Functional nanomechanical metamaterials driven by light, electromagnetic forces and sound

Nikolay I. Zheludev, Dimitrios Papas, Tongjun Liu, Jinxiang Li, Qiang Zhang, Dr. Jun-Yu Ou, Eric Plum, Kevin F. MacDonald

University of Southampton, UK & Nanyang Technological University, Singapore

Centre for Photonic Metamaterial, ORC
University of Southampton, UK
www.nanophotonics.org.uk

CLEO, San Jose CA, 11-15 May 2020
Symposium: Tunable and Nonlinear Optical Metasurfaces
May 11, 2020 11:00 AM US Pacific Time

Centre for Disruptive Photonic Technologies, TPI
NTU, Singapore
www.nanophotonics.sg

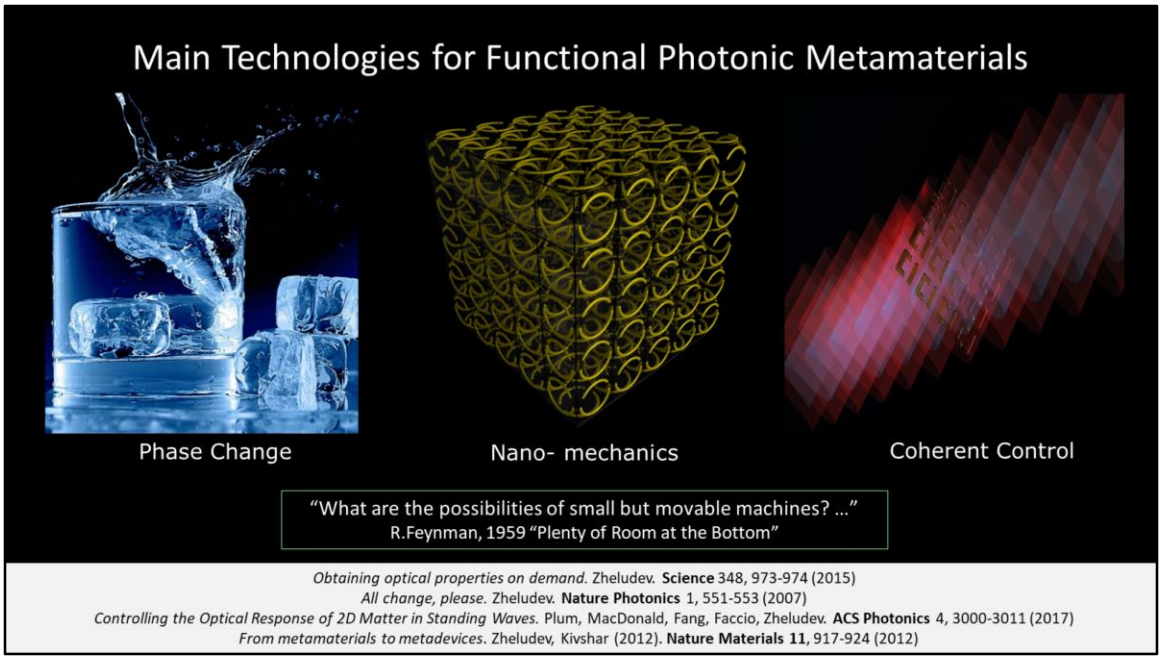

Zheludev, N. I. (2015). "Applied physics. Obtaining optical properties on demand." Science **348**(6238): 973-974.

Zheludev, N. (2007). "All change, please." Nature Photonics **1**(10): 551-553.

Plum, E., et al. (2017). "Controlling the Optical Response of 2D Matter in Standing Waves." Acs Photonics **4**(12): 3000-3011.
There is a major development unfolding in photonic technology that promises to impact optical data processing, spectroscopy, and nonlinear/quantum optics. This new direction relates to plasmonics, metamaterials and coherent optics. It exploits the difference in manifestations of optical properties of thin films in traveling waves and standing waves. In standing waves, "coherent control" of the energy exchange between incident and scattered waves leads to new technological opportunities including single photon gates, 100 THz all-optical modulators, sophisticated spectroscopy techniques that can for example distinguish different multipole contributions to absorption and quantum optical devices. We provide an overview of the rapidly growing body of work on the optics of films and metasurfaces in coherent light fields.

Zheludev, N. I. and Y. S. Kivshar (2012). "From metamaterials to metadevices." Nature Materials **11**(11): 917-924.
Metamaterials, artificial electromagnetic media that are structured on the subwavelength scale, were initially suggested for the negative-index 'superlens'. Later metamaterials became a paradigm for engineering electromagnetic space and controlling propagation of waves: the field of transformation optics was born. The research agenda is now shifting towards achieving tunable, switchable, nonlinear and sensing functionalities. It is therefore timely to discuss the emerging field of metadevices where we define the devices as having unique and useful functionalities that are realized by structuring of functional matter on the subwavelength scale. In this Review we summarize research on photonic, terahertz and microwave electromagnetic metamaterials and metadevices with functionalities attained through the exploitation of phase-change media, semiconductors, graphene, carbon nanotubes and liquid crystals. The Review also encompasses microelectromechanical metadevices, metadevices engaging the nonlinear and quantum response of superconductors, electrostatic and optomechanical forces and nonlinear metadevices incorporating lumped nonlinear components.

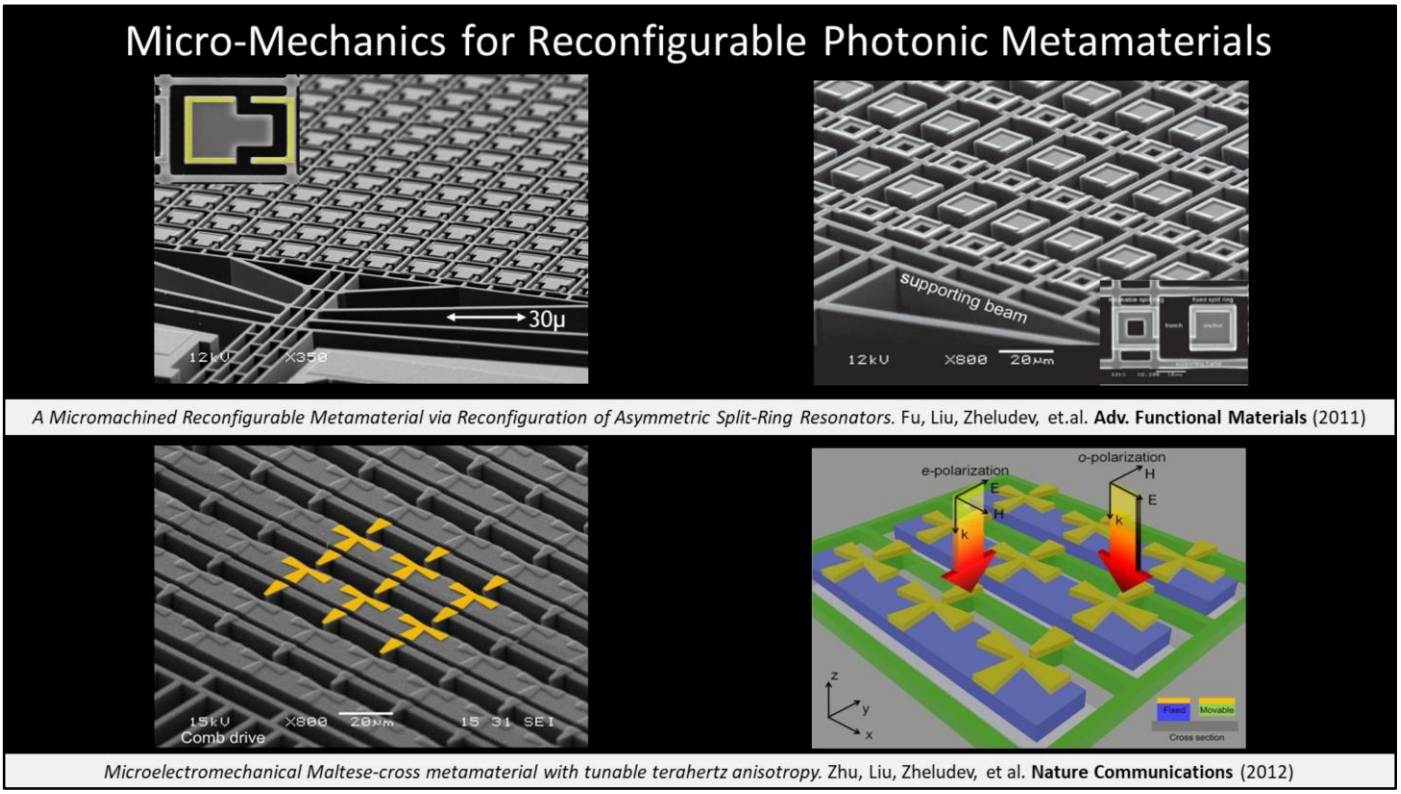

Zhu, W., et al. (2015). "A flat lens with tunable phase gradient by using random access reconfigurable metamaterial." Advanced Materials **27**(32): 4739-4743.

The first demonstration of an optofluidic metamaterial is reported where resonant properties of every individual metamolecule can be continuously tuned at will using a microfluidic system. This is called a random-access reconfigurable metamaterial, which is used to provide the first demonstration of a tunable flat lens with wavefront-reshaping capabilities.

Zhu, W. M., et al. (2012). "Microelectromechanical Maltese-cross metamaterial with tunable terahertz anisotropy." Nature Communications **3**: 1274.

Dichroic polarizers and waveplates exploiting anisotropic materials have vast applications in displays and numerous optical components, such as filters, beamsplitters and isolators. Artificial anisotropic media were recently suggested for the realization of negative refraction, cloaking, hyperlenses, and controlling luminescence. However, extending these applications into the terahertz domain is hampered by a lack of natural anisotropic media, while artificial metamaterials offer a strong engineered anisotropic response. Here we demonstrate a terahertz metamaterial with anisotropy tunable from positive to negative values. It is based on the Maltese-cross pattern, where anisotropy is induced by breaking the four-fold symmetry of the cross by displacing one of its beams. The symmetry breaking permits the excitation of a Fano mode active for one of the polarization eigenstates controlled by actuators using microelectromechanical systems. The metamaterial offers new opportunities for the development of terahertz variable waveplates, tunable filters and polarimetry.

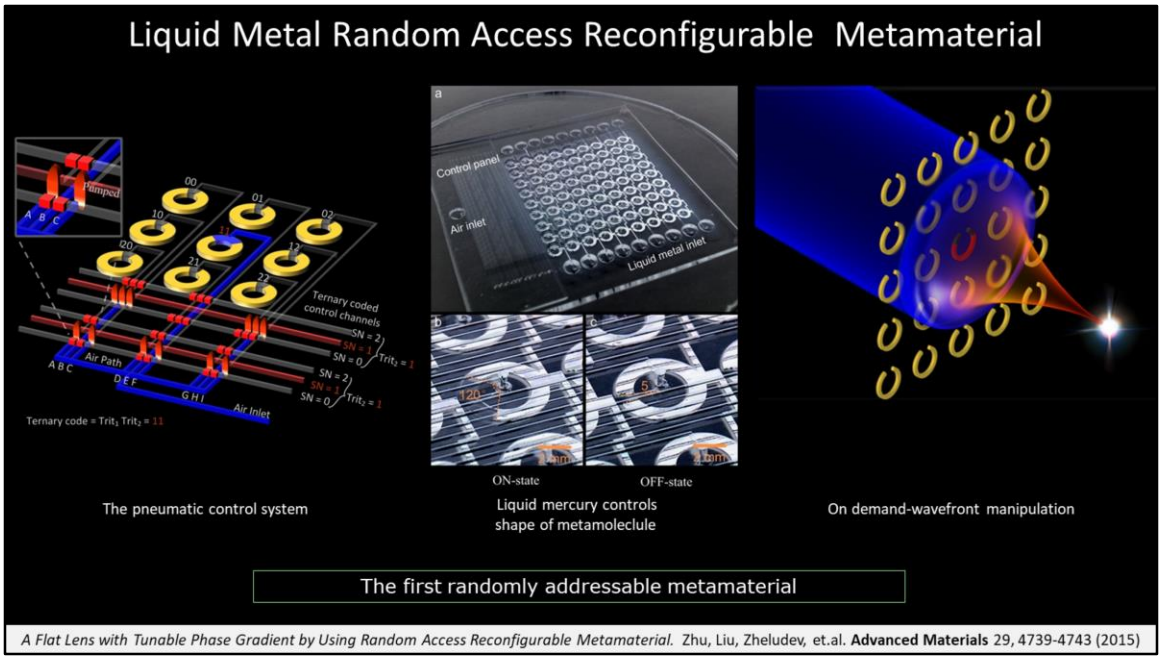

Zhu, W., et al. (2015). "A flat lens with tunable phase gradient by using random access reconfigurable metamaterial." Advanced Materials **27**(32): 4739-4743.

The first demonstration of an optofluidic metamaterial is reported where resonant properties of every individual metamolecule can be continuously tuned at will using a microfluidic system. This is called a random-access reconfigurable metamaterial, which is used to provide the first demonstration of a tunable flat lens with wavefront-reshaping capabilities.

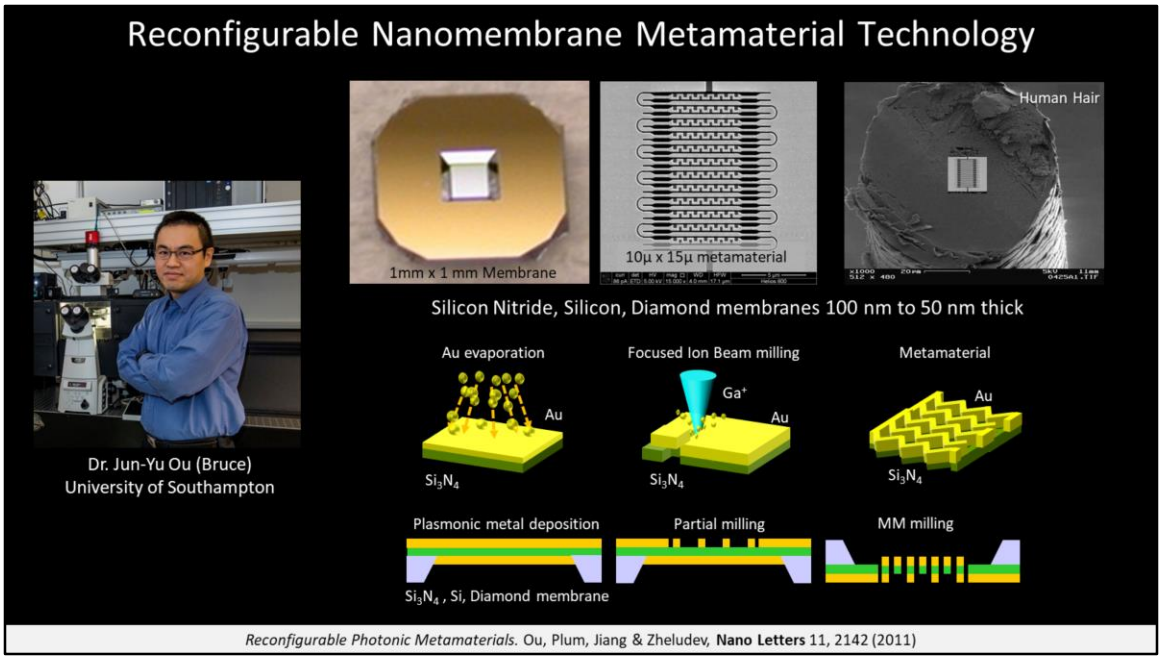

Ou, J. Y., et al. (2011). "Reconfigurable Photonic Metamaterials." Nano Letters **11**(5): 2142-2144

We introduce mechanically reconfigurable photonic metamaterials (RPMs) as a flexible platform for realizing metamaterial devices with reversible and large-range tunable characteristics in the optical part of the spectrum. Here we illustrate this concept for a temperature-driven RPM exhibiting reversible relative transmission changes of up to 50%.

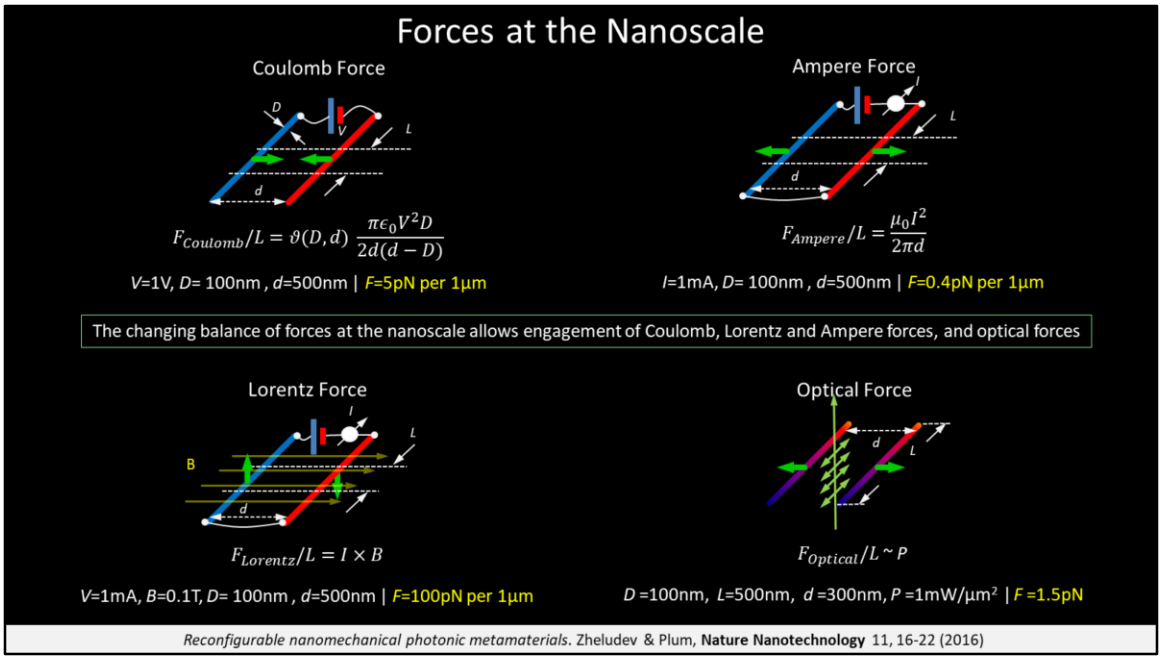

Zheludev, N. I. and E. Plum (2016). "Reconfigurable nanomechanical photonic metamaterials." Nat Nanotechnol **11**(1): 16-22.

The changing balance of forces at the nanoscale offers the opportunity to develop a new generation of spatially reconfigurable nanomembrane metamaterials in which electromagnetic Coulomb, Lorentz and Ampere forces, as well as thermal stimulation and optical signals, can be engaged to dynamically change their optical properties. Individual building blocks of such metamaterials, the metamolecules, and their arrays fabricated on elastic dielectric membranes can be reconfigured to achieve optical modulation at high frequencies, potentially reaching the gigahertz range. Mechanical and optical resonances enhance the magnitude of actuation and optical response within these nanostructures, which can be driven by electric signals of only a few volts or optical signals with power of only a few milliwatts. We envisage switchable, electro-optical, magneto-optical and nonlinear metamaterials that are compact and silicon-nanofabrication-technology compatible with functionalities surpassing those of natural media by orders of magnitude in some key design parameters.

The Coulomb force $F_{Coulomb}$ depends on the potential difference V between the nanowires, their diameter D and the distance d between them, where the dimensionless parameter $\vartheta(D,d)$ is of order unity for realistic geometries. For V=1V, D= 100nm and d=500nm the Coulomb force is about 5pN per 1μm of nanowire length L. This corresponds to an electric field acting between the nanowires that is close to the electric breakdown of air, which takes place at about 3MV/m [78]. With decreasing distance between the nanowires the Coulomb force increases rapidly.
The Ampere force F_{Ampere} depends on the current I in the nanowires and distance d between them. The achievable Ampere force tends to be smaller than the Coulomb force. For I =1mA and d=500nm the Ampere force is about 0.4pN per 1μm of nanowire length L. The Ampere force is limited by the current that a nanowire can sustain. A gold nanowire with diameter D =100nm cannot take more than 10mA continuous current due to the release heat that causes melting[79], but much higher current can be sustained in the pulsed regime.
The Lorentz force $F_{Lorentz}$ depends on the current I and magnetic field B and can be even stronger than the Coulomb force. The force is perpendicular to the current and magnetic field and moves wires apart. For I =1mA and B =100mT the Lorentz force is about 100pN per 1μm of nanowire length L. An external field B of about a Tesla can be easily achieved with permanent Neodymium and Samarium-Cobalt magnets.
Optical force. Nanowires can also be driven by illuminating them with light. A nanowire fragment that has a length of approximately half of the wavelength of incident radiation acts as a resonant antenna for light. Light-induced oscillating dipoles in the nanowires will repel with time-averaged optical force $F_{Optical}$ that is proportional to the incident light intensity P. When gold plasmonic nanowires of diameter D =100nm, length L=500nm and spacing d =300nm are illuminated by the wavelength of λ =925nm with intensity P =1mW/μm², the repelling optical force between them is about $F_{Optical}$ =1.5pN.

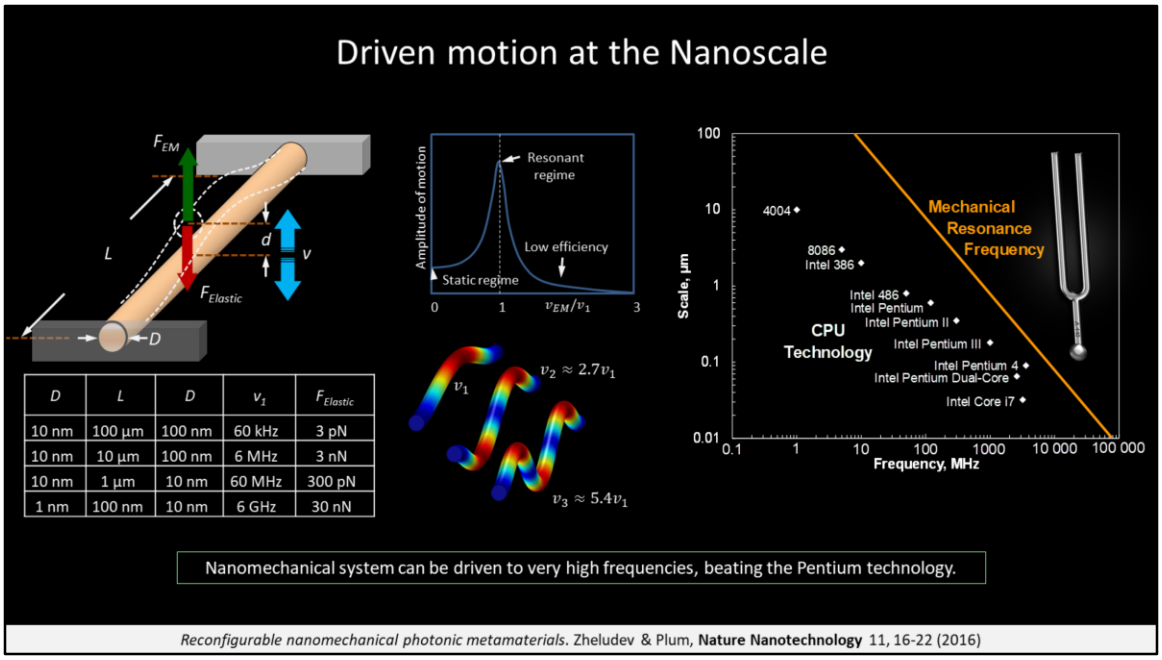

D	L	D	v_1	$F_{Elastic}$
10 nm	100 µm	100 nm	60 kHz	3 pN
10 nm	10 µm	100 nm	6 MHz	3 nN
10 nm	1 µm	10 nm	60 MHz	300 pN
1 nm	100 nm	10 nm	6 GHz	30 nN

Zheludev, N. I. and E. Plum (2016). "Reconfigurable nanomechanical photonic metamaterials." Nat Nanotechnol **11**(1): 16-22.

The changing balance of forces at the nanoscale offers the opportunity to develop a new generation of spatially reconfigurable nanomembrane metamaterials in which electromagnetic Coulomb, Lorentz and Ampere forces, as well as thermal stimulation and optical signals, can be engaged to dynamically change their optical properties. Individual building blocks of such metamaterials, the metamolecules, and their arrays fabricated on elastic dielectric membranes can be reconfigured to achieve optical modulation at high frequencies, potentially reaching the gigahertz range. Mechanical and optical resonances enhance the magnitude of actuation and optical response within these nanostructures, which can be driven by electric signals of only a few volts or optical signals with power of only a few milliwatts. We envisage switchable, electro-optical, magneto-optical and nonlinear metamaterials that are compact and silicon-nanofabrication-technology compatible with functionalities surpassing those of natural media by orders of magnitude in some key design parameters.

Motion at the nanoscale. (a) A nanowire mechanical oscillator of length *L*, diameter *D=L*/200, Young's modulus *E* and density *ρ* fabricated from a silicon nanomembrane will have natural frequency *v* that will rapidly increase with decreasing size of the oscillator. Using external electromagnetic force F_{EM} it will become possible to drive it to very high frequencies approaching the GHz range for sub-micron oscillators (see formula for the natural frequency of oscillation). Indeed, as can be seen from the generic resonance curve of a driven oscillator (b), driving at the mechanical resonance will lead to enhanced motion that is controlled by the quality factor of the mechanical oscillator, but driving at frequencies v_{EM} far above the resonance is inefficient. The force per unit length necessary to achieve static displacement *d* = *L*/100 of the nanowire's center to overcome the elastic force $F_{Elastic}$ decreases with size of the device (see formula for elastic force). However, the force per unit length required to achieve a fixed displacement of d=10nm does not depend on scaling of the device, but it is proportional to the nanowire's aspect ratio to the power of four $(D/L)^4$. (c) Often more complex movements are present and may be exploited for reconfiguration of nano-opto-mechanical metamaterials. For instance, depending on how the oscillator is driven, odd and even higher order modes can be excited, where in-plane and out-of-plane modes motions are allowed that appear at different natural frequencies for nanowires with elliptical or rectangular cross-sections.

Plurality of Optical Phenomena Without Change of Frequency

$D_i^{(1)}(\omega) = \varepsilon_{ij}(\omega, T) \times E_j(\omega)$	Absorption, refraction, linear birefringence and dichroism
$D_i^{(1*)}(\omega) = \mathrm{i}\, k_l \Gamma_{ijl}(\omega) \times E_j(\omega)$	Circular birefringence and dichroism (optical activity)
$D_i^{(2)}(\omega) = 2\chi_{ijl}^{(2)}(\omega, \omega, 0) \times E_j(\omega)\, E_l(0)$	Linear electro-optical effect (Pockels effect)
$D_i^{(2)}(\omega) = \xi_{ijlm}^{(3)}(\omega, \omega, 0, 0) \times E_j(\omega)\, E_l(0) H_m(0)$	Magneto-electric effect
$D_i^{(2*)}(\omega) = i\, k_n \Gamma_{ijln}^{(3)}(\omega, \omega, 0) \times E_j(\omega)\, E_l(0)$	Linear electrogiration
$D_i^{(3)}(\omega) = 6\chi_{ijlm}^{(3)}(\omega, \omega, \omega, -\omega) \times E_j(\omega)\, E_l(0) E_m^*(0)$	Quadratic electro-optical effect (Kerr effect)
$D_i^{(3)}(\omega) = 6\chi_{ijlm}^{(3)}(\omega, \omega, \omega, -\omega) \times E_j(\omega)\, E_l(\omega_p) E_m^*(\omega_p)$	Pump-probe interactions, nonlinear refraction & absorption
$D_i^{(3*)}(\omega) = i\, k_n \Gamma_{ijlmn}^{(3)}(\omega, \omega, 0, 0) \times E_j(\omega)\, E_l(0) E_m(0)$	Quadratic electrogyration
$D_i^{(3*)}(\omega) = i\, k_n \Gamma_{ijlmn}^{(3)}(\omega, \omega, \omega, -\omega) \times E_j(\omega)\, E_l(\omega) E_m(\omega)$	Nonlinear Optical Activity
$D_i^{(3)}(\omega) = 6N_{ijlm}^{(3)}(\omega, \omega, \omega, -\omega) \times E_j(\omega)\, E_l(\omega_p) E_m^*(\omega_p)$	Induced asymmetric transmission

Nano membrane reconfigurable metamaterials can deliver a wide range of photonic functionalities

Susceptibility Tensors for Nonlinear Optics. Svirko & Zheludev. IOP publishing (1995)

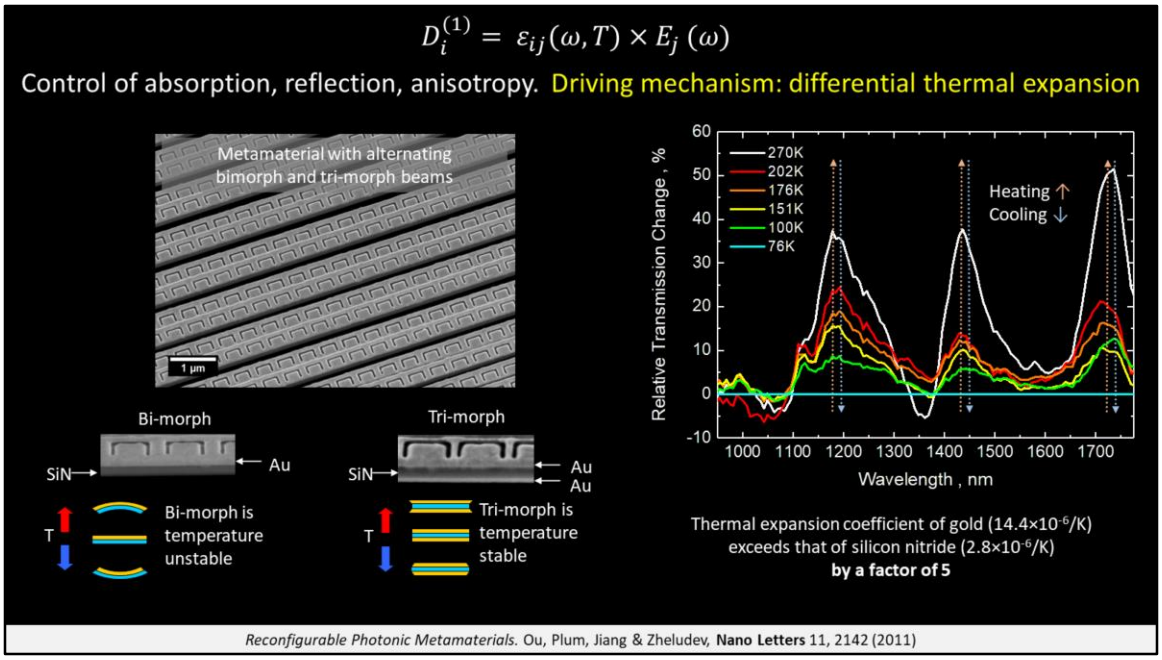

Ou, J. Y., et al. (2011). "Reconfigurable Photonic Metamaterials." Nano Letters **11**(5): 2142-2144

We introduce mechanically reconfigurable photonic metamaterials (RPMs) as a flexible platform for realizing metamaterial devices with reversible and large-range tunable characteristics in the optical part of the spectrum. Here we illustrate this concept for a temperature-driven RPM exhibiting reversible relative transmission changes of up to 50%.

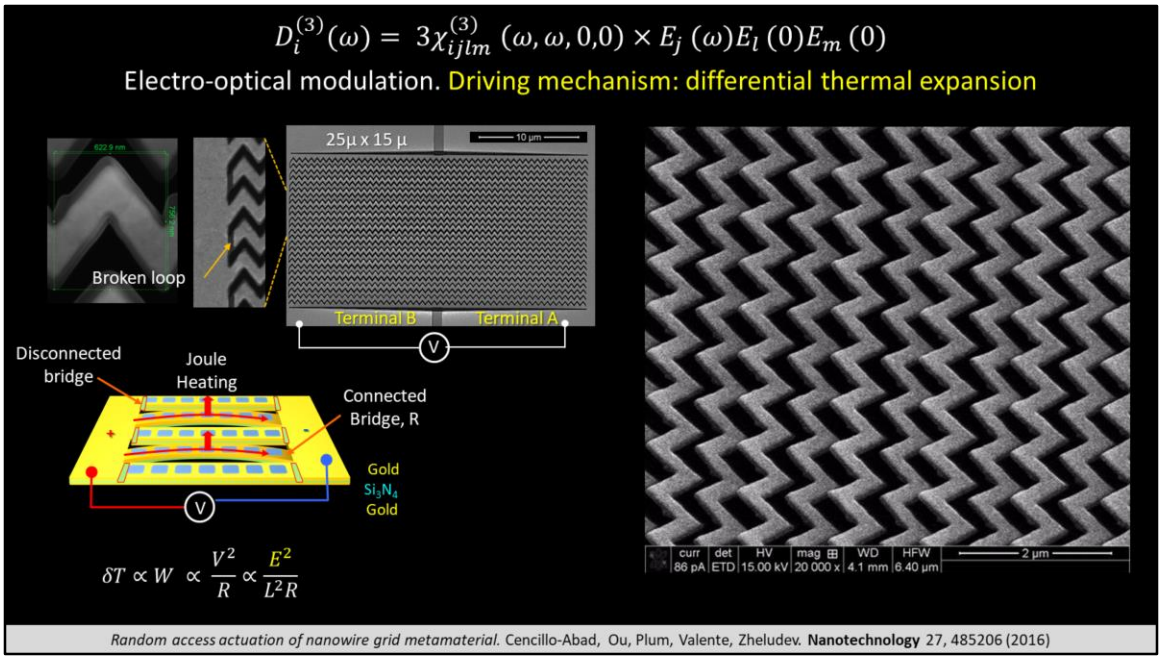

Cencillo-Abad, P., et al. (2016). "Random access actuation of nanowire grid metamaterial." Nanotechnology **27**(48).

While metamaterials offer engineered static optical properties, future artificial media with dynamic random-access control over shape and position of meta-molecules will provide arbitrary control of light propagation. The simplest example of such a reconfigurable metamaterial is a nanowire grid metasurface with subwavelength wire spacing. Recently we demonstrated computationally that such a metadevice with individually controlled wire positions could be used as dynamic diffraction grating, beam steering module and tunable focusing element. Here we report on the nanomembrane realization of such a nanowire grid metasurface constructed from individually addressable plasmonic chevron nanowires with a 230 nm x 100 nm cross-section, which consist of gold and silicon nitride. The active structure of the metadevice consists of 15 nanowires each 18 mu m long and is fabricated by a combination of electron beam lithography and ion beam milling. It is packaged as a microchip device where the nanowires can be individually actuated by control currents via differential thermal expansion.

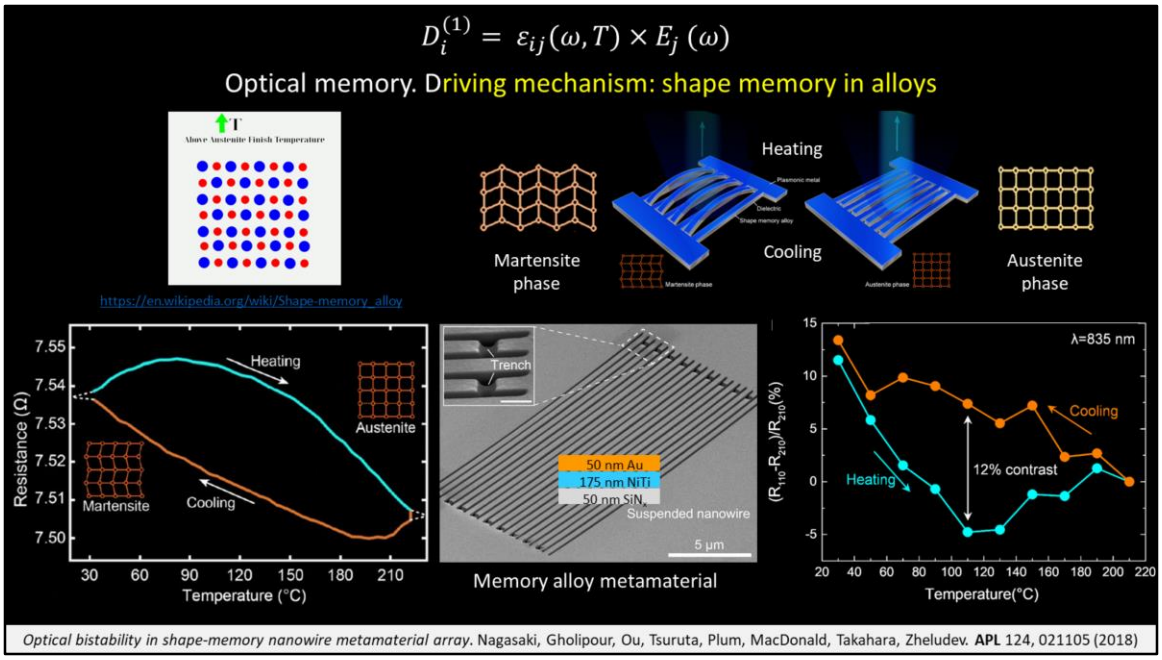

Nagasaki, Y., et al. (2018). "Optical bistability in shape-memory nanowire metamaterial array." Applied Physics Letters **113**(2).

Non-volatile temperature-induced structural phase transitions such as those found in chalcogenide glasses are known to lead to strong changes in optical properties and are widely used in rewritable optical disk technology. Herein, we demonstrate that thermally activated optical memory can be achieved via the nanostructural reconfiguration of a metallic nanowire metamaterial array made from a shape-memory alloy: A nickel-titanium film of nanoscale thickness structured on the subwavelength scale exhibits bistability of its optical properties upon temperature cycling between 30 degrees C and 210 degrees C. The structure, comprising an array of NiTi nanowires coated with a thin film of gold to enhance its plasmonic properties, can exist in two non-volatile states presenting an optical reflectivity differential of 12% via nanoscale mutual displacements of alternating nanowires in the structure. Such all-metal shape-memory photonic gratings and metamaterials may find applications in bistable optical devices. Published by AIP Publishing.

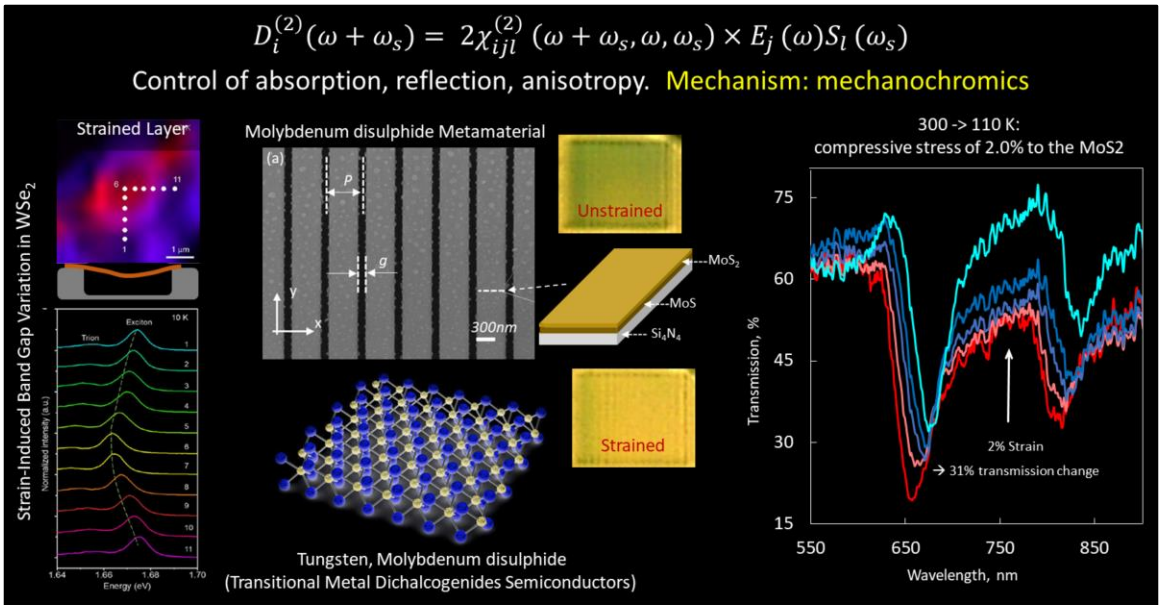

Mechanochromic Reconfigurable Metasurfaces. Karvounis, Aspiotis, Zeimpekis, Ou, Huang, Hewak, Zheludev. **Advanced Science** 6, 1900974 (2019)
Cathodoluminescence of Monolayer Transitional Metal Dichalcogenides Semiconductors. Zheng, So, Liu, Liu, Zheludev, Fan. **Nano Letters** 17, 6475−6480 (2017)

Karvounis, A., et al. (2019). "Mechanochromic Reconfigurable Metasurfaces." Advanced Science **6**(21): 1900974.
The change of optical properties that some usually natural compounds or polymeric materials show upon the application of external stress is named mechanochromism. Herein, an artificial nanomechanical metasurface formed by a subwavelength nanowire array made of molybdenum disulfide, molybdenum oxide, and silicon nitride changes color upon mechanical deformation. The aforementioned deformation induces reversible changes in the optical transmission (relative transmission change of 197% at 654 nm), thus demonstrating a giant mechanochromic effect. Moreover, these types of metasurfaces can exist in two nonvolatile states presenting a difference in optical transmission of 45% at 678 nm, when they are forced to bend rapidly. The wide optical tunability that photonic nanomechanical metasurfaces, such as the one presented here, possess by design, can provide a valuable platform for mechanochromic and bistable responses across the visible and near infrared regime and form a new family of smart materials with applications in reconfigurable, multifunctional photonic filters, switches, and stress sensors.

Giant Enhancement of Cathodoluminescence of Monolayer Transitional Metal Dichalcogenides Semiconductors, Zheng, So, Liu, Liu, Zheludev, Fan. Nano Lett. 17, 6475−6480 (2017)
Monolayer two-dimensional transitional metal dichalcogenides, such as MoS2, WS2, and WSe2, are direct band gap semiconductors with large exciton binding energy. They attract growing attentions for optoelectronic applications including solar cells, photodetectors, light-emitting diodes and phototransistors, capacitive energy storage, photodynamic cancer therapy, and sensing on flexible platforms. While light-induced luminescence has been widely studied, luminescence induced by injection of free electrons could promise another important applications of these new materials. However, cathodoluminescence is inefficient due to the low cross-section of the electron-hole creating process in the monolayers. Here for the first time we show that cathodoluminescence of monolayer chalcogenide semiconductors can be evidently observed in a van der Waals heterostructure when the monolayer semiconductor is sandwiched between layers of hexagonal boron nitride (hBN) with higher energy gap. The emission intensity shows a strong dependence on the thicknesses of surrounding layers and the enhancement factor is more than 500-fold. Strain-induced exciton peak shift in the suspended heterostructure is also investigated by the cathodoluminescence spectroscopy. Our results demonstrate that MoS2, WS2, and WSe2 could be promising cathodoluminescent materials for applications in single-photon emitters, high-energy particle detectors, transmission electron microscope displays, surface-conduction electron-emitter, and field emission display technologies.

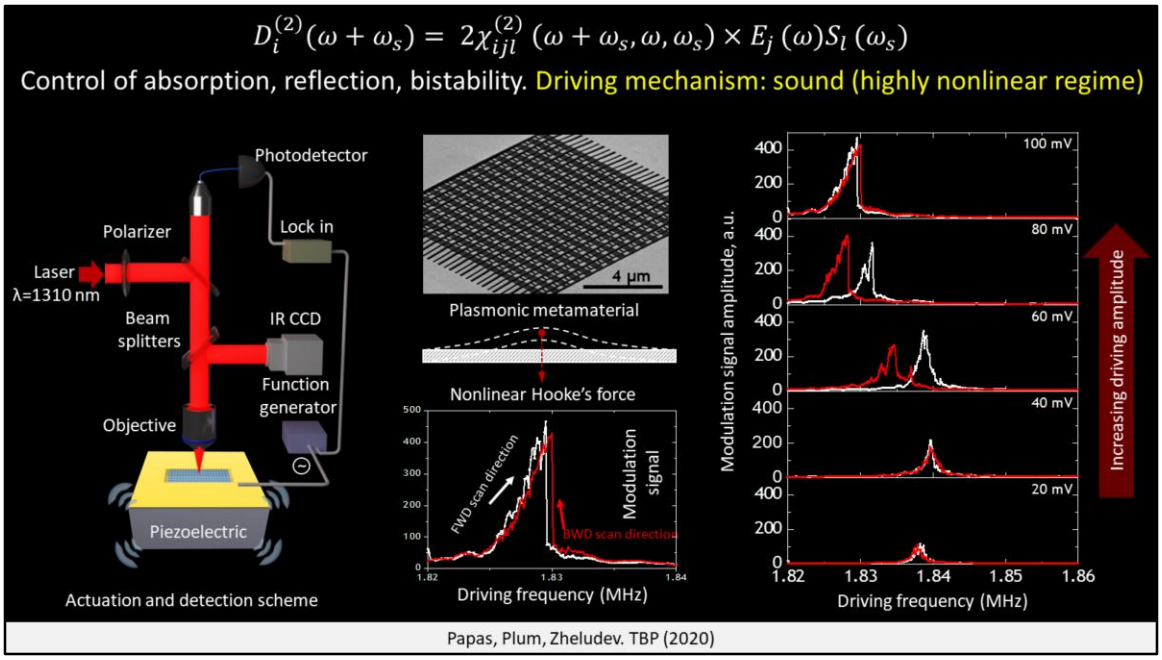

Optical metamaterial reconfigured with sound
D. Papas, J. Y. Ou, E. Plum, and N. I. Zheludev
Metamaterials'2019, Rome, Italy, 16 - 21 Sep 2019

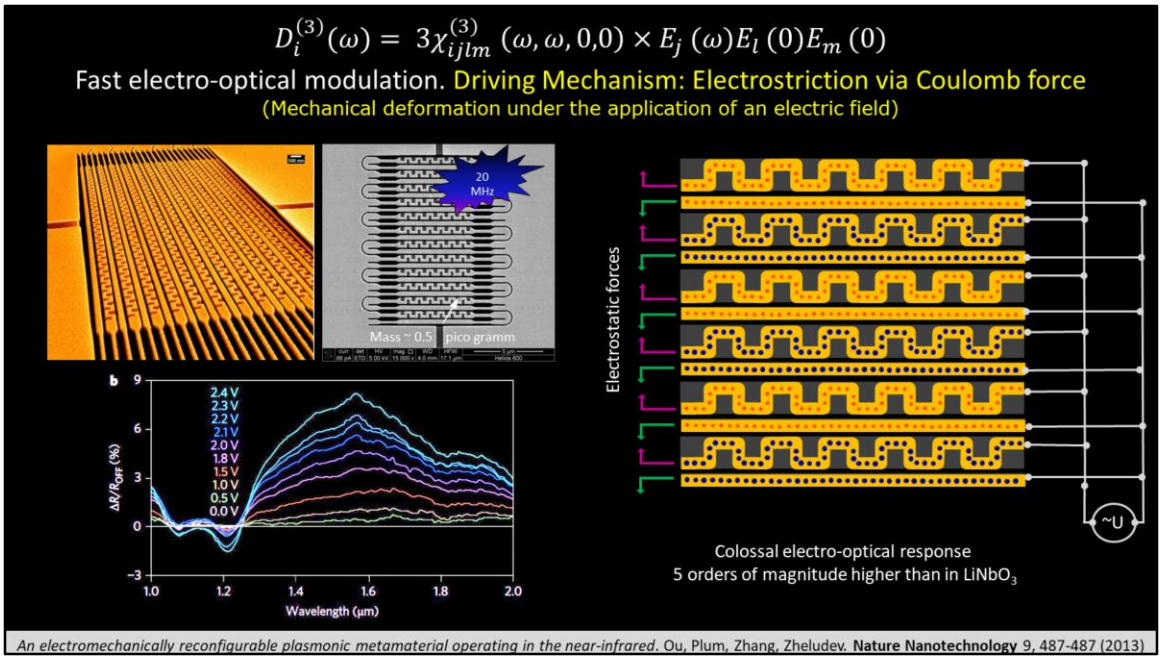

Ou, J. Y., et al. (2013). "An electromechanically reconfigurable plasmonic metamaterial operating in the near-infrared." Nature Nanotechnology **8**(4): 252-255.

Current efforts in metamaterials research focus on attaining dynamic functionalities such as tunability, switching and modulation of electromagnetic waves. To this end, various approaches have emerged, including embedded varactors, phase-change media, the use of liquid crystals, electrical modulation with graphene and superconductors, and carrier injection or depletion in semiconductor substrates. However, tuning, switching and modulating metamaterial properties in the visible and near-infrared range remain major technological challenges: indeed, the existing microelectromechanical solutions used for the sub-terahertz and terahertz regimes cannot be shrunk by two to three orders of magnitude to enter the optical spectral range. Here, we develop a new type of metamaterial operating in the optical part of the spectrum that is three orders of magnitude faster than previously reported electrically reconfigurable metamaterials. The metamaterial is actuated by electrostatic forces arising from the application of only a few volts to its nanoscale building blocks-the plasmonic metamolecules-that are supported by pairs of parallel strings cut from a flexible silicon nitride membrane of nanoscale thickness. These strings, of picogram mass, can be driven synchronously to megahertz frequencies to electromechanically reconfigure the metamolecules and dramatically change the transmission and reflection spectra of the metamaterial. The metamaterial's colossal electro-optical response (on the order of 10(-5)-10(-6) m V(-1)) allows for either fast continuous tuning of its optical properties (up to 8% optical signal modulation at up to megahertz rates) or high-contrast irreversible switching in a device only 100 nm thick, without the need for external polarizers and analysers.

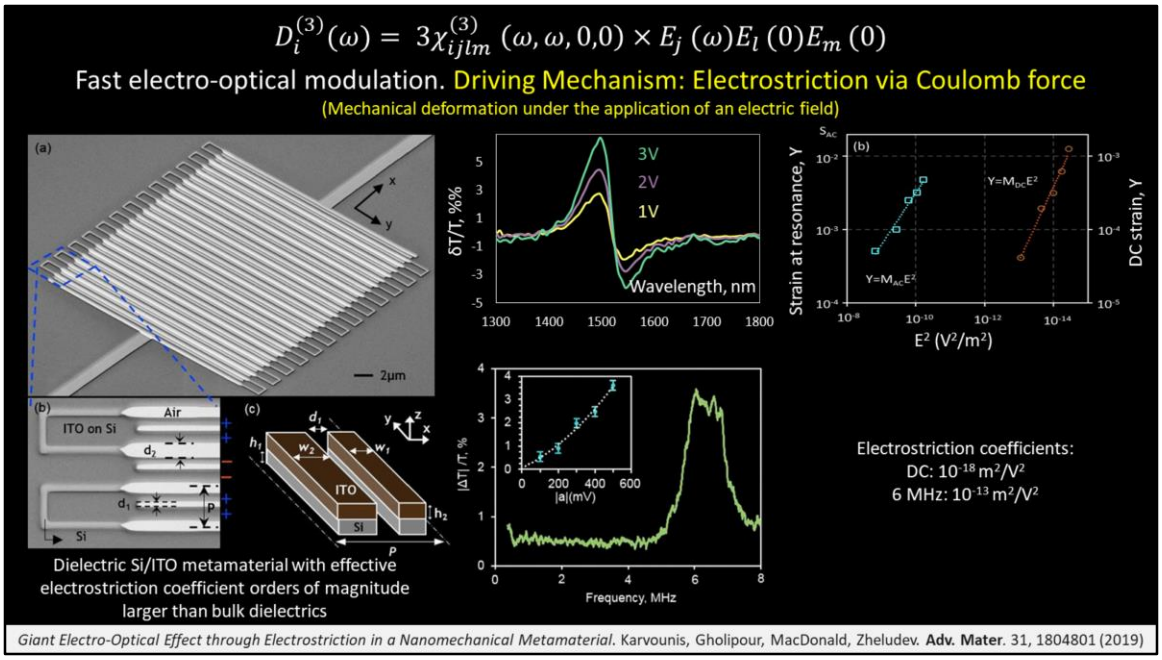

Karvounis, A., et al. (2019). "Giant Electro-Optical Effect through Electrostriction in a Nanomechanical Metamaterial." Advanced Materials **31**(1): e1804801.

Electrostriction is a property of all naturally occurring dielectrics whereby they are mechanically deformed under the application of an electric field. It is demonstrated here that an artificial metamaterial nanostructure comprising arrays of dielectric nanowires, made of silicon and indium tin oxide, is reversibly structurally deformed under the application of an electric field, and that this reconfiguration is accompanied by substantial changes in optical transmission and reflection, thus providing a strong electro-optic effect. Such metamaterials can be used as the functional elements of electro-optic modulators in the visible to near-infrared part of the spectrum. A modulator operating at 1550 nm with effective electrostriction and electro-optic coefficients of order 10(-13) m(2) V(-2) and 10(-6) m V(-1) , respectively, is demonstrated. Transmission changes of up to 3.5% are obtained with a 500 mV control signal at a modulation frequency of approximately 6.5 MHz. With a resonant optical response that can be spectrally tuned by design, modulators based on the artificial electrostrictive effect may be used for laser Q-switching and mode-locking among other applications that require modulation at megahertz frequencies.

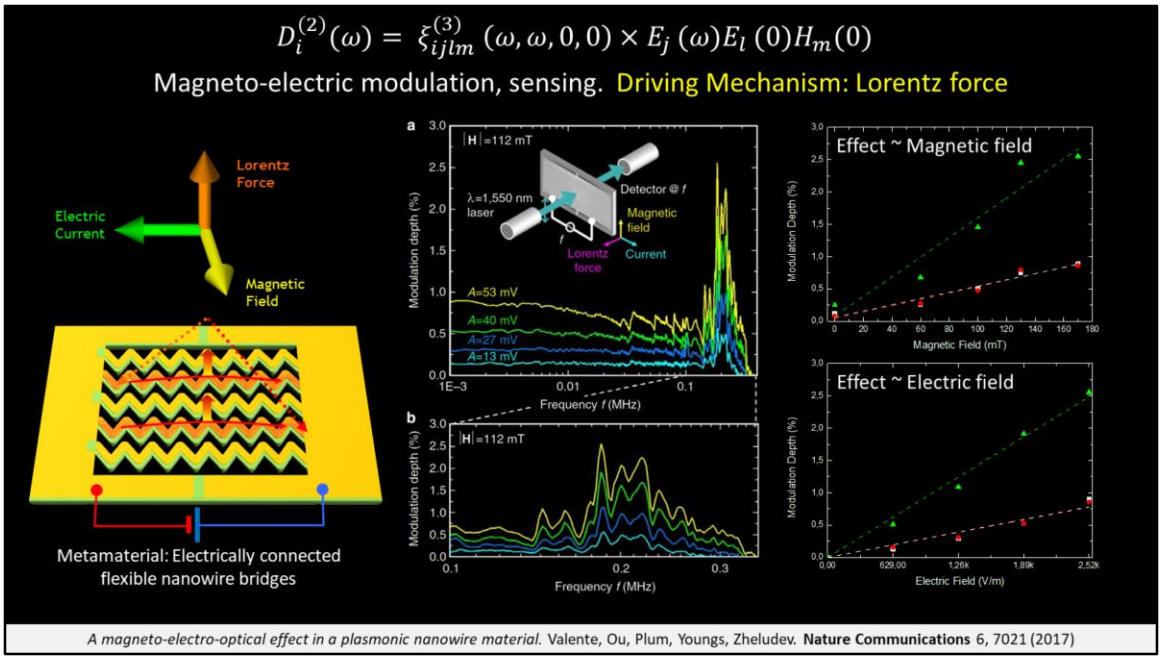

A magneto-electro-optical effect in a plasmonic nanowire material. Valente, Ou, Plum, Youngs, Zheludev. **Nature Communications** 6, 7021 (2017)

Valente, J., et al. (2015). "A magneto-electro-optical effect in a plasmonic nanowire material." Nature Communications **6**.

Electro- and magneto-optical phenomena play key roles in photonic technology enabling light modulators, optical data storage, sensors and numerous spectroscopic techniques. Optical effects, linear and quadratic in external electric and magnetic field are widely known and comprehensively studied. However, optical phenomena that depend on the simultaneous application of external electric and magnetic fields in conventional media are barely detectable and technologically insignificant. Here we report that a large reciprocal magneto-electro-optical effect can be observed in metamaterials. In an artificial chevron nanowire structure fabricated on an elastic nano-membrane, the Lorentz force drives reversible transmission changes on application of a fraction of a volt when the structure is placed in a fraction-of-tesla magnetic field. We show that magneto-electro-optical modulation can be driven to hundreds of thousands of cycles per second promising applications in magneto-electro-optical modulators and field sensors at nano-tesla levels.

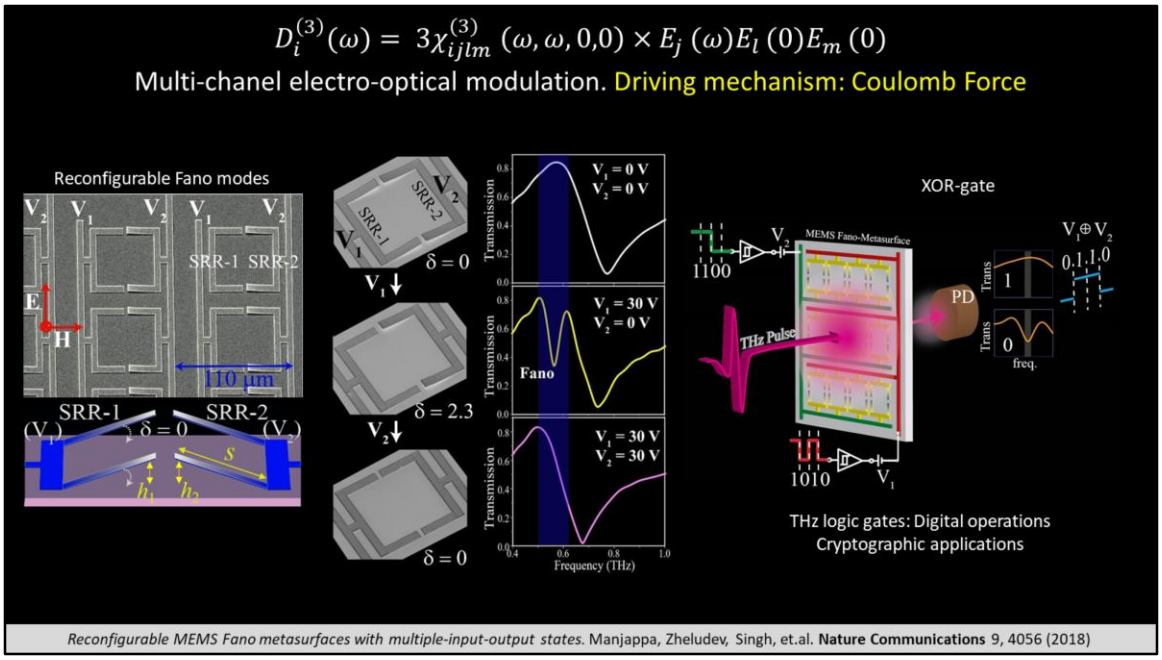

Reconfigurable MEMS Fano metasurfaces with multiple-input-output states. Manjappa, Zheludev, Singh, et.al. **Nature Communications** 9, 4056 (2018)

Manjappa, M., et al. (2018). "Reconfigurable MEMS Fano metasurfaces with multiple-input-output states for logic operations at terahertz frequencies." Nature Communications **9**(1): 4056.

A broad range of dynamic metasurfaces has been developed for manipulating the intensity, phase and wavefront of electromagnetic radiation from microwaves to optical frequencies. However, most of these metasurfaces operate in single-input-output state. Here, we experimentally demonstrate a reconfigurable MEMS Fano resonant metasurface possessing multiple-input-output (MIO) states that performs logic operations with two independently controlled electrical inputs and an optical readout at terahertz frequencies. The far-field behaviour of Fano resonance exhibits XOR and XNOR operations, while the near-field resonant confinement enables the NAND operation. The MIO configuration resembling hysteresis-type closed-loop behaviour is realized through inducing electromechanically tuneable out-of-plane anisotropy in the near-field coupling of constituent resonator structures. The XOR metamaterial gate possesses potential applications in cryptographically secured terahertz wireless communication networks. Furthermore, the MIO features could lay the foundation for the realization of programmable and randomly accessible metamaterials with enhanced electro-optical performance across terahertz, infrared and optical frequencies.

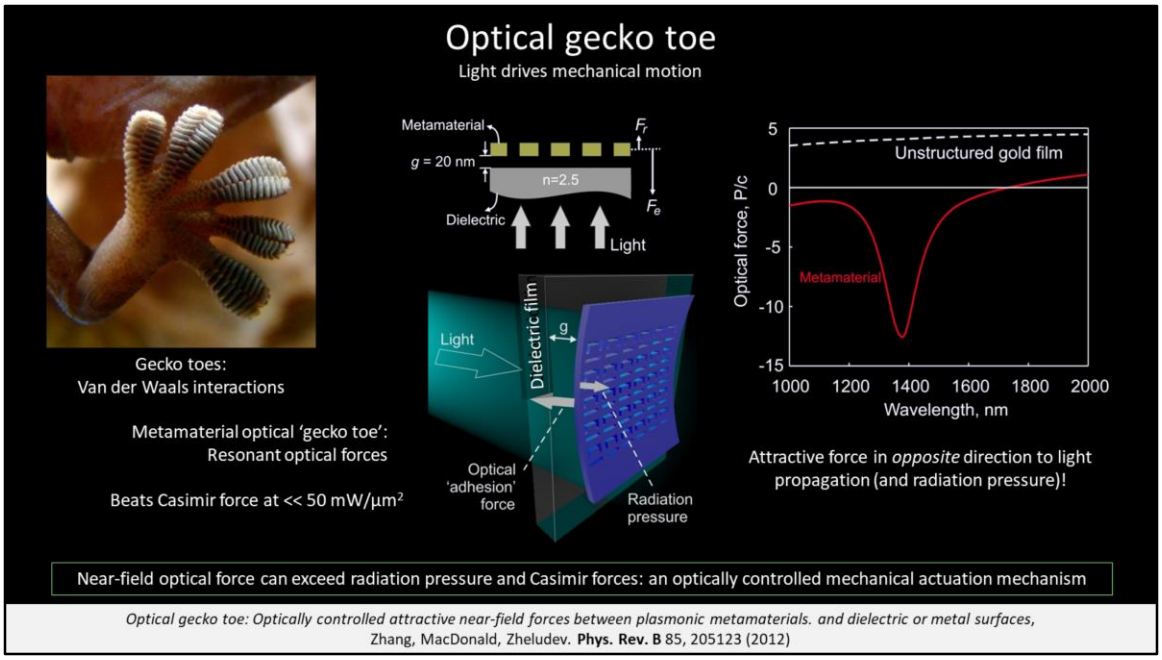

Zhang, J., et al. (2012). "Optical gecko toe: Optically controlled attractive near-field forces between plasmonic metamaterials and dielectric or metal surfaces." Physical Review B **85**(20).

On the mesoscopic scale, electromagnetic forces are of fundamental importance to an enormously diverse range of systems, from optical tweezers to the adhesion of gecko toes. Here we show that a strong light-driven force may be generated when a plasmonic metamaterial is illuminated in close proximity to a dielectric or metal surface. This near-field force can exceed radiation pressure and Casimir forces to provide an optically controlled adhesion mechanism mimicking the gecko toe: At illumination intensities of just a few tens of nW/mu m(2) it is sufficient to overcome the Earth's gravitational pull.

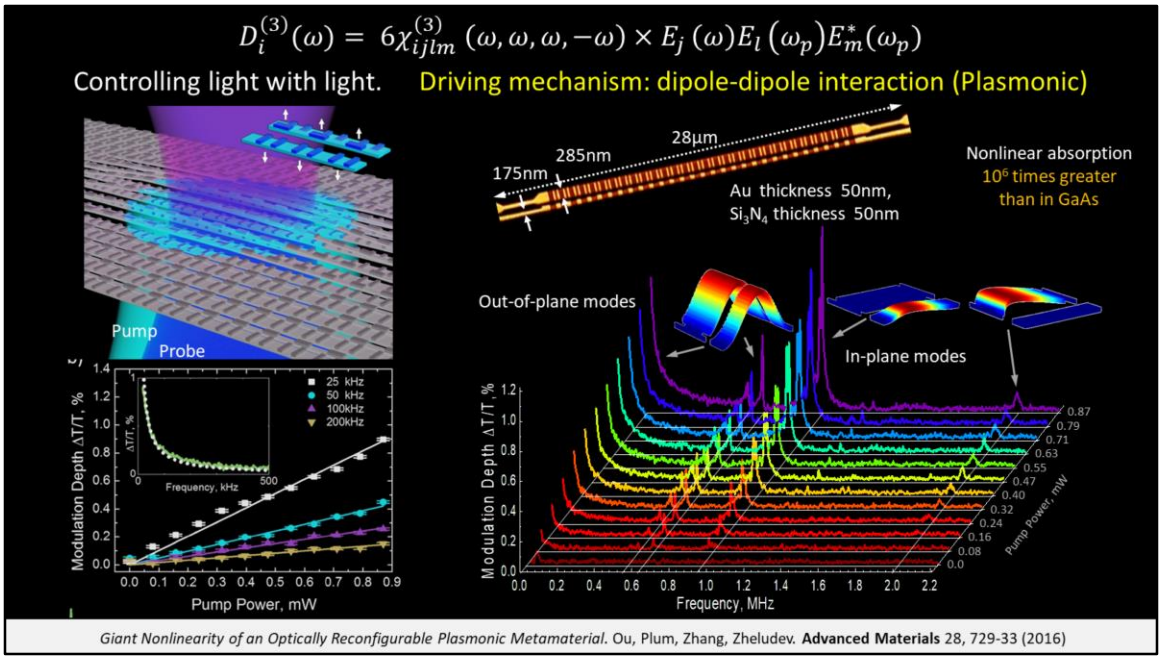

Ou, J. Y., et al. (2016). "Giant Nonlinearity of an Optically Reconfigurable Plasmonic Metamaterial." Advanced Materials **28**(4): 729-733.

Metamaterial nanostructures actuated by light give rise to a large optical nonlinearity. Plasmonic metamolecules on a flexible support structure cut from a dielectric membrane of nanoscale thickness are rearranged by optical illumination. This changes the optical properties of the strongly coupled plasmonic structure and therefore results in modulation of light with light.

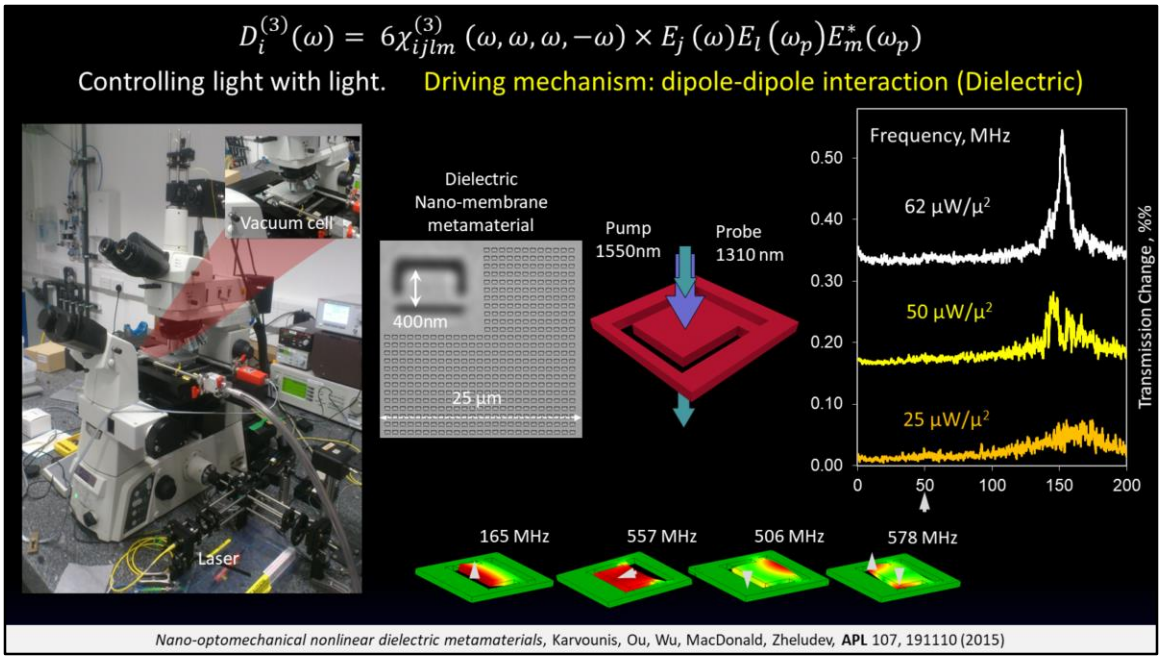

Karvounis, A., et al. (2015). "Nano-optomechanical nonlinear dielectric metamaterials." Applied Physics Letters **107**(19).

By harnessing the resonant nature of localized electromagnetic modes in a nanostructured silicon membrane, an all-dielectric metamaterial can act as nonlinear medium at optical telecommunications wavelengths. We show that such metamaterials provide extremely large optomechanical nonlinearities, operating at intensities of only a few mu W per unit cell and modulation frequencies as high as 152 MHz, thereby offering a path to fast, compact, and energy efficient all-optical metadevices. (C) 2015 AIP Publishing LLC.

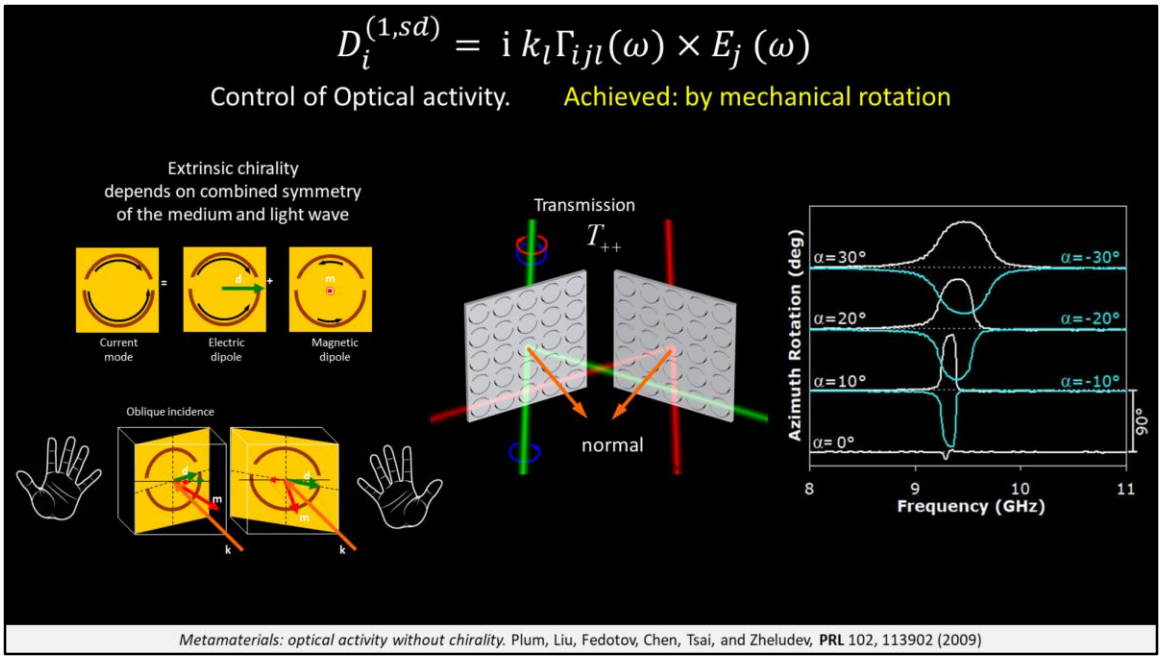

Plum, E., et al. (2009). "Metamaterials: Optical Activity without Chirality." Physical Review Letters **102**(11).

We report that the classical phenomenon of optical activity, which is traditionally associated with chirality (helicity) of organic molecules, proteins, and inorganic structures, can be observed in artificial planar media which exhibit neither 3D nor 2D chirality. We observe the effect in the microwave and optical parts of the spectrum at oblique incidence to regular arrays of nonchiral subwavelength metamolecules in the form of strong circular dichroism and birefringence indistinguishable from those of chiral three-dimensional media.

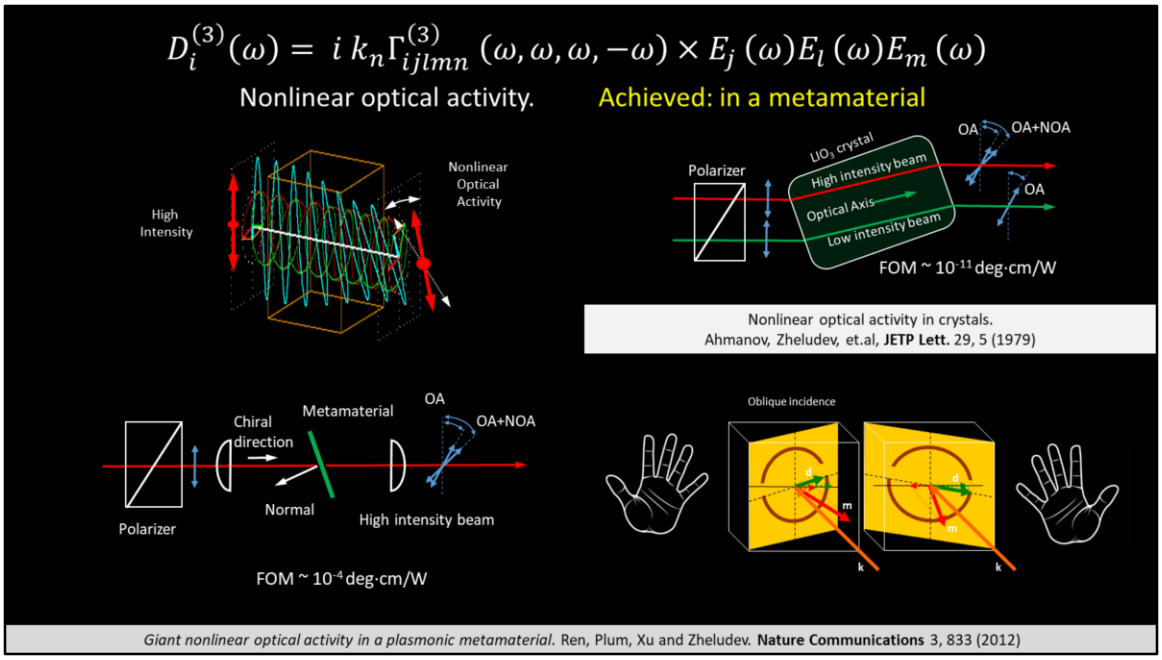

Ren, M., et al. (2012). "Giant nonlinear optical activity in a plasmonic metamaterial." Nature Communications **3**: 833.

In 1950, a quarter of a century after his first-ever nonlinear optical experiment when intensity-dependent absorption was observed in uranium-doped glass, Sergey Vavilov predicted that birefringence, dichroism and polarization rotatory power should be dependent on light intensity. It required the invention of the laser to observe the barely detectable effect of light intensity on the polarization rotatory power of the optically active lithium iodate crystal, the phenomenon now known as the nonlinear optical activity, a high-intensity counterpart of the fundamental optical effect of polarization rotation in chiral media. Here we report that a plasmonic metamaterial exhibits nonlinear optical activity 30 million times stronger than lithium iodate crystals, thus transforming this fundamental phenomenon of polarization nonlinear optics from an esoteric phenomenon into a major effect of nonlinear plasmonics with potential for practical applications.

Akhamanov, S. A., et al. (1979). "Non-Linear Optical-Activity in Crystals." Jetp Letters **29**(5): 264-268.

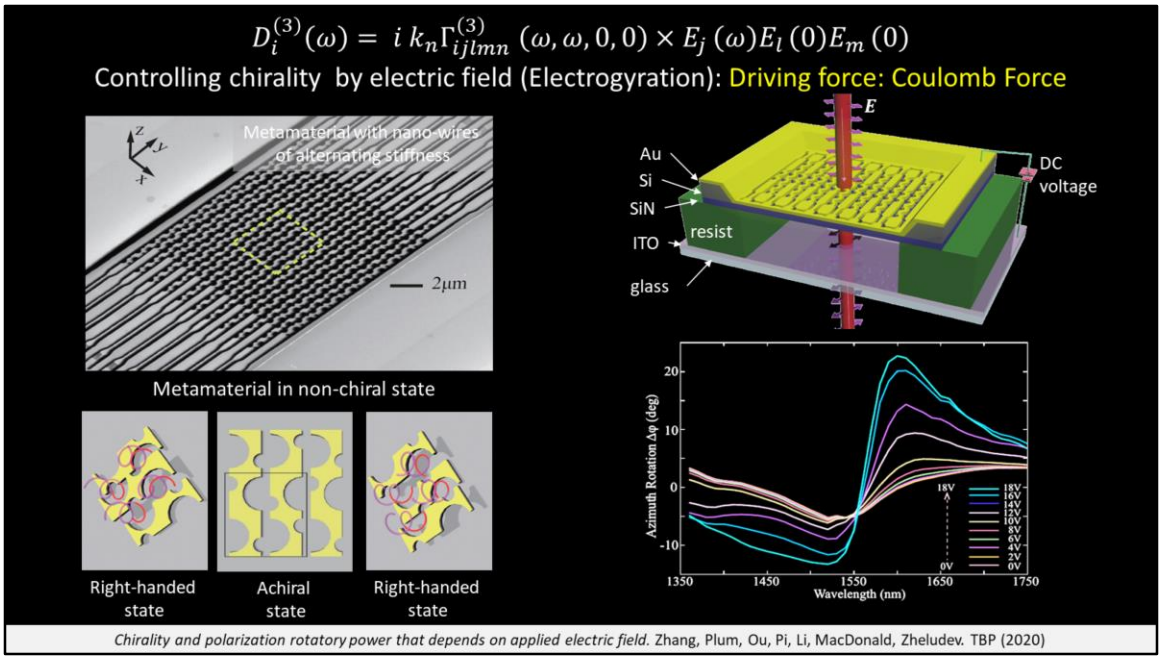

One of the most fascinating properties of chiral molecules is their ability to rotate the polarization state of light and since Faraday's experiments in 1845 it has been known that polarization rotation can be induced or changed by a magnetic field. But can molecular chirality and the associated polarization rotation be influenced by an electric field applied to a medium? In the 1960s K. Aizu and I. S. Zheludev described the phenomenon of electrogyration. In contrast to conventional linear (Pockels) and quadratic (Kerr) electro-optic effects, which lead to induced linear birefringence and dichroism, electrogyration induces circular birefringence and dichroism. Electrogyration has been observed in a variety of dielectrics, semiconductors and ferroelectrics, but the effect in naturally occurring materials is small. Here we demonstrate a nanostructured photonic metamaterial that exhibits quadratic electrogyration – proportional to the square of the applied electric field – 6 orders of magnitude stronger than has been observed in any natural medium. Giant quadratic electrogyration emerges as electrostatic forces acting against those of elasticity change the nanoscale chiral configuration of the metamaterial's building blocks and consequently its polarization rotatory power. The metamaterial does not manifest linear electrogyration. The discovered nano-mechanical mechanism of quadratic electrogyration transforms a fundamental but esoteric phenomenon of polarization optics into a substantive effect with practical applications potential.

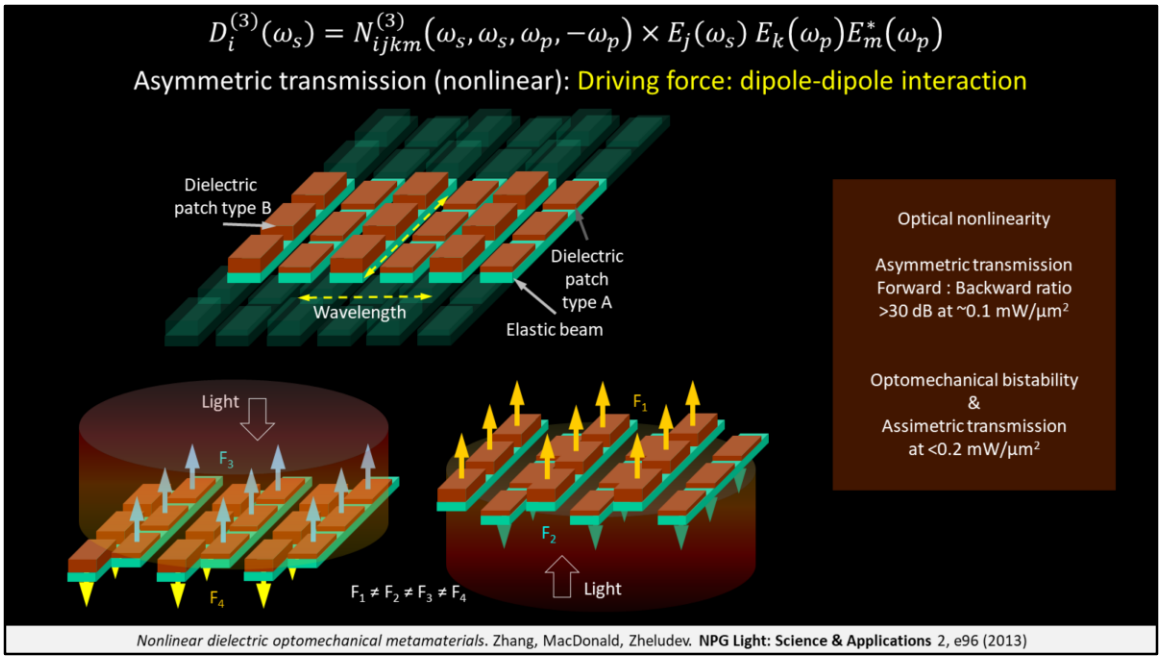

Zhang, J. F., et al. (2013). "Nonlinear dielectric optomechanical metamaterials." Light-Science & Applications **2**.

We introduce a dielectric photonic metamaterial presenting a giant nonlinear optical response driven by resonant optomechanical forces. Being inherently free of Joule losses, it exhibits optical bistability at intensity levels of less than 0.2 mW mu m(-2) and, furthermore, manifests nonlinear asymmetric transmission with a forward : backward optical extinction ratio of more than 30 dB.

$$D_i^{(3)}(\omega_s) = N_{ijkm}^{(3)}(\omega_s, \omega_s, \omega_p, -\omega_p) \times E_j(\omega_s)\, E_k(\omega_p) E_m^*(\omega_p)$$

Asymmetric transmission (nonlinear): Driving force: dipole-dipole interaction

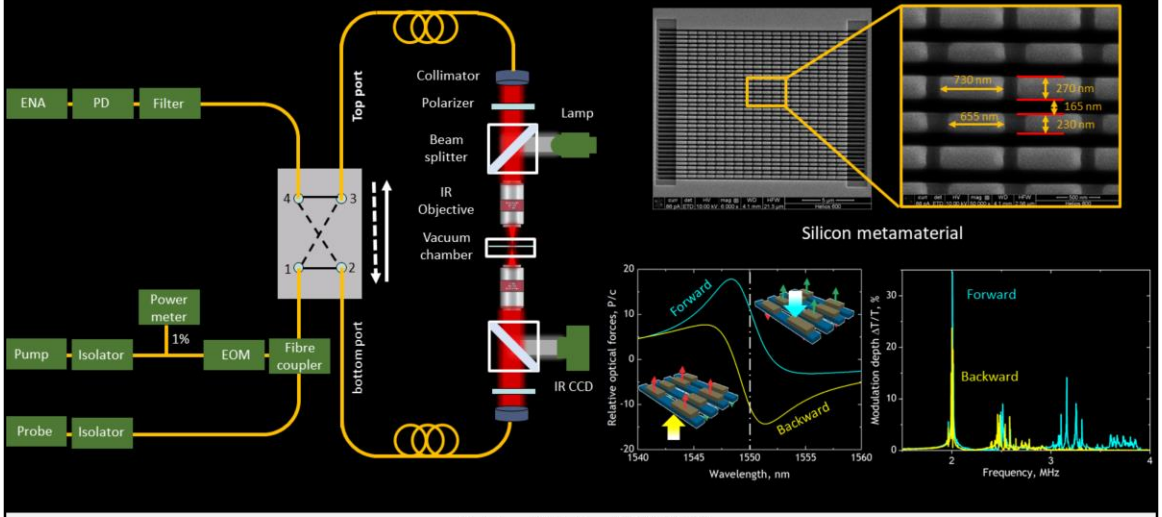

Zheludev, Li, MacDonald. TBP (2020)

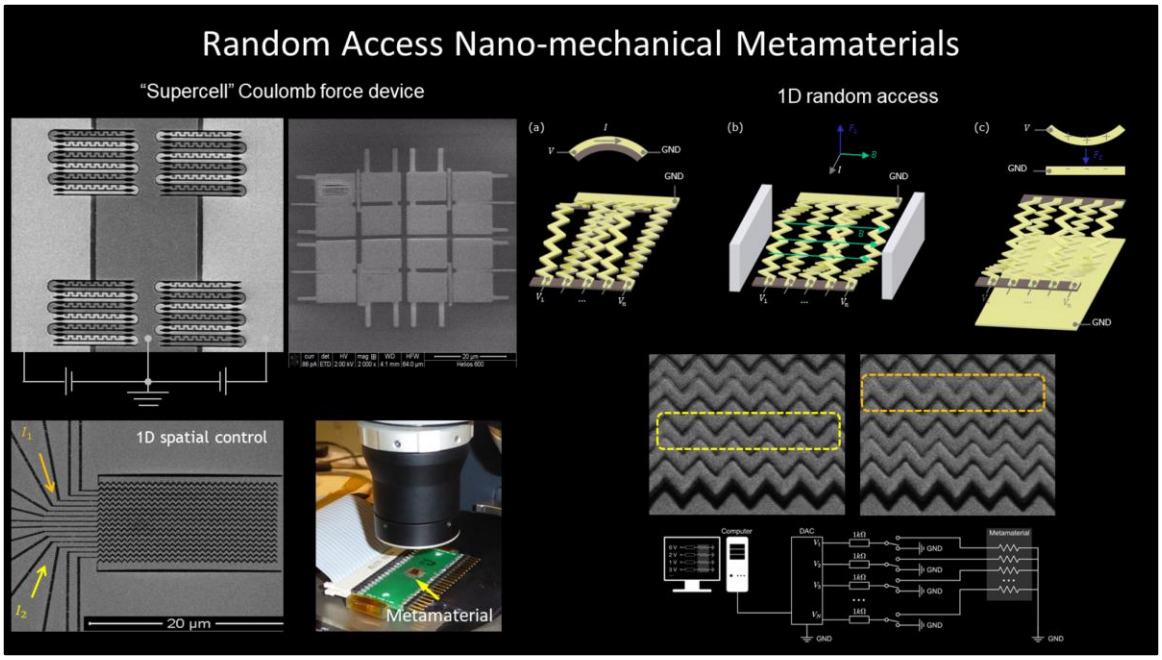
Random Access Nano-mechanical Metamaterials
"Supercell" Coulomb force device
1D random access
1D spatial control
20 μm
Metamaterial
GND
Computer
DAC
Metamaterial

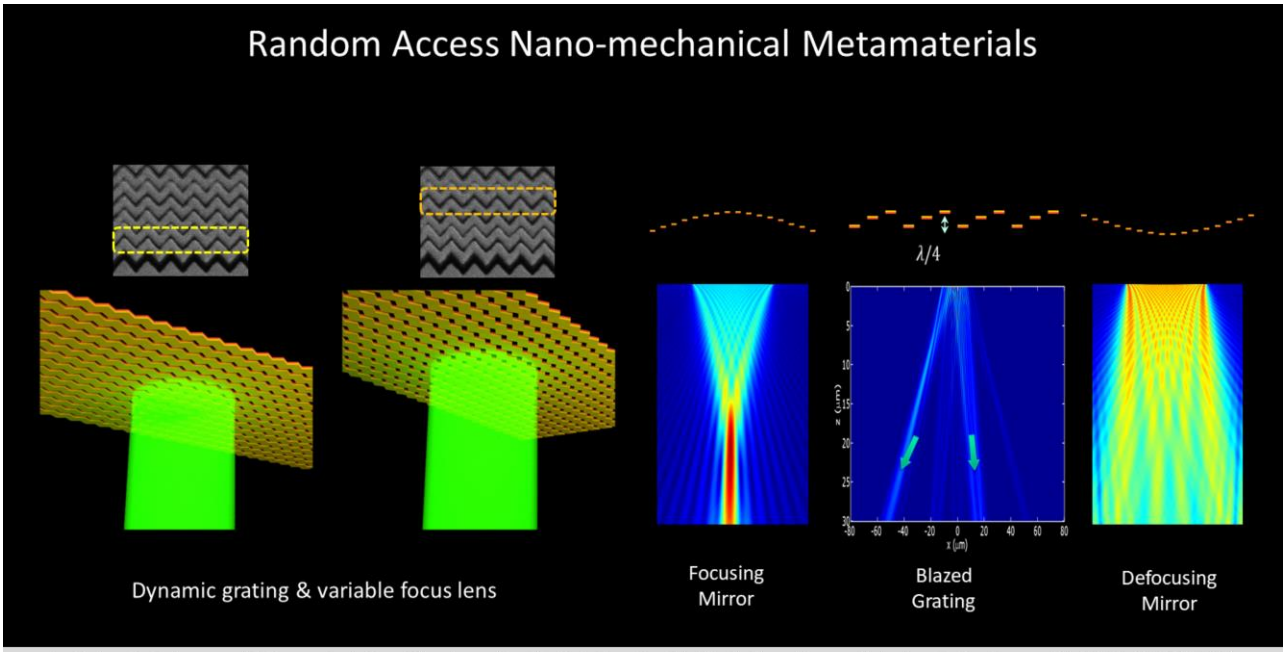

Spatial optical phase-modulating metadevice with subwavelength pixelation. Cencillo-Abad, Plum, Rogers, Zheludev. **Optics Express** 24, 18790-18798 (2016).
Random access actuation of nanowire grid metamaterial. Cencillo-Abad, Ou, Plum, Valente, Zheludev. **Nanotechnology** 27, 485206 (2016)
Metadevice for intensity modulation with sub-wavelength spatial resolution. Cencillo-Abad, Zheludev, Plum. **NPG Scientific Reports 6**, 37109 (2016)

Cencillo-Abad, P., et al. (2016). "Metadevice for intensity modulation with sub-wavelength spatial resolution." Scientific Reports NPG **6**: 37109.
Effectively continuous control over propagation of a beam of light requires light modulation with pixelation that is smaller than the optical wavelength. Here we propose a spatial intensity modulator with sub-wavelength resolution in one dimension. The metadevice combines recent advances in reconfigurable nanomembrane metamaterials and coherent all-optical control of metasurfaces. It uses nanomechanical actuation of metasurface absorber strips placed near a mirror in order to control their interaction with light from perfect absorption to negligible loss, promising a path towards dynamic diffraction and focusing of light as well as holography without unwanted diffraction artefacts.

Cencillo-Abad, P., et al. (2016). "Spatial optical phase-modulating metadevice with subwavelength pixelation." Optics Express **24**(16): 18790-18798.
Dynamic control over optical wavefronts enables focusing, diffraction and redirection of light on demand, however, sub-wavelength resolution is required to avoid unwanted diffracted beams that are present in commercial spatial light modulators. Here we propose a realistic metadevice that dynamically controls the optical phase of reflected beams with sub-wavelength pixelation in one dimension. Based on reconfigurable metamaterials and nanomembrane technology, it consists of individually moveable metallic nanowire actuators that control the phase of reflected light by modulating the optical path length. We demonstrate that the metadevice can provide on-demand optical wavefront shaping functionalities of diffraction gratings, beam splitters, phase-gradient metasurfaces, cylindrical mirrors and mirror arrays - with variable focal distance and numerical aperture - without unwanted diffraction.

Cencillo-Abad, P., et al. (2016). "Random access actuation of nanowire grid metamaterial." Nanotechnology **27**(48).
While metamaterials offer engineered static optical properties, future artificial media with dynamic random-access control over shape and position of meta-molecules will provide arbitrary control of light propagation. The simplest example of such a reconfigurable metamaterial is a nanowire grid metasurface with subwavelength wire spacing. Recently we demonstrated computationally that such a metadevice with individually controlled wire positions could be used as dynamic diffraction grating, beam steering module and tunable focusing element. Here we report on the nanomembrane realization of such a nanowire grid metasurface constructed from individually addressable plasmonic chevron nanowires with a 230 nm x 100 nm cross-section, which consist of gold and silicon nitride. The active structure of the metadevice consists of 15 nanowires each 18 mu m long and is fabricated by a combination of electron beam lithography and ion beam milling. It is packaged as a microchip device where the nanowires can be individually actuated by control currents via differential thermal expansion.

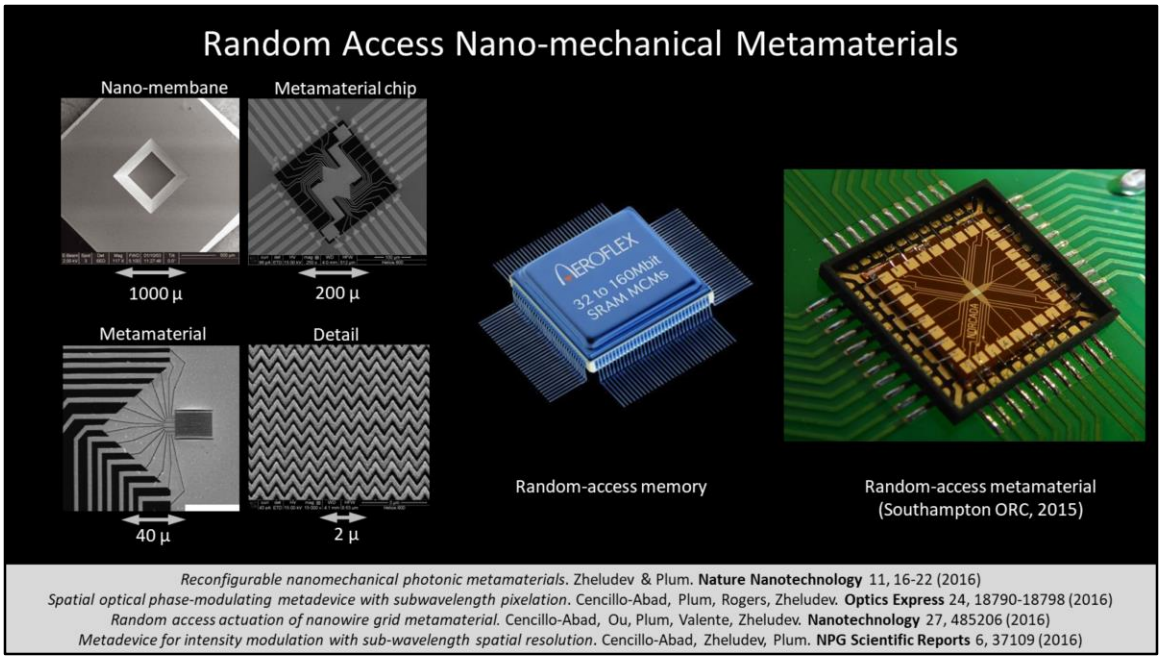

Zheludev, N. I. and E. Plum (2016). "Reconfigurable nanomechanical photonic metamaterials." Nat Nanotechnol **11**(1): 16-22.
The changing balance of forces at the nanoscale offers the opportunity to develop a new generation of spatially reconfigurable nanomembrane metamaterials in which electromagnetic Coulomb, Lorentz and Ampere forces, as well as thermal stimulation and optical signals, can be engaged to dynamically change their optical properties. Individual building blocks of such metamaterials, the metamolecules, and their arrays fabricated on elastic dielectric membranes can be reconfigured to achieve optical modulation at high frequencies, potentially reaching the gigahertz range. Mechanical and optical resonances enhance the magnitude of actuation and optical response within these nanostructures, which can be driven by electric signals of only a few volts or optical signals with power of only a few milliwatts. We envisage switchable, electro-optical, magneto-optical and nonlinear metamaterials that are compact and silicon-nanofabrication-technology compatible with functionalities surpassing those of natural media by orders of magnitude in some key design parameters.

Cencillo-Abad, P., et al. (2016). "Spatial optical phase-modulating metadevice with subwavelength pixelation." Optics Express **24**(16): 18790-18798.
Dynamic control over optical wavefronts enables focusing, diffraction and redirection of light on demand, however, sub-wavelength resolution is required to avoid unwanted diffracted beams that are present in commercial spatial light modulators. Here we propose a realistic metadevice that dynamically controls the optical phase of reflected beams with sub-wavelength pixelation in one dimension. Based on reconfigurable metamaterials and nanomembrane technology, it consists of individually moveable metallic nanowire actuators that control the phase of reflected light by modulating the optical path length. We demonstrate that the metadevice can provide on-demand optical wavefront shaping functionalities of diffraction gratings, beam splitters, phase-gradient metasurfaces, cylindrical mirrors and mirror arrays - with variable focal distance and numerical aperture - without unwanted diffraction.

Cencillo-Abad, P., et al. (2016). "Random access actuation of nanowire grid metamaterial." Nanotechnology **27**(48).
While metamaterials offer engineered static optical properties, future artificial media with dynamic random-access control over shape and position of meta-molecules will provide arbitrary control of light propagation. The simplest example of such a reconfigurable metamaterial is a nanowire grid metasurface with subwavelength wire spacing. Recently we demonstrated computationally that such a metadevice with individually controlled wire positions could be used as dynamic diffraction grating, beam steering module and tunable focusing element. Here we report on the nanomembrane realization of such a nanowire grid metasurface constructed from individually addressable plasmonic chevron nanowires with a 230 nm x 100 nm cross-section, which consist of gold and silicon nitride. The active structure of the metadevice consists of 15 nanowires each 18 mu m long and is fabricated by a combination of electron beam lithography and ion beam milling. It is packaged as a microchip device where the nanowires can be individually actuated by control currents via differential thermal expansion.

Cencillo-Abad, P., et al. (2016). "Metadevice for intensity modulation with sub-wavelength spatial resolution." Scientific Reports NPG **6**: 37109.
Effectively continuous control over propagation of a beam of light requires light modulation with pixelation that is smaller than the optical wavelength. Here we propose a spatial intensity modulator with sub-wavelength resolution in one dimension. The metadevice combines recent advances in reconfigurable nanomembrane metamaterials and coherent all-optical control of metasurfaces. It uses nanomechanical actuation of metasurface absorber strips placed near a mirror in order to control their interaction with light from perfect absorption to negligible loss, promising a path towards dynamic diffraction and focusing of light as well as holography without unwanted diffraction artefacts.

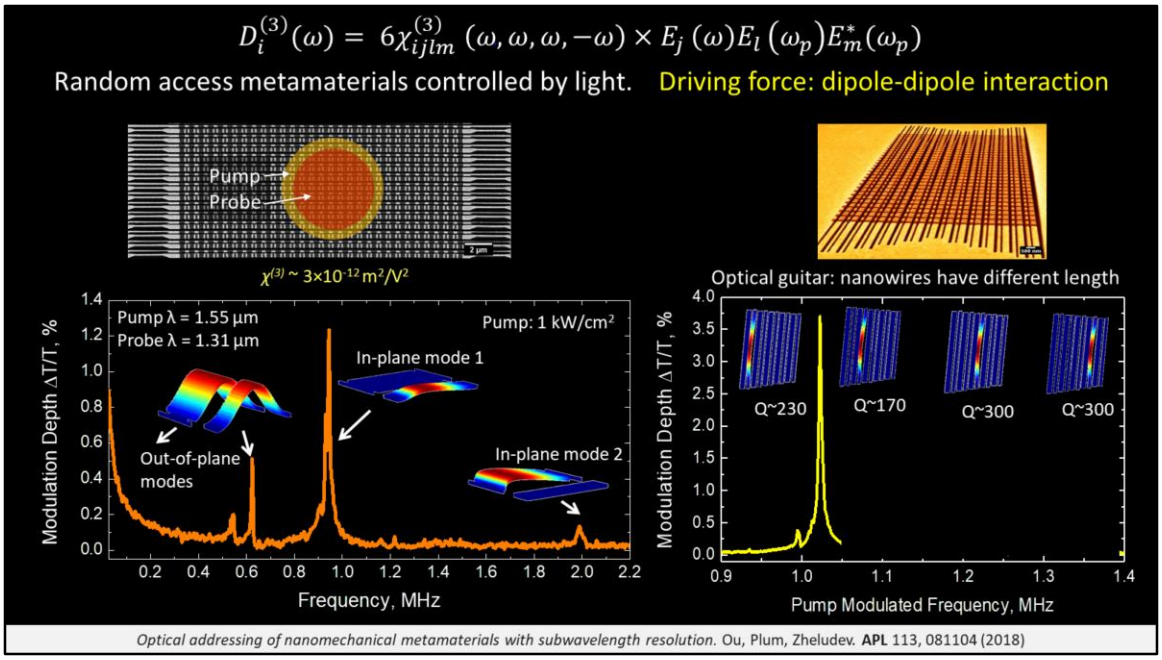

Ou, J. Y., et al. (2018). ".Optical addressing of nanomechanical metamaterials with subwavelength resolution." Applied Physics Letters **113**(8).

Metamaterials that offer "on-demand" control of individual metamolecules are termed "randomly accessible metamaterials." They can be useful for manipulation of the wavefront of electromagnetic radiation, for tailoring of the nearfield, and ultimately for multichannel data processing. Here, we demonstrate how light can be used to actuate individual metamaterial elements on demand. Selectivity is achieved by constructing the metamaterial from nanomechanical elements that are designed to have slightly different mechanical resonance frequencies. Actuation is controlled by modulation of the optical control signal at the mechanical resonance frequencies of targeted elements, providing an all-optical route to randomly accessible metamaterials with spatial resolution beyond the diffraction limit. Published by AIP Publishing.

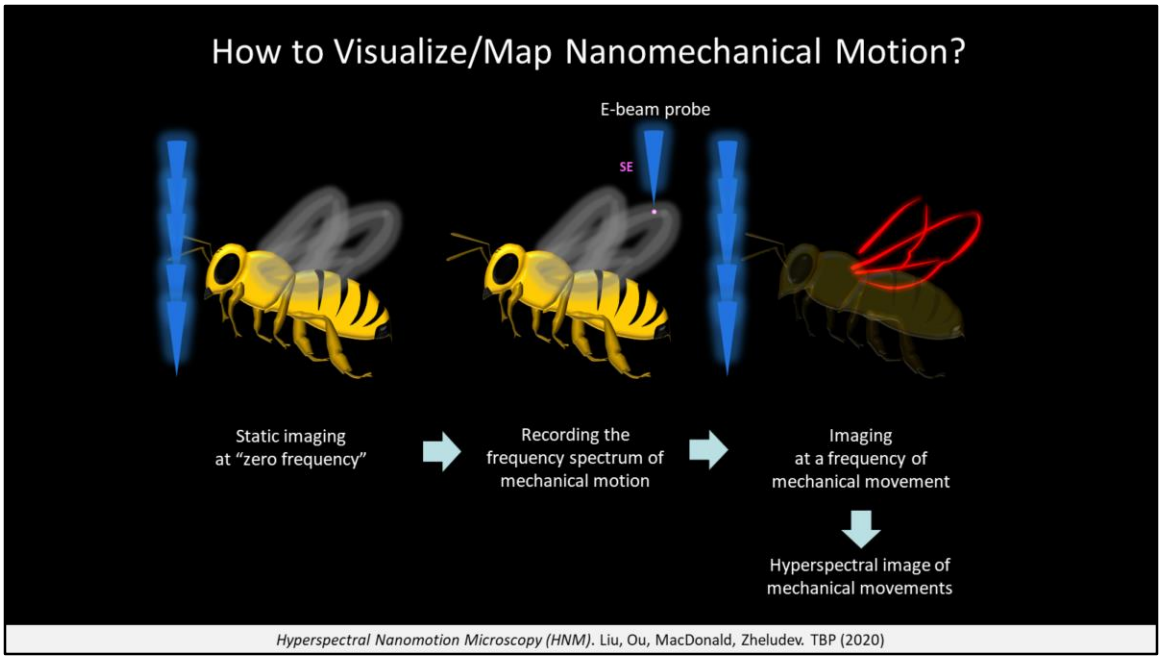

High-Frequency Nano-motion Electron Imaging for Artificial Nanostructures
T. Liu, J. Y. Ou, K. F. MacDonald, and N. I. Zheludev
Electron Beam Spectroscopy for Nanophotonics 2019 (EBSN2019), Paris, France, 16-19 Sept 2019

Imaging of high-frequency motion in artificial nanostructures
T. Liu, J. Y. Ou, K. F. MacDonald, and N. I. Zheludev
Metamaterials'2019, Rome, Italy, 16 - 21 Sep 2019

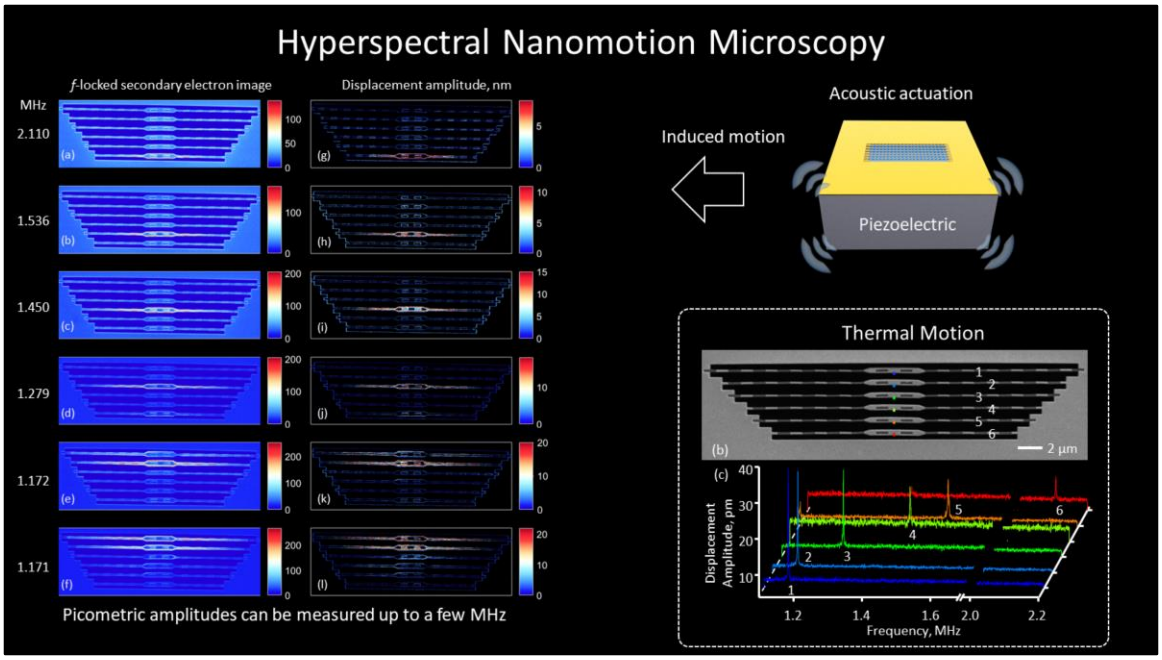

Hyperspectral Nanomotion Microscopy (HNM)

Tongjun Liu [1], Jun-Yu Ou [1(*)], Kevin F. MacDonald [1], Nikolay I. Zheludev [1, 2]
Corresponding author email: jo2c09@orc.soton.ac.uk
[1] Optoelectronics Research Centre and Centre for Photonic Metamaterials,
University of Southampton, Highfield, Southampton, SO17 1BJ, UK
[2] Centre for Disruptive Photonic Technologies, School of Physical and Mathematical Sciences and The Photonics Institute,
Nanyang Technological University, Singapore, 637378, Singapore

Abstract: We have developed a technique that extends static scanning electron microscopic imaging to include hyperspectral mapping of fast thermal and externally-driven movements at up to Megahertz frequencies. It is based on spectral analysis of the secondary electron flux generated by a focused electron beam incident on the moving object. We demonstrate detection of nanowire Brownian motion and hyperspectral mapping of stimulated flea setae oscillations with sub-nanometer displacement sensitivity

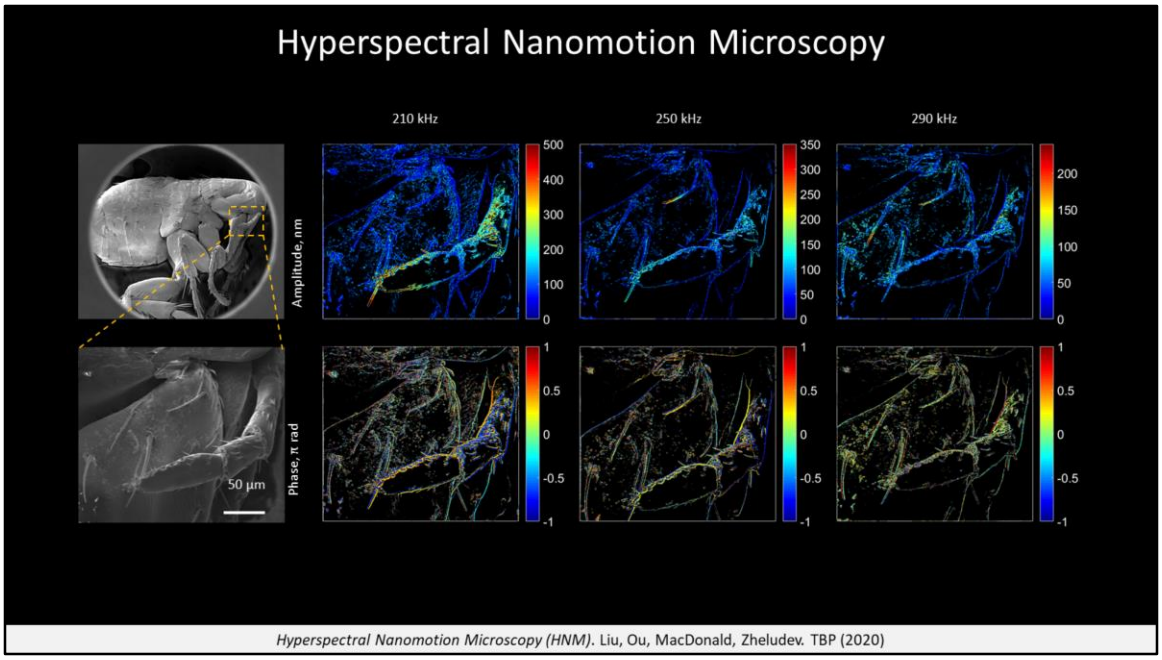

Hyperspectral Nanomotion Microscopy (HNM). Liu, Ou, MacDonald, Zheludev. TBP (2020)

Hyperspectral Nanomotion Microscopy (HNM)

Tongjun Liu [1], Jun-Yu Ou [1(*)], Kevin F. MacDonald [1], Nikolay I. Zheludev [1, 2]
Corresponding author email: jo2c09@orc.soton.ac.uk
[1] Optoelectronics Research Centre and Centre for Photonic Metamaterials,
University of Southampton, Highfield, Southampton, SO17 1BJ, UK
[2] Centre for Disruptive Photonic Technologies, School of Physical and Mathematical Sciences and The Photonics Institute,
Nanyang Technological University, Singapore, 637378, Singapore

Abstract: We have developed a technique that extends static scanning electron microscopic imaging to include hyperspectral mapping of fast thermal and externally-driven movements at up to Megahertz frequencies. It is based on spectral analysis of the secondary electron flux generated by a focused electron beam incident on the moving object. We demonstrate detection of nanowire Brownian motion and hyperspectral mapping of stimulated flea setae oscillations with sub-nanometer displacement sensitivity

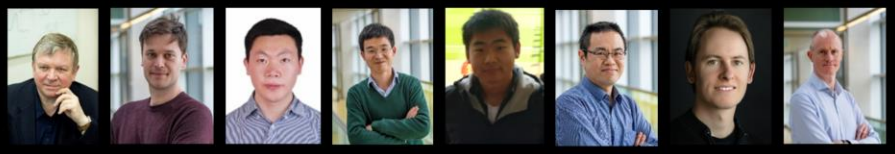

Nikolay I. Zheludev, Dimitrios Papas, Tongjun Liu, Jinxiang Li, Qiang Zhang, Dr. Jun-Yu Ou, Eric Plum, Kevin F. MacDonald

Reconfigurable Nanomembrane Metamaterial Technology
offers a plethora of photonic functionalities including:

Optical nonlinearity
Control of light with light
Electro-optical modulation
Magneto-optical modulation
Control of linear and circular dichroism
Asymmetric transmission

UKRI Engineering and Physical Sciences Research Council

This talk can be found on: www.nanophotonics.org.uk

Ministry of Education SINGAPORE

Nonlinear optical activity in crystals

S. A. Akhamanov, B. V. Zhdanov, N. I. Zheludev, N. I. Kovrigin, and V. I. Kuznetsov
M. V. Lomonosov Moscow State University

(Submitted 24 January 1979)

Pis'ma Zh. Eksp. Teor. Fiz. **29**, No. 5, 294–298 (5 March 1979)

We report on the first investigation of the effect of nonlinear optical activity (NOA) in crystals (dependence of the angle of rotation of the polarization plane on light intensity) which is dependent on the electronic nonlinearity. Measurements are made in $LiIO_3$ crystals. Electronic NOA is separated from the thermal effect background and is $(1\pm0.6)\times10^{-11}$ deg·cm·w^{-1}.

PACS numbers: 78.20.Ek, 42.65. – k

1. The object of this article is to present results of an experimental investigation involving the first study of nonlinear optical activity (NOA) in crystals (dependence of the angle of rotation of the polarization plane on light intensity) which is dependent on "fast" electronic nonlinearity.

Electronic NOA as identified in lithium iodate crystals in the background of slower thermal effects; the nonlinear rotation constant, measured at $\lambda = 0.532$ μm, was $(1 \pm 0.6)\times10^{-11}$ deg·cm·W^{-1}.

Measurement of NOA dispersion may, in our opinion, be a new effective method in nonlinear polarization spectroscopy of condensed media which yields unique information on the combined effects of anharmonicity and spatial dispersion.

2. The NOA effect was predicted in Ref. 1; phenomenologically, it is based on taking into account third-order terms of the optical field intensity in an expression for the polarization. The following holds for a medium with spatial dispersion, to within third-order field terms:

$$P_i = \chi_{ij}^{(1)} E_j + \chi_{ijk}^{(2)} E_j E_k + \chi_{ijkl}^{(3)} E_j E_k E_l + \gamma_{ijk}^{(1)} \frac{\partial E_j}{\partial x_k} - \gamma_{ijkl}^{(2)} E_j \frac{\partial E_k}{\partial x_l} + \gamma_{ijklm}^{(3)} E_j E_k \frac{\partial E_l}{\partial x_m}, \quad (1)$$

where the terms containing $\gamma^{(1)}$, $\gamma^{(2)}$, and $\gamma^{(3)}$ correspond, clearly, to the terms $\chi^{(1)}$, $\chi^{(2)}$, and $\chi^{(3)}$.

NOA is associated with nonlinear susceptibility $\gamma^{(3)}$; in the case of a gyrotropic cubic crystal the following obvious formula—using standard designations—may be written:

$$\mathbf{D} = \epsilon_0 \mathbf{E} - i f^L(\omega)[\mathbf{kE}] + i f^{NL} |\mathbf{E}|^2 [\mathbf{kE}],$$

where

$$f^L(\omega) = \mathrm{Re}\{\gamma^{(1)}(\omega)\}, \quad f^{NL}(\omega) = \mathrm{Re}\{\gamma^{(3)}(\omega)\}. \quad (2)$$

Here the term responsible for NOA has the same structure as that responsible for linear activity (LOA).

A detailed analysis of the tensor $\gamma^{(3)}$ is given in Ref. 2. The angles of linear and nonlinear rotation may be expressed as follows:

$$\phi^L = \frac{k^2 l}{2n_0} f^L(\omega), \qquad \phi^{NL} = \frac{k^2 l}{2n_0} f^{NL}(\omega) |\mathbf{E}|^2. \quad (3)$$

3. The same physical mechanisms contributing to self-interactions, described by the cubic nonlinear susceptibility $\chi^{(3)}$, contribute to NOA in the general case. In this connection, NOA can be called polarization self-interaction, the simplest manifestation of which is the heating of a medium by the laser beam. This mechanism was studied in Ref. 3, yielding results that are similar to those obtained for the temperature measurements of LOA.[1)] Coarse estimates of $\gamma^{(3)}$ (and, consequently, f^{NL}) which depend on electronic nonlinearity may be made for the following simple reasons. Away from the absorption bands, $\gamma^{(3)} \sim \chi^{(3)} a$, where a is the characteristic lattice dimension.[2)] In the case of typical nonlinear crystals in the optical region $\gamma^{(3)} \approx 10^{-20}$–$10^{-22}$ CGSE may be expected. Substituting this value into Eq. (3) yields a value of intensity $I = 10^8$ W/cm^2 and $l = 1$ cm, $\phi^{NL} \approx 3 \times 10^{-15}$–$3 \times 10^{-7}$ rad.

Thus, isolation of the intrinsic electronic NOA from the background of thermal effects and parasitic signals caused by frequency instability and LOA dispersion, is a

difficult task in itself.[3)] To solve this problem, we developed a two-channel pulsed polarimeter capable of measuring a change in the angle of rotation of the polarization plane during a single laser pulse, $\Delta\phi = 5\times10^{-5}$ rad ($\tau = 10^{-8}$ sec).

As the test object we used the $LiIO_3$, crystal which is characterized by a relatively high susceptibility $\chi^{(3)} = 3\times10^{-12}$ CGSE.

4. The NOA effect was studied in a 62-mm long $LiIO_3$ crystal at the second-harmonic frequency ($\lambda = 0.532\,\mu$m) of a monochromatic YAG : Nd laser. The experimental set-up is shown in Fig. 1.

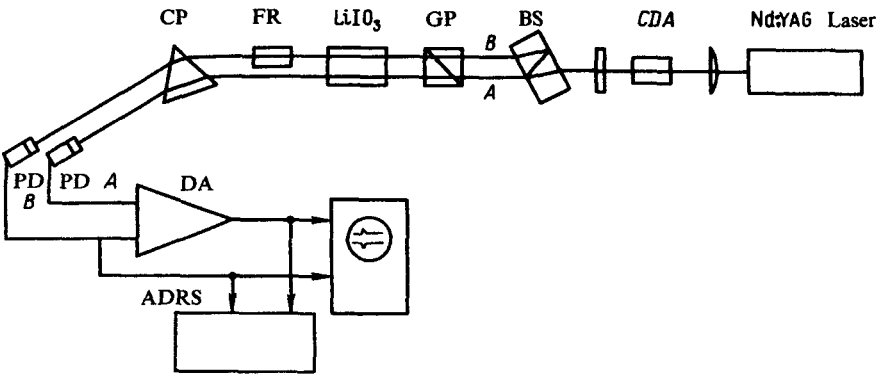

FIG. 1. Bloc diagram of the experimental setup.

The laser output was converted to the second harmonic (SH) by means of a CDA crystal, resulting in SH pulse width of 10 nsec and having the maximum energy $W_2 = 10$ mJ. The SH output was divided by the beam splitter (BS) into two parallel beams A and B with the intensity ratio $I_A/I_B = 30$. After being polarized by the Glann prism (GP), both beams were transmitted through the $LiIO_3$ crystal along the optical axis and, subsequently, through the Cotton prism (CP), a polarization analyzer. In addition to these, channel A contained a Faraday rotator (FR) that compensated for the difference of the linear rotation of the polarization planes of beams A and B which arises due to a difference in the optical path length in the two channels. The electrical part of the recording system consists of a differential amplifier (DA), two-beam oscilloscope and a two-channel pulsed analog-digital recording system (ADRS) with an output printer. Silicon photodiodes (PD) were used as photoreceivers. The nonlinear rotation effect was measured as a function of variations in the ratio of optical intensities in channels A and B produced by increasing the power of the beam propagating in the crystal. The sensitivity of the apparatus used in the NOA observations using the described method is characterized by a level of parasitic signals, associated with LOA, which did not exceed 8×10^{-5} rad.

5. Figure 2 shows the characteristic shape of signals generated at the polarimeter output (maximum beam intensity $I = 300$ MW/cm^2). The first pulses are constrained by electronic NOA; the effect was accompanied by the laser radiation depolarization effect (distinguishable from the NOA signal by changing the position of the working point of the polarimeter) which accumulated with each new laser burst and was,

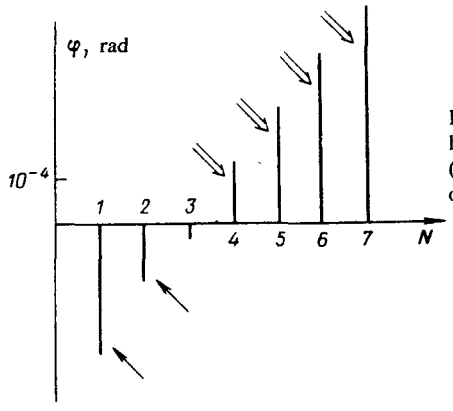

FIG. 2. Signals at the output of two-channel pulsed polarimeter after successive firing of YAG : Nd laser (→NOA signals, ⇒ change in signal sign, associated with optically-induced depolarization in a crystal).

clearly, associated with inhomogeneous heating of the crystal by the laser radiation. As the intensity decreases, so does the depolarization with the characteristic time $\tau_2 = 1$ sec which confirms its thermal origin. The effect of thermal rotation during a single laser pulse did not exceed 10% of the observed NOA effect in our experiments and was characterized by an opposite sign.

The experimental value of the optical rotation constant is $(1 \pm 0.6) \times 10^{-11}$ deg·cm·W^{-1}, and the effective value of the $\gamma^{(3)}$ tensor component (the beam propagating along the optical axis) is

$$\gamma^{(3)} = (6 \pm 4) \cdot 10^{-21} \text{ CGSE}.$$

Although as the NOA effect in $LiIO_3$ is relatively small and measuring it presents some difficulty, the generation of considerably greater effects may be expected. It suffices to point out that the susceptibility in crystals in the vicinity of biexciton resonances is $\chi^{(3)} \approx 10^{-8}$ CGSE (see Ref. 9).

The study of NOA in liquid crystals is of considerable interest; the use of tunable lasers will permit the development of NOA as a new method of nonlinear polarization spectroscopy which simultaneously yields information concerning anharmonicity and spatial dispersion.

Finally, the relation between NOA and the quadratic electrogyration effect is of considerable interest from the standpoint of crystal spectroscopy. A comparison of this kind is not possible at present since the measurement of NOA and quadratic electrogyration were made using different crystals.[10]

[1)]An interesting manifestation of the thermal effect in the dependence of the Faraday rotation on laser light intensity was first shown in Ref. 4.

[2)]This relation is actually used for a coarse evaluation of constants of linear gyration. Naturally, this is not a sufficient reason in support of this method of evaluation of the nonlinear constants; in this connection, it should be pointed out that such an evaluation is indirectly supported in Refs. 5–7 where the susceptibility $\gamma^{(2)}$ which describes the quadrupole generation of the second optical harmonic was determined.

[3)]In our opinion incomplete exclusion of the foregoing effects has affected the accuracy of results described in Ref. 8.

[1]S.A. Akhmanov and V.I. Zharikov, Pis'ma Zh. Eksp. Teor. Fiz. **6**, 644 (1967) [JETP Lett. **6**, 137 (1967)].
[2]B.V. Bokut', N.S. Kazak, and A.N. Serdyukov, Nelineĭnaya opticheskaya aktivnost' (Nonlinear optical cavity), Preprint Inst. Phys. BSSR Academy of Sciences, Minsk, 1971.
[3]D.V. Vlasov and V.P. Zaĭtsev, Pis'ma Zh. Eksp. Teor. Fiz. **14**, 171 (1971) [JETP Lett. **14**, 112 (1971)].
[4]V.S. Zapasskiĭ and P.P. Feofilov, Tezisy dokladov IX Vsesoyuznoĭ konferentsii po kogerentnoĭ i nelineĭnoĭ optike (Summaries of reports of the 9th All-Union Conference on Coherent and Nonlinear Optics), M., 1978, p. 154.
[5]S.A. Akhmanov and R.V. Khokhlov, Problemy nelineĭnoĭ optiki (Problems of Nonlinear Optics), M., 1964, p. 74.
[6]S.G. Dinev, S.M. Saltiel, K.V. Stamenov, K.A. Stankov, and V.G. Tunkin, Opt. Comm. **24**, 225 (1978).
[7]D.S. Bethune, R.W. Smith, and Y.R. Shen, U of C Preprint, 1977.
[8]V.V. Borshch, M.P. Lisitsa, P.E. Mozol', and I.V. Feshengazi, Kvantovaya Elektron. **5**, 672 (1978) [Sov. J. Quantum Electron. **8**, 393 (1978)].
[9]A. Marvani, J.L. Oudar, E. Batifol, and D. Chemla, Phys. Rev. Lett., (1979), in press.
[10]O.G. Vlokh and T.A. Kruzhel'nitskaya, Kristallografiya **15**, 587 (1970) [Sov. Phys. Crystallogr. **15**, 504 (1970)].

All change, please

NIKOLAY ZHELUDEV

is at the Optoelectronics Research Centre, University of Southampton, SO17 1BJ, UK.
e-mail: n.i.zheludev@soton.ac.uk

Examples of structural phase changes abound in the natural world around us. But if we can exploit such changes on the nanoscale using light, new nanophotonics technology may be just around the corner.

Melting polar ice caps or the fantasy of freezing oceans in cataclysmic Hollywood films are graphic illustrations of often badly understood thermodynamic processes involving a structural phase change in water (Fig. 1). What is less widely known is that similar phase change events occurring on the nanoscale lie at the foundation of one of today's most important data-storage technologies, the re-writable digital versatile disk (DVD), and that they are lining up to underpin the next generation of super-reliable, high-capacity electronic memories. Ultrasmall devices exploiting structural phase changes could also form the basis for the design of future active nanoscale optical circuits.

A radical change in the arrangement of atoms is called a structural phase transition, or phase change. Liquid water, in which the molecules are randomly arranged, undergoes a phase change to the regular crystalline atomic construction of ice on freezing, and back on melting. This is a phase change between disordered and ordered states.

So what use are such transformations for photonics? It appears that phase-change functionality can provide a way of shrinking optical switching devices all the way down to the nanoscale. They can help achieve the ultimate goal of nanophotonics — that is, to create devices smaller than or comparable in size to the carrier wavelength of the signals they handle, a relationship of proportions that is easily achieved in most electronic circuits.

The concept of all-optical logical memory elements has been studied extensively since the 1980s. Optical nonlinearities can be used together with a feedback mechanism to enhance the switching response of a material and lock it into one of two or more possible stable states. However, the minimum spatial size of early bistable and multistable optical devices was limited to one wavelength — too large for nanophotonic technology — because they involved feedback from the interference of light[1].

Two main hurdles obstruct the nanoscale miniaturization of photonic circuits: the need to guide optical signals in the narrow and sharply bending waveguides of a highly integrated environment; and the need to modulate these signals in very small active devices. It is now believed that the guiding problem can be successfully addressed using surface-plasmon-polariton waves as information carriers[2,3]. However, the modulation challenge seems to be much more difficult to tackle.

In essence, the modulation of a signal in a waveguide requires that its amplitude or phase be changed substantially by a control signal either through a change in propagation losses or propagation delays. This is practically achieved by modulating the absorption coefficient and refractive index of a length of waveguide over which a change in amplitude or phase then

ALEXANDER HAFEMANN

Figure 1 Processes similar to that of global climatic events involving melting icebergs also occur on the nanoscale, but quadrillions of times faster. By harnessing such phase changes, scientists could come up with fast and flexible nanophotonic circuit designs.

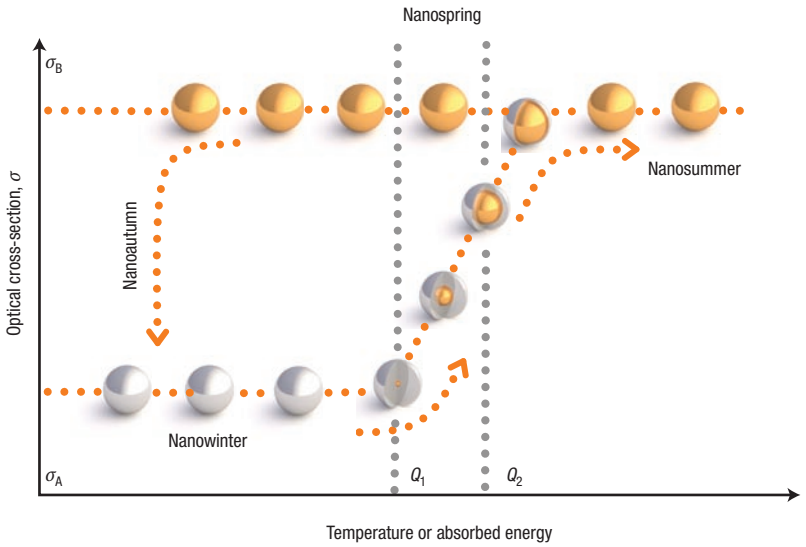

Figure 2 Phase change optical functionality in a nanoparticle: the dependence of optical cross-section σ on absorbed light energy Q for a nanoparticle undergoing a phase transition. At low temperature, the particle exists in phase A (nanowinter). Reversible changes occur when a light pulse of energy between Q_1 and Q_2 is used to excite the system (nanospring). Excitation energy levels above Q_2 herald in nanosummer and a memory effect: phase A fully transforms into phase B, and the particle remains in this metastable phase even as the excitation is withdrawn. A transition to the low-temperature phase takes place abruptly and only after overcooling (nanoautumn). The spherical structures indicate nanoparticles in phase A (silver), phase B (gold) and transitional mixed-phase states (silver and gold) occurring in the energy range between Q_1 and Q_2.

accumulates. But in optical nanocircuits, individual components are spaced on the nanoscale and there is not enough propagation distance to obtain effective modulation.

The only way to overcome the lack of propagation distance is to use nanometre-scale materials that can undergo a very strong change in absorption or refraction in response to an external control wave; for example, for a refractive index the real and imaginary parts would need to change on the order of unity. Traditional approaches such as the use of optical resonators to enhance modulation do not help here; any resonator must be at least one wavelength long (longer if possible, as resonator performance improves with length), and it will therefore simply not fit into nanoscale circuits. The required large changes in absorption and refraction are only possible in media where there is something substantial to change. And on this score, metals, which refract and absorb light strongly, fit the bill.

PHASE-DEPENDENT OPTICAL PROPERTIES

Large changes in the optical properties of metals can only be achieved through a phase change, and some metals — gallium, for example — can exist in phases with vastly different optical properties. This is the first piece of good news for nanophotonics. The stable ground-state phase in bulk is α-gallium, which has a very low melting point of only 29.8 °C and is likened to an inorganic polymer. When α-gallium melts at about room temperature, the modulus of its dielectric coefficient changes by more than a hundred. The α-phase is not normally observed in nanoparticulate form, but gallium nanoparticles can exist in a variety of other phases: from the highly metallic liquid phase to forms known as β-, γ-, δ- and ε-gallium, which display some marked departures from metallic behaviour. When gallium melts, the absorption and scattering cross-sections at the plasmonic resonance frequency change by an order of magnitude.

ENERGY EFFICIENT

The second piece of good news is that the energy difference between phases is often small, making phase-change-based devices extremely energy efficient. For instance in the case of optical nonlinearity associated with the bound electrons of a material, the maximum effect that the absorption of a single photon can have on the properties of a medium occurs when it knocks the molecule out of the light–matter interaction process (for example, by saturating the absorption) or, in contrast, when it 'switches on' the optical response of the molecule (for instance, by forcing it into a resonance). This requires one photon per atom. A similarly strong effect on the optical properties of a material may be achieved by providing the energy needed to move it from one phase to another. This energy 'price' is typically of the order of the characteristic phonon energy per atom. As phonon energy is three to four orders of magnitude lower than photon energy, changing the optical properties through a phase transition is much more energy efficient than relying on electronic nonlinearity. So the energy of only a handful of photons should be enough to convert an entire nanoparticle from one phase to another, say from a weakly absorbing 'semiconductor' phase to a strongly optically absorbing 'metallic' phase.

NANOSEASONS

The third piece of good news for nanophotonics is that structural phase transitions in nanoscale objects are different from those in bulk media. Depending on the regime of excitation, one can obtain either reversible or irreversible phase changes. Continuous and reversible changes occur through the intermediate coexistence of phases, and are suitable for controlling light with light. Irreversible changes are better suited to nanoscale optical memory elements.

Consider, for example, a nanoparticle that can exist in two different phases depending on temperature (Fig. 2). Continuing with the climatic analogy, the low-temperature phase represents winter when water is frozen into ice, whereas the high-temperature phase is that of summer, when ice melts into water. The seasons of spring and autumn in the nanoworld are interesting for photonics. Just as sunlight melts some of the ice on a spring day, a nanoparticle still in its low-temperature phase but with a rising ambient temperature, can be converted to the high-temperature phase by only a small amount of extra heat provided by a control light beam. If this phase change is only partial, then on removing the control light beam the particle will return to the low-temperature phase, like ice re-forming overnight in spring. These 'nanospring' processes can be reversible.

However, as the temperature increases further, there comes a point when the particle is converted completely into the high-temperature phase and it remains locked in 'nanosummer'. Full conversion to the high-temperature phase may also be achieved by providing sufficient energy in the form of a control light pulse hitting the nanoparticle, rather than by

changing the ambient temperature. Under these conditions the fully converted particle remains in the high-temperature phase even after the optical excitation is withdrawn. It could be said that the particle has a memory of past events written into its phase: reducing the temperature to the lowest nanospring level will not revert the particle back to its low-temperature phase. Much stronger cooling to a few tens of degrees below the lowest nanospring temperature (known as overcooling) is needed to trigger 'nanoautumn'. In fact, in some cases the nanoautumn transition may be stimulated by a short optical pulse.

Under the right conditions, therefore, a polymorphic nanoparticle can be locked into a metastable state, in which it remains regardless of changes in temperature. As the different crystalline phases of a single nanoparticle possess different optical absorption and scattering cross-sections, one can build a logical memory element by coding each distinct optical characteristic with a unique label. The transitions between the different phases, or equivalent logical states, may be activated by increasing or decreasing the temperature of the medium. In the case of optical data storage, this could be done by external excitation using optical pulses.

The phase-change approach to controlling the optical properties of a nanoparticle is deeply rooted in the nanoscale nature of the effect. The smaller the particle gets, the more rapidly and easily its optical properties (absorption, in this case) can be modulated by energy from an external light beam. Nanoparticles are particularly promising for all-optical data-storage applications because they provide intrinsic mechanisms of phase metastability, offer outstanding information-storage density in the terabits-per-square-inch territory and require a very small amount of energy per logical state to write. For example, in gallium an energy of just 0.4 fJ, which is equivalent to the energy of about 2,000 photons at a wavelength of 1 μm, is in principle enough to convert the state of a nanoparticle with a radius of 15 nm from the δ- to the β-solid phase. And absorbing the energy of just one photon could be sufficient to completely convert a particle with a diameter of a few nanometres into a different phase, thus making a single-photon all-optical switch a feasible proposition.

The ten orders of magnitude size difference between a melting iceberg and a nanoparticle changing its phase has welcome implications for nanophotonics: in the nanoworld spring and autumn may take only a few billionths of a second. Because the phase change proceeds through the coexistence of two phases, it involves the propagation of a boundary between the phases. Although this phase front does not travel particularly fast, and is normally much slower than the speed of sound, in nanoparticles it does not have far to travel, so switching times in the nanosecond range are possible. Subnanosecond switching times may even be possible if the 'explosive crystallization' regime — observed in thin metal films when crystallization velocities reach tens of metres per second — can be achieved in nanoparticles. A transition from a low-temperature to a high-temperature phase induced by an optical pulse may be even faster if the high-temperature phase is a disordered state of matter and the low-temperature phase is highly ordered. It only takes a few angstroms of atomic movement in a random direction to achieve such a transition. These processes occur on the picosecond timescale or even faster.

Nanophotonic switching and memory functionality underpinned by phase change has already been demonstrated using gallium nanoparticles. Solid-to-solid and solid-to-liquid light-induced phase transitions have been observed in various crystalline and amorphous phases of gallium[4]. Similarly, resonator-free all-optical memory has been achieved in this system[5,6]. The size of the memory element, which is equal to the size of the nanoparticle itself, is comparable to that of magnetic domains in state-of-the-art hard disks. Moreover, the energy needed to switch the nanoparticle (that is, to store one 'bit') is an order of magnitude smaller than that needed in DVD/DVR technology. These findings suggest that in the future photons driving structural phase changes could offer a practical way of controlling signals in plasmonic[7] and nanophotonic circuits[8].

References

1. Gibbs, H. M. *Optical Bistability: Controlling Light with Light* (Academic, Orlando, Florida, 1985).
2. Rashid, Z., Schuller, J. A., Chandran, A. & Brongersma, M. L. *Mater. Today* **9,** 20–27 (2006).
3. Atwater, H. A. *Sci. Am.* **296,** 56–63 (2007).
4. Soares, B. F., MacDonald, K. F., Fedotov, A. V. & Zheludev, N. I. *Nano Lett.* **5,** 2104–2107 (2005).
5. Soares, B. F., Jonsson, F. & Zheludev, N. I. *Phys. Rev. Lett.* **98,** 153905 (2007).
6. Soares, B. F., MacDonald, K. F. & Zheludev, N. I. *Appl. Phys. Lett.* **91,** 043115 (2007).
7. Krasavin, A. V. & Zheludev, N. I. *Appl. Phys. Lett.* **84,** 1416–1418 (2004).
8. Engheta, N., Salandrino, A. & Alù, A. *Phys. Rev. Lett.* **95,** 095504 (2005).

Metamaterials: Optical Activity without Chirality

E. Plum,[1] X.-X. Liu,[1,2] V. A. Fedotov,[1] Y. Chen,[3] D. P. Tsai,[2] and N. I. Zheludev[1,*]

[1]*Optoelectronics Research Centre, University of Southampton, SO17 1BJ, United Kingdom*
[2]*Department of Physics, National Taiwan University, Taipei, 10617, Taiwan, Republic of China*
[3]*Rutherford Appleton Laboratory, Chilton, Didcot, Oxon, OX11 0QX, United Kingdom*

(Received 28 July 2008; revised manuscript received 22 January 2009; published 19 March 2009)

We report that the classical phenomenon of optical activity, which is traditionally associated with chirality (helicity) of organic molecules, proteins, and inorganic structures, can be observed in artificial planar media which exhibit neither 3D nor 2D chirality. We observe the effect in the microwave and optical parts of the spectrum at oblique incidence to regular arrays of nonchiral subwavelength metamolecules in the form of strong circular dichroism and birefringence indistinguishable from those of chiral three-dimensional media.

DOI: 10.1103/PhysRevLett.102.113902 PACS numbers: 42.25.Ja, 41.20.Jb, 78.20.Ek

The phenomenon of optical activity, that is the ability to rotate the polarization state of light, is a fundamental effect of electrodynamics which is traditionally associated with mirror asymmetry (chirality) of organic molecules. The effect has enormous importance for analytical chemistry, crystallography, molecular biology, and is also a signature effect used to detect life forms in space missions. The recognition of chirality as a source negative refraction of light [1–9] needed for the creation of a perfect lens [10] inspired intense work in developing microwave and optical artificial chiral metamaterials [11–15] and yielded a demonstration of negative index due to chirality [11,16,17]. In this Letter, we present a somewhat surprising result that very strong optical activity may be seen in a metamaterial system consisting of metamolecules that itself are not chiral. Here, chirality is drawn extrinsically from the mutual orientation of the wave propagation direction and the two-dimensional metamaterial. We demonstrate the effect in both the microwave and optical parts of the spectrum using artificially created nonchiral planar metamaterial structures and show that they behave indistinguishably from 3D-chiral molecular systems manifesting resonant circular birefringence and dichroism. Our experiments also indicate that in such metamaterials, extrinsic chirality may also lead to negative refraction of circularly polarized electromagnetic waves.

The recent effort in creating artificial metamaterials with strong optical activity was focused on different types of arrays of 3D-chiral metamolecules [11–21]. It is significantly less acknowledged that the effect can also be seen when oriented nonchiral molecules make a chiral triad with the wave vector of light (extrinsic chirality). This mechanism was first described by Bunn [22] and detected in liquid crystals [23]. Here, we show that extrinsic chirality can lead to exceptionally large optical activity and circular dichroism in microwave and photonic *planar* metamaterials that possess neither 2D chirality [24] nor 3D chirality, and which are much simpler to fabricate than metamaterials based on arrays of 3D-chiral metamolecules.

We argue that to manifest optical activity, metamolecules of a planar metamaterial may have a line of mirror symmetry, but shall lack an inversion center, i.e., they will posses a polar direction s (see Fig. 1). A regular oriented array of such metamolecules will not show optical activity at normal incidence. However, the metamaterial will become optically active at oblique incidence provided that the plane of incidence does not contain the polar direction. Indeed, in this case, the wave vector k, normal to the metamolecule plane n and polar vector s, constitute a

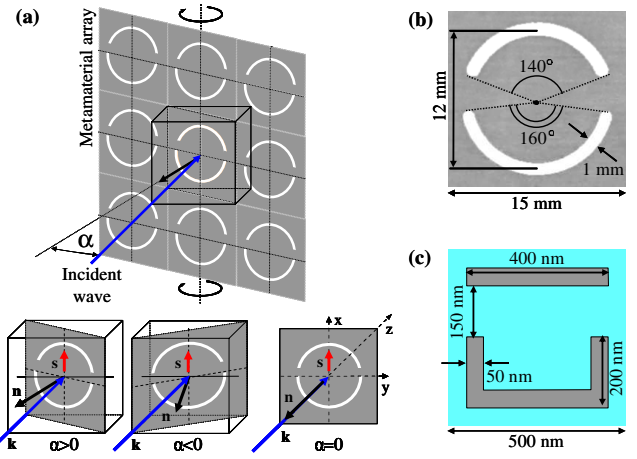

FIG. 1 (color online). (a) Planar metamaterials based on an array of asymmetrically split rings manifest optical activity and circular dichroism at oblique incidence of light. The direction of asymmetry is represented by a polar vector s (long to short arc). Optical activity is seen when the metamaterial plane is tilted around the x-axis so that the sample normal n and the incident wave vector k form an angle $\alpha \neq 0$. Configurations $\pm\alpha$ are enantiomeric arrangements showing optical activity of opposite signs. Configuration $\alpha = 0$, i.e., normal incidence, shows no optical activity. (b) Unit cell of the microwave metamaterial: an asymmetrically split ring aperture in a 1 mm thick aluminum sheet. (c) Unit cell of the photonic metamaterial containing 50 nm thick aluminum wires placed on a 500 μm-thick glass substrate.

3D-chiral triad. The enantiomeric configurations of these vectors corresponding to optical activity of opposite signs are created by tilting the plane of the structure in opposite directions with respect to the incident wave vector (compare $\alpha > 0$ and $\alpha < 0$ in Fig. 1).

The origin of the effect in such a planar nonchiral structure may be readily seen by considering a "unit cell," which contains a single tilted split ring (Fig. 1). Using the terminology of crystallography, the direction of light propagation will be a "screw direction" of the unit cell (that is to say, it will have a sense of twist), if several conditions are met [25]. First, the unit cell itself shall not have an inversion center. This is assured by an asymmetry of the split ring. Second, there should be no reflection symmetry in the plane perpendicular to the propagation direction, which is provided by oblique incidence. Third, there should be no inversion or mirror rotation axis along the propagation direction. This is provided by oblique incidence and the asymmetric split. And finally, there should be no reflection symmetry for any plane containing the propagation direction. This requirement is only fulfilled if the split is not perpendicular, and therefore vector s is not parallel, to the incidence plane yz. Therefore, with reference to Fig. 1(a), in cases $\alpha > 0$ and $\alpha < 0$, the direction of light propagation is a screw direction and supports optical activity. On the contrary, case $\alpha = 0$, i.e., normal incidence, fails the second, third, and forth conditions of the "screw direction" test. For instance, at normal incidence, there is a plane of reflection symmetry containing the propagation direction.

We observed optical activity in microwave and photonic metamaterials based on regular arrays of asymmetrically split rings. Each split ring has a line of mirror symmetry along the x-axis but has no axis of twofold rotation, which enables the introduction of a polar vector s that points towards the short arc [see Fig. 1(a)]. The microwave metamaterial is a self-standing aluminum plate with a size of $\approx 220 \times 220$ mm^2, which is perforated with split ring slits [see Fig. 1(b)]. The period of perforation is 15 mm rendering the structure nondiffracting at normal incidence for frequencies below 20 GHz. The photonic metamaterial consists of aluminum split nanorings manufactured by e-beam lithography on a glass substrate and has size of 500×500 μm^2 [see Fig. 1(c)]. The period of the nanostructure is 500 nm, which ensures no diffraction in the near IR.

The microwave metamaterial has a number of intriguing and useful properties. Being essentially a perforated sheet of metal, it is not transparent apart from a narrow spectral range around the resonant frequency, at which the wavelength is approximately twice the slit length. Transmission at the resonance is "extraordinarily" high and substantially exceeds the fraction of the area taken by the slits. As Joule losses in metals at microwave frequencies are negligible, the incident energy is split between reflected and transmitted radiation, and at the resonance reflection is low [26]. As illustrated below, the structure shows a strong bell-shaped resonance of circular birefringence leading to strong polarization rotation, while circular dichroism is zero at the resonance. This very useful feature is in striking contrast with optical activity in most molecular systems, where characteristically strong resonant polarization rotation is accompanied by substantial circular dichroism resulting in elliptical polarization. Moreover, at the optical activity resonance, the system shows *no linear birefringence* (anisotropy), and eigenstates are therefore two circular polarizations with equally moderate losses.

For microwaves, we measured the complex transmission matrix t relating the incident E^{in} and transmitted E^{out} circularly polarized electric fields and defined as $E_i^{\text{out}} = t_{ij} E_j^{\text{in}}$, where subscripts $+$ and $-$ denote right and left circularly polarized waves correspondingly. Our measure-

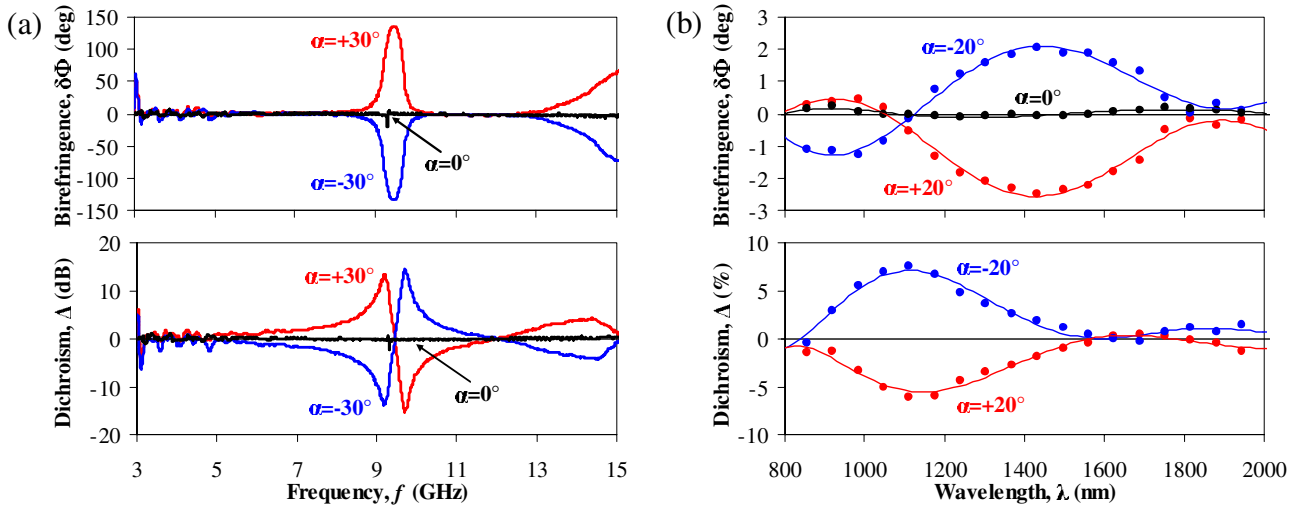

FIG. 2 (color online). Circular birefringence $\delta\phi$ and circular dichroism Δ observed in transmission for different tilt angles α: (a) microwave metamaterial (measured in an anechoic chamber using broadband horn antennas and a vector network analyzer) and (b) photonic structure (measured in a microspectrophotometer using linear polarizers and a superachromatic wave plate).

ments show that t_{++} and t_{--} are generally not equal, indicating true optical activity. The difference between their magnitudes $\Delta = |t_{++}|^2 - |t_{--}|^2$ is a measure of circular dichroism, while the corresponding phase difference $\delta\phi = \arg(t_{++}) - \arg(t_{--})$ is a measure of circular birefringence (see Fig. 2). t_{-+} and t_{+-} are equal within experimental accuracy, which indicates the expected presence of some linear anisotropy but also shows a complete absence of the asymmetric transmission effect recently discovered in planar chiral structures [24]. Importantly, the metamaterials' gyrotropic properties cannot be explained by linear anisotropy, which does not contribute to Δ and $\delta\phi$. Particularly, while linear anisotropy causes a polarization state dependent modulation of azimuth rotation, it has no effect on the material's average polarization rotary power, which is only determined by $\delta\phi$. For the photonic metamaterial, we measured the transmission difference Δ for right and left circular polarizations and the average polarization azimuth rotation $\delta\phi/2$ directly. In all cases, experiments performed in opposite directions of wave propagation show identical results.

In case of the lossless microwave structure, the observed effect has a resonant nature and is strongest around the resonance between 9 and 10 GHz, where the average arc length corresponds to approximately half of the free-space wavelength. For the photonic metamaterial, the effect is weaker and the resonances are broader due to the increase of losses in the metal wires. The following characteristic features of the effect have been observed in the experiments: i) no circular birefringence or dichroism is seen at incidence normal to the metamaterial array ($\alpha = 0$); ii) equal tilt in opposite directions yields circular dichroism and circular birefringence of opposite sign. On the absolute scale, the effect due to extrinsic chirality (polarization azimuth rotation, $|\delta\Phi/2|$, exceeds 60° for microwaves and 1° in optics) appears to be even stronger than that exhibited by microwave and photonic artificial 3D-chiral rosette structures [11,14,16]. Metamaterials of the proposed type, being essentially planar structures, are generally much easier to fabricate than the existing artificial chiral media, especially in the visible, and therefore are capable of superseding the latter as powerful ultrathin circular polarizers and polarization rotators.

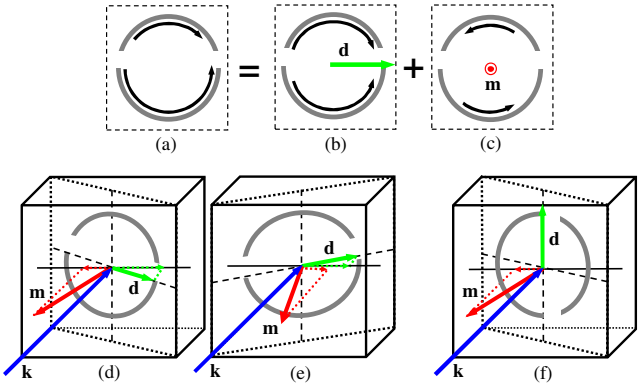

FIG. 3 (color online). Electric and magnetic responses in an asymmetrically split wire ring. Oscillating currents in the split ring (a) can be represented as a sum of symmetric (b) and antisymmetric (c) currents that correspond to the induced electric dipole in the plane of the ring d (green arrow) and magnetic dipole perpendicular to the plane m (red arrow). For tilted asymmetrically split rings, polarization rotation is strongest and of opposite sign if the projections of d and m onto the plane perpendicular to the k-vector (correspondingly green and red dashed arrows) are either antiparallel (d) or parallel (e). Optical activity is only absent if these projections are orthogonal (f).

The microscopic origin of optical activity in extrinsically chiral split wire rings can be easily understood (see Fig. 3, also see [27]). As with conventional optical activity exhibited by chiral molecules, the effect must result from the presence of both electric and magnetic responses. As illustrated in Fig. 3(a), a wave polarized along the split induces unequal oscillating currents in the upper and lower arches of the ring. This may be represented as a sum of symmetric and antisymmetric currents corresponding to the induced electric dipole in the plane of the ring and magnetic dipole perpendicular to the ring [see Figs. 3(b) and 3(c)]. Now we shall consider non-normal incidence of the wave onto the structure [see Figs. 3(d)–3(f)]. Here blue, red, and green solid arrows represent the wave vector k and induced magnetic m and electric d dipoles of the metamaterial's unit cell, while dashed arrows show projections of the corresponding dipole moments onto the plane perpendicular to the wave vector. The structure shows optical activity if the split is not perpendicular to the plane of incidence. Maximum optical activity is observed when the split is parallel to the plane of incidence; in this case, the wave vector and induced magnetic and electric dipoles are coplanar. The mutual phase difference between the electric and magnetic responses and thus the sign of optical activity depends on the sign of the tilt [compare projections of electric and magnetic dipoles in Figs. 3(d) and 3(e)]. Similarly to how it happens in conventional chiral media, when the wave vector and induced magnetic and electric dipoles of the "metamolecule" are coplanar, the oscillating dipole components perpendicular to the k-vector create scattered electromagnetic waves with orthogonal polarizations in the direction of wave propagation, and therefore the polarization of the transmitted wave rotates. On the contrary, if the split is perpendicular to the plane of incidence, the induced magnetic and electric dipoles as well as their projections are orthogonal and the structure does not show any optical activity [see Fig. 3(f)]: the oscillating magnetic and electric dipoles emit electromagnetic waves of the same polarization that propagate along the direction of the incident wave. According to Babinet's principle, the slit metamaterial, which is the Babinet complementary structure to the wire pattern discussed above, will exhibit similar polarization resonances in the same frequency band.

Intriguingly, in the slit metamaterial, in the resonance spectral band from about 9 to 10 GHz, phase velocity

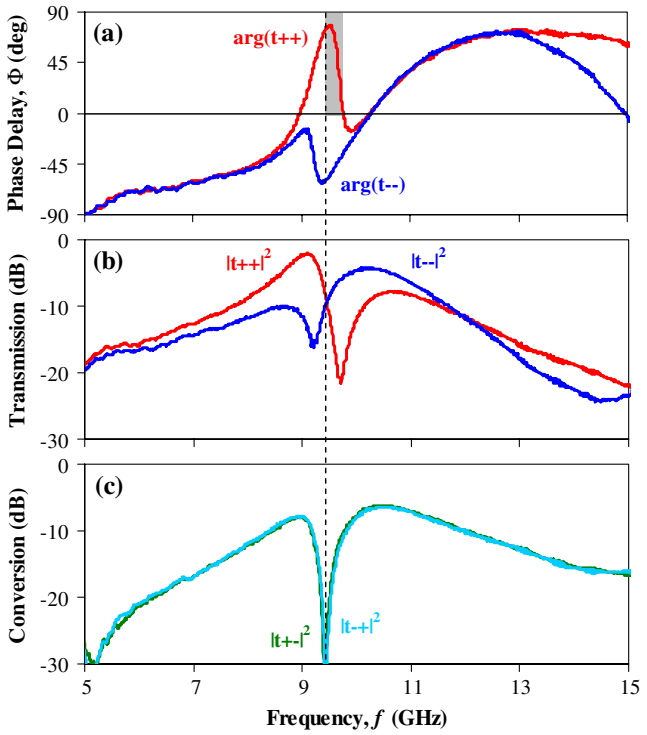

FIG. 4 (color online). (a) Dispersions of phase delay ϕ for transmitted left and right circularly polarized waves. The shaded area indicates the frequency range with almost circular eigenstates, where phase velocity v_p and group velocity v_g for right circular polarization have opposite signs. (b) Transmitted intensity of both left and right circularly polarized waves. (c) Efficiency of circular polarization conversion, which is a direct indication of anisotropy (linear birefringence) of the material response. All data correspond to incidence angle $\alpha = 30°$ onto the microwave metamaterial, see Fig. 1.

($v_p \sim \omega/\phi$, where $\omega = 2\pi f$) and group velocity ($v_g \sim d\omega/d\phi$) for right circular polarization have opposite signs indicating the appearance of a backward wave [see Fig. 4(a)]. In accordance with Pendry [1], this is a necessary condition or signature of negative refraction in bulk chiral media. Following Pendry, negative refraction should be seen at the resonance for one circular polarization only swapping to the other one in the medium's enantiomeric form. Indeed, our experiments show opposite signs of group and phase velocities for right circular polarization at $\alpha = 30°$ and for left circularly polarized waves for the enantiomeric arrangement, at $\alpha = -30°$. Importantly, linear anisotropy essentially disappears [negligible circular conversion $t_{+-} = t_{-+} = \frac{1}{2} \cdot (t_{xx} - t_{yy})$, see Fig. 4(c)]. Thus, the polarization eigenstates are very close to circular and in the k-vector direction, the material behaves as isotropic optically active medium. Moreover, in this spectral range, losses represented by $|t_{++}|^2$ and $|t_{--}|^2$ are relatively small [see Fig. 4(b)].

In conclusion, we have demonstrated strong optical activity and circular dichroism in nonchiral planar microwave and photonic metamaterials. The phenomena are due to extrinsic chirality, which arises from the mutual orientation of the metamaterial and the incident beam. The effect could be exploited for developing novel highly efficient polarization rotators and modulators, and vibration sensors, and may lead to the appearance of a new class of negative index metamaterials, in addition to the recently demonstrated conventional chiral negative index media [11,16,17].

Financial support of the Engineering and Physical Sciences Research Council, UK is acknowledged.

*niz@orc.soton.ac.uk
www.nanophotonics.org.uk/niz/

[1] J. B. Pendry, Science **306**, 1353 (2004).
[2] S. Tretyakov *et al.*, Photonics Nanostruct. Fundam. Appl. **3**, 107 (2005).
[3] C. Monzon and D. W. Forester, Phys. Rev. Lett. **95**, 123904 (2005).
[4] Y. Jin and S. He, Opt. Express **13**, 4974 (2005).
[5] Q. Cheng and T. J. Cui, Phys. Rev. B **73**, 113104 (2006).
[6] V. M. Agranovich *et al.*, Phys. Rev. B **73**, 045114 (2006).
[7] V. Yannopapas, J. Phys. Condens. Matter **18**, 6883 (2006).
[8] A. Baev *et al.*, Opt. Express **15**, 5730 (2007).
[9] D.-H. Kwon *et al.*, Opt. Express **16**, 11822 (2008).
[10] J. B. Pendry, Phys. Rev. Lett. **85**, 3966 (2000).
[11] A. V. Rogacheva *et al.*, Phys. Rev. Lett. **97**, 177401 (2006).
[12] M. D. M. Klein *et al.*, Opt. Lett. **32**, 856 (2007).
[13] K. Konishi *et al.*, Opt. Express **15**, 9575 (2007).
[14] E. Plum *et al.*, Appl. Phys. Lett. **90**, 223113 (2007).
[15] M. Thiel *et al.*, Adv. Mater. **19**, 207 (2007).
[16] E. Plum *et al.*, Phys. Rev. B **79**, 035407 (2009).
[17] S. Zhang *et al.* Phys. Rev. Lett. **102**, 023901 (2009).
[18] I. Tinoco and M. P. Freeman, J. Phys. Chem. **61**, 1196 (1957).
[19] D. L. Jaggard and N. Engheta, Electron. Lett. **25**, 173 (1989).
[20] F. Mariotte and N. Engheta, Radio Sci. **30**, 827 (1995).
[21] M. W. Horn *et al.*, Nanotechnology **15**, 303 (2004).
[22] C. W. Bunn, *Chemical Crystallography* (Oxford University Press, New York, 1945), p. 88.
[23] R. Williams, Phys. Rev. Lett. **21**, 342 (1968).
[24] V. A. Fedotov *et al.*, Phys. Rev. Lett. **97**, 167401 (2006).
[25] Y. I. Sirotin and M. P. Shaskolskaya, *Fundamentals of Crystal Physics* (Imported Publications, 1983).
[26] A. Roberts and R. C. McPhedran, IEEE Trans. Antennas Propagat. **36**, 607 (1988).
[27] E. Plum *et al.*, Appl. Phys. Lett. **93**, 191911 (2008).

A Micromachined Reconfigurable Metamaterial via Reconfiguration of Asymmetric Split-Ring Resonators

Yuan Hsing Fu, Ai Qun Liu, Wei Ming Zhu, Xu Ming Zhang, Din Ping Tsai, Jing Bo Zhang, Ting Mei, Ji Fang Tao, Hong Chen Guo, Xin Hai Zhang, Jing Hua Teng, Nikolay I. Zheludev, Guo Qiang Lo, and Dim Lee Kwong*

A micromachined reconfigurable metamaterial is presented, whose unit cell consists of a pair of asymmetric split-ring resonators (ASRRs); one is fixed to the substrate while the other is patterned on a movable frame. The reconfigurable metamaterial and the supporting structures (e.g., microactuators, anchors, supporting frames, etc.) are fabricated on a silicon-on-insulator wafer using deep reactive-ion etching (DRIE). By adjusting the distance between the two ASRRs, the strength of dipole–dipole coupling can be tuned continuously using the micromachined actuators and this enables tailoring of the electromagnetic response. The reconfiguration of unit cells endows the micromachined reconfigurable metamaterials with unique merits such as electromagnetic response under normal incidence and wide tuning of resonant frequency (measured as 31% and 22% for transverse electric polarization and transverse magnetic polarization, respectively). The reconfiguration could also allow switching between the polarization-dependent and polarization-independent states. With these features, the micromachined reconfigurable metamaterials may find potential applications in transformation optics devices, sensors, intelligent detectors, tunable frequency-selective surfaces, and spectral filters.

1. Introduction

Metamaterials are artificial composites which exhibit strong electric and magnetic responses to manipulate the amplitude, direction, polarization, wavelength, and phase of electromagnetic waves. By proper design of the unit cells, metamaterials have demonstrated amazing properties such as negative refraction,[1] super lens effect,[2] transformation optics,[3,4] chirality,[5] toroidal dipoles,[6] etc. Recently, reconfigurable metamaterials have attracted intense research interest since the active control of metamaterial characteristics is necessary to provide a flexible and versatile platform for mimicking fundamental physical effects.[7] In addition, the tunability could broaden the operation frequency range and enable reconfigurable metamaterial devices.[8,9] Tuning methods usually utilize capacitors/varactors,[10,11] semiconductors,[12] phase-change materials,[13,14] and ferromagnetic/ferroelectric materials.[15] However, most of these methods suffer from a limited tuning range as the variation of material properties is usually very small for the surrounding media and the metamaterial constituents. On the other hand, microelectromechanical systems (MEMS) technology has been well developed for fabrication and actuation of complicated micromechanical devices.[16,17] MEMS offers an ideal platform to directly reconfigure unit cells to overcome the limitations of the constituent materials.[18–20] As the unit cell is the fundamental building block of metamaterials, reconfiguration of the unit cell modifies the metamaterial properties and may promise unprecedented tunability. In our previous work,[20] a

Dr. Y. H. Fu, Prof. A. Q. Liu, Dr. W. M. Zhu, Prof. T. Mei, J. F. Tao
School of Electrical and Electronic Engineering
Nanyang Technological University
50 Nanyang Avenue, 639798, Singapore
E-mail: EAQLiu@ntu.edu.sg
Prof. X. M. Zhang
Department of Applied Physics
The Hong Kong Polytechnic University
Hung Hom, Kowloon, Hong Kong, P. R. China
Prof. D. P. Tsai
Department of Physics
National Taiwan University
1, Sec. 4, Roosevelt Road, Taipei 10617, Taiwan
Dr. H. C. Guo, Dr. X. H. Zhang, Dr. J. H. Teng
Institute of Materials Research and Engineering
3, Research Link, 117602, Singapore
Dr. Y. H. Fu, Dr. J. B. Zhang
Data Storage Institute
5, Engineering Drive 1, 117608, Singapore
Prof. N. I. Zheludev
Optoelectronics Research Centre
University of Southampton
Highfield, Southampton, SO17 1BJ, UK
Dr. G. Q. Lo, Dr. D. L. Kwong
Institute of Microelectronics
11 Science Park Road, 117685, Singapore

DOI: 10.1002/adfm.201101087

single split-ring resonator (SRR) was tuned by changing the gap between its two semisquare rings. Herein, two asymmetric split-ring resonators (ASRRs) are tuned by changing their separation distance, which dominates the coupling between both the electric and magnetic dipoles. The interactions between two adjacent ASRRs are demonstrated from the face-touch state to the back-touch state in real time. This reconfigurable metamaterial can be applied to many transmission-type applications which require normal incidence.

Two-dimensional (2D) metamaterials with one layer of metal pattern and another layer of dielectric substrate have been intensively studied experimentally thanks to their ease of fabrication.[21] However, a single layer of metal patterning makes it difficult to directly induce a magnetic response to normal incident light. An SRR with an asymmetric gap has been proposed as a paradigmatic design of a unit cell that would electrically induce the magnetic dipole.[22–24] The magnetic moment originates from the current loops in the fundamental inductive–capacitive (LC) resonant mode of the SRR. For this reason, the resonant frequency is strongly dependent on many factors that affect the current loops, such as the structure of a single SRR, the vertical coupling between stacked layers of SRRs,[25] and the lateral coupling of adjacent SRRs.[26–28] Among these factors, the lateral coupling of SRRs can be modified easily using micromachined actuators and also promises to be very efficient at tuning the metamaterial properties.

With this understanding, this paper demonstrates a reconfigurable metamaterial in which the unit cell is constructed using a pair of ASRRs. Previous work showed that induced magnetic-dipole resonance in the ASRR with two splits can only be excited by a normal incident wave when the polarization is perpendicular to the mirror line of the ASRR. This fact shows an important property of the "coherence" nature of the metamaterial, by adjusting the coupling between the ASRR.[24,29] Here, we investigate an ASRR with only one split and in which the symmetry is broken by displacing the gaps from the central line. Due to the asymmetry of the ASRR, a normal incident wave can excite a surface current loop to produce a magnetic dipole oscillation, regardless of the polarization direction of the normal incident wave. By adjusting the distance between two ASRRs using the micromachined actuators, the dipole–dipole couplings of both the magnetic field and the electric field are tuned simultaneously. These features provide the reconfigurable metamaterials with a unique merit of ability to wide tune the electromagnetic response.

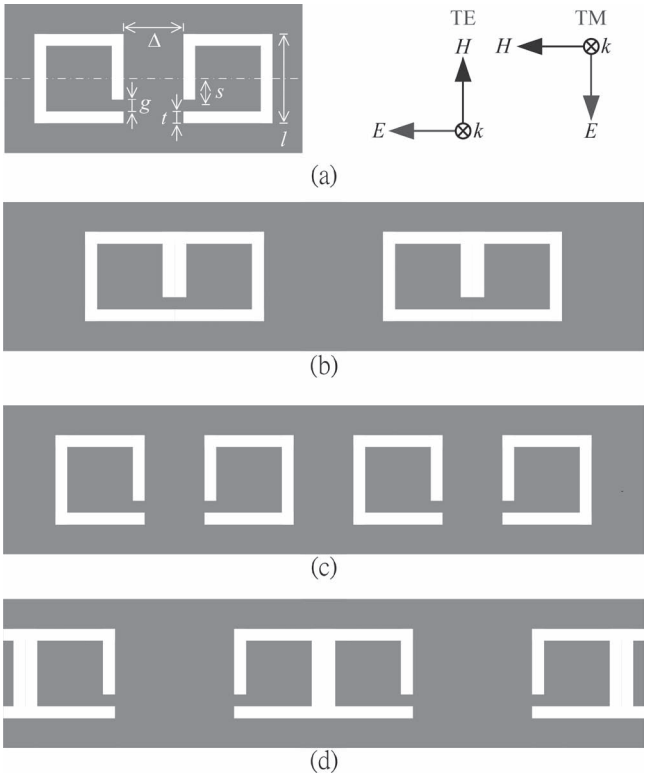

Figure 1. Schematic of the reconfigurable metamaterials. a) The gaps of the ASRRS are shifted from the central line by $s = 4.5$ μm. b–d) represent the unit cell in different configurations, b) for the face-touch state (i.e., $\Delta = 0$), c) for the separated state (i.e., $0 < \Delta < 20$ μm), and d) for the back-touch state (i.e., $\Delta = 20$ μm).

2. Results and Discussion

2.1. Design and Fabrication of the Unit Cell

The design of the unit cell for the reconfigurable metamaterial is shown in **Figure 1**a. The cell consists of a pair of square split rings with the split parts (i.e., the gaps) arranged opposite to each other. Asymmetry is achieved by displacing the gaps from the central line by $s = 4.5$ μm. As stated above, such asymmetry is essential to induce a magnetic dipole using the electric field component of normal incidence. The size of the unit cell is 50 μm × 25 μm ($L \times W$), and other dimensions are the sidewall length $l = 15$ μm, the width of the metal wire $t = 2$ μm, and the width of the gap $g = 2$ μm. The distance Δ between the paired ASRRs is an important tuning parameter since different configurations of the unit cell can be obtained by simply adjusting Δ. In an extreme case where $\Delta = 0$, the split rings touch face to face, which is called the face-touch configuration and is shown in Figure 1b. For $0 < \Delta < 20$ μm, the split rings are separated (called separated configuration) and their coupling strength varies with Δ. Figure 1c exemplifies a particular state of the separated configuration with $\Delta = 10$ μm. In another extreme case $\Delta = 20$ μm, the split rings touch back to back; this is called the back-touch configuration (Figure 1d). The diagrams in Figure 1b–d elucidate the key concept of micromachined reconfigurable metamaterials, namely, rearranging the metamaterial unit cell by simply displacing a part of the unit cell. For easy notation, the polarization of the incident wave is also indicated in Figure 1a. Transverse electric (TE) polarization state represents tthe case in which the electric field is perpendicular to the split side of the ring, while transverse magnetic (TM) occurs when the electric field is parallel to the split side.

The unit-cell design containing two oppositely arranged ASRRs has an intrinsic merit of high coupling between the two

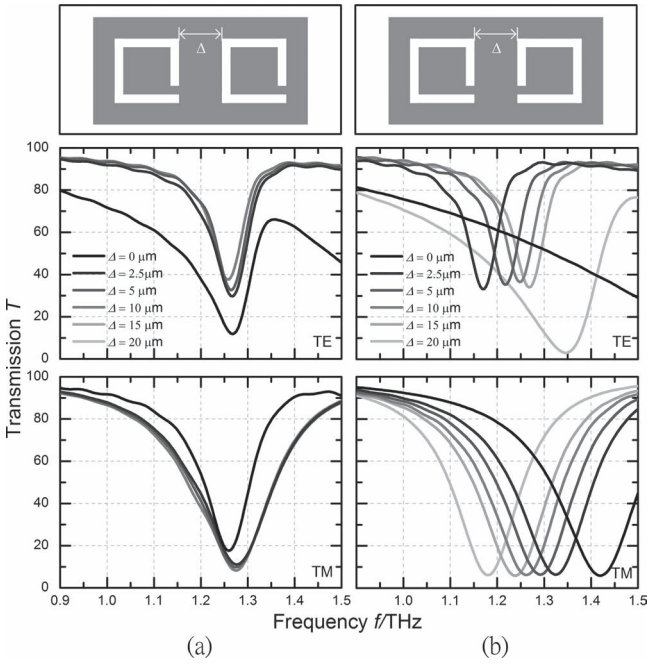

Figure 2. Transmission spectra of a) single ASRR and b) coupled ASRRs under TE- (upper row) and TM- (lower row) polarized incidence at various values of Δ. Δ was varied from 0 to 20 μm which is represented by the data curves from dark to light.

ASRRs and is thus expected to produce a wide tuning range, which is among the main interests of this work. For easy explanation of this feature, we compare this coupled ASRR design with another unit cell that is constructed by using two ASRRS with the same orientation, which equals to a single ASRR design (see **Figure 2**). In both designs, the coupling can be tuned by adjusting Δ. For the single ASRR design, resonant dips appear near 1.26 THz under the normal incidence of TE polarization (Figure 2a). However, the variation of Δ causes only a slight shift of the resonance frequency (0.6% at the maximum). Under the TM-polarized incidence, the shift of resonance dip is small also (0.8% at the maximum). Furthermore, changing Δ from 0 to 10 μm has the same effect as that of changing Δ from 20 to 10 μm due to the periodic symmetry of the unit cells, which further limits the tunability. In contrast, the coupled ASRR design exhibits very large tuning under either TE or TM incidence as shown in Figure 2b. For example, no LC-resonance dip occurs under TE polarization when Δ = 0 μm (see the upper panel of Figure 2b). We estimate that variation of Δ could cause > 20% shift of the resonance frequency, regardless of the polarization of incidence. This result verifies the large tunability of the coupled ASRRs and also shows the feasibility of reconfiguring the unit cells using the micromachined actuators.

The reconfigurable metamaterial and the supporting structures (e.g., microactuators, anchors, supporting frames, etc.) were fabricated on a silicon-on-insulator (SOI) wafer using deep reactive-ion etching (DRIE).[30] A close-up of the unit cell and an overview of the fabricated reconfigurable metamaterial are shown in **Figure 3**a and b, respectively. In the unit cell, one split ring is fixed while the other is movable. The fixed

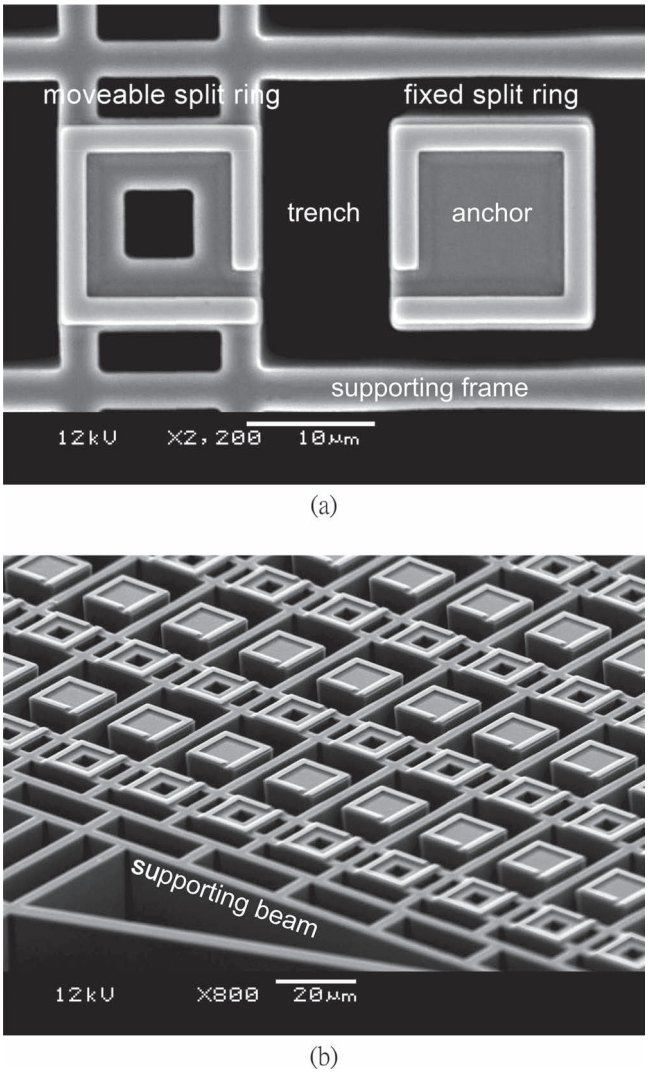

Figure 3. Scanning electron micrographs (SEMs) of the reconfigurable metamaterial. a) Close-up of the unit cell, which consists of a fixed split-ring resonator and a moveable ring. b) Overview of the reconfigurable metamaterial formed by an array of unit cells.

ring sits on an isolated anchor and the moveable one is on a floating frame connected to the comb-drive actuators with supporting beams. The split rings are formed by depositing and patterning an evaporated 500-nm aluminum layer. Some trenches surrounding the anchors are intentionally designed in to release the movable structures from the substrate and also provide space to move the supporting frame. The initial distance after fabrication is Δ = 10 μm. The reconfigurable metamaterial as shown in Figure 3b consists of 400 × 200 unit cells (footprint 1 × 1 cm); it employs two identical electrostatic comb-drive actuators on both sides for mechanically balanced translation of the supporting frame. Each comb-drive actuator provides a bidirectional in-plane translation following the actuation relationship $\Delta y = AV^2$, where Δy is the displacement, V the actuation voltage, and A = 0.05 μm V^{-2} is the actuation coefficient. The actuation range is from –10 to 10 μm, which corresponds to Δ = 0 to 20 μm.

2.2. Electromagnetic Response of the Reconfigurable Metamaterial

To characterize the electromagnetic response of the reconfigurable metamaterial, the transmission spectra of the metamaterials were measured using a terahertz time-domain spectrum (THz-TDS) system.[31] To understand the nature of the response, a simulation was also conducted using the finite diffraction-time domain (FDTD) solver. In the simulation, the electric conductivity of aluminum was chosen to be 2×10^7 S m^{-1} and the dielectric constant of the silicon substrate was 11.7. It is noted that although the surrounding media of the movable ASRR are different from those of the fixed ASRR due to the presence of the trenches and the supporting frame, the coupling effect is dominated by the relative positions between the ASRRs. In the numerical analysis, such substrate effect was taken into consideration.

The response to the TE normal incidence was first characterized. **Figure 4** shows both the measured and simulated transmission spectra in the frequency range of 0.9–1.5 THz for the TE polarization. The corresponding surface currents and magnetic-field components H_{normal} at resonance frequencies are also displayed on the right side of the spectra. Figure 4a represents the face-touch configuration and shows no LC resonance in the transmission spectrum. This absence can be explained by the observation that the surface currents on the two arms of the ASRR oscillate in parallel to the electric field and thus form no loop. Figure 4b shows the separated configuration in which Δ is tuned from 0 to 20 μm. In this configuration, circular surface current occurs on each ASRR, which results in two magnetic dipoles oscillating in phase. The quality factor (Q factor) of the resonance is approximately 13.8. When Δ = 2.5, 5, 10, and 15 μm, the resonant frequencies were positioned at 1.17, 1.21, 1.24, and 1.27 THz, respectively. An increase in Δ resulted in a blue shift of the resonant frequency. Figure 4c represents the back-touch configuration, and a broad resonance dip is present in the spectrum. It is observed that the surface currents on the contact sides (in the middle of the paired ASRRs) have near-zero amplitude, whereas those on the two arms oscillate in opposite directions and form a loop. The surface currents concentrate on the outside arms of the rings, which are similar to those of the asymmetric rings reported in previous work.[24]

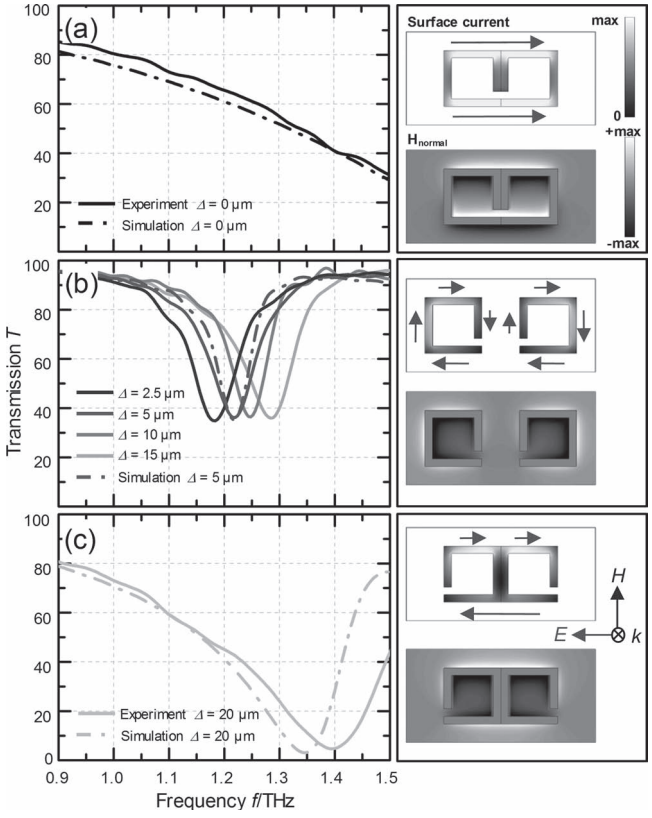

Figure 4. Transmission spectra for the TE polarization incident wave under the conditions of a) Δ = 0, b) Δ = 2.5, 5, 10, 15 μm (from dark to light) and c) Δ = 20 μm. The simulated surface currents and magnetic-field components H_{normal} are shown on the right side. The arrows and colors represent the directions and the intensities (the darker part shows the lower intensities and vice versa) of the surface currents (on the metal part), respectively. The maximum values of the surface current in (a), (b), and (c) were 0.015, 0.139, and 0.114 A m^{-1}, respectively. The maximum values of H_{normal} in (a), (b), and (c) were 0.012, 0.124, and 0.100 A m^{-1}, respectively. The values of the surface currents and H_{normal} were calculated assuming that the incident electric field was 1 V m^{-1}.

For TM polarization, the transmission spectra were also measured and simulated as shown in **Figure 5**. Because the electric field is oriented along a mirror plane for the ASRRs, the resonance is purely due to the electrical response, which is similar to the so-dubbed electric split-ring resonators (eSRRs).[32] In different unit-cell configurations, the circular surface currents are always excited but the two magnetic dipoles maintain a π phase shift, which results in a net zero magnetic dipole. However the frequency tuning is associated with the interaction of the two antiparallel magnetic dipoles. The resonant dips for Δ = 0, 2.5, 5, 10, 15, and 20 μm appear at 1.42, 1.32, 1.29, 1.24, 1.22, and 1.16 THz, respectively. The resonant frequency tends to have a red shift, which is opposite to the blue shift for the TE polarization, with increasing values of Δ. The Q factor of TM polarization (electric dipole resonance) for the separated configuration is approximately 7.8, which is approximately half of the Q factor of the TE polarization (LC resonance) under the same conditions.

2.3. Real-Time Tuning of Electromagnetic Response

To demonstrate the real-time tuning capability of the micromachined reconfigurable metamaterial, the tuning of the resonance dip under dynamic actuation was also characterized. The tuning time from minimum to maximum distance was experimentally determined to be about 500 μs, which corresponds to an operational frequency of 1 kHz. The Doppler effect is trivial in this case since the speed (0.04 m s^{-1}) was ten orders of magnitude smaller than the speed of light. Therefore, the responses in the real-time tuning process can be represented by the spectra of different static states. The simulated contour maps of the transmission at different time intervals are shown in **Figure 6** for both TE and TM polarization. It can be seen clearly that with the increase of time (and consequent larger values of Δ), the belt of resonance dips curves upwards for the TE polarization but bends down for TM polarization. Moreover, the belt of resonance dips for the TE polarization is

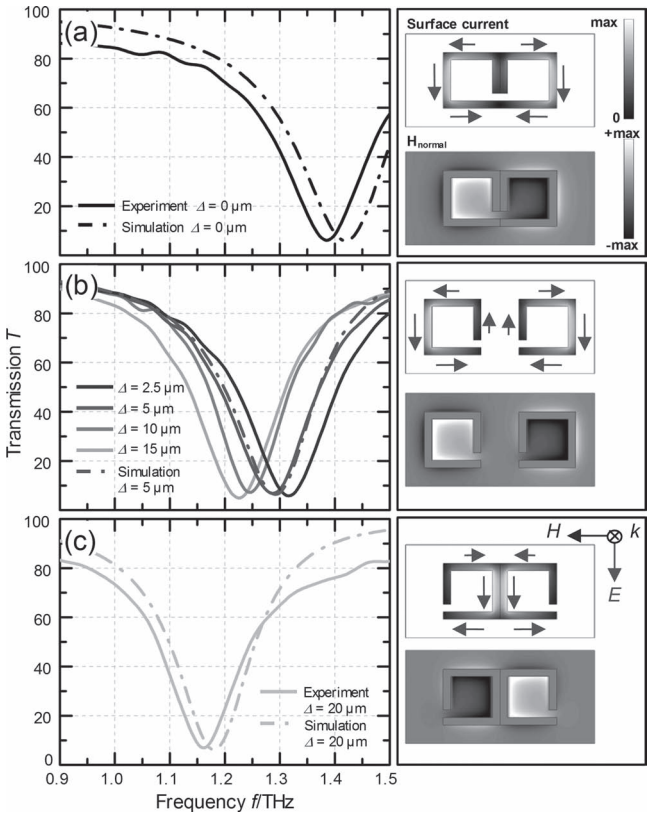

Figure 5. Transmission spectra for the TM polarization incident wave at a) $\Delta = 0$, b) $\Delta = 2.5$, 5, 10, 15 μm (from dark to light), and c) $\Delta = 20$ μm. The simulated surface currents and magnetic field components H_{normal} are shown on the right side. The arrows and the colors represent the directions and the intensities (the darker part shows the lower intensities and vice versa) of the surface currents (on the metal). The maximum values of the surface currents in (a), (b), and (c) are 0.103, 0.096, and 0.105 A m^{-1}, respectively. The maximum values of H_{normal} in (a), (b), and (c) are 0.092, 0.085, and 0.094 A m^{-1}, respectively. The values of the surface currents and H_{normal} were calculated assuming that the incident electric field was 1 V m^{-1}.

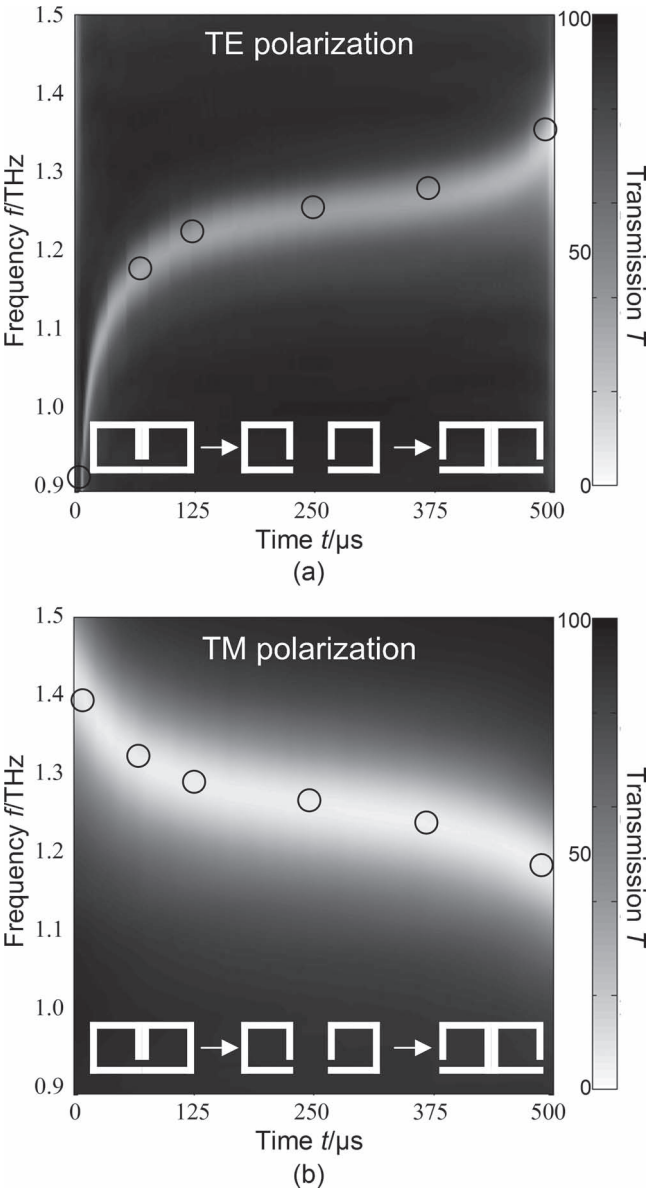

Figure 6. Real-time tuning of the transmission spectra as represented by the contour maps of transmission as functions of time and frequency for a) TE polarization and b) TM polarization. The circles represent the measured data points of resonance frequencies shown in Figure 4 and Figure 5. The insets indicate the changes of unit-cell configurations.

narrower (which corresponds to a higher Q factor) than that for the TM polarization. This distinction can be attributed to the differences in the excited electric and magnetic dipoles and the dipole–dipole coupling. More specifically, for the TE polarization the two electric dipoles are excited antiparallel at the gap whereas the two magnetic dipoles are in-phase in the center of the ASRR (see Figure 4b); for the TM polarization the opposite is true (see Figure 5b). The electric dipole coupling dominates the frequency shift when the tuning time is less than 250 μs, and the magnetic dipole coupling dominates thereafter. For transverse dipole–dipole coupling, the interaction of the parallelly oriented electric dipoles (in TM polarization) decreases the resonance frequency with increasing Δ.[27] The electric dipole–dipole coupling dominates this interaction, which results in the downwards trend of the belt of resonance over a tuning time from 0 to 250 μs, as shown in Figure 6b. For a tuning time between 250 to 500 μs, the two antiparallelly oriented magnetic dipoles become closer (in TM polarization), which tends to further decrease the resonance frequency. When the tuning time is approximately 250 μs, both the electric and magnetic dipole coupling are relatively weak, which results in a slight tuning of resonance frequency. Unlike with TM polarization, the electric dipoles are antiparallelly oriented while the magnetic dipoles are parallelly oriented, which results in a blue shift of the resonance frequency. For TE polarization, the tuning range of the resonance frequency is from 0.98 to 1.28 THz, which corresponds to a change of approximately 31% of the initial resonance frequency. For TM polarization, the tuning range of the resonance frequency is from 1.15 to 1.40 THz (approximately 22%). For easy comparison, the measured resonant dips (see Figure 4 and Figure 5) are superimposed onto

the contour maps. A reasonable agreement of the resonance positions is achieved between the simulation and the measurement. It is interesting to see that, at a particular time interval of 250 μs (corresponding to $\Delta = 10$ μm), the resonant dips of the TE and TM polarization overlap. This overlap is of profound importance since the response is polarization independent; it demonstrates the unique potential of the reconfigurable metamaterials in switching from a polarization-dependent state to a polarization-independent state for electromagnetic response, although the Q factors are not the same due to the asymmetry of the gaps in the split rings.

3. Conclusions

A reconfigurable metamaterial is presented by reconfiguring the unit cell, which consists of a pair of asymmetric split-ring resonators. The coupling distance between the pair of ASRRs is tuned by bidirectional micromachined actuators. Due to the asymmetry of the ASRRs, the inductive-capacitive resonance can be excited by a normal incident terahertz wave. The reconfigurable metamaterial not only has a wide tuning range of the resonance frequency up to 31% and 22% for the TE and the TM polarization, respectively, but also produces a high quality-factor resonance and an in-phase magnetic-dipole oscillation for the TE polarization. In the process of dynamic tuning, the reconfigurable metamaterial can be switched from the polarization-dependent state to the polarization-independent state. The metamaterial may find potential applications in transformation optics devices, sensors, intelligent detectors, tunable frequency-selective surfaces, and spectral filters.

4. Experimental Section

The transmission spectra characterization of the reconfigurable metamaterials was performed using a terahertz time-domain spectrum (THz-TDS) system. 100-fs optical pulses centered at 800 nm at a repetition rate of 76 MHz from a mode-locked Ti:sapphire laser were focused onto a photoconductive antenna of low-temperature-grown GaAs to generate the terahertz wave. A Fourier transform was used to extract the frequency spectrum from the time-domain data. A time range of the time-domain data was chosen to exclude Fabry-Pérot fringes that arise from the substrate. The transmission spectra were normalized with respect to the transmission of the pure silicon substrate (i.e., T_{sample}/T_{Si}).

Acknowledgements

This work was supported by the Science & Engineering Research Council (SERC) of A*STAR Singapore with project Metamaterials Programme: Nanoplasmonics (Grant No. SERC 092 154 0098) and EPSRC (UK).

Received: May 16, 2011
Revised: June 21, 2011
Published online: August 1, 2011

[1] D. R. Smith, D. C. Vier, N. Kroll, S. Schultz, *Appl. Phys. Lett.* **2000**, *77*, 2246.
[2] N. Fang, X. Zhang, *Appl. Phys. Lett.* **2003**, *82*, 161.
[3] U. Leonhardt, *Science* **2006**, *312*, 1777.
[4] J. B. Pendry, D. Schurig, D. R. Smith, *Science* **2006**, *312*, 1780.
[5] A. V. Rogacheva, V. A. Fedotov, A. S. Schwanecke, N. I. Zheludev, *Phys. Rev. Lett.* **2006**, *97*, 177401.
[6] T. Kaelberer, V. A. Fedotov, N. Papasimakis, D. P. Tsai, N. I. Zheludev, *Science* **2010**, *330*, 1510.
[7] N. I. Zheludev, *Science* **2010**, *328*, 582.
[8] H. T. Chen, W. J. Padilla, J. M. O. Zide, A. C. Gossard, A. J. Taylor, R. D. Averitt, *Nature* **2006**, *444*, 597.
[9] H. T. Chen, J. F. O'Hara, A. K. Azad, A. J. Taylor, R. D. Averitt, D. B. Shrekenhamer, W. J. Padilla, *Nat. Photonics* **2008**, *2*, 295.
[10] K. Aydin, E. Ozbay, *J. Appl. Phys.* **2007**, *101*, 024911.
[11] I. Gil, J. Garcia-Garcia, J. Bonache, F. Martin, M. Sorolla, R. Marques, *Electron. Lett.* **2004**, *40*, 1347.
[12] K. A. Boulais, D. W. Rule, S. Simmons, F. Santiago, V. Gehman, K. Long, A. Rayms-Keller, *Appl. Phys. Lett.* **2008**, *93*, 043518.
[13] M. J. Dicken, K. Aydin, I. M. Pryce, L. A. Sweatlock, E. M. Boyd, S. Walavalkar, J. Ma, H. A. Atwater, *Opt. Express* **2009**, *17*, 18330.
[14] Z. L. Samson, K. F. MacDonald, F. De Angelis, B. Gholipour, K. Knight, C. C. Huang, E. Di Fabrizio, D. W. Hewak, N. I. Zheludev, *Appl. Phys. Lett.* **2010**, *96*, 143105.
[15] L. Kang, Q. Zhao, H. J. Zhao, J. Zhou, *Opt. Express* **2008**, *16*, 8825.
[16] H. Cai, A. Q. Liu, X. M. Zhang, J. Tamil, D. Y. Tang, Q. X. Zhang, C. Lu, *Appl. Phys. Lett.* **2008**, *92*, 031105.
[17] W. M. Zhu, X. M. Zhang, A. Q. Liu, H. Cai, T. Jonathan, T. Bourouina, *Appl. Phys. Lett.* **2008**, *92*, 251101.
[18] H. Tao, A. C. Strikwerda, K. Fan, W. J. Padilla, X. Zhang, R. D. Averitt, *Phys. Rev. Lett.* **2009**, *103*, 147401.
[19] W. M. Zhu, H. Cai, T. Mei, T. Bourouina, J. F. Tao, G. Q. Lo, D. L. Kwong, A. Q. Liu, *IEEE Int. Conf. on Micro Electro Mech. Syst., Tech. Dig., 23rd (Hong Kong)* **2010**, 196.
[20] W. M. Zhu, A. Q. Liu, X. M. Zhang, D. P. Tsai, T. Bourouina, J. H. Teng, X. H. Zhang, H. C. Guo, H. Tanoto, T. Mei, G. Q. Lo, D. L. Kwong, *Adv. Mater.* **2011**, *23*, 1792.
[21] W. Withayachumnankul, D. Abbott, *IEEE Photonics J.* **2009**, *1*, 99.
[22] J. B. Pendry, A. J. Holden, D. J. Robbins, W. J. Stewart, *IEEE Trans. Microwave Theory Tech.* **1999**, *47*, 2075.
[23] R. Singh, I. A. I. Al-Naib, M. Koch, W. L. Zhang, *Opt. Express* **2010**, *18*, 13044.
[24] V. A. Fedotov, M. Rose, S. L. Prosvirnin, N. Papasimakis, N. I. Zheludev, *Phys. Rev. Lett.* **2007**, *99*, 147041.
[25] N. Liu, H. Liu, S. N. Zhu, H. Giessen, *Nat. Photonics* **2009**, *3*, 157.
[26] M. Decker, S. Linden, M. Wegener, *Opt. Lett.* **2009**, *34*, 1579.
[27] N. Feth, M. Konig, M. Husnik, K. Stannigel, J. Niegemann, K. Busch, M. Wegener, S. Linden, *Opt. Express* **2010**, *18*, 6545.
[28] I. Sersic, M. Frimmer, E. Verhagen, A. F. Koenderink, *Phys. Rev. Lett.* **2009**, *103*, 213902.
[29] N. Papasimakis, V. A. Fedotov, Y. H. Fu, D. P. Tsai, N. I. Zheludev, *Phys. Rev. B* **2009**, *80*, 041102.
[30] J. Li, A. Q. Liu, Q. X. Zhang, *Sens. Actuators A* **2006**, *125*, 494.
[31] H. C. Guo, X. H. Zhang, W. Liu, A. M. Yong, S. H. Tang, *J. Appl. Phys.* **2009**, *106*, 063104.
[32] D. Schurig, J. J. Mock, D. R. Smith, *Appl. Phys. Lett.* **2006**, *88*, 041109.

NANO LETTERS

LETTER

pubs.acs.org/NanoLett

Reconfigurable Photonic Metamaterials

J. Y. Ou,*,† E. Plum,*,† L. Jiang,‡ and N. I. Zheludev*,†

†Optoelectronics Research Centre and Centre for Photonic Metamaterials and ‡School of Engineering Sciences, University of Southampton, SO17 1BJ, United Kingdom

ABSTRACT: We introduce mechanically reconfigurable photonic metamaterials (RPMs) as a flexible platform for realizing metamaterial devices with reversible and large-range tunable characteristics in the optical part of the spectrum. Here we illustrate this concept for a temperature-driven RPM exhibiting reversible relative transmission changes of up to 50%.

KEYWORDS: Tunable metamaterial, reconfigurable nanostructure, bimaterial, nanophotonics

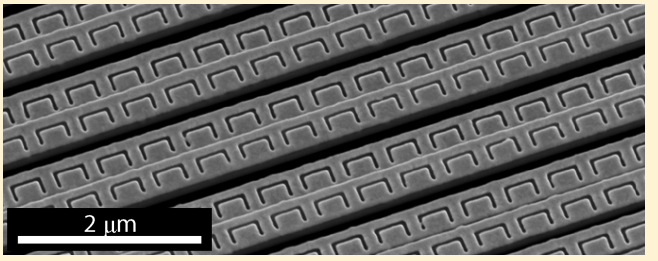

Switchable and tunable metamaterials are expanding areas of research driven by the development of nanophotonic all-optical data processing circuits, optical memory, smart surfaces, adaptable detection, imaging systems, and transformation optics devices.[1] Several avenues are being explored. Metamaterials where metal nanostructures are hybridized with nonlinear and switchable layers provide a way to achieve high-contrast optical switching and enhanced nonlinear responses. Indeed, a change in the refractive index or absorption in the hybridized material will modify the plasmon spectrum of the nanostructure. This can lead to a strong change in the resonant transmission and reflection characteristics of the hybrid structure. For instance the ability to change a metamaterial's response at terahertz frequencies by injection or optical generation of free carriers in a semiconductor substrate has been reported.[2,3] A layer of single-wall semiconductor carbon nanotubes deposited on a metamaterial shows an order of magnitude higher nonlinearity than the already extremely strong response of the nanotubes themselves due to resonant plasmon-exciton interactions.[4] Nanoscale metamaterial electro-optical switches using phase change chalcogenide glass[5] and vanadium dioxide[6] have already been demonstrated. Graphene is another favorite that promises to add electro-optical capability to metamaterials in particular in the infrared and terahertz domains by exploiting the spectral shift of the electromagnetic response that is driven by applied voltage.[7,8]

When high-speed switching is not the prime objective, metamaterials can be reliably and reversibly controlled by microelectromechanical (MEMS) actuators repositioning parts of the meta-molecules. MEMS-based metamaterials can provide continuous tuning, rather than steplike switching associated with phase-change materials and in contrast to approaches exploiting optical nonlinearities they are compatible with low intensities. This has been convincingly demonstrated for terahertz and far-infrared metamaterials consisting of specially designed deformable meta-molecules.[9,10] Reconfigurable photonic metamaterials (RPMs) operating in the visible and near-infrared parts of the spectrum require the development of components and actuators operating on the scale of a few tens of nanometers. Here, we demonstrate that RPM nanostructures based on metal-dielectric films of nanoscale thickness provide a generic platform for achieving large-range continuous reversible tuning of metamaterial properties in the optical part of the spectrum. By placing metamaterial resonators (meta-molecules) on a thermally reconfigurable bimaterial scaffold we control intermetamolecular coupling leading to a profound reversible change of the metamaterial's transmission of up to 50%.

The basic approach is illustrated by Figure 1a. Tunability will be introduced in almost any metamaterial system, if the distance and thus the coupling between neighboring meta-molecules can be controlled. For example, this may be achieved by placing the meta-molecules on alternating reconfigurable and nonreconfigurable support structures. This approach has two key advantages: (i) As it does not depend on the details of the meta-molecule design, it is applicable to a huge range of metamaterial patterns. (ii) It eliminates the need for reconfigurable elements on the size scale of the meta-molecules, which would be extremely challenging to achieve for the optical part of the spectrum.

As illustrated by Figure 1b, thermally reconfigurable support structures can be fabricated from a bilayer consisting of two materials with different thermal expansion coefficients, for example a plasmonic metal and a dielectric. Bending of the bimaterial structure will be caused by differential thermal expansion of the constituent materials. On the other hand, nonreconfigurable support structures can consist of either a single material or bending may be suppressed by using a symmetric sequence of layers such as metal-dielectric-metal.

Here we illustrate this concept for the reconfigurable photonic metamaterial shown in Figure 2. It consists of nanoscale "C"-shaped aperture plasmonic resonators (split rings) supported by alternating thermally reconfigurable and nonreconfigurable[11] bridges. The entire structure was fabricated by focused ion beam milling from a 100 nm thick silicon nitride membrane covered by 50 nm thick thermally evaporated gold layers on both sides. In order to create reconfigurable and nonreconfigurable support structures, the gold underlayer was removed from every second

Received: March 9, 2011
Revised: April 4, 2011
Published: April 11, 2011

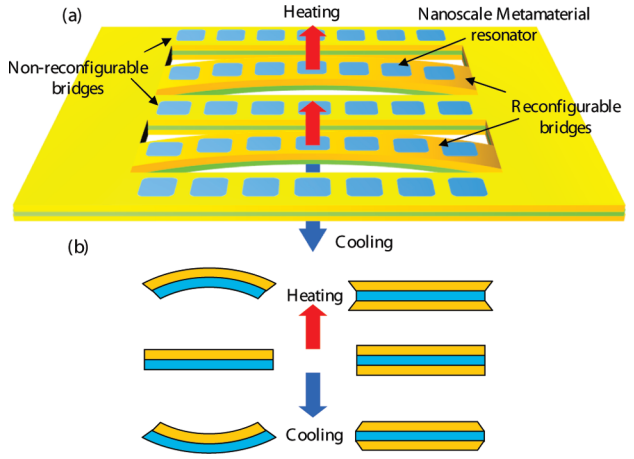

Figure 1. Thermally controlled metamaterial scaffold. (a) Thermally tunable metamaterial support structure consisting of alternating reconfigurable and nonreconfigurable bimaterial bridges. (b) Bilayered support beams consisting of materials with large (orange, for e.g., gold) and small (blue, e.g., silicon nitride) thermal expansion coefficients will bend in response to temperature changes, while bending is inhibited for a symmetric layer sequence.

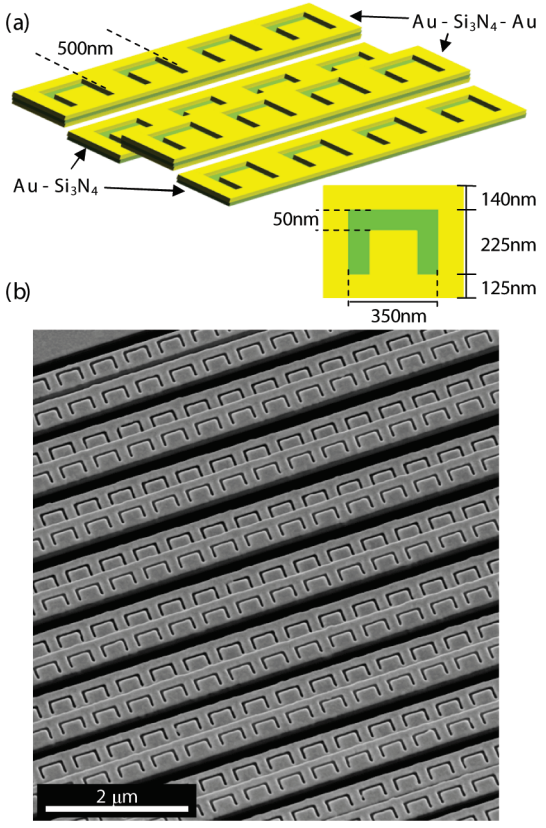

Figure 2. Thermally controlled reconfigurable photonic metamaterial. (a) Schematic with dimensions. (b) Scanning electron micrograph taken at room temperature.

bridge. Next the "C"-slit plasmonic resonator pattern was milled into the gold layer covering the front of the membrane. And finally the metamaterial membrane was cut into 50 μm long and 390 nm wide bridges separated by 110 nm gaps.

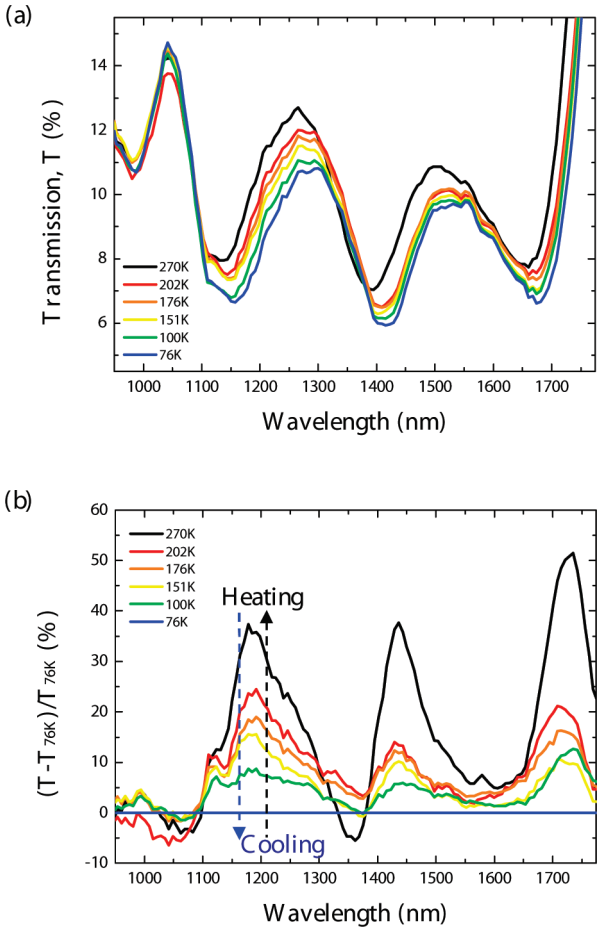

Figure 3. Temperature dependence of the reconfigurable metamaterial's transmission characteristics for waves polarized perpendicular to the supporting beams. (a) Transmission spectra measured at different temperatures. (b) Relative change of the metamaterial transmission normalized to a reference temperature of 76 K.

Because of the large thermal expansion coefficient of gold (14.4×10^{-6}/K), which exceeds that of silicon nitride (2.8×10^{-6}/K) by a factor of 5, the metamaterial bridges without gold underlayer will arch upward (downward) upon heating (cooling),[12] see the lowered bridges in Figure 2. On the other hand, thermal bending is suppressed for the more symmetric bridges with gold underlayer, which are raised in the scanning electron micrograph. We note that the metamaterial properties are position-dependent toward the end of the support structures, where the spacing between the metamaterial resonators gradually decreases. Therefore we investigated the central part of the structure, which is homogeneous and experiences the largest temperature-dependent changes.

The metamaterial's temperature-dependent transmission spectrum, which is shown in Figure 3a, was measured using a microspectrophotometer (CRAIC Technologies) equipped with a cryostatic sample stage. It reveals that the structure has resonant transmission minima in the near-infrared at about 1140, 1400, and 1670 nm. The resonant modes themselves are quite complex excitations of the coupled system of "C"-slit resonators and the gold underlayer on every second bridge. Importantly, the resonant properties of this system strongly depend on the coupling between neighboring bridges and therefore a continuous change of the physical configuration

dx.doi.org/10.1021/nl200791r |*Nano Lett.* 2011, 11, 2142–2144

of the nanostructure drives a dramatic change of its optical properties.

Figure 3b shows the change of the reconfigurable metamaterial's transmission characteristics relative to a reference temperature of 76 K. As the metamaterial is heated to 270 K, we observe dramatic 37, 38, and 51% relative increases of its transmission near its resonant transmission minima at 1180, 1435, and 1735 nm, respectively. These remarkably large relative increases in transmission are due to a 20 nm blue shift of the metamaterial spectrum combined with an overall transmission increase as the plasmonic resonators are moved closer together by differential thermal expansion driven by the ambient temperature increase. Importantly, as the structure is cooled back to its initial temperature of 76 K these changes of its transmission spectrum are reversed, indicating that the reconfigurable metamaterial returned to its initial state.

For practical applications, it may be important to achieve large-range tuning of metamaterial properties with much smaller temperature changes. This may be achieved with longer and thinner reconfigurable support structures and optimized material choices and layer thicknesses, as the mechanical tuning range of the reconfigurable bimaterial beams is proportional to $\Delta T \Delta\alpha L/t$, where ΔT and $\Delta\alpha$ are the temperature and thermal expansion coefficient differences and L/t is the length/thickness aspect ratio of the support structures. We chose gold for its good plasmonic properties and silicon nitride for its easy availability in form of membranes of nanoscale thickness. However, silicon nitride could be replaced by glass, which has a significantly smaller thermal expansion coefficient of only 0.4×10^{-6}/K.[12] Furthermore, intermetamolecular coupling could be enhanced by placing the supporting beams closer together and the relative thermal displacement of neighboring resonators could be doubled by alternating metal-on-dielectric and dielectric-on-metal reconfigurable structures, which would bend in opposite directions.

In summary, we show that reconfigurable photonic metamaterials provide a flexible platform for the realization of tunable metamaterials for the optical part of the spectrum. By placing nanoscale plasmonic resonators with useful functionalities at optical frequencies on reconfigurable support structures, their interaction can be controlled, which leads to large-range tunability of the system's electromagnetic properties. Potential applications of this generic approach include optical temperature sensors, tunable spectral filters, switches, modulators and any other planar metamaterial device where tunability is required or desirable. Reconfigurable photonic metamaterials can be prototyped by focused ion beam milling or electron beam lithography and could be mass-produced by standard semiconductor manufacturing techniques. Specifically, we have realized a thermally controlled reconfigurable photonic metamaterial exhibiting reversible relative changes in transmission of up to 50%.

AUTHOR INFORMATION

Corresponding Author

*E-mail: (J.Y.O.) jo2c09@orc.soton.ac.uk; (E.P.) erp@orc.soton.ac.uk; (N.I.Z.) niz@orc.soton.ac.uk.

ACKNOWLEDGMENT

The authors are grateful to S. M. Spearing for useful discussions on MEMS. This work is supported by the U.S. Office of Naval Research (grant N000141110474), The Leverhulme Trust, The Royal Society and the U.K.'s Engineering and Physical Sciences Research Council through the Metamaterials Programme Grant.

REFERENCES

(1) Zheludev, N. I. *Opt. Photonics News* **2011**, *22*, 30–35.
(2) Chen, H.-T.; Padilla, W. J.; Zide, J. M. O.; Gossard, A. C.; Taylor, A. J.; Averitt, R. D. *Nature* **2006**, *444*, 597.
(3) Kanda, N.; Konishi, K.; Kuwata-Gonokami, M. *Opt. Lett.* **2009**, *34*, 3000.
(4) Nikolaenko, A. E.; Angelis, F. D.; Boden, S. A.; Papasimakis, N.; Ashburn, P.; Fabrizio, E. D.; Zheludev, N. I. *Phys. Rev. Lett.* **2010**, *104*, 153902.
(5) Sámson, Z. L.; MacDonald, K. F.; Angelis, F. D.; Gholipour, B.; Knight, K.; Huang, C.-C.; Fabrizio, E. D.; Hewak, D. W.; Zheludev, N. I. *Appl. Phys. Lett.* **2010**, *96*, 143105.
(6) Driscoll, T.; Kim, H. T.; Chae, B. G.; Kim, B. J.; Lee, Y. W.; Jokerst, N. M.; Palit, S.; Smith, D. R.; Ventra, M. D.; Basov, D. N. *Science* **2009**, *325*, 1518.
(7) Wang, F.; Zhang, Y.; Tian, C.; Girit, C.; Zettl, A.; Crommie, M.; Shen, Y. R. *Science* **2008**, *320*, 206.
(8) Zheludev, N. I. *Science* **2010**, *328*, 582–583.
(9) Tao, H.; Strikwerda, A. C.; Fan, K.; Padilla, W. J.; Zhang, X.; Averitt, R. D. *Phys. Rev. Lett.* **2009**, *103*, 147401.
(10) Zhu, W. M.; Liu, A. Q.; Zhang, X. M.; Tsai, D. P.; Bourouina, T.; Teng, J. H.; Zhang, X. H.; Guo, H. C.; Tanoto, H.; Mei, T.; Lo, G. Q.; Kwong, D. L. *Adv. Mater.* **2011**, in press, DOI:10.1002/adma.201004341.
(11) Because of the patterned and unpatterned gold layers on their front and back, the "non-reconfigurable" support structures will bend slightly in the opposite direction to the "reconfigurable" support structures in response to changes of the ambient temperature.
(12) Prasanna, S.; Spearing, S. M. *J. Microelectromech. S.* **2007**, *16*, 248–259.

nature COMMUNICATIONS

ARTICLE

Received 2 Nov 2011 | Accepted 28 Mar 2012 | Published 15 May 2012

DOI: 10.1038/ncomms1805

Giant nonlinear optical activity in a plasmonic metamaterial

Mengxin Ren[1,2], Eric Plum[2], Jingjun Xu[1] & Nikolay I. Zheludev[2]

In 1950, a quarter of a century after his first-ever nonlinear optical experiment when intensity-dependent absorption was observed in uranium-doped glass, Sergey Vavilov predicted that birefringence, dichroism and polarization rotatory power should be dependent on light intensity. It required the invention of the laser to observe the barely detectable effect of light intensity on the polarization rotatory power of the optically active lithium iodate crystal, the phenomenon now known as the nonlinear optical activity, a high-intensity counterpart of the fundamental optical effect of polarization rotation in chiral media. Here we report that a plasmonic metamaterial exhibits nonlinear optical activity 30 million times stronger than lithium iodate crystals, thus transforming this fundamental phenomenon of polarization nonlinear optics from an esoteric phenomenon into a major effect of nonlinear plasmonics with potential for practical applications.

[1]Key Laboratory of Weak Light Nonlinear Photonics, Nankai University, Tianjin 300457, China. [2]Optoelectronics Research Centre and Centre for Photonic Metamaterials, University of Southampton, SO17 1BJ, UK. Correspondence and requests for materials should be addressed to E.P. (email: erp@orc.soton.ac.uk) or to N.I.Z.(email: niz@orc.soton.ac.uk).

Since its discovery by François J.D. Arago in 1811 (ref. 1), optical activity, that is the ability to rotate the polarization state of light, has acquired great importance in spectroscopy, analytical chemistry, crystallography and molecular biology, and it is associated with the biochemistry of life[2]. It is now well understood that the effect is linked to chirality. In dissipative media optical activity manifests itself as circular birefringence, leading to polarization rotation, and circular dichroism, that is, differential transmission of circularly polarized waves, that yields a change of the degree of ellipticity of the propagating wave. In contrast to the Faraday effect, which causes polarization rotation in the presence of static magnetic fields, polarization rotation due to natural optical activity is reciprocal and it does not distinguish between opposite directions of wave propagation.

The dependence of optical activity on the intensity of light was discussed by Vavilov in 1950 (ref. 3), a quarter of a century after the first effect of light self-action, the intensity-dependent absorption, was observed in uranium-doped glass[4]. The symmetry, wave propagation and quantum mechanical description of the phenomenon that later acquired the name of nonlinear optical activity (NOA) was then rigorously derived[5–11].

Observation of NOA due to the fast electronic mechanism of nonlinearity became possible in 1979, using a high-intensity single-mode nanosecond-pulsed laser and the natural crystal of lithium iodate that is simultaneously a highly nonlinear and strongly optically active medium[12] (Fig. 1a). Shortly after that, transient pump-probe measurements of NOA were performed in the chiral cholesteric phase of a liquid crystal exploiting the thermal mechanism of nonlinearity[13]. Thermal NOA was also seen in optically active crystals[14–16]. Since then NOA has been observed in a number of chiral liquids[17–20]. Nevertheless, the effect remained challenging to detect, making it unsuitable for routine practical applications, even in spectroscopy.

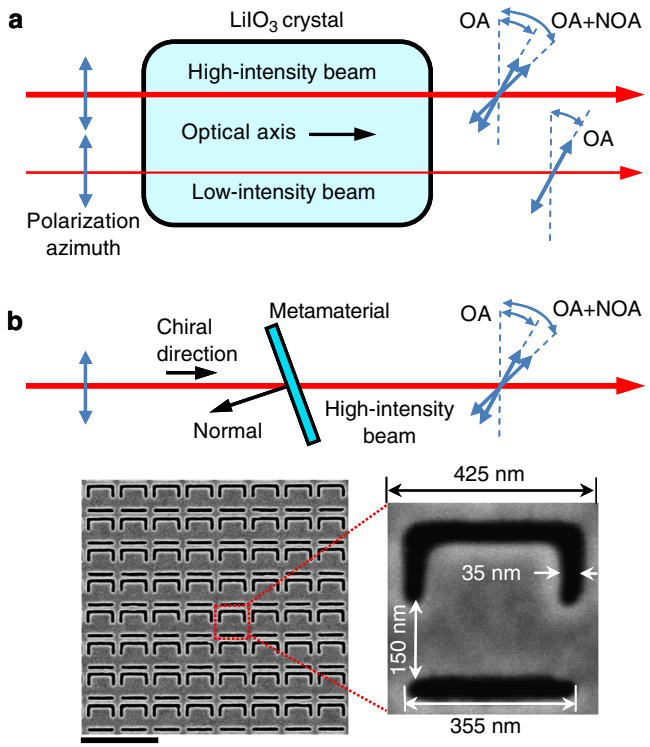

Figure 1 | Nonlinear optical activity. (**a**) To observe NOA in 1979 in a $LiIO_3$ crystal, intensity-dependent change of the polarization azimuth of about 0.02° was recovered on a background of 8,000° of natural rotation by comparing the polarization state in high-and-low intensity channels using a pulsed laser[12]. (**b**) Observation of NOA in a gold plasmonic metamaterial along a chiral direction, where nonlinearity is resonantly enhanced by nanoscale confinement of light. The scanning electron micrograph shows a fragment of the gold nanostructure (1-μm scale bar) and detailed dimensions of a single meta-molecule.

Although NOA in natural media was weak, hopes have been growing that a stronger effect could be found in artificial media. Indeed, an observation of optical activity in artificial media (twisted jute) in the millimeter wave part of the spectrum was reported by J.Bose as far back as 1898 (ref. 21). Recently, with the development of metamaterials (periodic media structured on the subwavelength scale), it has become possible to design optimized photonic structures with specific optical activity orders of magnitude larger than in natural media[22–25]. It was found, for instance, that artificial circular birefringence could be so strong that, whereas it is normally a correction to the refractive index, in some metamaterials it makes the refractive index negative for one circular polarization[26,27]. Moreover, recent experiments in waveguides revealed that a chiral inclusion containing a varactor nonlinear element forces a strong intensity-dependent rotation of the polarization state of microwave radiation and exhibits asymmetric transmission[28]. At the same time, resonant local field enhancement in plasmonic metamaterials can dramatically amplify the nonlinear response of hybridized materials, such as silicon[29,30] and carbon nanotubes[31], and even the metal forming the metamaterial framework itself[32,33].

The phenomenon of natural optical activity is inextricably linked to chirality. In many optically active media, chirality resides in the left–right asymmetry of the constituent components of the medium. For instance, a liquid consisting of only one form of chiral molecules, that is, molecules that are not congruent with their mirror image, is likely to exhibit optical activity. Here the best known natural example is sugar solution where optical activity is routinely used to measure the concentration of the syrup. Optical activity may also result from chiral arrangements of non-chiral molecules, as it may be found in crystals of quartz or lithium iodate. Chirality can also emerge from the mutual arrangement of the beam of light and the medium, creating what is known in crystallography as a screw direction. For instance a regular array of oriented molecules that are not chiral in their own right, could make an arrangement with a beam of light that lacks mirror symmetry and shows optical activity[34,35]. In general, only crystals whose point group contains no inversion centre could have screw directions. Polarization rotation in certain symmetric crystal classes is underpinned by this mechanism of optical activity[36], which is also routinely observed in liquid crystals[37] and metamaterials[38]. True circular birefringence and dichroism can be found in these cases.

Here we report that a plasmonic metamaterial exhibits a huge NOA in the optical part of the spectrum. It is 30 million times stronger than in the lithium iodate crystal[12]. This colossal magnitude of the nonlinear polarization effect was achieved by combining strong metamaterial optical activity due to extrinsic chirality with strong metamaterial optical nonlinearity: in this artificial medium, the figure of merit that represents specific nonlinear polarization rotation (° per cm) per unit of optical intensity (W cm^{-2}) is 3×10^{-4} °cm W^{-1} (compare with 10^{-11} °cm W^{-1} for lithium iodate). As a result, nonlinear rotation on the order of degrees can be seen at an average laser power level of only a few milliwatts.

Results

Optical activity due to extrinsic chirality. The metamaterial consists of a periodic array of asymmetric split ring slits, which were cut by focussed ion-beam milling through a 50 nm thick gold film supported by a 500 μm thick fused quartz substrate. The overall size of the metamaterial array is $100\times100\,\mu m^2$ with a period of 425 nm, and the individual meta-molecules lack inversion symmetry (Fig. 1b). Figure 2 illustrates the origin of chirality and optical

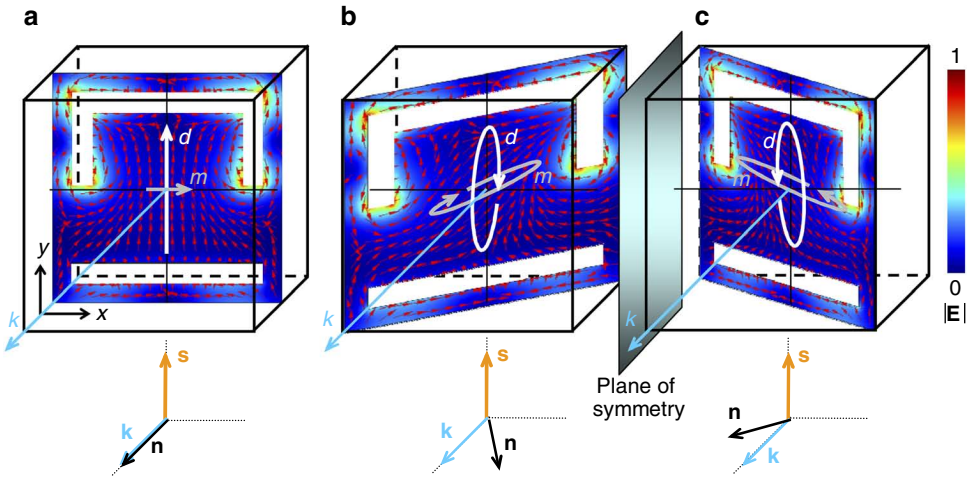

Figure 2 | Chiral scattering in plasmonic metamaterial. Electric field magnitude |**E**| (colour map) and instantaneous directions of the electric field (small red arrows) inside the metamaterial gold film, for excitation with *y*-polarized light at (**a**) normal incidence, (**b**) +20° oblique incidence (experimental case) and (**c**) −20° oblique incidence. At normal incidence, the unit cell's total electric *d* and magnetic *m* dipoles trace perpendicular directions. No polarization change is observed in this case (**a**). At oblique incidence, vectors *d* and *m* trace ellipses with main axes that are not perpendicular to one another. The scattered wave's polarization is now different from that of the incident wave. The polarization change reverses with reversing sense of chirality of the mutual arrangement of the incident light wave (vector **k**) and the metamaterial's normal **n** and symmetry axis **s**; scenarios (**b**) and (**c**) are mirror-symmetric and will show optical activity equal in amplitude but opposite in sign.

activity in this material for oblique incident angles. It is caused by circular differential forward scattering of incident photons that may be traced down to the scattering contributions of the unit cell's effective electric *d* and magnetic *m* dipole moments induced by the incident wave. It is well known from the molecular theory that optical activity requires the molecule to exhibit magnetic and electric responses simultaneously in such a way that there is a non-zero projection of the induced magnetic dipole on the induced electric dipole[2,39]. In this case, the forward scattered wave will exhibit polarization rotation, as electric and magnetic dipoles will emit orthogonal polarization components with a phase lag. The mechanism for extrinsic chirality in metamaterials is illustrated by the finite element method simulations in Fig. 2 for a single meta-molecule excited by an incident *y*-polarized wave. At normal incidence, the field distribution in the unit cell of the metamaterial is mirror-symmetric with respect to the *y*-direction. The total electric and magnetic moments of the unit cell oscillate along strictly perpendicular directions; no optical activity is observed in this case (Fig. 2a). At oblique incidence, the total induced magnetic and electric moments are tracing ellipses, whose main axes are no longer perpendicular and conditions are right for the meta-molecule to scatter with a polarization change. This polarization effect is optical activity and it will change sign with changing chirality of the arrangement, as illustrated by Fig. 2b,c.

Measurements of linear optical activity and anisotropy. We studied linear and intensity-dependent optical activity using a femtosecond mode-locked tunable laser with 115 fs pulse duration and 80 MHz repetition rate. Figure 3 illustrates the metamaterial's linear (low-power) optical properties for wavelengths between 930 and 954 nm, where the metamaterial has a plasmonic resonance and optical activity is largest. In general, in media of low symmetry optical activity coexists with anisotropy that manifests itself as differential refraction (birefringence) and transmission (dichroism) for orthogonal linear polarizations.

On propagation through an optically active and anisotropic medium, a wave with initially linear polarization becomes elliptically polarized and its polarization azimuth rotates. For moderate

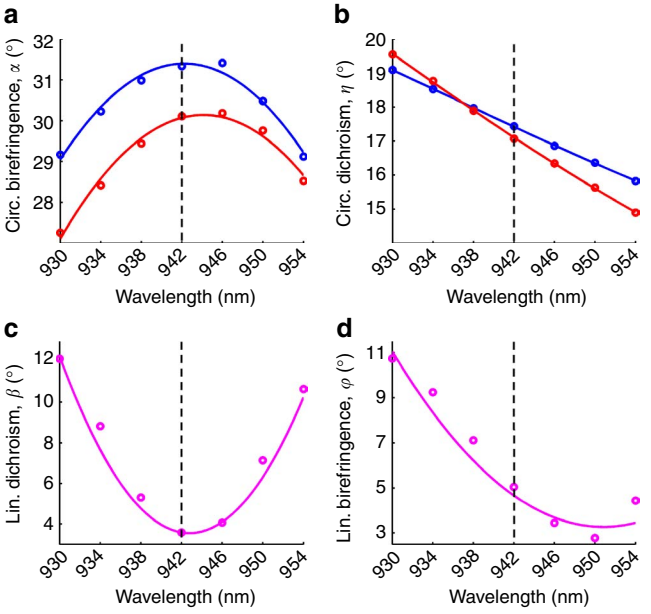

Figure 3 | Giant linear polarization effects in a plasmonic nanostructure. Optical activity in terms of (**a**) circular birefringence (polarization rotation) and (**b**) circular dichroism (ellipticity angle) at linear and nonlinear average power levels of 50 μW (blue) and 5 mW (red), respectively; optical anisotropy in terms of (**c**) linear dichroism and (**d**) linear birefringence at 50 μW average power. Vertical dashed lines indicate the wavelength of 942 nm for which the power dependence of NOA has been studied.

polarization changes, it may be shown that rotation of the polarization azimuth contains contributions resulting from circular birefringence α and linear dichroism β, while the ellipticity of the transmitted wave will contain contributions from circular dichroism η and linear birefringence φ. These four contributions can be separated

by measuring polarization rotation and ellipticity angle as functions of the input polarization azimuth of an initially linearly polarized wave, providing $\alpha, \beta, \eta, \varphi \ll \pi$ (see Methods).

Figure 3 presents measurements of circular birefringence and dichroism (optical activity) and linear birefringence and dichroism (anisotropy) in the metamaterial sample, observed as functions of wavelength at the incident angle of 20° to the normal (measurements taken at −20° show rotation and ellipticity angles of the same magnitude but opposite signs). We note that optical activity is the dominant contribution to the polarization azimuth and ellipticity changes at the resonance wavelength of 942 nm; here anisotropy contributes only up to 12% to the total polarization azimuth rotation and 30% to ellipticity. Detailed measurements of the intensity-dependent polarization changes, reported below, were performed at this wavelength.

Measurements of nonlinear optical activity. The intensity dependence of optical activity was studied using the same laser source as for the linear characterization. While we performed the linear measurements at an average power of 50 μW, the laser power was ramped up to 5 mW for nonlinear measurements, which corresponds to a peak intensity of $I = 2\,\mathrm{GW\,cm^{-2}}$ as the beam is focused to a spot size of 8 μm in diameter. This is sufficient to see a profound change of the light polarization state with intensity, as illustrated by Fig. 4a,b. Here results are represented in terms of changes relative to the low-intensity values of circular birefringence $\Delta\alpha$ and circular dichroism $\Delta\eta$. The most obvious effect of increasing intensity is a suppression of optical activity; at 942 nm polarization rotation is reduced by 1.0°, whereas the ellipticity angle drops 0.5°.

To determine the strength of NOA, we shall be concerned with the gradient of the polarization azimuth rotation change with increasing incident intensity that is measured to be about $\Delta\alpha/I = -0.8°\mathrm{cm^2}$ per GW, before nonlinear rotation starts to saturate above $1\,\mathrm{GW\,cm^{-2}}$. Here nonlinearity resides in the gold film of thickness 53 nm along the direction of propagation. Thus, the specific constant of NOA is $\Omega = 3\times10^{-4}\,°\mathrm{cm\,W^{-1}}$ (this accounts for the 50% reflection of the metamaterial sample). This is more than 7 orders of magnitude stronger than NOA in natural materials such as $LiIO_3$ ($10^{-11}\,°\mathrm{cm\,W^{-1}}$ (ref. 12)), sucrose ($2\times10^{-11}\,°\mathrm{cm\,W^{-1}}$ (refs 17,20)), α-pinene ($\leq10^{-11}\,°\mathrm{cm\,W^{-1}}$ (ref. 20)) and ruthenium salt solution[18,19].

The spectral dependence of NOA is shown by Fig. 4c,d. Nonlinear circular birefringence becomes more pronounced towards shorter wavelengths, whereas nonlinear circular dichroism changes sign at about 937 nm. As illustrated by Fig. 3a, the increase of light intensity reduces the overall polarization rotation throughout the studied spectral range.

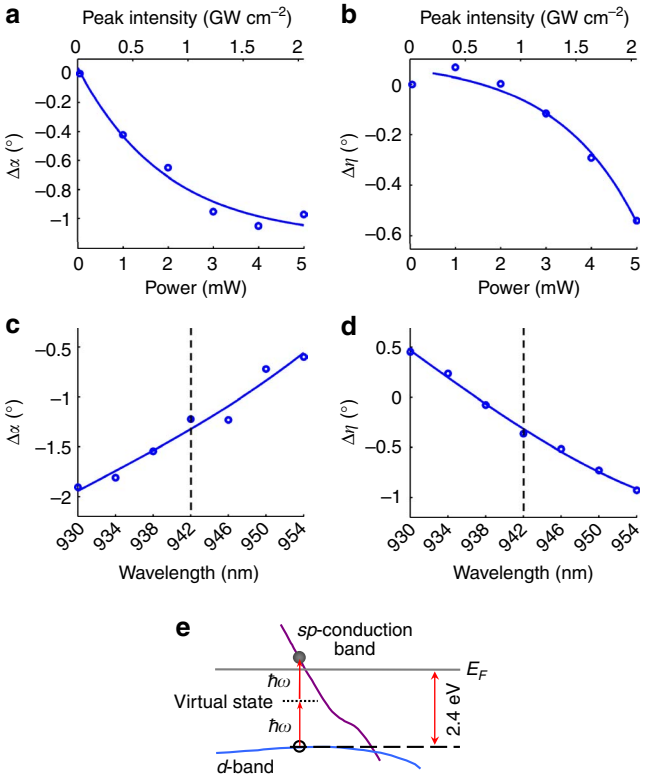

Figure 4 | Nonlinear optical activity of a plasmonic metamaterial. Power-dependent changes of the metamaterial's (**a**) circular birefringence $\Delta\alpha$ and (**b**) circular dichroism $\Delta\eta$ for a fixed wavelength of 942 nm. Spectral dependence of nonlinear (**c**) circular birefringence and (**d**) circular dichroism for a fixed average power of 5 mW (relative to 50 μW in all cases; guides to the eye are shown alongside experimental data points). The wavelength of 942 nm, for which the power dependence of NOA has been studied, is marked by dashed lines. (**e**) Sketch of the Au-band structure and the two-photon absorption process, where a *d*-band electron is excited to the *sp*-conduction band above the Fermi level E_F via absorption of two photons $\hbar\omega$.

Discussion

The nonlinearity of the metamaterial resides in the nonlinearity of its metal framework. It is mainly caused by the nonlinear process of direct two-photon absorption between the *d* and *sp* states in the gold band structure (Fig. 4e). Here direct two-photon absorption occurs through a virtual state when the energy $\hbar\omega$ of two incident photons is combined to bridge the gap $\Delta E = 2.4$ eV, between the *d* states and states above the Fermi level: $\Delta E/2 < \hbar\omega < \Delta E$. As the energy gap cannot be bridged by individual photons directly, 'Fermi-smearing', which dominates the nonlinearity of gold in the visible, is less important in our case. This inherited nonlinearity of gold is resonantly enhanced more than 300 times by the nanostructure through the virtue of strong field concentration at the edges of the grooves, which support a plasmonic mode (see bright hot-spots of field maps in Fig. 2)[32]. Pump-probe experiments[32] also confirmed that this is a very fast nonlinearity, because its main mechanism requires both the pump and the probe photons to be present simultaneously. This degenerate cubic optical nonlinearity gives rise to a nonlinear absorption coefficient on the order of $10^{-5}\,\mathrm{m\,W^{-1}}$. Importantly, the spectral maxima of the absorption nonlinearity and optical activity in this metamaterial overlap, as they are underpinned by the same plasmonic resonance, which arises from the asymmetry of the metamaterial pattern[25,32]. The asymmetry of the plasmonic structure results in excitation of a strong anti-phased current mode through weak free-space coupling, which ensures low radiation losses and therefore a narrow Fano-type optical resonance[40]. Here two-photon absorption reduces not only the intensity of light transmitted through the nanostructure, but it also hampers the chiral dipole scattering efficiency by dampening the underlying plasmon oscillations. Manifestation of this is a suppression of circular birefringence at high intensities (Fig. 3a).

It may be expected that similarly large nonlinear polarization effects can be observed at resonances in a wide range of plasmonic metamaterials. In particular, large NOA may also occur in intrinsically three-dimensionally chiral metamaterials while chiral plasmonic interfaces[41] may show nonlinear versions of other polarization effects such as asymmetric transmission[42].

In summary, we report that engineering of chiral and nonlinear optical properties in a plasmonic metamaterial allows the observation of NOA that is millions of times stronger than in natural crystals. Observation of this giant polarization effect provides a powerful

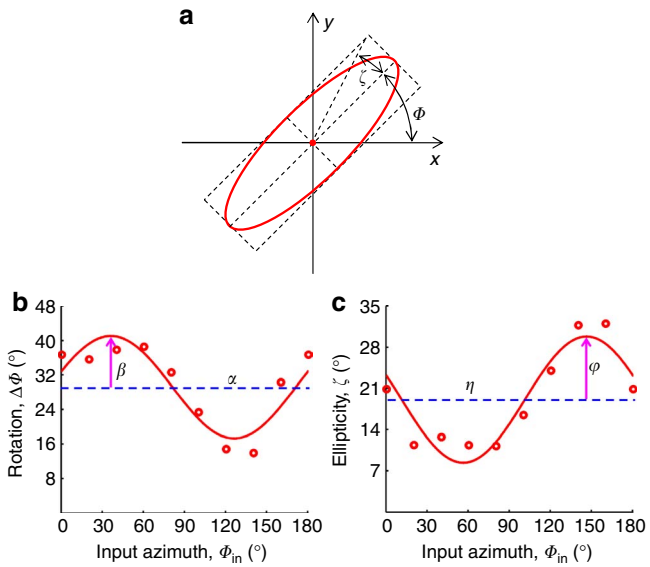

Figure 5 | Measuring optical activity and optical anisotropy. (**a**) Polarization azimuth Φ and ellipticity angle ζ of the polarization ellipse (red) define the polarization state of a polarized electromagnetic wave. (**b**) Polarization azimuth rotation $\Delta\Phi$ and (**c**) ellipticity angle ζ as a function of the azimuth Φ_{in} of the linearly polarized incident wave. The individual contributions of circular birefringence α and circular dichroism η correspond to the average levels of rotation and ellipticity of the transmitted wave, while the corresponding modulations arise from linear dichroism β and linear birefringence φ, respectively. The data shown was taken at 20° oblique incidence for a wavelength of 930 nm and low average power (50 μW).

illustration that nanoscale nonlinear plasmonics of metamaterials offers extremely strong effects unfolding in nanoscale volumes of nonlinear medium that could lead to applications in modulation of light intensity and polarization in nanophotonic devices.

Methods

Definition of polarization parameters. The polarization state of polarized light is characterized by the polarization azimuth Φ and the ellipticity angle ζ which are defined by the polarization ellipse, that is, the trace of the end of the electric field vector as seen by an observer looking into the beam (Fig. 5a).

Separation of optical activity and optical anisotropy. On propagation through an optically active and anisotropic medium, a wave with initially linear polarization becomes elliptically polarized and its polarization azimuth rotates. For moderate polarization changes, it may be shown that the polarization azimuth change $\Delta\Phi$ contains contributions resulting from circular birefringence α and linear dichroism β. On the other hand, the ellipticity angle ζ of the initially linearly polarized wave after interacting with the sample will contain contributions from circular dichroism η and linear birefringence φ.

Indeed, in the slow envelope approximation, evolution of the polarization state of light in linear media is governed by the following set of equations for the components of the four-dimensional Stokes vector **S**, which in a Cartesian coordinate frame can be written as follows (formula 3.24, ref. 10):

$$\frac{d}{dz}(S_\mu e^{2\mathrm{Im}\{k\}z}) = \frac{i\omega}{4c}(\Omega_\alpha E_j^* \sigma_{ji}^\mu \sigma_{ik}^\alpha E_k - \Omega_\alpha^* E_k^* \sigma_{kj}^\alpha \sigma_{ji}^\mu E_i) \quad (1)$$

Here z is the propagation direction, k and ω are the wave number and frequency, c is the speed of light, **E** is the electric field vector, σ^α are Pauli spin matrices, δ_{ij} is the Kronecker delta, and (formulae 3.19 and 3.21, ref. 10)

$$\Omega_\alpha = \sigma_{ji}^\alpha(\varepsilon_{ij} + ik\Gamma_{ijz} - n^2\delta_{ij})/n, \quad (2)$$

where ε_{ij} are cartesian components of the dielectric coefficient describing anisotropy and Γ_{ijz} are cartesian components of the nonlocality tensor describing optical activity. They are defined by the constitutive equation for the nonlocal anisotropic response (formula 2.14, ref. 10):

$$P_i = \frac{1}{4\pi}[(\varepsilon_{ij} - \delta_{ij})E_j + \Gamma_{ijn}\nabla_n E_j] \quad (3)$$

Therefore, it follows from the linear nature of equation (1) that small changes of the Stokes vector components and, thus, small polarization changes that are induced by the anisotropic and nonlocal effects are additive.

Now, by measuring the sample's polarization rotation $\Delta\Phi$ and ellipticity angle ζ as functions of the input polarization azimuth Φ_{in} of an initially linearly polarized wave, one can separate these four contributions, providing $\alpha, \beta, \eta, \varphi \ll \pi$.

Precise formulae for these contributions are given by formulae 3.41, 3.48 and 3.49 in ref. 10. For our consideration, here it is important that, for initially linearly polarized waves, polarization rotation and induced ellipticity are proportional to $\mathrm{Re}(\Gamma_{xyz})$ and $\mathrm{Im}(\Gamma_{xyz})$ describing circular birefringence and circular dichroism, correspondingly. Polarization rotation and induced ellipticity also have components that oscillate with the incident polarization azimuth Φ_{in} as $\sin(2\Phi_{in})$. They are proportional to linear dichroism described by $\mathrm{Im}(\varepsilon_{11} - \varepsilon_{22})$ and linear birefringence described by $\mathrm{Re}(\varepsilon_{11} - \varepsilon_{22})$.

Within this approximation, we retrieve circular birefringence α by measuring the Φ_{in}-independent (average) component of the polarization azimuth rotation; we retrieve circular dichroism η by measuring the Φ_{in}-independent (average) component of the ellipticity angle; we retrieve data on linear birefringence φ by measuring the amplitude of oscillation of the ellipticity angle with the incident polarization azimuth; we retrieve data on linear dichroism β by measuring the amplitude of oscillation of the polarization azimuth rotation with the incident polarization azimuth (Fig. 5b,c).

References

1. Arago, F. J. D. Mémoire sur une modification remarquable qu'éprouvent les rayons lumineux dans leur passage à travers certains corps diaphanes et sur quelques autres nouveaux phénomènes d'optique. *Mémoires de la classe des sciences math. et phys. de l'Institut Impérial de France* **1,** 93 (1811).
2. Barron, L. D. *Molecular Light Scattering and Optical Activity*, Cambridge University Press, 2004.
3. Vavilov, S. I. *Mikrostruktura Sveta (Microstructure of Light)*, USSR Academy of Sciences Publishing, Moscow, 1950.
4. Wawilow, S. I. & Lewschin, W. L. Die Beziehungen zwischen Fluoreszenz und Phosphoreszenz in festen und flüssigen Medien. *Z. Phys.* **35,** 920–936 (1926).
5. Zheludev, I. S. Axial tensors of the third rank and the physical effects they describe. *Sov. Phys. Crystallogr.* **9,** 418–420 (1965).
6. Akhmanov, S. A. & Zharikov, V. I. Nonlinear optics of gyrotropic media. *JETP Lett.* **6,** 137–140 (1967).
7. Kielich, S. Natural and magneto-optical rotation in the presence of an intense light beam. *Phys. Lett.* **25A,** 517–518 (1967).
8. Atkins, P. W. & Barron, L. D. Quantum field theory of optical birefringence phenomena. I. Linear and nonlinear optical rotation *P. Roy. Soc. Lond. A Mat.* **304,** 303–317 (1968).
9. Petrenko, A. & Zheludev, N. Physical mechanisms of nonlinear optical activity in crystals. *Optica Acta* **31,** 1177–1184 (1984).
10. Svirko, Y. P. & Zheludev, N. I. *Polarization of Light in Nonlinear Optics*, Wiley, New York, (1998).
11. Zheludev, N., Petrenko, A., Svirko, I. & Filippova, G. Nonlinear optical activity in weakly and strongly nonlinear media: direct and cascade processes-bistability and stochasticity. *Akademiia Nauk SSSR Izvestiia Seriia Fizicheskaia* **48,** 603–610 (1984).
12. Akhmanov, S. A., Zhdanov, B. V., Zheludev, N. I., Kovrigin, A. I. & Kuznetsov, V. I. Nonlinear optical activity in crystals. *JETP Lett.* **29,** 264–268 (1979).
13. Garibyan, O. V., Zhdanov, B. V., Zheludev, N. I., Kovrigin, A. I. & Kuznetsov, V. I. Thermal nonlinear optical rotation in cholesteric liquid crystals. *Kristallografiya (Soviet Physics Crystallography)* **26,** 787–791 (1981).
14. Vlasov, D. & Zaitsev, V. Experimental observation of nonlinear optical activity. *JETP Lett.* **14,** 112–115 (1971).
15. Borshch, V. V., Lisitsa, M. P., Mozol', P. E. & Fekeshgazi, I. V. Self-induced rotation of the direction of polarization of light in crystals of 422 symmetry. *Sov. J. Quantum Electron.* **8,** 393–395 (1978).
16. Zheludev, N., Ruddock, I. & Illingworth, R. Intensity dependence of thermal nonlinear optical activity in crystals. *Appl. Phys. B* **49,** 65–67 (1989).
17. Cameron, R. & Tabisz, G. Observation of two-photon optical rotation by molecules. *Mol. Phys.* **90,** 159–164 (1997).
18. Mesnil, H. & Hache, F. Experimental evidence of third-order nonlinear dichroism in a liquid of chiral molecules. *Phys. Rev. Lett.* **85,** 4257–4260 (2000).
19. Mesnil, H. *et al.* Experimental observation of nonlinear circular dichroism in a pump-probe experiment. *Chem. Phys. Lett.* **338,** 269–276 (2001).
20. Markowicz, P. *et al.* Modified z-scan techniques for investigations of nonlinear chiroptical effects. *Opt. Exp.* **12,** 5209–5214 (2004).

21. Bose, J. On the rotation of plane of polarisation of electric waves by a twisted structure. *Proc. R. Soc. Lond.* **63,** 146–152 (1898).
22. Plum, E., *et al.* Giant optical gyrotropy due to electromagnetic coupling. *Appl. Phys. Lett.* **90,** 223113 (2007).
23. Kuwata-Gonokami, M. *et al.* Giant optical activity in quasi-two-dimensional planar nanostructures. *Phys. Rev. Lett.* **95,** 227401 (2005).
24. Decker, M. *et al.* Strong optical activity from twisted-cross photonic metamaterials. *Opt. Lett.* **34,** 2501–2503 (2009).
25. Plum, E. *et al.* Metamaterials: optical activity without chirality. *Phys. Rev. Lett.* **102,** 113902 (2009).
26. Rogacheva, A. V., Fedotov, V. A., Schwanecke, A. S. & Zheludev, N. I. Giant gyrotropy due to electromagnetic-field coupling in a bilayered chiral structure. *Phys. Rev. Lett.* **97,** 177401 (2006).
27. Plum, E. *et al.* Metamaterial with negative index due to chirality. *Phys. Rev. B* **79,** 035407 (2009).
28. Shadrivov, I. V., Fedotov, V. A., Powell, D. A., Kivshar, Y. S. & Zheludev, N. I. Electromagnetic wave analogue of an electronic diode. *New J. Phys.* **13,** 033025 (2011).
29. Cho, D. *et al.* Ultrafast modulation of optical metamaterials. *Opt. Express* **17,** 17652–17657 (2009).
30. Dani, K. *et al.* Subpicosecond optical switching with a negative index metamaterial. *Nano Lett.* **9,** 3565–3569 (2009).
31. Nikolaenko, A. E. *et al.* Carbon nanotubes in a photonic metamaterial. *Phys. Rev. Lett.* **104,** 153902 (2010).
32. Ren, M. *et al.* Nanostructured plasmonic medium for terahertz bandwidth all-optical switching. *Adv. Mater.* **23,** 5540–5544 (2011).
33. Wurtz, G. *et al.* Designed ultrafast optical nonlinearity in a plasmonic nanorod metamaterial enhanced by nonlocality. *Nat. Nanotechnol.* **6,** 107–111 (2011).
34. Hameka, H. Resonance fluorescence in gases and molecular crystals. *J. Chem. Phys.* **38,** 2090–2111 (1963).
35. Buckingham, A. & Dunn, M. Optical activity of oriented molecules. *J. Chem. Soc. A* **38,** 1988–1991 (1971).
36. Sirotin, Y. & Shaskolskaya, M. *Fundamentals of Crystal Physics*, Imported Pubn, (1983).
37. Williams, R. Optical rotatory effect in the nematic liquid phase of *p*-azoxyanisole. *Phys. Rev. Lett.* **21,** 342–344 (1968).
38. Plum, E., Fedotov, V. A. & Zheludev, N. I. Optical activity in extrinsically chiral metamaterial. *Appl. Phys. Lett.* **93,** 191911 (2008).
39. Condon, E. Theories of optical rotatory power. *Rev. Mod. Phys.* **9,** 432–457 (1937).
40. Khardikov, V. V., Iarko, E. O. & Prosvirnin, S. L. Trapping of light by metal arrays. *J. Opt.* **12,** 045102 (2010).
41. Papakostas, A, Potts, A, Bagnall D. M., Prosvirnin, S. L., Coles H. J., Zheludev N. I. Optical manifestations of planar chirality. *Phys. Rev. Lett.* **90,** 107404 (2003).
42. Fedotov, V. A. *et al.* Asymmetric propagation of electromagnetic waves through a planar chiral structure. *Phys. Rev. Lett.* **97,** 167401 (2006).

Acknowledgements

We are grateful to Edward Rogers, Kevin F. MacDonald, Jun-Yu Ou and Andrey Nikolaenko for assistance with experiment and preparation of samples. This work was supported by The Leverhulme Trust, The Royal Society (London), the UK Engineering and Physical Sciences Research Council (programme grant EP/G060363/1) and the P. R. China ('111 Project' grant B07013 and '973 Program' grant 2007CB307002).

Author contributions

The idea of the experiment was conceived by N.I.Z. and E.P., M.R. assembled the polarimeter and carried out the measurements. N.I.Z. wrote the paper with assistance from E.P. All authors discussed the results and analysed the data; J.J.X. and N.I.Z. supervised the work.

Additional information

Competing financial interests: The authors declare no competing financial interests.

Reprints and permission information is available online at http://npg.nature.com/reprintsandpermissions/

How to cite this article: Ren, M. *et al.* Giant nonlinear optical activity in a plasmonic metamaterial. *Nat. Commun.* 3:833 doi: 10.1038/ncomms1805 (2012).

Optical gecko toe: Optically controlled attractive near-field forces between plasmonic metamaterials and dielectric or metal surfaces

J. Zhang, K. F. MacDonald, and N. I. Zheludev*

Optoelectronics Research Centre & Centre for Photonic Metamaterials, University of Southampton, Southampton SO17 1BJ, UK

(Received 30 December 2011; revised manuscript received 27 April 2012; published 14 May 2012)

On the mesoscopic scale, electromagnetic forces are of fundamental importance to an enormously diverse range of systems, from optical tweezers to the adhesion of gecko toes. Here we show that a strong light-driven force may be generated when a plasmonic metamaterial is illuminated in close proximity to a dielectric or metal surface. This near-field force can exceed radiation pressure and Casimir forces to provide an optically controlled adhesion mechanism mimicking the gecko toe: At illumination intensities of just a few tens of nW/μm^2 it is sufficient to overcome the Earth's gravitational pull.

DOI: 10.1103/PhysRevB.85.205123 PACS number(s): 78.67.Pt, 42.50.Wk

In various guises, electromagnetic forces are extremely important in mesoscopic systems: They are exploited in all forms of optical tweezing, manipulation, and binding,[1–4] in optomechanical photonic devices,[5–11] and may offer a mechanism of "quantum lubrication" between surfaces[12]; The fact that light exerts pressure upon any surface exposed to it (deduced theoretically by James Clerk Maxwell in 1871 and proven experimentally in 1901 by Lebedev[13] and in 1903 by Nichols & Hull[14]) can be exploited to generate "optical lift"[15]; And in nature, van der Waals interactions underpin the gecko's remarkable ability to overcome gravity by sticking to walls and ceilings.[16] In recent years it has become clear that plasmonic systems can provide unprecedented control over optical fields on the nanoscale, offering gigantic field enhancement, subwavelength light localization, and strongly enhanced interactions between nano-objects.[17–20] They present opportunities, for example, to extend/enhance the functionality of optical tweezers/traps[21] and to experimentally investigate the idea that structures with negative refractive indices will experience negative radiation pressure.[22,23]

Here we show that in addition to the conventional, well-understood force of radiation pressure a much stronger light-driven near-field force may be generated between an illuminated planar plasmonic metamaterial and a dielectric or metallic surface. This newly identified near-field force has a resonant nature linked to the excitation of the metamaterial's plasmonic mode and acts to close the gap between the metamaterial film and the surface (Fig. 1). This "optical adhesion" force exists alongside interfacial Casimir forces and can overcome both radiation pressure and, like the gecko toe, gravity.

Within the framework of classical electrodynamics the components of the total time-averaged force **F** acting on a metamaterial structure illuminated with light can be calculated using a surface integral:

$$\langle F_i \rangle = \oiint_S \langle T_{ij} \rangle \, n_j \, dS, \tag{1}$$

where S is a bounding surface around the metamaterial and T_{ij} is the time-averaged Maxwell stress tensor:

$$\langle T_{ij} \rangle = \frac{1}{2}\mathrm{Re}\left[\varepsilon_0\left(E_i E_j^* - \frac{1}{2}\sum_k E_k E_k^*\right) + \mu_0\left(H_i H_j^* - \frac{1}{2}\sum_k H_k H_k^*\right)\right]. \tag{2}$$

The stress tensor integral equation (1) encompasses both the radiation pressure and near-field force—the focus of this study. It does not include Casimir forces, which are derived from vacuum quantum fluctuation and thus exist even in the absence of illumination. (It will be demonstrated below that the classical electromagnetic force can be much stronger than the Casimir force.)

Radiation pressure arises through transfer of momentum between photons and any surface on which they impinge. It depends on the reflection R and absorption A coefficients of the surface according to the equation $F_r = (2R + A)P/c$, where c is the speed of light in vacuum and P is the power of the incident light, and assumes a maximum value of $2P/c$ when the reflectivity of a surface is 100%.

In addition to this radiation force, a near-field optical force emerges when a metamaterial is placed in close proximity to another object and the evanescent field of the nanostructure encounters that object. The magnitude of this force depends on how strongly optical energy is trapped in the metamaterial

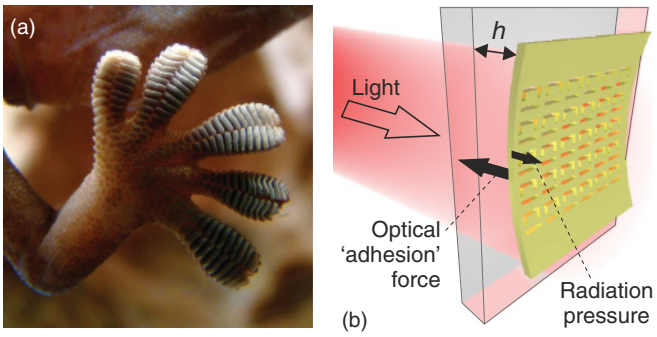

FIG. 1. (Color online) Gecko toes and their optical analog. (a) Gecko toes sticking to a smooth glass wall (Ref. 24). (b) Artistic impression of a metamaterial film attracted by a beam of light to a dielectric surface.

and on the electromagnetic properties of the nearby object. In general, the higher the refractive index of the nearby object is, the stronger the interaction will be and in all cases studied here the near-field optical force is attractive. In what follows, the ratio $|\mathbf{F}| : P/c$ is employed as a dimensionless measure of optical force.[25]

In the present study, forces acting on metamaterial structures are evaluated via the Maxwell stress tensor integral Eq. (1) with electric E and magnetic H field distributions obtained from fully three-dimensional finite-element Maxwell solver simulations (COMSOL MULTIPHYSICS). This analysis utilizes established experimental values of the complex dielectric parameters for gold,[26] excludes losses in dielectric media, and assumes normally incident, narrowband coherent illumination. By modeling a single "metamolecule" (translation unit cell of the metamaterial design) with periodic boundary conditions, calculations assumed a planar metamaterial array of infinite extent, parallel to the surface of a nearby semi-infinite metal or dielectric. The surface of integration S was defined as a rectangular parallelepiped enclosing the metamolecule, with walls along each of the four periodic boundaries and *outside* each of the two free surfaces of the metamaterial film. The same numerical model provides data on the transmission T and reflectance R of the structure. In all cases, stress tensor results are verified against independent calculations of force based on the variation with gap size of the total energy trapped in the system.[27]

We first consider optical forces between a gold metamaterial film and the surface of a semi-infinite transparent dielectric (Fig. 2). The metamaterial here is taken to comprise a two-dimensional square array of asymmetric split rings—a popular design recognized for its strong light confinement and simplicity of fabrication.[28,29] Dimensional details are shown inset to Fig. 2(a).

For a plasmonic metamaterial both the radiation pressure and near-field forces are resonant [Fig. 2(b)]. The dispersion of the radiation pressure force F_r is linked to variations in the metamaterial's absorbtion and reflection coefficients [Fig. 2(a)] and has a local maximum at a wavelength of 1320 nm corresponding to the reflectivity peak. When the structure is illuminated from free space the radiation pressure F_r and near-field evanescent F_e forces act in the same direction to reduce the gap h between the metamaterial and the dielectric surface. The evanescent force is resonant at 1370 nm, the wavelength of the absorption peak, and exceeds the radiation force across the entire spectral range from 1210 to 1550 nm, reaching a peak magnitude of approximately $6.7P/c$ as compared to only $1.2P/c$ for the radiation force. When light impinges on the sample through the transparent dielectric [Fig. 2(c)] the evanescent force acts *in opposition* to the radiation pressure and again acts to reduce h. In this configuration, if the gold film were unstructured the total light force would push it away from the dielectric surface, but for a metamaterial the attractive near-field force is dominant and pulls the metamaterial film toward the dielectric.

The near-field force is related to the nonpropagating evanescent field of localized plasmons in the nanostructure, which possesses no momentum. As such it does not contribute directly to the momentum balance with incident light; it simply adds to or subtracts from the radiation pressure force depending on the direction of the latter. The evanescent force works to change the energy trapped in the nanostructure when the metamaterial is brought into close proximity with a

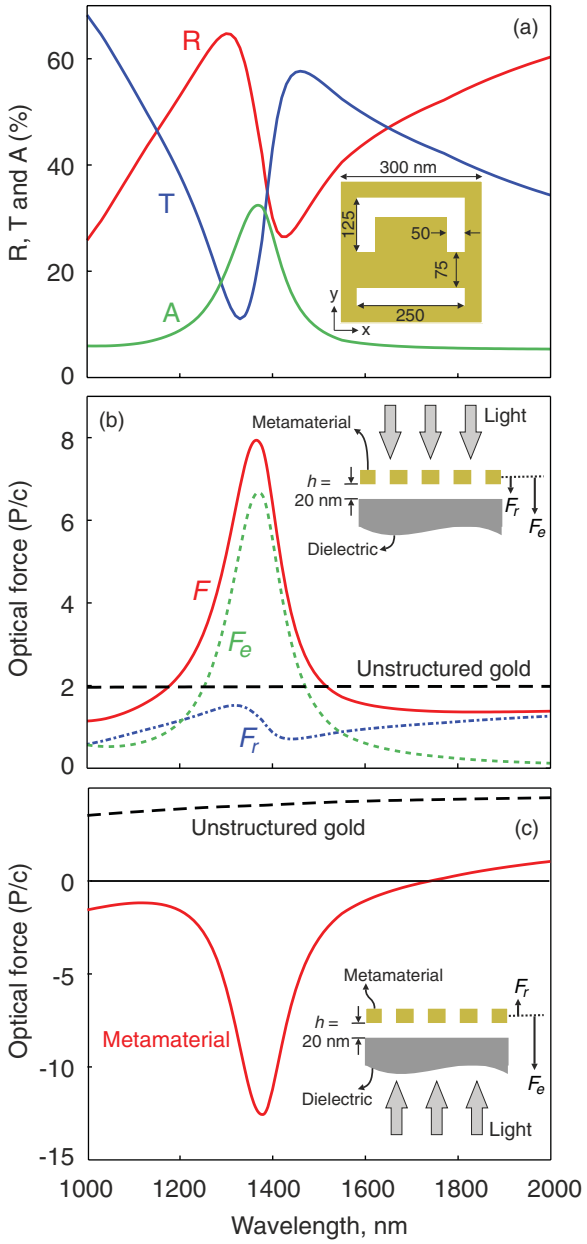

FIG. 2. (Color online) Optical forces between a plasmonic metamaterial and a dielectric surface. (a) Reflection R, transmission T, and absorption A spectra of a 50 nm thick gold metamaterial located at a distance $h = 20$ nm from the surface of a dielectric with refractive index $n = 2.5$ for y-polarized light normally incident from free space. The inset shows the metamaterial unit cell geometry. (b) Total optical force F acting on a metamaterial illuminated from free space as illustrated inset. Dashed lines show the evanescent F_e and light pressure F_r components of F. (c) Total optical force acting on a metamaterial illuminated through the dielectric. For comparison, the total force acting on an *unstructured* gold film in place of the metamaterial is shown in both (b) and (c). In all cases, positive values denote forces acting in the direction of incident light propagation.

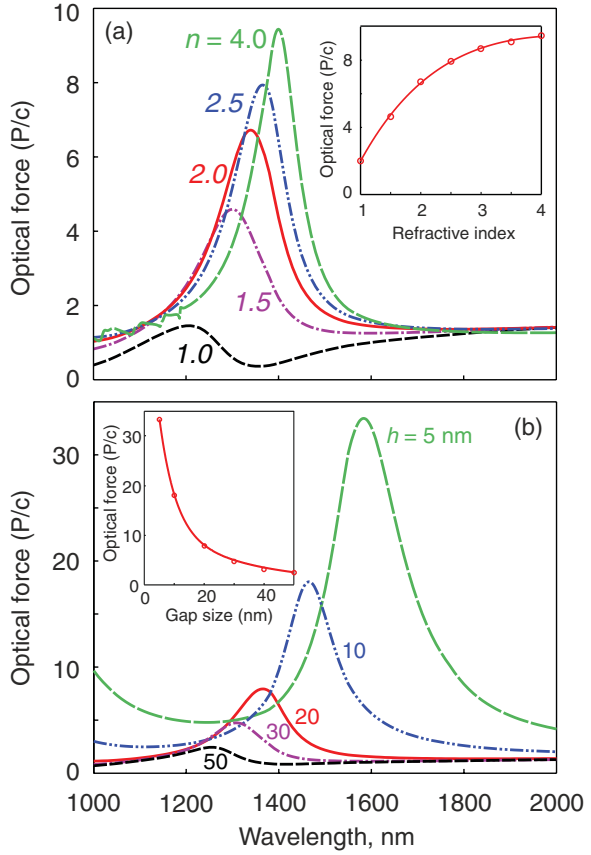

FIG. 3. (Color online) Optical forces between a plasmonic metamaterial and a dielectric surface. Spectral dispersion of the total optical force [under illumination from free space as illustrated inset to Fig. 2(b)] for different values, as labeled, of (a) dielectric refractive index n (at $h = 20$ nm) and (b) gap size h ($n = 2.5$). Insets show peak optical force as a function of n and h, respectively.

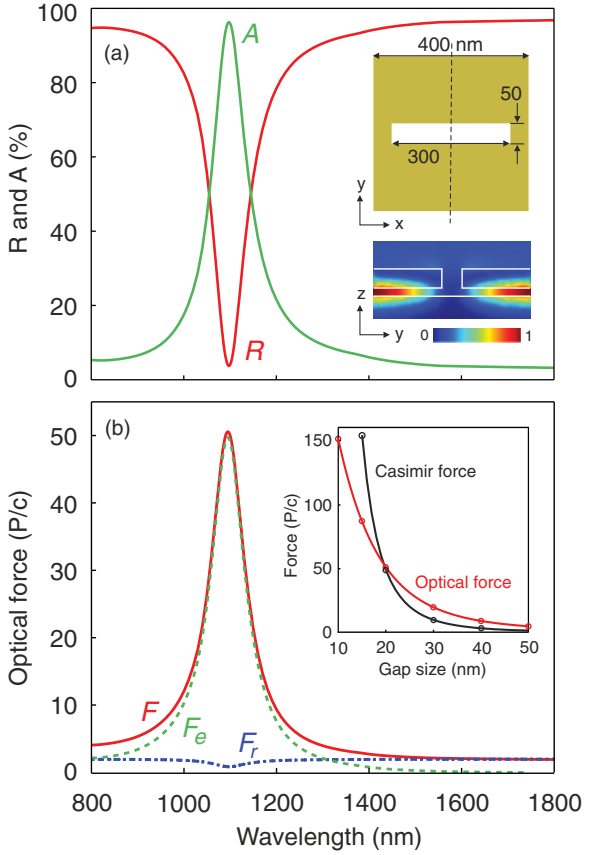

FIG. 4. (Color online) Optical forces between a plasmonic metamaterial and a metallic surface. (a) Normal incidence reflection R and absorption A spectra of a 50 nm thick gold metamaterial located at a distance $h = 20$ nm from a gold surface (incident light propagation in the $-z$ direction as defined inset). The insets show the metamaterial unit cell geometry and a map of the normalized magnetic field intensity distribution at the 1095 nm resonance wavelength for a cross-section along the dashed line in the y-z plane. (b) Evanescent F_e, radiation pressure F_r, and total optical force F acting on the metamaterial. The inset shows peak optical force as a function of gap size h and the corresponding dependence on h of the Casimir force between two perfectly conducting plates (scaled assuming $I = 50\ \mathrm{mW}/\mu\mathrm{m}^2$).

surface. As the eigenfrequencies of a metamaterial are always redshifted relative to their free-space values when the structure is close to or embedded in another medium with a refractive index exceeding unity, the closest possible presence of such a medium is energetically preferable. As a consequence, the resonant evanescent force between a metamaterial and nearby surface is always attractive.

Both the radiation pressure and evanescent forces are stronger when the metamaterial is illuminated through the dielectric than when light is incident on the structure from free space. In particular, higher values of $|F_e|$ (stronger evanescent fields between metamaterial and dielectric) are a consequence the metamaterial's higher absorption coefficient under illumination through the dielectric[30] (the increase in $|F_e|$ being proportional to that in A).

Figure 3 shows the dependence of total optical force on dielectric refractive index n and gap size h for free-space illumination [as in Fig. 2(b)]. As the refractive index of the dielectric increases from $n = 1$ to 4, the magnitude of the optical force increases and the resonance red-shifts. A similar trend is seen with decreasing gap size: At $h = 5$ nm the evanescent force is 33 times stronger than the radiation pressure. Both trends reflect the strong influence of near-field environment on the metamaterial resonances.

Near-field optical forces are even greater at metallic surfaces. In this case we consider a metamaterial comprising a square array of rectangular slots [see inset to Fig. 4(a)]. With a metallic backplane this structure supports a "magnetic resonance" (where anti-asymmetric currents are excited in the metamaterial and backplane) at which light is trapped [see inset to Fig. 4(b)] and strongly absorbed. Indeed, similar systems have previously been analyzed for "perfect" absorption applications.[31–33] Figure 4 shows the normal incidence reflection and absorption spectra of the structure and the dispersion of the optical forces acting on the metamaterial film. In this case the magnitude of the total optical force reaches $\sim 50P/c$ at the absorption peak around 1095 nm.

It is interesting to compare the enhanced optical forces between a metamaterial and metallic surface with the force of gravity on the metamaterial film. The gravitational force on a 50 nm thick gold film is of order $1 \times 10^{-14}\ \mathrm{N}/\mu\mathrm{m}^2$.

An optical force of the same magnitude can be achieved between a metallic (gold) surface and a metamaterial 20 nm away when the metamaterial is illuminated at the 1095 nm resonant wavelength at an intensity of around 60 nW/μm^2. Under such conditions the optical force will be sufficient to pull a metamaterial against gravity toward a surface. At shorter distances the pulling force becomes even stronger but other micro/nanoscale forces also become important. The Casimir force $F_c = -(\pi^2\hbar c)/(240d^4)$ between two perfectly conducting plates separated by 20 nm is (at $\sim$8 nN/μm^2) equivalent to the optical force achieved at the same separation between a gold metamaterial and planar gold surface for an illumination intensity I of approximately 50 mW/μm^2 [see inset to Fig. 4(b)]. However, for a perforated real metal thin film the Casimir force may easily be an order of magnitude smaller than the above estimate,[34–36] in which case it would be surpassed by the near-field optical force at much lower intensities.

Indeed, as the Casimir and near-field forces depend differently on distance—$F_c \propto h^{-4}$ (or h^{-3} for realistic metallic plates at values of h smaller than the metal's plasma wavelength[35]) while $F_e \propto Ie^{-h/a}$ (where a is the characteristic dimension of the nanostructural pattern)—above a threshold value of intensity I there will be a range of distances h where the near-field force is dominant, and this range will broaden with increasing intensity. As a result, the near-field force is likely to prevail where conditions such as surface roughness limit the proximity of two objects.

With regard to the experimental observation of the evanescent force described here, photonic metamaterials can readily tolerate mW/μm^2 illumination intensities under which F_e would exceed the gravitational force by several orders of magnitude. The great advantage of this near-field force for nanoscale manipulation is that it depends on both light intensity and wavelength, thereby offering dynamic controllability and spectral selectivity. Such forces could manifest themselves in a variety of resonant structural configurations including, for instance, single metamolecules or plasmonic elements and may serve applications in optical trapping/tweezing and in the control of light with light via optically reconfigurable metamaterials. For example, an optical fiber scanning probe tip capped with a plasmonic metamaterial may be employed to pick up and reposition individual nano-objects; an array of optically switchable adhesion elements may dynamically control patterns of particles/flakes; optically tuning the position of a metamaterial elastically suspended near a metal surface (varying illumination intensity to adjust the balance between near-field and mechanical forces) will deliver broadband changes in the reflectivity of the structure.

In summary, we have demonstrated that the attractive near-field optical forces between a nanostructured plasmonic metamaterial film and a dielectric or metal surface can greatly exceed the associated radiation pressure and outstrip the Casimir forces. This force is sufficient to overcome gravity at illumination intensities of just a few tens of nW/μm^2.

This work was supported by the Engineering and Physical Sciences Research Council (Project No. EP/G060363/1), the Royal Society (N.I.Z.), and the China Scholarship Council (J.Z.).

*niz@orc.soton.ac.uk; www.nanophotonics.org.uk/niz

[1] K. Dholakia and T. Čižmár, Nature Photon. **5**, 335 (2011).
[2] M. Padgett and R. Bowman, Nature Photon. **5**, 343 (2011).
[3] K. Dholakia and P. Zemánek, Rev. Mod. Phys. **82**, 1767 (2010).
[4] J. Chen, J. Ng, Z. Lin, and C. T. Chan, Nature Photon. **5**, 531 (2011).
[5] T. J. Kippenberg and K. J. Vahala, Science **321**, 1172 (2008).
[6] M. Li, W. H. P. Pernice, C. Xiong, T. Baehr-Jones, M. Hochberg, and H. X. Tang, Nature (London) **456**, 480 (2008).
[7] J. Ma and M. L. Povinelli, Opt. Exp. **19**, 10102 (2011).
[8] J. Roels, I. De Vlaminck, L. Lagae, B. Maes, D. Van Thourhout, and R. Baets, Nature Nanotech. **4**, 510 (2009).
[9] G. S. Wiederhecker, L. Chen, A. Gondarenko, and M. Lipson, Nature (London) **462**, 633 (2009).
[10] H. Taniyama, M. Notomi, E. Kuramochi, T. Yamamoto, Y. Yoshikawa, Y. Torii, and T. Kuga, Phys. Rev. B **78**, 165129 (2008).
[11] V. Liu, M. Povinelli, and S. Fan, Opt. Exp. **17**, 21897 (2009).
[12] J. N. Munday, F. Capasso, and V. A. Parsegian, Nature (London) **457**, 170 (2009).
[13] P. Lebedev, Ann. Phys. **311**, 433 (1901).
[14] E. F. Nichols and G. F. Hull, Phys. Rev. **17**, 26 (1903).
[15] G. A. Swartzlander Jr., T. J. Peterson, A. B. Artusio-Glimpse, and A. D. Raisanen, Nature Photon. **5**, 48 (2011).
[16] K. Autumn, M. Sitti, Y. A. Liang, A. M. Peattie, W. R. Hansen, S. Sponberg, T. W. Kenny, R. Fearing, J. N. Israelachvili, and R. J. Full, Proc. Natl. Acad. Sci. USA **99**, 12252 (2002).
[17] R. Zhao, P. Tassin, T. Koschny, and C. M. Soukoulis, Opt. Exp. **18**, 25665 (2010).
[18] M. Liu, T. Zentgraf, Y. Liu, G. Bartal, and X. Zhang, Nature Nanotech. **5**, 570 (2010).
[19] S. B. Wang, J. Ng, H. Liu, H. H. Zheng, Z. H. Hang, and C. T. Chan, Phys. Rev. B **84**, 075114 (2011).
[20] H. Liu, J. Ng, S. B. Wang, Z. F. Lin, Z. H. Hang, C. T. Chan, and S. N. Zhu, Phys. Rev. Lett. **106**, 087401 (2011).
[21] M. L. Juan, M. Righini, and R. Quidant, Nature Photon. **5**, 349 (2011).
[22] V. G. Veselago, Sov. Phys. Usp. **10**, 509 (1968).
[23] H. J. Lezec, A. Agarwal, and K. Chau, in *NanoMeta 2011* (Seefeld-in-Tirol, Austria, 2011).
[24] B. C. Tørrissen [http://en.wikipedia.org/wiki/File:Gecko_foot_on_glass.JPG] (CC BY-SA 3.0).
[25] A. W. Rodriguez, A. P. McCauley, P. C. Hui, D. Woolf, E. Iwase, F. Capasso, M. Lončar, and S. G. Johnson, Opt. Exp. **19**, 2225 (2011).
[26] E. D. Palik, ed., *Handbook of Optical Constants of Solids* (Academic Press, Orlando, 1984).
[27] M. L. Povinelli, S. G. Johnson, M. Lončar, M. Ibanescu, E. J. Smythe, F. Capasso, and J. D. Joannopoulos, Opt. Exp. **13**, 8286 (2005).

[28] K. Tanaka, E. Plum, J. Y. Ou, T. Uchino, and N. I. Zheludev, Phys. Rev. Lett. **105**, 227403 (2010).
[29] A. E. Nikolaenko, F. De Angelis, S. A. Boden, N. Papasimakis, P. Ashburn, E. Di Fabrizio, and N. I. Zheludev, Phys. Rev. Lett. **104**, 153902 (2010).
[30] K. Y. Bliokh, Y. P. Bliokh, V. Freilikher, S. Savel'ev, and F. Nori, Rev. Mod. Phys. **80**, 1201 (2008).
[31] N. Liu, M. Mensch, T. Weiss, M. Hentschel, and H. Giessen, Nano Lett. **10**, 2342 (2010).
[32] X. Liu, T. Starr, A. F. Starr, and W. J. Padilla, Phys. Rev. Lett. **104**, 207403 (2010).
[33] C. Hu, Z. Zhao, X. Chen, and X. Luo, Opt. Exp. **17**, 11039 (2009).
[34] V. B. Svetovoy, P. J. van Zwol, G. Palasantzas, and J. T. M. De Hosson, Phys. Rev. B **77**, 035439 (2008).
[35] A. W. Rodriguez, F. Capasso, and S. G. Johnson, Nature Photon. **5**, 211 (2011).
[36] M. Lisanti, D. Iannuzzi, and F. Capasso, Proc. Natl. Acad. Sci. USA **102**, 11989 (2005).

nature materials

REVIEW ARTICLE

PUBLISHED ONLINE: 23 OCTOBER 2012 | DOI: 10.1038/NMAT3431

From metamaterials to metadevices

Nikolay I. Zheludev[1,2]* and Yuri S. Kivshar[3]

Metamaterials, artificial electromagnetic media that are structured on the subwavelength scale, were initially suggested for the negative-index 'superlens'. Later metamaterials became a paradigm for engineering electromagnetic space and controlling propagation of waves: the field of transformation optics was born. The research agenda is now shifting towards achieving tunable, switchable, nonlinear and sensing functionalities. It is therefore timely to discuss the emerging field of metadevices where we define the devices as having unique and useful functionalities that are realized by structuring of functional matter on the subwavelength scale. In this Review we summarize research on photonic, terahertz and microwave electromagnetic metamaterials and metadevices with functionalities attained through the exploitation of phase-change media, semiconductors, graphene, carbon nanotubes and liquid crystals. The Review also encompasses microelectromechanical metadevices, metadevices engaging the nonlinear and quantum response of superconductors, electrostatic and optomechanical forces and nonlinear metadevices incorporating lumped nonlinear components.

For some years the metamaterials paradigm has mostly been considered as a means of engineering the electromagnetic response of passive micro- and nanostructured materials by engaging resonance excitations such as localized plasmonic modes. Remarkable results have been achieved in this way: they include, for instance, negative-index media that refract light in the opposite direction from that of conventional materials, chiral materials that rotate the polarization state of light hundreds of thousands of times more strongly than natural optical crystals, and structured thin films with remarkably strong dispersion that can slow light in much the same way as resonant atomic systems with electromagnetically induced transparency.

The ever-increasing demand for faster information transfer and processing drives efforts to remove the bottleneck between fibre-based optical telecommunication networks and electronic data handling and routing, improving data storage and developing parallel data processing operating in a compact space. Fulfilment of these tasks will require strong and fast nonlinearities for switching light with light, and much improved control of the electromagnetic properties of matter with external stimuli such as electric signals.

In this Review we illustrate that many of these functionalities may be greatly enhanced by hybridizing functional matter with metamaterials, by exploiting nonlinearity of the metamaterial framework itself, and by taking advantage of the changing balance of forces in systems with building blocks smaller than the wavelength of light. This leads to the concept of metadevices, a logical extension of the metamaterial paradigm, where interactions are nonlinear and responses are dynamic. Here we envisage that the future platform for highly integrated electromagnetic signal processing and distribution will emerge that will combine nonlinear, memory and switchable functionalities with transformation optics' ability to guide light via the engineered electromagnetic space, using metamaterials with spatially variable parameters.

Reconfigurable metadevices

Active tunability and switching of electromagnetic characteristics of metamaterials can be achieved by altering the shape of individual metamolecule resonators, or by manipulating the near-field interactions between them. The latter can be attained by changing the relative position of rows of the metamolecular structure[1] or by displacing arrays of metamolecules forming a three-dimensional metamaterial lattice[2] (Fig. 1a).

The potential of microelectromechanical systems (MEMS) for electromagnetic metamaterials was initially recognized for the tuning of transmission lines[3,4]. Shortly after the first publications on MEMS filters, microelectromechanical actuators were applied to reconfigure metamolecules[5], in the expectation that controlling the resonant properties of the individual elements could be used to make tunable negative-refractive-index metamaterial arrays. Reconfigurable metamaterials at terahertz frequencies were first produced by fabricating planar arrays of split-ring resonators on bimaterial cantilevers designed to bend out of plane in reaction to a thermal stimulus (Fig. 1b). A marked change of the electric and magnetic response was observed as the split-ring resonators synchrously reoriented within their unit cells[6]. Similar thermally activated structures may be used in infrared and terahertz detectors. A number of terahertz metamaterial designs with electrically activated MEMS switches have since been demonstrated[6–8]. One of the most elaborate designs is an array of pairs of asymmetric split-ring resonators, one fixed to the substrate and the other patterned on a movable frame[9] (Fig. 1c). Here the reconfigurable metamaterial and the supporting structures (microactuators, anchors, supporting frames and so on) are fabricated on a silicon-on-insulator wafer using deep reactive-ion etching. By adjusting the distance between the two rings using the micromachined actuators, the strength of dipole–dipole coupling can be tuned continuously, allowing efficient tailoring of the electromagnetic response. The reconfiguration of metamolecules also allows switching of polarization eigenstates of this anisotropic metamaterial.

Terahertz metamaterial structures that use flexing microelectromechanical cantilevers to tune the resonance frequency were suggested recently[10]. The cantilevers are coated with a magnetic thin film that can be actuated by an external magnetic field, enabling continuous control of the resonance frequency over a large frequency range[10]. Manufacturing arrays of plasmonic resonators on flexible, stretchable polymer substrates offers a practical way to dynamically tune the response of photonic metamaterials[11–13], and also allows them to be fabricated on curvilinear shapes

[1]Optoelectronics Research Centre, University of Southampton, Southampton SO17 1BJ, UK; [2]Centre for Disruptive Photonic Technologies, Nanyang Technological University, Singapore 637378, Singapore; [3]Nonlinear Physics Centre and CUDOS@ANU, Australian National University, Canberra ACT 0200, Australia. *e-mail: n.i.zheludev@soton.ac.uk

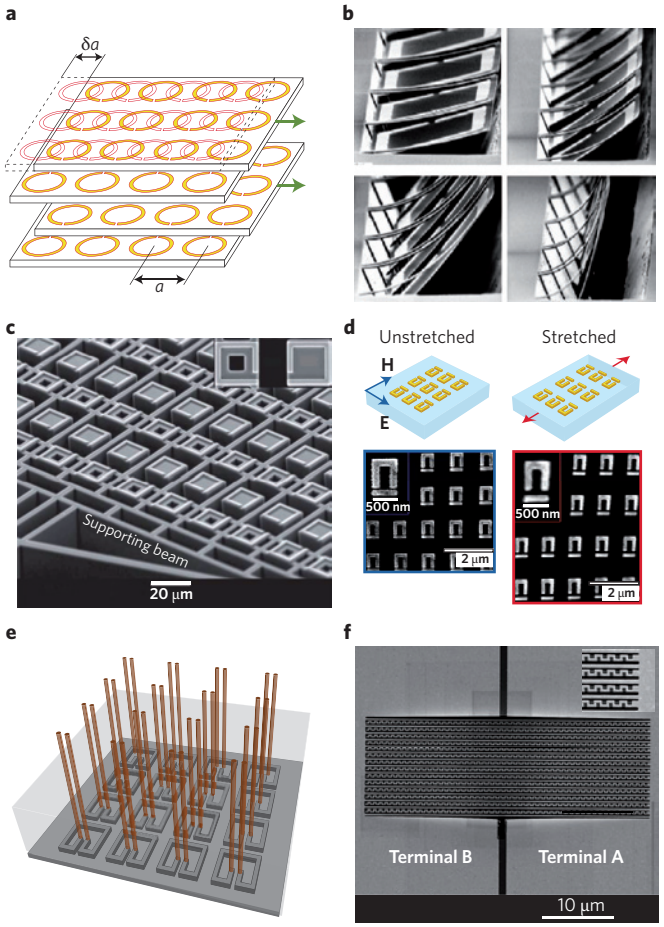

Figure 1 | Reconfigurable metamaterials. a, A metamaterial that is tuned by shifting the metamolecular planes of the lattice by δa relative to each other (artist's impression)[2]. **b**, Arrays of metamolecules of a terahertz metamaterial are switched from one configuration to the other by thermal activation (scanning electron micrograph, SEM)[6]. **c**, Terahertz metamaterial can be dynamically tuned by manufacturing the metamaterial array on a MEMS-driven silicon platform[9]. Inset: SEM showing the metamolecule consisting of static and movable split rings. **d**, Photonic metamaterials manufactured on polymer films can be tuned by manipulation of resonator components by stretching the substrate[11]. **E** (**H**) shows the direction of the incident electric (magnetic) field. **e**, Schematic impression of a microwave metamaterial that can be switched by injecting liquid metallic mercury into the capillary array in the shape of split-ring resonators[14]. **f**, Plasmonic metamaterials manufactured on dielectric strings cut from a silicon nitride membrane can be driven electrostatically to megahertz frequencies[15]. The inset is an SEM that shows a fragment of the array at the terminal end. Figure reproduced with permission from: **a**, ref. 2, © 2009 AIP; **b**, ref. 6, © 2009 APS; **c**, ref. 9, © 2011 Wiley; **d**, ref. 11, © 2010 ACS; **e**, ref. 14, © 2009 AIP; **f**, ref. 15, © 2012 OSA.

(Fig. 1d). Microfluidics can also be used to reconfigure microwave metadevices when a conductive liquid (such as mercury) is injected into the network of metamolecules, changing their electromagnetic spectra[14] (Fig. 1e).

Engineering dynamically reconfigurable photonic metamaterials with metamolecular features on the scale of tens of nanometres is a formidable technological challenge. However, working on the nanoscale also has some important advantages. The elastic forces and the forces of inertia acting on metamaterial elements scale differently with size in such a way that the mechanical frequencies of the system reach high values for submicrometre structures. Moreover, the electrostatic force, which is inversely proportional to the distance, becomes the dominant force at the nanoscale: potential differences of only a few volts induce a force that can overcome the elastic response of a metamaterial framework. A photonic metamaterial driven by electrostatic forces[15] has been developed, consisting of a gold plasmonic nanowire pattern fabricated on a dielectric membrane (Fig. 1f). Operating in the optical telecommunication range of wavelengths, it can be used as a megahertz-bandwidth modulator consuming only a few microwatts of power and can also perform non-volatile switching, providing high-contrast transmission change.

It is clear that the technological solutions developed in MEMS, NEMS and micro/nanofluidics technologies will have considerable impact on metadevices in the future. The mechanical oscillation frequencies of nanoscale components could be in the gigahertz range, allowing properly engineered arrays of metamolecules based on subwavelength-sized cantilevers to be driven at high bandwidth. In some applications this approach can directly compete with electro-optical modulators, simultaneously offering low-voltage operation and lending itself to high-density integration.

Electro-optical metadevices

An active metadevice capable of efficient real-time control of radiation with electric signals was first developed for the terahertz part of the spectrum[16]. It consisted of a gold metamaterial array fabricated on a semiconductor substrate. The array and substrate together effectively formed a Schottky diode, where dielectric properties of the substrate can be controlled by injection and depletion of carriers. An electric signal applied to the metamaterial affects the high-frequency conductivity of the substrate in critical areas near the metamolecules and thus affects their resonant response (Fig. 2a). This approach allows modulation of the terahertz transmission by 50%. These types of hybrid metamaterial devices offer frequency and modulation bandwidth potentially up to 10 MHz (ref. 17). A multi-pixel 4 × 4 voltage-controlled spatial modulator for terahertz beams has been developed using this type of active terahertz metamaterials (Fig. 2b). In the modulator each pixel is an array of subwavelength-sized split-ring resonator elements fabricated on a semiconductor substrate, and is independently controlled by applying an external voltage. The spatial modulator has a uniform modulation depth of around 40% and negligible crosstalk at the resonant frequency. It can operate at room temperature under small voltages, with low power consumption[18]. Researchers have also demonstrated that carrier photogeneration in the silicon substrate supporting a chiral terahertz metamaterial can lead to a switching of its optical activity in the form of reversed circular dichroism[19].

A very substantial change in the dielectric properties of a nanometre-thick layer may be achieved in conductive oxides through the injection of free carriers, which should be enough to control resonant transmission in a hybrid metamaterial[20]. Ferroelectrics can also be engaged in tuning a metamaterial response[21]. Graphene (Fig. 2c) is another favourite for constructing metamaterials[22,23] with electro-optical capability, in particular in the infrared and terahertz domains, by exploiting the modification of the electromagnetic response by an applied voltage[24]. Such a terahertz electro-optical modulator, consisting of engineered graphene microribbon arrays, was recently demonstrated (Fig. 2d)[24]. The graphene plasmon resonances were reported to have remarkably large oscillator strengths, resulting in prominent room-temperature optical absorption peaks. Moreover, the graphene's response can be tuned over a broad terahertz frequency range by electrostatic doping.

The main advantage that metamaterial technology can bring to electro-optical modulation is achieving deep modulation in thin, often subwavelength, metadevices. In many cases such metadevices can operate at low voltages, which is clearly a competitive advantage over conventional technology exploiting bulk and expensive electro-optical crystals.

Liquid-crystal metadevices

Tunability and a strongly nonlinear response can be achieved in metamaterials by infiltrating them with liquid crystals[25]. Electrical control of negative permeability in microwave metamaterials infiltrated with nematic liquid crystals was experimentally demonstrated for a periodic array of split-ring resonators[26], showing a reversible change of the transmission resonance with a maximum shift of about 210 MHz (Fig. 2e). A similar approach was later applied to demonstrate the tunability of wire-pair[27] and fishnet[28] microwave metamaterials, where the external electric field changes the orientation of infiltrated molecules, leading to an effective index variation within the negative-index regime. In a similar way, the tunability can be achieved with magnetic field[29].

Mastering control in the near-infrared and optical regimes is a much harder task, but thermal[30] and ultraviolet-irradiation-induced tunability of optical metamaterials with liquid crystals has been shown experimentally[31]. Light-induced control of fishnet metamaterials infiltrated with liquid crystals was also achieved recently[32] using a metal–dielectric (Au–MgF_2) sandwich nanostructure on a glass substrate infiltrated with a nematic liquid crystal (Fig. 2f). In such a device the transmission can be modulated up to 30% by both the electric voltage and incident optical power at the telecommunications wavelength of 1,550 nm.

Liquid crystals are a robust, proven and affordable technology offering a highly practical solution for controlling metamaterial devices when ambient temperatures and speed of operation are not critical issues, given that in most liquid crystals the response relaxation time is in the millisecond ballpark.

Phase-change metadevices

A radical change in the arrangement of atoms is called a structural phase transition, or phase change. Phase-change functionality of semiconductor chalcogenide glass has been used for decades in optical compact disks and DVDs, where the rewritable memory function is underpinned by a transition from amorphous to crystalline phase. Phase-change functionality in polymorphic metals can also provide a way to achieve nanoscale optical and plasmonic switching devices that can be fast and require little energy to activate[33]. Depending on the regime of stimulation and confinement of the active medium, phase changes can be either reversible or irreversible.

The first phase-change nanocomposite material for nonlinear optics and nonlinear plasmonics was created by grain-boundary penetration of gallium into the network of domains of an aluminium film[34]. Here, continuous and reversible changes occur through the intermediate coexistence of two different phases of gallium[35]. The change may be induced in a few picoseconds, and it relaxes back on a timescale of microseconds or nanoseconds. This optically and temperature-driven composite metamaterial forms a mirror-like interface with silica and shows an exceptionally broadband phase-transition-based switching response to optical excitation. It operates from the visible to near-infrared part of the spectrum and exhibits ~20% reflectivity change at optical fluence of about 1.5 mJ cm^{-2} with sub-100-ns response time.

Another important example of a phase-change medium is vanadium dioxide (VO_2), which shows a phase transition of a percolative nature in which 5–10-nm metallic puddles emerge and grow in the insulating host (Fig. 3a). It has attracted considerable attention as an active medium for hybrid metamaterial structures[36–39]. Hybridizing vanadium dioxide with a metamaterial shows 20% temperature-activated tuning of the transmission in the terahertz range. Similar switching has also been demonstrated in the near-infrared using a dual-bar gold metamaterial array[38]. A form of electrically activated memory function and persistent frequency tuning of a metamaterial, which allows lasting modification of its response by using a transient stimulus, have also been demonstrated in a hybrid VO_2 metadevice in the terahertz part of the spectrum[40].

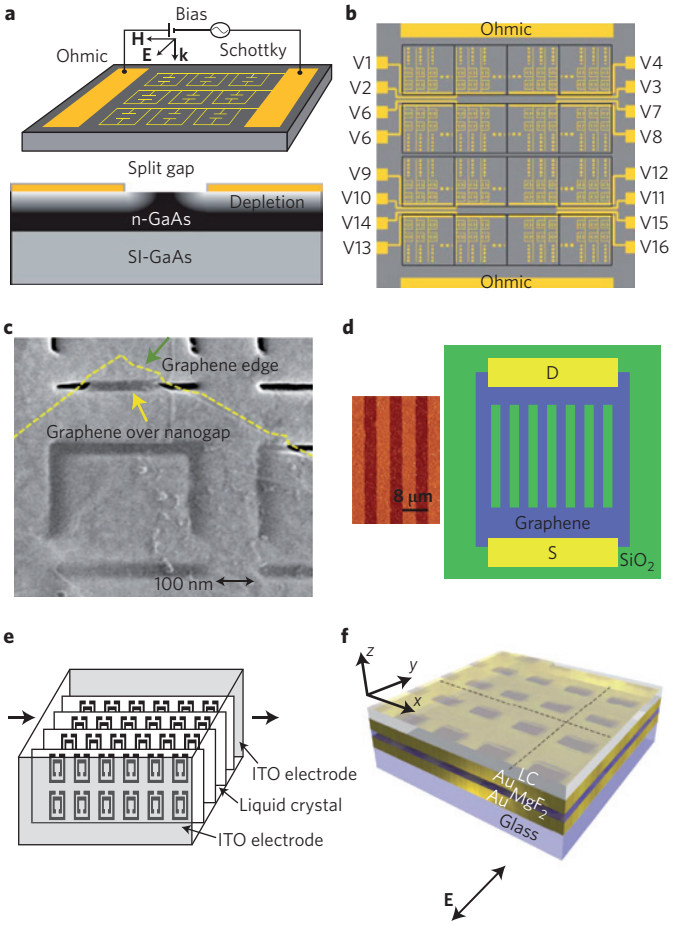

Figure 2 | Electro-optical and liquid-crystal metadevices. a, A terahertz metamaterial modulator fabricated on a semiconductor substrate (artist's impression) can be controlled by injection and depletion of carriers in response to an electric bias[16]. A vertical cross-section of the metamaterial structure near the resonator gap is shown below. **b**, Terahertz spatial light modulator based on metamaterial array elements that are individually addressable by electrical signals[18]. **c**, Graphene covering a metamaterial strongly modifies its plasmonic spectrum. A helium ion microscope image shows a fragment of the gold nano-slit array partially covered by graphene[22,71]. **d**, Right: A terahertz electro-optical modulator consisting of graphene microribbons with electrical terminals on a dielectric substrate (artist's impression)[24]. Left: An atomic force microscope image of the graphene array. S and D are the source and drain terminals. **e**, A negative-permeability microwave metamaterial consisting of an array of split rings infiltrated with nematic liquid crystals (artist's impression) can be continuously and reversibly adjusted by an applied electric field[26]. ITO, indium tin oxide. **f**, Optical nonlinearity of photonic fishnet metamaterials (artist's impression) infiltrated with nematic liquid crystal (LC). The material's optical properties can be tuned by an electric field[32]. Figure reproduced with permission from: **a**, ref. 16, © 2006 NPG; **b**, ref. 18, © 2009 AIP; **c**, ref. 71, © 2011 AIP; **d**, ref. 24, © 2011 NPG; **e**, ref. 26, © 2007 AIP; **f**, ref. 32, © 2012 AIP.

Combining the phase-change technology of chalcogenide glass semiconductors with metamaterials is a promising direction that offers high-contrast, near-infrared, electronically and optically addressable gating and switching. Its technological importance lies in the wide availability of chalcogenide glass production for optical data storage and the potential of integration with the future silicone and chalcogenide glass photonics technologies. Switching has been demonstrated by exploiting the frequency shift of a narrowband Fano resonance mode of a plasmonic planar metamaterial that

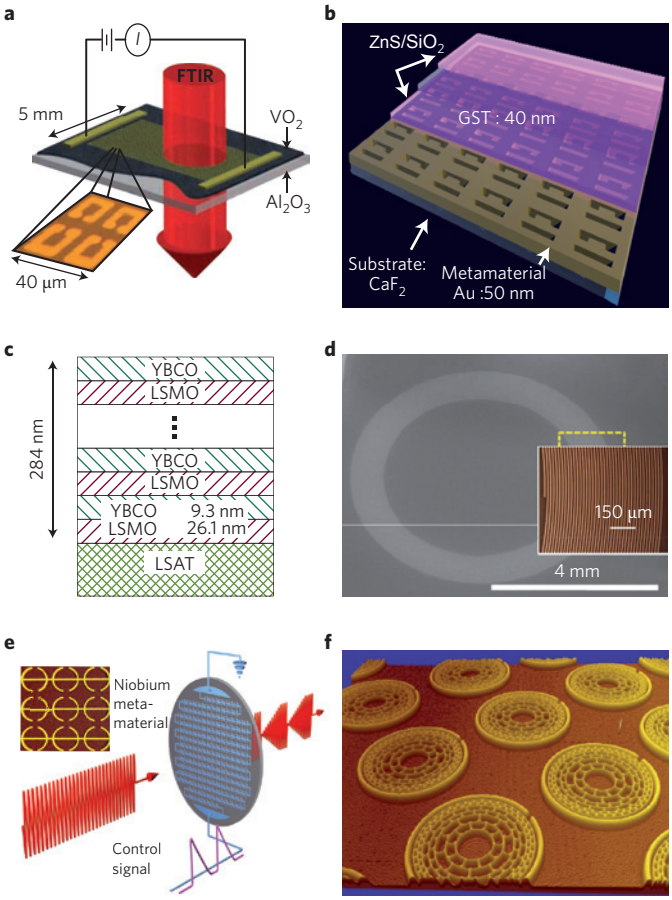

Figure 3 | Phase-change and superconducting metadevices. a, Metal-oxide memory hybrid-metamaterial device exploiting the temperature-driven phase transition of a vanadium oxide film (artist's impression)[40]. FTIR, Fourier transform infrared spectroscopy. **b**, Structure of the metamaterial all-optical switch using phase-change chalcogenide glass GST: the hybrid device consists of a planar gold plasmonic metamaterial on a silicon nitride membrane, covered with chalcogenide glass[41]. **c**, Negative-refraction, millimetre-wave metamaterial nanostructure based on ferromagnet–superconductor superlattice[52]. YBCO, yttrium barium copper oxide; LSMO, lanthanum strontium manganese oxide. **d**, A spiral metamolecule made from superconducting niobium is about 700 times smaller than its resonance wavelength[53]. **e**, Controlling sub-terahertz transmission of niobium superconducting metamaterial with electric current running through the network of metamolecules (inset shows optical image of the network of metamolecules connected by the control wire)[55]. **f**, Millimetre-wave quantum metamaterial exploiting the flux exclusion effect in superconductors manufactured from high-critical-temperature superconductor YBCO (profile image)[61]. Figure reproduced with permission from: **a**, ref. 40, © 2009 AAAS; **b**, ref. 41, © 2010 AIP; **c**, ref. 52, © 2005 APS; **d**, ref. 53, © 2011 IEEE; **e**, ref. 55, © OSA; **f**, ref. 61, © 2012 NPG.

was induced by a change in the dielectric properties of an adjacent 200-nm-thick film of chalcogenide glass[41]. The material used was a new gallium lanthanum sulphide chalcogenide glass, which was bistable and silicon-on-insulator compatible. An electrically stimulated transition between amorphous and crystalline forms of the glass brings about a 150-nm shift in the near-infrared resonance, providing transmission modulation with a contrast ratio of 4:1 in a layer of subwavelength thickness. One of the advantages of this technology is that devices may be structurally engineered to operate at any wavelength throughout the visible and infrared spectral range down to 11 μm. Recently, fully reversible bidirectional optically activated switching has been demonstrated in a gold plasmonic nanostructure combined with a conventional germanium–antimony–tellurium (GST) chalcogenide glass[42], making this technology compatible with real-world photonic applications (Fig. 3b).

Phase-change technology is gaining recognition in photonics applications. When non-volatile switching is required, its combination with metamaterials offers high contrast switching response with response times as low as nanoseconds and beyond[43] in devices of subwavelength thicknesses.

Superconducting metadevices

Negative dielectric constants and the dominant kinetic resistance make superconductors an intriguing plasmonic medium[44]. Applications of superconducting metamaterials are, however, limited to the microwave domain for niobium-based metamaterials, and to the terahertz spectral domain if high-temperature superconductors are used. This is because higher frequencies destroy the superconducting phase.

Researchers have demonstrated the fabrication of microwave and terahertz metamaterials where superconductors replace metals in conventional metamaterial designs. This includes the use of niobium[45] and patterned high-critical-temperature perovskite-related cuprates and niobioum nitride[46–51]. Negative refraction in a multilayer stack of ferromagnetic and superconducting thin films (Fig. 3c) has also been demonstrated[52]. Because a niobium thin film shows low losses at cryogenic temperatures, it allows the development of a metamaterial with extremely compact metamolecules that are as small as 1/658 of the free-space wavelength and have resonances with quality factors in excess of 5,000 (ref. 53; Fig. 3d).

Tuning of metamaterial resonances by temperature and external magnetic field is easy to achieve[45,47,50,51,54]. A superconducting metamaterial in the form of an interlinked network of subwavelength resonators can also be dynamically controlled by passing electrical current through it[55]: using a niobium metamaterial it was possible to achieve 45% intensity modulation at a carrier frequency of 100 GHz (Fig. 3e). The mechanism underpinning this functionality is a combination of the suppression of superconductivity by magnetic field and heat created by the control current. Superconducting metamaterials can be used in temperature-controllable slow light devices[56] and other applications[57].

Moreover, in superconducting metamaterials, it will be possible to switch from the plasmonic excitations of conventional metamaterial devices to quantum excitations underpinned by flux quantization and quantum interference effects. Indeed, the iconic object of metamaterials research — the ubiquitous split-ring metamolecule — has much in common with the fundamental superconductive element, the Josephson junction ring. An array of Josephson rings could be a truly quantum metamaterial, where each metamolecule is a multilevel quantum system supporting phase qubits[58–60]. However, Josephson junction devices require extremely high-quality nanofabrication and sub-kelvin temperatures. It was recently suggested[61] that a much simpler quantum superconducting metamaterial could be constructed that would exploit the magnetic flux quantization for switching, but would not require Josephson junctions (Fig. 3f). This metamaterial is an array of split-ring resonators enclosing a nest of superconducting rings[61]. To achieve a quantum regime of switching, it exploits the quantum exclusion of the oscillating magnetic field penetrating the superconducting rings when a magnetic field is generated by the current in the outer split ring driven by the incident wave.

A superconducting metamaterial can also be used to control static magnetic fields[62–64]. An anisotropic magnetic metamaterial consisting of an array of superconducting plates can be used for non-intrusive screening of weak d.c. magnetic fields. Moreover, a purposely designed cylindrical superconductor–ferromagnetic bilayer can cloak uniform static magnetic fields[65].

Superconducting metamaterials offer a radically new base for data processing and quantum information technologies.

Superconductors not only provide far lower losses, but also allow access to the extreme sensitivity of the superconducting state to external stimuli such as heat, electric and magnetic fields, light, current and mechanical stress. The cryo-cooling requirement is no longer a serious technological limitation as compact cryo-devices are now widely deployed in telecommunications and sensing installations.

Ultrafast photonic metadevices

Metamaterials in which metal nanostructures are hybridized with nonlinear and switchable dielectric or semiconductor layers and controlled by ultrafast optical pulses provide much faster switching than is attainable with MEMS/NEMS repositioning of parts, phase-change or voltage-driven carrier injection, liquid crystals or superconductivity modulation. A change in the refractive index or absorption in the layer adjacent to a plasmonic metamaterial array induced by the intense light modifies the plasmon spectrum of the nanostructure. This can lead to a strong change in the resonant transmission and reflection of the hybrid. Prime candidates for hybridization with metamaterials are semiconductors and semiconductor multiple-quantum-well structures used as substrates for a metallic framework, carbon nanotubes and graphene implanted into the fabric of the metamaterials.

The interaction of ultrafast optical pulses with metamaterial was initially studied for optical modulation of their terahertz responses: shunting the capacitive region of the metallic split-ring network by injecting optical carriers into the supporting ErAs/GaAs superlattice leads to a deep modulation of terahertz transmission characteristics of the planar metamaterial, with recovery time on the picosecond scale[66,67].

In the optical part of the spectrum the plasmonic resonance field enhancement created by the metamaterial network may be used to enhance the nonlinear response of the adjacent dielectric or semiconductor layer[68,69] (Fig. 4a). A threefold improvement of pump–probe response was observed in the near-infrared part of the spectrum in a fishnet metamaterial manufactured on an α-silicon substrate exhibiting up to 60% light-induced modulation at an excitation fluence of about 0.5 mJ cm^{-2}. Here the relaxation of nonlinearity is controlled by the electron relaxation time and happens within 2 ps (ref. 68).

Semiconductor carbon nanotubes are highly nonlinear media in their own right, where nonlinearity is associated with the optical saturation of excitonic transitions. Hybridization of single-walled carbon nanotubes with plasmonic metamaterials makes a photonic medium with an exceptionally strong ultrafast nonlinearity operating in the regime of plasmon–exciton coupling[70] (Fig. 4b). More than tenfold enhancement of the nonlinearity of nanotubes was achieved in a plasmonic nanostructure supporting Fano-type resonances, so a fluence of only 40 μJ cm^{-2} can create a 10% optical modulation with relaxation time less than 500 fs.

If the nonlinearity of carbon nanotubes has an essentially resonant nature, graphene is highly attractive as a medium with extremely broadband and fast nonlinear response. Unfortunately the achievable nonlinear transmission changes of atomic-thickness graphene films (which absorb only about 2% of incident light) are very small, in the region of 10^{-4}, even at intensities close to optical breakdown. The broadband nonlinear optical response of graphene can, however, be resonantly enhanced by more than an order of magnitude through hybridization with a plasmonic metamaterial[22], while retaining an ultrafast response time of about 1 ps (ref. 71). Transmission modulation close to 10% has been seen at a pump fluence of 30 μJ cm^{-2} (ref. 71). This approach allows the engineering of graphene's nonlinearity at a prescribed wavelength within a broad wavelength range, enabling applications in optical switching and pulse shaping.

In terms of data-processing applications, one of the most important figure of merit is the product of the fluence necessary to create an acceptable modulation contrast and the recovery time of response. Remarkably, in the optical part of the spectrum the metal metamaterial framework itself provides a source of nonlinearity that delivers one of the best performances. Indeed, metamaterial nanostructuring of a thin gold film increases the two-photon interband resonant absorption nonlinearity 300-fold, creating arguably one of the fastest and brightest nonlinear optical medium currently known[72]. Moreover, depending on the spectral position with respect to the plasmonic resonance, nonlinearity may change sign, thus switching from nonlinear dissipation to enhanced transmission. At a fluence of about 270 μJ cm^{-2}, modulation of up to 40% can be achieved with a recorded relaxation time that has a fast component

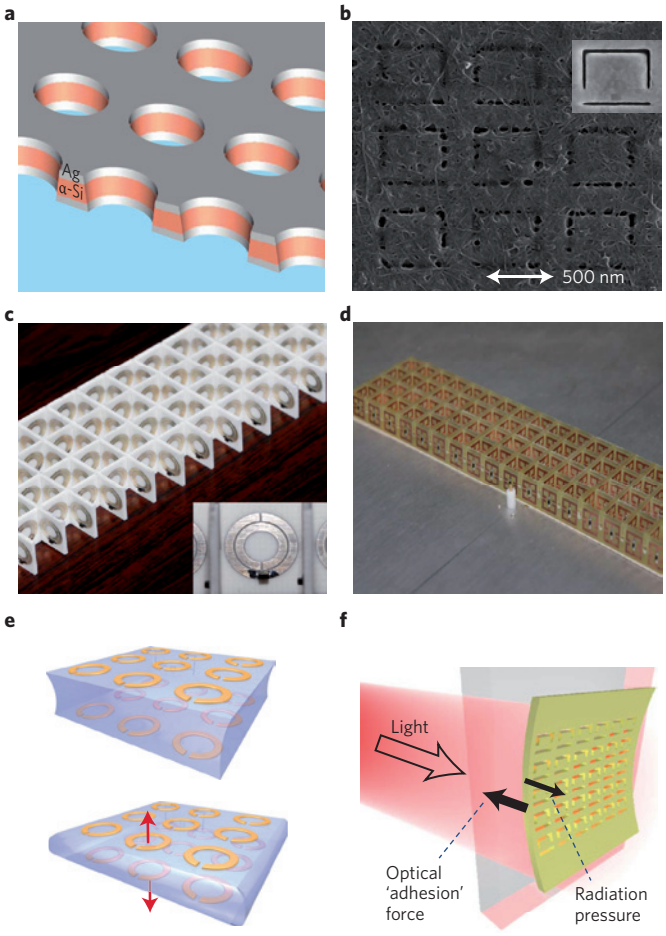

Figure 4 | Ultrafast metadevices, varactor metamaterials and electromagnetic forces. a, A fishnet photonic metamaterial with sub-picosecond optical response exploits fast carrier dynamics in the α-Si substrate[69]. **b**, A plasmonic metamaterial functionalized with carbon nanotubes shows strong sub-picosecond exciton–plasmon nonlinearity in the near-infrared part of the spectrum[70]. **c**, A nonlinear magnetic metamaterial with lumped varactor diodes embedded in the metamolecules[78]. Inset: a unit cell of the metamaterial before deposition of carbon nanotubes. **d**, Nonlinear electric metamaterials with varactor diodes[80]. **e**, A magnetoelastic metamaterial[99] is driven by the Ampère's force between excited metamolecules. Artist's impression of a metamaterial slab before (top) and after (bottom) illumination with light (the red arrows indicate the electromagnetic forces acting between the metamaterial elements). **f**, Optical gecko toe: artist's impression of a metamaterial film attracted by a beam of light to a dielectric surface[102]. Figure reproduced with permission from: **a**, ref. 69, © 2009 ACS; **b**, ref. 70, © 2010 APS; **c**, ref. 78, © 2008 OSA; **d**, ref. 80, © 2009 AIP; **e**, ref. 99, © 2012 NPG; **f**, ref. 102, © 2012 APS.

of about 100 fs (ref. 72). Enhanced nonlinearity of a gold metamaterial has been used to demonstrate a giant effect of intensity-dependent polarization rotation that is millions of time stronger than previously observed in natural crystalline materials[73].

In metals, optical excitation close to the edge of the Fermi level also offers a strong, but more slowly relaxing, nonlinear response. In this regime a metal nanowire metamaterial provides a 1-ps relaxation time with a good modulation contrast[74] at fluence of 7 mJ cm^{-2}.

Strong and fast nonlinearities are needed for controlling light with light because, according to the fundamental Huygens superposition principle, light beams travelling in a linear medium will pass though one another without mutual disturbance. Indeed, the field of photonics is based on the premise that controlling light signals with light requires intense laser fields to facilitate beam interactions in nonlinear media, where the superposition principle can be broken. This premise was recently challenged with help of a plasmonic metamaterial[75]: it was demonstrated that two coherent beams of light of arbitrarily low intensity can interact on a metamaterial layer of nanoscale thickness in such a way that one beam modulates the intensity of the other. The interference of beams can eliminate the plasmonic Joule losses of light energy in the metamaterial or, in contrast, can lead to almost total absorption of light. Applications of this phenomenon may lie in ultrafast all-optical pulse-recovery devices, coherence filters and terahertz-bandwidth light-by-light modulators.

Enhancement of ultrafast nonlinearities with metamaterials arguably offers the brightest and fastest nonlinear media with potential ground-breaking applications for terahertz-rate all-optical data processing as well as ultrafast optical limiters and laser saturable absorbers.

Nonlinear metadevices with varactors

Tuning metamaterials by taking advantage of the nonlinear response of lumped elements integrated into metamolecules of left-handed metamaterials was first suggested theoretically[76,77] and later implemented experimentally[78,79]. A similar approach has been explored for other types of metamaterial systems[17,80–82]. For instance, resonance of the split-ring metamolecule can be controlled by adding the capacitance of a varactor diode in series with the distributed capacitance of the resonator when placed at a point of maxima in the electric currents[83,84]. At low powers a split ring with embedded varactor exhibits nonlinearity of the second and third order[85,86], whereas at higher powers the nonlinear response becomes multivalued or bistable[84,87].

An example of a nonlinear magnetic metamaterial operating at microwave frequencies is shown in Fig. 4c. Here the varactor diodes are placed in each element of the composite structure[83,87]. By selecting the operating frequency to be near resonance, one can dynamically change the transmission properties of the metamaterial, for instance from opaque to transparent, by varying the input power. If a point-like dipole source is placed near the metamaterial, the metamolecules closer to the source will experience stronger fields, making the metamaterial more transparent, which can be seen as beaming of radiation emerging from the metamaterial[78]. A similar approach has been applied to the design of a tunable nonlinear electric response[80] (Fig. 4d).

Intensity-dependent (nonlinear) polarization rotation can also be achieved with a varactor-based chiral metadevice[88]. This polarization effect is almost negligible in any natural crystals, whereas in the nonlinear metamaterial the response of the structure has strongly resonant features caused by the excitation of currents in the left-handed metamolecule by the left-handed circularly polarized wave. At the same time, the right-handed circularly polarized wave does not noticeably excite any resonances in the structure. Changing the power of the incident wave shifts the resonance of the gyrotropic response to a higher frequency, and also leads to asymmetric transmission in the forward and backward directions[88].

The quadratic nonlinear response of the varactor-loaded metamaterials[89] can be used in various parametric processes, including phase conjugation[90], three- and four-wave mixing[91], and second-harmonic generation in quasi-phase-matched[92] and doubly resonant[93] structures. An unusual effect of phase matching between the backward and forward waves can also be realized in metamaterials that display negative refraction, giving rise to a range of exotic transmission and reflection features[92]. In applications that involve second-harmonic generation in metamaterials, momentum conservation can be satisfied in a process that creates backward harmonic radiation[94,95]. For other applications of lumped nonlinear devices in metamaterials see references 96–98.

Integration of lumped electronic components with metamaterial offers a highly efficient playground for modelling nonlinear systems and also provides a straightforward way of developing highly nonlinear and switchable media for the microwave part of the spectrum.

Metadevices driven by electromagnetic forces

In metamaterials composed of an anisotropic lattice of resonant elements, such as split-ring resonators or capacitively loaded 'meta-atoms', the currents induced in the resonators not only affect each other through mutual inductance, but also result in Ampère's force between the resonators (Fig. 4e), which is attractive, provided that the neighbouring currents are in phase. If the resonators are allowed to move, this force will displace them from their original positions, thus changing their mutual impedance, which in turn affects the current amplitudes and interaction forces. The balance is maintained by a restoring Hooke force, which originates from the elastic properties of the host medium. It enables the electromagnetically induced forces to change the metamaterial structure, dynamically tuning its effective properties. Reconfigurable metamaterials exploiting this force have been branded magnetoelastic metamaterials[99]. Related ideas involving conformational nonlinearity of chiral spiral metamolecules[100] and metamaterials with a gold nanowire pairs have also been discussed recently[101].

A strong light-driven force may be generated when a plasmonic metamaterial is illuminated in close proximity to a dielectric or metal surface[102] (Fig. 4f). This near-field force can exceed radiation pressure and Casimir forces to provide an optically controlled adhesion mechanism mimicking the gecko toe: at illumination intensities of just a few tens of nanowatts per square micrometre, it is sufficient to overcome the Earth's gravitational pull, thus offering a new opportunity for designing metadevices driven by electromagnetic forces.

The proliferation of nanostructured materials is magnifying the role of electromagnetic forces. In the near future, these could become a practical source of optical nonlinearity and photonic switching.

Outlook

Future technologies will demand a huge increase in photonic integration and energy efficiency far surpassing that of bulk optical components and silicon photonics. Such a level of integration can be achieved by embedding the data-processing and waveguiding functionalities at the material's level, creating the new paradigm of metadevices. We argue that robust and reliable metadevices will allow photonics to compete with electronics not only in telecommunication systems, but also at the level of 'Photonics Inside' consumer products such as mobile phones or automobiles. The main challenges in achieving this vision will be in developing cost-efficient fabrication and device integration technologies.

Received 22 June 2012; accepted 24 August 2012; published online 23 October 2012.

References

1. Ou, J. Y., Plum, E., Jiang, L. & Zheludev, N. I. Reconfigurable photonic metamaterials. *Nano Lett.* **11,** 2142–2144 (2011).
2. Lapine, M. *et al.* Structural tunability in metamaterials. *Appl. Phys. Lett.* **95,** 084105 (2009).
3. Karim, M. F., Liu, A. Q., Alphones, A. & Yu, A. B. A tunable bandstop filter via the capacitance change of micromachined switches. *J. Micromech. Microeng.* **16,** 851–861 (2006).
4. Gil, I., Martin, F., Rottenberg, X. & De Raedt, W. Tunable stop-band filter at Q-band based on RF-MEMS metamaterials. *Electron. Lett.* **43,** 1153–1154 (2007).
5. Hand, T. & Cummer, S. Characterization of tunable metamaterial elements using MEMS switches. *IEEE Antennas Wireless Propag. Lett.* **6,** 401–404 (2007).
6. Tao, H. *et al.* Reconfigurable terahertz metamaterials. *Phys. Rev. Lett.* **103,** 147401 (2009).
7. He, X., Lv, Z., Liu, B. & Li, Z. Tunable magnetic metamaterial based multi-split-ring resonator (MSRR) using MEMS switch components. *Microsyst. Technol. Micro Nanosyst. Inform. Storage Process. Syst.* **17,** 1263–1269 (2011).
8. Zhu, W. M. *et al.* Switchable magnetic metamaterials using micromachining processes. *Adv. Mater.* **23,** 1792–1796 (2011).
9. Fu, Y. H. *et al.* A micromachined reconfigurable metamaterial via reconfiguration of asymmetric split-ring resonators. *Adv. Funct. Mater.* **21,** 3589–3594 (2011).
10. Ozbey, B. & Aktas, O. Continuously tunable terahertz metamaterial employing magnetically actuated cantilevers. *Opt. Express* **19,** 5741–5752 (2011).
11. Pryce, I. M., Aydin, K., Kelaita, Y. A., Briggs, R. M. & Atwater, H. A. Highly strained compliant optical metamaterials with large frequency tunability. *Nano Lett.* **10,** 4222–4227 (2010).
12. Tao, H. *et al.* Metamaterial silk composites at terahertz frequencies. *Adv. Mater.* **22,** 3527–3531 (2010).
13. Aksu, S. *et al.* Flexible plasmonics on unconventional and nonplanar substrates. *Adv. Mater.* **23,** 4422–4430 (2011).
14. Kasirga, T. S., Ertas, Y. N. & Bayindir, M. Microfluidics for reconfigurable electromagnetic metamaterials. *Appl. Phys. Lett.* **95,** 214102 (2009).
15. Ou, J. Y., Plum, E. & Zheludev, N. I. MHz bandwidth electro-optical modulator based on a reconfigurable photonic metamaterial. *CLEO/QELS Conf. Poster* JW4A.11 (2012).
16. Chen, H-T. *et al.* Active terahertz metamaterial devices. *Nature* **444,** 597–600 (2006).
17. Shrekenhamer, D. *et al.* High speed terahertz modulation from metamaterials with embedded high electron mobility transistors. *Opt. Express* **19,** 9968–9975 (2011).
18. Chan, W. L. *et al.* A spatial light modulator for terahertz beams. *Appl. Phys. Lett.* **94,** 213511 (2009).
19. Zhang, S. *et al.* Photoinduced handedness switching in terahertz chiral metamolecules. *Nature Commun.* **3,** 942 (2012).
20. Feigenbaum, E., Diest, K. & Atwater, H. A. Unity-order index change in transparent conducting oxides at visible frequencies. *Nano Lett.* **10,** 2111–2116 (2010).
21. Gil, M. *et al.* Electrically tunable split-ring resonators at microwave frequencies based on barium-strontium-titanate thick films. *Electron. Lett.* **45,** 417–418 (2009).
22. Papasimakis, N. *et al.* Graphene in a photonic metamaterial. *Opt. Express* **18,** 8353–8359 (2010).
23. Yan, H. G. *et al.* Tunable infrared plasmonic devices using graphene/insulator stacks. *Nature Nanotech.* **7,** 330–334 (2012).
24. Ju, L. *et al.* Graphene plasmonics for tunable terahertz metamaterials. *Nature Nanotech.* **6,** 630–634 (2011).
25. Wang, X. *et al.* Tunable optical negative-index metamaterials employing anisotropic liquid crystals. *Appl. Phys. Lett.* **91,** 143122 (2007).
26. Zhao, Q. *et al.* Electrically tunable negative permeability metamaterials based on nematic liquid crystals. *Appl. Phys. Lett.* **90,** 011112 (2007).
27. Zhang, F. L. *et al.* Voltage tunable short wire-pair type of metamaterial infiltrated by nematic liquid crystal. *Appl. Phys. Lett.* **97,** 134103 (2010).
28. Zhang, F. L. *et al.* Electrically controllable fishnet metamaterial based on nematic liquid crystal. *Opt. Express* **19,** 1563–1568 (2011).
29. Zhang, F. *et al.* Magnetic control of negative permeability metamaterials based on liquid crystals. *Appl. Phys. Lett.* **92,** 193104 (2008).
30. Xiao, S. M. *et al.* Tunable magnetic response of metamaterials. *Appl. Phys. Lett.* **95,** 033115 (2009).
31. Kang, B. *et al.* Optical switching of near infrared light transmission in metamaterial-liquid crystal cell structure. *Opt. Express* **18,** 16492–16498 (2010).
32. Minovich, A. *et al.* Liquid crystal based nonlinear fishnet metamaterials. *Appl. Phys. Lett.* **100,** 121113 (2012).
33. Zheludev, N. All change, please. *Nature Photon.***1,** 551–553 (2007).
34. Krasavin, A. V., MacDonald, K. F., Schwanecke, A. S. & Zheludev, N. I. Gallium/aluminum nanocomposite material for nonlinear optics and nonlinear plasmonics. *Appl. Phys. Lett.* **89,** 031118 (2006).
35. Bennett, P. J. *et al.* A photonic switch based on a gigantic, reversible optical nonlinearity of liquefying gallium. *Appl. Phys. Lett.* **73,** 1787–1789 (1998).
36. Driscoll, T. *et al.* Dynamic tuning of an infrared hybrid-metamaterial resonance using vanadium dioxide. *Appl. Phys. Lett.* **93,** 024101 (2008).
37. Seo, M. *et al.* Active terahertz nanoantennas based on VO_2 phase transition. *Nano Lett.* **10,** 2064–2068 (2010).
38. Huang, W-x. *et al.* Optical switching of a metamaterial by temperature controlling. *Appl. Phys. Lett.* **96,** 261908 (2010).
39. Appavoo, K. & Haglund, R. F. Jr Detecting nanoscale size dependence in VO_2 phase transition using a split-ring resonator metamaterial. *Nano Lett.* **11,** 1025–1031 (2011).
40. Driscoll, T. *et al.* Memory metamaterials. *Science* **325,** 1518–1521 (2009).
41. Samson, Z. L. *et al.* Metamaterial electro-optic switch of nanoscale thickness. *Appl. Phys. Lett.* **96,** 143105 (2010).
42. Gholipour, B. *et al.* Chalcogenide glass photonics: non-volatile, bi-directional, all-optical switching in phase-change metamaterials. *CLEO/QELS Conf. Paper* CF2A.3 (2012).
43. Simpson, R. E. *et al.* Interfacial phase-change memory. *Nature Nanotech.* **6,** 501–505 (2011).
44. Tsiatmas, A., Fedotov, A. V. & Zheludev, N. I. Plasmonics without losses? (The case for terahertz superconducting plasmonics). *New J. Phys.* (in the press). Preprint at http://arxiv.org/abs/1105.3045 (2011).
45. Ricci, M., Orloff, N. & Anlage, S. M. Superconducting metamaterials. *Appl. Phys. Lett.* **87,** 034102 (2005).
46. Fedotov, V. A. *et al.* Temperature control of Fano resonances and transmission in superconducting metamaterials. *Opt. Express* **18,** 9015–9019 (2010).
47. Chen, H-T. *et al.* Tuning the resonance in high-temperature superconducting terahertz metamaterials. *Phys. Rev. Lett.* **105,** 247402 (2010).
48. Gu, J. Q. *et al.* Terahertz superconductor metamaterial. *Appl. Phys. Lett.* **97,** 071102 (2010).
49. Jin, B. B. *et al.* Low loss and magnetic field-tunable superconducting terahertz metamaterial. *Opt. Express* **18,** 17504–17509 (2010).
50. Tsiatmas, A. *et al.* Superconducting plasmonics and extraordinary transmission. *Appl. Phys. Lett.* **97,** 111106 (2010).
51. Wu, J. B. *et al.* Tuning of superconducting niobium nitride terahertz metamaterials. *Opt. Express* **19,** 12021–12026 (2011).
52. Pimenov, A., Loidl, A., Przyslupski, P. & Dabrowski, B. Negative refraction in ferromagnet-superconductor superlattices. *Phys. Rev. Lett.* **95,** 247009 (2005).
53. Kurter, C. *et al.* Superconducting RF metamaterials made with magnetically active planar spirals. *IEEE Trans. Appl. Supercond.* **21,** 709–712 (2011).
54. Ricci, M. C. *et al.* Tunability of superconducting metamaterials. *IEEE Trans. Appl. Supercond.* **17,** 918–921 (2007).
55. Savinov, V., Fedotov, V. A., de Groot, P. A. & Zheludev, N. I. Electro-optical modulation of sub-terahertz radiation with superconducting metamaterial. *CLEO/QELS Conf. Paper* CTh1D.1 (2012).
56. Kurter, C. *et al.* Classical analogue of electromagnetically induced transparency with a metal–superconductor hybrid metamaterial. *Phys. Rev. Lett.* **107,** 043901 (2011).
57. Kurter, C. *et al.* Switching nonlinearity in a superconductor-enhanced metamaterial. *Appl. Phys. Lett.* **100,** 121906 (2012).
58. Du, C. G., Chen, H. Y. & Li, S. Q. Quantum left-handed metamaterial from superconducting quantum-interference devices. *Phys. Rev. B* **74,** 113105 (2006).
59. Lazarides, N. & Tsironis, G. P. RF superconducting quantum interference device metamaterials. *Appl. Phys. Lett.* **90,** 163501 (2007).
60. Rakhmanov, A. L., Zagoskin, A. M., Savel'ev, S. & Nori, F. Quantum metamaterials: electromagnetic waves in a Josephson qubit line. *Phys. Rev. B* **77,** 144507 (2008).
61. Savinov, V. *et al.* Flux exclusion quantum superconducting metamaterial: towards quantum-level switching. *Sci. Rep.* **2,** 450 (2012).
62. Wood, B. *et al.* A d.c. magnetic metamaterial. *Nature Mater.* **7,** 295–297 (2008).
63. Navau, C., Chen, D. X., Sanchez, A. & Del-Valle, N. Magnetic properties of a dc metamaterial consisting of parallel square superconducting thin plates. *Appl. Phys. Lett.* **94,** 242501 (2009).
64. Sanchez, A., Navau, C., Prat-Camps, J. & Chen, D. X. Antimagnets: controlling magnetic fields with superconductor-metamaterial hybrids. *New J. Phys.* **13,** 093034 (2011).
65. Gomory, F. *et al.* Experimental realization of a magnetic cloak. *Science* **335,** 1466–1468 (2012).
66. Padilla, W. J., Taylor, A. J., Highstrete, C., Lee, M. & Averitt, R. D. Dynamical electric and magnetic metamaterial response at terahertz frequencies. *Phys. Rev. Lett.* **96,** 107401 (2006).
67. Chen, H-T. *et al.* Ultrafast optical switching of terahertz metamaterials fabricated on ErAs/GaAs nanoisland superlattices. *Opt. Lett.* **32,** 1620–1622 (2007).

68. Cho, D. J. *et al.* Ultrafast modulation of optical metamaterials. *Opt. Express* **17,** 17652–17657 (2009).
69. Dani, K. M. *et al.* Subpicosecond optical switching with a negative index metamaterial. *Nano Lett.* **9,** 3565–3569 (2009).
70. Nikolaenko, A. E. *et al.* Carbon nanotubes in a photonic metamaterial. *Phys. Rev. Lett.* **104,** 153902 (2010).
71. Nikolaenko, A. E. *et al.* Nonlinear graphene metamaterial. *Appl. Phys. Lett.* **100,** 181109 (2012).
72. Ren, M. X. *et al.* Nanostructured plasmonic medium for terahertz bandwidth all-optical switching. *Adv. Mater.* **23,** 5540–5544 (2011).
73. Ren, M., Plum, E., Xu, J. & Zheludev, N. I. Giant nonlinear optical activity in a plasmonic metamaterial. *Nature Commun.* **3,** 833 (2012).
74. Wurtz, G. A. *et al.* Designed ultrafast optical nonlinearity in a plasmonic nanorod metamaterial enhanced by nonlocality. *Nature Nanotech.* **6,** 106–110 (2011).
75. Zhang, J., MacDonald, K. F. & Zheludev, N. I. Controlling light-with-light without nonlinearity. *Light* **1,** e18 (2012).
76. Zharov, A. A., Shadrivov, I. V. & Kivshar, Y. S. Nonlinear properties of left-handed metamaterials. *Phys. Rev. Lett.* **91,** 037401 (2003).
77. Lapine, M., Gorkunov, M. & Ringhofer, K. H. Nonlinearity of a metamaterial arising from diode insertions into resonant conductive elements. *Phys. Rev. E* **67,** 065601 (2003).
78. Shadrivov, I. V., Kozyrev, A. B., van der Weide, D. & Kivshar, Y. S. Nonlinear magnetic metamaterials. *Opt. Express* **16,** 20266–20271 (2008).
79. Shadrivov, I. V., Kozyrev, A. B., van der Weide, D. W. & Kivshar, Y. S. Tunable transmission and harmonic generation in nonlinear metamaterials. *Appl. Phys. Lett.* **93,** 161903 (2008).
80. Powell, D. A., Shadrivov, I. V. & Kivshar, Y. S. Nonlinear electric metamaterials. *Appl. Phys. Lett.* **95,** 084102 (2009).
81. Carbonell, J., Boria, V. E. & Lippens, D. Nonlinear effects in split ring resonators loaded with heterostructure barrier varactors. *Microwave Opt. Technol. Lett.* **50,** 474–479 (2008).
82. Wiltshire, M. C. K. Tuning Swiss roll metamaterials. *J. Phys. D Appl. Phys.* **42,** 205001 (2009).
83. Shadrivov, I. V., Morrison, S. K. & Kivshar, Y. S. Tunable split-ring resonators for nonlinear negative-index metamaterials. *Opt. Express* **14,** 9344–9349 (2006).
84. Wang, B. N., Zhou, J. F., Koschny, T. & Soukoulis, C. M. Nonlinear properties of split-ring resonators. *Opt. Express* **16,** 16058–16063 (2008).
85. Huang, D., Poutrina, E. & Smith, D. R. Analysis of the power dependent tuning of a varactor-loaded metamaterial at microwave frequencies. *Appl. Phys. Lett.* **96,** 104104 (2010).
86. Poutrina, E., Huang, D. & Smith, D. R. Analysis of nonlinear electromagnetic metamaterials. *New J. Phys.* **12,** 093010 (2010).
87. Powell, D. A., Shadrivov, I. V., Kivshar, Y. S. & Gorkunov, M. V. Self-tuning mechanisms of nonlinear split-ring resonators. *Appl. Phys. Lett.* **91,** 144107 (2007).
88. Shadrivov, I. V., Fedotov, V. A., Powell, D. A., Kivshar, Y. S. & Zheludev, N. I. Electromagnetic wave analogue of an electronic diode. *New J. Phys.* **13,** 033025 (2011).
89. Larouche, S., Rose, A., Poutrina, E., Huang, D. & Smith, D. R. Experimental determination of the quadratic nonlinear magnetic susceptibility of a varactor-loaded split ring resonator metamaterial. *Appl. Phys. Lett.* **97,** 011109 (2010).
90. Katko, A. R. *et al.* Phase conjugation and negative refraction using nonlinear active metamaterials. *Phys. Rev. Lett.* **105,** 123905 (2010).
91. Huang, D., Rose, A., Poutrina, E., Larouche, S. & Smith, D. R. Wave mixing in nonlinear magnetic metacrystal. *Appl. Phys. Lett.* **98,** 204102 (2011).
92. Rose, A., Huang, D. & Smith, D. R. Controlling the second harmonic in a phase-matched negative-index metamaterial. *Phys. Rev. Lett.* **107,** 063902 (2011).
93. Kanazawa, T., Tamayama, Y., Nakanishi, T. & Kitano, M. Enhancement of second harmonic generation in a doubly resonant metamaterial. *Appl. Phys. Lett.* **99,** 024101 (2011).
94. Agranovich, V. M., Shen, Y. R., Baughman, R. H. & Zakhidov, A. A. Linear and nonlinear wave propagation in negative refraction metamaterials. *Phys. Rev. B* **69,** 165112 (2004).
95. Shadrivov, I. V., Zharov, A. A. & Kivshar, Y. S. Second-harmonic generation in nonlinear left-handed metamaterials. *J. Opt. Soc. Am. B* **23,** 529–534 (2006).
96. Gil, I., Bonache, J., Garcia-Garcia, J. & Martin, F. Tunable metamaterial transmission lines based on varactor-loaded split-ring resonators. *IEEE Trans. Microwave Theory Techniques* **54,** 2665–2674 (2006).
97. Velez, A., Bonache, J. & Martin, F. Doubly tuned metamaterial transmission lines based on complementary split-ring resonators. *Electromagnetics* **28,** 523–530 (2008).
98. Wang, Y. F., Yin, J. C., Yuan, G. S., Dong, X. C. & Du, C. L. Tunable I-shaped metamaterial by loading varactor diode for reconfigurable antenna. *Appl. Phys. A* **104,** 1243–1247 (2011).
99. Lapine, M., Shadrivov, I. V., Powell, D. A. & Kivshar, Y. S. Magnetoelastic metamaterials. *Nature Mater.* **11,** 30–33 (2012).
100. Lapine, M., Shadrivov, I. V., Powell, D. A. & Kivshar, Y. S. Metamaterials with conformational nonlinearity. *Sci. Rep.* **1,** 138 (2011).
101. Zhao, R. K., Tassin, P., Koschny, T. & Soukoulis, C. M. Optical forces in nanowire pairs and metamaterials. *Opt. Express* **18,** 25665–25676 (2010).
102. Zhang, J., MacDonald, F. M. & Zheludev, N. I. Optical gecko toe: optically controlled attractive near-field forces between plasmonic metamaterials and dielectric or metal surfaces. *Phys. Rev. B* **85,** 205123 (2012).

Acknowledgements

We thank I. Yangs for discussions, and T. Roy and D. Powel for assistance with preparing the manuscript. We acknowledge the support of the Defence Science and Technology Laboratory (UK), Engineering and Physical Sciences Research Council (UK), Royal Society (London), Australian Research Council and collaboration support through the Centre for Ultrahigh-bandwidth Devices for Optical Systems (Australia), and Ministry of Education, Singapore, grant number MOE2011-T3-1-005.

Author Contributions

N.I.Z initiated the sections on reconfigurable, electro-optical, phase change, superconducting and ultrafast metadevices; Y.S.K initiated the sections on liquid crystal metadevices, nonlinear metadevices with varactors and metadevices driven by electromagnetic forces; both authors contributed equally to editing.

Competing financial interests

The authors declare no competing financial interests.

nature COMMUNICATIONS

ARTICLE

Received 16 Apr 2012 | Accepted 14 Nov 2012 | Published 11 Dec 2012

DOI: 10.1038/ncomms2285

OPEN

Microelectromechanical Maltese-cross metamaterial with tunable terahertz anisotropy

W.M. Zhu[1], A.Q. Liu[1,2], T. Bourouina[3], D.P. Tsai[4,5], J.H. Teng[6], X.H. Zhang[6], G.Q. Lo[2], D.L. Kwong[2] & N.I. Zheludev[7,8]

Dichroic polarizers and waveplates exploiting anisotropic materials have vast applications in displays and numerous optical components, such as filters, beamsplitters and isolators. Artificial anisotropic media were recently suggested for the realization of negative refraction, cloaking, hyperlenses, and controlling luminescence. However, extending these applications into the terahertz domain is hampered by a lack of natural anisotropic media, while artificial metamaterials offer a strong engineered anisotropic response. Here we demonstrate a terahertz metamaterial with anisotropy tunable from positive to negative values. It is based on the Maltese-cross pattern, where anisotropy is induced by breaking the four-fold symmetry of the cross by displacing one of its beams. The symmetry breaking permits the excitation of a Fano mode active for one of the polarization eigenstates controlled by actuators using microelectromechanical systems. The metamaterial offers new opportunities for the development of terahertz variable waveplates, tunable filters and polarimetry.

[1] School of Electrical and Electronic Engineering, Nanyang Technological University, Singapore 639798, Singapore. [2] Institute of Microelectronics, 11 Science Park Road, Singapore 117685, Singapore. [3] School of Electrical and Electronic Engineering, ESIEE Université Paris-Est, Paris 93162, France. [4] Research Center for Applied Sciences, Academia Sinica, 10617 Taipei, Taiwan. [5] Department of Physics, National Taiwan University, 10617 Taipei, Taiwan. [6] Institute of Materials Research and Engineering, 3 Research Link, Singapore 117602, Singapore. [7] Optoelectronics Research Centre, Southampton SO17 1BJ, United Kingdom. [8] Centre for Disruptive Photonic Technologies, Nanyang Technological University, Singapore 639798, Singapore. Correspondence and requests for materials should be addressed to A.Q.L. (email: eaqliu@ntu.edu.sg).

Recently, in addition to traditional applications in optical filters and polarization components, anisotropic media was suggested for the realization of various important novel ideas, including negative refraction[1,2], cloaking[3,4], hyperlenses[5,6], and controlling luminescence[7,8]. However, although asymmetries of crystalline lattices and their constiuent molecules often result in optical anisotropy of natural materials, it is very difficult to find the required values of optical anisotropy for a prescribed wavelength, in particular in the far-infrared and terahertz parts of the spectrum. On the contrary, metamaterials can be rationally designed to achieve optical anisotropy[9–19] that can also be altered by changing the refractive index of the surrounding medium[20–23] or by emplying electrical or thermal effects in liquid crystals[24,25]. At the same time, substantial progress has been possible in developing metamaterials with unit cells reconfigurable with micro-actuators[26–35]. Here we report the active control of anisotropy in the terahertz spectral region in a metamaterial array of Maltese crosses driven by micro-actuators. By breaking the four-fold symmetry of the cross, we show that it is possible to tune linear birefringence and dichroism of the array between the positive and negative values.

Results

Tunable metamaterial with Maltese-cross-shaped unit cells. The metamaterial presented here is a two-dimensional square-lattice array of Maltese crosses with unit cell of $28 \times 28\,\mu m^2$ (Fig. 1a). It is designed to operate in the terahertz range of the spectrum and was characterized from 1 to 5 THz. The micro-actuator framework allowed for a simultaneous reconfiguration of all unit cells in the array. This was achieved by manufacturing one of the trapezoid metal beams in each unit cell on a movable actuated silicon framework (coloured green in Fig. 1). Three other beams of the Maltese cross are fixed to the substrate (blue in Fig. 1). The movable beam of the cross can be shifted away from the cross centre to a distance S up to half of its length. Figure 1b–d shows the unit cell for $S = 0$, 2.5 and 5 μm, respectively. The metamaterial sample with an overall size of approximately $1\,cm^2$ (400×400 unit cells) was fabricated on a silicon-on-insulator wafer as shown in Fig. 2a. Figure 2b shows a close-up view of the unit cells, which are formed by patterning a 0.5-μm thick evaporated aluminium layer. The design parameters are shown in Supplementary Fig. S1.

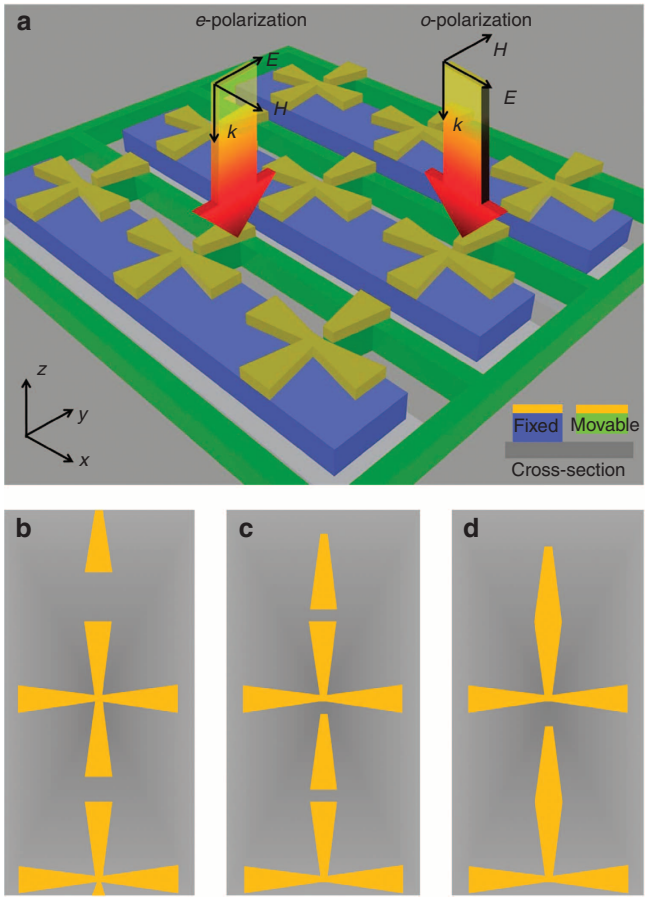

Figure 1 | Schematics of the micromachined Maltese-cross metamaterial. (**a**) The unit cell consists of four trapezoid metal stripes, one of which is located on the movable frames connected with the comb-drive actuator (green). The rest of the unit cell is located on the isolated islands (blue) fixed on the substrate. Inset shows the cross view of the unit cell. (**b**,**c**,**d**) The evolution of the unit cell when the movable trapezoid is shifted with the distance $S = 0$, 2.5 and 5 μm, respectively, is shown.

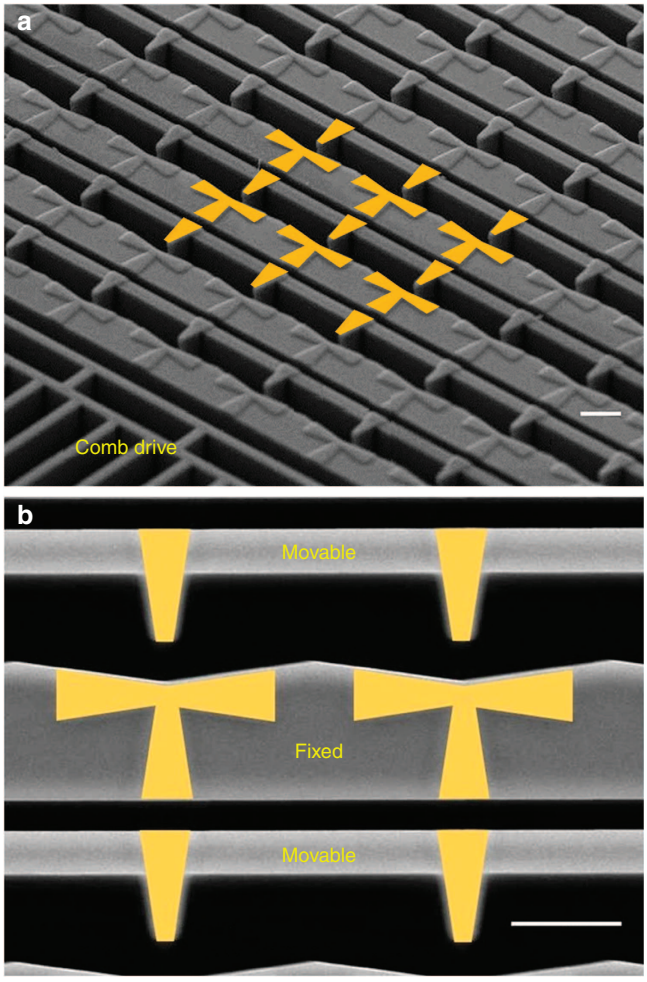

Figure 2 | Scanning electron microscopy image of the micromachined tunable metamaterial. (**a**) Overview of the unit cell array and comb drive. (**b**) Zoomed view of the Maltese-cross-shaped unit cell (the metal part is highlighted with false colour). The scale bars are 10 μm.

When the four metal trapezoid beams are arranged into the pattern of the Maltese cross that has a four-fold symmetry axis, the metamaterial array exhibits no birefringence for normally incident radiation. On the contrary, when the four-fold symmetry of the design is broken by moving one of the beams off-centre, the metamaterial retains a plane of symmetry and becomes birefringent for normally incident light. We define the extra-ordinary polarization (*e*-polarization) and ordinary polarization (*o*-polarization) of this metamaterial with reference to the mirror symmetry axis of the pattern (Supplementary Fig. S1). The *e*-polarization is parallel to the line of symmetry, whereas the *o*-polarization is perpendicular to it.

Experimental results on birefringence and dichroism. Optical anisotropy of the sample is completely characterized by its linear birefringence, and dichroism can be derived from its polarization-sensitive transmission and phase retardation spectra. The transmission spectra were measured by using an optical pump-terahertz probe (OPTP) system for different levels of asymmetry of the Maltese cross (Fig. 3). The experimental setup and data analysis approaches are discussed in the Methods and Supplementary Figs S2–S6. These measurements show that indeed at zero displacement *S*, when the cross has a four-fold symmetry, the metamaterial shows no dichroism: the recorded absorption spectra for both the *o*- and *e*- polarizations are nearly identical with the transmission peaks located at approximately 3.11 and 3.14 THz, respectively. Displacement of one of the beams of the cross is signified by a strong modification of the transmission spectrum for the *e*-polarization, including the appearance of a new transmission peak >4 THz, whereas the transmission spectrum for the *o*-polarization remains practically unchanged. The transmission peak moves from 3.11 to 2.73 THz, when the beam displacement changes from $S=0$ to 5 μm. See more detail on variation of dichroism in Supplementary Figs S7–S9.

Anisotropy of the metamaterial was also characterized by measuring the differential phase retardation $\Delta\Phi=\Phi_e-\Phi_o$ and transmitted power ratio T_e/T_o for *e*- and *o*-polarized waves as functions of *S* (see Fig. 4). Large phase changes of the transmission are observed at the frequency regions highlighted by grey colour as shown in Fig. 3a–f, where the transmission powers are bounced from the minimum to the maximum. Here the incident frequencies are fixed at 3.0 and 4.6 THz, which are the transmission peak frequencies at $S=2.5$ μm. However, large tunability of optical anisotropy of both 3.0- and 4.6-THz incidence is observed either at $0\,\mu m<S<1\,\mu m$ or $4\,\mu m<S<5\,\mu m$, when the gap between the movable beam and the fixed part is significantly small as shown in Fig. 4. The optical anisotropy is changed abruptly, when the movable beam is disconnected from the fixed ones. For $f=3$ THz, the phase difference is not sensitive to the shift distance *S* in the range from 1 to 4 μm. At the same time, the anisotropy monotonically increased at the high frequency of $f=4.6$ THz as shown in Fig. 4b. The anisotropy is more sensitive to the shift

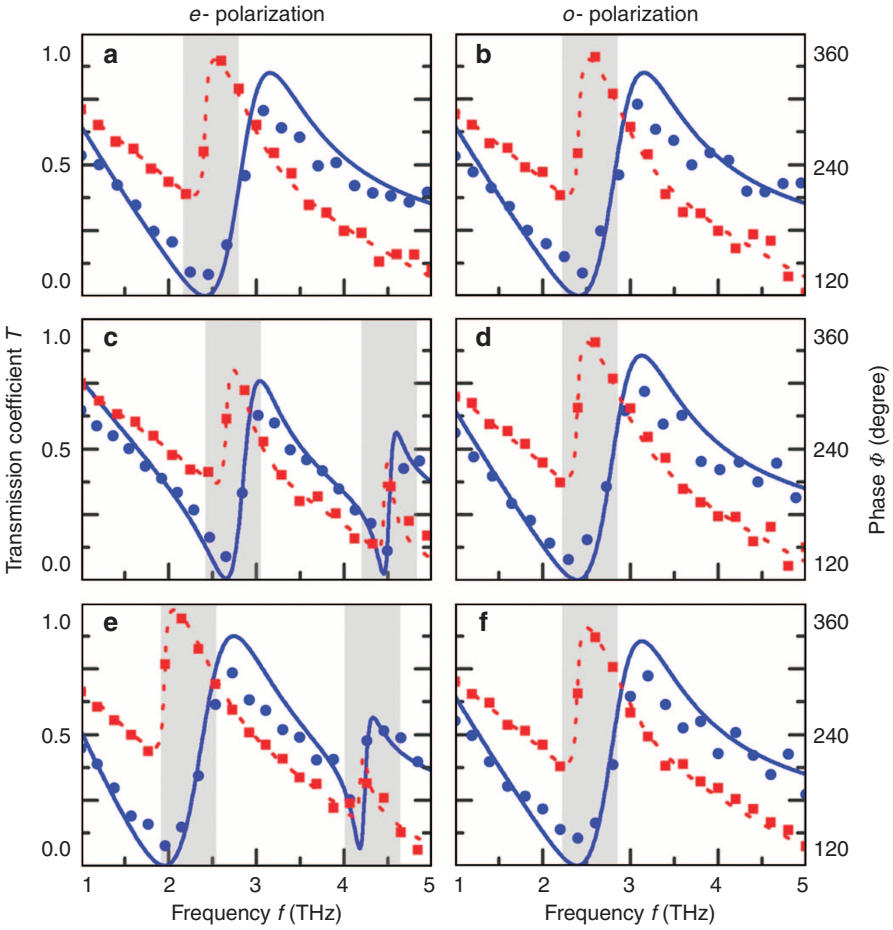

Figure 3 | Measured transmission and phase spectra of the Maltese-cross metamaterial. The first and second columns represent *e*- and *o*-polarized incident light, respectively. The blue solid lines and circular symbols show the numerical and experimental analyses of the transmission, respectively. The red dotted line and square symbols show the numerical and experimental analyses of the phase, respectively. The first, second and third rows show the spectra, when the shift distance is $S=0$ μm (**a**,**b**), 2.5 μm (**c**,**d**) and 5 μm (**e**,**f**), respectively. Rapid phase changes in the frequency domain are highlighted in gray.

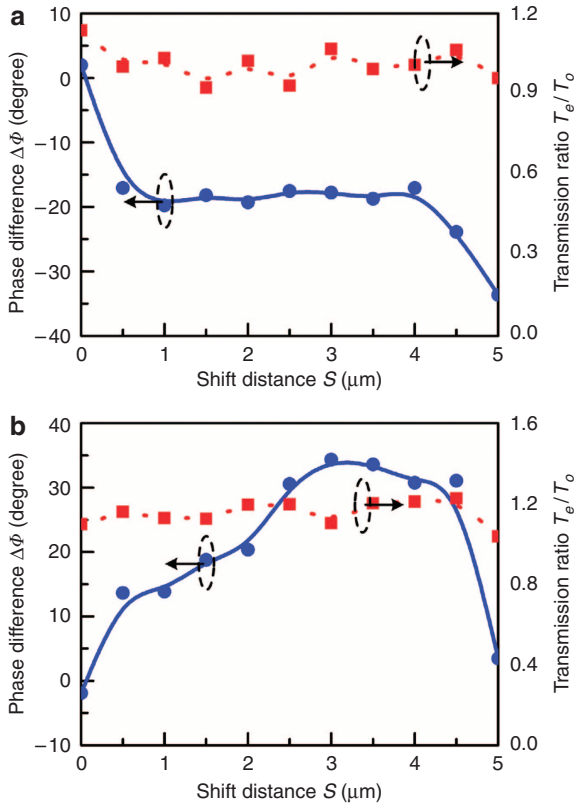

Figure 4 | Measured phase difference and transmitted power ratio between *e*- and *o*-polarized light as functions of the shift distance. (**a**,**b**) The measurement results when the incident frequency is fixed at 3.0 and 4.6 THz, respectively, are shown. The measurement results and their trend are shown by the symbols and lines, respectively.

distance S at 4.6 THz than that at 3.0 THz. The tuning of the anisotropy depends on the variation of the dipole resonance mode of the Maltese cross, which is shown in Fig. 5. The transmission ratio variation (T_e/T_o) is approximately 1 and 1.2 for $f = 3$ and 4.6 THz, respectively. The effective refractive index of the Maltese-cross metamaterials is derived by fitting the measured transmission spectra with the Fresnel equations[36]. The differences between the effective refractive indices of *o*- and *e*-polarized incidence are shown in Supplementary Fig. S9, which shows the same trend as the phase differences shown in Fig. 4.

Origin of the tunable optical anisotropy. The numerical analysis of the Maltese-cross structure without the substrate shows the dipole resonances of the surface current as shown in Fig. 5b–g, which result in transmission dips in the spectra. For example, when S = 2.5 μm, the dipole resonance at 5.94 and 9.85 THz (Fig. 5a) can be mapped to the two Fano resonance dips as shown in Fig. 3c. The existence of the substrate has two effects. One is shifting the resonance dips to low frequencies, which is due to the permittivity difference between air and silicon substrate[37]. The other effect is leading to Fano-type resonance profile, which is due to the coupling between the dipole resonance modes of the Maltese cross and the Fabry–Pérot mode of the substrate[38]. The resonance frequency shifts shown in Fig. 3a,c,e are mainly due to the resonance features of the Maltese-cross design. Because the influence of the substrate does not change with the reconfigurations of the cross, we can conclude that spectral changes observed with the movements of the beams are due to the changes in the dipole resonance of the cross pattern. When the Maltese cross has a four-fold symmetry, the surface current is resonant between two opposite beams of the Maltese cross, which are parallel to the incident electric field, as shown in Fig. 4b,c. The other two beams have trivial effect on the dipole resonance. Therefore, the shifting of the Maltese-cross beam has trivial

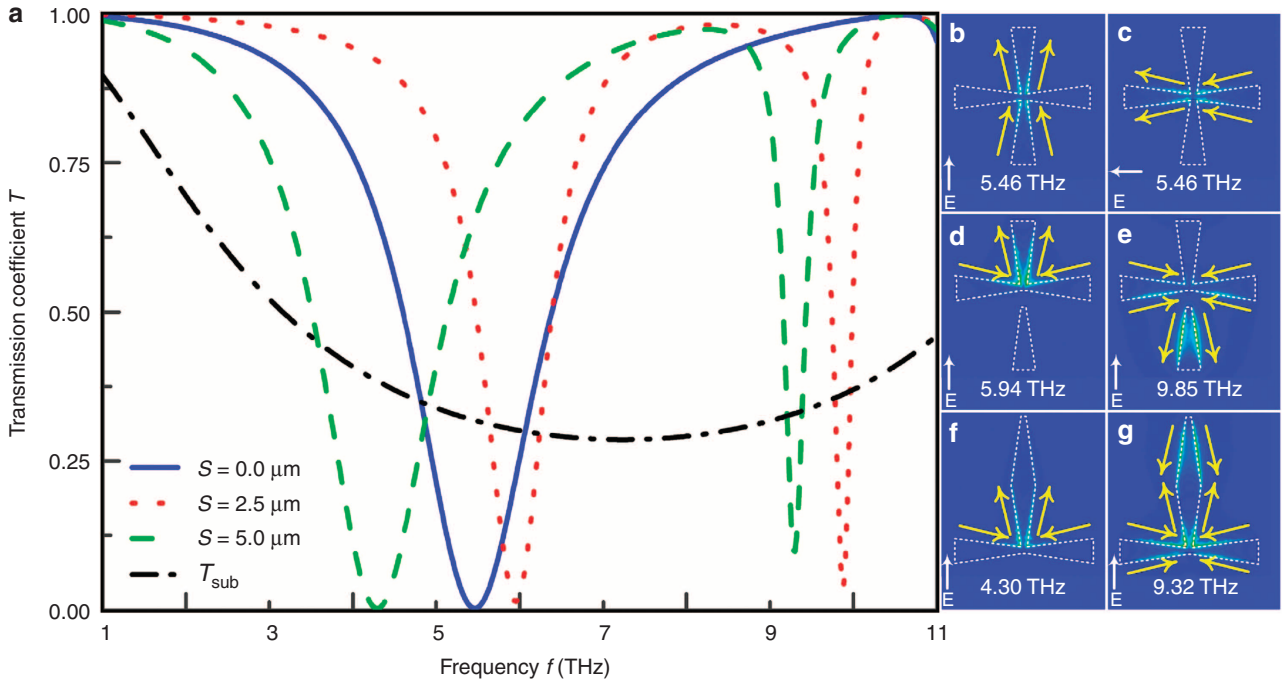

Figure 5 | Transmission spectra at different shift distance and surface current contour maps of the Maltese cross without substrate. (**a**) The solid, dotted and dashed lines represent the transmission spectra of the Maltese cross when the shift distance S is 0, 2.5 and 5 μm, respectively. The transmission of the 3-μm substrate is represented by the black dash dotted line. (**b**–**g**) The contour maps show surface currents under excitation by different frequencies of light. The lighter colour shows the high density of surface current, and the arrows show the surface current flux direction. The direction of the incident electric field is marked with the white arrow at the lower left corner. The direction of the surface current is marked with the yellow arrow.

effects on the resonance modes when the movable beam is perpendicular to the incident electric field (*o*-polarization). Considering the *e*-polarized incidence, however, the changing of the symmetry has vital effects on the dipole resonance modes due to the structural change of the beams, where most of the induced surface currents are concentrated on. This explains the difference between *e*- and *o*-polarized incidence of the transmission spectra as a function of shift distance *S*, which is shown in Fig. 3. The tuning of the anisotropy can also be explained by the change of the resonance mode of the Maltese cross when the movable beam is actuated. At low frequencies, the surface current cannot go to the movable beam, which is disconnected from the remaining parts of the Maltese cross. The surface current is mainly concentrated at the fixed beam parallel to the incident electric field. This beam is weakly coupled to the two perpendicular beams. Therefore, the change of the shift distance *S* has small effects on the resonance mode of the Maltese cross, which explains the small variation of the optical anisotropy, when *S* is in the range from 1 to 4 μm under 3.0-THz incidence (Fig. 4a). At high frequencies, the surface current is mainly concentrated at the movable beam and has a π phase difference from the incident electric field. Therefore, the surface current resonance is mainly induced by the capacitance coupling between the fixed and movable beams of the Maltese cross. This capacitance is a strong function of the shift distance *S*. Therefore, the resonance mode of the Maltese cross is a strong function of the shift distance *S*, which explains the rapid tuning of the anisotropy, when *S* is in the range from 1 to 4 μm under 4.6-THz incidence (Fig. 4b). There is an abrupt resonance mode change at both low and high frequencies when the movable beam is being disconnected from the fixed parts, which explains the abrupt anisotropy change observed either at $0\,\mu m < S < 1\,\mu m$ or $4\,\mu m < S < 5\,\mu m$ for both incident frequencies as shown in Fig. 4.

Insertion loss of the tunable metamaterial. The insertion loss of the tunable metamaterial consists of three parts, the ohmic loss due to the electron resonance within the metal structure, the reflection and the scattering loss of the imperfect surface and edge. In the experiment, the total insertion loss can be measured by monitoring the output transmission versus the source. Figure 6a shows the transmission and absorption spectra under the shift distance $S = 0.5\,\mu m$. Peak 1 and Peak 2 represent the transmission peaks, when the shift distance *S* is in the range from 0 to 5 μm, at low- and high-frequency region, respectively. The transmission peak and absorption peaks are staggered in the frequency domain, which is similar at different shift distance *S*. Therefore, the ohmic loss is maintained under 12% at low-frequency region and 6% at high-frequency region. The ohmic losses of the transmission peaks under different shift distances *S* are shown in Supplementary Fig. S8. The transmission peaks in high-frequency region have lower ohmic absorption because of the rapid decaying of the absorption profile at high-frequency region. The measured total insertion losses of the tunable metamaterial for Peak 1 and Peak 2 are shown in Fig. 6b. The symbols and lines show the experimental and numerical results, respectively. The differences of the experimental and numerical results are approximately 1 dB, which is due to the misalignment, surface roughness and edge scattering of the tunable metamaterial.

Discussion

The breaking of the Maltese-cross symmetry results in the splitting of the two parallel Maltese-cross beams and, subsequently, two different resonators, which can be excited by the *e*-polarized incidence. The breaking of the Maltese-cross symmetry splits and tunes the resonance modes of the *e*-polarized incidence but has minor effects on the *o*-polarized incidence with the electric field perpendicular to the mirror symmetry axis, which is unaltered during the tuning. The Maltese-cross metamaterial is tuned between positive anisotropy, negative anisotropy and isotropy states by actuators using microelectromechanical systems, which have promising applications such as waveplates, birefringent filters and light modulators.

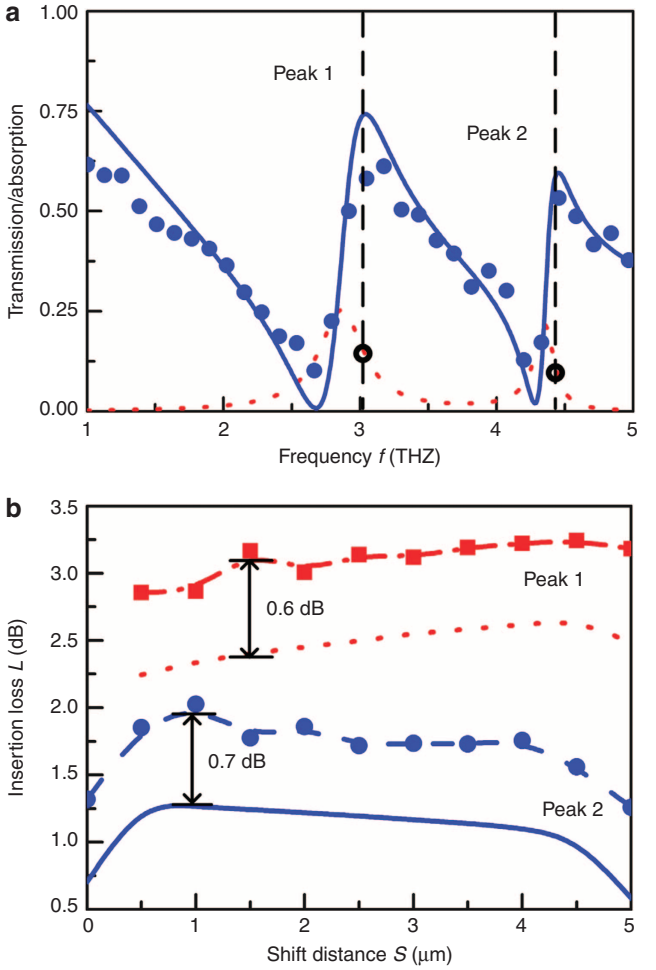

Figure 6 | Experimental and numerical analyses of the insertion loss for the reconfigurable metamaterial. (**a**) The transmission (blue solid line) and absorption (red dotted line) spectra under the shift distance $S = 0.5\,\mu m$. The transmission peak and absorption peaks are staggered in the frequency domain. (**b**) The insertion losses of each transmission peak, when the shift distance *S* ranges from 0 to 5 μm. Peak 1 and Peak 2 refer to the transmission peaks at the low- and high-frequency regions, respectively. The lines and symbols represent the numerical and measured results, respectively.

Methods

Fabrication processes. The structures of the tunable metamaterial are fabricated on a silicon-on-insulator wafer by using the deep reactive ion etching processes[39,40]. Figure 2a shows the overview of the micromachined tunable metamaterial imaged by using the scanning electron microscopy. Two identical micromachined comb drive actuators driven by the electrostatic force are placed on both sides of the unit cell array. Each actuator provides bidirectional in-plane translation (along the *x* direction) following the actuation relationship $\Delta x = AV^2$, where Δx is the displacement, *V* the actuation voltage and $A = 0.05\,\mu m\,V^{-2}$ is the actuation coefficient. The displacement of the actuator can be monitored by using vertical microscopic system. The actuation coefficient *A* is derived by fitting the measured displacement–voltage curve. The actuation frequency can reach 10 kHz based on the dynamic measurement results of our previous work[40]. Figure 2b

shows a close-up view of the unit cells. The micro-ring unit cells are formed by patterning a 0.5-μm thick evaporated aluminium layer on the top of the structure layer. The movable split rings are patterned on the central frame, which consists of many crossed narrow beams (2-μm width). The fixed split rings are patterned on the isolated anchors. Because each anchor encloses a larger area of the underlying oxide layer than the frame, it needs much longer time to remove all the oxide under the anchor than that under the frame. Therefore, the supporting frame is fully released and becomes freely movable, whereas the anchor remains fixed on the substrate by controlling the release time.

Experimental setup. Supplementary Figure S2 shows the experimental setup of the OPTP system used in the experiment. The terahertz probe pulse is generated by 35-fs pulses at centre wavelength of 800 nm with a repetition rate of 1 kHz by using the air-plasma technique. The spectral range of the terahertz pulse is from 0.3 to 8 THz, which is detected by free-space electro-optical (EO) sampling with a 0.3-mm thick <110> GaP crystal. The probe terahertz wave passes through the samples at normal incidence. The time domain terahertz signal is detected by the EO detector using a terahertz time-domain spectroscopy (TDS) delay system. It should be pointed out that the pump-probe system of the OPTP, which is highlighted as a red dashed line, is not used during the experiment because the Maltese-cross metamaterial is not tuned by laser pulses. Therefore, this OPTP system functions solely as a typical THz-TDS system in the experiment. The transmission spectra of both amplitude and phase, as shown in Supplementary Figs S5 and S6, are derived by using the Fourier transform of the time domain signal from the EO detector and then normalized with the source spectra. In Fig. 3, 20 equally spaced data points with the least mean-square error is chosen and compared with the simulation results.

References

1. Brazhe, R. A. & Meftakhutdinov, R. M. Negative optical refraction in crystals with strong birefringence. *Tech. Phys.* **52,** 793–795 (2007).
2. Burkat, T. M., Kostyuk, G. K. & Yakovlev, E. B. Structural anisotropy and double refraction in porous glass plates. *Fizika i Khimiya Stekia* **17,** 781–790 (1991).
3. Smolyaninov, I. I., Smolyaninova, V. N., Kildishev, A. V. & Shalaev, V. M. Anisotropic metamaterials emulated by tapered waveguides: application to optical cloaking. *Phys. Rev. Lett.* **102,** 213901 (2009).
4. Zhang, B. L., Luo, Y., Liu, X. G. & Barbastathis, G. Macroscopic invisibility cloak for visible light. *Phys. Rev. Lett.* **106,** 033901 (2011).
5. Salandrino, A. & Engheta, N. Far-field subdiffraction optical microscopy using metamaterial crystals: theory and simulations. *Phys. Rev. B* **74,** 075103 (2006).
6. Jacob, Z., Alekseyev, L. V. & Narimanov, E. Optical hyperlens: Far-field imaging beyond the diffraction limit. *Opt. Express* **14,** 8247–8256 (2006).
7. Tumkur, T., Zhu, G., Black, P., Barnakov, Y. A., Bonner, C. E. & Noginov, M. A. Control of spontaneous emission in a volume of functionalized hyperbolic metamaterial. *Appl. Phys. Lett.* **99,** 151115 (2011).
8. Jacob, Z., Kim, J. Y., Naik, G. V., Boltasseva, A., Narimanov, E. E. & Shalaev, V. M. Engineering photonic density of states using metamaterials. *Appl. Phys. B* **100,** 215–218 (2010).
9. Elser, J., Wangberg, R., Podolskiy, V. A. & Narimanov, E. E. Nanowire metamaterials with extreme optical anisotropy. *Appl. Phys. Lett.* **89,** 261102 (2006).
10. Singh, R., Plum, E., Zhang, W. & Zheludev, N. I. Highly tunable optical activity in planar achiral terahertz metamaterials. *Opt. Express* **18,** 13425–13430 (2010).
11. Zhu, W. M. *et al.* Polarization dependent state to polarization independent state change in THz metamaterials. *Appl. Phys. Lett.* **99,** 211102 (2011).
12. Sinchuk, K. *et al.* Tunable negative group index in metamaterial structures with large form birefringence. *Opt. Express* **18,** 463–472 (2010).
13. Anthony, J. *et al.* Negative refraction in semiconductor metamaterials. *Nat. Mater.* **6,** 946–950 (2007).
14. Che, M., Li, Z. Y. & Liu, R. J. Tunable optical anisotropy in three-dimensional photonic crystals. *Phys. Rev. A* **76,** 023809 (2007).
15. Boardman, A. D. *et al.* Active and tunable metamaterials. *Laser Photonics Rev.* **5,** 287–307 (2011).
16. Wu, K. D. & Wang, G. P. Transformation-optics-based nanopattern recognition. *J. Opt. Soc. Am. B* **28,** 2524–2528 (2011).
17. Lapine, M., Jelinek, L., Freire, M. J. & Marques, R. Realistic metamaterial lenses: Limitations imposed by discrete structure. *Phys. Rev. B* **82,** 165124 (2010).
18. Strikwerda, A. C., Fan, K., Tao, H., Pilon, D. V., Zhang, X. & Averitt, R. D. Comparison of birefringent electric split-ring resonator and meanderline structures as quarter-wave plates at terahertz frequencies. *Opt. Express* **17,** 136–149 (2009).
19. Kanda, N., Konishi, K. & Kuwata-Gonokami, M. Terahertz wave polarization rotation with double layered metal grating of complimentary chiral patterns. *Opt. Express* **15,** 11117–11125 (2007).
20. Chen, H. *et al.* Active terahertz metamaterial devices. *Nature* **444,** 597–600 (2006).
21. Xiao, S. *et al.* Tunable magnetic response of metamaterials. *App. Phys. Lett.* **95,** 033115 (2009).
22. Zhang, F. *et al.* Magnetically tunable left handed metamaterials by liquid crystal orientation. *Opt. Express* **17,** 4360–4366 (2009).
23. Zhang, S. *et al.* Photoinduced handedness switching in terahertz chiral metamolecules. *Nat. Commun.* **3,** 942 (2012).
24. Kahn, F. J. Electric-field-induced orientational deformation of nematic liquid crystals: tunable birefringence. *Appl. Phys. Lett.* **20,** 199–201 (1972).
25. Busch, K. & John, S. Liquid-crystal photonic-band-gap materials: the tunable electromagnetic vacuum. *Phys. Rev. Lett.* **83,** 967–970 (1999).
26. Tao, H., Strikwerda, A. C., Fan, K., Padilla, W. J., Zhang, X. & Averitt, R. Reconfigurable terahertz metamaterials. *Phys. Rev. Lett.* **103,** 147401 (2009).
27. Bouyge, D. *et al.* Split ring resonators (srrs) based on micro-electro-mechanical deflectable cantilever-type rings: application to tunable stopband filters. *IEEE Microw. Wirel. Co* **21,** 243–245 (2011).
28. Gil, I., Martin, F., Rottenberg, X. & De Raedt, W. Tunable stop-band filter at Q-band based on RF-MEMS metamaterials. *Electron. Lett.* **43,** 1153–1154 (2007).
29. He, X., Lv, Z., Liu, B. & Li, Z. Tunable magnetic metamaterial based multi-split-ring resonator (MSRR) using MEMS switch components. *Microsys. Tech.* **17,** 1263–1269 (2011).
30. Ozbey, B. & Aktas, O. Continuously tunable terahertz metamaterial employing magnetically actuated cantilevers. *Opt. Express* **19,** 5741–5752 (2011).
31. Perruisseau-Carrier, J., Topalli, K. & Akin, T. Low-loss Ku-band artificial transmission line with mems tuning capability. *IEEE Microw. Wirel. Co* **19,** 377–379 (2009).
32. Pryce, I. M., Aydin, K., Kelaita, Y. A., Briggs, R. M. & Atwater, H. A. Highly strained compliant optical metamaterials with large frequency tunability. *Nano Lett.* **10,** 4222–4227 (2010).
33. Xun-jun, H., Yue, W. & Tai-Long, G. MEMS switches controlled multi-split ring resonator as a tunable metamaterial component. *Microsys. Tech.* **16,** 1831–1837 (2010).
34. Zhu, W. M. *et al.* Switchable magnetic metamaterials using micromachining processes. *Adv. Mater.* **23,** 1792–1796 (2011).
35. Fu, Y. H. *et al.* A micromachined reconfigurable metamaterial via reconfiguration of asymmetric split-ring resonators. *Adv. Fun. Mater.* **21,** 3589–3594 (2011).
36. Driscoll, T., Basov, D. N., Padilla, W. J., Mock, J. J. & Smith, D. R. Electromagnetic characterization of planar metamaterials by oblique angle spectroscopic measurements. *Phys. Rev. B* **75,** 115114 (2007).
37. Munk, B. A. *Frequency Selective Surfaces: Theory and Design* (John Wiley & Sons, 2000).
38. Mousavi, S. H., Khanikaev, A. B. & Shvets, G. Optical properties of Fano-resonant metallic metasurfaces on a substrate. *Phys. Rev. B* **85,** 155429 (2012).
39. Li, J., Liu, A. Q. & Zhang, Q. X. Tolerance analysis for comb-drive actuator using DRIE fabrication. *Sens. Actu. A* **125,** 494–503 (2006).
40. Zhang, X. M., Zhao, Q. W., Liu, A. Q., Zhang, J., Lau, J. H. & Kam, C. H. Asymmetric tuning schemes of MEMS dual-shutter VOA. *J. Lightwave Tech.* **26,** 569–579 (208).

Acknowledgements

This work was supported by the Science and Engineering Research Council (SERC) of Singapore with project Metamaterials Programme: Nanoplasmonics (Grant No. SERC 092 154 0098), the MOE Singapore (Grant MOE2011-T3-1-005) and EPSRC (UK) Programme on Nanostructured Photonic Metamaterials.

Author contributions

W.M.Z and A.Q.L. jointly conceived the idea and prepared the manuscript. D.P.T. and T.B. assisted in the analysing and discussion of the results. J.H.T., X.H.Z., D.L. K. and G.Q.L. assisted in the experiment and fabrication. A.Q.L. and N.I.Z. supervised and coordinated all the work. All authors commented on the manuscript.

Additional information

Supplementary Information accompanies this paper at http://www.nature.com/naturecommunications

Competing financial interests: The authors declare no competing financial interests.

Reprints and permission information is available online at http://npg.nature.com/reprintsandpermissions/

How to cite this article: Zhu, W. M. *et al.* Microelectromechanical Maltese-cross metamaterial with tunable terahertz anisotropy. *Nat. Commun.* 3:1274 doi: 10.1038/ncomms2285 (2012).

LETTERS
PUBLISHED ONLINE: 17 MARCH 2013 | DOI: 10.1038/NNANO.2013.25
nature nanotechnology

An electromechanically reconfigurable plasmonic metamaterial operating in the near-infrared

Jun-Yu Ou[1], Eric Plum[1]*, Jianfa Zhang[1] and Nikolay I. Zheludev[1,2]*

Current efforts in metamaterials research focus on attaining dynamic functionalities such as tunability, switching and modulation of electromagnetic waves[1]. To this end, various approaches have emerged, including embedded varactors[2], phase-change media[3,4], the use of liquid crystals[5,6], electrical modulation with graphene[7,8] and superconductors[9], and carrier injection or depletion in semiconductor substrates[10,11]. However, tuning, switching and modulating metamaterial properties in the visible and near-infrared range remain major technological challenges: indeed, the existing microelectromechanical solutions used for the sub-terahertz[12] and terahertz[13–15] regimes cannot be shrunk by two to three orders of magnitude to enter the optical spectral range. Here, we develop a new type of metamaterial operating in the optical part of the spectrum that is three orders of magnitude faster than previously reported electrically reconfigurable metamaterials. The metamaterial is actuated by electrostatic forces arising from the application of only a few volts to its nanoscale building blocks—the plasmonic metamolecules—that are supported by pairs of parallel strings cut from a flexible silicon nitride membrane of nanoscale thickness. These strings, of picogram mass, can be driven synchronously to megahertz frequencies to electromechanically reconfigure the metamolecules and dramatically change the transmission and reflection spectra of the metamaterial. The metamaterial's colossal electro-optical response (on the order of 10^{-5}–10^{-6} m V^{-1}) allows for either fast continuous tuning of its optical properties (up to 8% optical signal modulation at up to megahertz rates) or high-contrast irreversible switching in a device only 100 nm thick, without the need for external polarizers and analysers.

Engineering fast, dynamically reconfigurable metamaterials for the optical spectral range, with metamolecular features on the scale of tens of nanometres, is a formidable technological challenge. However, working on the nanoscale also has some important advantages, because the electrostatic force, which is inversely proportional to distance, becomes dominant, allowing potential differences of only a few volts to overcome the elastic response of suitable nanostructures. Moreover, inertial and elastic forces scale differently with size, driving mechanical frequencies of microscale reconfigurable elements to megahertz values. However, existing electrically reconfigurable terahertz metamaterials, in which external comb-drive actuators drive the mass of the entire metamaterial[13–15], would not allow high-frequency operation, even if they could be scaled to the optical spectral range. Similarly, approaches based on the deformation of elastomeric substrates[16] lead to low resonance frequencies as they require macroscopic displacement of a comparatively high mass of low-stiffness material.

The electro-optical photonic metamaterial (Fig. 1) described here comprises a continuous plasmonic, metallic 'meander near the wire' pattern manufactured on a grid of flexible dielectric strings with picogram mass and megahertz mechanical resonances. Following

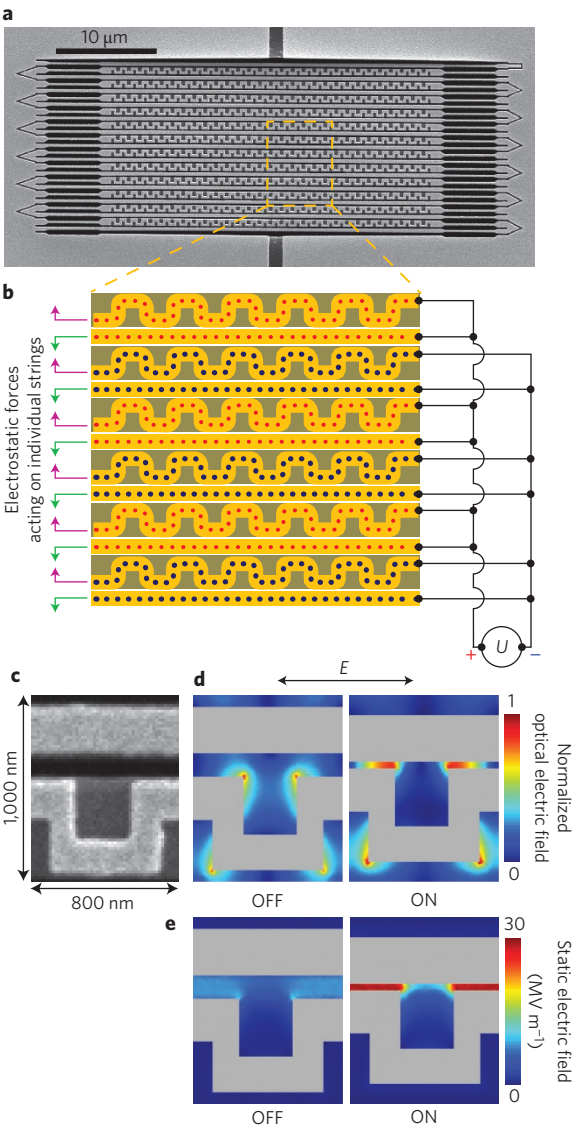

Figure 1 | Electrically reconfigurable photonic metamaterial. a, Scanning electron microscope (SEM) image of the device. **b**, Schematic of the driving circuit (black) and a section of the metamaterial pattern consisting of a gold nanostructure (yellow) supported by silicon nitride strings (brown). The driving voltage *U* causes positive (red) and negative (blue) charging and thus electrostatic forces acting in opposite directions (pink and green). **c**, SEM image of a single metamolecule. **d**, Plasmonic field distribution for the device OFF and ON states (excitation wavelength 1.6 µm; polarization *E*). **e**, Static electric field for an applied voltage of 1 V.

[1]Optoelectronics Research Centre and Centre for Photonic Metamaterials, University of Southampton, Southampton SO17 1BJ, UK, [2]Centre for Disruptive Photonic Technologies, Nanyang Technological University, Singapore 637371, Singapore. *e-mail: erp@orc.soton.ac.uk; niz@orc.soton.ac.uk

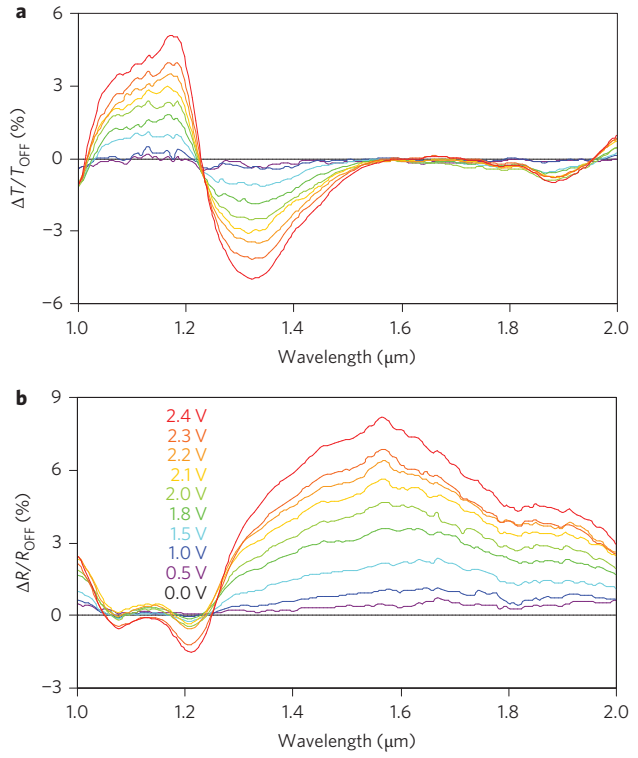

Figure 2 | Reversible electro-optical tuning and modulation. a,**b**, Spectral dependence of changes in transmission T (**a**) and reflection R (**b**) induced by applying a static voltage to the reconfigurable photonic metamaterial.

application of a few volts to neighbouring strings ('wire' and 'meander' conducting patterns), an attractive electrostatic force of a few nanonewtons moves the strings in the metamaterial plane, closing the gap between them. This strongly affects the resonant optical response of the meander pattern, which is linked to excitation of a plasmonic mode[17–19], allowing reversible transmission and reflection modulation with megahertz bandwidth as well as non-volatile switching of the metamaterial.

The nanostructure was manufactured by focused ion beam milling on a 50-nm-thick silicon nitride membrane (which provides a stable and flexible base for the plasmonic pattern) to form alternating 50-nm-thick gold straight and meander wires. The wires are supported by 500-nm- and 250-nm-wide strings cut from the membrane and separated by 125-nm gaps to provide room for mutual motion. Pairs of strings were connected alternately to two electrical terminals on opposite sides of the device. To increase flexibility, the string ends were narrowed to ~200 nm, as shown in the scanning electron microscopy (SEM) image in Fig. 1a. The entire nanostructure has dimensions of 12 μm × 35 μm. (For more fabrication details see Methods.)

When a voltage is applied across the device terminals, the strings are exposed to electrostatic forces resulting from strong fields in the gaps between them (~8 MV m^{-1} at an applied control signal of 1 V; Fig. 1e). In response, pairs of strings bend towards one another. While the restoring force grows linearly with string displacement, the electrostatic attraction tends to infinity as the gap approaches zero. At a critical voltage the electrostatic attraction irreversibly overcomes the restoring force. For driving voltages below this threshold, reversible modulation of the metamaterial pattern and optical properties is possible. Exceeding the critical voltage results in step-like non-volatile switching and an abrupt change in the optical properties of the structure. The critical voltage can be estimated from the balance of electrostatic attraction between two strings and their elastic restoring force as $U_c \approx \sqrt{(32Etw^3g_0^2)/(\pi\varepsilon_0 L^4)} \approx 3\text{V}$. Here, the average Young's modulus of silicon nitride and gold is $E = 169$ GPa and the initial gap size is $g_0 = 125$ nm. The string dimensions are thickness $t = 100$ nm, length $L = 35$ μm and average width $w = 375$ nm. In the following, we will present both regimes of operation separately.

In the device reported here the critical voltage was measured to be ~3 V, and continuous electro-optic modulation was possible at lower driving signals. Figure 2 shows the spectral dependence of the induced reversible changes in the transmission and reflection of the metamaterial relative to a reference case where no voltage is applied. The transmittance may be modulated by ~5% around wavelengths of 1.1 μm and 1.3 μm, and the reflectance can be modulated by up to 8% around 1.5 μm. (See Methods for characterization details.)

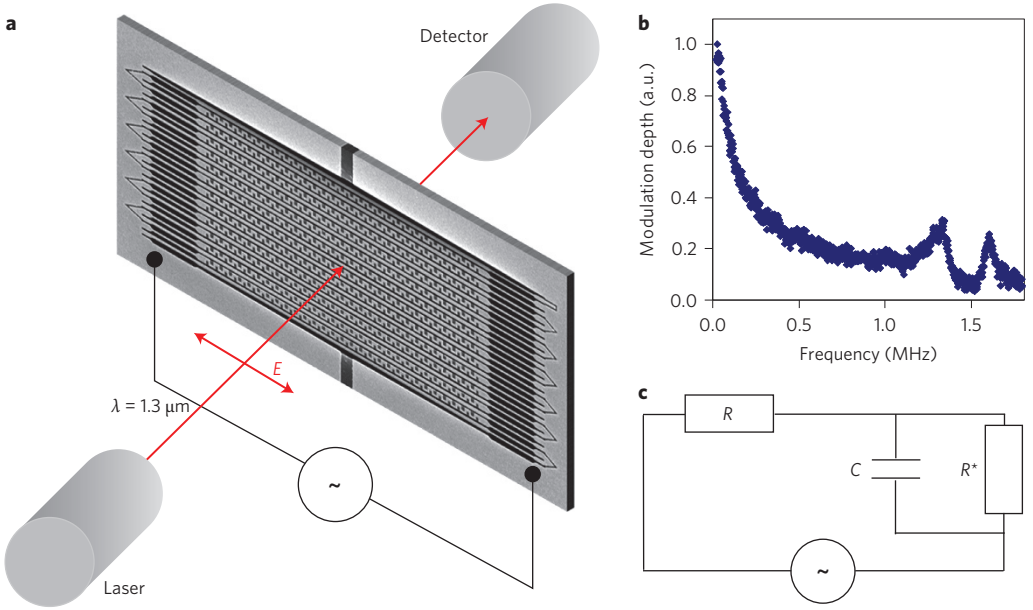

Figure 3 | Megahertz bandwidth electro-optical modulator. a, Modulator schematic. **b**, Frequency response function. **c**, Equivalent electric circuit diagram, where R stands for resistance and C for capacitance.

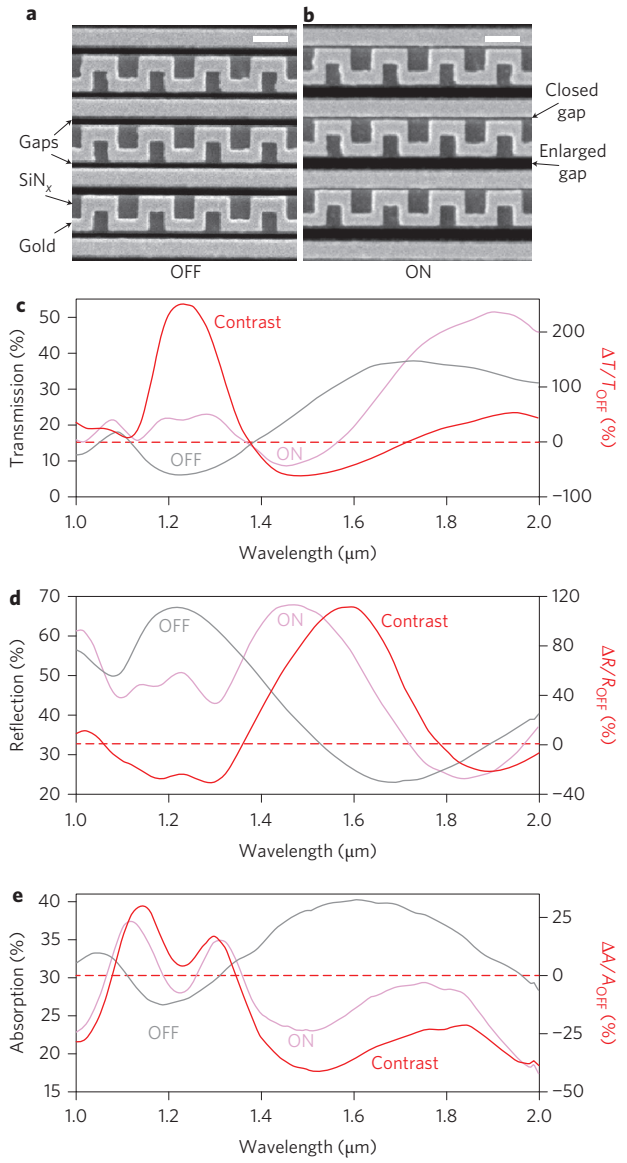

Figure 4 | High-contrast, non-volatile electro-optical switch. a,**b**, SEM images of the metamaterial in its OFF (**a**) and ON (**b**) states. Scale bar, 500 nm. **c**–**e**, Transmission (**c**), reflection (**d**) and absorption (**e**) spectra of the device in the OFF and ON states (left axis) and the corresponding switching contrast (right axis).

To understand the potential of electrostatically reconfigurable nanostructures for high-frequency modulation of metamaterial optical properties we estimated the fundamental mechanical resonance frequency of strings with rectangular cross-section based on classical beam theory as $f = (1/2\pi)\sqrt{(32E/\rho)}(w/L^2) \approx 1$ MHz, where $\rho = 11.4$ g cm^{-3} is an average density of the gold and silicon nitride. This simplified formula does not take into account the incomplete gold coverage and narrowing of the string ends.

Mechanical systems can be easily driven to frequencies up to their fundamental resonance, although in reality the frequency response is complicated by the resonant properties of the feeding electrical network. Indeed, when measuring the frequency dependence of optical modulation at a wavelength of 1.3 μm, we saw a complex spectral response with initial roll-off at ~0.5 MHz and two resonance peaks at 1.3 MHz and 1.6 MHz, which is in reasonable agreement with our estimates of the fundamental frequency f (Fig. 3).

By increasing the applied voltage beyond the structure's threshold voltage we enter the regime of step-like switching (see Supplementary Movie). Here, switching occurs at $U_c = 3$ V (the optical characteristics of the ON and OFF states of the device are presented in Fig. 4). In the telecommunications band, the transmission, reflection and absorption spectra of the metamaterial redshift by ~20% when the device switches, leading to dramatic 250% transmission changes around 1.2 μm and 110% reflectivity changes around 1.6 μm. Such switching is irreversible, as the metamaterial remains in its ON configuration supported by the van der Waals force, even after the driving field is withdrawn. (This 'sticking' effect could be eliminated by resorting to modified designs, materials and chemical surface treatments[20].) The origin of the drastic switching-induced change in the metamaterial's optical properties can be understood from Fig. 1d, which shows the optical electric field distribution before and after switching. For light polarized parallel to the wires, the resonances are mainly caused by excitation of plasmonic standing waves along the meander pattern. In the OFF state, interaction with the straight wires is relatively weak, and the electromagnetic field is mainly localized around the meander pattern. However, as straight and meander wires move closer together, their interaction becomes much stronger, the field redistributes into the narrow gap, and the resonances shift to longer wavelengths. In such a highly nonlinear system the switching dynamics are complex and strongly depend on the initial conditions and the shape of the control signal. However, by numerically solving the nonlinear equations of motion of a pair of strings, the characteristic switching time can be evaluated as ~500 ns for the metamaterial going from the initial OFF state to the fully switched ON state, if a control signal equal to the static switching voltage U_c is applied abruptly.

To evaluate the power consumption of the device we approximated it with the equivalent circuit presented in Fig. 3. The leakage resistance of $R^* = 400$ kΩ dominates the power consumption in the low-frequency limit, and $P = U^2/R^*$ gives the power needed to drive the modulator (only ~2.5 μW at $U = 1$ V). Simplifying the nanostructure as 12 parallel wire pairs, the capacitance can be estimated analytically as $C_0 \approx 15$ fF, increasing to ~20 fF at the static switching voltage U_c due to the decreasing gap between the wires. The energy required to switch the device from the OFF state to the ON state can be estimated as the energy required to charge the capacitive nanostructure to the static switching point and was determined numerically as ~100 fJ, a very small amount of energy.

It is interesting to compare the metamaterial's electro-optic properties to those of conventional electro-optic materials. Electro-optic modulation usually results from minute refractive index changes achieved by the application of an electric field across an electro-optic crystal, which is why applications require long crystals, high-voltage driving signals and polarizers to exploit birefringence-induced polarization effects. A similar solution using liquid crystals yields a slow response. In conventional electro-optic media such as perovskite-type ferroelectric lithium niobate, the electro-optic effect mainly comes from field-induced relative displacement of the central metal ion and the surrounding oxygen octahedron. This displacement changes the electronic band wavefunctions through electron–phonon coupling, which affects the refractive index of the lattice[21]. Similarly, in the reconfigurable metamaterial an electro-optic effect arises from electric field-induced relative displacement of its constitutive parts. This displacement changes the structure's collective plasmonic wavefunction, which affects the effective refractive index of the lattice. In light of these intriguing similarities in the microscopic mechanism and macroscopic manifestation, we estimated the reconfigurable metamaterial's effective electro-optic coefficient. Full three-dimensional Maxwell calculations showed that OFF to ON switching of the 100-nm-thick structure changes the transmitted wave's phase by up to $\pi/5$ at ~1.6 μm, corresponding to an effective refractive index change of $\Delta n = 1.6$. This results

from applying $U_c = 3$ V across $L = 35$ μm of metamaterial. Thus, the effective electro-optic coefficient of the metamaterial is approximately $\Delta nL/U_c \approx 10^{-5}$ m V^{-1} in the non-volatile regime, and $\sim 10^{-6}$ m V^{-1} in a fully reversible regime, which is about five to four orders of magnitude greater than in typical electro-optic media such as lithium niobate (3×10^{-11} m V^{-1}; ref. 22). This makes the metamaterial suitable for light modulation in small low-voltage devices without polarizers.

The novel technology presented here provides opportunities for further development, but it also has some limitations. Larger modulation depths can be achieved with metamaterial patterns that have narrower resonances[23]. Even faster modulation would result from smaller reconfigurable elements, where gigahertz modulation can be anticipated for electrostatic actuation within the individual meta-molecules. On the other hand, larger reconfigurable metamaterials based on longer strings will tend to be slower modulators, which can only be partially addressed by using stiffer materials. Also, bowing of the strings necessarily introduces some inhomogeneity, which can be reduced but not prevented by tapered string ends.

In summary, the novel class of reconfigurable nanostructures introduced here transfers electrically reconfigurable metamaterials from the terahertz to the optical part of the spectrum, while simultaneously increasing their modulation speed by three orders of magnitude. Such structures, with some modifications, are compatible with low-cost production using high-resolution complementary metal–oxide–semiconductor (CMOS) fabrication techniques and nanoimprinting. The approach, based on combining the elastic properties of a nanoscale-thickness dielectric membrane and nanoscale electrostatic forces in a planar plasmonic structure, provides a powerful generic platform for achieving tunable metamaterial characteristics in the optical spectral range. Such reconfigurable metamaterials can be operated at microwatt power levels and can provide continuous modulation of optical signals with megahertz bandwidth. A compact design integrating the actuation mechanism into the metamaterial, low-power consumption and direct control with a few volts makes electrostatically reconfigurable photonic metamaterials compatible with optoelectronic systems, for example as tunable spectral filters, switches, modulators and adaptable transformation optics devices. The low-energy, high-contrast, non-volatile switching mode of these devices may also have applications in protective optical circuitry and reconfigurable optical networks.

Methods

Reconfigurable photonic metamaterial fabrication. A 50-nm-thick gold layer (for the plasmonic metamaterial and contact electrodes) was thermally evaporated through a shadow mask onto a commercially available 50-nm-thick low-stress silicon nitride membrane. The gold-coated membrane was structured with a focused ion beam system (FEI Helios 600 NanoLab), with the contact electrodes connected to a source measurement unit (Keithley 2636) through a vacuum feedthrough for *in situ* electrical characterization. Using focused ion beam milling, the 'meander near the wire' pattern was first milled. The membrane was then cut into suspended silicon nitride strings with tapered ends, and the terminals at the string ends were electrically separated by removing the gold film in selected areas. The detailed dimensions of the nanostructure are given in the main text.

Experimental characterization. All imaging of the nanostructure was conducted using the scanning electron microscopy mode of the focused ion beam system (Figs 1,3 and 4). For the Supplementary Movie, the source measurement unit was used to induce switching.

The transmission and reflection spectra of the reconfigurable metamaterial were recorded using a microspectrophotometer (CRAIC Technologies) while applying various DC voltages (via the source measurement unit) to tune the mechanical configuration of the nanostructure (Figs 2 and 4).

High-frequency electro-optical modulation was studied by measuring the modulation of a 1.3-μm laser beam transmitted through the nanostructure, while modulating the metamaterial using a signal generator (Tabor 8551, rectangular modulation between 0 V and 1.1 V). The modulated signal was detected by an InGaAs photodetector (New Focus 1811) and a lock-in amplifier (Stanford Research SR844) (Fig. 3).

In all optical experiments, the incident electric field was polarized parallel to the strings.

Received 20 July 2012; accepted 31 January 2013; published online 17 March 2013; corrected online 22 March 2013; corrected after print 15 May 2014

References

1. Zheludev, N. I. & Kivshar, Y. S. From metamaterials to metadevices. *Nature Mater.* **11,** 917–924 (2012).
2. Gil, I., Bonache, J., Garcia-Garcia, J. & Martin, F. Tunable metamaterial transmission lines based on varactor-loaded split-ring resonators. *IEEE Trans. Microw. Theor.* **54,** 2665–2674 (2006).
3. Driscoll, T. *et al.* Memory metamaterials. *Science* **325,** 1518–1521 (2009).
4. Sámson, Z. L. *et al.* Metamaterial electro-optic switch of nanoscale thickness. *Appl. Phys. Lett.* **96,** 143105 (2010).
5. Zhao, Q. *et al.* Electrically tunable negative permeability metamaterials based on nematic liquid crystals. *Appl. Phys. Lett.* **90,** 011112 (2007).
6. Werner, D. H., Kwon, D-H., Khoo, I-C., Kildishev, A. V. & Shalaev, V. M. Liquid crystal clad near-infrared metamaterials with tunable negative–zero–positive refractive indices. *Opt. Express* **15,** 3342–3347 (2007).
7. Papasimakis, N. *et al.* Graphene in a photonic metamaterial. *Opt. Express* **18,** 8353–8359 (2010).
8. Ju, L. *et al.* Graphene plasmonics for tunable terahertz metamaterials. *Nature Nanotech.* **6,** 630–634 (2011).
9. Savinov, V., Fedotov, V. A., Anlage, S. M., de Groot, P. A. J. & Zheludev, N. I. Modulating sub-THz radiation with current in superconducting metamaterial. *Phys. Rev. Lett.* **109,** 243904 (2012).
10. Chen, H-T. *et al.* Active terahertz metamaterial devices. *Nature* **444,** 597–600 (2006).
11. Padilla, W. J., Taylor, A. J., Highstrete, C., Lee, M. & Averitt, R. D. Dynamical electric and magnetic metamaterial response at terahertz frequencies. *Phys. Rev. Lett.* **96,** 107401 (2006).
12. Chicherin, D. *et al.* MEMS-based high-impedance surfaces for millimeter and submillimeter wave applications. *Microw. Opt. Technol. Lett.* **48,** 2570–2573 (2006).
13. Zhu, W. M. *et al.* Switchable magnetic metamaterials using micromachining processes. *Adv. Mater.* **23,** 1792–1796 (2011).
14. Fu, Y. H. *et al.* A micromachined reconfigurable metamaterial via reconfiguration of asymmetric split-ring resonators. *Adv. Funct. Mater.* **21,** 3589–3594 (2011).
15. Zhu, W. M. *et al.* Microelectromechanical Maltese-cross metamaterial with tunable terahertz anisotropy. *Nature. Commun.* **3,** 1274 (2012).
16. Pryce, I. M., Aydin, K., Kelaita, Y. A., Briggs, R. M. & Atwater, H. A. Highly strained compliant optical metamaterials with large frequency tunability. *Nano Lett.* **10,** 4222–4227 (2010).
17. Fedotov, V. A., Mladyonov, P. L., Prosvirnin, S. L. & Zheludev, N. I. Planar electromagnetic metamaterial with a fish scale structure. *Phys. Rev. E* **72,** 056613 (2005).
18. Schwanecke, A. S. *et al.* Optical magnetic mirrors. *J. Opt. A* **9,** L1–L2 (2007).
19. Kao, T. S., Huang, F. M., Chen, Y., Rogers, E. T. F. & Zheludev, N. I. Metamaterial as a controllable template for nanoscale field localization. *Appl. Phys. Lett.* **96,** 041103 (2010).
20. Tasy, N., Sonnenberg, T., Jansen, H., Legtenberg, R. & Elwenspoek, M. Stiction in surface micromachining. *J. Micromech. Microeng.* **6,** 385–397 (1996).
21. Meng, X. Y., Wang, Z. Z., Zhu, Y. & Chen, C. T. Mechanism of the electro-optic effect in the perovskite-type ferroelectric $KNbO_3$ and $LiNbO_3$. *J. Appl. Phys.* **101,** 103506 (2007).
22. Turner, E. H. High-frequency electro-optic coefficients of lithium niobate. *Appl. Phys. Lett.* **8,** 303–304 (1966).
23. Lukyanchuk, B. *et al.* The Fano resonance in plasmonic nanostructures and metamaterials. *Nature Mater.* **9,** 707–715 (2010).

Acknowledgements

The authors thank Wei Ting Chen for assistance with metamaterial fabrication. This work is supported by the Leverhulme Trust, the Royal Society, the US Office of Naval Research (grant N000141110474), DSTL (UK), the MOE Singapore (grant MOE2011-T3-1-005) and the UK's Engineering and Physical Sciences Research Council through the Nanostructured Photonic Metamaterials Programme Grant.

Author contributions

N.I.Z. and E.P. conceived the idea for the experiment. J.Y.O. manufactured the sample and carried out the measurements. J.Z. simulated the nanostructure. All authors discussed the results and analysed the data. N.I.Z. and E.P. wrote the paper. N.I.Z. supervised the work.

Additional information

Supplementary information is available in the online version of the paper. Reprints and permissions information is available online at www.nature.com/reprints. Correspondence and requests for materials should be addressed to E.P. and N.I.Z.

Competing financial interests

The authors declare no competing financial interests.

ERRATUM

An electromechanically reconfigurable plasmonic metamaterial operating in the near-infrared

Jun-Yu Ou, Eric Plum, Jianfa Zhang and Nikolay I. Zheludev

Nature Nanotechnology http://dx.doi.org/10.1038/nnano.2013.25 (2013); published online 17 March 2013;
corrected online 22 March 2013.

In the version of this Letter originally published online, in the equation on page 2 the extent of the square root was incorrect. This has now been corrected in all versions of the Letter.

ERRATUM

An electromechanically reconfigurable plasmonic metamaterial operating in the near-infrared

Jun-Yu Ou, Eric Plum, Jianfa Zhang and Nikolay I. Zheludev

Nature Nanotechnology **8,** 252–255 (2013); published online 17 March 2013; corrected online 22 March 2013; corrected after print 15 May 2014.

In the version of this Letter originally published, in Fig. 4e, the position of the pink curve was incorrect. This has now been corrected in the online versions of the Letter.

Open

Light: Science & Applications (2013) 2, e96; doi:10.1038/lsa.2013.52

www.nature.com/lsa

ORIGINAL ARTICLE

Nonlinear dielectric optomechanical metamaterials

Jianfa Zhang[1], Kevin F MacDonald[1] and Nikolay I Zheludev[1,2]

We introduce a dielectric photonic metamaterial presenting a giant nonlinear optical response driven by resonant optomechanical forces. Being inherently free of Joule losses, it exhibits optical bistability at intensity levels of less than 0.2 mW μm^{-2} and, furthermore, manifests nonlinear asymmetric transmission with a forward : backward optical extinction ratio of more than 30 dB.
Light: Science & Applications (2013) **2,** e96; doi:10.1038/lsa.2013.52; published online 30 August 2013

Keywords: Metamaterial; optical bistability; optomechanical

INTRODUCTION

Optical forces are extremely important in mesoscopic systems: they are exploited in all forms of optical tweezing, manipulation and binding.[1–5] The dynamic back-action caused by optical forces has been proposed for optomechanical laser cooling and amplification and underpins the emerging field of 'cavity optomechanics'[6] where enormous progress has been made in recent years.[7–15] Optical forces can also be harnessed for actuation of nanophotonic devices.[16–19] Indeed, the convergence of nanophotonics and nanomechanics through optical forces presents enormous potential for all-optical operation of nanomechanical systems, reconfigurable and ultra-widely tunable nanophotonic devices, and novel nonlinear and self-adaptive photonic functionalities.[20–26]

Here we introduce the concept of optomechanical metamaterials as a new paradigm for achieving strong optical nonlinearity, optical bistability[27] and asymmetric transmission.[28–31] Metamaterials are artificial media with unusual and useful electromagnetic properties achieved through subwavelength structuring.[32] They provide a unique platform for manipulating electromagnetic fields, and thereby optical forces,[33,34] on the nanoscale. Numerical analyses reveal that optomechanical forces, acting within and among the constituent cells of a dielectric (silicon/silicon nitride) metamaterial, provide a strong nonlinear optical response mechanism (i.e., one through which light may change the optical properties of the medium) delivering high contrast, near-infrared asymmetric transmission and optical bistability at intensity levels of only a few hundred μW μm^{-2}.

MATERIALS AND METHODS

Within the framework of classical electrodynamics, the components of the total time-averaged force F acting on an object illuminated with light can be calculated using a surface integral:[35]

$$< F_i > = \oiint_S < T_{ij} > n_j \mathrm{d}S \qquad (1)$$

where S is a bounding surface around the object and T_{ij} is the time-averaged Maxwell stress tensor:

$$< T_{ij} > = \frac{1}{2}\mathrm{Re}\left[\varepsilon\varepsilon_0\left(E_i E_j^* - \frac{1}{2}\delta_{ij}|E|^2\right) + \mu\mu_0\left(H_i H_j^* - \frac{1}{2}\delta_{ij}|H|^2\right)\right] \qquad (2)$$

The stress tensor integral Equation (1) encompasses both radiation pressure, which arises through transfer of momentum between photons and any object on which they impinge, and the gradient force, which is associated with strong intensity variations in the local field around an object.[34]

Figure 1a shows an artistic impression and dimensions of the optomechanical metamaterial under consideration: it comprises an array of 250 nm wide, 690 nm long silicon 'nano-bars' with thicknesses alternating in the y direction between 100 and 150 nm; these are supported on parallel 100 nm thick, 250 nm wide silicon nitride strips running parallel to x and separated from each other (in y) by 200 nm. A unit cell of the metamaterial, with x and y dimensions of 900 nm, thus comprises a pair of dissimilar silicon nano-bars on parallel, independently mobile silicon nitride beams. It has recently been shown experimentally[36] that geometrically asymmetric silicon structures such as this support strong near-infrared magnetic resonances akin to the familiar 'trapped mode' of metallic asymmetric split ring designs.[37] Here we show computationally that in the vicinity of such a resonance (detailed further in the Supplementary Materials) strong optical forces are generated, which act to change the spatial arrangement of nano-bars within each cell and thereby the optical properties of the array:

- Electric E and magnetic H field distributions for the metamaterial are obtained from fully three-dimensional finite-element Maxwell solver simulations (in COMSOL Multiphysics). By modeling a single-unit cell with periodic boundary conditions in the x and y directions, these calculations assume an infinite planar array (which amounts in practical terms only to an assumption that one's probe beam is smaller than the array);

[1]Optoelectronics Research Centre & Centre for Photonic Metamaterials, University of Southampton, SO17 1BJ, UK and [2]Centre for Disruptive Photonic Technologies, Nanyang Technological University, Singapore 637371
Correspondence: Dr KF MacDonald, Optoelectronics Research Centre, University of Southampton, Highfield, Southampton, Hampshire, SO17 1BJ, UK
E-mail: kfm@orc.soton.ac.uk
Received 3 December 2012; revised 15 March 2013; accepted 23 April 2013

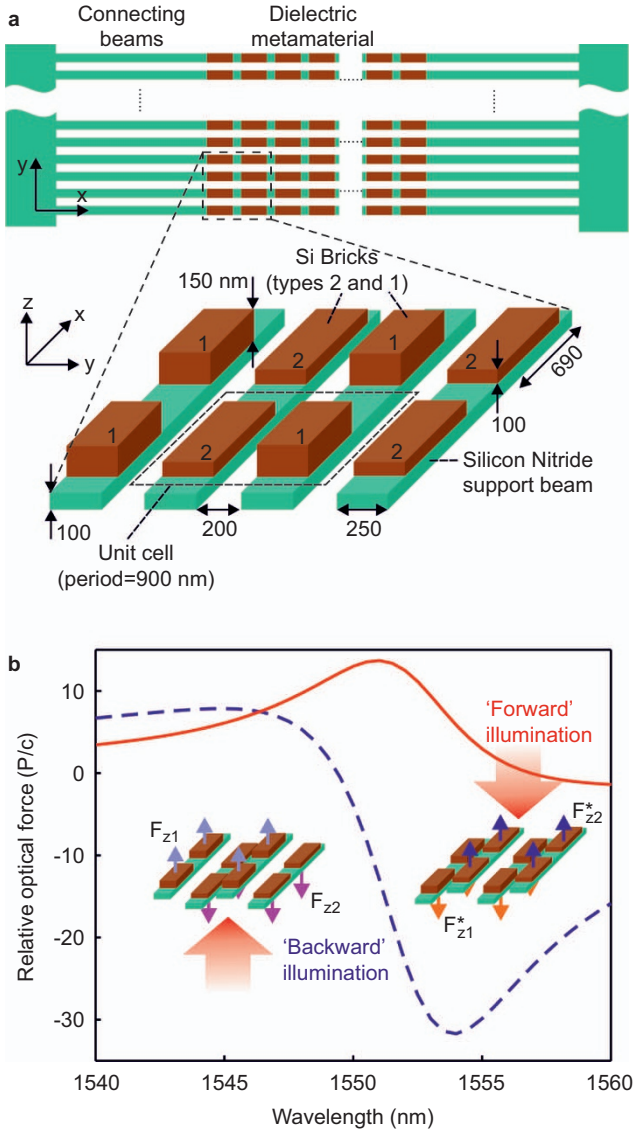

Figure 1 Asymmetric optomechanical forces in a dielectric photonic metamaterial. (**a**) Artistic impression and dimensional details of the parallel silicon nitride beam, silicon nano-bar metamaterial configuration studied. (**b**) Spectral dispersion of the relative optical force $F_{\text{opt.}}^{\text{cell}}$ on the two nanobar elements of a single metamaterial unit cell under normally incident *x*-polarized illumination for both forward ($-z$) and backward ($+z$) directions of light propagation ($F_{\text{opt.}}^{\text{cell}} = F_{z2} - F_{z1}$, where F_{z1} and F_{z2} are the optical forces on the thick and thin bars, respectively; Optical force is presented in units of P/c, where P is the incident power per unit cell and c is the speed of light in vacuum).

- Through the Maxwell stress tensor integral (Equation (1)), these E and H fields provide for the evaluation of optical force (on the nano-bar elements of a unit cell) as a function of relative displacement for selected wavelengths and/or incident power levels (as shown in Figure 2a).
- By translating these forces to a purely mechanical model of the silicon nitride beam structure (again in COMSOL), one may identify the equilibrium displacement position(s) at which the total optical force on each beam (for given illumination conditions) is balanced by the elastic restoring force. This mechanical model necessarily assumes a metamaterial array of finite extent in the x direction (12 Si nano-bars on a 10.8 μm long, 100 nm thick silicon nitride support), with the nitride beams extending, at a reduced thickness of 50 nm, to fixed mounting points 15 μm from the boundaries of the nano-bar array (edge effects relating to the finite number of silicon nano-bars on a beam are ignored because the optical force on each nano-bar is primarily a function of its electromagnetic interaction with dissimilar near-neighbors in the y direction.) By modeling a single pair of neighboring beams (one supporting 100 nm thick silicon nano-bars, the other 150 nm bars) the model effectively assumes an infinite array in the y direction—periodic boundary conditions being implied by the absence of any mechanical coupling between beams.
- The optical transmission coefficients for identified equilibrium states can then be obtained using the original model for the electromagnetic properties of the metamaterial array (the mechanical model shows that, within the range of applied force considered, less than 5% of the total out-of-plane beam deflection occurs across the central 100 nm thick section supporting the nano-bar array. As such, it validates the assumption of zero array curvature implied by the electromagnetic model's periodic boundary conditions).

Silicon and silicon nitride are assumed to be lossless with refractive indices of 3.5 and 2.0 respectively in the near-infrared range under consideration.[38] Further detail of modeling procedures may be found in the Supplementary Information.

All in-plane ('horizontal'; perpendicular to z) optical forces generated within the metamaterial structure are canceled and only out-of-plane ('vertical'; parallel to z) forces act on the dielectric beams. These drive each beam to move up or down until the optical forces are balanced by elastic restoring forces. While the electromagnetic components of the modeling procedure assume an infinite planar metamaterial array, optomechanical properties are presented below for a representative square domain of 12×12 unit cells subject to uniform (plane wave) illumination at a total incident power level P_0.

Figure 1b shows the relative magnitude of optical forces $F_{\text{opt.}}^{\text{cell}}$ acting on the pair of adjacent thick (150 nm) and thin (100 nm) nano-bars within a unit cell for light impinging on the metamaterial in the forward and backward directions—defined respectively as being incident on the silicon bar and supporting silicon nitride beam sides of the structure. A significant difference is found between these two configurations. The total force of radiation pressure on a unit cell is $\pm 2RP/c$ (where R is the reflection coefficient, P is the incident power per unit cell and c is the speed of light in vacuum), depending on the direction of incident light propagation. Forces on the individual nano-bar elements (see Supplementary Information) can be much larger in magnitude and may act against the direction of light propagation. Resonantly enhanced gradient forces are therefore the primary driver of the differential movement between neighboring beams, which gives rise to the asymmetric, nonlinear and bistable optical responses described below.

RESULTS AND DISCUSSION

Nonlinearity and asymmetric transmission

By providing a mechanism whereby light can induce changes in the spatial arrangement of a metamaterial's constituent parts, and thereby in its optical properties, the optomechanical effect described here acts as the foundation of a strong optical nonlinearity. Figure 2a shows the relative optical force acting on two neighboring beams $F_{\text{opt.}}^{\text{beam}}$ ($= NF_{\text{opt.}}^{\text{cell}}$ where $N=12$ is the number of silicon nano-bars on each beam within the mechanical model) as a function of mutual displacement D in the vertical (z) direction for a selection of incident light power levels at a wavelength $\lambda=1551$ nm. To achieve stable equilibrium, not only

doi:10.1038/lsa.2013.52

should the optical force be equal to the elastic restoring force $F_{el.}$, but they should also satisfy the conditions that $F_{opt.}^{beam} > F_{el.}|_{D-\Delta D}$ and $F_{opt.}^{beam} < F_{el.}|_{D+\Delta D}$. If these last conditions are not met, the equilibrium will be unstable and any perturbation would cause D to increase or decrease rapidly towards a stable balance point.

In the example shown, stable equilibrium is achieved for forward incidence of light with a power of 5 mW at a relative displacement of 9 nm (the point at which the black elastic force line intercepts the solid red 5 mW optical force line). For backward incidence, the direction of relative movement is inverted and equilibrium is achieved for the same power level at a mutual separation of −5 nm (the intersection of black and dashed red lines).

Figure 2b shows the dependence of relative beam displacement on optical power P_0 at a wavelength of 1551 nm for forward and backward light propagation directions. As a result of this movement, the dielectric metamaterial changes its optical properties as shown in Figure 2c. For forward propagation, transmission increases from a zero-illumination level of 3.2% to 68.3% at a power of 12.5 mW and then drops back to ~0.6% at 50 mW. The backward incidence optical transmission is less than 3.2% across the entirety of the 0–50 mW power range and at P_0=12.5 mW is only 0.034%, giving a forward:backward extinction ratio >30 dB.

Figure 3a shows the spectral dispersion of relative beam displacement under forward illumination at a selection of optical power levels and Figure 3b shows the corresponding transmission resonances, which become increasingly narrow and asymmetric as the optical power increases from 0 to 10 mW. This figure further illustrates the property of optomechanically-induced asymmetric transmission based on differing displacement responses for forward and backward directions of light propagation: at an optical power of only 10 mW, one observes an asymmetric transmission band centered at 1551 nm wherein the forward : backward extinction exceeds 20 dB.

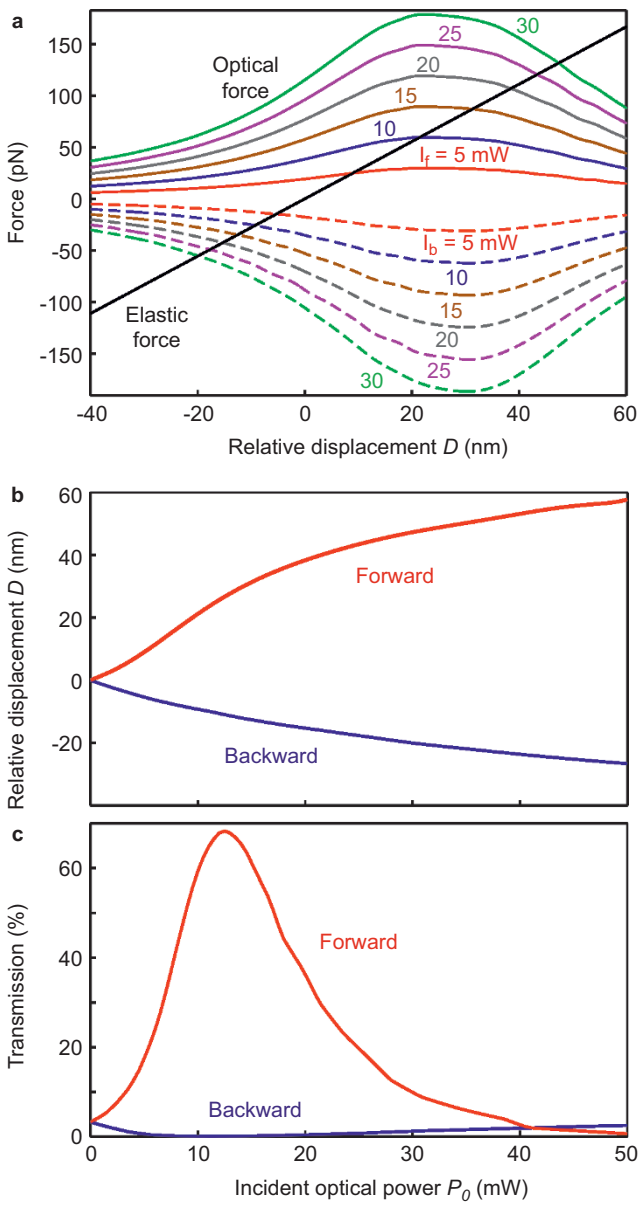

Figure 2 Nonlinear optical response and asymmetric transmission. (**a**) Dependence of the relative optical force $F_{opt.}^{beam}$ on the mutual out-of-plane displacement D of neighboring silicon nitride beams supporting thick and thin silicon nano-bars under 1551 nm forward (solid lines) and backward (dashed lines) illumination at a range of incident power levels P_0 (as labeled). The straight black line corresponds to the opposing elastic force. (**b**, **c**) Dependencies of (**b**) relative nano-beam displacement and (**c**) metamaterial optical transmission on total incident power at a wavelength of 1551 nm ($D=D_2-D_1$ where D_1 and D_2 are the absolute displacements of beams supporting thick and thin Si nano-bars respectively).

Bistability

The dielectric nano-bar metamaterial also exhibits optical bistability based on its nano-mechanical response:[27,39] Figure 4a presents the relative optical force (for forward incidence at a wavelength of λ=1555 nm) and the corresponding elastic restoring force acting on two neighboring beams as a function of relative displacement. At both low and high incident powers, the system has only one equilibrium

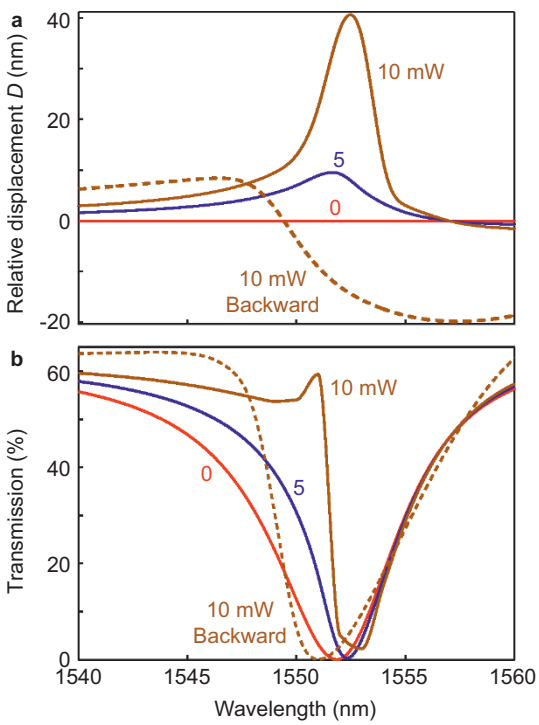

Figure 3 Optomechanical nonlinearity and asymmetric transmission resonances. (**a**) Spectral dispersion of the steady-state relative nano-beam displacement and (**b**) corresponding optical transmission for forward incidence of light (solid lines) at a selection of total incident power levels (as labeled) and backward incidence at 10 mW (dashed lines).

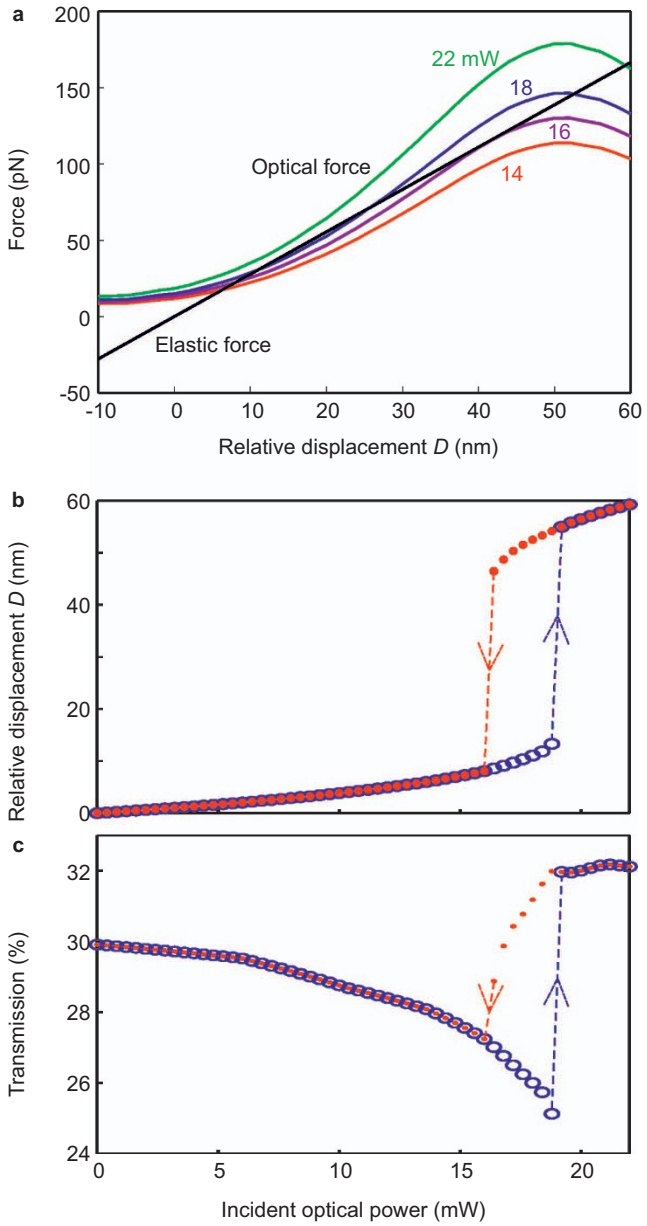

Figure 4 Optomechanical bistability. (**a**) Dependence of the relative optical force $F_{opt.}^{beam}$ and elastic restoring force $F_{el.}$ on the mutual out-of-plane separation D of neighboring silicon nitride nano-beams under 1555 nm forward illumination at a selection of incident power levels P_0 (as labeled). (**b**, **c**) Corresponding bistable incident power dependencies of (**b**) mutual displacement and (**c**) optical transmission.

position (the single points of intersection between $F_{el.}$ and $F_{opt.}^{beam}$ lines at D=6.3 nm for P_0=14 mW and at 59 nm for 22 mW). But at intermediate levels, here between about 16 and 19 mW, the optical and elastic force lines intersect at more than one point and the system becomes bistable, as illustrated by the relative displacement and corresponding optical transmission versus power curves in Figure 4b and 4c.

Switching dynamics

In such a highly nonlinear system, the switching dynamics are complex and depend strongly on initial conditions and control input dynamics. The above study is concerned with steady-state displacements of the nanostructure (i.e., assumes constant illumination at any given incident power level) and with the associated changes in optical properties, but an indicative estimate of switching time can be obtained by numerically solving the nonlinear equations of motion for individual beams. This analysis yields a characteristic transition time, from the zero-illumination equilibrium position to maximum deflection, of order 5 μs (assuming instantaneous application of a force equivalent to that generated at P_0=10 mW for forward illumination at a wavelength of 1551 nm, ignoring the damping of any subsequent oscillation).

CONCLUSIONS

In summary, we introduce a new type of dielectric metamaterial, inherently free of Joule losses, which exhibits strong optomechanical nonlinearity, asymmetric transmission and optical bistability at optical intensities of less than 0.2 mW μm^{-2}.

While changes in the transmission spectrum of a metamaterial such as considered here may also result from the Kerr nonlinearity of the silicon bars, this nonlinear response mechanism is around five orders of magnitude weaker than the optomecahnical nonlinearity.

With regard to the practical realization of optomechanical metamaterials, resonance quality factors will be affected slightly by the small but non-zero optical absorption coefficients of the constituent media, but more so by manufacturing imperfections. However, as the first experimental studies of dielectric metamaterials have shown,[36] neither of these factors is an obstacle to the achievement of near-infrared resonances at least as sharp as is possible in metallic metamaterials. Optical absorption (including two-photon absorption) and variations in ambient temperature may lead to thermomechanical changes in the structure. But while these would affect every beam equally, the nonlinear, asymmetric and bistable behaviors of interest are derived from differential movements of neighboring beams. As such, their visibility would not be compromised. The viscosity of the ambient medium, though not relevant to the steady state optical properties of such a system, will clearly be a determining factor in the limits of dynamic switching performance.

This metamaterial concept for nanoscale photonic functionality may exploit unique technological and manufacturing opportunities provided by semiconductor membrane technology and, in being driven by forces generated among its constituent parts (as opposed to external actuators), holds notable advantages over more conventional M/NEMS structures, particularly in relation to size scaling for different operational wavelength bands.

ACKNOWLEDGMENTS

The authors thank Dr Eric Plum and Professor Wei-Min Ye for fruitful discussions. This work was supported by the Engineering and Physical Sciences Research Council (grant EP/G060363/1) [All authors], the Royal Society and the Ministry of Education, Singapore (grant MOE2011-T3-1-005) [NIZ], and the China Scholarship Council [JZ].

1 Grier D. A revolution in optical manipulation. *Nature* 2003; **424**: 810–816.
2 Dholakia K, Čižmár T. Shaping the future of manipulation. *Nat Photon* 2011; **5**: 335–342.
3 Juan ML, Righini M, Quidant R. Plasmon nano-optical tweezers. *Nat Photon* 2011; **5**: 349–356.
4 Chen J, Ng J, Lin Z, Chan CT. Optical pulling force. *Nat Photon* 2011; **5**: 531–534.
5 Dholakia K, Zemánek P. Colloquium: gripped by light: optical binding. *Rev Mod Phys* 2010; **82**: 1767–1791.
6 Kippenberg TJ, Vahala KJ. Cavity optomechanics: back-action at the mesoscale. *Science* 2008; **321**: 1172–1176.
7 Eichenfield M, Jasper Chan J, Camacho RM, Vahala KJ, Painter O. Optomechanical crystals. *Nature* 2009; **462**: 78–82.
8 Favero I, Karrai K. Optomechanics of deformable optical cavities. *Nat Photon* 2009; **3**: 201–205.

doi:10.1038/lsa.2013.52

9 Anetsberger G, Arcizet O, Unterreithmeier QP, Rivière R, Schliesser A *et al*. Near-field cavity optomechanics with nanomechanical oscillators. *Nat Phys* 2009; **5**: 909–914.
10 Nunnenkamp A, Børkje K, Girvin SM. Single-photon optomechanics. *Phys Rev Lett* 2011; **107**: 063602.
11 Usami K, Naesby A, Bagci T, Melholt Nielsen B, Liu J *et al*. Optical cavity cooling of mechanical modes of a semiconductor nanomembrane. *Nat Phys* 2012; **8**: 168–172.
12 Ding L, Baker C, Senellart P, Lemaitre A, Ducci S *et al*. High frequency GaAs nano-optomechanical disk resonator. *Phys Rev Lett* 2010; **105**: 263903.
13 Favero I, Sebastian Stapfner S, Hunger D, Paulitschke P, Reichel J *et al*. Fluctuating nanomechanical system in a high finesse optical microcavity. *Opt Express* 2009; **17**: 12813–12820.
14 Ramos D, Gil-Santos E, Pini V, Llorens JM, Fernández-Regúlez M *et al*. Optomechanics with silicon nanowires by harnessing confined electromagnetic modes. *Nano Lett* 2012; **12**: 932–937.
15 Roh YG, Tanabe T, Shinya A, Taniyama H, Kuramochi E *et al*. Strong optomechanical interaction in a bilayer photonic crystal. *Phys Rev B* 2010; **81**: 121101(R).
16 Li M, Pernice WH, Xiong C, Baehr-Jones T, Hochberg M *et al*. Harnessing optical forces in integrated photonic circuits. *Nature* 2008; **456**: 480–485.
17 Eichenfield M, Michael CP, Perahia R, Painter O. Actuation of micro-optomechanical systems *via* cavity-enhanced optical dipole forces. *Nat Photon* 2007; **1**: 416–422.
18 Wiederhecker GS, Chen L, Gondarenko A, Lipson M. Controlling photonic structures using optical forces. *Nature* 2009; **462**: 633–637.
19 Van Thourhout D, Roels J. Optomechanical device actuation through the optical gradient force. *Nat Photon* 2010; **4**: 211–217.
20 Bagheri M, Poot M, Li M, Pernice WH, Tang HX. Dynamic manipulation of nanomechanical resonators in the high-amplitude regime and non-volatile mechanical memory operation. *Nat Nanotech* 2011; **6**: 726–732.
21 Lapine M, Shadrivov I, Powell DA, Kivshar Y. Magnetoelastic metamaterials. *Nat Mater* 2011; **11**: 30–33.
22 Deotare PB, Bulu I, Frank IW, Quan Q, Zhang Y *et al*. All optical reconfiguration of optomechanical filters. *Nat Commun* 2012; **3**: 846.
23 Rakich PT, Popović MA, Soljačić M, Ippen EP. Trapping, corralling and spectral bonding of optical resonances through optically induced potentials. *Nat Photon* 2007; **1**: 658–665.
24 Kang MS, Butsch A, Russell PS. Reconfigurable light-driven opto-acoustic isolators in photonic crystal fibre. *Nat Photon* 2011; **5**: 549–553.
25 Safavi-Naeini AH, Mayer Alegre TP, Chan J, Eichenfield M, Winger M *et al*. Electromagnetically induced transparency and slow light with optomechanics. *Nature* 2011; **472**: 69–73.
26 Lian Z, Horak P, Feng X, Xiao L, Frampton K *et al*. Nanomechanical optical fiber. *Opt Express* 2012; **20**: 29386–29394.
27 Gibbs HM. *Optical Bistability. Controlling Light with Light*. Orlando, FL: Academic Press; 1985.
28 Fedotov VA, Mladyonov PL, Prosvirnin SL, Rogacheva AV, Chen Y *et al*. Asymmetric propagation of electromagnetic waves through a planar chiral structure. *Phys Rev Lett* 2006; **97**: 167401.
29 Menzel C, Helgert C, Rockstuhl C, Kley EB, Tünnermann A *et al*. Asymmetric transmission of linearly polarized light at optical metamaterials. *Phys Rev Lett* 2010; **104**: 253902.
30 Mutlu M, Akosman AE, Serebryannikov AE, Ozbay E. Asymmetric transmission of linearly polarized waves and polarization angle dependent wave rotation using a chiral metamaterial. *Opt Express* 2011; **19**: 14290–14299.
31 Shadrivov I, Fedotov VA, Powell DA, Kivshar Y, Zheludev NI. Electromagnetic wave analogue of an electronic diode. *New J Phys* 2011; **13**: 033025.
32 Zheludev NI. The road ahead for metamaterials. *Science* 2010; **328**: 582–583.
33 Zhao R, Tassin P, Koschny T, Soukoulis CM. Optical forces in nanowire pairs and metamaterials. *Opt Express* 2010; **18**: 25665–25676.
34 Zhang J, MacDonald KF, Zheludev NI. Optical gecko toe: optically-controlled attractive near-field forces between plasmonic metamaterials and dielectric or metal surfaces. *Phys Rev B* 2012; **85**: 205123.
35 Jackson JD. *Classical Electrodynamics*. New York: John Wiley & Sons; 1998.
36 Zhang J, Ou JY, Chen R, Charlton MD, MacDonald KF *et al*. Optical magnetic response in all-dielectric metamaterial. In: Proceedings of the NanoMeta 2013; 3–6 January 2013; Seefeld-in-Tirol, Austria. ORC: Southampton, UK, 2013; Publication No: 5680.
37 Fedotov VA, Rose M, Prosvirnin SL, Papasimakis N, Zheludev NI. Sharp trapped-mode resonances in planar metamaterials with a broken structural symmetry. *Phys Rev Lett* 2007; **99**: 147401.
38 Palik ED, editor. *Handbook of Optical Constants of Solids*. Orlando, FL: Academic Press; 1998.
39 Yu YF, Zhang JB, Bourouina T, Liu AQ. Optical-force-induced bistability in nanomachined ring resonator systems. *Appl Phys Lett* 2012; **100**: 093108.

Supplementary Information for this article can be found on *Light: Science & Applications*' website (http://www.nature.com/lsa/)

AIP | Applied Physics Letters

Nano-optomechanical nonlinear dielectric metamaterials

Artemios Karvounis, Jun-Yu Ou, Weiping Wu, Kevin F. MacDonald, and Nikolay I. Zheludev

Citation: Applied Physics Letters **107**, 191110 (2015); doi: 10.1063/1.4935795
View online: http://dx.doi.org/10.1063/1.4935795
View Table of Contents: http://scitation.aip.org/content/aip/journal/apl/107/19?ver=pdfcov
Published by the AIP Publishing

Nano-optomechanical nonlinear dielectric metamaterials

Artemios Karvounis,[1] Jun-Yu Ou,[1] Weiping Wu,[1] Kevin F. MacDonald,[1] and Nikolay I. Zheludev[1,2]
[1]*Optoelectronics Research Centre and Centre for Photonic Metamaterials, University of Southampton, Southampton, SO17 1BJ, United Kingdom*
[2]*The Photonics Institute and Centre for Disruptive Photonic Technologies, Nanyang Technological University, Singapore 637371*

(Received 4 August 2015; accepted 3 November 2015; published online 13 November 2015)

By harnessing the resonant nature of localized electromagnetic modes in a nanostructured silicon membrane, an all-dielectric metamaterial can act as nonlinear medium at optical telecommunications wavelengths. We show that such metamaterials provide extremely large optomechanical nonlinearities, operating at intensities of only a few μW per unit cell and modulation frequencies as high as 152 MHz, thereby offering a path to fast, compact, and energy efficient all-optical metadevices. © *2015 AIP Publishing LLC*. [http://dx.doi.org/10.1063/1.4935795]

Non-metallic metamaterial nanostructures currently attract intense attention as they promise to reduce the losses and costs associated with the use of noble metals in traditional plasmonic architectures.[1] It has already been shown that oxides and nitrides,[2] graphene,[3] topological insulators,[4] and high-index dielectrics[5–13] can be used as platforms for the realization of high-Q resonant metamaterials. A variety of non-metallic media, such as graphene,[14] carbon nanotubes,[15] liquid crystals,[16] and semiconductors,[17,18] have also been engaged through hybridization with plasmonic metamaterials to create media with strongly enhanced optical nonlinearities, while a nano-optomechanical nonlinearity has recently been observed in a plasmonic metamaterial.[19] Here, we experimentally demonstrate an all-dielectric metamaterial, fabricated from a free-standing semiconductor nano-membrane, with sharp near-infrared optical resonances. It exhibits a strong optical nonlinearity associated with light-induced nano-mechanical oscillations of the structure, which change the physical configuration and thus the resonant response of the metamaterial array's constituent metamolecules.

Optical forces at the sub-micron scale can be comparable or even stronger than elastic forces, and resonantly enhanced optical forces in photonic metamaterials have been theoretically studied for both plasmonic and all-dielectric structures.[20–22] The exchange of energy between incident light and a nano-mechanical resonator can be further enhanced when the light is modulated at the mechanical eigenfrequency of the resonator; indeed, it has recently been shown that plasmonic metamaterials can be optically reconfigured on this basis with light modulated at MHz frequencies.[19] In consequence of the fact that the mechanical eigenfrequencies of objects are dictated by their stiffness (Young's modulus) and dimensions, nano-scale mechanical oscillators made of silicon offer the prospect of mechanical vibration at hundreds of MHz or even GHz frequencies.

Considerable efforts have been devoted to the reduction of radiative losses in resonant plasmonic metamaterials, as non-radiative losses (Joule heating) are unavoidable in the constituent metals. In "all-dielectric" metamaterials non-radiative losses are *a priori* limited, so with appropriate design they can present even stronger optical resonances, and thereby generate stronger optical forces, than plasmonic counterparts.[22] Previous works have demonstrated that high-index media such as silicon can support optical frequency resonances[5–13] and we harness that characteristic here to engineer an ultrathin medium with optical properties that are highly sensitive to structural reconfiguration.

The metamaterial is fabricated by direct focused ion beam (FIB) milling of a commercially sourced (Norcada, Inc.), 100 nm thick polycrystalline silicon membrane in a silicon frame (Fig. 1). To date, all-dielectric metamaterials have invariably been realized as "positive" structures—arrays of discrete high-index features (nanorods, discs, bars, etc.) supported on a lower-index substrate.[5–13] The metamaterial employed in the present study shows, however, that strong localized resonances can also be excited in "negative" dielectric nanostructures, i.e., a pattern formed by slots cut into a continuous layer of high-index material. The free-standing configuration has the additional advantage of maximizing refractive index contrast with the near-field environment and thereby resonance quality factor.[23] Each $1.05\,\mu\text{m} \times 1.05\,\mu\text{m}$ unit cell (metamolecule) contains a rectangular nano-cantilever of length $L = 300$ nm and width $W = 600$ nm, with an additional slot across the fixed end of the cantilever arm to increase flexibility (Fig. 1(c) shows a geometric schematic of the structure). The metamaterial array is composed of 25×25 metamolecules.

This structure supports several optical resonances in the near-infrared range, as illustrated by the microspectrophotometrically measured reflection, transmission, and derived absorption spectra presented in Figs. 1(d)–1(f). These data show good correlation with spectra obtained via 3D finite element numerical modelling (COMSOL Multiphysics), using a fixed complex refractive index for polycrystalline silicon of $3.2 + 0.04i$ (following Ref. 24 with an imaginary part tuned to match resonance quality with experimental observations, using the 1550 nm pump wavelength as a reference point: a value ≤ 0.01 for pristine polycrystalline silicon produces much sharper spectral features—the elevated value employed here effectively represents a variety of material and manufacturing imperfections including deviations from the ideal rectilinear, perfectly planar geometry of the model, surface roughness, and gallium contamination from the FIB milling process).

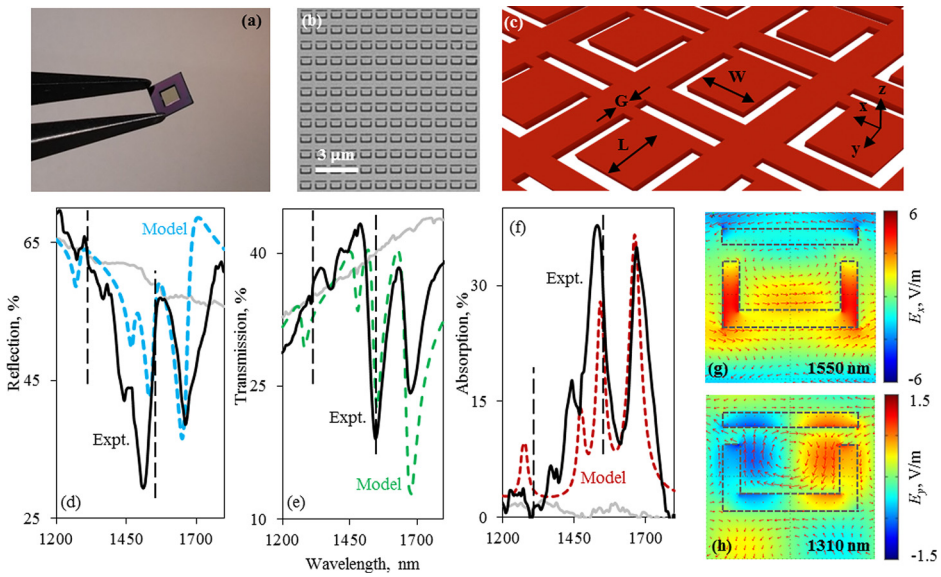

FIG. 1. Optical resonances in free-standing silicon nano-membrane metamaterials: (a) 100 nm thick Si membrane in 5 mm × 5 mm Si frame used as a platform for fabrication of free-standing all-dielectric metamaterials. (b) Scanning electron microscope image of part of a nano-cantilever metamaterial array fabricated in a Si membrane by focused ion beam milling [dark areas = slots cut through the membrane]. (c) Schematic oblique view of the nano-cantilever array: period = 1.05 μm; $L = 300$ nm; $W = 600$ nm; $G = 100$ nm; and slot width = 100 nm. (d)–(f) Normal incidence reflection, transmission, and absorption spectra of the metamaterial for x-polarized light. Black lines correspond to experimental measurements, dashed lines to numerical modelling results; grey lines show measured spectra for the unstructured silicon membrane. (g) and (h) Field maps, in the xy plane at the mid-point of the membrane thickness, for (g), the electric mode resonance at 1550 nm [E_x field component] and (h) the magnetic mode at 1310 nm [E_y field]—the experimental pump and probe wavelengths, respectively. The field maps are overlaid with arrows, indicating the direction and magnitude of electric displacement.

In order to achieve a strong optomechanical nonlinearity, we require a metamaterial that is highly sensitive at the probe wavelength (1310 nm in the present case) to structural reconfiguration driven by strong optical forces generated within the structure at the pump wavelength (1550 nm). Figure 2(a) shows simulated transmission around 1310 nm and corresponding maps of field distribution at this wavelength for three different configurations—tilt angles—of the metamolecule nano-cantilevers. The probe wavelength sits to one side of a resonance based upon a spatial distribution of electric field and displacement currents in the cantilever arms that generates magnetic dipoles (in the manner of the familiar plasmonic asymmetric split ring metamaterial "trapped mode"[25]). The spectral dispersion strongly depends on the cantilever tilt angle, with the resonance blue-shifting as the cantilever arms tilt out of plane (i.e., as their effective length decreases), resulting in a transmission increase at the fixed 1310 nm probe wavelength (there is a concomitant reflectivity decrease, and no meaningful change in absorption).

The absorption resonance in the 1550 nm waveband is derived from the excitation of an electric dipole, hybridized with higher order electric multipoles, within each unit cell (Fig. 1(g)), giving rise to a spatial distribution of optical forces that tilts the cantilever arms out of the sample plane. In classical electrodynamics, the components of the total time-averaged force F acting on an object illuminated with light can be calculated using the surface integral[26]

$$\langle F_i \rangle = \oiint_S \langle T_{ij} \rangle n_j dS, \tag{1}$$

S being a closed surface around the region of interest, n_j unit vector components pointing out of the surface, and $\langle T_{ij} \rangle$ the time-averaged Maxwell stress tensor defined by

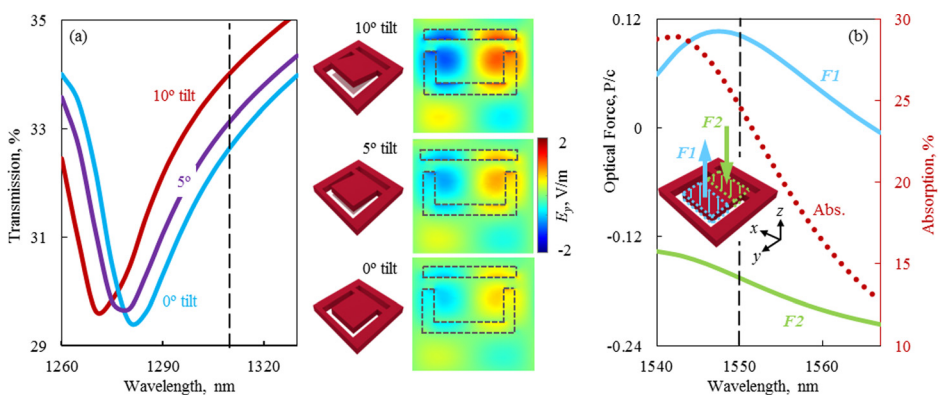

FIG. 2. Modelling optical forces and changes in optical properties resulting from structural reconfiguration: (a) Numerically simulated dispersion of metamaterial transmission around the experimental 1310 nm probe wavelength for a selection of nano-cantilever tilt angles, as labelled and illustrated schematically to the right, alongside corresponding Ey field maps for the xy plane at the mid-point of the membrane thickness at 1310 nm. (b) Spectral dispersion of the normalized out-of-plane optical forces acting on either end of the metamolecule nano-cantilevers [as illustrated inset], and of metamaterial absorption, around the experimental 1550 nm pump wavelength. [In all cases, simulations assume normally incident, x-polarized light.]

$$\langle T_{ij}\rangle = \frac{1}{2}Re\left[\varepsilon\varepsilon_0\left(E_iE_j^* - \frac{1}{2}\delta_{ij}|E|^2\right) + \mu\mu_0\left(H_iH_j^* - \frac{1}{2}\delta_{ij}|H|^2\right)\right]. \quad (2)$$

The optical force given by Eq. (1) encompasses both radiation pressure, which arises through the transfer of momentum between photons and any object on which they impinge, and the gradient force, which is associated with intensity variations in the local field around an object. Applied to the metamaterial unit cell (Fig. 2(b)), this stress tensor analysis reveals antiparallel forces acting on the two ends of the cantilever arms—a net "positive" force *F1* (in the $+z$ direction towards the light source) at the free end of the arm and an opposing force *F2* (in the $-z$ direction of light propagation) at the other.

In normalized units, these can, respectively, reach levels of 0.1 and $0.16\,P/c$ (where P is the incident power per unit cell and c is the speed of light). In absolute terms, for an illumination intensity of 60 μW/μm^2, this corresponds to a force of ~20 fN on the cantilever tip and an opposing force of ~35 fN at the hinge, which would be sufficient to induce a static deformation (i.e., tilt) of only 2″—displacing the tip of the cantilever arm by ~5 pm. However, much larger deformations can be achieved by the same instantaneous driving forces at the structure's mechanical resonances, where displacement will be enhanced by the quality factor of the mechanical resonator. Assuming a Young's modulus of 150 GPa for the silicon membrane,[27] the first mechanical eigenmode of the 300 nm metamolecule cantilevers—the out-of-plane oscillation of the arms—is expected from numerical simulations to occur at a frequency of 165 MHz.

The optomechanical nonlinearity of the free-standing silicon membrane metamaterial was evaluated using the pump-probe experimental configuration schematically illustrated in Fig. 3(a). Pump and probe beams at 1550 and 1310 nm, respectively, are generated by CW single-mode-fiber-coupled diode lasers, with the pump beam subsequently electro-optically modulated at frequencies up to 200 MHz. The beams are combined using a wavelength division multiplexer into a single fiber and then pass via a free-space collimator to the input port of an optical microscope operating in transmission mode. They are focused at normal incidence to concentric spots on the metamaterial, with diameters of ~10 μm. A fixed probe intensity of 25 μW/μm^2 is maintained at the sample, while peak pump intensity is varied up to a maximum level of 62.5 μW/μm^2. A low-pass filter blocks transmitted pump light and the probe signal are monitored using an InGaAs photodetector (New Focus 1811) connected to electrical network analyzer (Agilent Technologies E5071C). The sample is held under low vacuum conditions at ~0.1 mbar to reduce atmospheric damping of mechanical oscillations.

Figure 3(b) presents the relative pump-induced change in probe transmission as a function of pump modulation frequency. As the pump intensity increases, the observed optomechanical resonance grows in strength and collapses spectrally to a central frequency of 152 MHz, reaching a maximum modulation depth of 0.2%. From numerical modelling, a transmission change of this magnitude corresponds to an induced nano-cantilever tilt of order 10′, or a tip displacement of ~830 pm—some two orders of magnitude more than the expected static displacement at the same pump intensity. This implies a mechanical resonance quality factor of order 100, though we take this to be a lower limit on the value for individual silicon cantilevers inhomogenously broadened (due to slight manufacturing defects and structural variations) across the metamaterial array. Indeed, at low pump intensities, a spectrally disparate set of peaks emerges, suggestive of the distribution of individual cantilevers' different mechanical eigenfrequencies. At higher intensities, the coupling among oscillators leads to synchronization and collective oscillation at a common frequency, which is in good agreement with the computationally projected frequency of the structure's first mechanical eigenmode.

It is instructive to estimate what nonlinear susceptibility a hypothetical homogeneous medium would need to possess to provide a response of comparable magnitude to the nano-optomechanical silicon membrane metamaterial: Absorption in a nonlinear medium is conventionally described by the expression $-dI/dz = \alpha I + \beta I^2 + \cdots$, where I is the light intensity, z is the propagation distance in the medium, and α and β are the linear and nonlinear absorption coefficients, respectively. The observed nonlinear transmission change ΔT is proportional to the pump power, so can be quantified via an estimate of the

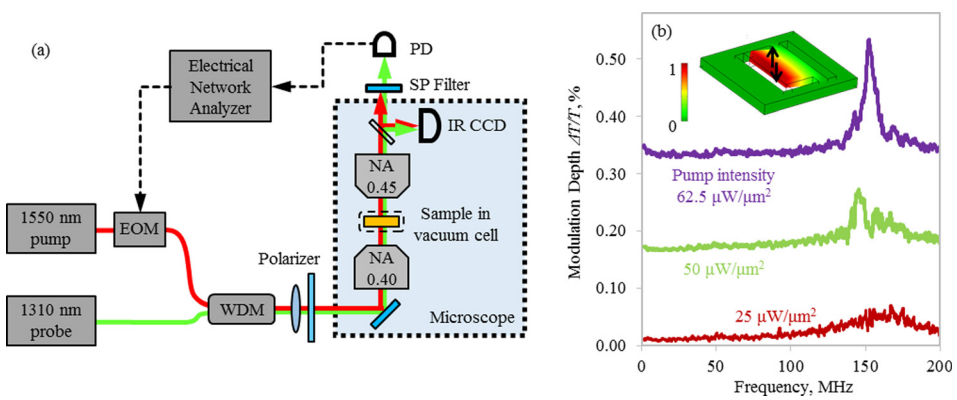

FIG. 3. Measuring the nonlinearity of nano-optomechanical all-dielectric metamaterials: (a) Schematic of the pump-probe experimental arrangement for transmission-mode measurements of metamaterial nonlinear response. (b) 1310 nm [probe] transmission modulation depth as a function of pump [1550 nm] modulation frequency for a selection of peak pump intensities [as labelled]. The inset shows a nano-cantilever unit cell colored according to the relative magnitude of out-of-plane displacement, from numerical modelling, for the structure's first mechanical eigenmode.

first nonlinear absorption coefficient $\beta \sim \Delta T/(It)$, where t is the metamaterial thickness. At the 152 MHz resonance frequency, $\beta \sim 7 \times 10^{-5}$ m/W, which corresponds to a nonlinear susceptibility of order $Im\{\chi^{(3)}\}/n^2 \sim 3.9 \times 10^{-14}$ m^2 V^{-2}.

In conclusion, by structuring a free-standing nano-membrane of silicon at the sub-wavelength scale, we engineer optical resonances strong enough to deliver a substantial optomechanical nonlinearity in an otherwise linear ultrathin medium. The nonlinear all-dielectric metamaterial operates at sub-GHz frequencies and μW/unit-cell intensities in the near-infrared spectral range. These free-standing all-dielectric metamaterials offer a compact, energy efficient, and fast active optoelectronic platform potentially suited to practical application in high speed photonic applications. Improvements may be made in the design and fabrication of membrane metamaterials to enhance the probe transmission or reflectivity change per degree of tilt or nanometre of displacement, and to maximize the efficacy with which optical forces can generate such movements. But even while absolute changes are small, their sharply resonant nonlinear character may serve a variety of sensing (e.g., gas pressure and chemical binding) applications.

This work was supported by the UK Engineering and Physical Sciences Research Council [Grant No. EP/G060363/1], the Samsung Advanced Institute of Technology [collaboration Project No. IO140325-01462-01], and The Royal Society, the Singapore Ministry of Education [Grant No. MOE2011-T3-1-005]. Following a period of embargo, the data from this paper can be obtained from the University of Southampton ePrints research repository, DOI: 10.5258/SOTON/383566.

[1]A. Boltasseva and H. A. Atwater, Science **331**, 290 (2011).
[2]G. V. Naik, V. M. Shalaev, and A. Boltasseva, Adv. Mater. **25**, 3264 (2013).
[3]N. Papasimakis, S. Thongrattanasiri, N. I. Zheludev, and F. J. García de Abajo, Light Sci. Appl. **2**, e78 (2013).
[4]J. Y. Ou, J. K. So, G. Adamo, A. Sulaev, L. Wang, and N. I. Zheludev, Nat. Commun. **5**, 5139 (2014).
[5]X. Meng, B. Bai, P. Karvinen, K. Konishi, J. Turunen, Y. Svirko, and M. Kuwata-Gonokami, Thin Solid Films **516**, 8745 (2008).
[6]S. Yun, J. A. Bossard, T. S. Mayer, and D. H. Werner, Appl. Phys. Lett. **96**, 223101 (2010).
[7]J. C. Ginn, I. Brener, D. W. Peters, J. R. Wendt, J. O. Stevens, P. F. Hines, L. I. Basilio, L. K. Warne, J. F. Ihlefeld, P. G. Clem, and M. B. Sinclair, Phys. Rev. Lett. **108**, 097402 (2012).
[8]J. Zhang, K. F. MacDonald, and N. I. Zheludev, Opt. Express **21**(22), 26721 (2013).
[9]C. Wu, N. Arju, G. Kelp, J. A. Fan, J. Dominguez, E. Gonzales, E. Tutuc, I. Brener, and G. Shvets, Nat. Commun. **5**, 3892 (2014).
[10]K. E. Chong, B. Hopkins, I. Staude, A. E. Miroshnichenko, J. Dominguez, M. Decker, D. N. Neshev, I. Brener, and Y. Kivshar, Small **10**, 1985 (2014).
[11]Y. Yang, I. I. Kravchenko, D. P. Briggs, and J. Valentine, Nat. Commun. **5**, 5753 (2014).
[12]P. Moitra, B. A. Slovick, Z. G. Yu, Y. S. Krishnamurthy, and J. Valentine, Appl. Phys. Lett. **104**, 171102 (2014).
[13]D. Lin, P. Fan, E. Hasman, and M. L. Brongersma, Science **345**, 298 (2014).
[14]A. E. Nikolaenko, N. Papasimakis, E. Atmatzakis, Z. Luo, Z. X. Shen, F. De Angelis, S. A. Boden, E. Di Fabrizio, and N. I. Zheludev, Appl. Phys. Lett. **100**, 181109 (2012).
[15]A. E. Nikolaenko, N. Papasimakis, A. Chipouline, F. De Angelis, E. Di Fabrizio, and N. I. Zheludev, Opt. Express **20**, 6068 (2012).
[16]A. Minovich, J. Farnell, D. N. Neshev, I. McKerracher, F. Karouta, J. Tian, D. A. Powell, I. V. Shadrivov, H. H. Tan, C. Jagadish, and Y. S. Kivshar, Appl. Phys. Lett. **100**, 121113 (2012).
[17]D. J. Cho, W. Wu, E. Ponizovskaya, P. Chaturvedi, A. M. Bratkovsky, S. Y. Wang, X. Zhang, F. Wang, and Y. R. Shen, Opt. Express **17**(20), 17652 (2009).
[18]K. M. Dani, Z. Ku, P. C. Upadhya, R. P. Prasankumar, S. R. J. Brueck, and A. J. Taylor, Nano Lett. **9**(10), 3565 (2009).
[19]J. Y. Ou, E. Plum, J. Zhang, and N. I. Zheludev, "Modulating light with light via giant nano-opto-mechanical nonlinearity of plasmonic metamaterial," Adv. Mater. (in press).
[20]V. Ginis, P. Tassin, C. M. Soukoulis, and I. Veretennicoff, Phys. Rev. Lett. **110**, 057401 (2013).
[21]J. Zhang, K. F. MacDonald, and N. I. Zheludev, Light Sci. Appl. **2**, e96 (2013).
[22]J. Zhang, K. F. MacDonald, and N. I. Zheludev, Opt. Lett. **39**, 4883 (2014).
[23]S. L. Prosvirnin, V. A. Dmitriev, Y. M. Kuleshov, and V. V. Khardikov, Appl. Opt. **54**(13), 3986 (2015).
[24]D. Maier-Schneider, S. Köprülülü, S. Ballhausen Holm, and E. Obermeier, J. Micromech. Microeng. **6**, 436 (1996).
[25]V. A. Fedotov, M. Rose, S. L. Prosvirnin, N. Papasimakis, and N. I. Zheludev, Phys. Rev. Lett. **99**, 147401 (2007).
[26]J. D. Jackson, *Classical Electrodynamics*, 3 ed. (John Wiley & Sons, New York, 1998).
[27]W. N. Sharpe, K. J. Hemker, and R. L. Edwards, *Mechanical Properties of MEMS Materials*, Report No. AFRL-IF-RS-TR-2004-76, 2004.

nature COMMUNICATIONS

ARTICLE

Received 3 Oct 2014 | Accepted 25 Mar 2015 | Published 24 Apr 2015 | Updated 7 Feb 2017 DOI: 10.1038/ncomms8021 OPEN

A magneto-electro-optical effect in a plasmonic nanowire material

João Valente[1], Jun-Yu Ou[1], Eric Plum[1], Ian J. Youngs[2] & Nikolay I. Zheludev[1,3]

Electro- and magneto-optical phenomena play key roles in photonic technology enabling light modulators, optical data storage, sensors and numerous spectroscopic techniques. Optical effects, linear and quadratic in external electric and magnetic field are widely known and comprehensively studied. However, optical phenomena that depend on the simultaneous application of external electric and magnetic fields in conventional media are barely detectable and technologically insignificant. Here we report that a large reciprocal magneto-electro-optical effect can be observed in metamaterials. In an artificial chevron nanowire structure fabricated on an elastic nano-membrane, the Lorentz force drives reversible transmission changes on application of a fraction of a volt when the structure is placed in a fraction-of-tesla magnetic field. We show that magneto-electro-optical modulation can be driven to hundreds of thousands of cycles per second promising applications in magneto-electro-optical modulators and field sensors at nano-tesla levels.

[1] Optoelectronics Research Centre and Centre for Photonic Metamaterials, University of Southampton, Highfield, Southampton SO17 1BJ, UK. [2] Physical Sciences Department, DSTL, Salisbury SP4 0JQ, UK. [3] The Photonics Institute and Centre for Disruptive Photonic Technologies, Nanyang Technological University, Singapore 637378, Singapore. Correspondence and requests for materials should be addressed to J.V. (email: jpv1f11@orc.soton.ac.uk) or to E.P. (email: erp@orc.soton.ac.uk) or to N.I.Z. (email: niz@orc.soton.ac.uk).

Dynamic control of metamaterials promises a radical expansion of photonic functionalities. The use of superconductors, phase change and nonlinear media, liquid crystals, carrier injection, graphene and coherent control[1–4] has been reported to achieve tuneable electromagnetic properties. Microwave magnetoelastic metamaterials[5], Terahertz MEMS metamaterials[6–10] and optical reconfigurable metamaterials driven by thermal expansion[11] and Coulomb forces[12] have been realized.

Several phenomena that allow the modulation of optical material properties with external electric or magnetic fields are known. We first recall the well-known linear electro-optical or Pockels effect of changing or inducing birefringence of crystals in the presence of static electric field **E** that is used in numerous light-modulation applications. In terms of the field-induced correction to the dielectric tensor ε_{ij} it may be introduced as $\delta\varepsilon_{ij} = \chi^{(2)}_{ijk}E_k$. Another example is the electro-optical Kerr effect that is normally observed in isotropic liquids and manifests itself as birefringence proportional to the square of applied electric field: $\delta\varepsilon_{ij} = \chi^{(3)}_{ijkl}E_kE_l$. Linear magneto-optical effects, i.e. the optical Faraday effect that induces circular birefringence and dichroism for transmission along a longitudinal magnetic field **H** and the polar, longitudinal and transversal magneto-optical Kerr effects that are usually observed for reflected waves, are well-known and applications include optical isolators and reading magnetically stored information with reflected light, $\delta\varepsilon_{ij} = \chi^{(2)}_{ijk}H_k$ (ref. 13). The quadratic magneto-optical effect of inducing optical birefringence by transverse magnetic field is also well documented and known as the Voigt effect in gases and the Cotton–Mouton effect in solids and liquids, $\delta\varepsilon_{ij} = \chi^{(3)}_{ijkl}H_kH_l$ (refs 14,15). Also known in the literature are phenomena of electro- and magneto-gyration that describe changes of optical activity in chiral media in the presence of electric and magnetic fields[16,17] and a nonreciprocal optical magneto-electric effect, leading to directional birefringence and dichroism[18–22].

Here we report the observation of a magneto-electro-optical effect that manifests itself as strong changes of optical properties of a metamaterial in response to simultaneous application of external electric and magnetic fields and does not depend on reversal of the propagation direction of the wave. It may be described by the following term in the constitutive equation:

$$\delta\varepsilon_{ij} = \chi^{(3)}_{ijkl}E_kH_l$$

Results

Magneto-electro-optical nanowire metamaterial. To create a metamaterial exhibiting strong magneto-electric changes of its optical response, we designed a flexible plasmonic nanostructure that can be reconfigured by the Lorentz force on simultaneous application of external electric **E** and magnetic **H** fields, see Fig. 1. To engage the Lorentz force, we used a continuous conductive chevron nanowire array of length L along which we applied electric voltage V to introduce an electric field $|\mathbf{E}| = V/L$ and a current **I** that is necessary for the appearance of the Lorenz force, $\mathbf{F} = L\mathbf{I} \times \mathbf{H}$. The chevron pattern was chosen as it has good longitudinal elasticity due to its spring-like structure, while providing plasmonic optical resonances, continuous electrical paths that can support currents and simplicity in terms of nanofabrication.

Optical properties of metallic nanostructures, such as the metamaterial investigated here, are determined by the localized plasmonic response of coupled oscillations of conduction electrons and the electromagnetic near field induced by the incident light. The near-field distribution and thus the plasmonic response are highly sensitive to the geometry of the structure. Therefore, changes on the nanometric scale, that are induced by the action of the Lorentz force, can have a strong effect on the nanostructure's optical properties. This is illustrated by Fig. 1b–d using somewhat exaggerated levels of displacement (for clarity): the electric field distribution in the near-field of the structure changes dramatically on out-of-plane movement of every second nanowire of the array.

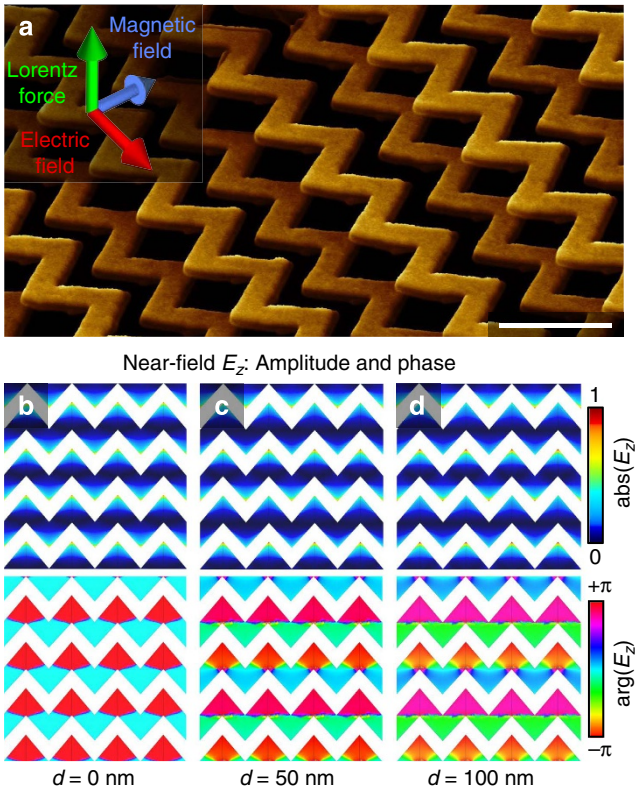

Figure 1 | Lorentz magneto-electro-optical metamaterial. (**a**) Artistic impression of the nanostructure of current-carrying flexible chevron strips that are driven by the Lorentz force. The scale bar, 1 μm. (**b**–**d**) To illustrate reconfiguration-induced changes of the plasmonic response of the nanostructure, we show the magnitude and phase of the near-field E_z perpendicular to the plane of the metamaterial, 10 nm above the chevron strips. This field component is linked to the light-induced oscillating charge separation in the gold layer. The effect of displacing every second nanowire can be seen in both amplitude and phase patterns, most dramatically in the latter: the increasing displacement d from (**b**) 0 to (**c**) 50 and (**d**) 100 nm leads to a growing phase difference between alternating rows. In these field maps, the nanowires are separated by white areas and the first and third complete chevron strips are being displaced. Incident light is at the wavelength of 1,550 nm and linearly polarized with the electric field perpendicular to the nanowires.

The magneto-electro-optical effect appears concurrently with thermally-induced changes of the optical properties that are driven by the release of Joule heat in the nanostructure. This thermo-optic effect appears even in the absence of the external magnetic field and is not sensitive to the current direction. In the first approximation, it is proportional to the power dissipated in the array and thus to $|\mathbf{I}|^2 \sim V^2 \sim |\mathbf{E}|^2$. As the nanowire material used in our experiments was non-magnetic, we observed no optical response on application of the external magnetic field **H** alone.

In our experiments, we targeted the magneto-electro-optical response in the near-infrared part of the spectrum, at telecom frequencies. The metamaterial reported here is an array of

separated gold nanowires of length $L = 35\,\mu m$ manufactured on a 50-nm-thick silicon nitride membrane that was cut into separate elastic chevron strips with 770 nm chevron period (see Methods and Fig. 2). The nanowire strips form a regular grid with pitch of 775 nm. Alternating nanowires were electrically connected to terminals on both ends, so that electric field applied across the metamaterial array induces a current **I** in every second strip. Optical transmission of the metamaterial has plasmonic resonances in the near infrared, see Fig. 2b.

In the presence of external magnetic field **H**, nanowires that bear current are subject to the Lorentz force $\mathbf{F} = L\mathbf{I} \times \mathbf{H}$ that moves them from the plane of the array against the elasticity force to a maximum displacement of few tens of nanometres, see Fig. 2d. In the reconfigurable metamaterial with anchored ends of the strips, the Lorentz force leads to homogeneous displacement at the centre that contributes most to the modulation of optical properties of the metamaterial. This deformation changes the electromagnetic coupling between neighbouring nanowires and thus the plasmonic response of the array at optical frequencies. At zero displacement, symmetry dictates identical light-induced charge oscillations in all chevron strips, see Fig. 1b. With displacement of every second strip, charges in neighbouring strips oscillate with an increasing phase difference and with lower (higher) amplitude in repositioned (stationary) strips, see Fig. 1c,d.

In general, the Lorentz force-induced change of the optical properties has components that are even and odd functions of the nanowire displacement along the z-direction. Indeed, if initially all strips are located in the plane of the membrane, any change of optical properties is insensitive to the direction of displacement z. However, if alternated nanowires are pre-displaced in the z-direction, the change in the optical properties will be sensitive to the direction of displacement z. The out-of-plane motion of every second strip increases the nanostructure's periodicity perpendicular to the strips, so that the metamaterial's unit cell in the dynamic regime is $770 \times 1{,}550$ nm. Strictly speaking, for the metamaterial to be an effective medium film, that is, to transmit and reflect light without scattering, the optical wavelength shall be longer than the unit cell in all directions. Characterization of the sample was performed at the edge of the effective medium regime of the deformed structure at the telecommunications wavelength of 1,550 nm. Therefore, our results shall be interpreted as indication on what changes in permittivity ε of a hypothetical homogeneous medium shall be obtained to reach the same modulation depth as the actual nanostructure.

Experimental characterization of the effect. To detect the magneto-electro-optical effect, we characterized transmission changes of the metamaterial induced by simultaneous application of the electric and magnetic fields. The magneto-electro-optical effect and the thermo-optical effect can be effectively separated by changing the magnetic field strength. Moreover, with a harmonically modulated external electric control signal the thermal

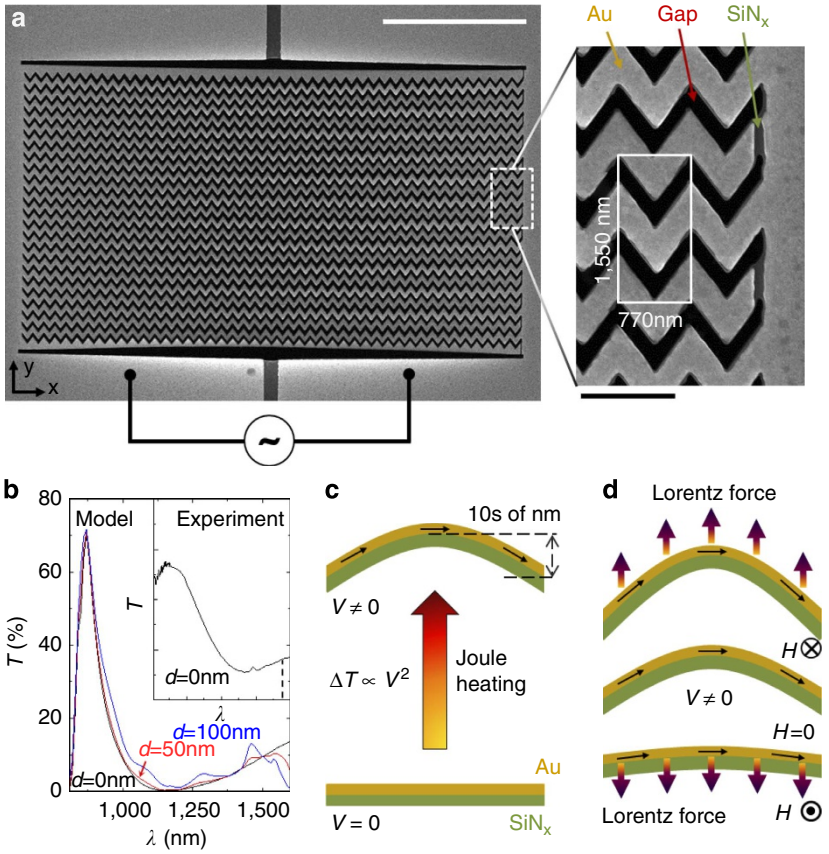

Figure 2 | Lorentz and thermal forces in reconfigurable metamaterial. (**a**) Scanning electron microscopy image showing the metamaterial device with chevron nanowires. The white scale bar, 10 μm, the black scale bar in the inset, 1 μm. (**b**) Transmission T of the nanostructure as a function of wavelength λ for several displacements d. Experimental results and numerical simulations are plotted on identical scales and the wavelength used in the modulation experiments is marked by a dashed line. (**c**) Electro-thermal and elastic forces compete in the bimorph nanowire consisting of gold (yellow) and silicon nitride (green) when an applied voltage V leads to a temperature increase ΔT due to Joule heating. (**d**) Current in a magnetic field **H** produces a Lorentz force competing with the thermal effect.

mechanism will respond at the doubled frequency of modulation due to its quadratic nature. However, the Lorentz mechanism will create a modulated optical response at the control frequency.

Results for non-zero values of the magnetic field strength are presented on Fig. 3. It shows the optical modulation depth recorded at the frequency f for different amplitudes and frequencies of the control signal $V=A\cos(2\pi ft)$. A high-frequency zoom-up displays the resonant feature. Correspondingly, Fig. 4 shows the optical modulation depth as a function of control signal amplitude A and magnetic field $\mathbf{H}$ at characteristic frequencies of modulation.

The results clearly indicate a linear dependence of the sample's transmissivity on the external magnetic and electric fields and this can be described as linear magneto-electro-optical effect $\delta\varepsilon_{yy}=\chi^{(3)}_{yyxy}E_xH_y$. The effect has a clear resonant nature (a peak at about 200 kHz) that is related to the mechanical resonance of the chevron nanowires that are supported at both ends. Off-resonance the effect is weakly dependent on the frequency of modulation. The effect is enabled by the Lorentz force acting against the elasticity of the membrane. Indeed the modulation vanishes at zero magnetic field. Based on the nanostructure's resistance of $R=27\,\Omega$, a voltage of $V=53$ mV leads to $I_s=V/(12R)=160\,\mu$A current in each of the 12 electrically connected strips, corresponding to a maximum Lorentz force of $F_s=LI_s|\mathbf{H}|=640$ pN per strip in our experiments when $|\mathbf{H}|=112$ mT magnetic field is applied. The proportionality of the effect to the driving voltage seen in Fig. 4 is only possible if the 'hot' nanowires bearing the current are pre-displaced from the plane of the membrane. We argue that such displacement results from post-fabrication bow-type deformation of the sample and/or is induced by the Joule heating of the bimorph nanowires.

Indeed, the equilibrium temperature of the heated strips is proportional to power dissipation. The dissipated power at $V=53$ mV is $V^2/R=100\,\mu$W, corresponding to about 40 K temperature increase at current-carrying nanowire centres compared with their ends. Such temperature increase will cause few tens of nanometres static strip displacement due to differential thermal expansion of gold and silicon nitride[23].

In contrast, Fig. 5a shows the optical modulation depth recorded at frequency $2f$ at zero magnetic field $\mathbf{H}$ for different amplitudes A and frequencies f of the control signal V. Correspondingly, Fig. 5b shows the optical modulation depth as a function of control signal amplitude A at characteristic frequencies of modulation. The results show a quadratic dependence of the sample's transmissivity change on the external electric field, which shall be expected for the thermo-optic effect. Similar to the magneto-electro-optical contribution, the effect has a peak at the mechanical resonance of the metamaterial. Off-resonance, the effect progressively rolls off with the frequency of modulation. Indeed, the thermo-optical effect depends on heating and cooling of the nanostructure, which is controlled by conductive heat transport from the nanowires to the surrounding

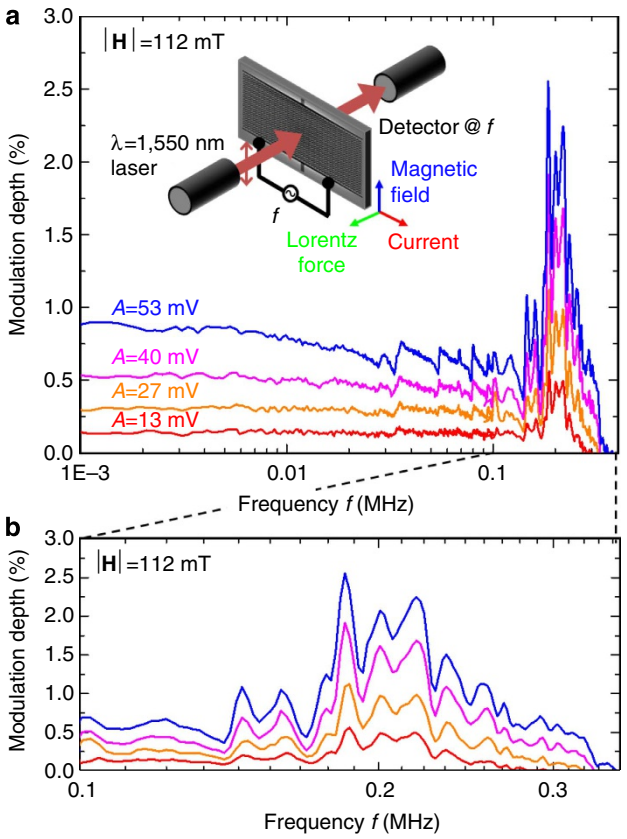

Figure 3 | Magneto-electro-optical modulation. Modulation of transmission with an external electrical control signal of amplitude A at different frequencies f in a static magnetic field $\mathbf{H}$. Transmission modulation is detected at the frequency of electric modulation.

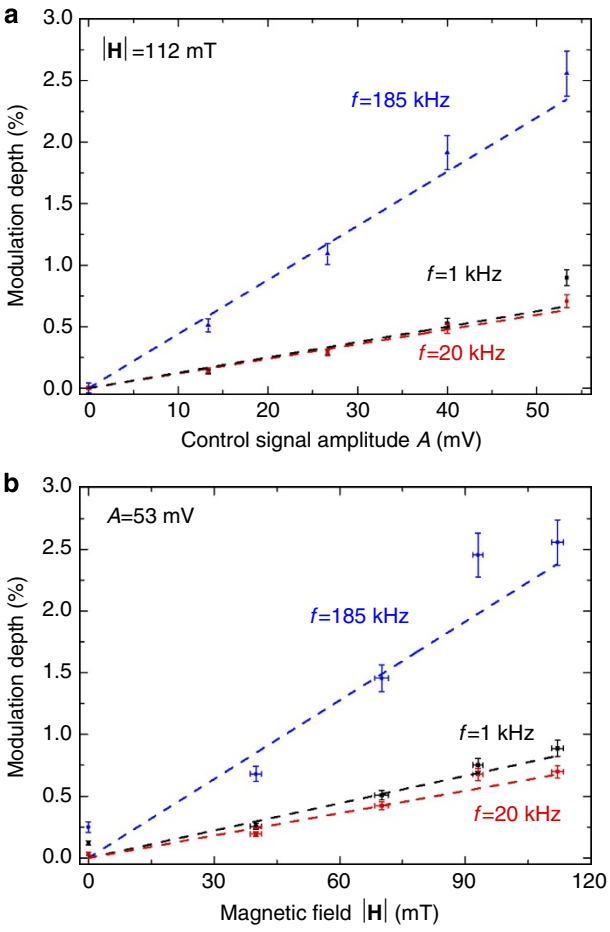

Figure 4 | Magneto-electro-optic effect. Linear relation between transmission change and applied external control signals detected at selected modulation frequencies f. Transmission modulation as a function of (**a**) electric modulation amplitude for a $|\mathbf{H}|=112$ mT static magnetic field and (**b**) magnetic field for a fixed electric modulation amplitude of $A=53$ mV ($|\mathbf{E}|=1.5\,\mathrm{kV\,m^{-1}}$). Error bars show the s.d. and dashed lines are linear fits through the origin.

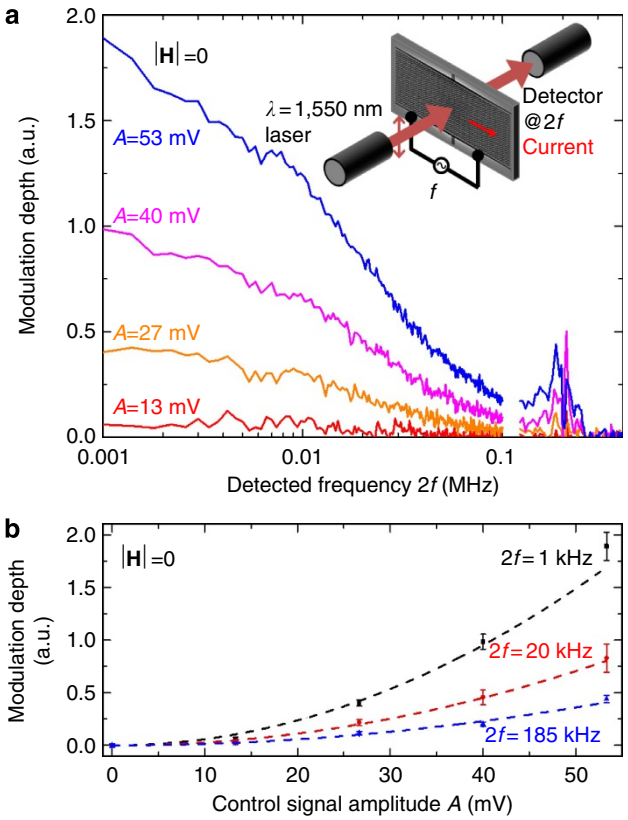

Figure 5 | Thermal modulation. Transmission modulation with an external electrical control signal at different frequencies without magnetic field. Detection at twice the frequency of modulation 2*f*. Modulation depth as a function of (**a**) frequency and (**b**) electrical modulation amplitude. Error bars show the s.d. and dashed lines are quadratic fits through the origin.

membrane and then to the supporting silicon frame. Our calculations starting from the law of heat conduction and published values for the thermal properties of 50-nm-thick films of gold [24] and silicon nitride [25] predict a characteristic roll-off frequency of few tens of kilohertz, which is consistent with the experimentally observed roll-off (Fig. 5).

Discussion

We are not aware of any highly flexible natural media structured on the nanoscale with distinctly anisotropic conductivity that could exhibit a similar magneto-electro-optical effect. Therefore our work is a further illustration of the power of the metamaterial paradigm to create materials with novel properties. In the past this included negative optical magnetism[26], negative refraction[27], asymmetric transmission[28], toroidal resonances[29], as well as extremely high nonlinear[30] and electro-optical coefficients[12]. Here we extend this to the observation of a magneto-electro-optical effect that has never been observed before. We note that Lorentz force based MEMS magnetic field sensors have been reported [31,32], but cannot be approximated as effective media. From our experimental data, we can estimate the order of magnitude of $\chi^{(3)}$ in $\delta\varepsilon_{yy} = \chi^{(3)}_{yyxy} E_x H_y$ as $\chi^{(3)}/n \sim 10^{-4}(\mathrm{m\,V^{-1}T^{-1}})$, where n is the refractive index.

We note that a nonreciprocal optical magneto-electric effect is also known. It results from bi-anisotropic constitutive equations that have terms mixing the polarization (magnetization) of the medium with the magnetic field (electric field) of the wave at optical frequencies, resulting in a dependence of the effect on the propagation direction of the wave[18–22]. The phenomenon observed here is different: in the constitutive equation it results only from the term that describes the change of the dielectric tensor in response to the slowly variable externally applied electric and magnetic fields, which control the deformation of the nanostructure. Such change therefore does not depend on the wave propagation direction, and therefore leads to a reciprocal effect. Control experiments confirm within experimental accuracy that the effect is the same for opposite directions of wave propagation, see Table 1.

Table 1 | Reciprocity of the magneto-electro-optical effect.

Modulation frequency *f* (kHz)	$\frac{\left(\frac{\Delta T}{T}\right)_{SiN} - \left(\frac{\Delta T}{T}\right)_{Au}}{\left(\frac{\Delta T}{T}\right)_{SiN} + \left(\frac{\Delta T}{T}\right)_{Au}}$
1	+0.00 ± 0.07
4	−0.03 ± 0.07
7	−0.04 ± 0.07
10	−0.03 ± 0.07
40	+0.04 ± 0.07
70	−0.01 ± 0.07
100	+0.01 ± 0.07

Difference of the magneto-electro-optical modulation depths $\Delta T/T$ for opposite directions of wave propagation normalized by the magnitude of the effect. Indices SiN and Au mark modulation depths for illumination of the silicon nitride and gold sides of the nanowire metamaterial, which are found to be identical within experimental accuracy. The transmission is modulated with an external electrical control signal of amplitude $A = 53$ mV at different frequencies f in a static magnetic field $|\mathbf{H}| = 130$ mT and detected at the frequency of electric modulation. The magnetic field is directed perpendicular to the chevron nanowires in the metamaterial plane. Incident light is polarized perpendicular to the chevron nanowires at the wavelength of 1,550 nm.

Both lateral uniformity and magnitude of the observed optical effect can be improved by thinning the chevron nanowires at their ends, which will lead to larger and more uniform displacement of the more rigid central part of the pattern, as has been suggested in ref. 33. The use of stronger currents and magnetic fields will lead to stronger Lorentz force and larger displacements of the strips, but the Joule heat dissipation and inelastic deformation of the nanostructure will limit the parameter field in which reversible and reproducible changes and consistent signal modulation can be achieved. The main obstacle in achieving higher modulation depth will be thermal damage to the device that we expect to fail at a few hundred millivolts of driving signal. Displacements and optical modulation can also be increased by using longer nanowires to increase the elasticity of the structure and by using more elastic membranes. A considerable increase in the amplitude of high-frequency resonant responses can be attained by reducing the damping associated with the ambient air in which the nanowires move, thus placing the metamaterial in a vacuum cell will help to increase the *Q*-factor of the response. Furthermore, the design of the plasmonic resonators can be optimized and their spacing reduced to couple them more strongly, increasing the sensitivity of optical properties to nanoscale displacements.

In conclusion, we observe a magneto-electro-optical effect that is driven by the Lorentz force acting on an array of nanowires. Already the effect in the chevron nanowire array can be used for magnetic field-sensing applications, where availability of the second control parameter (the electric field) can be exploited to engage highly sensitive zero balance phase detection techniques to realize sensitivity at nano-Tesla levels. Moreover, we argue that a dedicated optimization of the metamaterial design can lead to the observation of stronger effects suitable for practical application in light-modulation devices.

Methods

Reconfigurable photonic metamaterial fabrication. The reconfigurable nanostructure was fabricated from a 50-nm-thick low stress silicon nitride membrane, which is $500 \times 500\,\mu m^2$ in size and supported by a silicon frame. A 50-nm-thick

gold layer was thermally evaporated onto the membrane and structured with a focused ion beam system (FEI Helios 600 NanoLab), with the contact electrodes connected to a source measurement unit (Keithley 2636) through a vacuum feedthrough for *in situ* electrical characterization. Using focused ion beam milling, the chevron pattern was milled through both gold and silicon nitride layers, creating both the plasmonic resonators and the supporting suspended silicon nitride strips in one step. Then the terminals at the strip ends were electrically separated by removing the gold film in selected areas. The overall size of the metamaterial array is $35 \times 20\,\mu m$.

Experimental and numerical characterization. In the numerical simulations shown in Figs 1b–d and 2b and the optical experiments presented in Figs 2–5, the nanostructure was illuminated from the silicon nitride side with the optical electric field polarized perpendicular to the strips. High-frequency modulation was studied with a 1,550 nm laser transmitted through the nanostructure, while modulating the electric signal applied to the metamaterial using a signal generator and applying static magnetic fields with neodymium magnets. The modulated signal was detected by an InGaAs photodetector (New Focus 1811) and two lock-in amplifiers (Stanford Research SR830 up to 100 kHz and SR844 >100 kHz). The numerical simulations are full three-dimensional Maxwell calculations based on a finite element method solver (Comsol). One unit cell consisting of a chevron pair was modelled with periodic boundary conditions.

References

1. Zheludev, N. I. & Kivshar, Y. S. From metamaterials to metadevices. *Nat. Mater.* **11,** 917–924 (2012).
2. Zhang, J., MacDonald, K. F. & Zheludev, N. I. Controlling light-with-light without nonlinearity. *Light* **1,** e18 (2012).
3. Mousavi, S. A., Plum, E., Shi, J. & Zheludev, N. I. Coherent control of birefringence and optical activity. *Appl. Phys. Lett.* **105,** 011906 (2014).
4. Fang, X. *et al.* Ultrafast all-optical switching via coherent modulation of metamaterial absorption. *Appl. Phys. Lett.* **104,** 141102 (2014).
5. Lapine, M., Shadrivov, I. V., Powell, D. A. & Kivshar, Y. S. Magnetoelastic metamaterials. *Nat. Mater.* **11,** 30–33 (2012).
6. Tao, H. *et al.* Reconfigurable terahertz metamaterials. *Phys. Rev. Lett.* **103,** 147401 (2009).
7. Chicherin, D. *et al.* MEMS-based high-impedance surfaces for millimeter and submillimeter wave applications. *Microw. Opt. Technol. Lett.* **48,** 2570–2573 (2006).
8. Zhu, W. M. *et al.* Switchable magnetic metamaterials using micromachining processes. *Adv. Mater.* **23,** 1792–1796 (2011).
9. Fu, Y. H. *et al.* A micromachined reconfigurable metamaterial via reconfiguration of asymmetric split-ring resonators. *Adv. Funct. Mater.* **21,** 3589–3594 (2011).
10. Zhu, W. M. *et al.* Microelectromechanical Maltese-cross metamaterial with tunable terahertz anisotropy. *Nat. Commun.* **3,** 1274 (2012).
11. Ou, J. Y., Plum, E., Jiang, L. & Zheludev, N. I. Reconfigurable photonic metamaterials. *Nano Lett.* **11,** 2142–2144 (2011).
12. Ou, J. Y., Plum, E., Zhang, J. & Zheludev, N. I. An electromechanically reconfigurable plasmonic metamaterial operating in the near infrared. *Nat. Nanotechnol.* **8,** 252–255 (2013).
13. Višňovský, Š. Magneto-optical effects in crystals at the normal incidence. *Czech. J. Phys. B* **37,** 218–231 (1987).
14. Cotton, A. & Mouton, H. Nouvelle propriete optique (birefringence magnetique) de certains liquids organiques non colloïdaux. *C.R. Acad. Sci.* **145,** 229–230 (1907).
15. Voigt, W. *Magneto- und Elektrooptik* 161–185 (Teubner, 1908).
16. Zheludev, I. S. & Vlokh, O. G. Electro- and magnetogyration. *Proc. Indian Acad. Sci. (Chem. Sci.)* **92,** 421–427 (1983).
17. Vlokh, O. G. & Vlokh, R. O. The electrogyration effect. *Opt. Photon. News* **20,** 34–39 (2009).
18. Markelov, V. A., Novikov, M. & Turkin, A. A. Experimental observation of a new nonreciprocal magneto-optical effect. *JETP Lett.* **25,** 378–380 (1977).
19. Graham, E. & Raab, R. A molecular theory of linear birefringence induced by crossed electric and magnetic fields. *Mol. Phys.* **52,** 1241–1249 (1984).
20. Jung, J. H. *et al.* Optical magnetoelectric effect in the polar GaFeO3 ferrimagnet. *Phys. Rev. Lett.* **93,** 037403 (2004).
21. Kida, N. *et al.* Enhanced optical magnetoelectric effect in a patterned polar ferrimagnet. *Phys. Rev. Lett.* **96,** 167202 (2006).
22. Saito, M., Taniguchi, K. & Arima, T.-H. Gigantic optical magnetoelectric effect in CuB2O4. *J. Phys. Soc. Jpn.* **77,** 013705 (2008).
23. Prasanna, S. & Spearing, S. M. Materials selection and design of microelectrothermal bimaterial actuators. *J. Microelectromech. Syst.* **16,** 248–259 (2007).
24. Chen, G. & Hui, P. Thermal conductivities of evaporated gold films on silicon and glass. *Appl. Phys. Lett.* **74,** 2942–2944 (1999).
25. Queen, D. R. & Hellman, F. Thin film nanocalorimeter for heat capacity measurements of 30 nm films. *Rev. Sci. Instrum.* **80,** 063901 (2009).
26. Linden, S. *et al.* Magnetic response of metamaterials at 100 terahertz. *Science* **306,** 1351–1353 (2004).
27. Shelby, R. A., Smith, D. R. & Schultz, S. Experimental verification of a negative index of refraction. *Science* **292,** 77–79 (2001).
28. Fedotov, V. A. *et al.* Asymmetric propagation of electromagnetic waves through a planar chiral structure. *Phys. Rev. Lett.* **97,** 167401 (2006).
29. Kaelberer, T., Fedotov, V. A., Papasimakis, N., Tsai, D. P. & Zheludev, N. I. Toroidal dipolar response in a metamaterial. *Science* **330,** 1510–1512 (2010).
30. Ren, M. *et al.* Nanostructured plasmonic medium for terahertz bandwidth all-optical switching. *Adv. Mater.* **23,** 5540–5544 (2011).
31. Keplinger, F. *et al.* Lorentz force based magnetic field sensor with optical readout. *Sens. Actuators A* **110,** 112–118 (2004).
32. Wickenden, D. K. *et al.* Micromachined polysilicon resonating xylophone bar magnetometer. *Acta Astronaut.* **52,** 421–425 (2003).
33. Zhang, J., MacDonald, K. F. & Zheludev, N. I. Nonlinear dielectric optomechanical metamaterials. *Light* **2,** e96 (2013).

Acknowledgements

This work is supported by the UK's Defence Science and Technology Laboratory (grant DSTLX1000064081), the US Office of Naval Research (grant N000141110474), the MOE Singapore (grant MOE2011-T3-1-005), the Leverhulme Trust, the Royal Society and the UK's Engineering and Physical Sciences Research Council (grant EP/G060363/1).

Author contributions

The idea of the experiment was conceived by N.I.Z. and E.P.; J.V. manufactured the sample and carried out the measurements; J.-Y.O advised on all experimental procedures; all authors discussed the results and analysed the data; J.V., N.I.Z. and E.P. wrote the paper; N.I.Z. and I.J.Y. supervised the work.

Additional Information

Competing financial interests: The authors declare no competing financial interests.

Reprints and permission information is available online at http://npg.nature.com/reprintsandpermissions/

How to cite this article: Valente, J. *et al.* A magneto-electro-optical effect in a plasmonic nanowire material. *Nat. Commun.* 6:7021 doi: 10.1038/ncomms8021 (2015).

nature COMMUNICATIONS

DOI: 10.1038/ncomms14497 OPEN

Corrigendum: A magneto-electro-optical effect in a plasmonic nanowire material

João Valente, Jun-Yu Ou, Eric Plum, Ian J. Youngs & Nikolay I. Zheludev

Nature Communications 6:7021 doi: 10.1038/ncomms8021 (2015); Published 24 Apr 2015; Updated 7 Feb 2017

APPLIED PHYSICS

Obtaining optical properties on demand

Reconfigurable metamaterials provide a flexible platform for nanophotonic technology

By **Nikolay I. Zheludev**[1,2]

With the developments in nanotechnology that enable atoms, singly or in clumps, to be moved and arranged at will, we now have the capability of creating metamaterials that can display properties not found in naturally occurring media. Today lenses are being developed that image more sharply than glass lenses, and materials can be designed that make objects invisible or bend light beams into any chosen trajectory. We look here at the impact that metamaterials are having on photonics (see the figure).

Despite the achievements so far, photonic metamaterials cannot yet be used for many practical applications because of limitations associated with energy dissipation in the metals used to construct them. Alternatives are being sought in oxides and nitrides (*1*), topological insulators, and two-dimensional materials, which could offer improved plasmonic response, and in high-index dielectrics delivering resonant metamaterial properties with negligible losses (*2*). Planar phase and intensity holograms exploiting metamaterials with spatially variable characteristics may have potential for novel applications (*3*, *4*). Metamaterials with zero dielectric permittivity (*5*) and topologically protected surface modes (*6*) promise new waveguide technologies; metamaterials with tailored hyperbolic dispersion (*7*) can enhance luminescence and improve optical gain. An emerging direction is to use metamaterials for optical computation (*8*) and thermal and radiation management.

The most remarkable recent development in this materials science is that we can now tune and switch metamaterial optical properties (*9*). However, today's challenge is not only to achieve homogeneous change of optical response across the entire volume of the metamaterial, but to develop the "on-demand" control of individual metamolecules in the material. By analogy with electronic random access memory, such structures are called "randomly accessible metamaterials." These metamaterials will not only allow for modulation of light's intensity or phase, but will offer full active control of the wavefront of electromagnetic radiation, tailoring of the near field, and ultimately multichannel data processing. Developing randomly accessible photonic metamaterials is a challenge: The metamolecules would have to be subwavelength optical switches with a physical volume of about 10^{-19} m^3. To have an impact on telecommunications technologies, such switches must also be fast and energy-efficient.

Do we have in sight physical processes that can sufficiently alter the optical properties of individual metamolecules such that they can change the phase and intensity of the transmitted and reflected light? Liquid crystal and digital micromirror spatial light modulators are well known, but they have pixels at least a few micrometers in size, too big for metamaterial applications, and their bandwidth is only a few tens of kilohertz at best, whereas electro-optical crystal modulators are fast but bulky. However, there are emerging technologies that can deliver not only metamolecular-level switching controlled by electric or magnetic signals, but also switching with light. These are nano-optomechanical, phase-change, and coherent control technologies.

Some exceptional opportunities are provided by nano-optomechanics that takes advantage of the changing balance of forces at the nanoscale. At the submicrometer dimensions of the metamolecules, electromagnetic forces compete with elastic forces and can thus be used to reconfigure the shape of individual metamolecules or their mutual arrangement. Structured semiconductor nanomembranes are the ideal platform for such nano-optomechanical reconfigurable metamaterials (*10*). These structures can be driven thermoelastically, electrically, and magnetically. They can also be reconfigured by light-induced forces between elements of illuminated metamolecules. Their nonlinear, switching, electro-optical and magneto-optical characteristics can surpass those of natural media by orders of magnitude. Moreover, the nanoscale metamaterial building

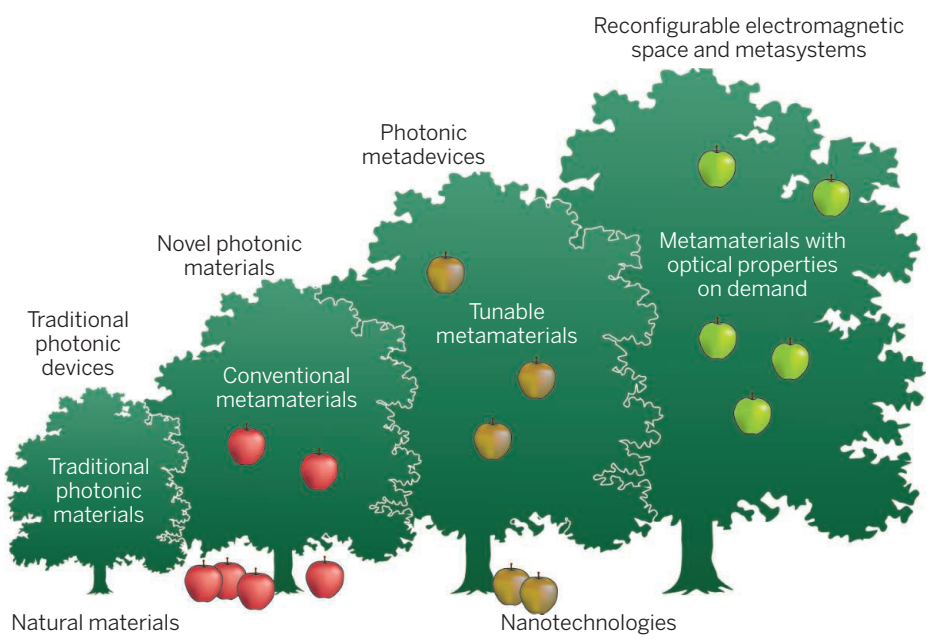

Mighty metamaterials forest. Metamaterials were first developed as artificial media structured on a size scale smaller than the wavelength of external stimuli. They showed novel, now well-understood electromagnetic properties, such as negative index of refraction or optical magnetism, allowing devices such as optical cloaks and superresolution lenses. Tunable, nonlinear, switchable, gain-assisted, sensor, and quantum metamaterials appeared and increased the potential for device integration of metamaterial technology. The coming challenge is to develop metamaterials with on-demand optical properties that may be independently controlled for every individual metamolecule of the nanostructure.

[1]*Centre for Photonic Metamaterials, Optoelectronics Research Center, University of Southampton, Southampton SO17 1BJ, UK.* [2]*Centre for Disruptive Photonic Technologies, The Photonics Institute, Nanyang Technological University, Singapore 637371. E-mail:niz@orc.soton.ac.uk*

ILLUSTRATION: P. HUEY/*SCIENCE*; ADAPTED FROM N. I. ZHELUDEV

blocks can be moved very fast, potentially offering gigahertz bandwidth switching. The first generation of randomly accessible reconfigurable metamaterials or nanomembranes, providing control in a single spatial dimension, have been realized and can function as refocusable lenses or dynamic diffraction gratings.

Phase change is another technology that can work for metamolecular-level switching. Initially developed for rewritable optical discs, it offers a mechanism for nonvolatile switching of optical properties within a nanoscale volume (*11*). This provides a new platform for creating optical components that are written, erased, and rewritten as two-dimensional binary or grayscale patterns into a film of chalcogenide glass using tailored trains of femtosecond pulses. Reconfigurable bichromatic and multifocus Fresnel zone plates, superoscillatory lenses with subwavelength focus, grayscale holograms, and a dielectric metamaterial with on-demand resonances have been demonstrated.

Another emerging technology for controlling and switching the manifestation of optical properties in metamaterials is coherent control. A highly absorbing plasmonic metamaterial film of subwavelength thickness that is placed in the node of a standing wave formed by counterpropagating control and signal waves will see zero electric field and so will not absorb the light. Any change in the phase or intensity of the control wave will distort the standing wave pattern and destroy the regime of zero absorption. This effect can underpin various forms of optical switching (*12*) operating down to the level of a few photons and with a modulation bandwidth up to 100 THz, presenting powerful opportunities for laser spectroscopies, image processing, and data handling in the locally coherent networks that are increasingly part of the mainstream telecommunications agenda. ■

REFERENCES

1. G. V. Naik, V. M. Shalaev, A. Boltasseva, *Adv. Mater.* **25**, 3264 (2013).
2. Y. Yang, I. I. Kravchenko, D. P. Briggs, J. Valentine, *Nat. Commun.* **5**, 5753 (2014).
3. N. Yu, F. Capasso, *Nat. Mater.* **13**, 139 (2014).
4. S. Larouche, Y. J. Tsai, T. Tyler, N. M. Jokerst, D. R. Smith, *Nat. Mater.* **11**, 450 (2012).
5. R. Maas, J. Parsons, N. Engheta, A. Polman, *Nat. Photonics* **7**, 907 (2013).
6. A. B. Khanikaev *et al.*, *Nat. Mater.* **12**, 233 (2013).
7. A. Poddubny, I. Iorsh, P. Belov, Y. Kivshar, *Nat. Photonics* **7**, 948 (2013).
8. A. Silva *et al.*, *Science* **343**, 160 (2014).
9. N. I. Zheludev, Y. S. Kivshar, *Nat. Mater.* **11**, 917 (2012).
10. J. Valente, J. Y. Ou, E. Plum, I. J. Youngs, N. I. Zheludev, *Nat. Commun.* **6**, 7021 (2015).
11. Q. Wang *et al.*, *Appl. Phys. Lett.* **104**, 121105 (2014).
12. X. Fang, K. F. MacDonald, N. I. Zheludev, *Light Sci. Appl.* **4**, e292 (2015).

10.1126/science.aac4360

INFECTIOUS DISEASES

Overcoming neglect of kinetoplastid diseases

Drug development offers hope for controlling diseases that affect millions of people worldwide

By **Graeme Bilbe**

INFECTIOUS DISEASE SERIES

Of the 17 neglected tropical diseases listed by the World Health Organization (WHO) (*1*), three are caused by parasitic kinetoplastid protozoa: human African trypanosomiasis (HAT; also known as sleeping sickness), leishmaniasis, and Chagas disease. The three diseases are responsible for high mortality and morbidity among the world's poorest populations. Although these and other neglected diseases have received increased attention over the past decade, new drugs are still scarce: From 2000 to 2011, only 4% of new drugs and vaccines were registered for neglected diseases (*2*). However, the drug development pipeline, with sustained resources and research efforts, should see the delivery of new drugs for these diseases over the next decade.

KINETOPLASTID DISEASES. Transmitted by insects, these poverty-related infectious diseases are genetically highly diverse. They cause a spectrum of often chronic visceral and disfiguring skin diseases that can be fatal and that exact a high socioeconomic burden on patients and their families. Most cases occur in impoverished countries with poor health resources, but the diseases are also reemerging in Europe and the United States.

HAT is caused by *Trypanosoma brucei* (see the first figure). It is transmitted by the bite of an infected tsetse fly and is fatal without treatment. Active case detection and treatment have led to a fall in the number of cases, currently estimated at 20,000, and sustained efforts are vital to ensure that the WHO's target to eliminate HAT as a public health problem by 2020 is achieved and maintained. The initial hemolymphatic phase of the disease generally goes undiagnosed without active surveillance.

Leishmaniasis is caused by *Leishmania* parasites that are transmitted by phlebotomine sandflies. Visceral leishmaniasis (fatal without treatment) and cutaneous leishmaniasis are the two most common forms of the disease, which is prevalent in 98 countries with 350 million people at risk. Leishmaniasis was long considered not to be a public health threat to high-income countries, but population increases, migration, and climate change may be spreading it, as highlighted by a recent serious outbreak in Madrid, Spain (*3*). Of even greater concern is the change in epidemiology of the more serious visceral form due to the spread of HIV (*4*).

Chagas disease is caused by *T. cruzi* parasites. An estimated 6 million to 7 million people worldwide are infected with the parasite. The disease is endemic in 21 countries of Latin America, where it causes more deaths than malaria, but can remain asymp-

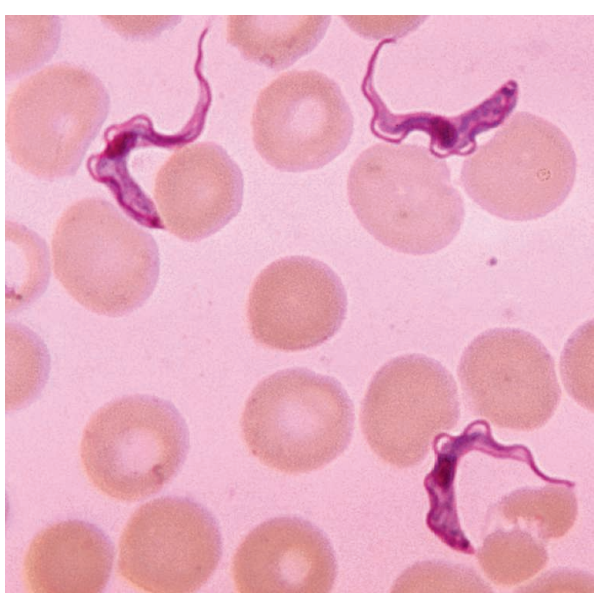

Trypanosoma sp. parasites in blood smear from a patient with African trypanosomiasis. The parasites are about 16 to 42 μm long.

ILLUSTRATION: C. SMITH/*SCIENCE*; IMAGE: CDC/MYRON G. SCHULTZ

Obtaining optical properties on demand

Nikolay I. Zheludev (May 28, 2015)

Science **348** (6238), 973-974. [doi: 10.1126/science.aac4360]

Editor's Summary

Science (print ISSN 0036-8075; online ISSN 1095-9203) is published weekly, except the last week in December, by the American Association for the Advancement of Science, 1200 New York Avenue NW, Washington, DC 20005.

A Flat Lens with Tunable Phase Gradient by Using Random Access Reconfigurable Metamaterial

Weiming Zhu, Qinghua Song, Libin Yan, Wu Zhang, Pin-Chieh Wu, Lip Ket Chin, Hong Cai, Din Ping Tsai, Zhong Xiang Shen, Tian Wei Deng, Sing Kwong Ting, Yuandong Gu, Guo Qiang Lo, Dim Lee Kwong, Zhen Chuan Yang, Ru Huang, Ai-Qun Liu, and Nikolay Zheludev**

The concept of metamaterials, electromagnetic media structured on sub-wavelength scale, has created a platform of new opportunities for manipulating light across the entire electromagnetic spectrum. Metamaterial with manageable dispersion allows access to unusual permittivities and permeabilities, leading to negative index,[1,2] zero epsilon,[3] giant chirality,[4] or exotic and useful hyperbolic dispersion anisotropy.[5] Metamaterials can form "invisible" metallic structures and exhibit extraordinary resonant transparency.[6–9] Controlling boundary conditions with metamaterial offers perfect absorbing media[10,11] and "magnetic" mirrors.[12] Metamaterials are now widely exploited to enhance nonlinear, switching and light emission[13] performance of conventional active materials. Metamaterials allow waveform manipulation[14] and offer exciting opportunities for cloaking,[15,16] waveguiding,[17] and localization of light. Moreover, metamaterials are now used as a platform for exploration and modeling of new physical effects[18,19] and developing practical sensor solutions.[20,21] These thrilling technological prospects have stimulated a wide search for developing metamaterials with tunable and switchable properties using Microelectromechanical Systems (MEMS), phase change media, liquid crystal, magnetic media, and superconductors.[22–26] Efficient modulation of reflection and transmission of metamaterial array in the terahertz and sub-terahertz parts of the spectrum can also be achieved by injecting current into the supporting semiconductor substrate[27] or into a wire loop continuously connecting all metamolecules.[28] In addition, controlling physical shape or mutual position of metamolecules in metamaterial arrays allows for a very efficient tuning of their characteristics, which can now be achieved with megahertz bandwidth in the optical part of the spectrum.[29]

One of the most exciting breakthroughs based on metamaterials is the planar lens. Traditional optical lenses tailor the incident wavefront by accumulating the spatial phase difference induced by their geometries, which are typically difficult to be manufactured, e.g., aberration-free lens. Furthermore, the tunability of traditional lens is limited by the low refractive index contrast and mechanical properties of the transparent materials available in nature. Therefore, compact lens arrays are required for most lens-based devices such as cameras and microscopes, which are difficult to be minimized. Researchers are now exploring planar metamaterials with spatially variable characteristics as diffraction grating[30–32] and for focusing.[33–35] The planar metamaterial lenses tailor the wavefront by spatial phase gradient induced by the predesigned metamolecules, which cannot be tuned once fabricated. The ability to control resonant properties of every individual metamolecule in a planar metamaterial will offer an ultimate freedom for dynamically shaping wavefronts via reconfigurable spatial phase gradient, which is essential for applications such as tunable flat lenses, dynamic holograms, spatial intensity, and phase modulators with sub-wavelength pixilation. However, metamolecules in a planar array are difficult to be individually tuned using current techniques based on integrating lump active elements in the metamolecules (transistors or diodes), current injection, or suppression of superconductivity. Those methods depend for modulation on undesirable Joule losses[36,37] and require a network of wires, individual electrical connections to all metamolecules,

Dr. W. M. Zhu, L. B. Yan, Dr. W. Zhang, Dr. P. C. Wu, Dr. L. K. Chin, Prof. Z. X. Shen, Prof. A. Q. Liu
School of Electrical and Electronic Engineering
Nanyang Technological University
Singapore 639798
E-mail: eaqliu@ntu.edu.sg

Q. H. Song
Université Paris-Est
UPEM, Marne-la-Vallée
Paris F-77454, France

Dr. H. Cai, Dr. Y. D. Gu, Dr. G. Q. Lo, Dr. D. L. Kwong
Institute of Microelectronics
A*STAR
Singapore 117686

Prof. D. P. Tsai
Department of Physics
National Taiwan University
Taipei 10617, Taiwan

Dr. T. W. Deng, S. K. Ting
Temasek Laboratories
5A Engineering Drive 1
Singapore 117411

Prof. Z. C. Yang, Prof. R. Huang
Institute of Microelectronics
Peking University
Beijing 100871, China

Prof. N. I. Zheludev
Optoelectronics Research Centre
Southampton SO17 1BJ, UK
E-mail: nzheludev@ntu.edu.sg

Prof. N. I. Zheludev
Centre for Disruptive Photonic Technologies
School of Physical and Mathematical Sciences
Nanyang Technological University
Singapore 637371

DOI: 10.1002/adma.201501943

which will inevitably interfere and could spoil electromagnetic resonant properties of the metamaterial.

Here we report for the first time a proof-of-principle demonstration of a planar metamaterial where resonant properties of every individual metamolecule can be continuously controlled at will, which is called a random access reconfigurable metamaterial (RARM). RARMs are passive structures that are designed to control wavefront of external source of radiation. They shall be distinguished from phased antenna arrays that are active structures, shaping radiated pattern by controlling phase and intensity characteristics of every emitter through a complex feed arrangement. Using the developed RARM, we also provide the first demonstration of a metamaterial lens that is tunable in focal distance at will. To achieve RARM, we have created an array of cavities that can be filled with liquid metal[38–41] in a controllable fashion[42] using microfluidic technology and pneumatic valves. A microfluidic network addressing every individual element of the array provides the mechanism to dynamically change the filling factor of resonators and thus their resonant electromagnetic properties at will, continuously and with random access. Such individually addressable cavities of sub-wavelength size form a metamaterial array of sub-wavelength resonators where modulation of transmitted wavefront is achieved practically without Joule losses[43] via changing the spatial phase gradient of the array. Our metamaterial does not have massive moving parts characteristic to comb-driven MEMS metamaterial[44] while by using pneumatic valves the proposed solution minimizes the network of conductive elements that could disturb electromagnetic properties of the array and can be used with metamolecules of broad variety of shapes, from simple antennas to complex connected and disconnected 3D structures. Our proof-of-principle demonstration is based on microfluidic elements allowing RARMs operating in microwave regime. However, with recent progress in nanofluidics (for instance, the flow of liquids through carbon nanotubes is being investigated[45] one can envisage a realization of nanocapillary RARM that could translate the concept into higher frequencies, including the optical range.

The metamaterial reported here consists of a 2D square array of metallic split rings and two perpendicularly placed metal gratings (**Figure 1**a). The metal gratings consist of 1 mm wide copper wires with period spacing of 2.5 mm, which is fabricated on 0.635 mm thick Taconic substrate (TLY-5-520, ε_r = 2.2). The split ring element has a radius of 2 mm in a 60 × 60 lattice with periodic spacing of 5 mm, which has a total footprint of 300 mm. It is designed to operate in the GHz range from 12 to 18 GHz (Ku band). The split ring metamolecules are formed by filling liquid mercury into the ring-shaped microcavities. If completely filled with mercury the ring metamolecule exhibits a dipole absorption resonance at the wavelength linked to the half-length of the ring. The resonance wavelength can be progressively reduced if a section of the ring is removed by introducing a gap into the ring. This can simply be achieved by substituting the liquid metal in the cavity with a gas bubble. To create and control the gaps of the rings individually, they are connected by microchannels to pneumatic valves, which regulate air pressure in the channels. By increasing the pressure in the channel, air pushes mercury away from the ring cavity, substituting it with an air bubble (Figure 1b-c). The process can be made continuous and fully reversible by changing the balance of air and mercury pressures. Here mercury is chosen for its low melting point (–38.8 °C) and high electrical conductivity (1.04×10^6 S m^{-1}), which is only one order of magnitude lower than that of copper (5.96×10^7 S m^{-1}). The metamaterial is supported on a polymethyl methacrylate (PMMA, ε_r = 2.57) substrate of 1 mm thickness while the architecture of microchannels and cavities is imbedded into a polydimethylsiloxane (PDMS, ε_r = 2.69) layered structure of 2 mm thickness. Ring cavities are located in the layer bonded with the PMMA substrate that also hosts mercury filling channels. Narrow air channels directed across the rings connect each cavity with the vertical air loading channels that are linked to the pattern of pneumatic valves and air inlet in the layers above. The control system is fabricated within a PDMS layered structure of 1 mm thick. In the heart of the air control system is a purposely designed ternary valve multiplexer, addressing metamolecules in the array individually (see details in the Supporting Information, Figure S2). The metamolecules are different row by row along the *x*-direction, which creates a 1D spatial phase distribution.

Here, we illustrate the opportunities provided by the flexibility of random access metamaterial by functionalizing it into a tunable flat lens (**Figure 2**). The microfluidic layer with liquid metal rings functions as a polarization converter of the linear polarized excitations as the slope angles between the symmetric axes of the rings and the incident electric field are

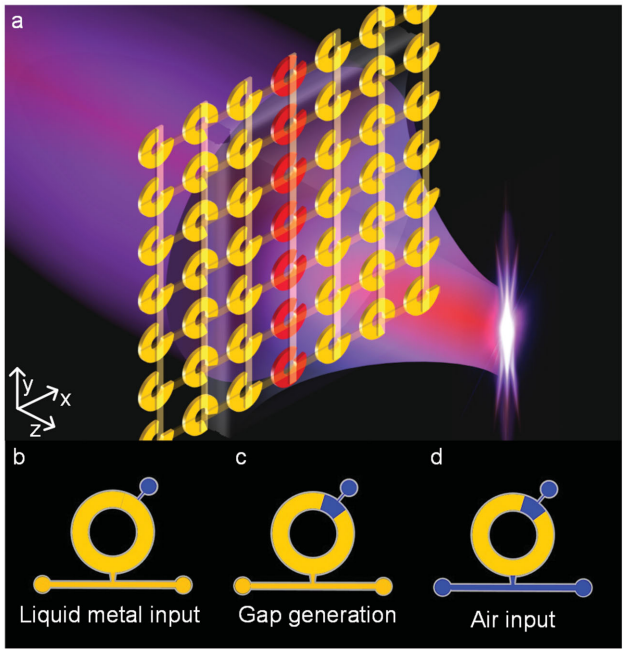

Figure 1. Schematic of tunable flat lens. a) The randomly addressable metamaterial can be used as a flat lens with tunable focal distance when resonant properties of a split ring in the array are altered by changing the metal filling fraction. The RARM is formed by loading liquid metal into the ring microcavities fabricated in transparent dielectric. b) The liquid metal (light grey) is injected into the microchannels and filled in the wide channels with controlled pressure. c) The gap is defined by regulating air pressure in the pneumatic valves, injecting air (dark grey) from the narrow channels. d) The extra liquid metal in the wide channel are expelled by air.

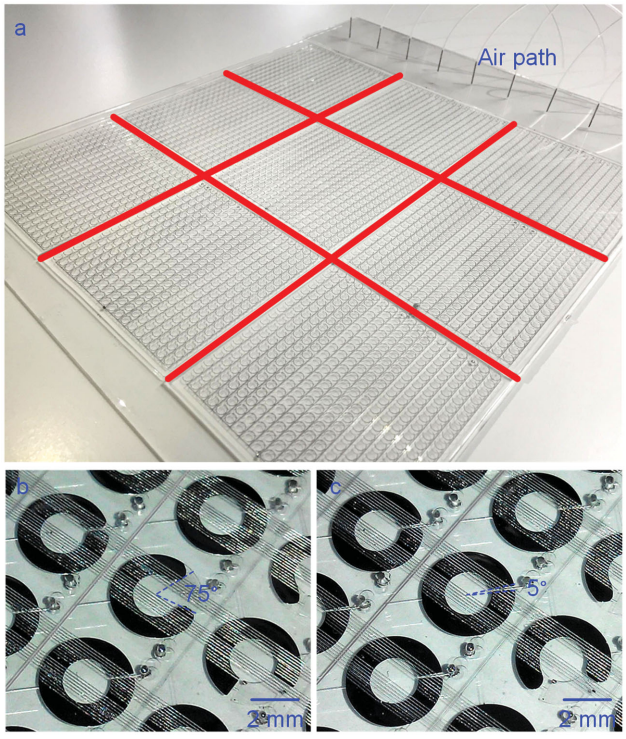

Figure 2. Photographs of the flat lens. a) An overview photograph of the flat lens, which consists of a 60 × 60 square array of SRRs partially filled with the liquid metal, microchannels pneumatic array, and a ternary valve multiplexer addressing metamolecules in the array individually at will. The flat lens is divided into nine independently controlled SRR arrays, which are highlighted with the red line. b) Zoomed-in view of one single pneumatic valve when air pushes mercury away from the cavity void forming the air gap of approximately 75°. c) The gap of the SRR restored to 5° when air pressure in reduced. The gaps of the cavity can be continuously tuned by changing the pressure of the pneumatic valves. The small channels on the top of the cavities are the air channels.

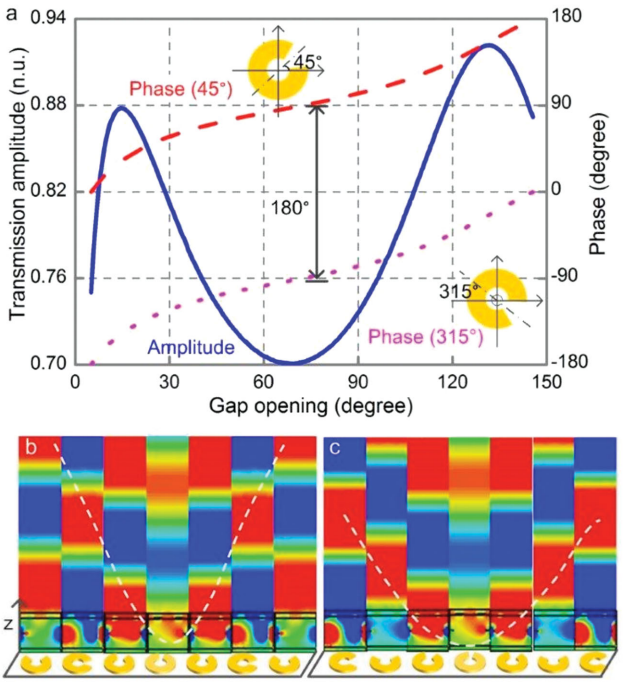

Figure 3. Simulation on the transmission amplitude and phase as the function of the gap openings. a) Simulation results of the transmission amplitude and phase as functions of the gap openings and orientations of the metamolecules. The incidence is linear polarized with the electric field along *y*-direction. b,c) Phase profile of different metamolecules arrayed with the period of 5 mm, which shows the feasibility of tuning the wavefront by controlling the SRRs.

either 45° or 315°. The two metal gratings enhance the cross-polarization transmission due to the Fabry–Pérot resonance.[46] The phase and amplitude modulations of the transmitted electromagnetic wave are highly depending on the gap opening of the metamolecules. **Figure 3**a shows the phase and amplitude of the cross-polarized transmission as functions of the gap openings and orientations of the symmetric axes. Here, the incident electric field is along the *y*-direction with the frequency of 16 GHz. The metamolecules with different gap openings are numerically characterized under periodic boundary conditions. The transmission phase can be tuned continuously with 2-π range while maintaining the normalized amplitude larger than 0.7. Figure 3b,c shows the phase profile when the incident wave passed through each metamolecule. Here, the wavefront can be tailored via changing the gap opening and orientations of the metamolecules individually. For the purpose of demonstrating a convex lensing function, the incident wave frequency was chosen at 16 GHz.

Experimental results of electromagnetic wave focusing with RARM are presented in **Figure 4**. Here the metamaterial is illuminated by a plane wave that propagates along *z*-direction, normal to the plane of the metamolecules array and is polarized along the *y*-direction. All measurements are performed in a microwave anechoic chamber using a vector network analyzer with horn antenna as the wave source and a monopole antenna mounted on an *xy* scanner as a probe. To map the transmitted field, the receiving probe is scanned at different *z* distances from the sample with steps of 5 mm. During the experiment, the air inlets are sealed using the microplugs for the sake of the stability and safety issues. The experimental results and the corresponding simulation results of different phase gradient distributions are shown in Figure 4a–c, when the designed focal length is 5λ, 10λ, and 15λ, respectively. The 3D full Maxwell numerical modeling of the electric field intensity distributions at *xz* plane are shown in the first column to compare with the experimental results of *xz* plane and *xy* plane in the second and third columns, respectively. The simulation is done by using Computer Simulation Technology (CST) microwave studio with the periodic boundary along *y*-direction and open boundary along *x*- and *z*-directions. The diffraction efficiency η of the flat lens is defined as $\eta = P_f/P_i$, where P_f and P_i are the total optical power measured at the hotspots and total input power measured without the sample, respectively. In the experiment, the measured diffraction efficiency is approximately 10%, which is much larger than most flat lens design.[33] The diffraction efficiency can be further increased by maintaining the transmission coefficient during the gap tuning, which can be realized by the optimization of the cavities. The corresponding spatial phase distributions are shown in the fourth column, which are

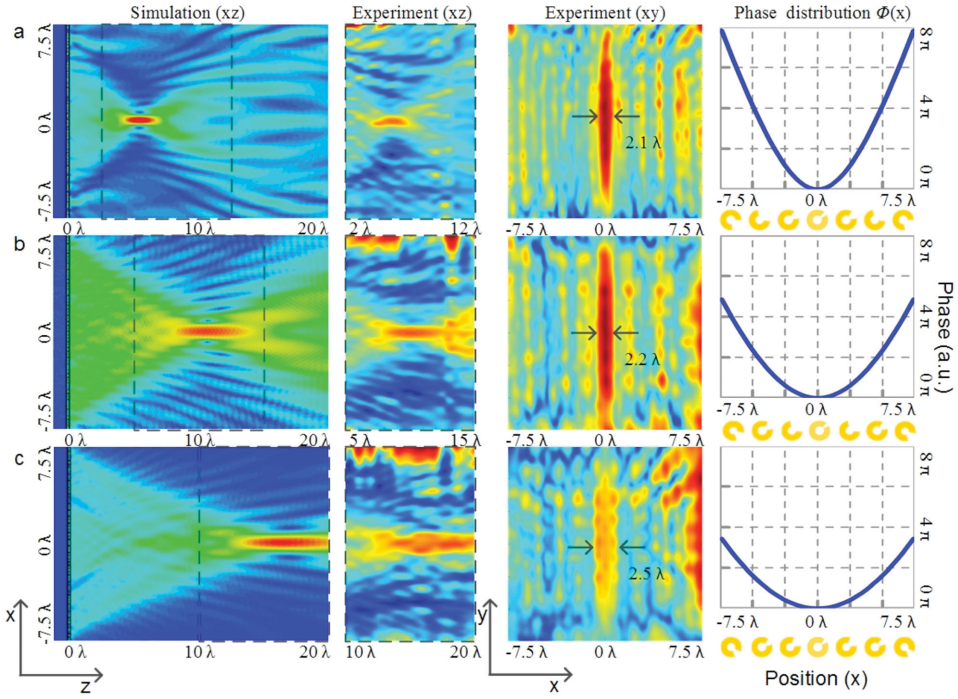

Figure 4. The tuning of the RARM lens hotspot when the spatial phase distribution is changed. Panels a–c) show the experimental results and the corresponding simulation results of different phase gradient distributions when the designed focal length is 5λ, 10λ, and 15λ, respectively. The 3D full Maxwell numerical modeling of the electric field intensity distributions at *xz* plane are shown in the first column to compare with the experimental results of *xz* plane and *xy* plane in the second and third columns, respectively. The corresponding spatial phase distributions are shown in the fourth column, which are obtained by hyperbolic lens equation. The schematics of the corresponding SRR arrays are shown in the insets. The incident 16 GHz wave is linear polarized with the electric field along *y*-direction and propagation direction along *z*-direction (perpendicular to the surface of the flat lens).

obtained by hyperbolic lens equation. The *xz* and *xy* cross-sections illustrate that the beam can be confined into an intensity linear hotspot with FWHM = 2.1λ when the measured focal length F = 5.1λ. Figure 4a–c shows that the focal length F can be tuned from 5.1λ to 15.2λ by adjusting the spatial phase gradient. Here, the focal length is defined as the distance between the central of the hotspot and the surface of the flat lens. The measured focal lengths agree with the 3D simulation well as shown in Figure 4.

In conclusion, a RARM formed by casting liquid metal microwave resonators through microfluidic channels is demonstrated to have function as reconfigurable wavefront manipulation, which has been illustrated by showing a tunable flat lens. The RARM can be used as densely integrated tunable lens array, which has potential applications in high resolution display, sensor, and imaging systems. We expect that in the future RARM will be developed for the entire electromagnetic spectral range up to optical frequencies. This will make possible various applications such as 3D holographic displays for mobile phones, high-performance devices for space division multiplexing in the next generation telecommunication networks, and adaptive wavefront correction devices, to name just a few.

Supporting Information

Supporting Information is available from the Wiley Online Library or from the author.

Acknowledgements

The work is mainly supported by the Singapore National Research Foundation under its Environmental & Water Technologies Strategic Research Programme (Grant No. 1102-IRIS-05) and administered by the Environment & Water Industry Programme Office (EWI) of the PUB; Singapore Ministry of Education (MOE) (Grant No. MOE2011-T3-1-005 and RG 89/13) and EPSRC (UK) Programme on Nanostructured Photonic Metamaterials and National Science Council of Taiwan (Grant Nos. NSC 101-2811-P-002-004 and NSC 102-2745-M-002-005-ASP).
Note: The author first names were missing from the author byline on initial online publication; these were added on August 20, 2015; Figure 1 and 3 were also reset.

Received: April 23, 2015
Revised: June 3, 2015
Published online: July 16, 2015

[1] D. R. Smith, J. B. Pendry, M. C. K. Wiltshire, *Science* **2004**, *305*, 847.
[2] T. Xu, M. Abashin, A. Agrawal, K. J. Chau, H. J. Lezec, *Nature* **2013**, *497*, 470.
[3] M. Silveirinha, N. Engheta, *Phys. Rev. Lett.* **2006**, *97*, 157403.
[4] A. V. Rogacheva, V. A. Fedotov, A. S. Schwanecke, N. I. Zheludev, *Phys. Rev. Lett.* **2006**, *97*, 177401.
[5] J. Elser, R. Wangberg, V. A. Podolskiy, E. E. Narimanov, *Appl. Phys. Lett.* **2006**, *89*, 261102.
[6] A. Alu, N. Engheta, *Phys. Rev. E* **2005**, *72*, 016623.
[7] V. A. Fedotov, M. Rose, S. L. Prosvirnin, N. Papasimakis, N. I. Zheludev, *Phys. Rev. Lett.* **2007**, *99*, 147401.

[8] N. Papasimakis, V. A. Fedotov, N. I. Zheludev, *Phys. Rev. Lett.* **2008**, *101*, 253903.
[9] N. Liu, L. Langguth, T. Weiss, J. Kastel, M. Fleishhauer, T. Pfau, H. Giessen, *Nat. Mater.* **2009**, *8*, 758.
[10] V. A. Fedotov, P. L. Mladyonov, S. L. Prosvirnin, N. I. Zheludev, *Phys. Rev. E* **2005**, *72*, 056613.
[11] N. I. Landy, S. Sajuyigbe, J. J. Mock, D. R. Smith, W. J. Padilla, *Phys. Rev. Lett.* **2008**, *100*, 207402.
[12] V. A. Fedotov, A. V. Rogacheva, N. I. Zheludev, P. L. Mladyonov, S. L. Prosvirnin, *Appl. Phys. Lett.* **2006**, *88*, 091119.
[13] O. Hess, J. B. Pendry, S. A. Maier, R. F. Oulton, J. M. Hamm, K. L. Tsakmakidis, *Nat. Mater.* **2012**, *11*, 573.
[14] N. Yu, P. Genevet, F. Aieta, M. A. Kats, R. Blanchard, G. Aoust, J. P. Tetienne, Z. Gaburro, F. Capasso, *IEEE J. Sel. Top. Quant. Electron.* **2013**, *19*, 4700423.
[15] D. Schurig, J. J. Mock, B. J. Justice, S. A. Cummer, J. B. Pendry, A. F. Starr, D. R. Smith, *Science* **2006**, *314*, 977.
[16] P. Y. Chen, J. Soric, A. Alu, *Adv. Mater.* **2012**, *24*, OP281.
[17] K. L. Tsakmakidis, A. D. Boardman, O. Hess, *Nature* **2007**, *450*, 397.
[18] T. Kaelberer, V. A. Fedotov, N. Papasimakis, D. P. Tsai, N. I. Zheludev, *Science* **2010**, *330*, 1510.
[19] A. G. Dentcho, S. Zhang, X. Zhang, *Nat. Phys.* **2009**, *5*, 687.
[20] N. Liu, M. Mesch, T. Weiss, M. Hentschel, H. Giessen, *Nano Lett.* **2010**, *10*, 2342.
[21] B. Gallinet, T. Siegfried, H. Sigg, P. Nordlander, O. J. F. Martin, *Nano Lett.* **2013**, *13*, 497.
[22] W. M. Zhu, A. Q. Liu, X. M. Zhang, D. P. Tsai, T. Bourouina, J. H. Teng, X. H. Zhang, H. C. Guo, H. Tanoto, T. Mei, G. Q. Lo, D. L. Kwong, *Adv. Mater.* **2011**, *23*, 1792.
[23] A. Q. Liu, W. M. Zhu, D. P. Tsai, N. I. Zheludev, *J. Opt.* **2012**, *14*, 114009.
[24] W. M. Zhu, A. Q. Liu, T. Bourouina, D. P. Tsai, J. H. Teng, X. H. Zhang, G. Q. Lo, D. L. Kwong, N. I. Zheludev, *Nat. Commun.* **2012**, *3*, 1274.
[25] N. I. Zheludev, Y. S. Kivshar, *Nat. Mater.* **2012**, *11*, 917.
[26] A. D. Boardman, *Laser Photon. Rev.* **2011**, *5*, 287.
[27] H. T. Chen, W. J. Padilla, J. M. O. Zide, A. C. Gossard, A. J. Taylor, R. D. Averitt, *Nature* **2006**, *444*, 597.
[28] V. Savinov, V. A. Fedotov, S. M. Anlage, P. A. J. Groot, N. I. Zheludev, *Phys. Rev. Lett.* **2012**, *109*, 243904.
[29] J. Y. Ou, E. Plum, J. Zhang, N. I. Zheludev, *Nat. Nanotech.* **2013**, *8*, 252.
[30] N. Yu, P. Genevet, M. A. Kats, F. Aieta, J. P. Tetienne, F. Capasso, Z. Gaburro, *Science* **2011**, *334*, 333.
[31] A. V. Kildishev, A. Boltasseva, V. M. Shalaev, *Science* **2013**, *339*, 6125.
[32] S. Sun, K. Y. Yang, C. Wang, T. Juan, W. T. Chen, C. Y. Liao, Q. He, S. Xiao, W. T. Kung, G. Guo, L. Zhou, D. P. Tsai, *Nano Lett.* **2012**, *12*, 6223.
[33] F. Aieta, P. Genevet, M. A. Kats, N. Yu, R. Blanchard, Z. Gaburro, F. Capasso, *Nano Lett.* **2012**, *12*, 4932.
[34] R. Yang, W. Tang, Y. Hao, *Opt. Express* **2011**, *19*, 12348.
[35] T. Roy, E. T. F. Rogers, N. I. Zheludev, *Opt. Express* **2013**, *21*, 7577.
[36] W. L. Chan, H. T. Chen, A. J. Taylor, I. Brener, M. J. Chich, D. M. A. Mittleman, *Appl. Phys. Lett.* **2009**, *94*, 213511.
[37] Z. W. Xie, X. K. Wang, J. S. Ye, S. F. Feng, W. F. Sun, T. Akalin, Y. Zhang, *Sci. Rep.* **2013**, *3*, 3347.
[38] T. S. Kasirga, Y. N. Ertas, M. Bayindir, *Appl. Phys. Lett.* **2009**, *95*, 214102.
[39] A. V. Krasavin, N. I. Zheludev, *Appl. Phys. Lett.* **2004**, *84*, 1416.
[40] J. Q. Wang, S. C. Liu, Z. V. Vardeny, A. Nahata, *Opt. Express* **2012**, *20*, 2346.
[41] S. R. C. Vivekchand, C. J. Engel, S. M. Lubin, M. G. Blaber, W. Zhou, J. Yong Suh, G. C. Schatz, T. W. Odom, *Nano Lett.* **2012**, *12*, 4324.
[42] T. Thorsen, S. J. Maerkl, S. R. Quake, *Science* **2002**, *298*, 580.
[43] O. Hess, K. L. Tsakmakidis, *Science* **2013**, *339*, 654.
[44] W. Zhang, W. M. Zhu, E. P. Li, H. Tanoto, Q. Y. Wu, J. H. Teng, X. H. Zhang, J. M. Tsai, G. Q. Lo, D. L. Kwong, A. Q. Liu, *Appl. Phys. Lett.* **2012**, *101*, 151902.
[45] A. Noya, H. G. Parka, F. Fornasieroa, J. K. Holta, C. P. Grigoropoulosb, O. Bakajina, *Nano Today* **2007**, *2*, 22.
[46] N. K. Grady, J. E. Heyes, D. R. Chowdhury, Y. Zeng, M. T. Reiten, A. K. Azad, A. J. Taylor, D. A. R. Dalvit, H. Chen, *Science* **2013**, *14*, 1304.

Random access actuation of nanowire grid metamaterial

2016 Nanotechnology 27 485206

(http://iopscience.iop.org/0957-4484/27/48/485206)

OPEN ACCESS
IOP Publishing
Nanotechnology

Nanotechnology **27** (2016) 485206 (6pp)
doi:10.1088/0957-4484/27/48/485206

Random access actuation of nanowire grid metamaterial

Pablo Cencillo-Abad[1], Jun-Yu Ou[1], Eric Plum[1,3], João Valente[1,4] and Nikolay I Zheludev[1,2,3,5]

[1] Optoelectronics Research Centre and Centre for Photonic Metamaterials, University of Southampton, Highfield, Southampton, SO17 1BJ, UK
[2] Centre for Disruptive Photonic Technologies, School of Physical and Mathematical Sciences and The Photonics Institute, Nanyang Technological University, Singapore 637371, Singapore

E-mail: erp@orc.soton.ac.uk and niz@orc.soton.ac.uk

Received 26 August 2016, revised 10 October 2016
Accepted for publication 12 October 2016
Published 4 November 2016

Abstract

While metamaterials offer engineered static optical properties, future artificial media with dynamic random-access control over shape and position of meta-molecules will provide arbitrary control of light propagation. The simplest example of such a reconfigurable metamaterial is a nanowire grid metasurface with subwavelength wire spacing. Recently we demonstrated computationally that such a metadevice with individually controlled wire positions could be used as dynamic diffraction grating, beam steering module and tunable focusing element. Here we report on the nanomembrane realization of such a nanowire grid metasurface constructed from individually addressable plasmonic chevron nanowires with a 230 nm $\times$ 100 nm cross-section, which consist of gold and silicon nitride. The active structure of the metadevice consists of 15 nanowires each 18 μm long and is fabricated by a combination of electron beam lithography and ion beam milling. It is packaged as a microchip device where the nanowires can be individually actuated by control currents via differential thermal expansion.

S Online supplementary data available from stacks.iop.org/nano/27/485206/mmedia

Keywords: reconfigurable metamaterial, nanowire, metadevice, nanoelectromechanical system

(Some figures may appear in colour only in the online journal)

Full active control over diffraction and focusing of light, beam steering and video holography require dynamic control over amplitude and phase of light with sub-wavelength resolution, i.e. a device where optical properties of points spaced by less than the wavelength of operation can be controlled independently. However, sub-wavelength pixelation is out of reach for established spatial light modulator technologies based on digital micromirrors or liquid crystal cells that have a characteristic size of 10 μm [1–3] as well as deformable mirrors that have a typical actuator pitch of hundreds of microns. Opportunities for fast dynamic control over light with much higher resolution are now emerging in metamaterials, i.e. media that obtain enhanced or unusual optical properties from structuring with characteristic dimensions that are smaller than their wavelength range of operation. Approaches to achieving dynamic control over metamaterial properties can be grouped into three categories. (i) All-optical control over the light–matter interaction using multiple coherent light waves [4, 5], (ii) modification of the materials making up the metamaterial nanostructure, e.g. based on optical nonlinearities [6, 7], phase transitions [8] or electronic doping [9], and (iii) spatial rearrangement of

[3] Author to whom any correspondence should be addressed
[4] Present address: Department of Electronic & Electrical Engineering, University College London, Torrington Place, London, WC1E 7JE, UK.
[5] Homepage: http://www.nanophotonics.org.uk.

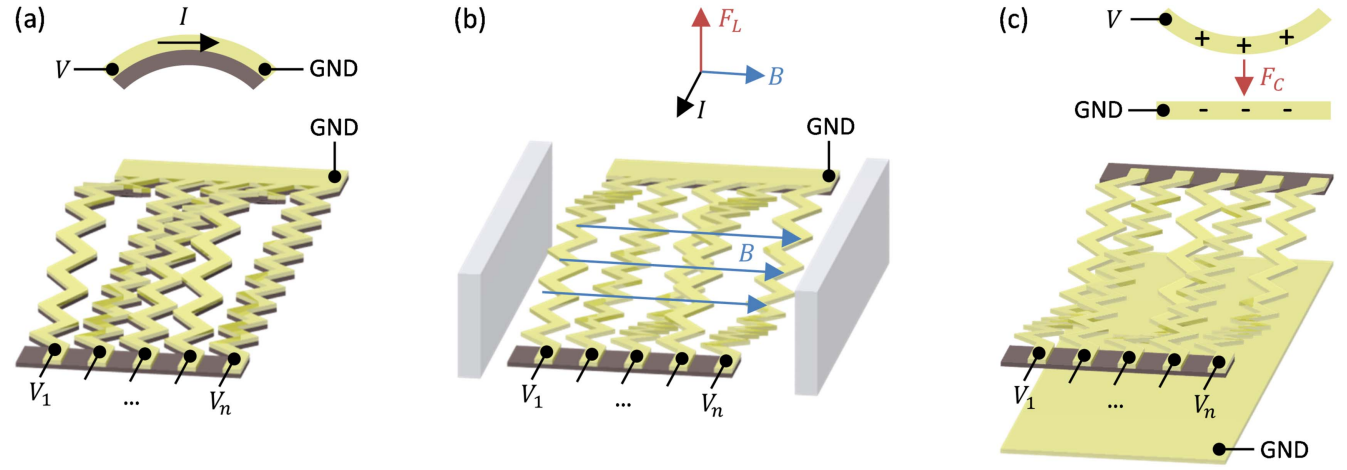

Figure 1. Random-access electrical actuation of reconfigurable nanowire metamaterials. (a) Electrothermal actuation, which is employed here, exploits differential thermal expansion of materials with different thermal expansion coefficients in response to resistive heating by a current I to displace a nanowire. (b) Magnetic actuation uses the Lorentz force F_L on moving charges to actuate a current-carrying metamaterial strip placed in an external magnetic field B. (c) Electrostatic actuation is driven by the Coulomb force F_C between charged nanowires or between a nanowire and a ground plane (GND). V_i indicate nanowire actuation voltages in all cases.

the metamaterial components [10–15]. However, dynamic control over metamaterial properties with sub-wavelength resolution remains a challenge. Spatial resolution of all-optical approaches involving coherent light–matter interactions, optical nonlinearities or phase transitions is limited by the ability to focus light, in contrast, this limitation is avoided by nanoelectromechanically actuated metamaterials, whose pixelation is determined by nanofabrication technology rather than light. It has been predicted that selective actuation of nanowires in nanowire grid metamaterials would enable spatial phase and intensity modulation with one-dimensional sub-wavelength pixelation providing focusing, diffraction and beam steering functionalities on demand [16, 17]. We refer to such metamaterials that allow selective control of each individual element as random access metamaterials.

Here we report the nanofabrication of a random access metadevice consisting of individually addressable plasmonic nanowire actuators. The nanowires are arranged in a grid, forming a metamaterial with a chevron-shaped unit cell. We demonstrate selective electrical actuation of individual nanowires, which allows the metamaterial nanostructure to be controlled with 620 nm pixelation in one dimension.

Reconfigurable metamaterials [14, 18–21] and similar optomechanical nanostructures [22–25] operating in the visible to near infrared part of the spectrum have been developed based on dielectric membranes of nanoscale thickness. Such membranes serve as a flexible support for a plasmonic metal or high index dielectric thin film, which can be structured by standard nanofabrication processes to create metamaterial nanostructures and actuators. Electrical actuation is most easily achieved by cutting a membrane with an electrically conductive layer into freestanding metamaterial strips. Deformation of such nanowires with microsecond scale response times can then be driven by Coulomb or Lorentz forces, or resistive heating, resulting in very large electro-optical and magneto-electro-optical effects [18–20].

Selective electrical actuation of individual nanowires requires the wires to be controlled by independent electrical signals. Bimorph nanowires can be actuated by resistive heating, where the same temperature change of materials with different thermal expansion coefficients causes nanowire deformation due to differential thermal expansion (figure 1(a)). Current-carrying nanowires can be actuated by the magnetic Lorentz force that acts on moving charges in a magnetic field (figure 1(b)). Electrically charged nanowires can be actuated by electrostatic forces due to a nearby plane (or neighboring wires) that has a different electric potential (figure 1(c)). Here we have chosen actuation of bimorph nanowires due to differential thermal expansion in response to resistive heating as this allows simultaneous nanowire observation by scanning electron microscopy. Prior work on electrically actuated nanowire grid metamaterials was limited to equal actuation of every second nanowire controlled by a total of two electrical terminals [18–20]. Here we report independent selective actuation of individual nanowires, which is required to enable spatial light modulation applications. In contrast to prior art, the number of nanoscale electrical terminals scales with the number of nanowires, and we address the resulting increase in complexity by combining multiple nanofabrication processes and introducing standard electronic packaging and standard electronic interfaces, as well as computer control.

We fabricated such an electrically addressable metamaterial nanostructure, starting with a commercially available (Norcada Inc, figure 2(a)) 250 × 250 μm^2 low stress silicon nitride membrane of 50 nm thickness. The membrane is supported by a 5 × 5 mm^2 silicon frame with 32 electrodes and contact pads consisting of 50 nm thick gold with a chromium adhesive layer that were made by standard photolithography, metal deposition and lift-off processes.

In order to create the plasmonic metal film for metamaterial fabrication on the membrane and to transition from the 30 μm electrode spacing at the membrane edge to the sub-

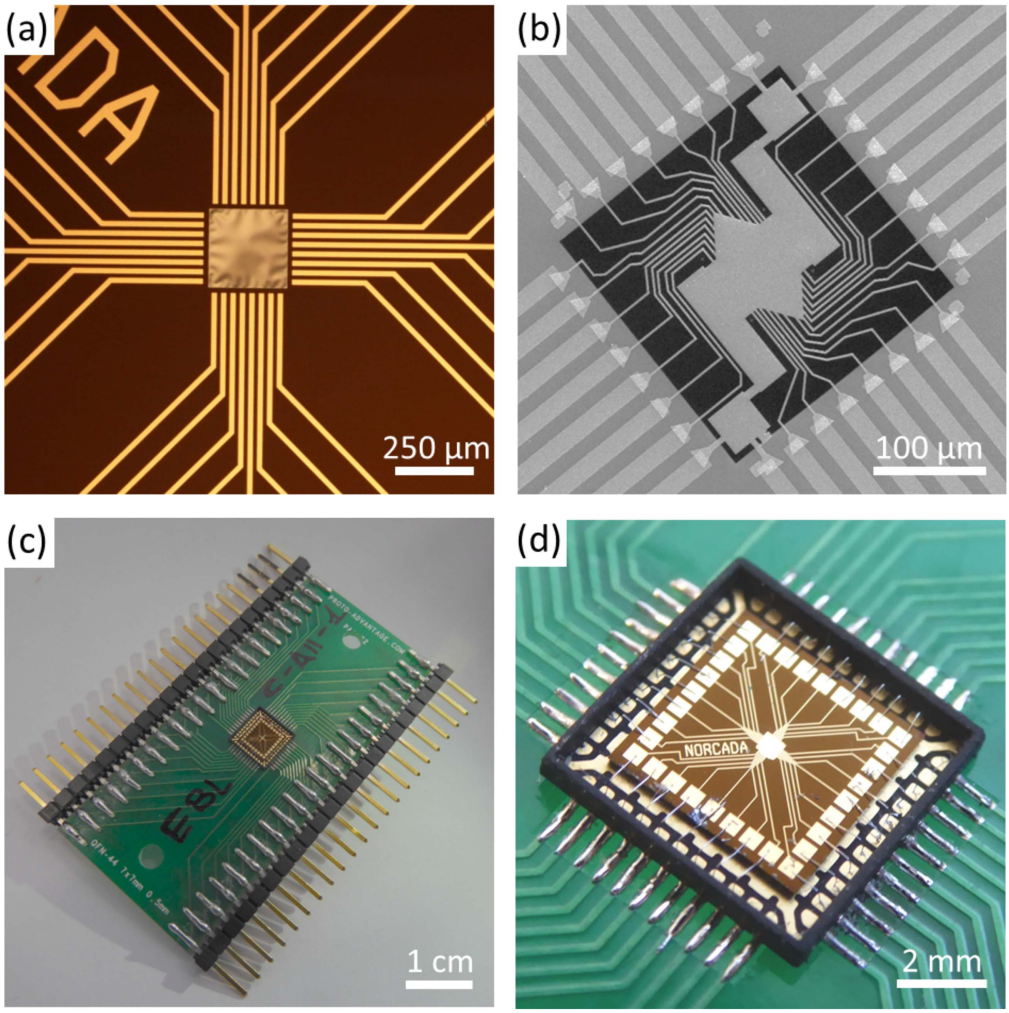

Figure 2. Contacting a nanomembrane. (a) Commercial 250 × 250 μm^2 silicon nitride membrane of 50 nm thickness on a 5 × 5 mm silicon frame with 32 electrodes. (b) Nanoscale gold contacts and gold areas for testing and metadevice fabrication made by e-beam lithography. (c) Addressable metamaterial device placed in a standard QFN to DIP package. (d) Close-up image of the metadevice in the QFN carrier.

micron electrode spacing that is required at the metamaterial edge, we performed electron beam lithography (figure 2(b)). A 1 μm thick layer of poly(methyl methacrylate) e-beam resist was spin-coated onto the membrane chip, then the electrode pattern and areas for metamaterial fabrication were exposed by standard electron beam lithography. The electrode pattern was developed for 60 s in a 1:3 MIBK:IPA solution at room temperature, rinsed with IPA and dried with N_2, followed by thermal evaporation of 50 nm of gold and subsequent lift-off.

In order to create a reliable and standardized electrical interface for the membrane chip, we used an open QFN (quad flat no-leads) chip carrier that had been surface-mounted by soldering to a QFN to DIP adapter (figure 2(c)). The membrane chip was attached inside the QFN chip carrier and the contact pads on the membrane frame were wire-bonded to the contacts of the chip carrier (figure 2(d)). The resulting chip assembly connects to a 16-way flat ribbon cable.

The metamaterial nanostructure was fabricated by gallium focused ion beam (FIB) milling and positioned relative to the e-beam lithography pattern using standard alignment techniques (figure 3(a)). Fifteen freestanding 18-μm-long chevron nanowires with a 230 nm × 100 nm cross-section were created by milling through both the gold and silicon nitride layers. Plasmonic chevron metamaterial strips were chosen for their suitability for electrothermal and magnetic actuation, their spring-like mechanical properties and their optical resonances [19, 20]. The chevron metamaterial unit cell is 600 × 620 nm^2 in size, corresponding to an active metamaterial area of 18 μm × 9 μm with a one-dimensional metadevice pixelation of 620 nm (figure 3(b)). Then the electrical connections of the 13 central nanowires to the contacts of the e-beam lithography pattern were separated by manual FIB milling at a reduced dose in order to remove the gold layer while keeping the silicon nitride membrane intact to ensure structural integrity of the device.

In order to realize a computer-controlled 'programmable' metadevice, the reconfigurable metamaterial was connected to a computer using a 16-channel digital-to-analog converter and a protective circuit that provides a 1 kΩ series resistor for each nanowire as well as grounding to avoid electrical shock to the nanostructure (figure 4(a)). A LabVIEW interface

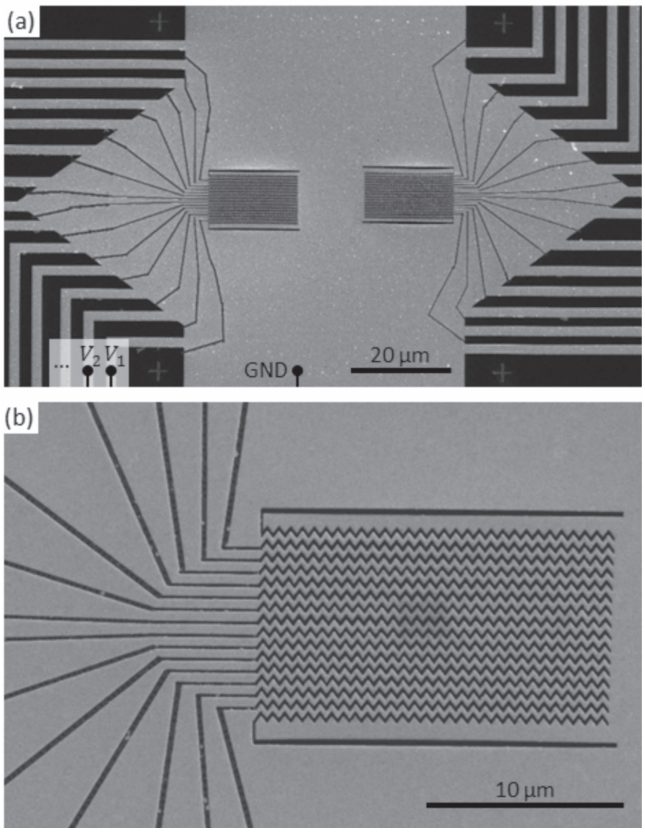

Figure 3. Addressable reconfigurable nanomembrane metadevices. (a) SEM image of the central membrane area with two contacted metadevices and alignment marks for automated FIB milling. V_i indicate electrical terminals for actuation of individual nanowires and GND indicates the common ground terminal. (b) High-resolution image of the nanowire grid metamaterial nanostructure.

allows computer-controlled actuation of individual metamaterial strips by setting the DAC output voltages.

Actuation of individual nanowires is illustrated by figures 4(b)–(d) and the online supplementary video, which show scanning electron micrographs of the central part of the metadevice at a viewing angle of 50° from the normal in order to visualize out-of-plane displacements of individual nanowires. The left and right panels show actuation of the third and fifth nanowires from the bottom with DAC control voltages of 3 V, while the middle panel shows a reference image without applied electrical signals. The nanowire resistance is small compared to the 1 kΩ protective resistor, therefore, the nanowire actuation current is almost 3 mA, with <9 mW (<1 mW) power dissipation per metamaterial strip including (excluding) the protective circuit. The movement of the actuated nanowires relative to their neighbors is clearly visible and corresponds to about 100 nm vertical displacement.

The actuation is caused by resistive heating of the nanowires, which leads to differential thermal expansion as the thermal expansion coefficient of gold (14.2×10^{-6} K^{-1}) is five times larger than that of silicon nitride (2.8×10^{-6} K^{-1}). Neglecting temperature variation along the wire for simplicity, the resulting displacement is proportional to $\Delta T \Delta \alpha L^2/t$, where the temperature change ΔT is proportional to the square of the applied current, the difference in thermal expansion coefficients $\Delta\alpha$ depends on the chosen materials, and L and t correspond to nanowire length and thickness, respectively [26]. Therefore, larger nanowire displacements and lower current operation are most easily achieved with longer nanowires or by placing the metadevice in a static magnetic field in order to combine electrothermal actuation with magnetic actuation driven by the Lorentz force. We found in our experiments that currents exceeding 3 mA (about 3×10^{11} A m^{-2} current density) are likely to damage our metadevice due to reaching the melting point of gold in positions where fabrication imperfections cause the nanowire to have a smaller gold cross-section. The exact nanowire damage threshold depends on the gold film quality, nanofabrication accuracy as well as the nanowire dimensions, see [27] for a detailed study. Therefore, an increased range of nanowire displacement due to a larger temperature range would require higher nanofabrication accuracy, a cooled environment or replacement of gold with a conductive material that has a higher melting point. Potential thermal issues such as heat transfer between nanowires still need to be investigated and the overall current applied to the metadevice may need to be limited to avoid possible overheating during simultaneous actuation of all nanowires. Such thermal issues can be minimized by fabricating the metadevice on a smaller membrane so that the thick supporting frame that acts as a heat sink is located at the nanowire ends. Reducing the size of the membrane will also enhance the mechanical stability of the structure. The device packaging could be improved with a transparent anti-reflection-coated protective lid to create a sealed unit. The speed of the thermal actuation process is determined by the cooling timescale of the nanowires, which is on the order of 10 μs and scales with L^2 according to conductive cooling estimates, while faster actuation could be driven by magnetic and electrostatic forces as illustrated by figures 1(b) and (c).

Potential optical functionalities of such programmable metadevices have been studied numerically by references [16] and [17], which show that similar metadevices can modulate the phase or intensity of reflected light in one dimension by controlling either the optical path length or light absorption separately with each nanowire, enabling functionalities of gratings, phase-gradient metasurfaces and curved mirrors on demand and without unwanted diffracted beams for wavelengths of operation that exceed the nanowire period, here 620 nm. Our metadevice design is intended to operate in the red to infrared band at wavelengths λ longer than the nanowire period, but small compared to the overall size of the nanowire array, i.e. 620 nm $<\lambda \ll 9$ μm. Beyond photonics, actuation of structured nanowires may also provide opportunities for manipulation of their thermal and phononic properties, which have been shown to depend on nanostructuring and strain [28].

In summary, we report the nanofabrication of an electrically addressable reconfigurable metadevice with 620 nm pixelation in one dimension. We demonstrate selective actuation of individual rows of metamaterial unit cells. Potential applications of such random access metadevices

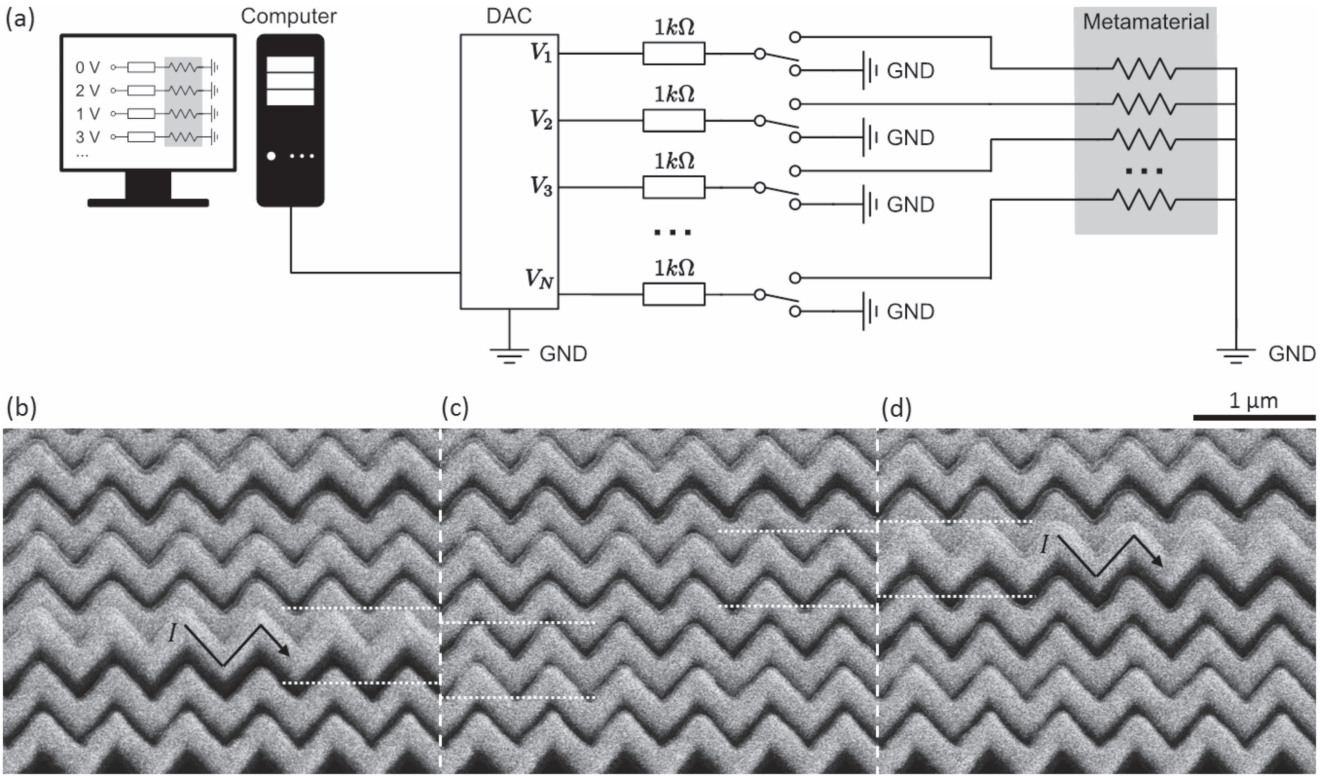

Figure 4. Selective electrical actuation of individual nanowires. (a) Schematic of the computer-controlled actuation circuit, where DAC indicates the digital-to-analog converter and GND indicates ground. (b)–(d) Strip actuation—SEM images showing the nanostructure at a viewing angle of 50° from the normal (b) with $V_3 = 3$ V applied to nanowire 3 from the bottom, (c) without voltage application and (d) with $V_5 = 3$ V applied to nanowire 5 from the bottom.

include spatial light modulators with sub-wavelength pixelation.

Acknowledgments

The authors thank Jeff Hooker for assistance with assembling the electronic interfaces. This work is supported by the Leverhulme Trust, the MOE Singapore (grant MOE2011-T3-1-005) and the UK Engineering and Physical Sciences Research Council (grants EP/G060363/1 and EP/M009122/1). The data from this paper can be obtained from the University of Southampton ePrints research repository: http://dx.doi.org/10.5258/SOTON/399811.

References

[1] Efron U 1994 *Spatial Light Modulator Technology: Materials Devices, and Applications* (Boca Raton, FL: CRC Press)
[2] Lazarev G, Hermerschmidt A, Krüger S and Osten S 2012 LCOS spatial light modulators: trends and applications *Optical Imaging and Metrology: Advanced Technologies* (Weinheim: Wiley-VCH) pp 1–29
[3] Yu H, Park J, Lee K, Yoon J, Kim K, Lee S and Park Y 2015 Recent advances in wavefront shaping techniques for biomedical applications *Curr. Appl. Phys.* **15** 632–41
[4] Zhang J, MacDonald K F and Zheludev N I 2012 Controlling light-with-light without nonlinearity *Light Sci. Appl.* **1** e18
[5] Papaioannou M, Plum E, Valente J, Rogers E and Zheludev N 2015 Two-dimensional control of light with light on metasurfaces *Light Sci. Appl.* **5** e16070
[6] Cho D J, Wu W, Ponizovskaya E, Chaturvedi P, Bratkovsky A M, Wang S Y, Zhang X, Wang F and Shen Y R 2009 Ultrafast modulation of optical metamaterials *Opt. Express* **17** 17652–7
[7] Dani K M, Ku Z, Upadhya P C, Prasankumar R P, Brueck S R J and Taylor A J 2009 Subpicosecond optical switching with a negative index metamaterial *Nano Lett.* **9** 3565–9
[8] Driscoll T, Kim H T, Chae B G, Kim B J, Lee Y W, Jokerst N M, Palit S, Smith D R, Ventra M D and Basov D N 2009 Memory metamaterials *Science* **325** 1518–21
[9] Huang Y-W, Lee H W H, Sokhoyan R, Pala R A, Thyagarajan K, Han S, Tsai D P and Atwater H A 2009 Gate-tunable conducting oxide metasurfaces *Nano Lett.* **16** 5319–25
[10] Lapine M, Powell D, Gorkunov M, Shadrivov I, Marqués R and Kivshar Y 2009 Structural tunability in metamaterials *Appl. Phys. Lett.* **95** 084105
[11] Tao H, Strikwerda A C, Fan K, Padilla W J, Zhang X and Averitt R D 2009 Reconfigurable terahertz metamaterials *Phys. Rev. Lett.* **103** 147401
[12] Pryce I M, Aydin K, Kelaita Y A, Briggs R M and Atwater H A 2010 Highly strained compliant optical metamaterials with large frequency tunability *Nano Lett.* **10** 4222–7
[13] Zhu W M *et al* 2011 Switchable magnetic metamaterials using micromachining processes *Adv. Mater.* **23** 1792–6

[14] Ou J Y, Plum E, Jiang L and Zheludev N I 2011 Reconfigurable photonic metamaterials *Nano Lett.* **11** 2142–4
[15] Zheludev N I and Plum E 2016 Reconfigurable nanomechanical photonic metamaterials *Nat. Nanotechnol* **11** 16–22
[16] Cencillo-Abad P, Plum E, Rogers E T F and Zheludev N I 2016 Spatial optical phase-modulating metadevice with subwavelength pixelation *Opt. Express* **24** 18790–8
[17] Cencillo-Abad P, Zheludev N I and Plum E 2016 Metadevice for intensity modulation with sub-wavelength spatial resolution *Sci. Rep.* at press(arXiv:1610.06791)
[18] Ou J Y, Plum E, Zhang J and Zheludev N I 2013 An electromechanically reconfigurable plasmonic metamaterial operating in the near-infrared *Nat. Nanotechnol* **8** 252–5
[19] Valente J, Ou J Y, Plum E, Youngs I J and Zheludev N I 2015 Reconfiguring photonic metamaterials with currents and magnetic fields *Appl. Phys. Lett.* **106** 111905
[20] Valente J, Ou J Y, Plum E, Youngs I J and Zheludev N I 2015 A magneto-electro-optical effect in a plasmonic nanowire material *Nat. Commun.* **6** 7021
[21] Karvounis A, Ou J Y, Wu W, MacDonald K F and Zheludev N I 2015 Nano-optomechanical nonlinear dielectric metamaterials *Appl. Phys. Lett.* **107** 191110
[22] Thijssen R, Verhagen E, Kippenberg T J and Polman A 2013 Plasmon nanomechanical coupling for nanoscale transduction *Nano Lett.* **13** 3293–7
[23] Thijssen R, Kippenberg T J, Polman A and Verhagen E 2014 Parallel transduction of nanomechanical motion using plasmonic resonators *ACS Photon.* **1** 1181–8
[24] Yamaguchi K, Fujii M, Okamoto T and Haraguchi M 2014 Electrically driven plasmon chip: active plasmon filter *Appl. Phys. Express* **7** 012201
[25] Thijssen R, Kippenberg T J, Polman A and Verhagen E 2015 Plasmomechanical resonators based on dimer nanoantennas *Nano Lett.* **15** 3971–6
[26] Prasanna S and Spearing S M 2007 Materials selection and design of microelectrothermal bimaterial actuators *J. Microelectromech. Syst.* **16** 248–59
[27] Karim S, Maaz K, Ali G and Ensinger W 2009 Diameter dependent failure current density of gold nanowires *J. Phys. D: Appl. Phys.* **42** 185403
[28] Zhu T and Ertekin E 2015 Resolving anomalous strain effects on two-dimensional phonon flows: the cases of graphene, boron nitride, and planar superlattices *Phys. Rev.* B **91** 205429

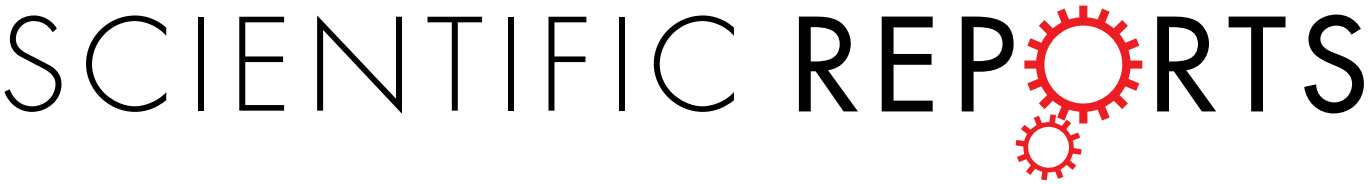

OPEN

Metadevice for intensity modulation with sub-wavelength spatial resolution

Received: 25 July 2016
Accepted: 25 October 2016
Published: 18 November 2016

Pablo Cencillo-Abad[1], Nikolay I. Zheludev[1,2] & Eric Plum[1]

Effectively continuous control over propagation of a beam of light requires light modulation with pixelation that is smaller than the optical wavelength. Here we propose a spatial intensity modulator with sub-wavelength resolution in one dimension. The metadevice combines recent advances in reconfigurable nanomembrane metamaterials and coherent all-optical control of metasurfaces. It uses nanomechanical actuation of metasurface absorber strips placed near a mirror in order to control their interaction with light from perfect absorption to negligible loss, promising a path towards dynamic diffraction and focusing of light as well as holography without unwanted diffraction artefacts.

Spatial control over the intensity of light is the basis of optical components such as diffraction gratings, Fresnel zone plates and amplitude holograms. Dynamic spatial control over light intensity can — in principle — provide their functionalities on demand, however, established spatial light modulators based on liquid crystal or digital micromirror technology suffer from low resolution and unwanted diffraction due to their pixelation on the order of 10 μm[1–3]. Sub-wavelength resolution would be required to avoid unwanted diffraction and to achieve truly arbitrary and effectively continuous spatial control over the intensity of light. The required sub-wavelength scale structuring is a defining characteristic of metamaterials and metasurfaces and leads to locally homogeneous optical properties. Static spatial variation of metamaterial structures has given rise to the fields of transformation optics[4–7] and gradient metasurfaces[8–15], while emerging technologies based on phase transitions[16,17], nonlinearities[18,19], coherent light-matter interactions[20–23] and nanomechanical actuation[24–33] now enable the temporal modulation of metamaterial properties[34].

Here we propose a metadevice that controls coherent absorption of light by selective actuation of metamaterial nanostructures to provide arbitrary dynamic control over its reflectivity with sub-wavelength spatial resolution in one dimension, see Fig. 1a.

Absorbtion of light in a planar absorber of sub-wavelength thickness is limited to 50%, if it is illuminated from only one side[35]. However, if it is placed within a standing wave formed by counterpropagating coherent waves, then absorption will depend on its position relative to the standing wave's nodes and anti-nodes. At an electric field node, the planar structure cannot interact with the wave and therefore absorption is nominally zero, while absorption at an electric field anti-node can in principle reach 100% (ref. 20). Projection of images onto a metasurface absorber with coherent light has enabled all-optical control of light absorption with diffraction-limited resolution[23], however, this approach cannot beat the diffraction limit and it requires a stable interferometer as well as coherent light. Instead, we propose a mechanically reconfigurable nanoscale version of a Salisbury screen[36–39], where individually addressable absorbing metamaterial strips are placed at a variable nanoscale distance from a mirror in order to exploit coherent perfect absorption and transparency on demand. As illustrated by Fig. 1, the incident light and multiple reflections by mirror and metasurface form a standing wave, without a macroscopic interferometer and even for incoherent illumination provided that the coherence length is large compared to the metasurface-to-mirror spacing d (measured from the middle of the metasurface to the mirror surface). Furthermore, the spatial resolution of the metadevice will be determined by the pitch of the metamaterial strip actuators, i.e. it will be controlled by nanofabrication technology, rather than the diffraction limit. Thermal, electric, magnetic and optical actuation of such metamaterial strips[28–31] as well as actuation of similar optomechanical nanostructures[40–43] has been reported. Recently, selective actuation of individual metamaterial strips has been demonstrated[44] and suggested as a method for spatial phase modulation[45]. Structures for the optical part of the

[1]Optoelectronics Research Centre and Centre for Photonic Metamaterials, University of Southampton, Highfield, Southampton, SO17 1BJ, UK. [2]Centre for Disruptive Photonic Technologies, School of Physical and Mathematical Sciences and The Photonics Institute, Nanyang Technological University, Singapore 637371. Correspondence and requests for materials should be addressed to E.P. (email: erp@orc.soton.ac.uk)

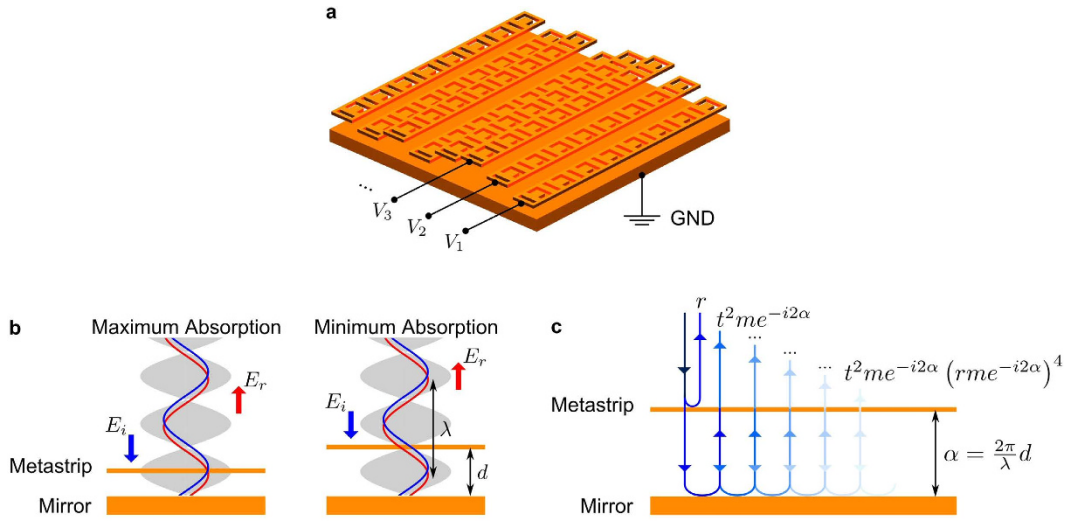

Figure 1. Intensity modulation based on coherent metasurface absorption. (**a**) Artistic impression of a spatial intensity modulator based on selective actuation of metastrips above a grounded metallic mirror (GND), where V_i indicate metastrip actuation voltages. (**b**) Incident E_i and reflected E_r electromagnetic waves form a standing wave (grey). The largest absorption occurs for metastrips placed at an electric field anti-node, while negligible absorption occurs for metastrips positioned at an electric field node. (**c**) Multiple reflections at a metasurface with reflection coefficient r and transmission coefficient t placed at a distance d in front of a mirror with reflection coefficient m.

spectrum are typically based on a dielectric membrane of nanoscale thickness (e.g. silicon nitride) which is coated by a plasmonic material (e.g. gold) or a high index dielectric (e.g. silicon), which is then structured by reactive ion etching and focused ion beam milling to create the metamaterial pattern and strip actuators with or without the original dielectric layer[46].

Results and Discussion

The metadevice considered here consists of a reconfigurable metasurface in front of a metallic mirror, see Fig. 1a. The metasurface is composed of parallel gold strips of 400 nm width and 50 nm thickness that are separated by 100 nm gaps and perforated with asymmetrically split ring apertures, see Fig. 2. A unit cell size of 500 nm was chosen to enable non-diffracting operation in the red to infrared spectral range where gold is highly reflective. Asymmetrically split ring apertures were chosen as they are well-studied[47] and known to provide coherent perfect absorption[20]. The size of the split rings was determined by the available space on the gold strips prescribing a minimum feature size of 50 nm that can be routinely achieved with both focused ion beam milling and electron beam lithography. The optical properties of metasurface and metadevice were simulated for normal incidence illumination by a coherent plane wave using finite element modelling (COMSOL Multiphysics 4.4) in three dimensions, approximating the device with metastrips that have prescribed displacements and infinite length. We consider linearly polarised light with the electric field parallel to the strips in all cases to avoid the excitation of metal-insulator-metal waveguide modes. The electric permittivity of gold is computed from a Drude-Lorentz model with 3 oscillators[48]. Figure 2a illustrates the optical properties of the flat metasurface without the backing mirror. The split ring aperture array has rich transmission, reflection and absorption spectra with several resonances corresponding to the fundamental and higher order modes of the split ring slits, see Fig. 2c.

The optical properties of the structure change dramatically when it is combined with a mirror. For an optically thick mirror, transmission is zero and reflectivity R and absorption A are given by the superposition of the waves that are multiply reflected by mirror and metasurface as illustrated by Fig. 1c. Neglecting near-field effects,

$$A = 1 - R = 1 - \left| r + \frac{e^{-i2\alpha} m t^2}{1 - e^{-i2\alpha} m r} \right|^2 \quad (1)$$

where r and t are the complex Fresnel reflection and transmission coefficients of the flat metasurface, m is the reflection coefficient of the mirror and $\alpha = 2\pi d/\lambda$ is the phase accumulated during propagation of the wave of wavelength λ from metasurface to mirror.

Assuming an ideal mirror ($m = -1$), the metadevice absorption is that of the metasurface. In this case, the electric field at the metasurface position — which controls absorption — corresponds to the superposition of the incident wave with the wave that is transmitted by the metasurface and then multiply reflected between mirror and metasurface. The metasurface absorption A is proportional to the square of the resulting electric field enhancement. For an ideal planar metasurface ($t = r + 1$),

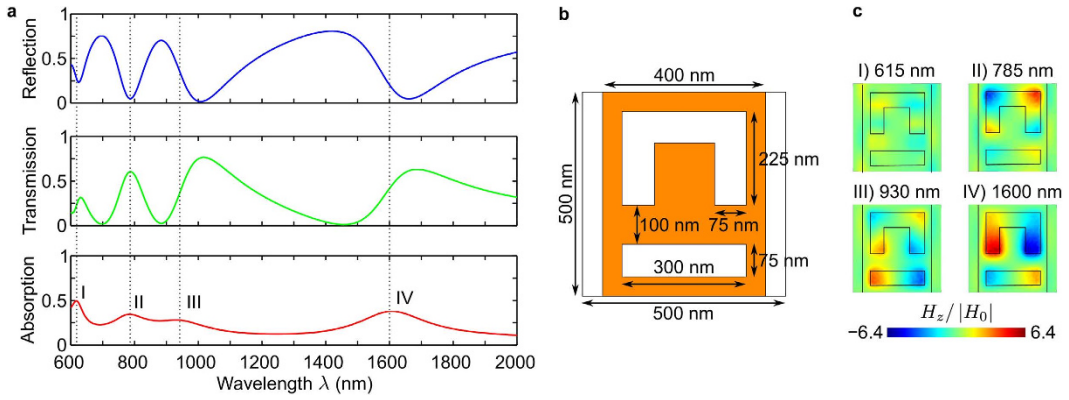

Figure 2. The metamaterial and its resonances. (**a**) Reflection, transmission and absorption of the flat metasurface without mirror. (**b**) Schematic of the unit cell. (**c**) Modes of excitation at the absorption maxima in terms of the instantaneous magnetic field H_z 10 nm above the gold surface relative to the incident wave's magnetic field amplitude $|H_0|$.

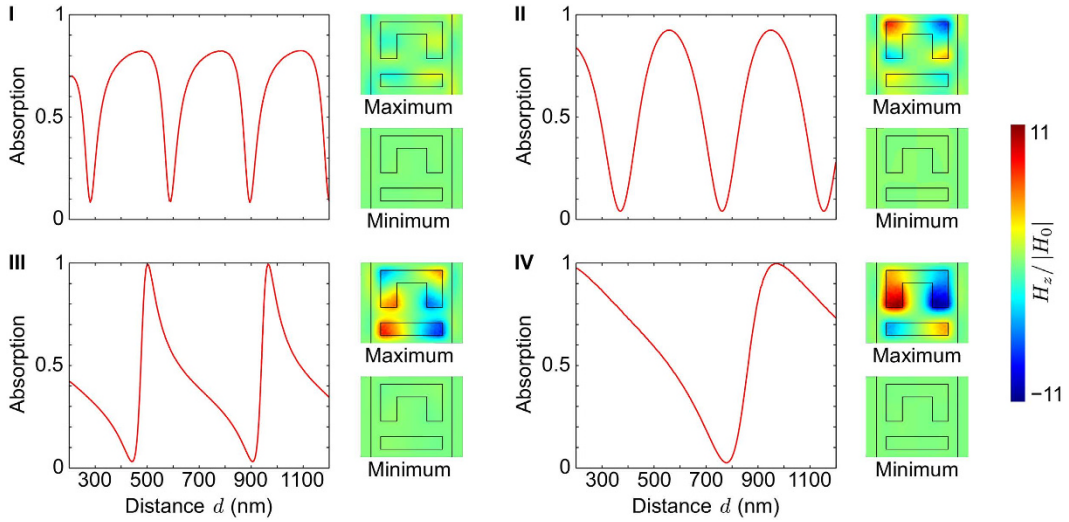

Figure 3. Metadevice absorption at the metasurface absorption maxima. Dependence of absorption on the metasurface-to-mirror spacing d at wavelengths of (**I**) 615 nm, (**II**) 785 nm, (**III**) 930 nm and (**IV**) 1600 nm. Colour maps show the instantaneous magnetic field H_z 10 nm above the gold surface relative to the incident wave's magnetic field amplitude $|H_0|$ for absorption maxima and minima.

$$A = \frac{1 - \cos 2\alpha}{\left|1 + e^{-i2\alpha} r\right|^2} 2A_0 \tag{2}$$

where $A_0 = 1 - |r|^2 - |r + 1|^2$ is the metasurface absorption without the mirror. Notably, this analytical model predicts that absorption vanishes completely due to electric field cancellation at the metasurface when α is a multiple of π, i.e. when the metasurface-to-mirror spacing d becomes a multiple of $\lambda/2$.

As illustrated by Fig. 3, this behaviour is confirmed by numerical simulations. Absorption of the metadevice is strongly dependent on the metasurface-to-mirror spacing and reduces to few % for wavelengths corresponding approximately to multiples of $\lambda/2$. The small residual reflectivity and 10s-of-nm deviations in the spectral position of the absorption minima result from (i) the metasurface not being perfectly planar due to having a finite thickness of 50 nm ($t \simeq r + 1$) and (ii) the gold mirror not being an ideal mirror due to small absorption losses and slight deviations from reflection with a π phase change ($m \simeq -1$). For intermediate spacings, the metasurface's resonant modes are excited (compare Figs 2c and 3) and the strength of the metasurface excitation is controlled by the distance d that determines the interference of incident and (multiply) reflected waves on the metasurface. Constructive interference results in stronger excitation and higher levels of absorption (>99% for selected wavelengths) than for the metasurface without the backing mirror, compare with Fig. 2a. Destructive interference suppresses metasurface excitation resulting in negligible absorption as discussed above. We note that absorption

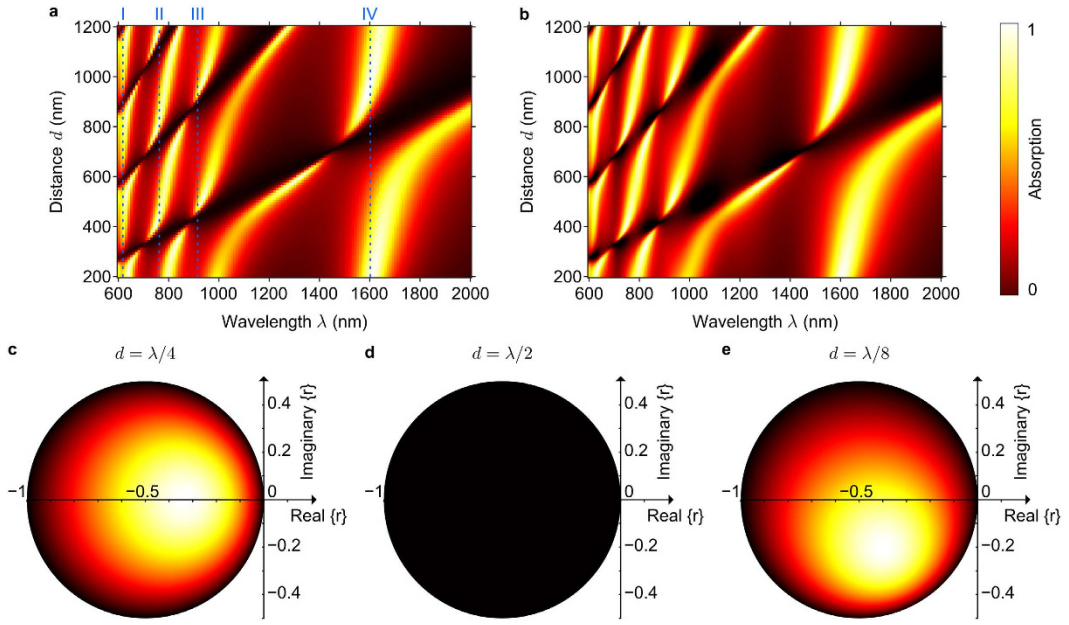

Figure 4. Metadevice absorption according to numerical and analytical models. Dependence of absorption on metasurface-to-mirror spacing d and wavelength λ based on (**a**) numerical modelling of the entire metadevice and (**b**) the semi-analytical model given by equation (1). (**c**–**e**) Dependence of absorption on the metasurface scattering coefficient r for metasurface-to-mirror distances (**c**) $d = \lambda/4$, (d) $\lambda/2$ and (**e**) an intermediate spacing of $\lambda/8$ based on the analytical model given by equation (2).

as a function of the metasurface-to-mirror spacing is generally periodic with period $\lambda/2$ (provided that d is small compared to the coherence length of the illuminating light), however, some deviations due to near-field interactions between metasurface and mirror are observed for small gaps d approaching 200 nm.

Figure 4a,b shows the absorption spectrum of the metadevice as a function of the metasurface-to-mirror spacing d, where panel (a) shows results for numerical modelling of the entire metadevice, while panel (b) shows semi-analytical results based on equation (1), where the metasurface properties, r and t, were determined separately by numerical modelling and the reflectivity of the gold mirror m was calculated using the Fresnel equations. The results are almost indistinguishable and they reveal that the metadevice's absorption can be strongly modulated in wide spectral bands around the metasurface's resonances I-IV (see Fig. 3). These bands of operation are separated by the metasurface's transmission minima at 700, 885 and 1455 nm (compare to Fig. 2a) and the absorption wavelength can be moved continuously across each band by adjusting the metasurface-to-mirror spacing, resulting in a wavelength-tuneable metadevice. Notably, the bands of operation include the red part of the visible spectrum and the main telecommunications bands around 1310 nm and 1550 nm wavelength. The absence of absorption when the metasurface-to-mirror spacing coincides with a multiple of $\lambda/2$ corresponds to the straight dark bands across the colormaps.

Figure 4c–e illustrates based on equation (2) how the metadevice absorption depends on the metasurface's complex scattering coefficient r for characteristic metasurface-to-mirror spacings d. As should be expected, absorption vanishes for lossless metasurfaces, which satisfy $|r + 0.5| = 0.5$, and, as shown above, absorption vanishes for $d = \lambda/2$ regardless of the metasurface's scattering coefficient. For lossy metasurfaces, the dependence of absorption on d is symmetric for real scattering coefficients (as in Fig. 3I, II) and asymmetric for complex scattering coefficients (as in Fig. 3III, IV).

As indicated on Fig. 1a, actuation of individual metamaterial strips can be driven by electrostatic forces resulting from grounding the mirror and application of an electric potential to an individual nanowire as in commercial grating light valves[49,50]. In-plane strip deformation can be neglected as the strips deform about 100× more easily towards the mirror than towards their neighbours due to their perforated center and their width/thickness aspect ratio of 8 (ref. 51). Spatial intensity modulation results from positioning different metastrips at different distances from the mirror. This is illustrated by Fig. 5 for a metastrip configuration that corresponds to a Fresnel zone plate operating at $\lambda = 785$ nm wavelength. The zone plate consists of reflective and absorbing areas arranged in such a way that all scattered fields will constructively interfere at the intended focus as illustrated by panel (a). Here, the zone plate is realised by placing the metastrips at positions of either negligible ($d = 370$ nm) or almost complete ($d = 560$ nm) absorption as shown. In order to achieve a line focus 2 μm above the metadevice, light scattered by the reflective areas must constructively interfere on the focal line. Therefore, all strips for which the strip-to-focus optical path length p_i satisfies $0 \leq p_i/\lambda - N_i - C < 0.5$, where N_i is an integer and $C = 0.6$ is an arbitrarily chosen real number, were set to the reflective position, while all other strips were set to the absorbing position. The simulations show that coupling between neighboring strips is sufficiently small to allow weak excitation of strips at $d = 370$ nm and strong excitation of strips at $d = 560$ nm even in the most extreme case when these reflective and absorbing strips alternate, see panel (b). The same panel also shows the complex pattern of standing waves that

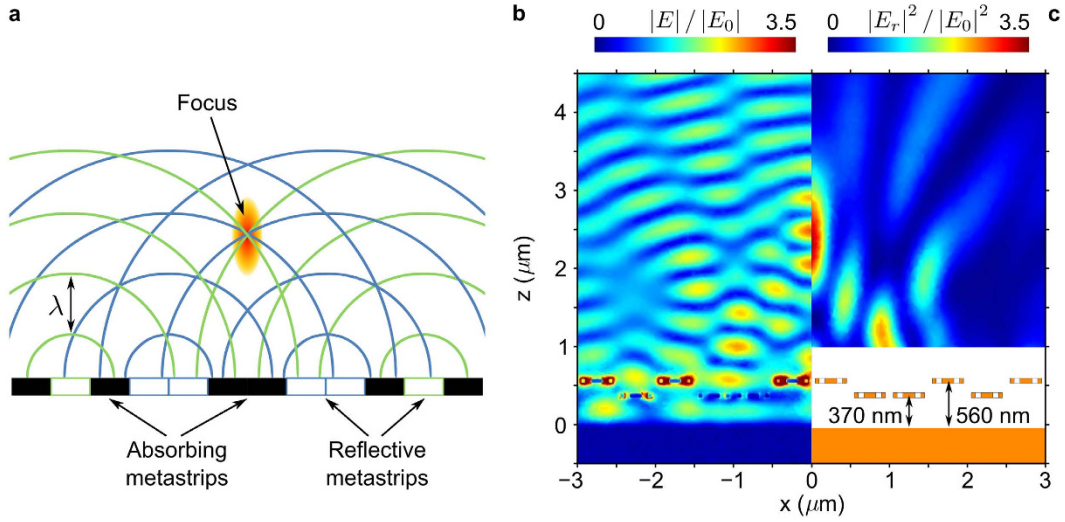

Figure 5. Fresnel zone plate application of a metadevice with 12 metastrips operating at $\lambda = 785$ nm wavelength. (**a**) Basic operating principle of the zone plate: all reflective areas are sources of scattered fields, which interfere constructively at the focal spot. (**b**,**c**) A focal spot at a distance of 2 μm results from metastrip-to-mirror spacings of $d = 370$ nm (negligible absorption) and 560 nm (perfect absorption) as shown. The colour maps show (**b**) the total electric field amplitude $|E|$ and (**c**) the square of the reflected electric field's amplitude $|E_r|^2$ normalised to the incident wave E_0.

forms above the actuated metadevice due to interference of incident and scattered fields. Panel (c) shows the focal spot that forms 2 μm above the metadevice in its Fresnel zone plate configuration due to constructive interference of the fields scattered by the weakly absorbing strips.

Regarding the experimental feasibility of the metadevice, actuation of metastrips of similar complexity and characteristic dimensions has already been demonstrated[46]. Metastrips will generally be fixed at both ends and therefore voltage application will result in metastrip bending towards the ground plane, where only the middle section of each strip will achieve the desired displacement. The size of this optically useful middle section of the metastrips scales with the overall strip length and it can be enlarged by making the end sections of the strips more elastic (e.g. thinner). Permanent metastrip deformation was not found to be a major issue in prior work and could be addressed by adding an elastic dielectric supporting layer (e.g. silicon or silicon nitride). However, we note that the electrostatic force will overcome the elastic restoring force of the metastrips as the metastrip-to-mirror spacing decreases towards half of its original size[29]. In order to achieve reliable electrostatic operation without such accidental switching of the device, metastrips should only be displaced by substantially less than half of their original distance from the ground plane. Slight differences in response and rest position of different metastrips could arise from fabrication imperfections, but could be offset using adjusted actuation voltages after device calibration. Achievable modulation rates of metastrips are limited by their mechanical resonances and the associated resonance frequencies are inversely proportional to the square of the metastrip length. Typical metastrips of 10 s of μm length have mechanical resonances at 100 s of kHz to MHz and could have actuation voltages of several V if placed 100 s of nm away from a ground plane[29,32,46].

Conclusion

In summary, we demonstrate that nanoscale actuation of metamaterial strips placed at a nanoscale distance from a mirror could be the basis for a spatial light modulator with sub-wavelength spatial resolution in one dimension and — in principle — unlimited optical contrast resulting from complete reflection and coherent perfect absorption. We argue that recent breakthroughs in reconfigurable nanomembrane metamaterials and coherent all-optical control of metasurfaces make such a device a realistic proposition. Potential application areas of such metadevices include dynamic diffraction, focusing and attenuation of light as well as holography.

Data availability. The data from this paper can be obtained from the University of Southampton ePrints research repository: http://dx.doi.org/10.5258/SOTON/398132.

References

1. Efron, U. (ed.) *Spatial Light Modulator Technology: Materials, Devices, and Applications* (CRC Press, 1994).
2. Lazarev, G., Hermerschmidt, A., Krüger, S. & Osten, S. *Optical Imaging and Metrology: Advanced Technologies.* chap. 1. LCOS Spatial Light Modulators: Trends and Applications. 1–29 (Wiley-VCH Verlag GmbH & Co. KGaA, 2012).
3. Yu, H. *et al.* Recent advances in wavefront shaping techniques for biomedical applications. *Curr. Appl. Phys.* **15,** 632–641 (2015).
4. Leonhardt, U. Optical conformal mapping. *Science* **312,** 1777–1780 (2006).
5. Schurig, D. *et al.* Metamaterial electromagnetic cloak at microwave frequencies. *Science* **314,** 977–980 (2006).
6. Cai, W., Chettiar, U. K., Kildishev, A. V. & Shalaev, V. M. Optical cloaking with metamaterials. *Nat. Photonics* **1,** 224–227 (2007).
7. Valentine, J., Li, J., Zentgraf, T., Bartal, G. & Zhang, X. An optical cloak made of dielectrics. *Nat. Mater.* **8,** 568–571 (2009).

8. Yu, N. F. *et al.* Light propagation with phase discontinuities: generalized laws of reflection and refraction. *Science* **334,** 333–337 (2011).
9. Sun, S. L. *et al.* High-efficiency broadband anomalous reflection by gradient meta-surfaces. *Nano Lett.* **12,** 6223–6229 (2012).
10. Walther, B., Helgert, C., Rockstuhl, C., Setzpfandt, F. & Eilenberger, F. Spatial and spectral light shaping with metamaterials. *Adv. Mater.* **24,** 6300–6304 (2012).
11. Roy, T., Nikolaenko, A. E. & Rogers, E. T. A meta-diffraction-grating for visible light. *J. Opt.* **15,** 85101 (2013).
12. Ni, X. J., Ishii, S., Kildishev, A. V. & Shalaev, V. M. Ultra-thin, planar, babinet-inverted plasmonic metalenses. *Light. Sci. Appl.* **2,** e72 (2013).
13. Lin, D. M., Fan, P. Y., Hasman, E. & Brongersma, M. L. Dielectric gradient metasurface optical elements. *Science* **345,** 298–302 (2014).
14. Chen, W. T. *et al.* High-efficiency broadband meta-hologram with polarization-controlled dual images. *Nano Lett.* **14,** 225–230 (2014).
15. Veksler, D., Maguid, E., Shitrit, N., Ozeri, D. & Kleiner, V. Multiple wavefront shaping by metasurface based on mixed random antenna groups. *ACS Photonics* **2,** 661–667 (2015).
16. Driscoll, T. *et al.* Memory metamaterials. *Science* **325,** 1518–1521 (2009).
17. Sámson, Z. L. *et al.* Metamaterial electro-optic switch of nanoscale thickness. *Appl. Phys. Lett.* **96,** 143105 (2010).
18. Cho, D. J. *et al.* Ultrafast modulation of optical metamaterials. *Opt. Express* **17,** 17652–17657 (2009).
19. Dani, K. M. *et al.* Subpicosecond optical switching with a negative index metamaterial. *Nano Lett.* **9,** 3565–3569 (2009).
20. Zhang, J., MacDonald, K. F. & Zheludev, N. I. Controlling light-with-light without nonlinearity. *Light Sci. Appl.* **1,** e18 (2012).
21. Fang, X. *et al.* Ultrafast all-optical switching via coherent modulation of metamaterial absorption. *Appl. Phys. Lett.* **104,** 141102 (2014).
22. Shi, J. *et al.* Coherent control of snell's law at metasurfaces. *Opt. Express* **22,** 21051–21060 (2014).
23. Papaioannou, M., Plum, E., Valente, J., Rogers, E. & Zheludev, N. Two-dimensional control of light with light on metasurfaces. *Light Sci. Appl.* **5,** e16070 (2015).
24. Lapine, M. *et al.* Structural tunability in metamaterials. *Appl. Phys. Lett.* **95,** 084105 (2009).
25. Tao, H. *et al.* Reconfigurable terahertz metamaterials. *Phys. Rev. Lett.* **103,** 147401 (2009).
26. Pryce, I. M., Aydin, K., Kelaita, Y. A., Briggs, R. M. & Atwater, H. A. Highly strained compliant optical metamaterials with large frequency tunability. *Nano Lett.* **10,** 4222–4227 (2010).
27. Zhu, W. M. *et al.* Switchable magnetic metamaterials using micromachining processes. *Adv. Mater.* **23,** 1792–1796 (2011).
28. Ou, J. Y., Plum, E., Jiang, L. & Zheludev, N. I. Reconfigurable photonic metamaterials. *Nano Lett.* **11,** 2142–2144 (2011).
29. Ou, J. Y., Plum, E., Zhang, J. & Zheludev, N. I. An electromechanically reconfigurable plasmonic metamaterial operating in the near-infrared. *Nat. Nanotechnol.* **8,** 252–255 (2013).
30. Valente, J., Ou, J. Y., Plum, E., Youngs, I. J. & Zheludev, N. I. Reconfiguring photonic metamaterials with currents and magnetic fields. *Appl. Phys. Lett.* **106,** 111905 (2015).
31. Ou, J. Y., Plum, E., Zhang, J. & Zheludev, N. I. Giant nonlinearity of an optically reconfigurable plasmonic metamaterial. *Adv. Mater.* **28,** 729–733 (2016).
32. Valente, J., Ou, J. Y., Plum, E., Youngs, I. J. & Zheludev, N. I. A magneto-electro-optical effect in a plasmonic nanowire material. *Nat. Commun.* **6,** 7021 (2015).
33. Liu, X. & Padilla, W. J. Dynamic manipulation of infrared radiation with mems metamaterials. Adv. *Opt. Mater.* **1,** 559–562 (2013).
34. Zheludev, N. I. Obtaining optical properties on demand. *Science* **348,** 973–974 (2015).
35. Thongrattanasiri, S., Koppens, F. H. L. & de Abajo, F. J. G. Complete optical absorption in periodically patterned graphene. *Phys. Rev. Lett.* **108,** 047401 (2012).
36. Fante, R. L. & McCormack, M. T. Reflection properties of the salisbury screen. *IEEE Trans. Antennas. Propag.* **36,** 1443–1454 (1988).
37. Munk, B. A. *Frequency Selective Surfaces: Theory and Design* (John Wiley & Sons, 2000).
38. Engheta, N. Thin absorbing screens using metamaterial surfaces. In *Antennas and Propagation Society International Symposium* **2,** 392–395 (2002).
39. Schwanecke, A. S., Fedotov, V. A., Khardikov, V. V., Y. C., Prosvirnin, S. L. & Zheludev, N. I. Optical magnetic mirrors. *J. Opt. A: Pure Appl. Opt.* **9,** L1–L2 (2007).
40. Thijssen, R., Verhagen, E., Kippenberg, T. J. & Polman, A. Plasmon nanomechanical coupling for nanoscale transduction. *Nano Lett.* **13,** 3293–3297 (2013).
41. Thijssen, R., Kippenberg, T. J., Polman, A. & Verhagen, E. Parallel transduction of nanomechanical motion using plasmonic resonators. *ACS Photonics* **1,** 1181–1188 (2014).
42. Yamaguchi, K., Fujii, M., Okamoto, T. & Haraguchi, M. Electrically driven plasmon chip: Active plasmon filter. *Appl. Phys. Express* **7,** 012201 (2014).
43. Thijssen, R., Kippenberg, T. J., Polman, A. & Verhagen, E. Plasmomechanical resonators based on dimer nanoantennas. *Nano Lett.* **15,** 3971–3976 (2015).
44. Cencillo-Abad, P., Ou, J. Y., Plum, E., Valente, J. & Zheludev, N. I. Random access actuation of nanowire grid metamaterial. *Nanotechnology* **27,** 485206 (2016).
45. Cencillo-Abad, P., Plum, E., Rogers, E. T. F. & Zheludev, N. I. Spatial optical phase-modulating metadevice with subwavelength pixelation. *Opt. Express* in press (2016).
46. Zheludev, N. I. & Plum, E. Reconfigurable nanomechanical photonic metamaterials. *Nat. Nanotechnol.* **11,** 16–22 (2016).
47. Plum, E. *et al.* A combinatorial approach to metamaterials discovery. *J. Opt.* **13,** 055102 (2011).
48. Liu, Z. *et al.* Plasmonic nanoantenna arrays for the visible. *Metamaterials* **2,** 45–51 (2008).
49. Bloom, D. M. Grating light valve: revolutionizing display technology. *Proc. SPIE* **3013,** 165–171 (1997).
50. Solgaard, O. *Photonic Microsystems: Micro and Nanotechnology Applied to Optical Devices and Systems* (Springer Science & Business Media, 2009).
51. Timoshenko, S. P. & Gere, J. M. *Theory of Elastic Stability* (Dover Publications Inc., 2009).

Acknowledgements

This work is supported by the MOE Singapore (grant MOE2011-T3-1-005) and the UK's Engineering and Physical Sciences Research Council (grants EP/G060363/1 and EP/M009122/1). The authors acknowledge the use of the IRIDIS High Performance Computing Facility, and associated support services at the University of Southampton, in the completion of this work.

Author Contributions

P.C.A. caried out the simulations and performed the data analysis. P.C.A. and E.P. conceived the study and drafted the manuscript. E.P. and N.I.Z. supervised the work and all authors read and approved the manuscript.

Additional Information

Competing financial interests: The authors declare no competing financial interests.

How to cite this article: Cencillo-Abad, P. *et al.* Metadevice for intensity modulation with sub-wavelength spatial resolution. *Sci. Rep.* **6**, 37109; doi: 10.1038/srep37109 (2016).

Publisher's note: Springer Nature remains neutral with regard to jurisdictional claims in published maps and institutional affiliations.

Research Article | Vol. 24, No. 16 | 8 Aug 2016 | OPTICS EXPRESS 18790

Optics EXPRESS

Spatial optical phase-modulating metadevice with subwavelength pixelation

Pablo Cencillo-Abad,[1] Eric Plum,[1,*] Edward T. F. Rogers,[1,2] and Nikolay I. Zheludev[1,3]

[1] *Optoelectronics Research Centre and Centre for Photonic Metamaterials, University of Southampton, Highfield, Southampton, SO17 1BJ, UK*
[2] *Institute for Life Sciences, University of Southampton, Highfield, Southampton, SO17 1BJ, UK*
[3] *The Photonics Institute and Centre for Disruptive Photonic Technologies, Nanyang Technological University, Singapore 637371, Singapore*
[*] *erp@orc.soton.ac.uk*
http://www.nanophotonics.org.uk

Abstract: Dynamic control over optical wavefronts enables focusing, diffraction and redirection of light on demand, however, sub-wavelength resolution is required to avoid unwanted diffracted beams that are present in commercial spatial light modulators. Here we propose a realistic metadevice that dynamically controls the optical phase of reflected beams with sub-wavelength pixelation in one dimension. Based on reconfigurable metamaterials and nanomembrane technology, it consists of individually moveable metallic nanowire actuators that control the phase of reflected light by modulating the optical path length. We demonstrate that the metadevice can provide on-demand optical wavefront shaping functionalities of diffraction gratings, beam splitters, phase-gradient metasurfaces, cylindrical mirrors and mirror arrays — with variable focal distance and numerical aperture — without unwanted diffraction.

OCIS codes: (240.0240) Optics at surfaces, (050.0050) Diffraction and gratings, (130.0130) Integrated optics, (160.3918) Metamaterials, (230.6120) Spatial light modulators.

References and links

1. U. Efron, ed., *Spatial Light Modulator Technology: Materials, Devices, and Applications* (CRC, 1994).
2. G. Lazarev, A. Hermerschmidt, S. Krüger, and S. Osten, *Optical Imaging and Metrology: Advanced Technologies* (Wiley-VCH Verlag GmbH & Co. KGaA, 2012, Chap. 1. LCOS Spatial Light Modulators: Trends and Applications, pp. 1–29).
3. H. Yu, J. Park, K. Lee, J. Yoon, K. Kim, S. Lee, and Y. Park, "Recent advances in wavefront shaping techniques for biomedical applications," Curr. Appl. Phys. **15**, 632–641 (2015).
4. N. I. Zheludev, "Obtaining optical properties on demand," Science **348**, 973–974 (2015).
5. T. Driscoll, H.-T. Kim, B.-G. Chae, B.-J. Kim, Y.-W. Lee, N. M. Jokerst, S. Palit, D. R. Smith, M. D. Ventra, and D. N. Basov, "Memory metamaterials," Science **325**, 1518–1521 (2009).
6. Z. L. Sámson, K. F. MacDonald, F. D. Angelis, B. Gholipour, K. Knight, C. C. Huang, E. D. Fabrizio, D. W. Hewak, and N. I. Zheludev, "Metamaterial electro-optic switch of nanoscale thickness," Appl. Phys. Lett. **96**, 143105 (2010).
7. D. J. Cho, W. Wu, E. Ponizovskaya, P. Chaturvedi, A. M. Bratkovsky, S.-Y. Wang, X. Zhang, F. Wang, and Y. R. Shen, "Ultrafast modulation of optical metamaterials," Opt. Express **17**, 17652–17657 (2009).
8. K. M. Dani, Z. Ku, P. C. Upadhya, R. P. Prasankumar, S. R. J. Brueck, and A. J. Taylor, "Subpicosecond optical switching with a negative index metamaterial," Nano Lett. **9**, 3565–3569 (2009).
9. A. E. Nikolaenko, N. Papasimakis, E. Atmatzakis, Z. Luo, Z. X. Shen, F. D. Angelis, S. A. Boden, E. D. Fabrizio, and N. I. Zheludev, "Nonlinear graphene metamaterial," Appl. Phys. Lett. **100**, 181109 (2012).
10. J. Zhang, K. F. MacDonald, and N. I. Zheludev, "Controlling light-with-light without nonlinearity," Light Sci. Appl. **1**, e18 (2012).
11. X. Fang, M. L. Tseng, J. Y. Ou, K. F. MacDonald, D. P. Tsai, and N. I. Zheludev, "Ultrafast all-optical switching via coherent modulation of metamaterial absorption," Appl. Phys. Lett. **104**, 141102 (2014).
12. J. Shi, X. Fang, E. T. F. Rogers, E. Plum, K. F. MacDonald, and N. I. Zheludev, "Coherent control of snell's law at metasurfaces," Opt. Express **22**, 21051–21060 (2014).
13. M. Papaioannou, E. Plum, J. Valente, E. Rogers, and N. Zheludev, "Two-dimensional control of light with light on metasurfaces," Light Sci. Appl. **5**, e16070 (2015).

#263883 http://dx.doi.org/10.1364/OE.24.018790
Journal © 2016 Received 23 Apr 2016; revised 3 Jun 2016; accepted 10 Jun 2016; published 5 Aug 2016
Corrected: 08 August 2016

Optics EXPRESS

14. M. Lapine, D. Powell, M. Gorkunov, I. Shadrivov, R. Marqués, and Y. Kivshar, "Structural tunability in metamaterials," Appl. Phys. Lett. **95**, 084105 (2009).
15. H. Tao, A. C. Strikwerda, K. Fan, W. J. Padilla, X. Zhang, and R. D. Averitt, "Reconfigurable terahertz metamaterials," Phys. Rev. Lett. **103**, 147401 (2009).
16. I. M. Pryce, K. Aydin, Y. A. Kelaita, R. M. Briggs, and H. A. Atwater, "Highly strained compliant optical metamaterials with large frequency tunability," Nano Lett. **10**, 4222–4227 (2010).
17. W. M. Zhu, A. Q. Liu, X. M. Zhang, D. P. Tsai, T. Bourouina, J. H. Teng, X. H. Zhang, H. C. Guo, H. Tanoto, T. Mei, G. Q. Lo, and D. L. Kwong, "Switchable magnetic metamaterials using micromachining processes," Adv. Mater. **23**, 1792–1796 (2011).
18. J. Y. Ou, E. Plum, L. Jiang, and N. I. Zheludev, "Reconfigurable photonic metamaterials," Nano Lett. **11**, 2142–2144 (2011).
19. J. Y. Ou, E. Plum, J. Zhang, and N. I. Zheludev, "An electromechanically reconfigurable plasmonic metamaterial operating in the near-infrared," Nat. Nanotechnol. **8**, 252–255 (2013).
20. J. Valente, J. Y. Ou, E. Plum, I. J. Youngs, and N. I. Zheludev, "Reconfiguring photonic metamaterials with currents and magnetic fields," Appl. Phys. Lett. **106**, 111905 (2015).
21. J. Valente, J. Y. Ou, E. Plum, I. J. Youngs, and N. I. Zheludev, "A magneto-electro-optical effect in a plasmonic nanowire material," Nat. Commun. **6**, 7021 (2015).
22. R. Thijssen, E. Verhagen, T. J. Kippenberg, and A. Polman, "Plasmon nanomechanical coupling for nanoscale transduction," Nano Lett. **13**, 3293–3297 (2013).
23. R. Thijssen, T. J. Kippenberg, A. Polman, and E. Verhagen, "Parallel transduction of nanomechanical motion using plasmonic resonators," ACS Photonics **1**, 1181–1188 (2014).
24. K. Yamaguchi, M. Fujii, T. Okamoto, and M. Haraguchi, "Electrically driven plasmon chip: Active plasmon filter," Appl. Phys. Express **7**, 012201 (2014).
25. R. Thijssen, T. J. Kippenberg, A. Polman, and E. Verhagen, "Plasmomechanical resonators based on dimer nanoantennas," Nano Lett. **15**, 3971–3976 (2015).
26. N. I. Zheludev and E. Plum, "Reconfigurable nanomechanical photonic metamaterials," Nat. Nanotechnol. **11**, 16–22 (2016).
27. S. Prasanna and S. M. Spearing, "Materials selection and design of microelectrothermal bimaterial actuators," J. Microelectromech. Syst. **16**, 248–259 (2007).
28. P. Cencillo-Abad, E. Plum, E. T. F. Rogers and N. I. Zheludev, "Spatial optical phase-modulating metadevice with subwavelength pixelation," University of Southampton ePrints research repository (2016), http://dx.doi.org/10.5258/SOTON/384976.
29. O. K. Ersoy, *Diffraction, Fourier Optics and Imaging* (John Wiley & Sons, 2006).
30. Z. Liu, A. Boltasseva, R. H. Pedersen, R. Bakker, A. V. Kildishev, V. P. Drachev, and V. M. Shalaev, "Plasmonic nanoantenna arrays for the visible," Metamaterials **2**, 45–51 (2008).
31. D. M. Bloom, "Grating light valve: revolutionizing display technology," Proc. SPIE **3013**, 165–171 (1997).
32. O. Solgaard, *Photonic Microsystems: Micro and Nanotechnology Applied to Optical Devices and Systems* (Springer Science & Business Media, 2009).
33. E. Hasman, V. Kleiner, G. Biener, and A. Niv, "Polarization dependent focusing lens by use of quantized pancharatnam-berry phase diffractive optics," Appl. Phys. Lett. **82**, 328–330 (2003).
34. N. Yu, P. Genevet, M. A. Kats, F. Aieta, J.-P. Tetienne, F. Capasso, and Z. Gaburro, "Light propagation with phase discontinuities: Generalized laws of reflection and refraction," Science **334**, 333–337 (2011).
35. S. Sun, K.-Y. Yang, C.-M. Wang, T.-K. Juan, W. T. Chen, C. Y. Liao, Q. He, S. Xiao, W.-T. Kung, G.-Y. Guo, L. Zhou, and D. P. Tsai, "High-efficiency broadband anomalous reflection by gradient meta-surfaces," Nano Lett. **12**, 6223–6229 (2012).
36. T. Roy, A. E. Nikolaenko, and E. T. F. Rogers, "A meta-diffraction-grating for visible light," J. Opt. **15**, 085101 (2013).
37. P. Cencillo-Abad, J. Y. Ou, J. Valente, E. Plum, and N. I. Zheludev, "Randomly addressable reconfigurable photonic metamaterials." in "5th Int. Topical Meeting on Nanophotonics and Metamaterials, Seefeld in Tirol, Austria," (2015).

1. Introduction

The ability to control amplitude and phase of light at will with sub-wavelength spatial resolution would enable applications from dynamic focusing, diffraction and beam steering to video holography and programmable transformation optics. Sub-wavelength spatial control would allow effectively continuous variation of optical properties, avoiding unwanted diffracted beams that necessarily occur in established spatial light modulators based on liquid crystal or digital micromirror technology due to their pixelation on the order of 10 μm [1–3]. While deformable mirror technologies avoid diffraction, they suffer from even lower resolution determined by their typical actuator pitch of hundreds of microns. In this manuscript we define "resolution" as the

Optics EXPRESS

smallest characteristic distance between points where the optical properties of the spatial light modulator can be independently controlled.

Technologies with the potential to achieve fast dynamic control over light with much higher spatial resolution are now emerging in the field of metamaterials and metasurfaces [4]. Metamaterials are media that obtain enhanced or unusual properties from artificial structuring on the sub-wavelength scale and therefore they do not suffer from unwanted diffraction, however, dynamic control over their optical properties with sub-wavelength resolution remains a challenge. In principle, dynamic control of light by a metamaterial can be achieved by (i) modification of constituent materials based on phase transitions [5,6] or nonlinearities [7–9], (ii) coherent optical control of the light-matter interaction [10–13] or (iii) mechanical rearrangement of the metamaterial's structure [14–21]. While the spatial resolution of — optically induced — phase transitions, nonlinearities and coherent control can be far greater than that of conventional spatial light modulators, it is still diffraction limited. In contrast, the pixelation of nano-electro-mechanically actuated metamaterials is determined by nanofabrication technology, rather than light. Recently, nanomembrane technology emerged as a practical solution for such reconfigurable metamaterials [18–21] and similar optomechanical nanostructures [22–25] operating in the optical part of the spectrum: a dielectric membrane of nanoscale thickness (typically silicon nitride) serves as a flexible support for a thin film of plasmonic metal (typically gold) or high index dielectric (such as silicon), which is then structured by reactive ion etching and focused ion beam milling to selectively remove either one or both layers, creating both metamaterial resonators and moving parts. Electrical reconfiguration is most easily achieved by cutting a metal-coated nanomembrane into freestanding parallel nanowires, which may be actuated with microsecond scale response times by electrostatic forces [19], resistive heating or the magnetic Lorentz force [20, 21].

The scope of this paper is to propose a feasible design of a randomly addressable metadevice and to study the optical functionalities it can provide numerically. We propose a metasurface device that modulates the phase of light with sub-wavelength spatial resolution in one dimension. The metadevice consists of an array of plasmonic nanowires of sub-wavelength spacing, which can be actuated individually by electrical signals in order to control the phase of reflected waves and it is feasible based on recent advances in reconfigurable photonic metamaterials [26]. We demonstrate that such a metadevice can perform functionalities of gratings, phase-gradient metasurfaces and curved mirrors on demand and without unwanted diffracted beams that necessarily occur in conventional technology. Thus, this work illustrates the ultimate level of control over light that becomes possible when a metadevice becomes a spatial light modulator with one-dimensional subwavelength pixelation by studying the optical functionalities of a randomly addressable reconfigurable nanowire metamaterial for the first time. In contrast to previous reconfigurable nanowire metamaterials, the proposed device is non-resonant, broadband / wavelength tuneable, provides spatial light modulation in addition to temporal light modulation and manipulates reflected rather than transmitted light.

2. Results and discussion

The nanomembrane device considered here can be made by focused ion beam milling and consists of 32 parallel nanowires of 300 nm width separated by 100 nm gaps, Fig. 1(a) shows a feasibility test with fewer nanowires of slightly larger period. The nanowires are fixed at both ends and consist of a gold layer of 50 nm thickness supported by a silicon nitride layer of the same thickness. One end of each nanowire is connected to a common ground, while the other is connected to one of 32 electrical control channels to allow independent actuation of each nanowire. The nanowires reflect electromagnetic waves that are linearly polarized with the electric field along the wire without polarization change and the phase of the reflected wave is controlled by displacing the nanowire in the direction normal to the device plane. As illustrated by Fig. 1(b), at normal incidence, a nanowire displacement of Δz changes the path of the reflected

Optics EXPRESS

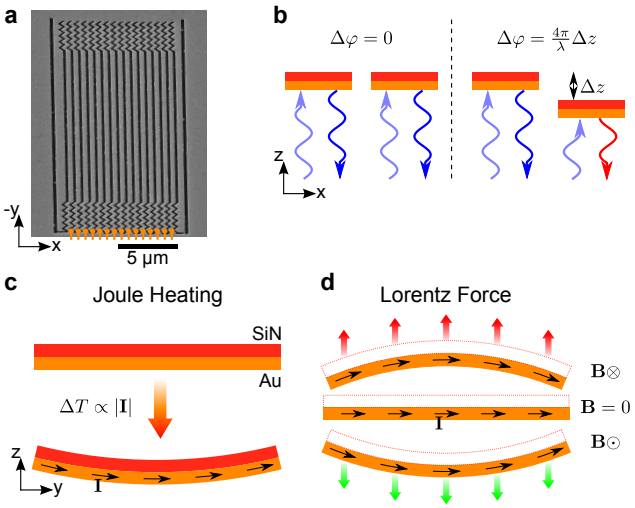

Fig. 1. Phase modulation by nanomechanical actuation. (a) Scanning electron microscope image of freestanding nanowires suitable for thermal and magnetic actuation. The nanowires consist of 50 nm of gold on 50 nm of silicon nitride, their overall length is 20 μm including 3 μm elastic springs at either end and their period is about 600 nm. (b) Out-of-plane nanowire displacement Δz changes the phase of the reflected wave by $\Delta\varphi = 4\pi\lambda\Delta z$. (c) Electrothermal actuation: resistive heating by electrical currents induces nanowire displacement by differential thermal expansion [20]. (d) Magnetic actuation: The magnetic Lorentz force displaces current-carrying wires placed in a magnetic field directed perpendicular to the current flow [21]. Magnetic actuation does not require the silicon nitride layer (red dotted line).

wave by $-2\Delta z$, resulting in a phase change $\Delta\varphi = 4\pi\lambda\Delta z$. As this is a non-resonant effect, the metadevice operates over the full wavelength range where its nanowire periodicity p_0 is smaller than the wavelength ($\lambda > p_0 = 400$ nm) — which avoids unwanted diffraction — and where the achievable maximum nanowire displacement is at least half a wavelength so that the full range of phases can be accessed ($\lambda \leq 2\Delta z_{max}$). Therefore, our non-resonant plasmonic structure is a wavelength tuneable metadevice, making it very different from the resonant, and therefore narrow-band, functionalities offered by most metamaterials.

Electrical actuation of the nanowires can be achieved exploiting two mechanisms. As illustrated by Fig. 1(c), resistive heating of a gold/silicon nitride nanowire by an electrical current I will bend the nanowire due to differential thermal expansion as the thermal expansion coefficient of gold ($14.2 \times 10^{-6}K^{-1}$) exceeds that of silicon nitride ($2.8 \times 10^{-6}K^{-1}$) by a factor of 5. Neglecting the temperature variation along the wire for simplicity, the resulting nanowire displacement is proportional to $\Delta T\Delta\alpha L^2/t$, where ΔT is the temperature change (proportional to the applied current), $\Delta\alpha$ the difference in thermal expansion coefficients, L the nanowire length and t its thickness [27]. If the nanowire metadevice is placed in a magnetic field $\vec{B}$, then it can also be actuated by the magnetic Lorentz force $\vec{F} = LI \times \vec{B}$ resulting in displacement of the nanowires of width w that is proportional to $\vec{F}L^3/(t^3w)$. Such magnetic actuation can also be applied to electrically conductive nanowires consisting of a single material and it allows the actuation direction to be inverted by reversing the direction of either current or magnetic field, see Fig. 1(d). Electrothermal displacements of 100s of nm due to application of sub-mA currents to nanowires of 10s of μm length have been reported and similar magnetic displacements have been observed for magnetic fields of 100s of mT [20]. For such structures, electrothermal actuation is limited by the nanowire cooling timescale to 10s of kHz, while mechanical resonances limit magnetic

Optics EXPRESS

actuation to 100s of kHz [21]. Here we present simulations of on-demand optical functionalities that can be expected from the metadevice.

Grating and mirror functionalities were simulated using finite element modelling (COMSOL Multiphysics 4.4), approximating the device with nanowires that have prescribed displacements and infinite length. The simulation results are shown by Figs. 2-4 and the data are available as Dataset 1 (Ref. [28]). In order to minimize computational requirements, the field reflected from the grating structures (that require larger models due to diffracted beams, see Figs. 2 and 4) was extracted at a distance of 2 μm from the metadevice and propagated in free space by the beam propagation method using Matlab [29]. The gold side of the nanowire device is illuminated by a normally incident coherent plane wave of green light (wavelength $\lambda = 550$ nm) that is polarized with the electric field parallel to the wires. Gold and silicon nitride were modelled using electric permittivities of $\varepsilon_{Au} = -5.8 + i1.6$ and $\varepsilon_{SiN} = 4.0$, respectively [30]. All simulations presented here consider nanowires consisting of 50 nm of gold supported by 50 nm of silicon nitride. For gold-side illumination as discussed below, we note that simulations of the same nanowire arrangement with and without the silicon nitride layer yield almost identical results.

Grating functionalities result from displacing the nanowires periodically in space, see Fig. 2, where diffraction of order m at an angle θ from the normal is determined by the grating period p_g of the structure following $\sin\theta = m\lambda/p_g$. Thus, without nanowire displacement, the metadevice's period of 400 nm does not allow diffraction of visible light at normal incidence. Equal displacement of every second nanowire results in a diffraction grating of 800 nm period. It can be operated as a beam splitter or grating light valve [31, 32], where a displacement of $\lambda/4$ causes destructive interference of 0^{th} order reflection due to the π phase difference for waves reflected from neighboring nanowires and thus all reflected light is redirected into the 1^{st} diffraction order [panel (a)]. We note that only one of the nanowires at the device edges is displaced as the metadevice has an even number of nanowires, resulting in a small asymmetry that can be seen around $x = 0$. Equal displacement of every third nanowire switches the metadevice to a grating of 1200 nm period, resulting in diffraction up to the 2^{nd} order. Here, mirror-symmetric displacement results in equal intensities of diffraction orders $\pm m$ [panel (b)], while mirror-asymmetric displacement such as a sawtooth configuration corresponds to a blazed grating and allows light to be preferentially diffracted into selected diffraction orders [panel (c)]. A sawtooth configuration can also be used to create a constant phase gradient along the metadevice surface by displacing the nanowires in N steps of $\lambda/(2N)$, corresponding to phase steps of $2\pi/N$ and a phase gradient of $2\pi/(Np_0)$. In the phase-gradient configuration, the metadevice will reflect the incident light into a single 1^{st} diffraction order, for example, for $N = 4$ the phase gradient is $2\pi/(1600\text{ nm})$, resulting in (almost) complete reflection of the normally incident beam at 20° from the surface normal [panel (d)]. Arbitrary phase gradients can be realized by interpolation. In this way, the metadevice can provide anomalous reflection of phase-gradient metasurfaces [33–36], but, crucially, the device is electrically controllable allowing on-demand beam steering.

Broadband focusing and defocusing cylindrical mirrors can be realized by displacing the nanowires to approximate a cylindrical segment, where the focal distance corresponds to half of the radius of curvature, see Fig. 3. Concave mirrors focus light [panel (a)], where a focal distance of 38.5 μm results from a maximum nanowire displacement of only 250 nm. A defocusing mirror is realized by a convex nanowire configuration [panel (b)], where the same maximum displacement results in reflection of the incident plane wave as if it originated from an imaginary focal point 38.5 μm behind the metadevice. Independent control of every nanowire can be used to create multifocal devices where the position and numerical aperture of every focus can be set independently, for example, a reflector with 3 focal points consisting of 3 concave cylindrical mirrors formed by 11 nanowires each [panel (c)]. We note that neighboring concave mirrors have one nanowire in common, leaving an extra nanowire at one edge of the 32-nanowire-metadevice that causes a small asymmetry. Such mirrors are broadband, suitable for

Optics EXPRESS

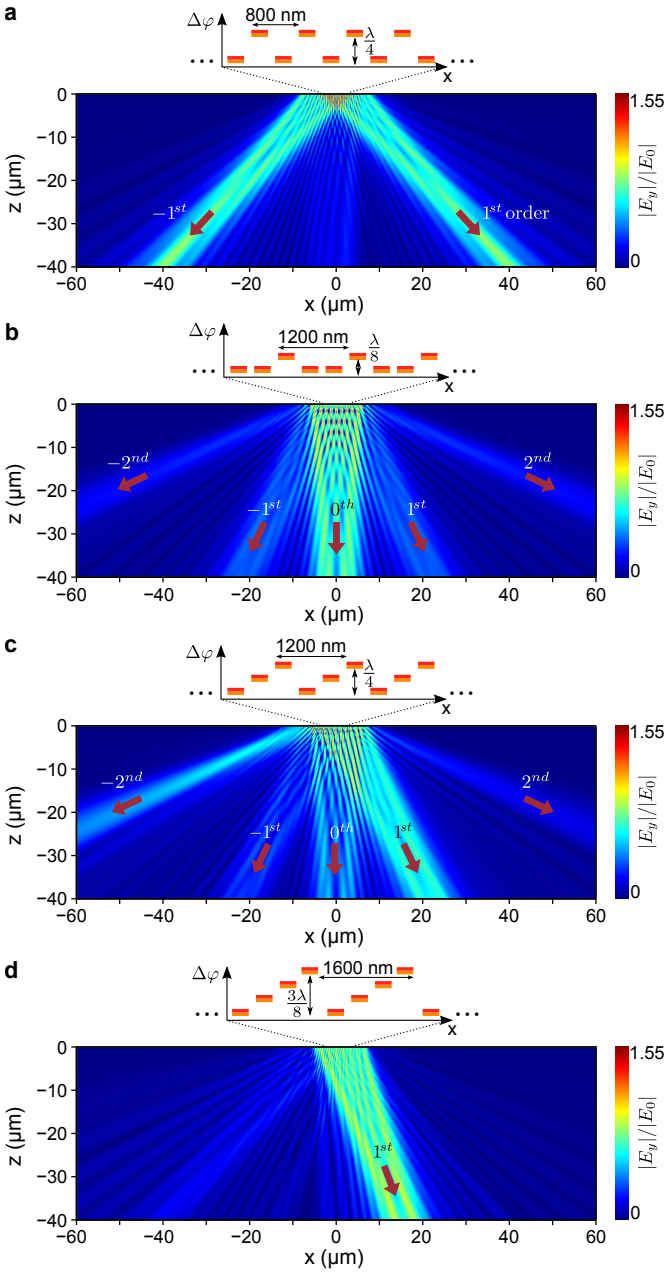

Fig. 2. Reconfigurable gratings are formed by spatially periodic vertical displacement of the nanowires. (a) Grating light valve (beam splitter) of period $p_g = 800$ nm realized by $\lambda/4$ actuation of every second nanowire. (b) Grating of period $p_g = 1200$ nm resulting from $\lambda/8$ displacement of every third nanowire. (c) Blazed grating ($p_g = 1200$ nm) and (d) phase-gradient surface ($p_g = 1600$ nm) based on a sawtooth configuration of the nanowires that are displaced in steps of $\lambda/8$. The magnitude of the only non-zero reflected electric field component $|E_y|$ is shown and the metadevice, that is located at $z = +2$ μm, is illuminated by a y-polarized plane wave of 550 nm wavelength and electric field amplitude $|E_0|$ propagating along the positive z-axis. The diffraction orders are labelled and marked by arrows.

Optics EXPRESS

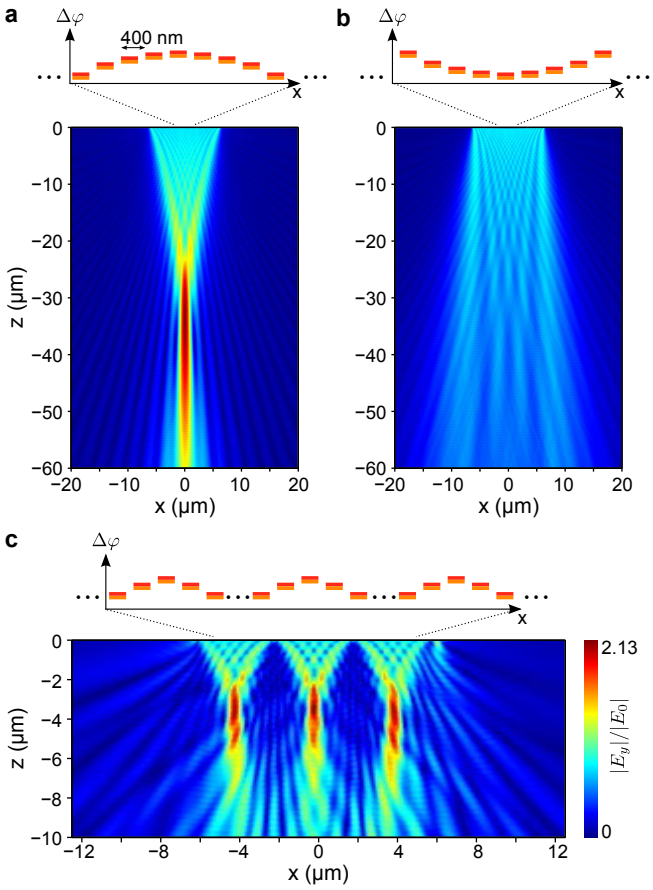

Fig. 3. Reconfigurable mirrors. (a) Focusing and (b) defocusing mirrors with 38.5 μm focal length formed by arranging the nanowires to form concave and convex cylindrical segments, respectively. (c) Multifocal mirror array, where each mirror of 3.3 μm focal length is formed by a concave cylindrical arrangement of 11 nanowires. The maximum nanowire displacement is 250 nm in all cases. The magnitude of the only non-zero reflected electric field component $|E_y|$ is shown and the metadevice, that is located at $z = 0$, is illuminated by a y-polarized plane wave of 550 nm wavelength and electric field amplitude $|E_0|$ propagating along the positive z-axis.

Optics EXPRESS

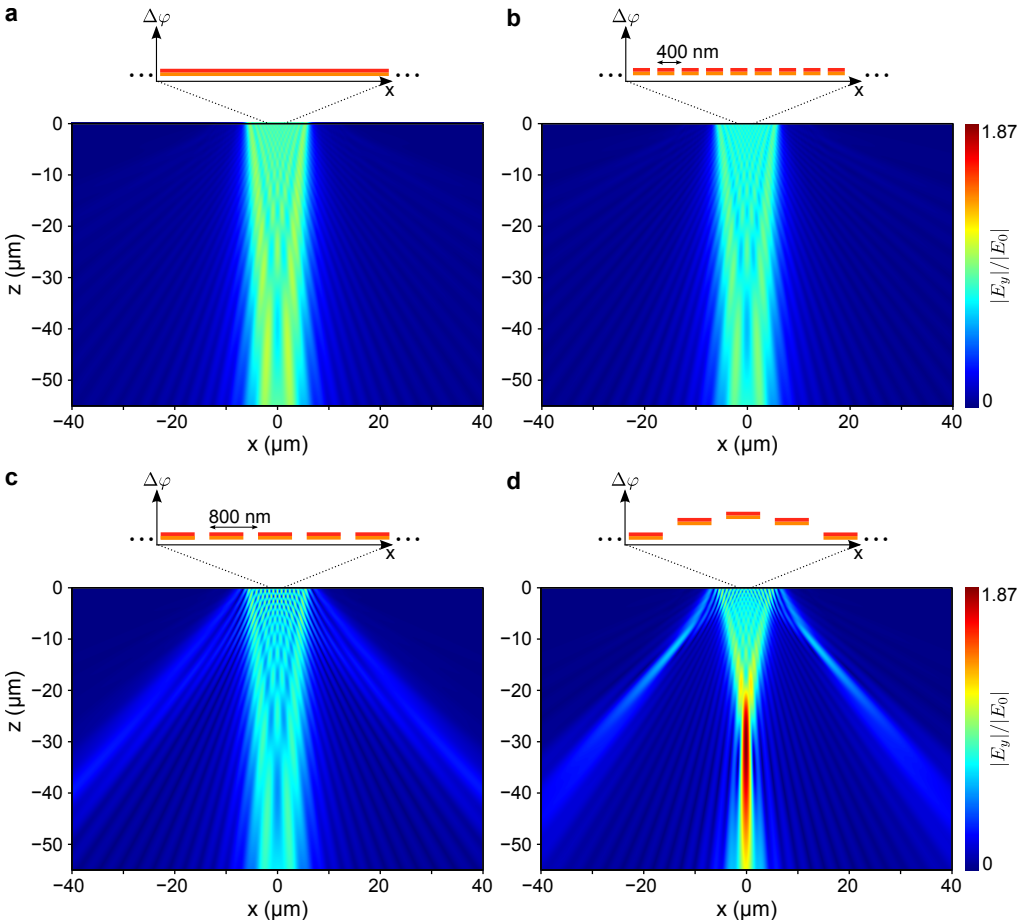

Fig. 4. Metadevices with and without sub-wavelength nanowire actuator pitch. (a) Flat continuous mirror of 12.7 μm width. (b) Flat mirror configuration of the nanowire metadevice with sub-wavelength period of 400 nm and overall width of 12.7 μm. (c) Flat mirror configu-ration of a coarser metadevice, where the period is doubled to 800 nm. (d) The metadevice with 800 nm periodicity in the same focusing mirror configuration as presented in Fig. 3(a) for the metadevice of period 400 nm. The magnitude of the only non-zero reflected electric field component $|E_y|$ is shown and the structures, that are located at $z = +2$ μm, are illuminated by a y-polarized plane wave of 550 nm wavelength and electric field amplitude $|E_0|$propagating along the positive z-axis.

illuimination wavelengths that are larger than the nanowire periodicity p_0 while being small compared to the size of each individual cylindrical mirror.

In contrast to established spatial light modulators, the proposed metadevice offers sub-wavelength pixelation and Fig. 4 illustrates the importance of this. Without actuation, the metadevice reflects the incident visible light without diffracted beams like a flat mirror [compare panels (a) and (b)]. The microstructure that can be seen in the field distribution originates from diffraction of the incident plane wave on the device edges in the same way as it does for the flat continuous mirror of the same size and it vanishes during propagation to the far field. In contrast, a coarser structure with a period that is larger than the wavelength of the incident wave will have diffracted beams [panel (c)] and these unwanted beams will be present in any applications [such as focusing, panel (d)], just as they are present in the case of commercial spatial light modulators.

Optics EXPRESS

As such potentially dangerous stray beams remove intensity from the intended application, their absence in case of our metadevice increases both safety and energy efficiency.

With respect to the realization of a functional device, we demonstrate that the fabrication of a suitable nanowire structure is possible. Indeed, similar metadevices are being developed and individual electrical actuation of several selected nanowires was recently demonstrated [37]. We note that aluminum and silver (with a protective coating to prevent oxidation) may be more suitable alternatives to gold, due to their higher reflectivity in the blue part of the spectrum. Here, we consider gold as both electrothermal and magnetic actuation of gold-based nanowire structures has been demonstrated experimentally [20, 21]. Furthermore, the actuated nanowires will be flat only at their center, but curved towards their ends. Therefore, optical illumination should be limited to the central part of the nanowires in order to ensure a homogeneous optical response. While independent and simultaneous addressing of 32 nanowires remains an engineering challenge, such devices are feasible using existing fabrication techniques, and should be realisable in the near future. All required ingredients are available, the challenge is one of design, optimization and engineering in order to ensure reliable and simultaneous independent actuation of all nanowires.

3. Summary

In summary, we propose a metadevice providing dynamic spatial modulation of optical phase with sub-wavelength pixelation in one dimension. We show that the realization of such a device is feasible and demonstrate based on numerical modelling that it can focus and redirect light by providing optical functionalities of various types of gratings, beam splitters, phase-gradient surfaces and curved mirrors on demand. In contrast to existing spatial light modulator technologies, our proposed device does not create unwanted diffracted beams, making it safer and more optically efficient than current solutions in addition to allowing higher resolution modulation.

Acknowledgments

This work is supported by the MOE Singapore (grant MOE2011-T3-1-005), the Leverhulme Trust and the UK's Engineering and Physical Sciences Research Council (grants EP/G060363/1 and EP/M009122/1). The data from this paper are available as Dataset 1 (Ref. [28]).

Giant Nonlinearity of an Optically Reconfigurable Plasmonic Metamaterial

Jun-Yu Ou, Eric Plum, Jianfa Zhang, and Nikolay I. Zheludev**

From the demonstration of saturable absorption by Wawilow and Levshin in 1926,[1] and with invention of the laser, unavailability of strongly nonlinear materials was a key obstacle for developing optical signal processing, in particular in transparent telecommunication networks. Today, most advanced photonic switching materials exploit gain dynamics[2] and near-band and excitonic effects in semiconductors,[3] nonlinearities in organic media with weakly-localized electrons[4] and nonlinearities enhanced by hybridization with metamaterials.[5] Here we report on a new type of artificial nonlinearity that is nano-optomechanical in nature. It was observed in an artificial metamaterial array of plasmonic metamolecules supported by a flexible nanomembrane. The nonlinearity is underpinned by a reversible light-induced reconfiguration of the nanostructure. In a film of only 100 nm thickness, we demonstrate modulation of light with light using milliwatt power telecom diode lasers.

Some exceptional opportunities for developing engineered nonlinear media are provided by reconfigurable nanostructures that take advantage of the changing balance of forces at the nanoscale.[6–9] With the decrease in the physical dimensions of a system, the electromagnetic forces between constituent elements grow, as may be illustrated by the repulsion of electrons as their separation diminishes. In contrast, elastic forces, such as the force restoring a compressed spring, decrease with size. Moreover, nanoscale metamaterial building blocks have high natural frequencies and thus can be moved very fast, potentially offering GHz switching bandwidth for elements of sub-micrometer size.

Recently, this was exploited to develop reconfigurable metamaterials fabricated on elastic membranes of nanoscale thickness. These photonic metamaterials can be driven thermally[10] and by electromagnetic forces, such as the Coulomb force between charged elements of the nanostructure,[11] or the Lorentz force acting on currents running through conductive elements in magnetic field.[12] Their electro-optical and magneto-optical switching characteristics surpass those of natural media by orders of magnitude.

Metamaterials are in essence arrays of optical resonators where light-induced nanomechanical phenomena can play crucial roles. For instance, it has been suggested that near-field[13] and Casimir forces[14,15] in metamaterials are modified by the presence of light. Forces between oscillating plasmonic or displacement currents induced by light in metamolecules were also theoretically shown to be sufficient to drive reconfiguration of a metamaterial structure in the optical part of the spectrum,[16–18] and proof-of-principle experiments on such interactions between individual metamolecules have been reported at microwave frequencies.[19]

Here we show that reversible reconfiguration of a plasmonic metamaterial nanostructure driven by optical forces between its illuminated elements can be the source of a strong optical nonlinearity. We show that this cubic nonlinearity may be used to modulate light with light at milliwatt power levels. Moreover, although for the majority of media the magnitude of nonlinearity tends to be proportional to its response time, the nano-optomechnical nonlinearity can modulate light at three orders of magnitude higher frequencies than could be expected from this otherwise universal trend.

The plasmonic nanomechanical metamaterial was fabricated on strips of suspended dielectric membrane of nanoscale thickness in such a way that plasmonic elements of the metamolecules were located on different strips. Here light illumination leads to electromagnetic and thermal forces that induce nanoscale strip displacements and thus reconfiguration of individual metamolecules in a way that affects their plasmonic resonances, see **Figure 1**. This leads to modulation of the metamaterial's transmissivity at different wavelengths. The nonlinear response of metamaterial, that is only 100 nm thick, can be observed at only a few milliwatts of continuous laser power, using lasers operating at telecommunication wavelengths.

We developed optically reconfigurable metamaterial on the basis of a Π-shaped resonator design known for exhibiting plasmon-induced transparency,[20,21] see Figure 1 and Figure S1a (Supporting Information). To allow mechanical deformation of the 700 nm × 700 nm plasmonic Π metamolecules, the horizontal and vertical gold bars were supported by different flexible silicon nitride strips of 28 μm length spaced by alternating gaps of 95 and 145 nm. The nanostructure was fabricated by focused ion beam milling from a 50 nm thick silicon nitride membrane covered by 50 nm of gold. Such structures can be reconfigured: i) by differential thermal expansion through light-induced heating of the bimorph gold and silicon nitride layers, and ii) by near-field optical forces acting between elements of illuminated plasmonic resonators.

Dr. J. Y. Ou, Dr. E. Plum, Dr. J. Zhang, Prof. N. I. Zheludev
Optoelectronics Research Centre and Centre for Photonic Metamaterials
University of Southampton
Southampton SO17 1BJ, UK
E-mail: erp@orc.soton.ac.uk; niz@orc.soton.ac.uk
Dr. J. Zhang
College of Optoelectronic Science and Engineering
National University of Defense Technology
Changsha 410073, China
Prof. N. I. Zheludev
The Photonics Institute and Centre for Disruptive Photonic Technologies
Nanyang Technological University
Singapore 637378, Singapore

DOI: 10.1002/adma.201504467

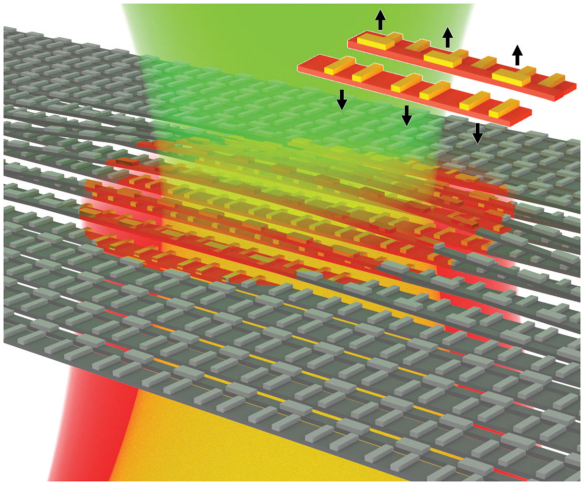

Figure 1. Nonlinearity in optically reconfigurable metamaterial. Light-induced (red) forces in the plasmonic metamaterial array cause nanoscale reversible displacements of its small and light building blocks supported by an elastic nanomembrane. They move fast, with a response time reaching microseconds. These displacements change the plasmonic spectra of the metamaterial array and its transmission. This is used to modulate another, weaker beam of light (green) at a different wavelength.

Experimental measurements and full 3D Maxwell simulations show a pronounced near-infrared absorption resonance at ≈1240 nm wavelength, see **Figure 2**a and Figure S1b (Supporting Information). Maxwell stress tensor calculations[16] assuming normal incidence illumination of the nondiffracting, periodic metamaterial reveal optical forces acting on the Π-resonators around this resonance, see Figure 2b,c. As the normally incident photons only carry momentum along the z-direction the net force must be directed along z and must comply with the momentum transfer associated with absorption A and reflection R, $F_{z1} + F_{z2} = (A + 2R)P/c$, where P is the incident power per unit cell area and c is the speed of light in vacuum. In close agreement with this relationship, our simulations show substantial differential optical forces $F_2 - F_1$ between the unit cell's strip segments reaching ≈0.4 P/c along y and 2.8 P/c along z.

Optical forces in such metamaterial nanostructures can be understood as time-averaged Coulomb and Lorentz forces acting between the currents and oscillating dipole charges of the plasmonic resonators in the presence of the illuminating electromagnetic wave.[18] For example, repulsive and attractive optical forces within the metamaterial plane for illumination at wavelengths of 1310 and 1550 nm correspond to repulsive and attractive interaction of the dipole charges on neighboring strips, see Figure 2a,b. Forces normal to the metamaterial plane result from a combination of optical pressure and the Lorentz force acting on the moving charges of the plasmonic mode in the presence of the incident wave's magnetic field.

We investigated the nonlinear optical properties of the metamaterial in a pump–probe experiment as presented in **Figure 3**a. As the pump and probe optical sources we used fiber-coupled telecommunication laser diodes operating at the wavelengths of 1550 and 1310 nm, respectively. The intensity of the pump beam was modulated by a fiber-coupled electro-optical modulator. The pump and probe were then combined into a single beam

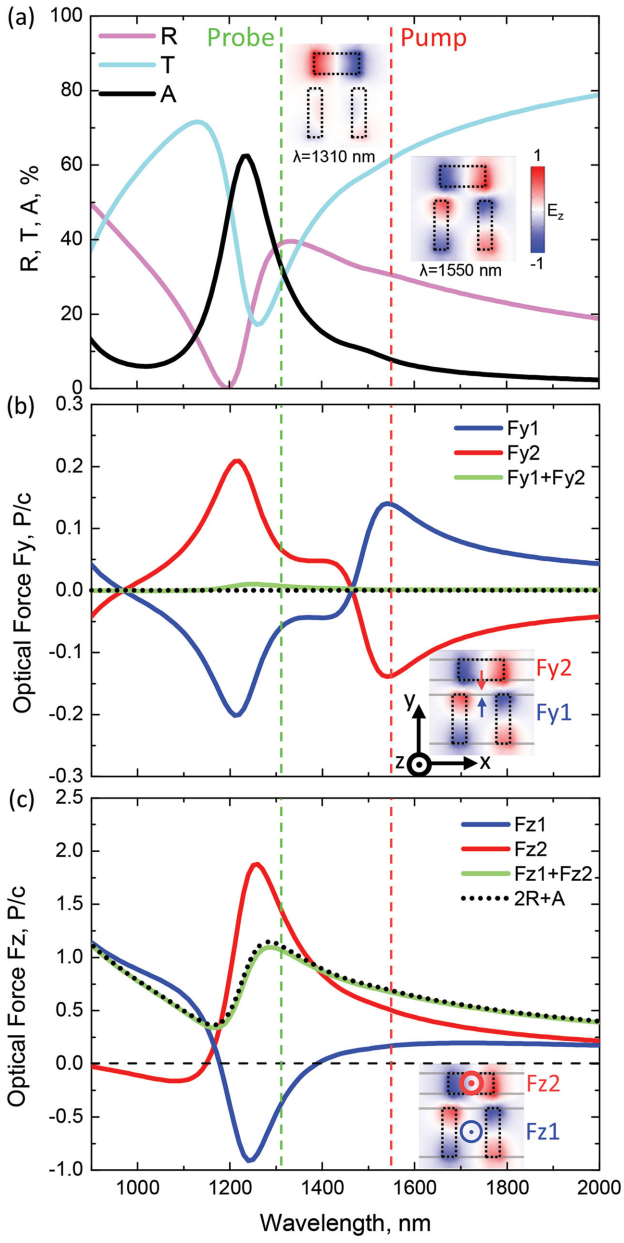

Figure 2. Optical spectra and optical forces. a) Simulated metamaterial refection R, transmission T, and absorption A spectra. Insets show maps of the optically induced charge distributions at the probe and pump wavelengths in terms of the instantaneous electric field E_z that these charges generate normal to the metamaterial surface. The maps are normalized to the maximum of E_z. b) In-plane-of-metamaterial component of optical forces $F_{y1,2}$ acting between the strip segments of an individual unit cell according to Maxwell stress tensor calculations. c) Normal to the metamaterial component of optical forces $F_{z1,2}$ acting on the strip segments along the light propagation direction. The total optical force on the unit cell (green line) is presented alongside the value expected from reflection and absorption (dotted black line). Forces are shown per unit cell in units of P/c, where P is the incident power per unit cell and c is the speed of light in vacuum. All quantities are shown for x-polarized illumination of the silicon nitride side.

using a fiber coupler, decoupled into free space and focused on the sample placed in a microscope using focusing and collection objectives. The sample was placed in a cell evacuated to

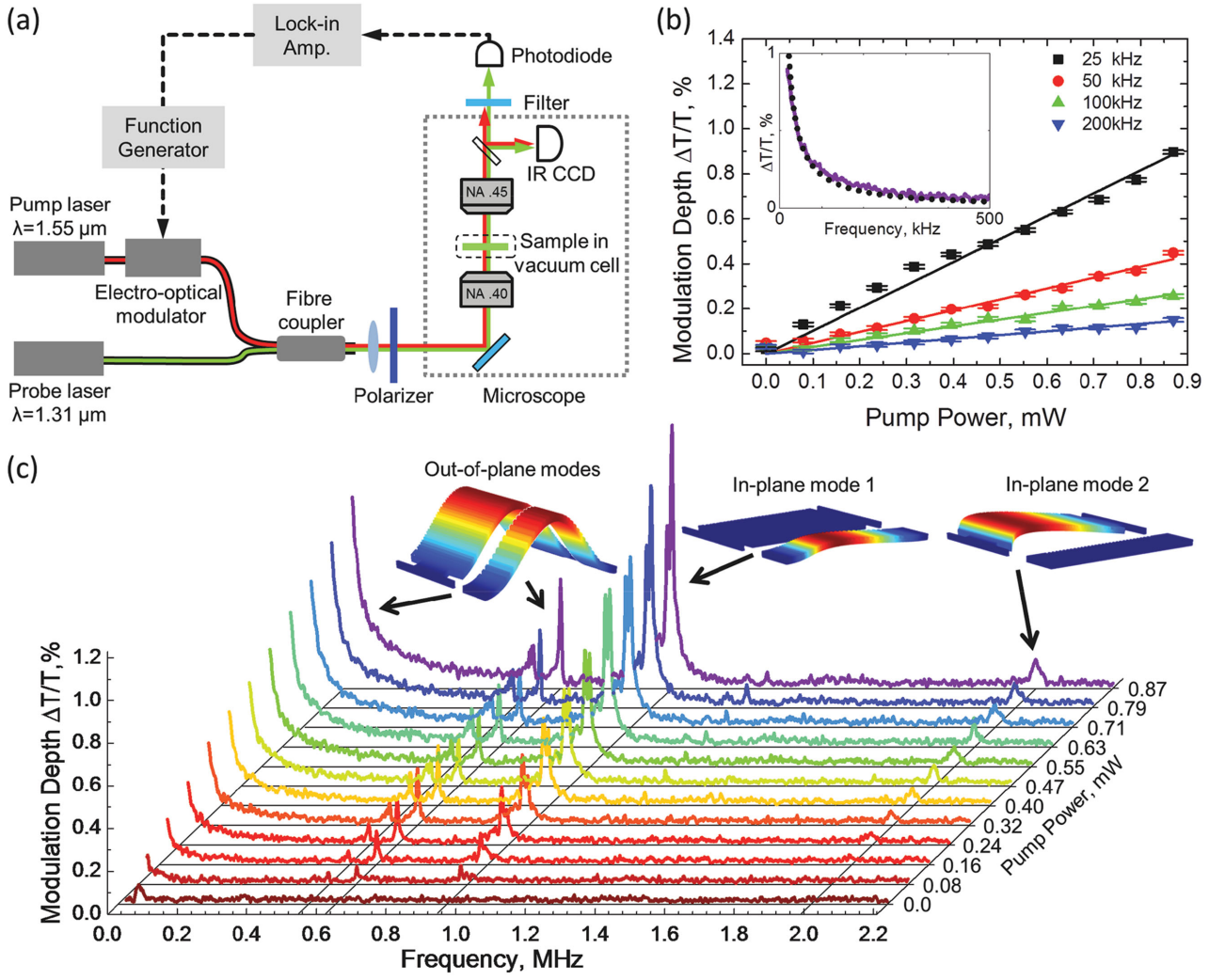

Figure 3. Modulating light with light using optically reconfigurable metamaterial. a) Schematic of the pump–probe experimental setup. b) Probe transmission modulation depth at $\lambda = 1310$ nm as a function of pump power for several pump modulation frequencies ν with linear fits (solid lines). The inset shows a hyperbolic fit (proportional to $1/\nu$, black dotted line) of the thermal modulation tail for a pump power of 0.9 mW. c) Modulation depth as a function of pump laser power and modulation frequency. Corresponding mechanical modes of the metamaterial nanostructure are shown near resonant peaks. The pump modulation depth is close to 100% in all cases.

the pressure of 30 Pa to prevent damping of the nanomechanical motion. Probe light transmitted through the sample was detected by an InGaAs photodetector and a lock-in amplifier locked to the pump modulation frequency. In order to optimize the light-induced nano-optomechanical modulation, we pumped the nanostructure at 1550 nm just above its absorption resonance, where simulations predict significant in-plane forces.

At low modulation frequencies, below 100 kHz, the optical pump leads to pronounced modulation of the metamaterial's transmission at the probe wavelength, see Figure 3c. For 0.9 mW pump power (peak intensity 9.2 μW μm^{-2}) a modulation amplitude on the order of 1% is observed at 25 kHz modulation. This is an exceptionally large effect considering that the interaction length of light and metamaterial is less than one tenth of a wavelength. In contrast, in conventional nonlinear optical media interaction lengths much larger than the wavelength are required to accumulate significant effects.

The low-frequency component of the nonlinear response has a thermal nature and drops rapidly with increasing modulation frequency, fading at a few 100s of kHz. In this frequency range, the modulation amplitude halves as the modulation frequency doubles which is consistent with a thermal deformation of the bimorph Au/SiN_x membrane, see inset to Figure 3b. This is also consistent with thermal calculations for 50 nm gold[22] and silicon nitride[23] layers, which predict conductive cooling timescales on the order of 20–30 μs. The light-induced heating of the nanostructure is balanced by heat conduction along the metamaterial strips and according to our calculations can reach hundreds of degrees for a pump intensity of 10 μW μm^{-2}. As the thermal expansion coefficient of gold (14.4×10^{-6} K^{-1}) exceeds that of silicon nitride (2.8×10^{-6} K^{-1}) fivefold such large temperature changes will bend the strips. When heated to the same temperature, narrow strips will rise higher than wider strips due to more complete

gold coverage; the metamolecule changes its shape and therefore its plasmonic absorption and transmission for the probe wavelength change.

While the thermal nonlinearity easily dominates at low modulation frequencies, other modulation mechanisms are at play at higher frequencies. Indeed, as differential thermal expansion in the layered structure can only drive motion out of the metamaterial plane, it should not drive in-plane resonant oscillations of the metamaterial strips. Several resonant peaks of nonlinear response are seen at much higher frequencies ≈600 kHz, 1 MHz, and 2 MHz, see Figure 3c. Mechanical eigenmode calculations identify the resonances as the fundamental modes of oscillation of the narrow and wide strips, corresponding to vibration normal to the metamaterial plane (≈600 kHz) and motion within the metamaterial plane (at MHz frequencies), see insets. Comparing the sub-microsecond heating and cooling cycles to the characteristic strip cooling timescale, we argue for their nonthermal origin.

To assess the origin of the high frequency modulation, we estimate the optomechanical deformation that can be expected from the optical forces acting between different parts of the metamolecular resonator. Based on the simulations presented in Figure 2c, pump-induced optical forces reach 0.5 P/c (0.2 P/c) for the narrow (wide) strips. For a strip pair with 29 unit cells and 9.2 μW μm^{-2} pump intensity, this corresponds to ≈220 fN (90 fN) force per strip. Estimating the spring constant k from strip mass m and measured resonance frequency ν as $k = (2\pi\nu)^2 m = 28$ fN pm^{-1} (56 fN pm^{-1}) for out-of-plane deformation, we may expect the gap between strips and thus between elements of the metamolecule to change by 6 pm. Corresponding estimates for in-plane deformation predict a gap change on the order of 1 pm. Such modulation is not sufficient to create a detectable level of nonresonant high-frequency modulation. However, much larger displacements are expected at the structure's mechanical resonances, where the displacement will be enhanced by the quality factor of the mechanical resonator. Our optical measurements show mechanical resonance quality factors on the order of 100, which may serve as a lower limit for the quality factor of mechanical resonances of individual strips as the overall resonance profile is affected by inhomogeneous broadening due to slight structural variations from strip to strip. Taking this enhancement into account, optical forces should be sufficient to induce resonant strip displacements on the order of 1 nm, which is consistent with the observed resonant transmission modulation on the order of 1%. Therefore we argue that the resonant response at 600 kHz, 1 MHz, and 2 MHz is predominantly driven by nonthermal, optical forces.

Absorption in a nonlinear medium is conventionally described by the expression:

$$-\frac{\mathrm{d}I}{\mathrm{d}z} = \alpha I + \beta I^2 + \ldots \quad (1)$$

where I is the light intensity, z is the propagation distance, and α and β are the linear and nonlinear absorption coefficients. As the observed nonlinear transmission change is proportional to the pump power, we can quantify the nonlinearity of the reconfigurable photonic metamaterial by estimating its first nonlinear absorption coefficient β. Assuming that the nonlinear transmission change ΔT results from nonlinear absorption, $\beta \approx \Delta T/(It)$, where t is the metamaterial's thickness. At 1 MHz modulation frequency, $\beta \approx 5 \times 10^{-3}$ m W^{-1} corresponding to a nonlinear susceptibility on the order of $Im(\chi^{(3)})/n^2 \approx 10^{-12}$ m^2 V^{-2} and a nonlinear imaginary refractive index change $\Delta\kappa \approx 5 \times 10^{-3}$ at 9.2 μW μm^{-2} pump intensity. We argue here that the observed nano-optomechanical nonlinearity is special as it exhibits a departure from the prevailing relation between speed and magnitude of nonlinear responses (**Figure 4**). This happens in a way that allows larger nonlinearity or higher modulation frequency to be achieved than could be expected from traditional media. Indeed, it appears that for many mechanisms of optical nonlinearity the achievable modulation frequency ν is related to the magnitude of the nonlinearity $\chi^{(3)}$ in such a way that $\chi^{(3)}\nu \approx 10^{-9}$ m^2 V^{-2} s^{-1}.[24] At the resonance of in-plane motion, MHz rate modulation can be achieved at 10 μW μm^{-2} of light intensity corresponding to $\chi^{(3)}\nu \approx 10^{-6}$ m^2 V^{-2} s^{-1}.

The magnitude of the observed nonlinearity is controlled by the magnitude of the light-induced strip displacement and the displacement sensitivity of the metamaterial's optical properties. Therefore, the observed nonlinearity may be increased further by optimizing the design of the metamolecules to achieve higher quality factor optical resonances and stronger electromagnetic coupling between the moving parts of the unit cell at the pump and near the probe wavelengths. Higher quality factor optical resonances exhibit higher sensitivity to perturbations as well as increased optical forces and they may be achieved by substituting gold for a lower loss plasmonic material, such as silver, or an almost lossless high index dielectric as suggested recently.[16] Stronger electromagnetic coupling between the moving parts of the unit cell may also be achieved by reducing their spacing. Furthermore, longer strips will increase the magnitude of the nonlinearity by increasing the light-induced displacement but

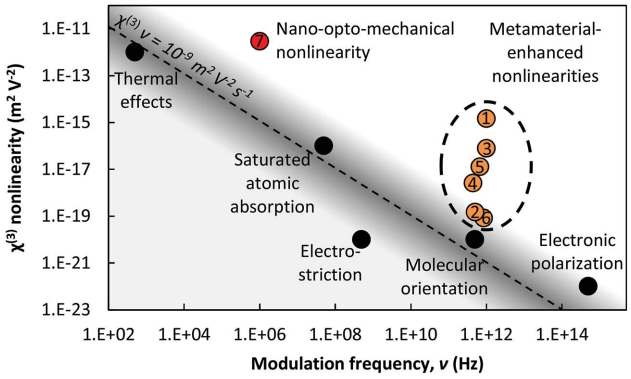

Figure 4. Optical nonlinearities in metamaterials and conventional media. Cubic optical nonlinearities due to thermal effects, saturated absorption, molecular orientation, and electronic anharmonicity follow a general trend of decreasing achievable modulation frequency ν with increasing magnitude of the nonlinearity: $\chi^{(3)}\nu \approx 10^{-9}$ m^2 V^{-2} s^{-1}.[24] Metamaterial patterning of plasmonic metal[25,26] (points 1 and 2) as well as hybridization of carbon nanotubes[27] (point 3), graphene[28] (point 4), and semiconductors[29,30] (points 5 and 6) with metamaterials resonantly enhances the magnitude of the nonlinear response without affecting its response time. Optically reconfigurable metamaterial demonstrated in the present work also departs from the common trend exhibiting $\chi^{(3)}\nu$ that is three orders of magnitude bigger than in conventional nonlinear media (point 7).

will also have lower mechanical resonance frequencies due to a reduced spring constant and increased mass.

Larger modulation amplitudes will result from nanomechanical structures with higher nonlinearity (as detailed above) as well as increasing the pump power (Figure 3). Thus, the achievable modulation amplitude for a given structure is limited by its thermal damage threshold. For slow modulation—relative to the structure's cooling timescale—thermal damage is controlled by the peak intensity, while thermal damage for fast modulation is controlled by the average intensity, thus allowing for a two times higher peak intensity. Therefore, we expect that the resonant high frequency modulation in our experimental structure can be increased to several percent by increasing the pump power.

In summary, we provide the first experimental demonstration of a giant nano-optomechanical nonlinearity in plasmonic metamaterial that allows modulation of light with light at MHz frequencies and milliwatt power levels. Bimorph deformation resulting from optical heating at low modulation frequencies and electromagnetic forces between elements of plasmonic resonators drive the nonlinear response. The magnitude and spectral position of the underlying optical resonance can be controlled across the optical spectral range by design of the plasmonic resonators and the supporting nanomembrane strips.

Experimental Section

Plasmonmechanical Metamaterial Fabrication: Starting with a commercially available 50 nm thick low stress silicon nitride membrane, a 50 nm thick gold layer for the plasmonic metamaterial was thermally evaporated. The gold-coated membrane was structured with a focused ion beam system (FEI Helios 600 NanoLab). The pattern of plasmonic resonators was milled and then the supporting silicon nitride membrane was cut into suspended strips with tapered ends. Detailed dimensions of the nanostructure are given in Figure S1b (Supporting Information).

Experimental Characterization: The cubic nonlinearity was measured by detecting the pump-induced modulation of the metamaterial's transmission (Figure 3a). The probe beam at wavelength 1310 nm was generated by a fiber-coupled telecom laser diode (Thorlabs FPL1053S). The pump beam from a fiber-coupled laser diode at wavelength 1550 nm (Thorlabs FPL1009S) was modulated with a fiberized electro-optical modulator (EOSpace AX-0K5-10-PFA-UL) and then combined with the probe beam in a fiber coupler (JDSU L2SWM1310/1550BB). The transmitted beam was filtered to remove the pump and the probe signal was detected by an InGaAs photodetector (New Focus 1811) and a lock-in amplifier (Stanford Research SR844). In all optical experiments and simulations the electric field was *x*-polarized (parallel to the strips) and incident on the silicon nitride side of the sample.

Supporting Information

Supporting Information is available from the Wiley Online Library or from the author. The data from this paper can be obtained from the University of Southampton ePrints research repository: http://dx.doi.org/10.5258/SOTON/377861.

Acknowledgements

The authors are grateful to Artemios Karvounis for fruitful discussions and to Pablo Cencillo-Abad for assistance in preparing the paper. This work was supported by the Leverhulme Trust, the Royal Society, the U.S. Office of Naval Research (Grant No. N000141110474), the MOE Singapore (Grant No. MOE2011-T3-1-005), and the UK's Engineering and Physical Sciences Research Council (Grant No. EP/G060363/1).

Received: September 11, 2015
Revised: October 1, 2015
Published online: November 30, 2015

[1] S. J. Wawilow, W. L. Lewschin, *Z. Phys.* **1926**, *35*, 920.
[2] D. Cotter, R. J. Manning, K. J. Blow, A. D. Ellis, A. E. Kelly, D. Nesset, I. D. Phillips, A. J. Poustie, D. C. Rogers, *Science* **1999**, *286*, 1523.
[3] U. Keller, *Nature* **2003**, *424*, 831
[4] C. Bosshard, K. Sutter, P. Prêtre, J. Hulliger, M. Flörsheimer, P. Kaatz, P. Günter, *Organic Nonlinear Optical Materials*, CRC Press, Basel, Switzerland, **2001**.
[5] M. Lapine, I. V. Shadrivov, Y. S. Kivshar, *Rev. Mod. Phys.* **2014**, *86*, 1093.
[6] M. Aspelmeyer, P. Meystre, K. Schwab, *Phys. Today* **2012**, *65*, 29.
[7] R. Thijssen, E. Verhagen, T. J. Kippenberg, A. Polman, *Nano Lett.* **2013**, *13*, 3293.
[8] V. V. Yakovlev, W. Dickson, A. Murphy, J. McPhillips, R. J. Pollard, V. A. Podolskiy, A. V. Zayats, *Adv. Mater.* **2013**, *25*, 2351.
[9] R. Thijssen, T. J. Kippenberg, A. Polman, E. Verhagen, *ACS Photonics* **2014**, *1*, 1181.
[10] J. Y. Ou, E. Plum, L. Jiang, N. I. Zheludev, *Nano Lett.* **2011**, *11*, 2142.
[11] J. Y. Ou, E. Plum, J. Zhang, N. I. Zheludev, *Nat. Nanotechnol.* **2013**, *8*, 252.
[12] J. Valente, J. Y. Ou, E. Plum, I. J. Youngs, N. I. Zheludev, *Nat. Commun.* **2015**, *6*, 7021.
[13] J. Zhang, K. F. MacDonald, N. I. Zheludev, *Phys. Rev. B* **2012**, *85*, 205123.
[14] F. Rosa, D. Dalvit, P. Milonni, *Phys. Rev. Lett.* **2008**, *100*, 183602.
[15] R. Zhao, J. Zhou, T. Koschny, E. Economou, C. Soukoulis, *Phys. Rev. Lett.* **2009**, *103*, 103602.
[16] J. Zhang, K. F. MacDonald, N. I. Zheludev, *Light Sci. Appl.* **2013**, *2*, e96.
[17] R. Zhao, P. Tassin, T. Koschny, C. M. Soukoulis, *Opt. Express* **2010**, *18*, 256656.
[18] J. Zhang, K. F. MacDonald, N. I. Zheludev, *Opt. Lett.* **2014**, *39*, 4883.
[19] M. Lapine, I. V. Shadrivov, D. A. Powell, Y. S. Kivshar, *Nat. Mater.* **2012**, *11*, 30.
[20] S. Zhang, D. A. Genov, Y. Wang, M. Liu, X. Zhang, *Phys. Rev. Lett.* **2008**, *101*, 047401.
[21] N. Papasimakis, N. I. Zheludev, *Opt. Photonics News* **2009**, *20*, 22.
[22] G. Chen, P. Hui, *Appl. Phys. Lett.* **1999**, *74*, 2942.
[23] D. R. Queen, F. Hellman, *Rev. Sci. Instrum.* **2009**, *80*, 063901.
[24] R. W. Boyd, *Nonlinear Optics*, 3rd ed., Academic Press, San Diego, CA, USA, **2008**.
[25] M. Ren, B. Jia, J. Y. Ou, E. Plum, J. Zhang, K. F. MacDonald, A. E. Nikolaenko, J. Xu, M. Gu, N. I. Zheludev, *Adv. Mater.* **2011**, *23*, 5540.
[26] G. A. Wurtz, R. Pollard, W. Hendren, G. P. Wiederrecht, D. J. Gosztola, V. A. Podolskiy, A. V. Zayats, *Nat. Nanotechnol.* **2011**, *6*, 107.
[27] A. E. Nikolaenko, N. Papasimakis, A. Chipouline, F. D. Angelis, E. D. Fabrizio, N. I. Zheludev, *Opt. Express* **2012**, *20*, 6068.
[28] A. E. Nikolaenko, N. Papasimakis, E. Atmatzakis, Z. Luo, Z. X. Shen, F. D. Angelis, S. A. Boden, E. D. Fabrizio, N. I. Zheludev, *Appl. Phys. Lett.* **2012**, *100*, 181109.
[29] D. Cho, W. Wu, E. Ponizovskaya, P. Chaturvedi, A. Bratkovsky, S. Wang, X. Zhang, F. Wang, Y. Shen, *Opt. Express* **2009**, *17*, 176527.
[30] K. M. Dani, Z. Ku, P. C. Upadhya, R. P. Prasankumar, S. R. J. Brueck, A. J. Taylor, *Nano Lett.* **2009**, *9*, 3565.

PERSPECTIVE | FOCUS
PUBLISHED ONLINE: 7 JANUARY 2016 | DOI: 10.1038/NNANO.2015.302
nature nanotechnology

Reconfigurable nanomechanical photonic metamaterials

Nikolay I. Zheludev[1,2] and Eric Plum[1]

The changing balance of forces at the nanoscale offers the opportunity to develop a new generation of spatially reconfigurable nanomembrane metamaterials in which electromagnetic Coulomb, Lorentz and Ampère forces, as well as thermal stimulation and optical signals, can be engaged to dynamically change their optical properties. Individual building blocks of such metamaterials, the metamolecules, and their arrays fabricated on elastic dielectric membranes can be reconfigured to achieve optical modulation at high frequencies, potentially reaching the gigahertz range. Mechanical and optical resonances enhance the magnitude of actuation and optical response within these nanostructures, which can be driven by electric signals of only a few volts or optical signals with power of only a few milliwatts. We envisage switchable, electro-optical, magneto-optical and nonlinear metamaterials that are compact and silicon-nanofabrication-technology compatible with functionalities surpassing those of natural media by orders of magnitude in some key design parameters.

Metamaterials — artificial electromagnetic media structured on a size scale smaller than the wavelength of external stimuli — were first developed to exhibit unusual properties, such as negative index of refraction, asymmetric transmission, invisibility or optical magnetism. They stimulated the development of devices such as optical cloaks and super-resolution lenses. Now research is focused on tunable, nonlinear, switchable, gain-assisted, sensor and quantum metamaterials that show growing potential for practical device integration[1]. The next challenge is to develop random access metamaterials with on-demand optical properties, where every individual 'metamolecule' may be independently controlled at any given point in space and at any moment of time. This will allow modulation of the intensity and phase of light, as well as control of the wavefront and the near-field of electromagnetic radiation, thus enabling multi-channel optical data processing[2]. Compared with commercial liquid crystal spatial light modulators offering kilohertz modulation and pixel sizes of about $10 \times 10\ \mu m^2$, emerging technologies for random access metamaterials promise two orders of magnitude higher pixel densities and up to six orders of magnitude faster modulation frequencies. However, the development of randomly accessible photonic metamaterials is challenging: the metamolecules must be subwavelength optical switches with a fraction of a square micrometre footprint and a physical volume of only $\sim 10^{-19}\ m^3$. To have an impact on telecommunications technologies, such switches must be fast and consume energy at a competitive level not prohibitive to their deployment.

Exceptional opportunities to address this challenge are provided by nanomechanical devices that take advantage of the changing balance of forces at the nanoscale (Box 1). With the decrease in the physical dimensions of a system, the electromagnetic forces between constituent elements grow, as illustrated by the repulsive force between electrons as their separation diminishes. In contrast, elastic forces, such as the force restoring a deformed beam, decrease with size (Box 2). At the submicrometre dimensions of the metamolecules in photonic metamaterials, electromagnetic Coulomb, Lorentz and Ampère forces compete with elastic forces and can thus be used to reconfigure the shape of individual metamolecules or to change their mutual arrangement. Here, even small movements can lead to a substantial change of the metamaterial's optical properties (Fig. 1). The nanoscale metamaterial building blocks can be moved fast, potentially offering modulation at gigahertz frequencies. Such structures can also be driven thermoelastically or by light, through optical forces arising within illuminated metamolecules (Fig. 2). Elastic structured nanomembranes are the ideal platform for such nanomechanical reconfigurable metamaterials.

This new high-throughput and silicon-compatible technology benefits from related advances in nano-optomechanics[3], which have led to the demonstration of thermally driven plasmonic nanomechanical oscillators[4,5] and resonators[6]. Nanomechanical metamaterials are being developed alongside other approaches for creating nonlinear, tunable and switchable metamaterials from the microwave to the optical parts of the spectrum, such as the phase change[7–9] and liquid crystal[10–13] hybrid metamaterial technologies, coherent control[14–19], structural reconfiguration[20,21] of metamaterials based on stretchable polymer substrates[22–26], microelectromechanical systems (MEMS)[27–37], microfluidics[38,39] and magnetic forces[40,41]; carrier injection in semiconductor metamaterial substrates[42,43] and graphene[44,45]; and superconducting metamaterials[46,47]. A detailed account of these approaches is available in recent reviews[1,48–53].

The technology for growing high-quality free-standing nanomembranes, such as ultrathin films of silicon nitride[54,55], silicon[56] and diamond[57], that are supported by bulk semiconductor frames is well established[58,59]. Such membranes are commercially available, packaged as individual membranes, arrays of membranes on silicon wafers or chip prototypes with prefabricated terminal wires (for example, Norcada, www.norcada.com; Silson, www.silson.com; Ted Pella, www.tedpella.com; SPI Supplies, www.2spi.com). Individual membranes, both polycrystalline or nearly single crystal, typically have thicknesses ranging from a few tens of nanometres to one micrometre, with overall sizes up to a few square millimetres. They are mechanically robust, chemically stable and can support plasmonic metal films deposited on them by thermal evaporation and sputtering. For prototyping work, focused ion beam milling (FIB) is extensively used to fabricate plasmonic and dielectric metamaterial patterns on such membranes, including cutting through the membrane to form individual metamolecules and free-standing strips of them[60–65]. When using FIB, the typical prototype fabrication time is between a few minutes and a few hours, depending on the complexity of the design, and faster lithographic fabrication of metamaterial patterns on membranes is being developed. Supplementary Movie 1 shows FIB fabrication of an array of metamaterial samples on a silicon nitride membrane.

[1]Optoelectronics Research Centre and Centre for Photonic Metamaterials, University of Southampton, Southampton SO17 1BJ, UK. [2]The Photonics Institute and Centre for Disruptive Photonic Technologies, Nanyang Technological University, 637371 Singapore, Singapore. e-mail: niz@orc.soton.ac.uk; erp@orc.soton.ac.uk

Box 1 | Electromagnetic forces at the nanoscale.

Elements of reconfigurable metamaterials can often be represented as nanowires. At the nanoscale, electromagnetic forces acting on such nanowires are comparable with elastic forces of the supporting structure (see Box 2) and therefore can be used to reconfigure metamaterials. Even small mutual motion of the elements of the metamaterial array can create substantial changes in its interaction with light and its optical properties (see Fig. 1).

For simplicity, let us consider two cylindrical nanowires of diameter D spaced by a centre-to-centre distance d and evaluate forces acting on a segment of nanowire of length L.

The Coulomb force. $F_{Coulomb}$ depends on the potential difference V between the nanowires, their diameter D and the distance d between them (panel **a**). The dimensionless parameter $\vartheta(D,d) \approx 1$ for realistic geometries and ε_0 is the permittivity of vacuum. For $V = 1$ V, $D = 100$ nm and $d = 500$ nm, the Coulomb force is about 5 pN per 1 μm of nanowire length L. This corresponds to an electric field acting between the nanowires that is close to the electric breakdown of air, which takes place at about 3 MV m^{-1} (ref. 82). With decreasing distance between the nanowires, the Coulomb force increases rapidly.

The Ampère force. $F_{Ampère}$ depends on the current I in the nanowires and the distance d between them (**b**); μ_0 is the vacuum permeability. It may be understood as the Lorentz force acting on the current in one nanowire due to the magnetic field caused by the current in the other. The achievable Ampère force tends to be smaller than the Coulomb force. For $I = 1$ mA and $d = 500$ nm, the Ampère force is about 0.4 pN per 1 μm of nanowire length L. The Ampère force is limited by the current that a nanowire can sustain. A gold nanowire with diameter $D = 100$ nm cannot take more than 10 mA continuous current due to the release of heat that causes melting[83], but much higher current can be sustained in the pulsed regime.

The Lorentz force. $F_{Lorentz}$ depends on the current I and magnetic field B and can be even stronger than the Coulomb force (**c**). The force is perpendicular to the current and magnetic field. For $I = 1$ mA and $B = 100$ mT, the Lorentz force is about 100 pN per 1 μm of nanowire length L. An external field B of hundreds of mT can be easily achieved with permanent neodymium and samarium-cobalt magnets.

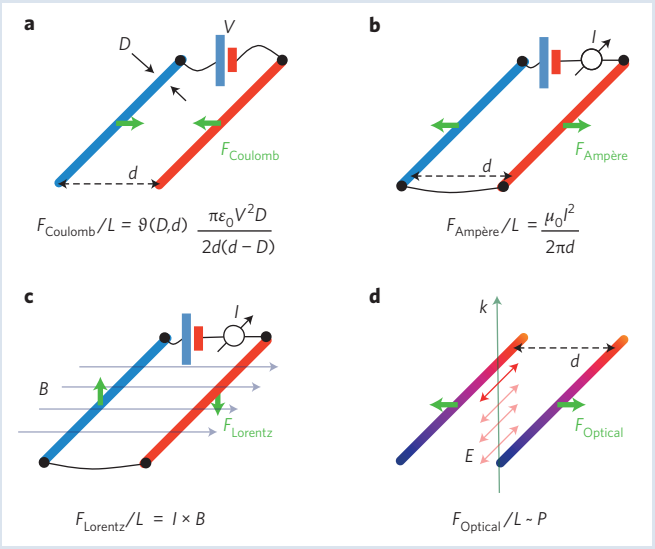

Optical force. Nanowires can also be driven by illuminating them with light. Nanowires that have a length L of approximately half of the wavelength of incident radiation act as resonant antennas for light. Light-induced oscillating dipoles in a pair of parallel nanowires will repel with time-averaged optical force $F_{Optical}$ that is proportional to the incident light intensity P, if the radiation is polarized with the electric field E parallel to the nanowires and the optical wavevector k is directed perpendicular to the plane defined by them (**d**). When such gold plasmonic nanowires of diameter $D = 100$ nm, length $L = 500$ nm and spacing $d = 300$ nm are illuminated by light with wavelength $\lambda = 925$ nm and intensity $P = 1$ mW μm^{-2}, the repelling optical force between them is about 1.5 pN.

Thermal actuation

Following the successful implementation of a thermally switchable terahertz metamaterial[21] (Fig. 2a), the first tunable nanomembrane metamaterial for the optical part of the spectrum[60] exploited thermally activated deformations of a multilayered plasmonic structure that was built by sophisticated dual-side ion beam milling on a silicon nitride membrane. It consisted of an array of plasmonic metamolecules supported by pairs of strings cut from the membrane and designed in a way that one string of the pair exhibited temperature-activated deformation while the other did not. The thermally activated string was a two-layer sandwich of materials with different thermal expansion coefficients: a 50-nm-thick gold layer and a 100-nm-thick silicon nitride layer. On increasing the ambient temperature, the bimorph string bent towards its gold side, as the thermal expansion coefficient of gold is five times larger than that of silicon nitride (Fig. 2d). The other, thermally insensitive string of the pair had a symmetric three-layered structure made of gold, silicon nitride and gold films. The alternating thermally active and thermally passive strings supported rows of C-shaped aperture resonators (split rings) with a 500 nm × 500 nm footprint. On change of the ambient temperature, relative displacement of neighbouring strings caused a change in the electromagnetic coupling of adjacent split rings. Such reconfiguration of the metamaterial, which involved nanoscale displacements of rows, strongly affected the transmission spectrum of the entire array: a temperature increase from 76 K to 270 K caused a transmission change of up to 50% at plasmonic resonances in the spectral range from 1,200 nm to 1,700 nm. Potential applications of this thermally activated metamaterial include temperature sensors, tunable spectral filters, switches and modulators. However, this simple and robust technology is relatively slow: the reaction time τ depends on the thermal conductivity of the materials involved and the geometry of the string, and can be estimated as $\tau \approx L^2 C_L/12Ak$, where L is the string length, C_L is the heat capacity per unit length, A is the cross-section of the string and k is the thermal conductivity. For metamaterial arrays with an overall size of tens of micrometres, the response time is typically on the microsecond to millisecond scale, but the practically achievable reaction time is likely to be controlled by the rate at which the ambient temperature can be changed, unless the nanostructure's temperature is controlled directly using local resistive heating by electrical currents[62,63] or heating by pulses of light[65] or an electron beam[66]. Supplementary Movie 2 shows the thermal actuation of a nanomembrane chevron metamaterial.

NATURE NANOTECHNOLOGY DOI: 10.1038/NNANO.2015.302

Box 2 | Motion at the nanoscale.

Nanowires anchored at either one or two ends are fundamental parts of the toolkit for nanomechanically reconfigurable metamaterials. A nanowire anchored at both ends of length L, diameter D, Young's modulus E and density ρ will have a fundamental natural frequency ν_1 that will rapidly increase with decreasing size of the wire (panel **a**). Using an external electromagnetic force F_{EM} it will become possible to drive submicrometre wires to frequencies approaching the gigahertz range. Indeed, as can be seen from the generic resonance curve of a driven oscillator (**b**), driving at the mechanical resonance $\nu_{EM} \approx \nu_1$ will lead to enhanced motion, the amplitude of which is controlled by the quality factor of the mechanical oscillator, but driving at frequencies far above the resonance is inefficient. The force necessary to achieve a static displacement d of the nanowire's centre against the elastic force $F_{Elastic}$ depends on the size and aspect ratio of the nanowire, as illustrated in the table for silicon nanowires (**c**): a much smaller force is needed to drive a displacement d = 10 nm in a nanowire of 100 μm length and 100 nm diameter than in a short nanowire of 1 μm length and 10 nm diameter. The same nanowire anchored at only one end (a cantilever) will have an about seven times lower resonance frequency and it will reach the same end displacement in response to a 48 times weaker force. Often more complex movements are present in nanostructures that may be exploited for spatial reconfiguration of metamaterials. For instance, depending on how the oscillator is driven and anchored, odd and even higher order modes can be excited, where in-plane and out-of-plane modes of oscillation are allowed (**d**). Note that in a nanowire with finite aspect ratio the frequencies of higher modes (ν_2 and ν_3) are not integer multiples of the fundamental natural frequency ν_1, as could be expected for an infinitely thin string, thus leading to a rich pattern of mechanical excitations that can be seen in nanostructures.

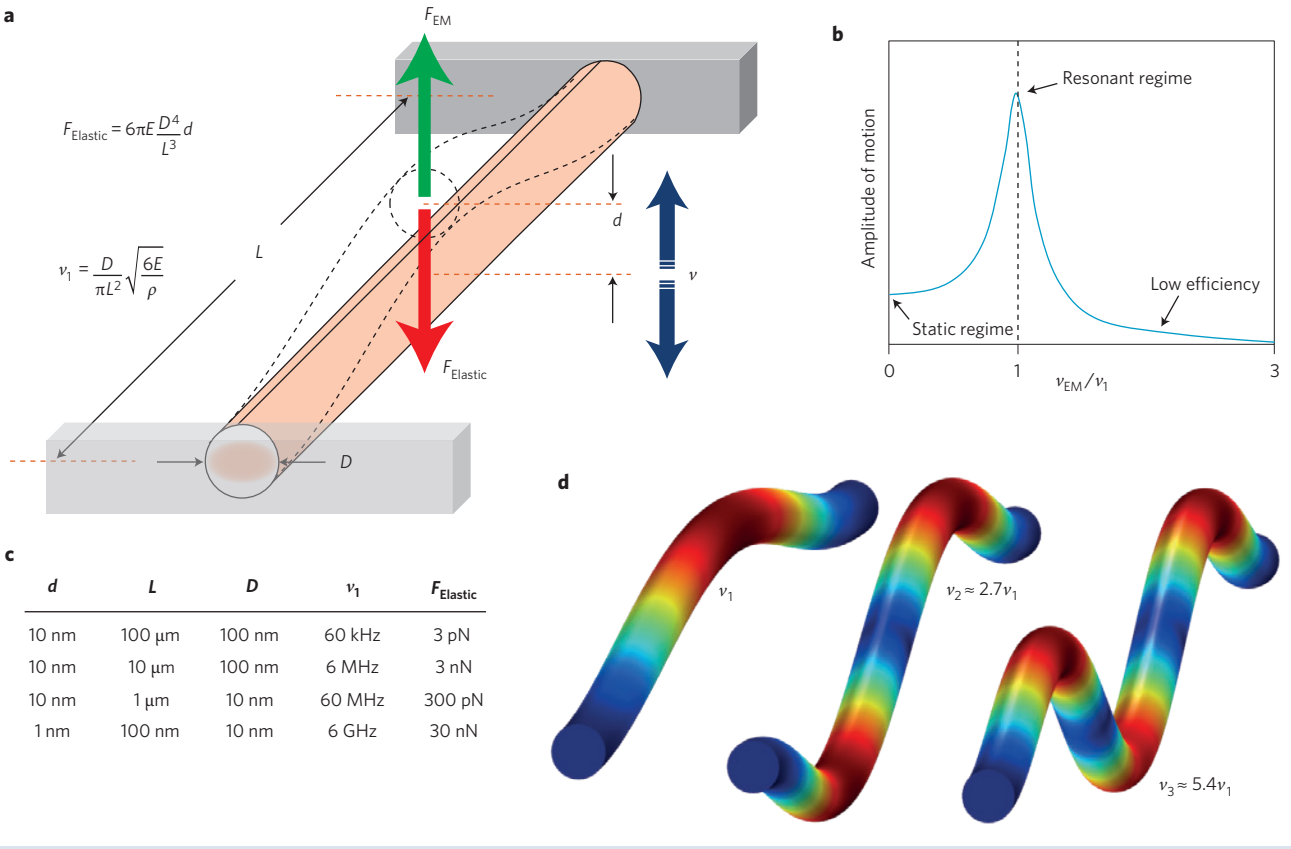

c

d	L	D	ν_1	$F_{Elastic}$
10 nm	100 μm	100 nm	60 kHz	3 pN
10 nm	10 μm	100 nm	6 MHz	3 nN
10 nm	1 μm	10 nm	60 MHz	300 pN
1 nm	100 nm	10 nm	6 GHz	30 nN

Electrostatic actuation

Engagement of the Coulomb force (panel a in Box 1) allows for the development of membrane-based devices[67] and metamaterials[61] controlled by electrical signals, which work in the visible and near-infrared spectral bands. They are orders of magnitude faster and far more compact than previously reported electrically reconfigurable terahertz MEMS comb-drive metamaterials (Fig. 2b) and — in contrast to metamaterials with opaque adjustable ground plane designs — membrane-based metamaterials can be used in transmission and reflection modes[27–37]. In the metamaterial shown in Fig. 2e, 'wire' and 'meander' parts of the metamolecules were fabricated on separate strings cut from a 100-nm-thick gold-coated silicon nitride membrane in a way that two parts of each metamolecule were placed on neighbouring strings. To increase the flexibility of the strings, their ends, which are anchored in the unstructured membrane, were narrowed to about 200 nm. Such a metamaterial can be actuated by electrostatic forces arising from the application of only a few volts to each pair of parallel strings. These strings of picogram mass can be driven to reconfigure the metamolecules synchronously across the entire array in the static and dynamic regimes. This actuation significantly changes the transmission and reflection spectra of the array. In the static regime, reversible changes of transmission and reflection spectra reaching 8% at the plasmonic resonances in the near-infrared spectral range were observed on application of voltages up to 2.4 V. Beyond that level of voltage, the neighbouring strings come so close to one another that the electrostatic force grows more rapidly than the elastic restoring force; as a result, the strings came into contact and stuck to each other due to

surface (van der Waals) forces, fusing together and short-circuiting the device. A large, irreversible 250% transmission jump around the wavelength of 1,200 nm and 110% reflectivity changes around 1,600 nm occurred due to the change of electromagnetic coupling between the plasmonic wire and meander structures (Fig. 1a). Below the critical switching voltage, the structure can be driven reversibly up to megahertz frequencies (the main natural frequency of the strings is about 1 MHz). Driving the array at mechanical resonance frequencies enhances the amplitude of motion and modulation of its optical properties. The metamaterial exhibits a complex dependence of its optical response on the frequency of electrical modulation with initial roll-off at about 0.5 MHz and resonant peaks at 1.3 and 1.6 MHz. The effective electro-optical coefficient of such an electrically driven nanomechanical metamaterial is on the order of 10^{-5}–10^{-6} m V^{-1} (at 1,600 nm wavelength), which is about four to five orders of magnitude greater than in reference natural electro-optic media, such as lithium niobate (3×10^{-11} m V^{-1} at 633 nm wavelength). Thus, electro-optical nanomembrane metamaterials could become a compact alternative for modulator applications at frequencies well into the megahertz range, where they can complement and compete with conventional bulky modulators based on the electro-optical Pockels effect in crystals. The energy required to switch the metamaterial device from the off state to the on state can be estimated as the energy required to charge the capacitive nanostructure and is as little as ~100 fJ for the entire array. Such reconfigurable metamaterials can be operated with microwatt power consumption, making them suitable for applications in ultracompact tunable spectral filters, displays, switches, modulators, adaptable transformation optics devices, protective optical circuitry and reconfigurable optical networks. Supplementary Movie 3 shows switching of a nanomembrane electro-optical metamaterial by the Coulomb force.

Magnetic actuation

Engaging the Lorentz force (panel c in Box 1) provides another mechanism for reconfiguring nanomembrane metamaterials. In a recently demonstrated artificial 'chevron' gold nanowire structure fabricated on an elastic dielectric nanomembrane, the Lorentz force drives reversible transmission changes on application of a fraction of a volt when the structure is placed in a magnetic field of a fraction of 1 T (refs 62,63). Typically, the current is less than 1 mA in each of the actuated wires of the array. The chevron pattern was chosen because it is easy to fabricate and has good longitudinal elasticity due to its spring-like shape, while providing plasmonic optical resonances and continuous electrical paths for control currents (Fig. 2f). The metamaterial was placed between the poles of permanent neodymium magnets in such a way that the field was directed along the surface of the array, but perpendicular to the nanowires. The electrical current used as the control signal is run through every second nanowire, forcing out-of-plane motion of alternating strips. The magneto-electro-optical response of this metamaterial can be separated from its thermal response caused by resistive heating by observing modulation at different frequencies. Modulation up to frequencies of hundreds of kilohertz was observed. The corresponding optical response may be quantified in terms of the change δ to the dielectric tensor ε_{ij} of the medium that is simultaneously proportional to the applied electric field E that drives the current and the magnetic field B: $\delta\varepsilon_{ij} = \chi_{ijkl}E_kB_l$ where the indices can take the values of the Cartesian coordinates x, y and z. Here the magneto-electro-optical susceptibility χ reaches a value of $\chi_{yyxy}/n \approx 10^{-4}$ mV^{-1} T^{-1}, where n is the refractive index. Remarkably, no natural media are known that show a noticeable magneto-electro-optical phenomenon of this type. This change of the dielectric properties is reciprocal, as it does not depend on the wave propagation direction[63] and the phenomenon is therefore radically different from the conventional magneto-optical Faraday effect. By engaging highly sensitive zero-balance phase detection techniques, this magnetically actuated metamaterial could be used to realize micrometre-size magnetic field sensors with sensitivity at the nanotesla level. Moreover, we argue that a dedicated optimization of the metamaterial design can lead to stronger effects suitable for practical application in light-modulation devices controllable by electrical signals and magnetic fields.

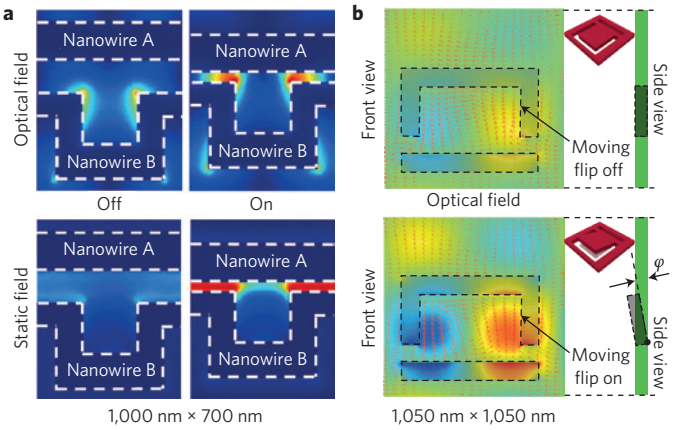

Figure 1 | Nanoscale motion and fields. a, In a plasmonic reconfigurable metamaterial[61] with a 1,000 nm × 700 nm unit cell (see also Fig. 2e) relative displacement of electrically charged nanowires A and B towards each other by about 125 nm driven by the Coulomb force leads to a large change of the resonant optical field trapped in the structure around 1,800 nm wavelength (top row), and thus to a change in the optical reflectivity and transmission of the metamaterial array. The distribution of the static electric field that drives the reconfiguration also changes dramatically (bottom row). Blue and red indicate the smallest and largest electric field, respectively. **b**, A dielectric reconfigurable metamaterial[72] with a 1,050 nm × 1,050 nm unit cell consisting of an asymmetric split-ring aperture in a silicon nanomembrane creating a moving flip (see also Fig. 2h). Dashed lines indicate areas where the membrane was removed. Both images show optical field maps (colours indicate the field strength along the unit cell's symmetry axis, where blue and red correspond to largest fields of opposite sign) and displacement currents (arrows) for illumination at a wavelength of 1,280 nm. The field distribution changes significantly when the flip is turned by an angle $\varphi = 10°$ out of the plane of the membrane. In-phase oscillations of the flips in the metamaterial array may be caused by optical forces and will lead to a change of the metamaterial's optical properties.

Optical actuation

Optical forces (panel d in Box 1) allow photonic metamaterials to be driven by light, and this leads to optical nonlinearity[41,68–71]. Building on the experimental demonstration of such nonlinearity in a microwave metamaterial[41] (Fig. 2c), this idea was extended to the optical part of the spectrum using a dielectric optomechanical metamaterial. The proposed metamaterial consists of arrays of silicon 'nanobricks' with subwavelength footprint and thicknesses alternating between 100 and 150 nm (ref. 64). Pairs of such 'bricks' support a high-quality 'trapped-mode' optical resonance. These bricks are mounted on 100-nm-thick, 250-nm-wide elastic silicon nitride strips running parallel and separated from each other by a nanoscale gap. When the wavelength of light illuminating the array is close to the trapped mode resonance, strong optical forces are generated, which act to change the spatial arrangement of the nanobricks within each unit cell and thereby the optical properties of the array. Numerical Maxwell stress tensor analysis reveals that optical forces, acting within and among the constituent cells of the dielectric metamaterial, are sufficient to produce relative movements of neighbouring beams, providing a strongly nonlinear

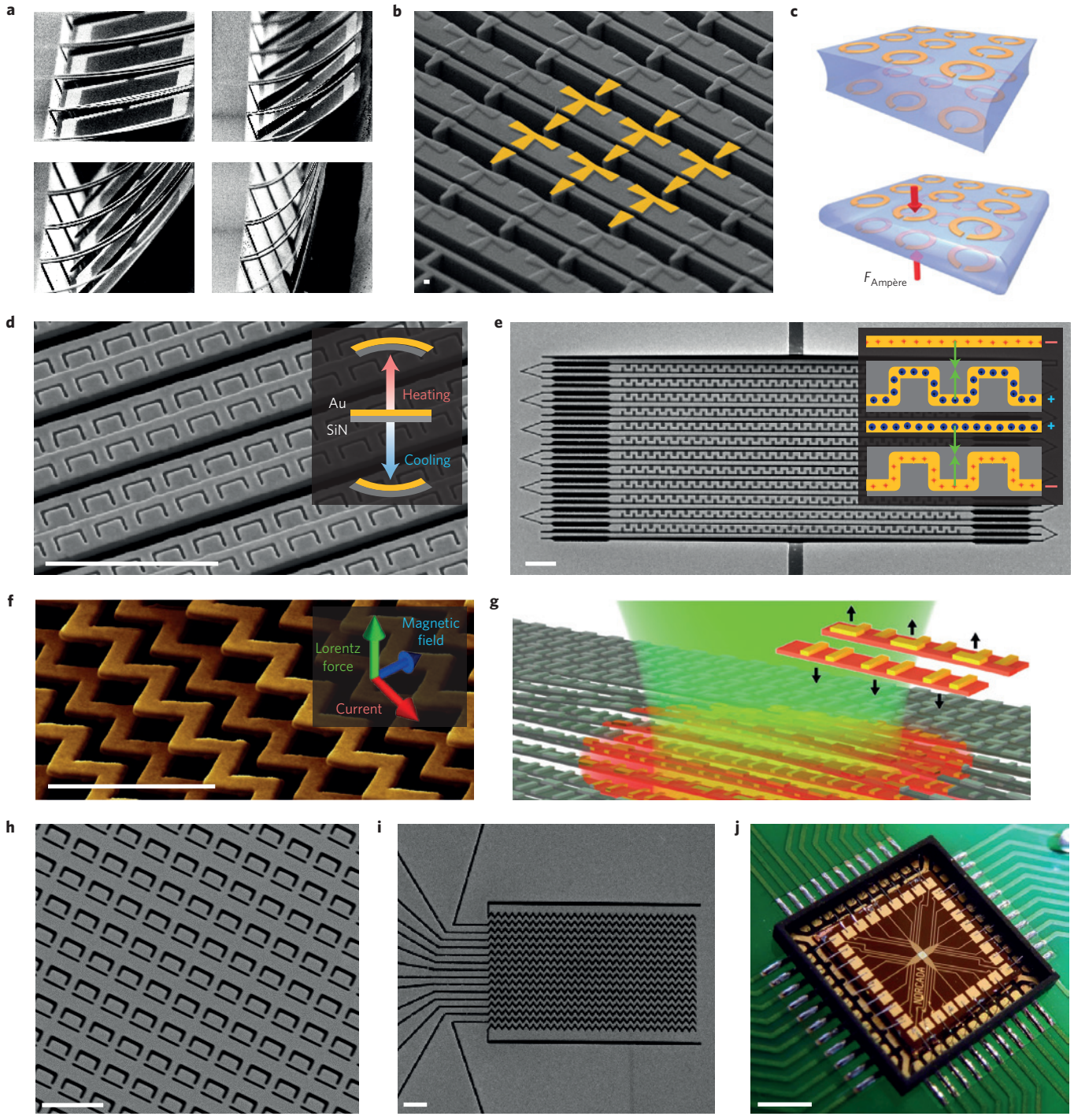

Figure 2 | Implementations of spatially reconfigurable nanomembrane metamaterials. a–c, Earlier reconfigurable metamaterials included a thermally switchable terahertz metamaterial actuated by rapid thermal annealing[21] (**a**), a terahertz metamaterial tuned by MEMS actuators[33] (**b**) and a magnetoelastic microwave metamaterial driven by Ampère's force, $F_{Ampère}$, between excited metamolecules, shown in its relaxed (top) and actuated (bottom) states[41] (**c**). **d–j**, Reconfigurable optical metadevices based on flexible strips or nanowires cut from membranes of nanoscale thickness supporting a thin film of plasmonic metal or high index dielectric. Structures controlled by various forces on the nanoscale have been reported recently. **d**, A thermally reconfigurable metamaterial driven by differential thermal expansion between gold and silicon nitride layers[60]. **e**, An electro-optical modulator: metadevice driven by electrostatic forces (green arrows) between oppositely charged nanowires (+, –)[61]. **f**, A magneto-optical modulator: nanowire structure actuated by the Lorentz force that is controlled by currents and magnetic field[63]. **g**, An all-optical modulator: plasmonic metamaterial actuated by a milliwatt of light power at telecom wavelengths, a pump beam (red) reconfigures the nanostructure (inset) resulting in modulation of a probe beam (green)[65]. **h**, A nonlinear device: all-dielectric metamaterial with a large optomechanical nonlinearity[72]. **i,j**, A spatial light modulator: electrically addressable metadevice randomly reconfigurable in one dimension. Panel **i** shows an array of individually controlled nanowires and panel **j** shows the packaging arrangement for the device[81]. Scale bars in **b**,**d**,**e**,**f**,**h**,**i**, 2 μm; **j**, 2 mm. Figure adapted with permission from: **a**, ref. 21, APS; **b**, ref. 33, Nature Publishing Group; **c**, ref. 41, Nature Publishing Group.

optical response that gives rise to high contrast all-optical modulation, asymmetric transmission and could lead to optical bistability at excitation intensity levels of only a few hundred μW μm^{-2}. An all-dielectric metamaterial exhibiting an optomechanical nonlinearity that allows modulation of light with light at 150 MHz has recently been demonstrated experimentally[72] (Fig. 2h).

Furthermore, a nano-optomechanical metamaterial was reported that realized a similar optical actuation and nonlinearity, but using plasmonic resonant structures rather than dielectric ones[65] (Fig. 2g). The nonlinearity also results from the reversible light-induced reconfiguration of the structure. Cross-wavelength modulation of light with light using continuous-wave milliwatt power telecom diode lasers operating at wavelengths of 1,310 nm and 1,550 nm was demonstrated in a nanostructure of only 100 nm thickness. To allow mechanical reconfiguration of the 700 nm × 700 nm plasmonic metamolecules, their constituent parts were supported by different flexible silicon nitride strips of 28 μm length spaced by alternating nanoscale gaps of different width. Plasmonic resonances play a key role here: a plasmonic resonance increases the driving force that reconfigures the metamaterial. Moreover, a steep plasmonic resonance near the wavelength of light probing the nanostructure enhances transmission and reflection changes caused by the reconfiguration. The nano-optomechanical plasmonically enhanced nonlinearity reaches a very large value of $\chi^{(3)}/n^2 \approx 10^{-12}$ m^2 V^{-2}, while remaining three orders of magnitude faster than could be expected from the otherwise universal trend linking response speed and magnitude of $\chi^{(3)}$ nonlinearities[73]. The optical response of the structure can be modulated to up to a few megahertz frequency and it exhibits a complex pattern that corresponds to different modes of mechanical oscillation of the strips (Box 2). At such frequencies, the viscosity of air significantly damps oscillations: placing the metamaterial in a vacuum cell increases the quality factor of its mechanical resonances and thus the magnitude of the nonlinearity.

Outlook

In conclusion, the recent proof-of-principle demonstrations of nonlinear, switching, electro-optical and magneto-optical functionalities in nanomechanical devices indicate the appearance of a new important direction for developing functional metamaterials and metadevices. We expect that nanomechanical metamaterials will impact photonic technology significantly, as they can provide light modulation in micrometre-size devices. Further improvements beyond the proof-of-principle stage are possible. Indeed, high-index dielectric resonators[72,74–79] promise lower losses and larger optical forces than plasmonic structures[80]. Silicon and silicon nitride membranes as scaffolding materials may be replaced by diamond membranes that offer higher mechanical resonances and superior thermal properties. Following the recent demonstration of microwave metamaterials with random access to individual metamolecules[39], the first generation of photonic metamaterials providing random access in a single spatial dimension has already been realized using nanomembrane technology[81] (Fig. 2i,j). Such devices can function as re-focusable lenses or dynamic dispersion elements and could be used for signal multiplexing in multi-mode or multi-core optical telecommunication technology. Supplementary Movie 4 shows actuation of individual wires in a randomly reconfigurable nanomembrane metamaterial.

Received 23 June 2015; accepted 18 November 2015; published online 7 January 2016

References

1. Zheludev, N. I. & Kivshar, Y. S. From metamaterials to metadevices. *Nature Mater.* **11,** 917–924 (2012).
2. Zheludev, N. I. Obtaining optical properties on demand. *Science* **348,** 973–974 (2015).
3. Aspelmeyer, M., Kippenberg, T. J. & Marquardt, F. Cavity optomechanics. *Rev. Mod. Phys.* **86,** 1391–1452 (2014).
4. Thijssen, R., Verhagen, E., Kippenberg, T. J. & Polman, A. Plasmon nanomechanical coupling for nanoscale transduction. *Nano Lett.* **13,** 3293–3297 (2013).
5. Thijssen, R., Kippenberg, T. J., Polman, A. & Verhagen, E. Parallel transduction of nanomechanical motion using plasmonic resonators. *ACS Photon.* **1,** 1181–1188 (2014).
6. Thijssen, R., Kippenberg, T. J., Polman, A. & Verhagen, E. Plasmomechanical resonators based on dimer nanoantennas. *Nano Lett.* **15,** 3971–3976 (2015).
7. Dicken, M. J. *et al.* Frequency tunable near-infrared metamaterials based on VO_2 phase transition. *Opt. Express* **17,** 18330–18339 (2009).
8. Driscoll, T. *et al.* Memory metamaterials. *Science* **325,** 1518–1521 (2009).
9. Sámson, Z. L. *et al.* Metamaterial electro-optic switch of nanoscale thickness. *Appl. Phys. Lett.* **96,** 143105 (2010).
10. Werner, D. H., Kwon, D.-H., Khoo, I.-C., Kildishev, A. V. & Shalaev, V. M. Liquid crystal clad near-infrared metamaterials with tunable negative-zero-positive refractive indices. *Opt. Express* **15,** 3342–3347 (2007).
11. Zhao, Q. *et al.* Electrically tunable negative permeability metamaterials based on nematic liquid crystals. *Appl. Phys. Lett.* **90,** 011112 (2007).
12. Minovich, A. *et al.* Liquid crystal based nonlinear fishnet metamaterials. *Appl. Phys. Lett.* **100,** 121113 (2012).
13. Buchnev, O., Ou, J. Y., Kaczmarek, M., Zheludev, N. I. & Fedotov, V. A. Electro-optical control in a plasmonic metamaterial hybridised with a liquid-crystal cell. *Opt. Express* **21,** 1633–1638 (2013).
14. Zhang, J., MacDonald, K. F. & Zheludev, N. I. Controlling light-with-light without nonlinearity. *Light Sci. Appl.* **1,** e18 (2012).
15. Fang, X. *et al.* Ultrafast all-optical switching via coherent modulation of metamaterial absorption. *Appl. Phys. Lett.* **104,** 141102 (2014).
16. Mousavi, S. A., Plum, E., Shi, J. & Zheludev, N. I. Coherent control of birefringence and optical activity. *Appl. Phys. Lett.* **105,** 011906 (2014).
17. Shi, J. *et al.* Coherent control of Snell's law at metasurfaces. *Opt. Express* **22,** 21051–21060 (2014).
18. Fang, X., MacDonald, K. F. & Zheludev, N. I. Controlling light with light using coherent metadevices: all-optical transistor, summator and invertor. *Light Sci. Appl.* **4,** e292 (2015).
19. Roger, T. *et al.* Coherent perfect absorption in deeply subwavelength films in the single-photon regime. *Nature Commun.* **6,** 7031 (2015).
20. Lapine, M. *et al.* Structural tunability in metamaterials. *Appl. Phys. Lett.* **95,** 084105 (2009).
This paper reports the first mechanically reconfigurable microwave metamaterial.
21. Tao, H. *et al.* Reconfigurable terahertz metamaterials. *Phys. Rev. Lett.* **103,** 147401 (2009).
This paper reports the first mechanically reconfigurable terahertz metamaterial.
22. Pryce, I. M., Aydin, K., Kelaita, Y. A., Briggs, R. M. & Atwater, H. A. Highly strained compliant optical metamaterials with large frequency tunability. *Nano Lett.* **10,** 4222–4227 (2010).
This paper reports the first mechanically reconfigurable optical metamaterial.
23. Aksu, S. *et al.* Flexible plasmonics on unconventional and nonplanar substrates. *Adv. Mater.* **23,** 4422–4430 (2011).
24. Cui, Y., Zhou, J., Tamma, V. A. & Park, P. Dynamic tuning and symmetry lowering of Fano resonance in plasmonic nanostructure. *ACS Nano* **6,** 2385–2393 (2012).
25. Lee, S. *et al.* Reversibly stretchable and tunable terahertz metamaterials with wrinkled layouts. *Adv. Mater.* **24,** 3491–3497 (2012).
26. Walia, S. *et al.* Flexible metasurfaces and metamaterials: a review of materials and fabrication processes at micro- and nano-scales. *Appl. Phys. Rev.* **2,** 011303 (2015).
27. Chicherin, D. *et al.* MEMS-based high-impedance surfaces for millimeter and submillimeter wave applications. *Microw. Opt. Technol. Lett.* **48,** 2570–2573 (2006).
28. Hand, T. Characterization of tunable metamaterial elements using MEMS switches. *IEEE Antenn. Wireless Propag. Lett.* **6,** 401–404 (2007).
29. Fu, Y. H. *et al.* A micromachined reconfigurable metamaterial via reconfiguration of asymmetric split-ring resonators. *Adv. Funct. Mater.* **21,** 3589–3594 (2011).
30. He, X., Lv, Z., Liu, B. & Li, Z. Tunable magnetic metamaterial based multi-split-ring resonator (MSRR) using MEMS switch components. *Microsys. Technol.* **17,** 1263–1269 (2011).
31. Zhu, W. M. *et al.* Switchable magnetic metamaterials using micromachining processes. *Adv. Mater.* **23,** 1792–1796 (2011).
32. Zhang, W. *et al.* Micromachined switchable metamaterial with dual resonance. *Appl. Phys. Lett.* **101,** 151902 (2012).
33. Zhu, W. M. *et al.* Microelectromechanical Maltese-cross metamaterial with tunable terahertz anisotropy. *Nature Commun.* **3,** 1274 (2012).
34. Ho, C. P. *et al.* Electrothermally actuated microelectromechanical systems based omega-ring terahertz metamaterial with polarization dependent characteristics. *Appl. Phys. Lett.* **104,** 161104 (2014).

35. Lin, Y.-S. & Lee, C. Tuning characteristics of mirrorlike T-shape terahertz metamaterial using out-of-plane actuated cantilevers. *Appl. Phys. Lett.* **104,** 251914 (2014).
36. Pitchappa, P. *et al.* Micro-electro-mechanically switchable near infrared complementary metamaterial absorber. *Appl. Phys. Lett.* **104,** 201114 (2014).
37. Liu, A. Q., Zhu, W. M., Tsai, D. P. & Zheludev, N. I. Micromachined tunable metamaterials: a review. *J. Opt.* **14,** 114009 (2012).
38. Kasirga, T. S., Ertas, Y. N. & Bayindir, M. Microfluidics for reconfigurable electromagnetic metamaterials. *Appl. Phys. Lett.* **95,** 214102 (2009).
39. Zhu, W. M. *et al.* A flat lens with tunable phase gradient by using random access reconfigurable metamaterial. *Adv. Mater.* **27,** 4739–4743 (2015).
This paper presents the first randomly addressable reconfigurable microwave metamaterial.
40. Ozbey, B. & Aktas, O. Continuously tunable terahertz metamaterial employing magnetically actuated cantilevers. *Opt. Express* **19,** 5741–5752 (2011).
41. Lapine, M., Shadrivov, I. V., Powell, D. A. & Kivshar, Y. S. Magnetoelastic metamaterials. *Nature Mater.* **11,** 30–33 (2012).
This paper reports the first microwave metamaterial that is actuated by electromagnetic forces.
42. Chen, H. T. *et al.* Active terahertz metamaterial devices. *Nature* **444,** 597–600 (2006).
43. Padilla, W. J., Taylor, A. J., Highstrete, C., Lee, M. & Averitt, R. D. Dynamical electric and magnetic metamaterial response at terahertz frequencies. *Phys. Rev. Lett.* **96,** 107401 (2006).
44. Ju, L. *et al.* Graphene plasmonics for tunable terahertz metamaterials. *Nature Nanotech.* **6,** 630–634 (2011).
45. Lee, S. H. *et al.* Switching terahertz waves with gate-controlled active graphene metamaterials. *Nature Mater.* **11,** 936–941 (2012).
46. Ricci, M., Orloff, N. & Anlage, S. M. Superconducting metamaterials. *Appl. Phys. Lett.* **87,** 034102 (2005).
47. Savinov, V., Fedotov, V. A., Anlage, S. M., de Groot, P. A. J. & Zheludev, N. I. Modulating sub-THz radiation with current in superconducting metamaterial. *Phys. Rev. Lett.* **109,** 243904 (2012).
48. Boardman, A. D. *et al.* Active and tunable metamaterials. *Laser Photon. Rev.* **5,** 287–307 (2011).
49. Keiser, G. R., Fan, K., Zhang, X. & Averitt, R. D. Towards dynamic, tunable, and nonlinear metamaterials via near field interactions: a review. *J. Infrared Millim. Terahertz Waves* **34,** 709–723 (2013).
50. Lapine, M., Shadrivov, I. V. & Kivshar, Y. S. Colloquium: nonlinear metamaterials. *Rev. Mod. Phys.* **86,** 1093–1123 (2014).
51. Shadrivov, I., Lapine, M. & Kivshar, Y. S. (eds) *Nonlinear, Tunable and Active Metamaterials* (Springer, 2014).
52. Turpin, J. P., Bossard, J. A., Morgan, K. L., Werner, D. H. & Werner, P. L. Reconfigurable and tunable metamaterials: a review of the theory and applications. *Int. J. Antenn. Propag.* **2014,** 1–18 (2014).
53. Fan, K. & Padilla, W. J. Dynamic electromagnetic metamaterials. *Mater. Today* **18,** 39–50 (January–February, 2015).
54. Toivola, Y., Thurn, J., Cook, R. F., Cibuzar, G. & Roberts, K. Influence of deposition conditions on mechanical properties of low-pressure chemical vapor deposited low-stress silicon nitride films. *J. Appl. Phys.* **94,** 6915–6922 (2003).
55. Zwickl, B. M. *et al.* High quality mechanical and optical properties of commercial silicon nitride membranes. *Appl. Phys. Lett.* **92,** 103125 (2008).
56. Petersen, K. E. Silicon as a mechanical material. *Proc. IEEE* **70,** 420–457 (1982).
57. Fairchild, B. A. *et al.* Fabrication of ultrathin single-crystal diamond membranes. *Adv. Mater.* **20,** 4793–4798 (2008).
58. Rogers, J. A., Lagally, M. G. & Nuzzo, R. G. Synthesis, assembly and applications of semiconductor nanomembranes. *Nature* **477,** 45–53 (2011).
59. Lagally, M. G. *et al.* Semiconductor nanomembranes: a platform for new science and technology. *Proc. SPIE* **8031,** 803107 (2011).
60. Ou, J. Y., Plum, E., Jiang, L. & Zheludev, N. I. Reconfigurable photonic metamaterials. *Nano Lett.* **11,** 2142–2144 (2011).
This paper reports the first thermally actuated optical nanomembrane metamaterial.
61. Ou, J. Y., Plum, E., Zhang, J. & Zheludev, N. I. An electromechanically reconfigurable plasmonic metamaterial operating in the near-infrared. *Nature Nanotech.* **8,** 252–255 (2013).
This paper reports the first electrostatically actuated optical nanomembrane metamaterial.
62. Valente, J., Ou, J. Y., Plum, E., Youngs, I. J. & Zheludev, N. I. Reconfiguring photonic metamaterials with currents and magnetic fields. *Appl. Phys. Lett.* **106,** 111905 (2015).
63. Valente, J., Ou, J. Y., Plum, E., Youngs, I. J. & Zheludev, N. I. A magneto-electro-optical effect in a plasmonic nanowire material. *Nature Commun.* **6,** 7021 (2015).
This paper reports the first magnetically actuated optical nanomembrane metamaterial.
64. Zhang, J., MacDonald, K. F. & Zheludev, N. I. Nonlinear dielectric optomechanical metamaterials. *Light Sci. Appl.* **2,** e96 (2013).
This theoretical paper predicts giant nonlinear optical effects in nanomembrane metamaterials actuated by optical forces.
65. Ou, J. Y., Plum, E., Zhang, J. & Zheludev, N. I. Giant nonlinearity of an optically reconfigurable plasmonic metamaterial. *Adv. Mater.* http://dx.doi.org/10.1002/adma.201504467 (2015).
This paper reports the first optically actuated nano-optomechanical metamaterial operating in the optical part of the spectrum.
66. Chen, C. C. *et al.* Fabrication of three dimensional split ring resonators by stress-driven assembly method. *Opt. Express* **20,** 9415–9420 (2012).
67. Yamaguchi, K., Fujii, M., Okamoto, T. & Haraguchi, M. Electrically driven plasmon chip: active plasmon filter. *Appl. Phys. Express* **7,** 012201 (2014).
68. Zhao, R., Tassin, P., Koschny, T. & Soukoulis, C. M. Optical forces in nanowire pairs and metamaterials. *Opt. Express* **18,** 25665–25676 (2010).
69. Zhang, J., MacDonald, K. F. & Zheludev, N. I. Optical gecko toe: optically controlled attractive near-field forces between plasmonic metamaterials and dielectric or metal surfaces. *Phys. Rev. B* **85,** 205123 (2012).
70. Slobozhanyuk, A. P. *et al.* Flexible helices for nonlinear metamaterials. *Adv. Mater.* **25,** 3409–3412 (2013).
71. Ginis, V., Tassin, P., Soukoulis, C. M. & Veretennicoff, I. Enhancing optical gradient forces with metamaterials. *Phys. Rev. Lett.* **110,** 057401 (2013).
72. Karvounis, A., Ou, J. Y., Wu, W., MacDonald, K. F. & Zheludev, N. I. Nano-optomechanical nonlinear dielectric metamaterials. *Appl. Phys. Lett.* **107,** 191110 (2015).
This paper reports the first dielectric nano-optomechanical metamaterial.
73. Boyd, R. W. *Nonlinear Optics* 3rd edn (Academic Press, 2008).
74. Semouchkina, E. A., Semouchkin, G. B., Lanagan, M. & Randall, C. A. FDTD study of resonance processes in metamaterials. *IEEE Trans. Microw. Theory Tech.* **53,** 1477–1487 (2005).
75. Ginn, J. C. *et al.* Realizing optical magnetism from dielectric metamaterials. *Phys. Rev. Lett.* **108,** 097402 (2012).
76. Zhang, J., MacDonald, K. F. & Zheludev, N. I. Near-infrared trapped mode magnetic resonance in an all-dielectric metamaterial. *Opt. Express* **21,** 26721–26728 (2013).
77. Chong, K. E. *et al.* Observation of Fano resonances in all-dielectric nanoparticle oligomers. *Small* **10,** 1985–1990 (2014).
78. Wang, Q. *et al.* 1.7 Gbit/in.^{2} gray-scale continuous-phase-change femtosecond image storage. *Appl. Phys. Lett.* **104,** 121105 (2014).
79. Wang, Q. *et al.* Optically switchable and rewritable phase-change (dielectric) metamaterials. In *2015 MRS Spring Meeting, San Francisco* (2015); http://eprints.soton.ac.uk/379172
80. Zhang, J., MacDonald, K. F. & Zheludev, N. I. Giant optical forces in planar dielectric photonic metamaterials. *Opt. Lett.* **39,** 4883–4886 (2014).
81. Cencillo-Abad, P., Ou, J. Y., Valente, J., Plum, E. & Zheludev, N. I. Randomly addressable reconfigurable photonic metamaterials. In *5th Int. Topical Meeting on Nanophotonics and Metamaterials, Seefeld* (2015); http://eprints.soton.ac.uk/375824
This conference paper presents the first randomly addressable reconfigurable nanomembrane metamaterial.
82. Rigden, J. S. *Macmillan Encyclopedia of Physics* (Simon and Schuster Macmillan, 1996).
83. Karim, S., Maaz, K., Ali, G. & Ensinger, W. Diameter dependent failure current density of gold nanowires. *J. Phys. D* **42,** 185403 (2009).

Acknowledgements

We are grateful to A. Karvounis and V. Savinov for their help preparing the manuscript. We are also grateful to P. Cencillo-Abad, J. P. Valente and J. Y. Ou for preparing the Supplementary Movies and K. F. MacDonald for discussions. This work is supported by the Leverhulme Trust, the MOE Singapore (grant MOE2011-T3-1-005) and the UK's Engineering and Physical Sciences Research Council (grants EP/G060363/1 and EP/M009122/1).

Author contributions

N.I.Z. and E.P. made equal contributions to the preparation of this Perspective.

Additional information

Supplementary information is available in the online version of this paper. Reprints and permission information is available online at www.nature.com/reprints. The data from this paper can be obtained from the University of Southampton ePrints research repository: http://dx.doi.org/10.5258/SOTON/378243. Correspondence and requests for materials should be addressed to N.I.Z. and E.P.

Competing financial interests

The authors declare no competing financial interests.

ACS Photonics

Review

pubs.acs.org/journal/apchd5

Controlling the Optical Response of 2D Matter in Standing Waves

Eric Plum,*[,†] Kevin F. MacDonald,*[,†] Xu Fang,[‡] Daniele Faccio,[§] and Nikolay I. Zheludev*[,†,∥]

[†]Optoelectronics Research Centre and Centre for Photonic Metamaterials and [‡]Department of Electronics and Computer Science, University of Southampton, Highfield, Southampton, SO17 1BJ, United Kingdom

[§]School of Engineering and Physical Sciences, SUPA, Heriot-Watt University, Edinburgh EH14 4AS, United Kingdom

[∥]Centre for Disruptive Photonic Technologies, School of Physical and Mathematical Sciences and The Photonics Institute, Nanyang Technological University, Singapore 637371

ABSTRACT: There is a major development unfolding in photonic technology that promises to impact optical data processing, spectroscopy, and nonlinear/quantum optics. This new direction relates to plasmonics, metamaterials and coherent optics. It exploits the difference in manifestations of optical properties of thin films in traveling waves and standing waves. In standing waves, "coherent control" of the energy exchange between incident and scattered waves leads to new technological opportunities including single photon gates, 100 THz all-optical modulators, sophisticated spectroscopy techniques that can for example distinguish different multipole contributions to absorption and quantum optical devices. We provide an overview of the rapidly growing body of work on the optics of films and metasurfaces in coherent light fields.

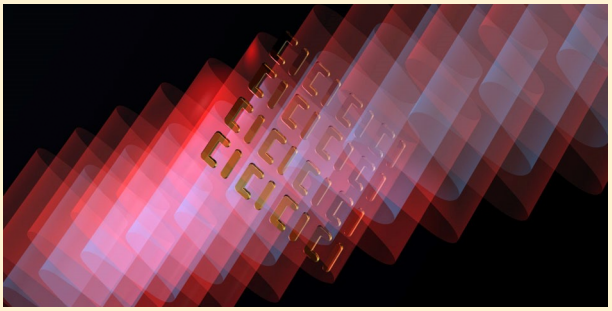

KEYWORDS: *standing wave, metamaterial, metasurface, plasmonics, all-optical, coherent perfect absorption*

Coherent control is a well-understood concept in quantum mechanics,[1] where it is used to direct dynamic processes with light by engaging quantum interference phenomena. Coherent control has also been employed to manipulate electron motion in semiconductors,[2] breaking of chemical bonds,[3] the absorption[4−8] and localization[9−13] of light in cavities and at surfaces, transmission of light by metal-dielectric stacks,[14,15] light modulation in waveguides,[16−18] nonlinear optical phenomena in periodic structures[19] and nanoparticles,[20] polarization rotation in Faraday media,[21,22] optical effects in optomechanical systems,[23,24] and the excitation and propagation of surface plasmon polaritons at metal/dielectric interfaces,[25−27] as well as the absorption of acoustic waves,[28,29] see Figure 1.

Here we review how coherent control of standing waves can be used to manipulate all kinds of light-matter interactions in thin films where one can change reflection, transmission, absorption and polarization properties. We begin with a theoretical description of such interactions followed by a review of the resulting opportunities from all-optical modulation of intensity, propagation direction, and polarization of light to their applications in data and image processing as well as quantum technologies.

Interaction of Coherent Light with 2D Matter. Consider a layer of absorbing material illuminated at normal incidence by a pair of counter-propagating, collinearly polarized coherent light waves: The incident fields E_α and E_β represent input signals; the transmitted and reflected waves (fields E_γ and E_δ) propagating away from the film on either side constitute output signals (Figure 2). Assuming a purely linear, isotropic dipolar response of the film, with no change in the polarization state of light, the input and output fields are related by a complex scattering matrix[30] $\mathbf{S}$:

$$\begin{bmatrix} E_\delta \\ E_\gamma \end{bmatrix} = \begin{bmatrix} \mathbf{S}_{11} & \mathbf{S}_{12} \\ \mathbf{S}_{21} & \mathbf{S}_{22} \end{bmatrix} \begin{bmatrix} E_\alpha \\ E_\beta \end{bmatrix} \quad (1)$$

where $\mathbf{S}_{11}$ and $\mathbf{S}_{21}$ are, respectively, the reflection and transmission coefficients for light incident on the medium from side 1; $\mathbf{S}_{22}$ and $\mathbf{S}_{12}$ being the same for incidence on side 2. In the absence of any magneto-optical effects, reciprocity dictates that $\mathbf{S}_{12} = \mathbf{S}_{21}$, so three independent parameters are necessary to describe the optical properties of such a device.

In this four-port optical device linearity of the film's properties implies that if both input signals are scaled by the same factor η, both of the resulting output signals must also scale by η. However, linearity of the film's response does not imply any proportional scaling of one, other, or both outputs when only one of the inputs is changed. In fact, the relationship between a given input port and a given output port in a coherent four-port device can be nonlinear. This nonlinear response results from the coherent redistribution of energy between the ports.

Planar metamaterials or metasurfaces—man-made media structured on the subwavelength scale—provide unprecedented

Special Issue: 2D Materials for Nanophotonics

Received: August 15, 2017
Published: October 19, 2017

DOI: 10.1021/acsphotonics.7b00921
ACS Photonics 2017, 4, 3000−3011

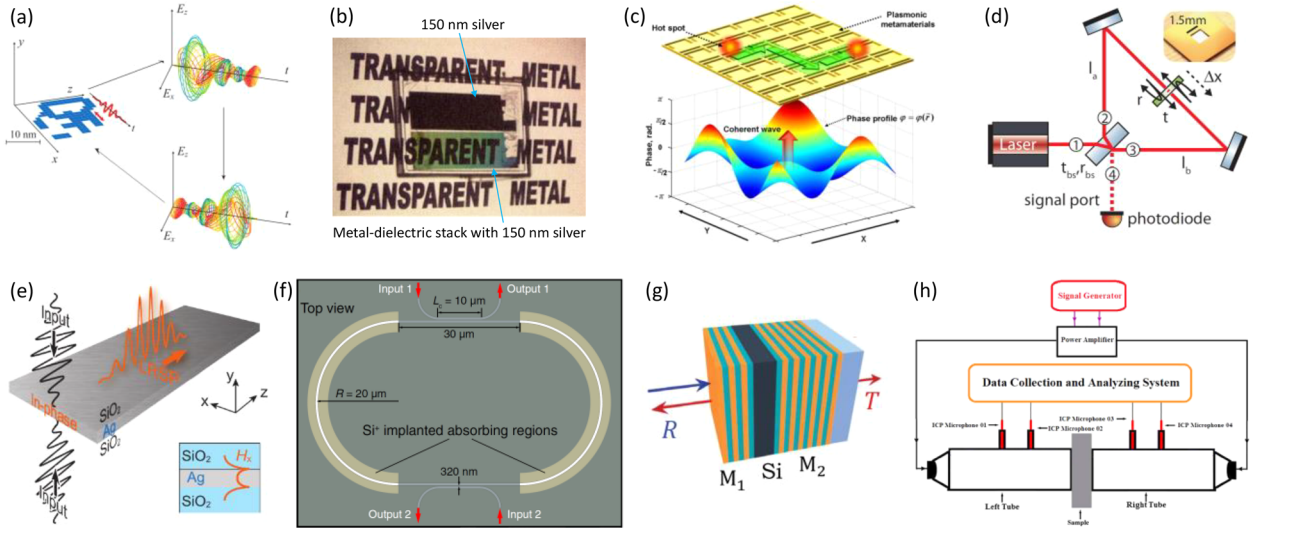

Figure 1. Coherent control of various phenomana across many disciplines. (a) Nanosecond-femtosecond spatiotemporal field localization in plasmonic systems by time reversal.[10] (b) Transparent metal-dielectric stacks.[15] (c) Nanoscale light localization in metamaterials.[11] (d) Quantum opto-mechanics based on destructive interference on a nanomembrane oscillator.[23] (e) Selective excitation of long-range surface plasmon polaritons.[27] (f) Silicon photonic modulator based on coherent perfect absorption.[18] (g) Multiband coherent perfect absorption in silicon controlled by aperiodic dielectric mirrors M.[8] (h) Coherent perfect absorption of sound.[29]

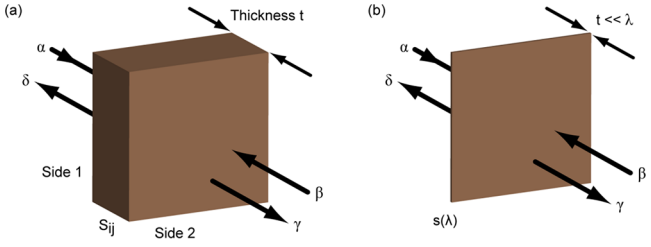

Figure 2. Generic four-port coherent control device. (a) A medium, with optical properties described by a complex scattering matrix $\mathbf{S}_{ij}$ containing three independent parameters, is illuminated by counter-propagating coherent input light waves α and β; waves γ and δ are the device outputs. (b) In the limit of substantially subwavelength thickness, the medium can be described by a single complex scattering coefficient $s(\lambda)$.

freedom to engineer the balance among resonant absorption, reflection and transmission almost at will in ultrathin metal, dielectric and semiconductor films. Nanostructuring of thin-film materials introduces optical resonances with a strength and spectral position that is controlled by the geometry and size of the nanostructure, allowing strong light−matter interactions to be achieved in films of nanoscale thickness and enabling the four-port optical device to be configured to deliver a broad range of functionalities.

Consider now a film of sufficient thinness that retardation effects across it can be ignored, that is, we may consider each constituent molecule to be exposed to the same electric field, the combined field $E_\alpha + E_\beta$ of the incident waves. Here energy will be reradiated equally in the forward and backward directions with an efficiency dependent on the excitation wavelength λ, resulting in a reradiated field $s(\lambda)(E_\alpha + E_\beta)$, where $s(\lambda)$ is the complex wavelength-dependent scattering coefficient for the film as measured in a traveling wave.[31] The magnitude and phase of $s(\lambda)$ respectively correspond to the relative amplitude of the reradiated field and to the phase lag between reradiated and driving fields. $s(\lambda)$ may include losses and thereby excludes any assumption of equality between the combined incident and combined output beam intensities. Requirements of field continuity then dictate the following scattering matrix expression relating input and output fields for a coherent four-port device based upon a vanishingly thin film (Figure 2b):

$$\begin{bmatrix} E_\delta \\ E_\gamma \end{bmatrix} = \begin{bmatrix} s(\lambda) & s(\lambda)+1 \\ s(\lambda)+1 & s(\lambda) \end{bmatrix} \begin{bmatrix} E_\alpha \\ E_\beta \end{bmatrix} \quad (2)$$

In cases where the contribution from interference among multiply reflected/transmitted beams is small, eq 2 can serve as an approximation to eq 1 for films of substantially subwavelength thickness and greatly simplifies the analysis of four-port coherent device functionalities by reducing the number of free parameters required to describe the system from three ($\mathbf{S}_{ij}$) to one, in the form of $s(\lambda)$.

At the node of a standing wave formed by counter-propagating coherent incident beams, $E_\alpha = -E_\beta$. With an ultrathin medium positioned at the node, E_γ will thus always be equal to E_α, and E_δ to E_β, regardless to the value of the film's scattering parameter $s(\lambda)$. This is the "coherent perfect transmission" regime, a situation in which there is no light−matter interaction because the film is located at a point where the electric field is zero. (It should be noted here that the regime of coherent perfect transparency of weakly absorbing films has long been exploited for intra-cavity laser mode selection.[32−37]) At an antinode of the standing wave, on the other hand, $E_\alpha = E_\beta$. Here, both E_γ and E_δ can be reduced to zero if $s(\lambda) = -0.5$, whereby the film exhibits the maximum possible level of zero-thickness single-beam absorption[38,39] of 50%. This is the regime of "coherent perfect absorption". It is interesting to note here that while perfect transparency requires an absorber of substantially subwavelength thickness,[40] the phenomenon of coherent perfect absorption does not. Indeed, the latter has been demonstrated in a variety of optically thick media and spectral domains.[5,8,41−43]

The effective optical nonlinearity of coherent four-port devices, that is, the nonlinear relationship between selected

DOI: 10.1021/acsphotonics.7b00921
ACS Photonics 2017, 4, 3000−3011

input and output port intensities, is illustrated by the intensity (defined as $I = EE^*$) of output γ:

$$I_\gamma = |1 + s(\lambda)|^2 I_\alpha + |s(\lambda)|^2 I_\beta + 2Re\{(1 + s(\lambda))s^*(\lambda)E_\alpha E_\beta^*\} \quad (3)$$

Clearly, if one of the two input signals is removed, the output signal intensities are strictly proportional to that of the remaining input. And, if input intensities I_α and I_β are increased or decreased in proportion, there will be a correspondingly proportional increase or decrease in I_γ. However, if I_α remains fixed and only I_β changes, then I_γ will respond in a nonlinear fashion, as illustrated in Figure 3 for the case where $s(\lambda) = -0.5$ and $I_\alpha = 1$: here the dependence of I_γ on I_β is nonlinear.

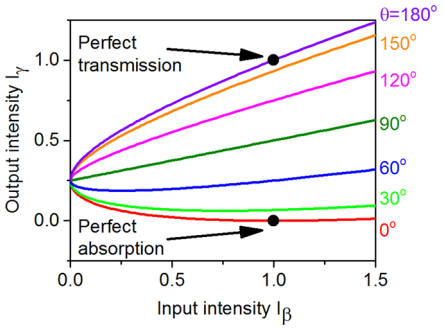

Figure 3. Nonlinear response function of a generic four-port coherent device. Dependence of output intensity I_γ on input intensity I_β for a fixed input intensity $I_\alpha = 1$, for a selection of mutual phase settings θ between E_α and E_β (as labeled) in the plane of a vanishingly thin absorber with a scattering parameter $s(\lambda) = -0.5$.

Light propagating in a conventional nonlinear (bulk) medium experiences harmonic distortion, which can lead ultimately to optical instability and multistability. The nonlinear character of a four-port coherent device, however, is different: it is based on the redistribution of energy among ports and does not cause harmonic distortion; it is underpinned only by linear interference effects and as such is of course strictly compliant with energy conservation; a variety of functionalities is enabled by the fact that the level of absorption in such devices is strongly dependent on the balance of intensities and mutual phase of the input beams.

It is apparent from the above analysis that an effective nonlinearity may be obtained using any ultrathin film, for example, a 50:50 beamsplitter. However, in dissipation-free films the range of achievable input-output functions is constrained. In this context, photonic metamaterials provide access to an otherwise inaccessible range of ultrathin-film scattering coefficients $s(\lambda)$ at any desired wavelength by nanostructural design, and thereby to a wide range of nonlinear response functions.

Before illustrating specific metamaterial designs and four-port device functionalities based upon such structures, we shall consider the meaning of $s(\lambda)$ scattering coefficients. For instance, single-pass absorption is governed by the expression

$$A = 1 - |s(\lambda)|^2 - |s(\lambda) + 1|^2 \quad (4)$$

Figure 4a maps levels of single-beam absorption onto the complex $s(\lambda)$ parameter space. The red circular line corresponds to $A = 0$ and describes lossless media that neither absorb nor amplify incident light. It defines a boundary between absorbing materials ($A > 0$, inside the circle) and gain media ($A < 0$, outside the circle). The central point of the circle $A = 0.5$ represents the maximum possible level of single-beam absorption permitted by field continuity constraints in a vanishingly thin film.[38,39] It corresponds to a film with a scattering parameter $s(\lambda) = -0.5$.

A perfectly transparent thin film that does not inflict any phase change corresponds to $s(\lambda) = 0$. A thin film of perfect electric conductor (PEC), on the other hand, will reflect 100% of incident light at any wavelength with a π phase change corresponding to $s(\lambda) = -1$. Scattering coefficients for glass films with a refractive index of 1.5 also sit on the zero-loss contour, being represented over a given wavelength range by a segment of a circle, as opposed to a singular point, as plotted in Figure 4b for glass films of 10 and 50 nm thicknesses for wavelengths from 750 to 1050 nm. Gold thin films are dispersive but highly reflective and weakly absorbing, so they appear in $s(\lambda)$ space as curves lying just inside the zero-loss contour.

In contrast, metamaterial nanostructures can provide access by design to the full parameter space. This is illustrated by Figure 4c, showing the range of scatting coefficients accessible with several planar metamaterial designs of sub-100 nm

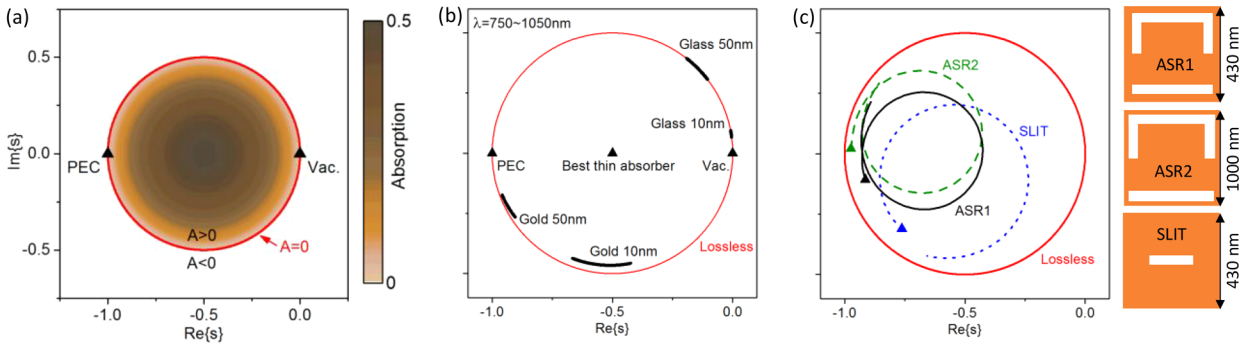

Figure 4. Scattering coefficient $s(\lambda)$ of ultrathin films and associated properties. (a) Level of absorption A of an ultrathin film illuminated from only one side as a function of its scattering coefficinet s. (b) Scattering coefficients for homogeneous thin film media in the 750−1050 nm wavelength range. (c) Scattering coefficients for selected periodic planar metamaterials indicated by their unit cells, modeled in COMSOL Multiphysics. The designs ASR1, ASR2, and SLIT consist of gold on silicon nitride with layer thicknesses of 50/30, 50/30, and 30/30 nm and the scattering coefficients are plotted for wavelength ranges of 750−1050, 1250−1850, and 750−1050 nm, respectively, with a triangular marker indicating the shortest wavelength. Modeling assumed a Drude-Lorentz model for the properties of gold and a fixed refractive index of 2.0 for silicon nitride, with normal monochromatic plane-wave illumination linearly polarized with the electric field parallel to the common symmetry axis of the nanostructures.

DOI: 10.1021/acsphotonics.7b00921
ACS Photonics 2017, 4, 3000−3011

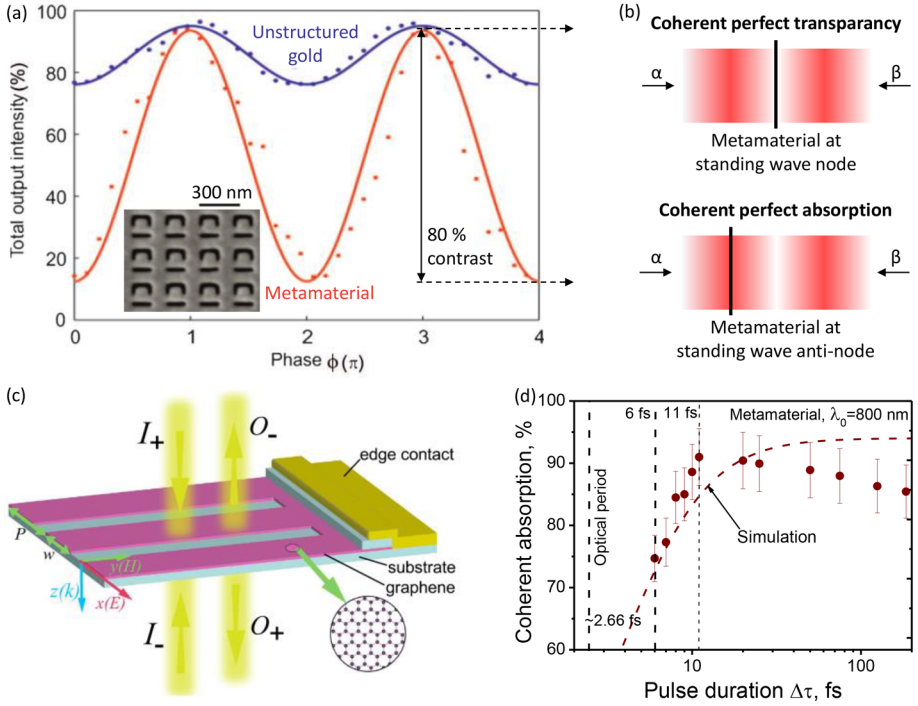

Figure 5. Coherent absorption modulation in 2D matter. (a) First observation of coherent absorption and transparency for a planar metamaterial (50 nm thick nanostructured gold supported by glass) illuminated by counterpropagating coherent laser beams at 633 nm wavelength linearly polarized parallel to the symmetry axis of the nanostructure.[40] (b) Schematic illustrating coherent perfect transparency and absorption resulting from destructive and constructive interference of incident electric fields α and β on a planar metamaterial. (c) Proposed scheme for electric control of mid-infrared coherent absorption in structured graphene.[50] (d) Coherent absorption at the standing wave antinode measured with counterpropagating coherent femtosecond laser pulses for a plasmonic metamaterial consisting of a freestanding 60 nm thick gold film perforated with an ASR aperture array of 320 nm period.[47]

thickness. These are arrays of asymmetric split ring (ASR) and slot apertures in a bilayer of gold and silicon nitride. ASR designs have been employed and optimized in numerous previous studies,[44,45] including the first experimental demonstrations of coherent absorption modulation.[40,46] The scattering coefficients of metamaterial ASR1 for wavelengths between 750 and 1050 nm describe a loop extending from the neighborhood of the zero-loss contour, toward the center of the $A > 0$ domain with "ideal, zero-thickness absorber" characteristics at 870 nm wavelength, and back. The metamaterial response can be modified simply by adjusting the dimensions of the design: the ASR2 line for example represents a similar pattern with an absorption resonance centered at 1550 nm. The third trace presented in Figure 4c corresponds to a metamaterial comprising an array of linear slots in a gold film on silicon nitride. Thus, metamaterials can provide otherwise unattainable thin film optical properties by nanostructural design.

Coherent Modulation of Absorption. As explained above, the interference of coherent light beams on an ultrathin layer of material, much thinner than the wavelength of light, can selectively render the medium almost perfectly transparent or facilitate near-perfect optical absorption, thus enabling high bandwidth light-by-light modulation[47] at low intensity.[48]

As noted earlier, coherent control of absorption in standing waves has long been exploited for laser mode selection, whereby a lossy thin film is placed within the laser cavity at a node of the desired mode to selectively absorb competing modes.[32−37] Coherent perfect absorption in thick structures,[8,41] − sometimes referred to as time-reversed lasing,[4,5,42,43] has also been known for some time.

Dynamic coherent control of thin film absorption from coherent perfect transparency to coherent perfect absorption was first observed by Zhang et al.[40] for a 50 nm thick gold film perforated with an ASR aperture array and supported by a glass substrate using a HeNe laser (Figure 5a). In the absorber, that was 13× thinner than the laser wavelength, a full span of modulation from nearly perfect absorption to nearly perfect transmission was demonstrated. When the absorber is placed at an electric field node of the standing wave no light-matter interaction occurs (Figure 5b). In contrast, if the metasurface is located at an antinode of the standing wave, the light−matter interaction is enhanced, resulting in nearly complete absorption of all incident light. Apart from photonic metasurfaces made from plasmonic materials,[40] dielectrics,[49] or graphene,[50] coherent perfect absorption and transparency has also been investigated in multiband microwave metamaterials[51] and heavily doped silicon thin films for terahertz waves[52] as well as observed in 9 nm thick (30-layer) graphene,[53] which exhibits broadband 50% absorption when illuminated by a single beam of light. Notably, the electric tunability of layered or structured graphene absorbers offers the interesting opportunity of electric modulation of coherent absorption,[50] see Figure 5c.

While optical nonlinearities suffer from a trade-off between speed and magnitude,[54] Xu, Nalla, and coauthors[46,47] have demonstrated that coherent absorption offers intensity-independent high contrast modulation of light-with-light even at femtosecond time scales which can be used for generation of "dark pulses". Figure 5d shows coherent absorption measured in a plasmonic metasurface with femtosecond laser pulses. Absorption of about 90% can be achieved with laser pulses as

DOI: 10.1021/acsphotonics.7b00921
ACS Photonics 2017, 4, 3000−3011

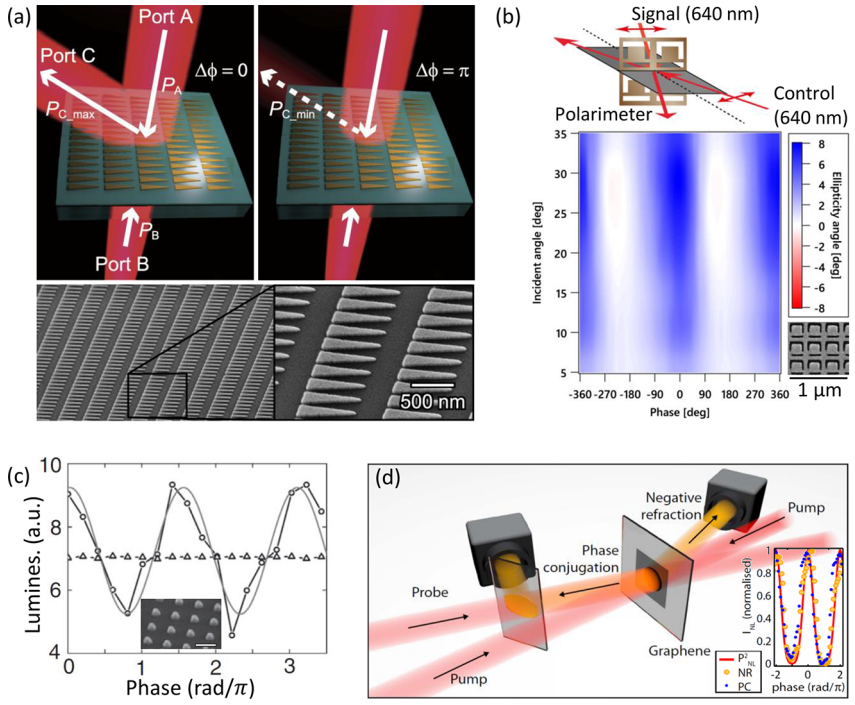

Figure 6. Coherent control of diffraction, polarization effects, and nonlinear phenomena in the optical part of the spectrum. (a) Constructive interference (left) of incident waves A and B on a phase-gradient metasurface leads to efficient redirection of light to Port C, while the diffracted beam vanishes almost completely in case of destructive interference (right).[57] (b) Manifestation of optical activity of a metasurface controlled by constructive interference (phase 0) and destructive interference (phase ± 180°) of 640 nm wavelength signal and control beams illuminating the nanostructure.[65] (c) Photoluminescence of dye molecules on aluminum nanopyramids (300 nm scale bar) as a function of the phase difference between coherent (circles) and incoherent (triangles) counterpropagating pump beams.[66] (d) Nonlinear response of 30-layer graphene controlled by constructive (phase 0) and destructive (phase π) interference of counterpropagating coherent pump beams on the nonlinear thin film at 780 nm wavelength. Time-averaged nonlinear polarization P^2_{NL}, as well as negatively refracted (NR) and phase-conjugated (PC) beam amplitudes, are shown.[67]

short as 10 fs, corresponding to about four optical cycles and a bandwidth on the order of 100 THz.

The ability to control absorption of light-with-light without a nonlinear medium, with 100 THz bandwidth and without need for high intensities opens up a broad range of possibilities. As discussed later on, the resulting effective nonlinearity may be used to achieve various logical functions for ultrafast all-optical data processing, image recognition and analysis, as well as small-signal amplification and coherence filtering.

Coherent Control of Diffraction, Polarization Effects, and Nonlinear Optical Phenomena. While the ability to control absorption is very important, coherent interaction of light-with-light on planar materials can go much further. The superposition of coherent waves allows control over both the local electric and the local magnetic field from zero (destructive interference) to enhancement (constructive interference). By controlling the field in the plane of a 2D material, the interaction of coherent light fields may therefore be used to control the optical excitation of the material and thus the manifestation of any optical functionality the material may have. Opportunities include control over diffraction from gratings or phase-gradient metasurfaces, the manifestation of linear and circular birefringence and dichroism, and the efficiency of nonlinear optical responses, promising new functionalities for wavefront shaping and signal processing.

For example, Shi et al.[55] studied coherent control of phase-gradient metasurfaces, which are planar metamaterials consisting of "meta-molecules" that scatter light with a spatially varying phase, resulting in diffraction, transmission and reflection of light.[56] Exploiting destructive interference of coherent light fields incident on the metasurface from opposite sides, scattering and thus diffraction may be turned off, whereas constructive interference yields diffraction with enhanced efficiency, enabling dynamic redirection of light. An experimental realization was recently reported by Kita et al.[57] using a gold phase-gradient nanostructure with a partial back reflector that directs scattered light preferentially to one side of the nanostructure, see Figure 6a. Such all-optical beam deflection could have applications in signal routing and the concept could be extended to planar meta-lenses[58,59] and meta-holograms,[60,61] that could also be coherently controlled.

Coherent control of polarization phenomena with very high contrast has been reported at microwave frequencies using anisotropic as well as 3D-chiral structures that are thin compared to the wavelength.[62] Coherent interaction of microwaves on an anisotropic metamaterial, resembling a wave plate, has allowed full control over the orientation of the plane of polarization. Arbitrary levels of polarization rotation have also been achieved with a chiral thin film consisting of mutually twisted metal patterns in parallel planes spaced by a distance of a small fraction of a wavelength. Optical activity—an ability to rotate the polarization state of light (circular birefringence), and differential throughput for left- and right-handed circular polarizations (circular dichroism)—is usually observed in such 3D-chiral structures (that is, in structures that cannot be superimposed with their mirror image). While 3D-chiral structures can be very thin, they cannot be planar, however optical activity does not require chiral materials.

DOI: 10.1021/acsphotonics.7b00921
ACS Photonics 2017, 4, 3000−3011

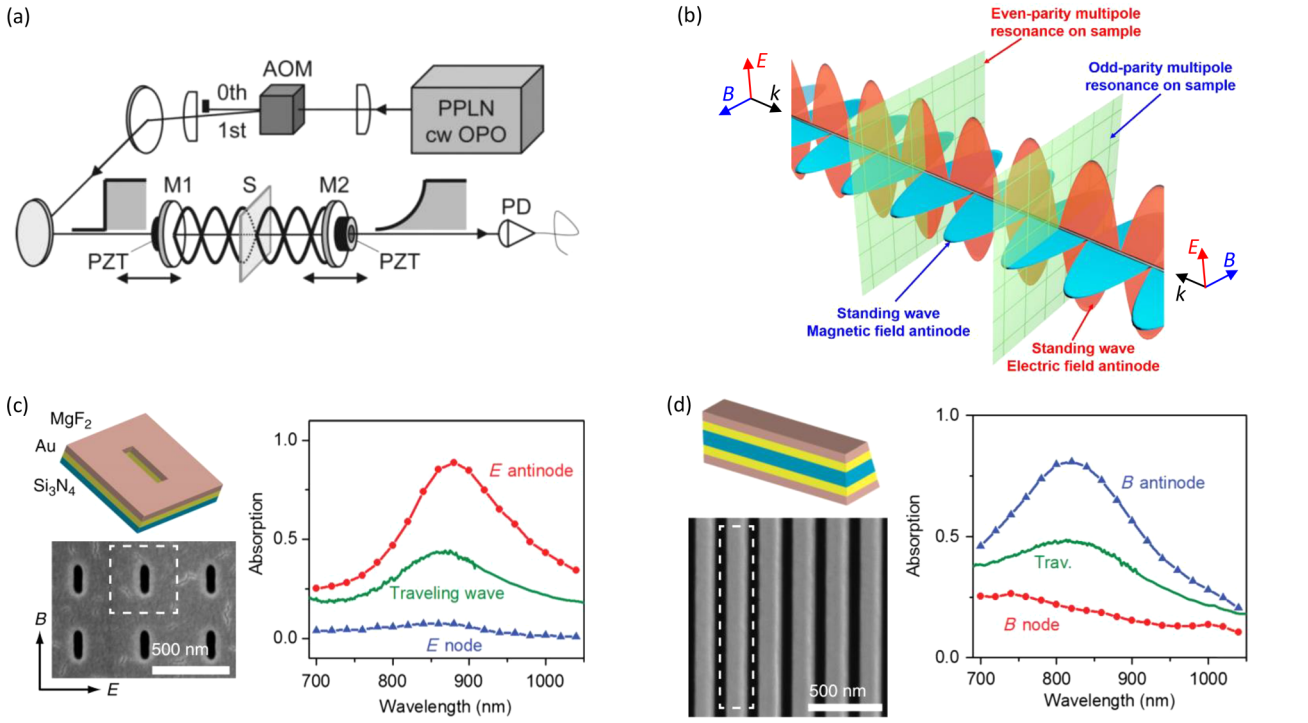

Figure 7. Coherent spectroscopy in standing waves. (a) Schematic setup for photon-trap spectroscopy, a generalized form of cavity ringdown spectroscopy where a thin sample interacts with the standing wave formed in a Fabry–Perot cavity.[70] (b) Coherent counterpropagating waves of the same linear polarization form a standing wave of alternating electric and magnetic field antinodes that are sensitive to different multipole resonances.[72] (c) The electric dipole resonance of a plasmonic slot aperture metamaterial can be detected at the electric field antinode, but not at the magnetic field antinode (E node).[73] (d) The magnetic dipole and electric quadrupole resonance of stacked plasmonic wires can be detected at the magnetic field antinode, but not at the electric field antinode (B node).[73]

Instead, optical activity may be observed if the mirror-symmetry of the experimental arrangement is broken by the illumination direction. Such so-called "extrinsic 3D chirality" leads to very large optical activity in planar metamaterials lacking rotational symmetry[63] and this effect can also be coherently controlled. Coherent interaction of microwaves on an array of asymmetrically split metallic rings has allowed almost complete control over the ellipticity of electromagnetic waves from right-handed to left-handed circular polarization.[64] Figure 6b illustrates the first demonstration of such polarization control in the visible part of the spectrum.[65] Constructive (or destructive) interference at oblique incidence is achieved by illuminating both sides of the metamaterial with coherent waves incident in the same plane with the same incidence angle on the same side of the surface normal as shown. This way, the phase difference between the incident waves is constant across the metamaterial. The metamaterial is an asymmetric split ring aperture array in a gold film with ~300 nm period. Oblique incidence yields an extrinsically chiral experimental arrangement (except when the structure's line of symmetry coincides with the plane of incidence). The manifestation of the resulting optical activity is then controlled by the phase difference of the incident waves. For constructive interference of the incident electric fields significant circular dichroism (as well as circular birefringence) is observed, which increases with increasing angle of incidence. In contrast, destructive interference renders the nanostructure essentially transparent causing all polarization effects to vanish.

Coherent interaction of light-with-light on thin films can also be exploited to control light emission. For example, Pirruccio et al. reported that photoluminescence may be enhanced or suppressed through interference of pump light on a luminescent thin film[68] or on plasmonic nanostructures coupled to a luminescent material[66] (Figure 6c), providing a route to phase-modulated light sources.

Not only linear, but also nonlinear phenomena can be controlled by two coherent beams of light. This has been explored by Rao et al.[67] who studied nonlinear four-wave mixing in 30-layer graphene, which is about 9 nm thick, at a wavelength of 780 nm. By controlling the interference of two counterpropagating coherent pump beams on the thin graphene film (or one pump beam and its reflection on a mirror), the authors were able to control phase conjugation in the graphene film, see Figure 6d.

Coherent Excitation-Selective Spectroscopy. Important differences between interactions of light and matter in traveling and standing waves have previously been noted in the context of cavity ringdown spectroscopy[69,70] (Figure 7a), where different levels of absorption were observed for thin samples positioned at a node or antinode of a standing wave formed within a cavity. Standing waves, formed by counter-propagating coherent waves, offer degrees of freedom that allow probing of materials of substantially subwavelength thickness in ways that are not possible with traveling waves. For example, non-radiating anapoles, formed by destructive interference of electric and toroidal dipoles, can be excited in this way.[71]

In particular, copolarized, counter-propagating, coherent linearly polarized waves form a standing wave of alternating electric and magnetic field nodes and antinodes, see Figure 7b. As electric field antinodes correspond to magnetic field nodes, and vice versa, this allows selective material excitation with electric or magnetic field only. This enables the selective detection of even parity multipole resonances (e.g., electric

DOI: 10.1021/acsphotonics.7b00921
ACS Photonics 2017, 4, 3000–3011

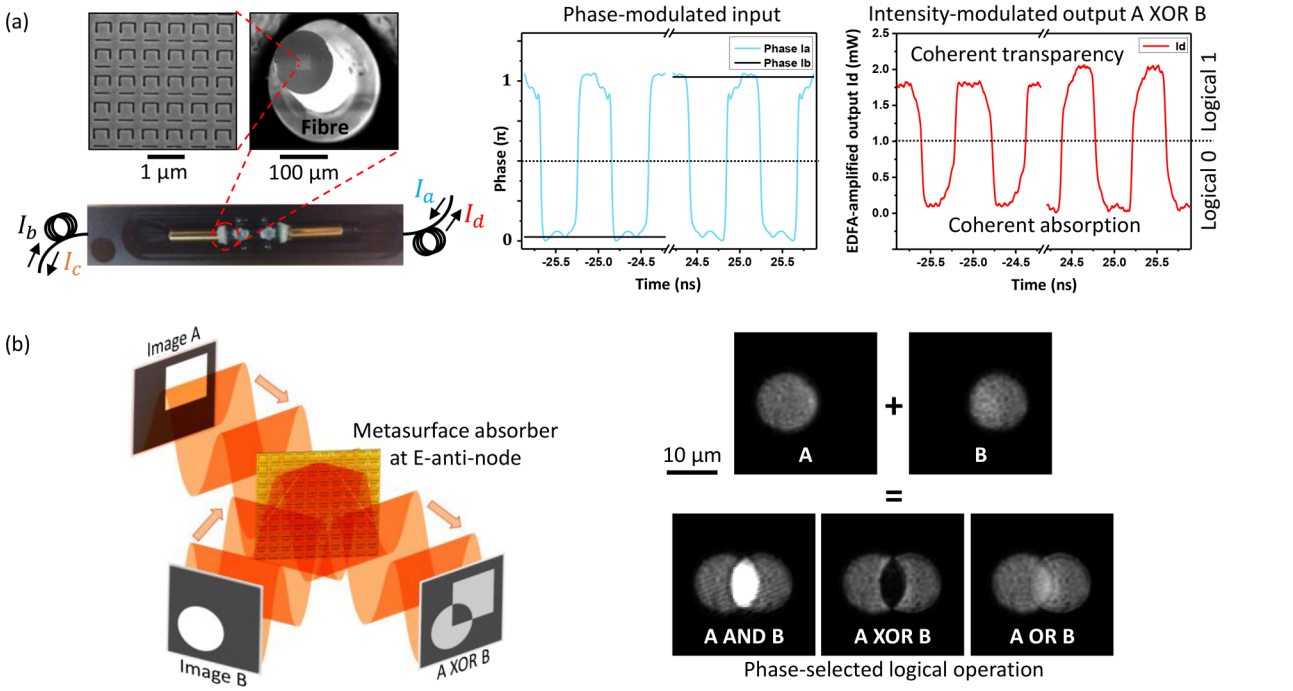

Figure 8. Coherent data and image processing. (a) Fiberized coherent data processing metadevice consisting of a gold metasurface absorber fabricated on the cleaved end of an optical fiber. Phase-modulated input signals I_a and I_b interact on the metasurface such that identical bits are absorbed and opposite bits are transmitted, yielding an output signal I_d corresponding to an intensity-modulated signal A XOR B with a modulation rate of 1.2 GHz.[76] (b) Logical operations between images, A and B, based on projection of both images onto a metasurface absorber using coherent light. The optical phase difference in areas of image overlap controls absorption from coherent perfect transparency to coherent perfect absorption and may be set to realize logical operations A AND B, A XOR B, and A OR B between the images.[77]

dipole) of a thin sample placed at an electric field antinode and detection of odd parity multipole resonances (e.g., magnetic dipole and electric quadrupole) at magnetic field antinodes.[72] Such excitation-selective spectroscopy in standing waves has been demonstrated experimentally by Fang et al.[73] using thin plasmonic metamaterials. The electric dipole resonance of an array of slots in a single plasmonic metal layer was clearly visible for electric field excitation but could not be detected with magnetic excitation (Figure 7c). In contrast, the magnetic dipole and electric quadrupole resonance of plasmonic wire pairs could only be detected with magnetic excitation of the nanostructure (Figure 7d).

Standing waves formed by copolarized, counterpropagating waves are only one type within a much bigger family of electromagnetic energy and polarization standing waves[74] promising further spectroscopic opportunities. Energy standing waves can be formed by counterpropagating coherent waves of parallel linear polarization or opposite circular polarizations and they are characterized by spatially oscillating electric and magnetic energy densities. Polarization standing waves are formed by counterpropagating waves of orthogonal linear polarization or identical circular polarization and they are characterized by a spatially oscillating local polarization state. As Fang et al.[74] have shown recently, they offer an additional degree of freedom for spectroscopy and control of light-matter interactions dependent on planar structural symmetries.

Data and Image Processing with Coherent Metadevices. The signal processing opportunities presented by coherent interaction of light-with-light on 2D matter in a four-port device, as discussed above, have been investigated in detail in a theoretical study by Fang et al.,[75] followed by recent experimental demonstrations.[76−78] They include transistor-like small-signal amplification as well as logical operations NOT, XOR, XNOR on phase-modulated data and NOT, XOR, AND, OR on intensity-modulated data, promising fast and low energy information processing in the locally coherent networks that are becoming part of the mainstream telecommunications agenda. With 100 THz bandwidth[47] and energy requirements at the quantum level[48] (see next section), coherent control of light-with-light on 2D matter may therefore provide part of the answer to the bandwidth and energy challenges in optical telecommunications.

Recently, a first fiberized coherent data processing system has been demonstrated,[76] see Figure 8a. It consists of a plasmonic metasurface absorber fabricated on the core area of a cleaved optical fiber coupled to a second optical fiber by a pair of microcollimator lenses. The fully packaged four-port metadevice connects directly to standard telecoms fibers. It exhibits the effective nonlinearity introduced in Figure 3 as well as several logical functions. For example, an XOR operation on binary phase-modulated data, where logical states of "1" and "0" are represented by equal intensity and opposite phase, is shown by Figure 8a. The XOR operation between input signals A and B results from absorption of identical bits due to constructive interference on the metasurface absorber and transmission of opposite bits due to destructive interference on the metasurface, yielding an intensity-modulated output signal A XOR B that has been demonstrated at modulation frequencies of up to 1.2 GHz. Other signal processing functions such as signal inversion have been demonstrated at effective bitrates of up to 40 Gbit/s.

In contrast to electronics, where every signal requires a separate wire, massively parallel information processing is easily realized in optics, where imaging systems transmit essentially

DOI: 10.1021/acsphotonics.7b00921
ACS Photonics 2017, 4, 3000−3011

separate information channels spaced by the diffraction limit. Therefore, "zero-dimensional" coherent control of one beam of light with another, as considered above, may be extended to "two-dimensional" coherent control of light with light by projecting different images onto opposite sides of a metasurface absorber using coherent light, see Figure 8b. This has been demonstrated by Papaioannou et al.[77] for the simple case of imaging two misaligned apertures onto a metasurface absorber. In the regions of image overlap, the phase difference between the illuminating light beams controls absorption of light by the metasurface. Destructive interference in areas of image overlap highlights the similarities of images A and B due to coherent perfect transparency and therefore yields an output image A AND B. On the other hand, constructive interference deletes the similarities by coherent absorption, leaving only the image differences and therefore yields an output image A XOR B. The phase-dependent power variation of the output image is therefore proportional to the area of image overlap, while the minimum power contained in the output image is a measure of the image differences, enabling pattern recognition and image analysis applications.[79] Further importance is derived from the exponential growth of telecommunications bandwidth that will require information transfer in multiple spatial information channels, for example, in multicore optical fibers. Here, two-dimensional control of light with light can provide solutions for both ultrafast parallel data processing as well as selection and deletion of selected information channels.[78]

However, despite demonstrations of various single-channel and multichannel signal processing operations, there are still significant challenges that need to be overcome before complex coherent information processing systems can become a reality,[80] for example relating to phase stability and cascading of multiple signal processing steps. The phase stability that will be required across the entire system may be achieved by miniaturization and a monolithic platform that could be based on silicon photonics. Cascading of coherent signal processing steps will require the output of one coherent interaction to be a suitable input for the next, implying that signal regeneration may be needed in between signal processing steps to avoid accumulation of noise.

Coherent Absorption of Light in the Quantum Regime. Conventional modulation of light-with-light based on optical nonlinearities is strongly intensity-dependent and requires a minimum level of intensity to activate the nonlinear response. In contrast, coherent control of light-with-light as discussed above is linear in the sense that equal scaling of all coherent signals incident on a 2D material will result in scaling of all output signals by the same factor. Recently, it has been demonstrated that this remains true at arbitrarily low intensities and even in the single photon regime,[48] unlocking interesting and counterintuitive opportunities for deterministic control of single as well as entangled quanta of light.

Historically, losses and dissipation have typically been considered highly undesirable in the field of quantum optics[81] as losses occur at the expense of additional fluctuations and noise in the system.[82,83] It was therefore generally thought that dissipation should at all costs be minimized or avoided. However, recent advances in the field of quantum plasmonics[84] have paved the way to the study of quantum effects in the context of coherent perfect absorption. While absorption of photons from a traveling wave is probabilistic, coherent perfect absorption can be observed deterministically even with a single photon, which may be coupled into a localized plasmon with nearly 100% probability.[48] Also, two-photon N00N states can be commanded to exclusively exhibit either single- or two-photon absorption.[85] A counterintuitive and currently debated possibility is that dissipation can actually lengthen the coherence time of a certain subsystem thus possibly even providing a route for the observation of quantum effects in "warm" environments such as photosynthesis or other biological systems.[86−88]

More specifically to the control of photon states, the presence of loss, if properly harnessed, can be used as a resource that can shape the specific output modes from a beamsplitter in ways that are not achievable without loss. The first theoretical studies in this sense were carried out by Barnett and co-workers who analyzed the behavior of a lossy beamsplitter inserted in a Hong-Ou-Mandel interferometer.[89]

Hong-Ou-Mandel interference is a quantum effect whereby two photons simultaneously entering two ports of a beam splitter will be forced to bunch together, that is, they can exit from either output port, but both photons must exit from the same port.[90] It is not possible to know which output port the two photons will bunch into. Therefore, two photons interfering at the beamsplitter will create what is known as a N00N state at the beamsplitter output. A N00N state is an entangled state and is so-called after the bra-ket notation used to describe the situation in which 2 photons (or N photons) are in a superposition state of being either N in one arm or N in the other arm of an interferometer. Such path-entangled states can be used as a resource for quantum metrology as they can provide an *N*-fold enhancement in interferometer-based phase measurements. N00N states from photon bunching at a beamsplitter are generally obtained with a lossless beamsplitter. The more general case in which loss occurs at the beamsplitter leads to more complicated output states. Without going into the details of the most general case studied by Barnett et al.,[89] we will consider the specific situation in which absorption is equal to exactly 50% in a very thin film (compared to the wavelength of the photon). For the simplest case of a single photon input state ($N = 1$) with appropriate phases, the single photon is either deterministically absorbed or completely transmitted, thus, providing a "lossless lossy beamsplitter".[91] This of course is just a quantum restatement of coherent perfect absorption for a single photon.[92] Coherent perfect absorption of a single photon was verified experimentally by Roger et al., thereby extending coherent perfect absorption into the single photon regime.[48] For appropriate two-photon input states ($N = 2$), the lossy beam splitter can yield deterministic absorption of a single photon as well as situations where the two photons must be either both transmitted or both absorbed. The latter is reminiscent of nonlinear absorption processes although it is important to recall that the "linear" two-photon absorption described here requires linear absorption at the input wavelength of the two input photons (in contrast to nonlinear two-photon absorption that can occur in a medium that is transparent at the input wavelength). Thus, quantum states in the regime of coherent perfect absorption can lead to rather unexpected output states and situations such as linear two-photon absorption that do not have a direct analogue in classical optics. The first experimental verification of coherent perfect absorption with two-photon N00N states was performed by Roger et al. and was carried out using a multilayer graphene beamsplitter.[85] By tailoring the number of layers (2.3% absorption per layer), it is possible to achieve close to ideal 50% absorption in a graphene film of several nm

DOI: 10.1021/acsphotonics.7b00921
ACS Photonics 2017, 4, 3000−3011

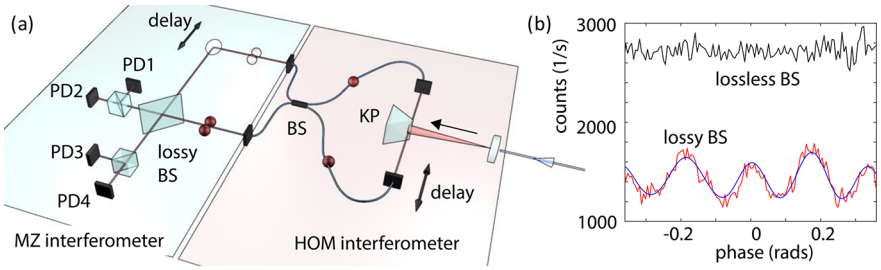

Figure 9. Coherent absorption in the quantum regime. (a) Experimental layout used to measure coherent perfect absorption with entangled N00N states. Photon pairs generated in a BBO crystal are filtered and split at a knife edge prism (KP). They are then coupled into the Hong-Ou-Mandel interferometer with single mode fibers and directed to a 50/50 beamsplitter (BS). A delay stage ensures the photons arrive at the same time on the beamsplitter and hence bunch, forming a N00N state. The $N = 2$ N00N state is directed into a Sagnac or, in this case, a Mach−Zehnder (MZ) interferometer. The N00N state interferes with itself on the lossy beam splitter and the output states are characterized by a series of four photon detectors (PD) and beamsplitters. (b) By scanning the N00N state phase with a delay stage, oscillations are seen in the total output coincidence counts. These correspond to the output state oscillating between a mixed state and a pure entangled N00N state with one photon less ($N = 1$). The black line shows the same measurement performed with a lossless beamsplitter: no oscillations in the coincidence counts are observed, reflecting the fact that the photon number is conserved.

thickness deposited on a glass substrate that is then used as the lossy beamsplitter. The input states are generated in a Hong-Ou-Mandel interferometer that is, in turn, illuminated with photon pairs obtained by parametric down-conversion in a BBO crystal. The output of the Hong-Ou-Mandel interferometer is fed into a Sagnac-interferometer, similar to that used for classical coherent perfect absorption measurements. The output states are then measured by extracting 50% of the photons with beamsplitters placed on either side of the lossy film. In this way it was indeed possible to verify that by changing the phase of the input states, the total photon counts oscillate, thus providing indirect evidence of the oscillation between single and two-photon absorption.

The extra degree of freedom offered by loss can also be used to achieve other forms of coherent control of quantum states. For example, Vest et al, showed that loss can lead to antibunching of bosons in a Hong-Ou-Mandel interferometer,[93] that is, the Hong-Ou-Mandel interferometer "dip" is replaced by a "peak". This Fermionic anticoalescence of photons at a beamsplitter, here obtained as a result of dissipation at the beamsplitter, had only been observed before by purposely shaping the input photons so that their wave functions where antisymmetric. Here, the common notion of boson bunching on a dielectric beamsplitter is overturned by resorting to the unique degree of freedom offered by lossy beamsplitters in tailoring the exact phase relation between reflection and transmission.

As a last example of progress in the field, we highlight recent work that extends previous quantum eraser experiments to include coherent perfect absorption.[94] If we consider the simple case of single photon interference, this may be inhibited by providing which-path information in the interferometer (e.g., by polarization rotation with a wave plate in one arm). During the postmeasurement process, it is however possible to "erase" the information by postselecting data based on measurements performed on a nonlocal detector.[95,96] The erasure scheme is enabled by entanglement of the photon inside the interferometer and the "control" photon, detected outside (nonlocally to) the interferometer. In the experiment by Altuzarra et al., a single photon is sent into a coherent perfect absorption interferometer such as that shown in Figure 9. The photon is one of a pair of polarization entangled photons; for example, the polarization of an individual photon is either vertical or horizontal but is not predetermined in a single measurement. However, measurement of the polarization of one photon fixes the polarization of the other to be opposite. Which-path information is introduced by a half-wave plate oriented at 45° inside only one arm of the interferometer: H-polarized photons traveling in that arm will be rotated to V and vice versa. Therefore, measurements performed on the single photon in the interferometer do not reveal any coherent perfect absorption effects due to the fact that the counterpropagating photon mode functions are oppositely polarized and can no longer form an energy standing wave. However, polarization sensitive measurements on the second (nonlocal) photon allow to immediately establish the polarization of the other photon: by postselecting all measurements corresponding to a fixed polarization of $\pm 45°$ at the nonlocal detector, one fixes the polarization to $\mp 45°$ in the interferometer (that is not modified by the half-wave plate): which-path information is erased and coherent perfect absorption interference fringes are now observed. The quantum nature of this process is also directly verified by reducing the degree of entanglement of the two input photons and thus observing a corresponding decrease in the coherent perfect absorption visibility.[94]

This brief overview of recent results shows how absorption is gaining recognition as a resource in quantum optics and as such, coherent control of absorption presents new opportunities for both fundamental studies and applications alike, enriching the quantum toolbox.

SUMMARY

Control of light-with-light used to be the domain of nonlinear optics, however, the coherent interaction of light-with-light on linear dispersive planar materials and metamaterials enables control over a huge range of optical phenomena. Instead of relying on optically nonlinear materials, dynamic control of light-with-light is derived from the fact that the interference of two coherent beams of light controls the local field that interacts with the film. This allows the manifestation of the film's optical functionalities to be controlled from complete suppression by destructive interference to enhancement by constructive interference. In contrast to optical nonlinearities, such coherent control of light-with-light offers high contrast and high bandwidth and works at arbitrary intensities down to the single photon regime. Therefore, this approach offers a broad range of novel and interesting opportunities for classical all-optical signal and image processing as well as quantum

DOI: 10.1021/acsphotonics.7b00921
ACS Photonics 2017, 4, 3000−3011

technologies. In addition, interference of coherent light fields allows selective probing of thin films with either electric or magnetic fields, opening up novel opportunities for spectroscopy.

AUTHOR INFORMATION

Corresponding Authors

*E-mail: erp@orc.soton.ac.uk.
*E-mail: kfm@orc.soton.ac.uk.
*E-mail: niz@orc.soton.ac.uk.

ORCID

Eric Plum: 0000-0002-1552-1840

Notes

The authors declare no competing financial interest.

ACKNOWLEDGMENTS

The authors thank Jianfa Zhang, Maria Papaioannou, Angelos Xomalis, Yidong Chong, and Robert Boyd for fruitful discussions. This work is supported by the U.K.'s Engineering and Physical Sciences Research Council (Grant EP/M009122/1) and the MOE Singapore (Grant MOE2011-T3-1-005). No new data were created as part of this review.

REFERENCES

(1) Shapiro M, B. P. *Principles of the Quantum Control of Molecular Processes*; John Wiley & Sons Inc.: New York, 2003.
(2) Reiter, D. E.; Sherman, E. Y.; Najmaie, A.; Sipe, J. E. Coherent control of electron propagation and capture in semiconductor heterostructures. *Europhys. Lett.* **2009**, *88* (6), 67005.
(3) Assion, A.; Baumert, T.; Bergt, M.; Brixner, T.; Kiefer, B.; Seyfried, V.; Strehle, M.; Gerber, G. Control of Chemical Reactions by Feedback-Optimized Phase-Shaped Femtosecond Laser Pulses. *Science* **1998**, *282* (5390), 919−922.
(4) Chong, Y. D.; Ge, L.; Cao, H.; Stone, A. D. Coherent Perfect Absorbers: Time-Reversed Lasers. *Phys. Rev. Lett.* **2010**, *105*, 053901.
(5) Wan, W.; Chong, Y.; Ge, L.; Noh, H.; Stone, A. D.; Cao, H. Time-Reversed Lasing and Interferometric Control of Absorption. *Science* **2011**, *331*, 889−892.
(6) Yoon, J. W.; Koh, G. M.; Song, S. H.; Magnusson, R. Measurement and Modeling of a Complete Optical Absorption and Scattering by Coherent Surface Plasmon-Polariton Excitation Using a Silver Thin-Film Grating. *Phys. Rev. Lett.* **2012**, *109*, 257402.
(7) Noh, H.; Chong, Y.; Stone, A. D.; Cao, H. Perfect coupling of light to surface plasmons by coherent absorption. *Phys. Rev. Lett.* **2012**, *108*, 186805.
(8) Pye, L. N.; Villinger, M. L.; Shabahang, S.; Larson, W. D.; Martin, L.; Abouraddy, A. F. Octave-spanning coherent perfect absorption in a thin silicon film. *Opt. Lett.* **2017**, *42* (1), 151−154.
(9) Stockman, M. I.; Faleev, S. V.; Bergman, D. J. Coherent Control of Femtosecond Energy Localization in Nanosystems. *Phys. Rev. Lett.* **2002**, *88*, 067402.
(10) Li, X.; Stockman, M. I. Highly efficient spatiotemporal coherent control in nanoplasmonics on a nanometer-femtosecond scale by time reversal. *Phys. Rev. B: Condens. Matter Mater. Phys.* **2008**, *77*, 195109.
(11) Kao, T. S.; Jenkins, S. D.; Ruostekoski, J.; Zheludev, N. I. Coherent Control of Nanoscale Light Localization in Metamaterial: Creating and Positioning Isolated Subwavelength Energy Hot Spots. *Phys. Rev. Lett.* **2011**, *106*, 085501.
(12) Gjonaj, B.; Aulbach, J.; Johnson, P. M.; Mosk, A. P.; Kuipers, L.; Lagendijk, A. Active spatial control of plasmonic fields. *Nat. Photonics* **2011**, *5*, 360−363.
(13) Brinks, D.; Castro-Lopez, M.; Hildner, R.; van Hulst, N. F. Plasmonic antennas as design elements for coherent ultrafast nanophotonics. *Proc. Natl. Acad. Sci. U. S. A.* **2013**, *110*, 18386−18390.
(14) Scalora, M.; Bloemer, M. J.; Pethel, A. S.; Dowling, J. P.; Bowden, C. M.; Manka, A. S. Transparent, metallo-dielectric, one-dimensional, photonic band-gap structures. *J. Appl. Phys.* **1998**, *83* (5), 2377−2383.
(15) Scalora, M.; Bloemer, M. J.; Bowden, C. M. Metals under a new light. *Opt. Photonics News* **1999**, *10* (9), 25−27.
(16) Bruck, R.; Muskens, O. L. Plasmonic nanoantennas as integrated coherent perfect absorbers on SOI waveguides for modulators and all-optical switches. *Opt. Express* **2013**, *21* (23), 27662−71.
(17) Park, H.; Lee, S. Y.; Kim, J.; Lee, B.; Kim, H. Near-infrared coherent perfect absorption in plasmonic metal-insulator-metal waveguide. *Opt. Express* **2015**, *23* (19), 24464−74.
(18) Rothenberg, J. M.; Chen, C. P.; Ackert, J. J.; Dadap, J. I.; Knights, A. P.; Bergman, K.; Osgood, R. M.; Grote, R. R. Experimental demonstration of coherent perfect absorption in a silicon photonic racetrack resonator. *Opt. Lett.* **2016**, *41* (11), 2537−40.
(19) Utikal, T.; Stockman, M. I.; Heberle, A. P.; Lippitz, M.; Giessen, H. All-Optical Control of the Ultrafast Dynamics of a Hybrid Plasmonic System. *Phys. Rev. Lett.* **2010**, *104*, 113903.
(20) Papoff, F.; McArthur, D.; Hourahine, B. Coherent control of radiation patterns of nonlinear multiphoton processes in nanoparticles. *Sci. Rep.* **2015**, *5*, 12040.
(21) Crescimanno, M.; Dawson, N. J.; Andrews, J. H. Coherent perfect rotation. *Phys. Rev. A: At., Mol., Opt. Phys.* **2012**, *86*, 031807.
(22) Crescimanno, M.; Zhou, C.; Andrews, J. H.; Baker, M. A. Structure and symmetry in coherent perfect polarization rotation. *Phys. Rev. A: At., Mol., Opt. Phys.* **2015**, *91* (1), 013845.
(23) Friedrich, D.; Kaufer, H.; Westphal, T.; Yamamoto, K.; Sawadsky, A.; Khalili, F. Y.; Danilishin, S. L.; Goßler, S.; Danzmann, K.; Schnabel, R. Laser interferometry with translucent and absorbing mechanical oscillators. *New J. Phys.* **2011**, *13*, 093017.
(24) Yan, X. B.; Cui, C. L.; Gu, K. H.; Tian, X. D.; Fu, C. B.; Wu, J. H. Coherent perfect absorption, transmission, and synthesis in a double-cavity optomechanical system. *Opt. Express* **2014**, *22* (5), 4886−4895.
(25) Choi, S. B.; Park, D. J.; Jeong, Y. K.; Yun, Y. C.; Jeong, M. S.; Byeon, C. C.; Kang, J. H.; Park, Q. H.; Kim, D. S. Directional control of surface plasmon polariton waves propagating through an asymmetric Bragg resonator. *Appl. Phys. Lett.* **2009**, *94*, 063115.
(26) Li, Z.; Zhang, S.; Halas, N. J.; Nordlander, P.; Xu, H. Coherent Modulation of Propagating Plasmons in Silver-Nanowire-Based Structures. *Small* **2011**, *7*, 593−596.
(27) Miyata, M.; Takahara, J. Excitation control of long-range surface plasmons by two incident beams. *Opt. Express* **2012**, *20*, 9493−9500.
(28) Wei, P.; Croënne, C.; Tak Chu, S.; Li, J. Symmetrical and anti-symmetrical coherent perfect absorption for acoustic waves. *Appl. Phys. Lett.* **2014**, *104* (12), 121902.
(29) Meng, C.; Zhang, X.; Tang, S. T.; Yang, M.; Yang, Z. Acoustic Coherent Perfect Absorbers as Sensitive Null Detectors. *Sci. Rep.* **2017**, *7*, 43574.
(30) Pozar, D. M. *Microwave Engineering*, 2nd ed.; John Wiley & Sons Inc., 1998.
(31) Jackson, J. D. *Classical Electrodynamics*, 3rd ed.; John Wiley & Sons: New York, 1998.
(32) Troitskii, Y. V. Optical resonator with a thin absorbing film as a mode selector. *Opt. Spectrosc.* **1968**, *25*, 309−313.
(33) Troitskii, Y. V.; Goldina, N. D. Separation of one mode in a laser. *JETP Lett.* **1968**, *7*, 36.
(34) Smith, P. W.; Schneider, M. V.; Danielmeyer, H. G. High-Power Single-Frequency Lasers Using Thin Metal Film Mode-Selection Filters. *Bell Syst. Tech. J.* **1969**, *48*, 1405.
(35) Avtonomov, V. P.; Antropov, E. T.; Sobolev, N. N.; Troitskii, Y. V. Separation of rotational lines of a CO2 laser with a film selector in the resonator. *Sov. J. Quantum Electron* **1972**, *2* (3), 300−302.
(36) Miller, A. B. Laser tuners and wavelength-selective detectors based on absorbers in standing waves. *IEEE J. Quantum Electron.* **1994**, *30* (3), 732−749.
(37) Babin, S. A.; Kablukov, S. I.; Terentiev, V. S. Reflection interferometer based on the Troitsky thin film for frequency selection in fiber lasers. *Laser Phys.* **2008**, *18* (11), 1241−1245.

DOI: 10.1021/acsphotonics.7b00921
ACS Photonics 2017, 4, 3000−3011

(38) Hägglund, C.; Apell, S. P.; Kasemo, B. Maximized Optical Absorption in Ultrathin Films and Its Application to Plasmon-Based Two-Dimensional Photovoltaics. *Nano Lett.* **2010**, *10*, 3135−3141.
(39) Thongrattanasiri, S.; Koppens, F. H. L.; García de Abajo, F. J. Complete Optical Absorption in Periodically Patterned Graphene. *Phys. Rev. Lett.* **2012**, *108*, 047401.
(40) Zhang, J.; MacDonald, K. F.; Zheludev, N. I. Controlling light-with-light without nonlinearity. *Light: Sci. Appl.* **2012**, *1*, e18.
(41) Dutta-Gupta, S.; Martin, O. J. F.; Dutta Gupta, S.; Agarwal, G. S. Controllable coherent perfect absorption in a composite film. *Opt. Express* **2012**, *20*, 1330−1336.
(42) Yu, S.; Piao, X.; Hong, J.; Park, N. Progress toward high-Qperfect absorption: A Fano antilaser. *Phys. Rev. A: At., Mol., Opt. Phys.* **2015**, *92* (1), 011802(R).
(43) Wong, Z. J.; Xu, Y.-L.; Kim, J.; O'Brien, K.; Wang, Y.; Feng, L.; Zhang, X. Lasing and anti-lasing in a single cavity. *Nat. Photonics* **2016**, *10* (12), 796−801.
(44) Zheludev, N. I.; Kivshar, Y. S. From metamaterials to metadevices. *Nat. Mater.* **2012**, *11*, 917−924.
(45) Plum, E.; Tanaka, K.; Chen, W. T.; Fedotov, V. A.; Tsai, D. P.; Zheludev, N. I. A combinatorial approach to metamaterials discovery. *J. Opt.* **2011**, *13*, 055102.
(46) Fang, X.; Tseng, M. L.; Ou, J. Y.; MacDonald, K. F.; Tsai, D. P.; Zheludev, N. I. Ultrafast all-optical switching via coherent modulation of metamaterial absorption. *Appl. Phys. Lett.* **2014**, *104*, 141102.
(47) Nalla, V.; Valente, J.; Sun, H.; Zheludev, N. I. 11-fs dark pluses generated via coherent absorption in plasmonic metamaterial. *Opt. Express* **2017**, *25* (19), 22620−22625.
(48) Roger, T.; Vezzoli, S.; Bolduc, E.; Valente, J.; Heitz, J. J. F.; Jeffers, J.; Soci, C.; Leach, J.; Couteau, C.; Zheludev, N. I.; Faccio, D. Coherent perfect absorption in deeply subwavelength films in the single-photon regime. *Nat. Commun.* **2015**, *6*, 7031.
(49) Nalla, V.; Karvounis, A.; Valente, J.; Sun, H. D.; Zheludev, N. I. Ultrafast Regimes of Coherent Absorption in Plasmonic and Dielectric Diamond-Based Metasurfaces. *ICMAT2017*, Singapore, 2017.
(50) Fan, Y.; Liu, Z.; Zhang, F.; Zhao, Q.; Wei, Z.; Fu, Q.; Li, J.; Gu, C.; Li, H. Tunable mid-infrared coherent perfect absorption in a graphene meta-surface. *Sci. Rep.* **2015**, *5*, 13956.
(51) Nie, G.; Shi, Q.; Zhu, Z.; Shi, J. Selective coherent perfect absorption in metamaterials. *Appl. Phys. Lett.* **2014**, *105*, 201909.
(52) Pu, M.; Feng, Q.; Wang, M.; Hu, C.; Huang, C.; Ma, X.; Zhao, Z.; Wang, C.; Luo, X. Ultrathin broadband nearly perfect absorber with symmetrical coherent illumination. *Opt. Express* **2012**, *20*, 2246−2254.
(53) Rao, S. M.; Heitz, J. J. F.; Roger, T.; Westerberg, N.; Faccio, D. Coherent control of light interaction with graphene. *Opt. Lett.* **2014**, *39* (18), 5345−5374.
(54) Boyd, R. W. *Nonlinear Opt.*, 3rd ed.; Academic Press: San Diego, CA, U.S.A., 2008.
(55) Shi, J.; Fang, X.; Rogers, E. T. F.; Plum, E.; MacDonald, K. F.; Zheludev, N. I. Coherent control of Snell's law at metasurfaces. *Opt. Express* **2014**, *22* (17), 21051−21060.
(56) Yu, N.; Genevet, P.; Kats, M. A.; Aieta, F.; Tetienne, J.-P.; Capasso, F.; Gaburro, Z. Light Propagation with Phase Discontinuities: Generalized Laws of Reflection and Refraction. *Science* **2011**, *334* (6054), 333−337.
(57) Kita, S.; Takata, K.; Ono, M.; Nozaki, K.; Kuramochi, E.; Takeda, K.; Notomi, M. Coherent control of high efficiency metasurface beam deflectors with a back partial reflector. *APL Photonics* **2017**, *2* (4), 046104.
(58) Ni, X.; Ishii, S.; Kildishev, A. V.; Shalaev, V. M. Ultra-thin, planar, Babinet-inverted plasmonic metalenses. *Light: Sci. Appl.* **2013**, *2* (4), e72.
(59) Chen, X.; Huang, L.; Muhlenbernd, H.; Li, G.; Bai, B.; Tan, Q.; Jin, G.; Qiu, C. W.; Zhang, S.; Zentgraf, T. Dual-polarity plasmonic metalens for visible light. *Nat. Commun.* **2012**, *3*, 1198.
(60) Ni, X.; Kildishev, A. V.; Shalaev, V. M. Metasurface holograms for visible light. *Nat. Commun.* **2013**, *4*, 2807.
(61) Huang, L.; Chen, X.; Mühlenbernd, H.; Zhang, H.; Chen, S.; Bai, B.; Tan, Q.; Jin, G.; Cheah, K.-W.; Qiu, C.-W.; Li, J.; Zentgraf, T.; Zhang, S. Three-dimensional optical holography using a plasmonic metasurface. *Nat. Commun.* **2013**, *4*, 2808.
(62) Mousavi, S. A.; Plum, E.; Shi, J.; Zheludev, N. I. Coherent control of birefringence and optical activity. *Appl. Phys. Lett.* **2014**, *105*, 011906.
(63) Plum, E.; Liu, X. X.; Fedotov, V. A.; Chen, Y.; Tsai, D. P.; Zheludev, N. I. Metamaterials: optical activity without chirality. *Phys. Rev. Lett.* **2009**, *102* (11), 113902.
(64) Mousavi, S. A.; Plum, E.; Shi, J.; Zheludev, N. I. Coherent control of optical polarization effects in metamaterials. *Sci. Rep.* **2015**, *5*, 8977.
(65) Hiramatsu, K.; Plum, E.; Valente, J.; MacDonald, K. F.; Zheludev, N. I. *Coherent Spectroscopy of Optical Activity*. *CLEO/Europe-EQEC 2015*, Munich, Germany, 21−25 June 2015; Munich, Germany, 2015.
(66) Pirruccio, G.; Ramezani, M.; Rodriguez, S. R.; Rivas, J. G. Coherent Control of the Optical Absorption in a Plasmonic Lattice Coupled to a Luminescent Layer. *Phys. Rev. Lett.* **2016**, *116* (10), 103002.
(67) Rao, S. M.; Lyons, A.; Roger, T.; Clerici, M.; Zheludev, N. I.; Faccio, D. Geometries for the coherent control of four-wave mixing in graphene multilayers. *Sci. Rep.* **2015**, *5*, 15399.
(68) Pirruccio, G.; Rivas, J. G. Modulated light absorption and emission of a luminescent layer by phase-controlled multiple beam illumination. *Opt. Express* **2015**, *23* (14), 18166−80.
(69) Terasaki, A.; Kondow, T.; Egashira, K. Continuous-wave cavity ringdown spectroscopy applied to solids: properties of a Fabry-Perot cavity containing a transparent substrate. *J. Opt. Soc. Am. B* **2005**, *22* (3), 675−686.
(70) Egashira, K.; Terasaki, A.; Kondow, T. Photon-trap spectroscopy applied to molecules adsorbed on a solid surface: probing with a standing wave versus a propagating wave. *Appl. Opt.* **2010**, *49* (7), 1151−1157.
(71) Wei, L.; Xi, Z.; Bhattacharya, N.; Urbach, H. P. Excitation of the radiationless anapole mode. *Optica* **2016**, *3* (8), 799.
(72) Tseng, M. L.; Fang, X.; Savinov, V.; Wu, P. C.; Ou, J. Y.; Zheludev, N. I.; Tsai, D. P. Coherent selection of invisible high-order electromagnetic excitations. *Sci. Rep.* **2017**, *7*, 44488.
(73) Fang, X.; Tseng, M. L.; Tsai, D. P.; Zheludev, N. I. Coherent Excitation-Selective Spectroscopy of Multipole Resonances. *Phys. Rev. Appl.* **2016**, *5*, 014010.
(74) Fang, X.; MacDonald, K. F.; Plum, E.; Zheludev, N. I. Coherent control of light-matter interactions in polarization standing waves. *Sci. Rep.* **2016**, *6*, 31141.
(75) Fang, X.; MacDonald, K. F.; Zheludev, N. I. Controlling light with light using coherent metadevices: all-optical transistor, summator and invertor. *Light: Sci. Appl.* **2015**, *4*, e292.
(76) Xomalis, A.; Demirtzioglou, I.; Plum, E.; Jung, Y.; Nalla, V.; Lacava, C.; MacDonald, K. F.; Petropoulos, P.; Richardson, D. J.; Zheludev, N. I. Fibre-optic metadevice for all-optical signal modulation based on coherent absorption. *arXiv1709.05357*, **2017**.
(77) Papaioannou, M.; Plum, E.; Valente, J.; Rogers, E. T. F.; Zheludev, N. I. Two-dimensional control of light with light on metasurfaces. *Light: Sci. Appl.* **2016**, *5*, e16070.
(78) Papaioannou, M.; Plum, E.; Valente, J.; Rogers, E. T. F.; Zheludev, N. I. All-optical multichannel logic based on coherent perfect absorption in a plasmonic metamaterial. *APL Photonics* **2016**, *1*, 090801.
(79) Papaioannou, M.; Plum, E.; Zheludev, N. I. All-Optical Pattern Recognition and Image Processing on a Metamaterial Beam Splitter. *ACS Photonics* **2017**, *4* (2), 217−222.
(80) Miller, D. A. B. Are optical transistors the logical next step? *Nat. Photonics* **2010**, *4* (1), 3−5.
(81) Walls, D. F.; Milburn, G. J. Effect of dissipation on quantum coherence. *Phys. Rev. A: At., Mol., Opt. Phys.* **1985**, *31* (4), 2403−2408.
(82) Callen, H. B.; Welton, T. A. Irreversibility and Generalized Noise. *Phys. Rev.* **1951**, *83* (1), 34−40.

DOI: 10.1021/acsphotonics.7b00921
ACS Photonics 2017, 4, 3000−3011

(83) Kubo, R. The fluctuation-dissipation theorem. *Rep. Prog. Phys.* **1966**, *29*, 255.
(84) Tame, M. S.; McEnery, K. R.; Özdemir, Ş. K.; Lee, J.; Maier, S. A.; Kim, M. S. Quantum plasmonics. *Nat. Phys.* **2013**, *9* (6), 329−340.
(85) Roger, T.; Restuccia, S.; Lyons, A.; Giovannini, D.; Romero, J.; Jeffers, J.; Padgett, M.; Faccio, D. Coherent Absorption of N00N States. *Phys. Rev. Lett.* **2016**, *117*, 023601.
(86) Müller, M.; Diehl, S.; Pupillo, G.; Zoller, P. Engineered Open Systems and Quantum Simulations with Atoms and Ions. *Adv. At., Mol., Opt. Phys.* **2012**, *61*, 1−80.
(87) Verstraete, F.; Wolf, M. M.; Ignacio Cirac, J. Quantum computation and quantum-state engineering driven by dissipation. *Nat. Phys.* **2009**, *5* (9), 633−636.
(88) Barreiro, J. T.; Muller, M.; Schindler, P.; Nigg, D.; Monz, T.; Chwalla, M.; Hennrich, M.; Roos, C. F.; Zoller, P.; Blatt, R. An open-system quantum simulator with trapped ions. *Nature* **2011**, *470* (7335), 486−491.
(89) Barnett, S.; Jeffers, J.; Gatti, A.; Loudon, R. Quantum optics of lossy beam splitters. *Phys. Rev. A: At., Mol., Opt. Phys.* **1998**, *57*, 2134−2145.
(90) Hong, C. K.; Ou, Z. Y.; Mandel, L. Measurement of Subpicosecond Time Intervals between Two Photons by Interference. *Phys. Rev. Lett.* **1987**, *59* (18), 2044−2046.
(91) Jeffers, J. Interference and the lossless lossy beam splitter. *J. Mod. Opt.* **2000**, *47*, 10.
(92) Huang, S.; Agarwal, G. S. Coherent perfect absorption of path entangled single photons. *Opt. Express* **2014**, *22* (17), 20936.
(93) Vest, B.; Dheur, M.-C.; Devaux, É.; Baron, A.; Rousseau, E.; Hugonin, J.-P.; Greffet, J.-J.; Messin, G.; Marquier, F. Anti-coalescence of bosons on a lossy beam splitter. *Science* **2017**, *356*, 1373.
(94) Altuzarra, C. M. X.; Vezzoli, S.; Valente, J.; Gao, W.; Soci, C.; Faccio, D.; Couteau, C. Coherent perfect absorption in metamaterials with entangled photons. *ACS Photonics* **2017**, *4*, 2124.
(95) Scully, M. O.; Drühl, K. Quantum eraser: A proposed photon correlation experiment concerning observation and "delayed choice" in quantum mechanics. *Phys. Rev. A: At., Mol., Opt. Phys.* **1982**, *25* (4), 2208−2213.
(96) Walborn, S. P.; Terra Cunha, M. O.; Pádua, S.; Monken, C. H. Double-slit quantum eraser. *Phys. Rev. A: At., Mol., Opt. Phys.* **2002**, *65* (3), 033818.

DOI: 10.1021/acsphotonics.7b00921
ACS Photonics 2017, 4, 3000−3011

NANO LETTERS

Letter

pubs.acs.org/NanoLett

Giant Enhancement of Cathodoluminescence of Monolayer Transitional Metal Dichalcogenides Semiconductors

Shoujun Zheng,[†] Jin-Kyu So,[†] Fucai Liu,[‡] Zheng Liu,[‡] Nikolay Zheludev,*[,†,§] and Hong Jin Fan*[,†,∥]

[†]Centre for Disruptive Photonic Technologies, School of Physical and Mathematical Sciences and The Photonics Institute, Nanyang Technological University, Singapore 637371

[‡]School of Materials Science and Engineering, Nanyang Technological University, 639798, Singapore

[§]Optoelectronics Research Centre and Centre for Photonic Metamaterials, University of Southampton, Southampton SO17 1BJ, United Kingdom

[∥]Division of Physics and Applied Physics, School of Physical and Mathematical Sciences, Nanyang Technological University, 637371, Singapore

S *Supporting Information*

ABSTRACT: Monolayer two-dimensional transitional metal dichalcogenides, such as MoS_2, WS_2, and WSe_2, are direct band gap semiconductors with large exciton binding energy. They attract growing attentions for optoelectronic applications including solar cells, photodetectors, light-emitting diodes and phototransistors, capacitive energy storage, photodynamic cancer therapy, and sensing on flexible platforms. While light-induced luminescence has been widely studied, luminescence induced by injection of free electrons could promise another important applications of these new materials. However, cathodoluminescence is inefficient due to the low cross-section of the electron−hole creating process in the monolayers. Here for the first time we show that cathodoluminescence of monolayer chalcogenide semiconductors can be evidently observed in a van der Waals heterostructure when the monolayer semiconductor is sandwiched between layers of hexagonal boron nitride (hBN) with higher energy gap. The emission intensity shows a strong dependence on the thicknesses of surrounding layers and the enhancement factor is more than 500-fold. Strain-induced exciton peak shift in the suspended heterostructure is also investigated by the cathodoluminescence spectroscopy. Our results demonstrate that MoS_2, WS_2, and WSe_2 could be promising cathodoluminescent materials for applications in single-photon emitters, high-energy particle detectors, transmission electron microscope displays, surface-conduction electron-emitter, and field emission display technologies.

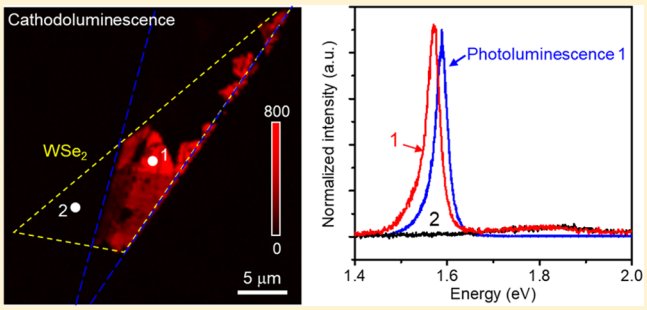

KEYWORDS: *2D materials, van der Waals heterostructures, cathodoluminescence, carrier confinement, photoluminescence*

Two-dimensional (2D) layered semiconductors, due to their weak interlayer van der Waals bonds, can be easily thinned down to atomic thickness by mechanical[1] and chemical[2] exfoliation methods, for example, graphene[3] and hexagonal boron nitride (hBN).[4] Monolayer transitional metal dichalcogenides (TMDCs) with the formula of MX_2 (M = Mo, W; X = S, Se, Te) are a type of unique semiconductors with narrow direct band gaps, large exciton binding energies, high optoconductivity, and high photoelectrochemical activity. Moreover, due to the inversion symmetry breaking, monolayer MX_2 are widely employed for the study of valley polarization and spin-valley coupling.[5,6] Recently, van der Waals heterostructures, composed of different 2D materials with unique band alignment and interlayer coupling, attract growing attentions not only for fundamental new physics but also for many potential applications such as tunneling transistors[7−9] and light-emitting diodes.[10]

Considering the low dimensionality and unavoidable defects, grain boundaries, and local strain of 2D TMDCs, it is essential to characterize their electronic, structural, and optical properties with the spatial resolution down to the relevant length scales which are mostly at the nanoscale. With the well-established scanning tunneling microscopes[11] or transmission electron microscopes,[12] characterizing the electronic and structural properties of monolayer TMDCs has been straightforward down to the atomic-scale. However, the optical characterization of excitonic excitations in monolayer TMDCs by photoluminescence (PL) is diffraction-limited due to the spot size of a laser, which should be resolved by creating optical excitations with subwavelength probes such as scanning probes[13] or focused electron beams.

Received: August 21, 2017
Revised: September 16, 2017
Published: September 21, 2017

DOI: 10.1021/acs.nanolett.7b03585
Nano Lett. 2017, 17, 6475−6480

Cathodoluminescence (CL), photon emission excited by a high-energy electron beam, is widely applied in the analysis of mineral compositions,[14] light-emitting diodes,[15,16] surface plasmon mapping.[17] Compared to PL excited by light, CL offers a much higher excitation energy allowing the study of wide band gap materials including diamond[18] and hexagonal boron nitride.[19,20] Due to a small excitation hotspot CL has been extensively used to study nanostructures including hyperspectral imaging of plasmonic gratings,[21] nanoparticles,[22] nanoantenna,[23] quantum well,[24,25] three-dimensional nanoscale visualization of metal-dielectric nanoresonators,[26] and nanoscale light sources.[27,28] Therefore, CL is an ideal candidate to investigate optical properties of 2D TMDCs in nanoscale.

In monolayers of TMDCs, it is challenging to detect the interband CL signal as the electron−hole creation cross section is extremely small. Moreover, the spatial distribution of electron−hole pairs at the interface, which is near the point of free-electron injection, is close to a three-dimensional spherical shape of a few microns in diameter. Only a negligible fraction of recombination takes place in the top 2D material and most of them happen in the supporting slab. So far only a few reports are available on CL study of 2D materials, including six atomic layer thick flakes of boron nitride.[29−31] However, observation of CL from monolayer TMDCs has not been achieved.

In this report, we show that CL emissions from monolayer MX_2 (MoS_2, WS_2 and WSe_2) can be enhanced and efficiently detected in a van der Waals heterostructure, in which the luminescent MX_2 layer is sandwiched between layers of hexagonal boron nitride (hBN) with higher energy gap (see schematics in Figure 1a). Here the hBN/MX_2/hBN heterostructure can effectively increase the recombination probability of electron−hole pairs in the monolayer MX_2 in such a way that a good fraction of the electrons and holes generated in the hBN layers diffuse to and then radiatively recombine in the MX_2 layer, leading to significant enhancement of the emission, comparatively to an isolated layer (Figure 1b).

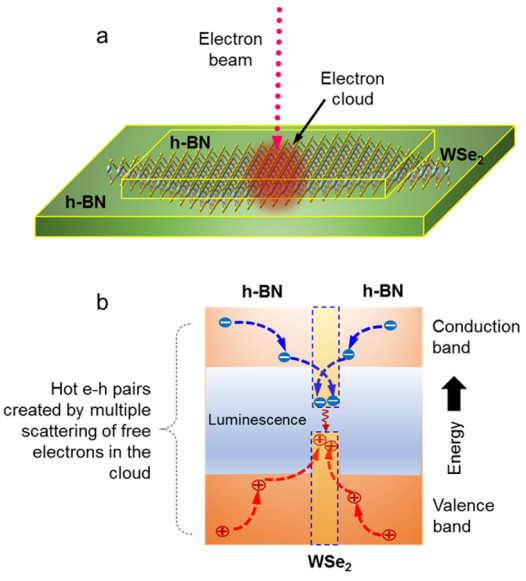

Figure 1. Electron beam-induced light emission in a TMDC heterostructure. (a) Illustration of cathodoluminescence in an hBN/MX_2/hBN van der Waals heterostructure. (b) Process of the generation, diffusion, and recombination of electron−hole (e-h) pairs. The minor number of e-h pairs generated in the MX_2 layer is ignored.

Cathodoluminescence of hBN/Monolayer WSe_2/hBN Heterostructure. Heterostructures of hBN/TMDC/hBN were prepared by stacking individual flakes with a dry transfer technique,[1,32] where mechanically exfoliated flakes are picked up in sequence by van der Waals forces (see Methods and Supporting Information Figure S1). Molybdenum disulfide (MoS_2), tungsten disulfide (WS_2) and tungsten diselenide (WSe_2) were tested as TMDC monolayers. Figure 2a is an optical image of a heterostructure hBN/WSe_2/hBN at an intermediate stage, where hBN (4.2 nm thick) and WSe_2 layers are clearly identified with an overlapped region. The heterostructure is completed by stamping this stack on another hBN layer (~100 nm thick) on a SiO_2/Si substrate as in Figure 2b. The TMDC monolayer and hBN layers constituting the heterostructures were further identified with micro-Raman (Supporting Information Figure S2).

Secondary electron imaging and CL measurements of prepared samples were performed in a scanning electron microscope equipped with a dedicated CL detection system. The emitted light induced by electron beam irradiation onto samples was collected by an achromatic reflective objective with a high numerical aperture (NA 0.72) and sent to a UV−vis spectrometer equipped with a thermoelectrically cooled silicon CCD array. To produce hyperspectral images,[21] the focused electron beam (electron energy 5 keV; beam current ~36 nA; dwell time 10−50 ms) scanned the samples according to a predefined resolution of the image while recording the light emission spectrum synchronously.

Figure 2c shows the CL intensity map of the heterostructure hBN/WSe_2/hBN near 1.572 eV which corresponds to the exciton energy of monolayer WSe_2. Here, WSe_2 monolayer glows only if sandwiched by the two hBN layers, which confirms the model for enhancing CL in monolayer TMDCs described in Figure 1. The extra e-h pairs created in the adjacent hBN layers diffuse, trap, and recombine in the monolayer TMDCs. The CL spectra from WSe_2 monolayer on (position 1) and off (position 2) the heterostructure are shown in Figure 2d. The small redshift of CL spectrum, 16.8 meV, from the PL spectrum in Figure 2d is attributed to the temperature-induced band gap shrinkage[33] of the semiconductor caused by the local heating by the electron beam.[34] Similar redshifts were also observed from other TMDCs, such as MoS_2 and WS_2, studied in this work. The patchy emission pattern within the sandwiched region in Figure 2c is due to poor interface contacts developed during the dry transfer. The CL intensity was proportional to the beam current and remained linear within the available beam current (Supporting Information Figure S2e).

Effect of hBN Thickness on CL Enhancement. In electroluminescence or PL configuration, hBN layers in such heterostructures would only work as tunneling barriers for electrically or optically injected charge carriers. In CL configuration, they should also work as a source for extra e-h pairs due to the broadband pumping capability of swift electrons. Part of them can diffuse into and trapped in the sandwiched monolayer TMDCs before they recombine in hBN layers. To verify this aspect of hBN layers, we prepared two types of heterostructures where either the top or bottom hBN layer is manipulated to have a selection of thickness and studied the effect of barrier thickness on the CL intensity.

DOI: 10.1021/acs.nanolett.7b03585
Nano Lett. 2017, 17, 6475−6480

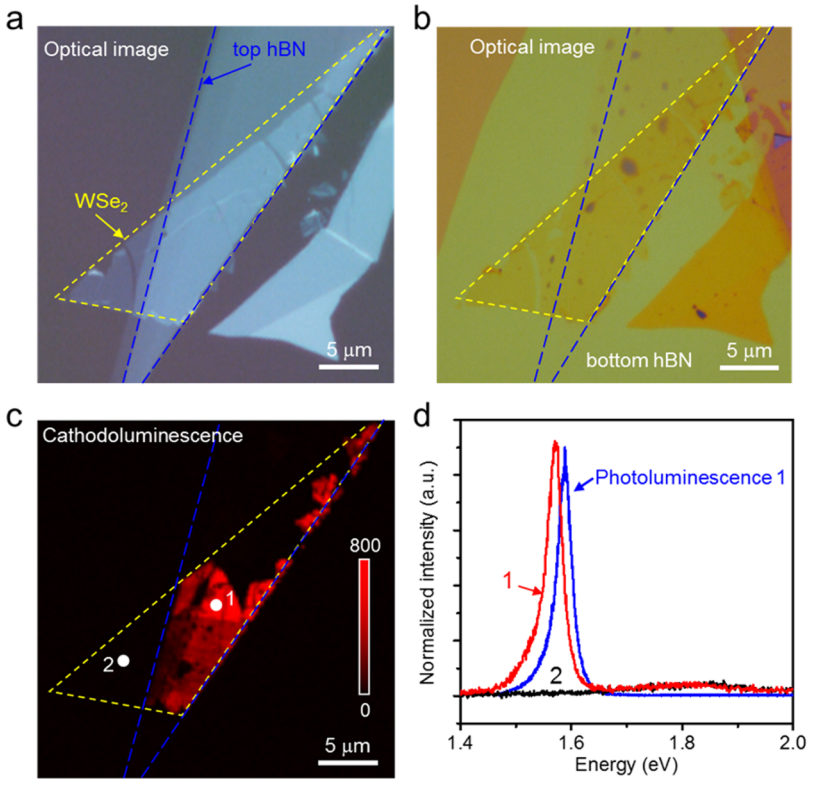

Figure 2. Optical characterization of a heterostructure hBN/WSe_2/hBN. Optical microscope images of a heterostructure hBN/WSe_2/hBN (a) before and (b) after the final dry transfer onto a bottom hBN layer. While Top hBN flake (blue) and monolayer WSe_2 (yellow) can be identified as small flakes, the edge of larger bottom hBN flake is not seen in the images. (c) Monochromatic CL map of the heterostructure at WSe_2 emission energy, 1.66 eV (color coded in red). (d) CL spectra generated by electron beam impact on WSe_2 at position 1 and 2 in (c) are shown together with a PL spectrum acquired at position 1 in (c).

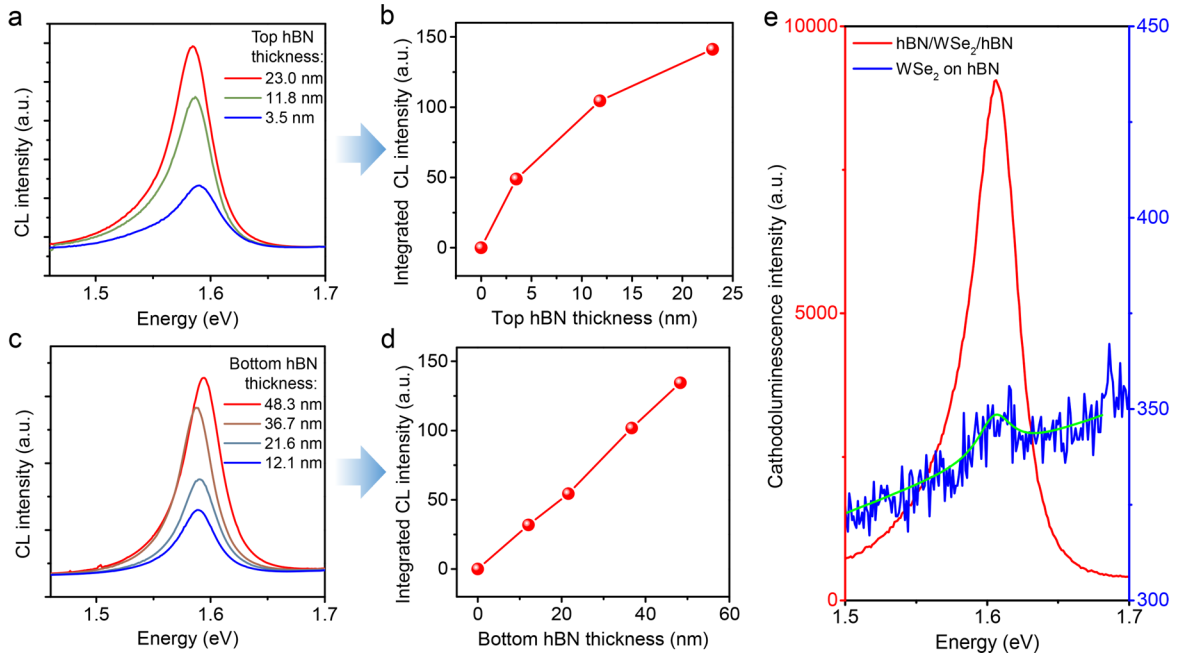

Figure 3. Effects of hBN layers on CL intensity. CL spectra acquired from regions with different (a) top and (c) bottom hBN thickness. The CL integrated intensity is shown as a function of (b) top and (d) bottom hBN thickness. (e) Comparison of CL intensity of sandwiched WSe_2 (with 19.8 nm top and 123.9 nm bottom hBN layers, red line) and WSe_2 with only bottom hBN layer (blue line). Green line is the Lorenz fitting of the blue line. The enhancement factor is estimated to be more than 500.

To see the effect of top hBN layer, a heterostructure hBN/WSe_2/hBN was fabricated from a bottom hBN layer with a uniform thickness of 165.3 nm and a top hBN layer with three regions of different thickness from 3.5, 11.8, and 23.0 nm. The

DOI: 10.1021/acs.nanolett.7b03585
Nano Lett. 2017, 17, 6475−6480

CL mapping for WSe_2 emission shows a clear contrast in intensity between the three regions (see Supporting Information Figure S3a–c). Figure 3a shows CL spectra from the three regions where each spectrum is an average of multiple spectra acquired from 20 positions within each region to remove the intensity inhomogeneity. The peak CL intensity increases with the top hBN thickness in a nearly linear fashion (Figure 3b).

To see the effect of bottom hBN layer, another heterostructure hBN/WSe_2/hBN which was prepared from a top hBN layer with a uniform thickness of 20.0 nm and a bottom hBN layer with four regions of thickness from 12.1, 21.6, 36.7, 48.3 nm. The CL mapping shows a similar dependence of increasing CL intensity with bottom hBN thickness (Figure 3c,d and Supporting Information Figure S3d–f). The slight variations in CL peak positions between regions in both samples might be arising from local strain and/or heterostructure inhomogeneity. The dependence of CL intensity on the top and bottom hBN thickness was also confirmed in another set of samples. This dependence confirms our model in Figure 1 that majority of e-h pairs which recombine in TMDC monolayers originate from the adjacent hBN layers. The diffusion lengths of electrons and holes in hBN are known to be in the micrometer range,[35] so large amounts of e-h pairs created in both top and bottom hBN layers in the heterostructure can diffuse into the TMDC monolayer layer before recombination. As hBN layers with larger thickness would support larger interaction volume for e-h pair creation, the amount of e-h pairs that are eventually trapped in TMDC monolayer should be proportional to the hBN layer thickness. It is noteworthy that the bottom hBN layer cannot be replaced by the amorphous SiO_2 substrate, as the latter does not provide an atomically flat surface as well as perfect contact. In order to roughly estimate the enhancement factor in our experiments, we compare the intensity ratio of the sandwiched hBN/WSe_2/hBN to that of the WSe_2/hBN (i.e., with only bottom hBN), which is more than 500 times (see Figure 3e).

Nanoscale Imaging of Strain-Induced Band Gap Variation. To demonstrate the full potential of CL spectroscopy as a nanoscale optical characterization tool for monolayer TMDCs, we created a heterostructure hBN/WSe_2/hBN possessing nanoscale variation of strain by placing the heterostructure on a prepatterned Si substrate with holes of 1–2 μm diameter (see inset of Figure 4a and Supporting Information Figure S4). Part of the heterostructure sitting above the holes are suspended and develops spatially varying strain which induces band gap shrinkage of the monolayer WSe_2 accordingly. This strain-induced band gap engineering is well established both theoretically[36] and experimentally.[37−39] Interestingly, the CL intensity from the suspended part of the heterostructure is much higher than the rest of the heterostructure (Figure 4a). This is attributed to the funnel effect[40] where the e-h pairs in the monolayer drift toward the strained part due to the lowered band gap and recombine. To enhance the spectral resolution for resolving the strain-induced peak shifts, the sample was cooled down to 10 K where the exciton and trion peaks well separated. Position-dependent spectra at 10 K (Figure 4b,c) clearly shows that the excitonic peak redshift with a maximum shift of 11.2 meV from the edge to the center of the hole due to strain.

In addition to the strain induced by suspension, local strain can be introduced in the heterostructures during the transfer process. Such inhomogeneous local strain in the heterostructures is also detectable by CL spectroscopy. Indeed two energy domains were observed from the hBN/WSe_2/hBN (indicated by purple and green colors in Supporting Information Figure S5a) sample in terms of the exciton peak position at 77 K. From the CL spectra from selected points (Supporting Information Figure S5b), two emission peaks can be resolved at both point A and B. The two peaks correspond to the emissions of neutral excitons and trions (charged excitons).[41] However, the peak positions of excitons and trions at point A are 1.640 and 1.614 eV, respectively, while 1.657 and 1.623 eV are at point B. The peak position difference between point A and B in the heterostructure may be caused by strain, which is possibly generated during the transfer process (e.g., bubbles).

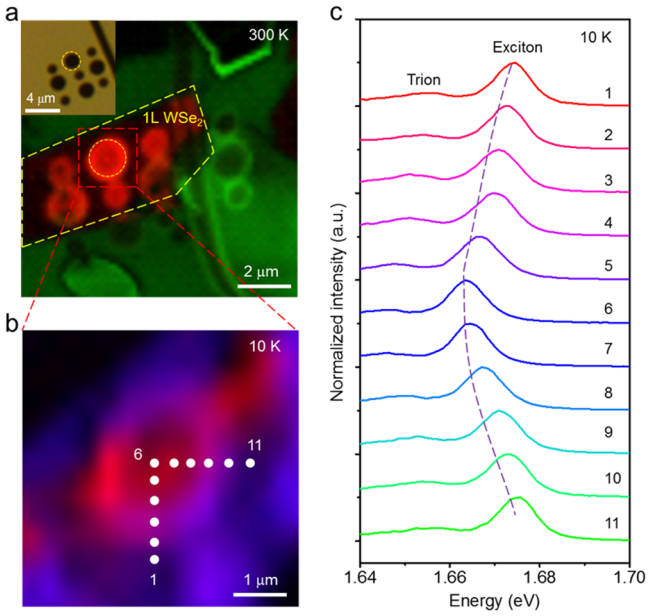

Figure 4. Imaging of the strain-induced band gap variation. (a) CL image of an hBN/WSe_2/hBN heterostructure on a patterned Si substrate at room temperature. The pseudocolors correspond to the luminescence in 307–331 nm (green) and 733–788 nm (red). Inset: Scanning electron microscopy image of the patterned silicon substrate without the heterostructure. (b) CL mapping acquired for the hole highlighted in (a) with higher magnification at 10 K. The pseudocolors correspond to the luminescence in 707–716 nm (blue) and 716–726 nm (red). (c) Position-dependent spectra taken from a selection of data points in (b).

Temperature-dependent CL spectra of the point B were plotted (Supporting Information Figure S5c). The peak positions of both excitons and trions are fitted (Supporting Information Figure S5d) according to the semiempirical semiconductor band gap equation[33,42] of $E_g(T) = E_g(0) - S\hbar\omega[\coth(\frac{\hbar\omega}{2kT})-1]$, where $E_g(0)$ is the excitonic energy at 0 K, S is a dimensionless coupling constant, and $\hbar\omega$ is an average phonon energy. From the fitting curves, we extract $E_g(0)$ of the exciton and trion of the monolayer WSe_2 to be 1.665 and 1.634 eV, respectively. So, the binding energy of the trion is calculated to be ~30.8 meV which is consistent with the previous report (30 meV).[32]

CL Enhancement in Heterostructures with MoS_2 and WS_2. In addition to WSe_2, we also performed CL experiments to monolayer WS_2 and MoS_2 in a van der Waals heterostructure (sandwiched by two hBN layers). The emission peak position from the WS_2 heterostructure is located at 1.933 eV (Figure 5a)

DOI: 10.1021/acs.nanolett.7b03585
Nano Lett. 2017, 17, 6475–6480

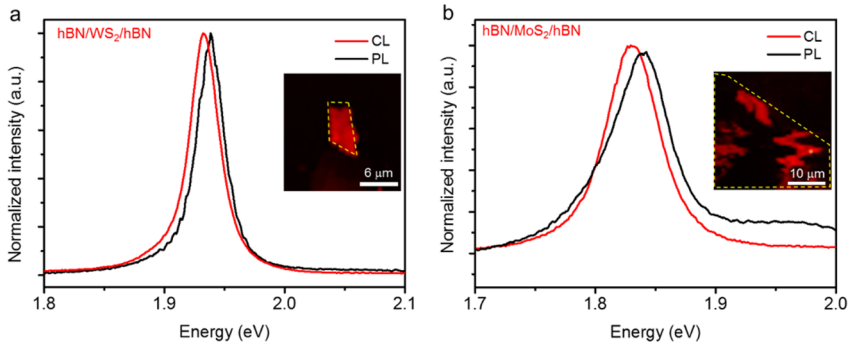

Figure 5. Cathodoluminescence of monolayer WS_2 and MoS_2. (a) CL and PL spectra of the monolayer WS_2 in the top-hBN (7.5 nm)/WS_2/bottom-hBN (299.4 nm). (b) CL and PL spectra of the monolayer MoS_2 in the top-hBN (13.5 nm)/MoS_2/bottom-hBN (168.6 nm). Insets are the corresponding CL intensity mappings.

and that from the MoS_2 in the heterostructure is at 1.831 eV (Figure 5b). The emission peak positions of both two heterostructures redshift with respect to their PL peak positions, similar to the case of hBN/WSe_2/hBN. The CL mapping is inhomogeneous at the MoS_2 sample, which is most likely due to a poor interface contact. Therefore, we have attested that sandwiching a monolayer TMDC into two hBN layers is a universal approach to study its CL emission.

In summary, for the first time we have obtained evident CL emissions from monolayer TMDCs, including WSe_2, MoS_2 and WS_2, via a van der Waals heterostructure configuration. In the hBN/TMDC/hBN heterostructure, electron beam induced e-h pairs can transfer to and be trapped in the middle TMDC layer, leading to increased recombination probability within the TMDC layer. Moreover, we demonstrate that CL spectroscopy can be applied to study the strain-induced excitonic peak shift in monolayer TMDCs. Because of its high spatial resolution and high beam energy, our demonstration makes CL spectroscopy a powerful technique to the study of 2D materials in various forms such as alloy, heterostructures or defects. The 2D monolayer-based heterostructure may promise potential applications in single-photon emitters, surface-conduction electron-emitter, and field emission display technologies.

Methods. *Heterostructure Preparation.* Heterostructures of hBN/TMDC/hBN were prepared using a dry transfer technique.[1,32] hBN and monolayer TMDC flakes were mechanically exfoliated from bulk hBN and TMDC single crystals synthesized by chemical vapor transport method with Scotch tape and deposited on 300 nm thick SiO_2 on Si (SiO_2/Si)substrates. Mono- and few-layer flakes were identified by optical contrast (Nikon optical microscope), Raman spectroscopy, and atomic force microscopy (AFM) (see Supporting Information Figure S2). As adhesion layer, poly(vinyl alcohol) (PVA) was used as it is water-soluble with a moderate adhesion. A PVA solution (9% weight in water) was spin coated on a polydimethylsiloxane (PDMS) film (~0.5 mm thick). After baking at 90 °C on a hot plate, the PDMS/PVA film was attached on a glass slide and the whole stack was mounted on a micromanipulator. Under an optical microscope, the PDMS/PVA stack was aligned to an hBN flake on a SiO_2/Si substrate and brought into contact with the flake underneath. The flake can be easily picked up due to its stronger adhesion to PVA than SiO_2. The procedure was repeated to pick up a monolayer TMDC flake. Then, the hBN/TMDC on the stack was aligned and brought into contact to another hBN flake on a Si/SiO_2 substrate. The PDMS/PVA film was released from the heterostructure on SiO_2/Si by slowly peeling the PDMS film from the PVA film at 70 °C leaving the PVA film on the Si/SiO_2. The PVA film was washed off by dipping in water for half an hour. Fewer bubbles and better contacts were created with the latter approach since the heterostructure was not stretched during the removal of the PDMS film. For the patterning of the Si substrate in Figure 4, a focused ion beam (FEI Helios NanoLab) was used to mill holes with 1−2 μm diameter and 1 μm depth.

AFM and Optical Characterization. The thickness of hBN flakes was measured using a Cypher ES scanning probe microscopy in AC tapping mode. A Witec alpha300 R confocal Raman spectrum was used to collect Raman and photolulminescence spectra where a pump laser at 532 nm at power of 0.2 mW was used to illuminate the samples through a 100× objective.

CL Measurements. CL measurements were performed in a scanning electron microscope equipped with a CL detection system, Attolight Allalin 4027 Chronos. A focused electron beam (electron energy 5 keV; beam current ~36 nA; dewell time 10−50 ms) scanned the samples while recording the light emission spectrum synchronously to produce hyperspectral images. The emitted light was collected by an achromatic reflective objective with a high numerical aperture (NA 0.72) and sent to a UV−vis spectrometer (Horiba iHR320) equipped with a thermoelectrically cooled silicon CCD array (Andor Newton). For low-temperature measurements, samples were cooled down with an open-cycle cryostat by continuously flowing either liquid nitrogen or liquid helium.

■ ASSOCIATED CONTENT

Supporting Information

The Supporting Information is available free of charge on the ACS Publications website at DOI: 10.1021/acs.nanolett.7b03585.

Further information on sample transfer, more AFM and optical images, and CL spectra (PDF)

■ AUTHOR INFORMATION

Corresponding Authors

*E-mail: NZheludev@ntu.edu.sg (N. Z).
*E-mail: fanhj@ntu.edu.sg (H.J. F).

ORCID

Hong Jin Fan: 0000-0003-1237-4555

DOI: 10.1021/acs.nanolett.7b03585
Nano Lett. 2017, 17, 6475−6480

Author Contributions

S.Z. conceived the idea of using vdW heterostructures and prepared samples. J.K.S. and S.Z. conducted CL measurements. F.L. provided the hBN and TMDCs crystals and conducted Raman and PL measurements. S.Z. and J.K.S. prepared the manuscript. All authors contributed to the analysis and interpretation of results and writing of the paper. H.J.F. supervised the project. S.Z. and J.K.S. contributed equally.

Notes

The authors declare no competing financial interest.

■ ACKNOWLEDGMENTS

This work was supported by Singapore Ministry of Education Academic Research Fund Tier 3 (Grant MOE2011-T3-1-005), the Singapore National Research Foundation under NRF RF Award No. NRF-RF2013-08, the start-up funding from Nanyang Technological University (M4081137.070), and Nanyang Technological University Strategic Research Facilities Initiative.

■ REFERENCES

(1) Castellanos-Gomez, A.; Buscema, M.; Molenaar, R.; Singh, V.; Janssen, L.; van der Zant, H. S. J.; Steele, G. A. *2D Mater.* **2014**, *1* (1), 011002.
(2) Chhowalla, M.; Shin, H. S.; Eda, G.; Li, L. J.; Loh, K. P.; Zhang, H. *Nat. Chem.* **2013**, *5* (4), 263−275.
(3) Novoselov, K. S.; Geim, A. K.; Morozov, S. V.; Jiang, D.; Zhang, Y.; Dubonos, S. V.; Grigorieva, I. V.; Firsov, A. A. *Science* **2004**, *306* (5696), 666−669.
(4) Dean, C. R.; Young, A. F.; Meric, I.; Lee, C.; Wang, L.; Sorgenfrei, S.; Watanabe, K.; Taniguchi, T.; Kim, P.; Shepard, K.; et al. *Nat. Nanotechnol.* **2010**, *5* (10), 722−726.
(5) Zeng, H. L.; Dai, J. F.; Yao, W.; Xiao, D.; Cui, X. D. *Nat. Nanotechnol.* **2012**, *7* (8), 490−493.
(6) Shan, W. Y.; Lu, H. Z.; Xiao, D. *Phys. Rev. B: Condens. Matter Mater. Phys.* **2013**, *88* (12), 125301.
(7) Britnell, L.; Gorbachev, R.; Geim, A.; Ponomarenko, L.; Mishchenko, A.; Greenaway, M.; Fromhold, T.; Novoselov, K.; Eaves, L. *Nat. Commun.* **2013**, *4*, 1794.
(8) Nguyen, L.-N.; Lan, Y.-W.; Chen, J.-H.; Chang, T.-R.; Zhong, Y.-L.; Jeng, H.-T.; Li, L.-J.; Chen, C.-D. *Nano Lett.* **2014**, *14* (5), 2381−2386.
(9) Campbell, P. M.; Tarasov, A.; Joiner, C. A.; Ready, W. J.; Vogel, E. M. *ACS Nano* **2015**, *9* (5), 5000−5008.
(10) Withers, F.; Del Pozo-Zamudio, O.; Mishchenko, A.; Rooney, A. P.; Gholinia, A.; Watanabe, K.; Taniguchi, T.; Haigh, S. J.; Geim, A. K.; Tartakovskii, A. I.; Novoselov, K. S. *Nat. Mater.* **2015**, *14* (3), 301−306.
(11) Helveg, S.; Lauritsen, J. V.; Laegsgaard, E.; Stensgaard, I.; Norskov, J. K.; Clausen, B. S.; Topsoe, H.; Besenbacher, F. *Phys. Rev. Lett.* **2000**, *84* (5), 951−954.
(12) Van Der Zande, A. M.; Huang, P. Y.; Chenet, D. A.; Berkelbach, T. C.; You, Y.; Lee, G.-H.; Heinz, T. F.; Reichman, D. R.; Muller, D. A.; Hone, J. C. *Nat. Mater.* **2013**, *12* (6), 554−561.
(13) Bao, W.; Melli, M.; Caselli, N.; Riboli, F.; Wiersma, D.; Staffaroni, M.; Choo, H.; Ogletree, D.; Aloni, S.; Bokor, J.; et al. *Science* **2012**, *338* (6112), 1317−1321.
(14) Boggs, S.; Krinsley, D. *Application of cathodoluminescence imaging to the study of sedimentary rocks*; Cambridge University Press, 2006; p 7.
(15) Chin, A. K.; Zipfel, C. L.; Mahajan, S.; Ermanis, F.; Digiuseppe, M. A. *Appl. Phys. Lett.* **1982**, *41* (6), 555−557.
(16) Griffiths, J. T.; Zhang, S.; Rouet-Leduc, B.; Fu, W. Y.; Bao, A.; Zhu, D.; Wallis, D. J.; Howkins, A.; Boyd, I.; Stowe, D.; Kappers, M. J.; Humphreys, C. J.; Oliver, R. A. *Nano Lett.* **2015**, *15* (11), 7639−43.
(17) Zhao, M.; Bosman, M.; Danesh, M.; Zeng, M.; Song, P.; Darma, Y.; Rusydi, A.; Lin, H.; Qiu, C. W.; Loh, K. P. *Nano Lett.* **2015**, *15* (12), 8331−8335.
(18) Ruf, T.; Cardona, M.; Sternschulte, H.; Wahl, S.; Thonke, K.; Sauer, R.; Pavone, P.; Anthony, T. R. *Solid State Commun.* **1998**, *105* (5), 311−316.
(19) Watanabe, K.; Taniguchi, T.; Kanda, H. *Nat. Mater.* **2004**, *3* (6), 404−409.
(20) Arnaud, B.; Lebegue, S.; Rabiller, P.; Alouani, M. *Phys. Rev. Lett.* **2006**, *96* (2), 026402.
(21) Bashevoy, M.; Jonsson, F.; MacDonald, K.; Chen, Y.; Zheludev, N. *Opt. Express* **2007**, *15* (18), 11313−11320.
(22) Tikhomirov, V.; Adamo, G.; Nikolaenko, A.; Rodriguez, V.; Gredin, P.; Mortier, M.; Zheludev, N.; Moshchalkov, V. *Opt. Express* **2010**, *18* (9), 8836−8846.
(23) Denisyuk, A.; Adamo, G.; MacDonald, K.; Edgar, J.; Arnold, M.; Myroshnychenko, V.; Ford, M.; García de Abajo, F. J.; Zheludev, N. *Nano Lett.* **2010**, *10* (9), 3250−3252.
(24) Xu, J.; Chen, L.; Yu, L.; Liang, H.; Zhang, B.; Lau, K. M. *J. Electron. Mater.* **2007**, *36* (9), 1144−1148.
(25) Priesol, J.; Satka, A.; Uherek, F.; Donoval, D.; Shields, P.; Allsopp, D. W. E. *Appl. Surf. Sci.* **2013**, *269*, 155−160.
(26) Atre, A. C.; Brenny, B. J.; Coenen, T.; Garcia-Etxarri, A.; Polman, A.; Dionne, J. A. *Nat. Nanotechnol.* **2015**, *10* (5), 429−436.
(27) Adamo, G.; MacDonald, K. F.; Fu, Y.; Wang, C.; Tsai, D.; Garcia de Abajo, F.; Zheludev, N. *Phys. Rev. Lett.* **2009**, *103* (11), 113901.
(28) Li, G.; Clarke, B. P.; So, J. K.; MacDonald, K. F.; Zheludev, N. I. *Nat. Commun.* **2016**, *7*, 13705.
(29) Bourrellier, R.; Amato, M.; Tizei, L. H. G.; Giorgetti, C.; Gloter, A.; Heggie, M. I.; March, K.; Stephan, O.; Reining, L.; Kociak, M.; Zobelli, A. *ACS Photonics* **2014**, *1* (9), 857−862.
(30) Watanabe, K.; Taniguchi, T.; Niiyama, T.; Miya, K.; Taniguchi, M. *Nat. Photonics* **2009**, *3* (10), 591−594.
(31) Schue, L.; Berini, B.; Betz, A. C.; Placais, B.; Ducastelle, F.; Barjon, J.; Loiseau, A. *Nanoscale* **2016**, *8* (13), 6986−6993.
(32) Pizzocchero, F.; Gammelgaard, L.; Jessen, B. S.; Caridad, J. M.; Wang, L.; Hone, J.; Boggild, P.; Booth, T. J. *Nat. Commun.* **2016**, *7*, 11894.
(33) O'Donnell, K.; Chen, X. *Appl. Phys. Lett.* **1991**, *58* (25), 2924−2926.
(34) Rodriguez-Viejo, J.; Jensen, K.; Mattoussi, H.; Michel, J.; Dabbousi, B.; Bawendi, M. *Appl. Phys. Lett.* **1997**, *70* (16), 2132−2134.
(35) Maity, A.; Doan, T. C.; Li, J.; Lin, J. Y.; Jiang, H. X. *Appl. Phys. Lett.* **2016**, *109* (7), 072101.
(36) Amin, B.; Kaloni, T. P.; Schwingenschlogl, U. *RSC Adv.* **2014**, *4* (65), 34561−34565.
(37) Castellanos-Gomez, A.; Roldán, R.; Cappelluti, E.; Buscema, M.; Guinea, F.; van der Zant, H. S.; Steele, G. A. *Nano Lett.* **2013**, *13* (11), 5361−5366.
(38) Conley, H. J.; Wang, B.; Ziegler, J. I.; Haglund, R. F., Jr.; Pantelides, S. T.; Bolotin, K. I. *Nano Lett.* **2013**, *13* (8), 3626−3630.
(39) Desai, S. B.; Seol, G.; Kang, J. S.; Fang, H.; Battaglia, C.; Kapadia, R.; Ager, J. W.; Guo, J.; Javey, A. *Nano Lett.* **2014**, *14* (8), 4592−4597.
(40) Feng, J.; Qian, X.; Huang, C.-W.; Li, J. *Nat. Photonics* **2012**, *6* (12), 866−872.
(41) Wang, G.; Bouet, L.; Lagarde, D.; Vidal, M.; Balocchi, A.; Amand, T.; Marie, X.; Urbaszek, B. *Phys. Rev. B: Condens. Matter Mater. Phys.* **2014**, *90* (7), 075413.
(42) Ross, J. S.; Wu, S.; Yu, H.; Ghimire, N. J.; Jones, A. M.; Aivazian, G.; Yan, J.; Mandrus, D. G.; Xiao, D.; Yao, W.; Xu, X. *Nat. Commun.* **2013**, *4*, 1474.

DOI: 10.1021/acs.nanolett.7b03585
Nano Lett. 2017, 17, 6475−6480

ADVANCED MATERIALS
www.advmat.de

Giant Electro-Optical Effect through Electrostriction in a Nanomechanical Metamaterial

Artemios Karvounis, Behrad Gholipour, Kevin F. MacDonald, and Nikolay I. Zheludev*

Electrostriction is a property of all naturally occurring dielectrics whereby they are mechanically deformed under the application of an electric field. It is demonstrated here that an artificial metamaterial nanostructure comprising arrays of dielectric nanowires, made of silicon and indium tin oxide, is reversibly structurally deformed under the application of an electric field, and that this reconfiguration is accompanied by substantial changes in optical transmission and reflection, thus providing a strong electro-optic effect. Such metamaterials can be used as the functional elements of electro-optic modulators in the visible to near-infrared part of the spectrum. A modulator operating at 1550 nm with effective electrostriction and electro-optic coefficients of order 10^{-13} m^2 V^{-2} and 10^{-6} m V^{-1}, respectively, is demonstrated. Transmission changes of up to 3.5% are obtained with a 500 mV control signal at a modulation frequency of ≈6.5 MHz. With a resonant optical response that can be spectrally tuned by design, modulators based on the artificial electrostrictive effect may be used for laser *Q*-switching and mode-locking among other applications that require modulation at megahertz frequencies.

In regard to the pervasive technological challenge of electrically controlling (i.e., modulating/routing) guided and free-space optical signals (at macro-, micro-, and lately nanoscopic scales), mechanisms for electrically switching and tuning the optical properties of bulk or thin film media and surfaces have been the subject of research interest over many decades. The Kerr and Pockels electro-optic effects are widely used in amplitude, phase, and polarization modulators; carrier-induced changes in doped semiconductors are harnessed in optoelectronic and silicon photonic devices[1]; liquid crystals reliant upon electric-field-induced molecular reorientation, acousto-optic modulators, and microelectromechanical systems (MEMS) are the foundation of numerous display, spatial light modulation, and adaptive optics technologies.[2–6]

In recent years, photonic metamaterials—manmade media with nanostructurally engineered optical properties[7,8]—have emerged as an enabling technology platform within which all kinds of light–matter interaction can be resonantly enhanced and dynamically controlled. Large electro-optic (EO) switching and tuning effects have been demonstrated through the hybridization of plasmonic metamaterials with active media, including oxides/semiconductors,[9,10] graphene,[11–13] phase-change materials,[14,15] and liquid crystals,[16,17] and in nanomechanically reconfigurable metamaterials.[18] Indeed, the latter can also provide unique (e.g., electro-magneto-optical) response functions that have no counterpart in bulk optical media. In these nanoelectromechanical structures, Coulomb and Lorentz forces are harnessed to manipulate the conformation of constituent plasmonic metal unit cell elements fabricated on flexible dielectric nanomembranes, the elastic deformation of which provides the necessary restoring force.

"All-dielectric" metamaterials are typically manufactured from high-index–low-loss media such as silicon, and rely upon the excitation of displacement current as opposed to plasmonic resonances.[19–24] They have attracted considerable attention of late, not least for their potential to mitigate the drawbacks associated with plasmonic metal architectures in various applications at optical frequencies. However, while their optical properties are readily amenable to active control via hybridization,[25] macroscopic substrate deformation,[26] phase-change,[27,28] and photoexcitation[29,30] (including nanostructural reconfiguration induced by optical forces[31]), in being usually composed of discrete dielectric or semiconductor "particles," they are not immediately suited to delivering nanoelectromechanical optical switching/tuning functions. Here we report on the realization of a free-standing, all-dielectric, metamaterial EO modulator in which indium tin oxide (ITO) is employed as a transparent, low-index conductor in tandem with nanostructured silicon, to enable low-power modulation of near-infrared transmission at MHz frequencies via electrostrictive nanomechanical reconfiguration. Silicon, as the archetypal high-index, low-loss platform for optical-frequency all-dielectric

Dr. A. Karvounis, Dr. B. Gholipour, Prof. K. F. MacDonald, Prof. N. I. Zheludev
Optoelectronics Research Centre and Centre for Photonic Metamaterials
University of Southampton
Southampton SO17 1BJ, UK
E-mail: ak1c13@soton.ac.uk
Dr. B. Gholipour
Department of Chemistry
University of Southampton
Southampton SO17 1BJ, UK
Prof. N. I. Zheludev
Centre for Disruptive Photonic Technologies
School of Physical and Mathematical Sciences and
The Photonics Institute
Nanyang Technological University
Singapore 637371
The ORCID identification number(s) for the author(s) of this article can be found under https://doi.org/10.1002/adma.201804801.

DOI: 10.1002/adma.201804801

metamaterials[20–22] provides the resonant optical response necessary to enhance low-voltage modulation contrast, while ITO, as perhaps the best-known member of the conductive oxide family (which also includes Al- and Ga-doped zinc oxides) provides conductivity for electrostatic actuation without introducing the optical losses that would come with use of a metal.

Electrostriction is a property of all bulk dielectrics, arising from a quadratic coupling between strain and electric field, which manifests itself as a small field-induced mechanical deformation dependent upon the magnitude but not the polarity of the field. The largest electrostrictive coefficients reaching $\approx 10^{-16}$ m^2 V^{-2} are found in certain ceramics[32,33] and polymers,[34–38] which have been investigated for potential applications ranging from sonar and high-precision positional actuation[39,40] to MEMS textile fibers.[41] Recent analytical and computational studies have considered the enhancement of electrostriction in artificial composite (meta)materials comprising metal, dielectric, or semiconductor nanoparticles embedded in a dielectric matrix.[42,43] In the present case, the electric-field-induced deformation of the metamaterial unit cell structure is driven by Maxwell stress[44,45]—specifically the electrostatic force between neighboring, oppositely charged nanowires, providing a resonantly enhanced effective electrostriction coefficient of order 10^{-13} m^2 V^{-2}, and an associated EO coefficient of $\approx 10^{-6}$ m V^{-1}.

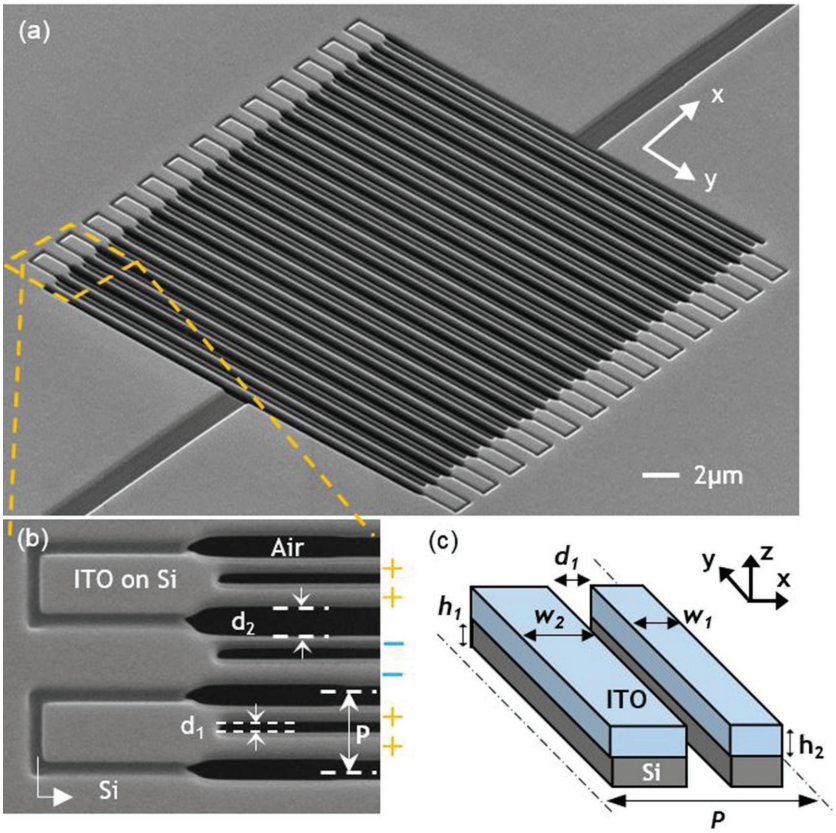

Figure 1. All-dielectric, nanomechanical metamaterial electro-optic modulator. a) Scanning electron microscopy image of a nanowire array metamaterial manufactured on a silicon/ITO bilayer membrane. b) Detail of the structure at the ends of the nanowires. c) Schematic cross-section of the asymmetric Si/ITO nanowire pair within each period of the metamaterial array (P = 800, h_1 = 100, h_2 = 70, w_1 = 200, w_2 = 300, d_1 = 100 nm, d_2 = 200 nm).

The metamaterial EO modulator in **Figure 1** comprises an array of nanowires with length L = 18 μm manufactured on a free-standing bilayer membrane of silicon and ITO (see Experimental Section), with each period containing an asymmetric pair of closely spaced Si/ITO strips—one being wider than the other. The optical response of the nanowire array is predominantly determined by the structural geometry of the high-refractive index silicon component. Dimensions are selected here, for a bilayer of h_1 = 100 nm Si and h_2 = 70 nm ITO, to achieve transmission/reflection resonances in the near-infrared telecommunications band around 1550 nm (**Figure 2**): a sub-wavelength period P = 800 nm, nanowire widths $w_{1,2}$ = 200, 300 nm, and gap size $d_{1,2}$ = 100, 200 nm. The ITO layer meanwhile provides electrical connectivity to facilitate electrostatic tuning of the gap sizes. For this purpose, the ITO layer is patterned at each end of the nanowires such that neighboring pairs are electrically isolated from each other and connected to opposing terminals of the device, such that alternate pairs are alternately biased as annotated in Figure 1b.

Normal incidence reflection and transmission spectra for the metamaterial device are measured using a microspectrophotometer (see Experimental Section). For incident light polarized parallel to the nanowires (the transverse electric or TE-mode of illumination), the metamaterial presents a Fano-type resonant response as shown in Figure 2a, with a quality factor Q of ≈35. This is based upon the excitation of antiparallel displacement currents in the dimensionally asymmetric nanowire pairs,[46,47] predominantly within the silicon, as illustrated by the numerically simulated cross-sectional field maps in Figure 2b. In contrast, spectra for the orthogonal transverse magnetic (TM) polarization are essentially flat, with transmission >80% and reflection ≈10% across the entire near-IR spectral range.

The resonant optical properties of the Si/ITO metamaterial are strongly dependent on the nanowire pair separations $d_{1,2}$, which can be continuously and to a point reversibly controlled by applying an electrical bias. In the + + − − configuration indicated in Figure 1b, the nanowires in each asymmetric pair are subject to electrostatic forces of mutual repulsion and (more weakly by virtue of greater separation) of attraction to the nearest neighboring wires of the adjacent pairs. In consequence, the two nanowires in each pair move away from one another, increasing the gap size d_1 and decreasing d_2. This nanomechanical reconfiguration redshifts the TE resonance, leading to changes in transmission and reflection that are most pronounced where the dispersion is steepest.

We first evaluate induced changes in transmission as a function of applied static bias. **Figure 3**a presents the spectral dispersion of relative transmission change $\Delta T/T_0$, where

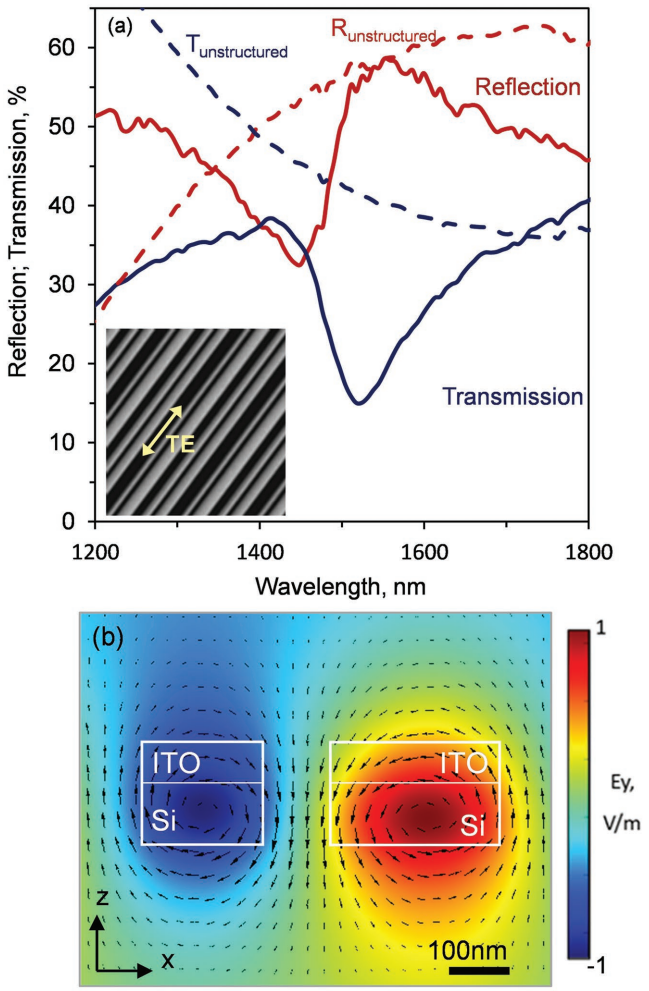

Figure 2. Optical characteristics of the Si/ITO nanowire metamaterial. a) Measured transmission (solid blue line) and reflection (solid red line) spectra of the Si/ITO nanowire metamaterial shown in Figure 1 for TE-polarized light and corresponding (polarization independent) spectra for the unstructured Si/ITO bilayer (dashed lines). b) Numerically simulated distribution of the *y*-component of electric field in the *xz* plane, overlaid with arrows denoting the direction and magnitude of magnetic field, for one pair of asymmetric width nanowires as described in Figure 1b, at the 1520 nm transmission resonance wavelength.

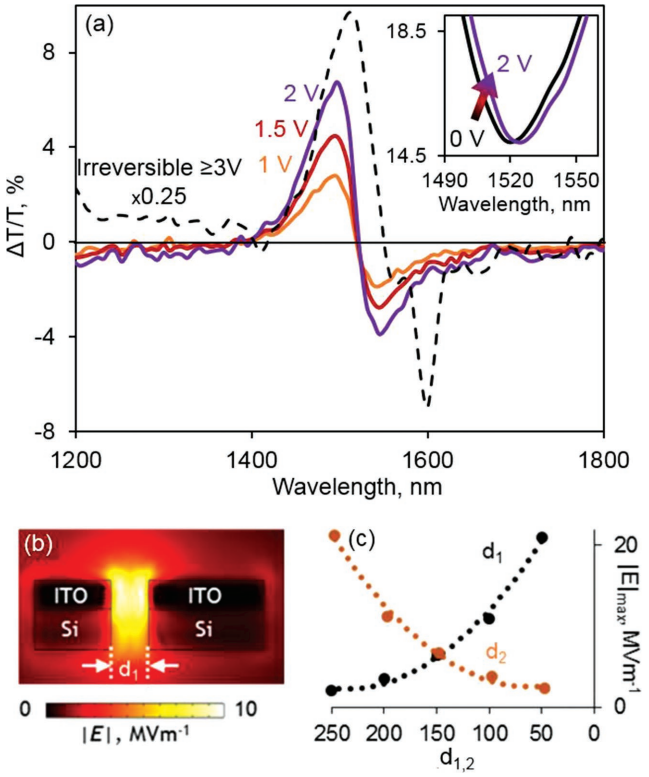

Figure 3. EO tuning of Si/ITO metamaterial transmission. a) Spectral dispersion of the relative change in transmission of the Si/ITO nanowire metamaterial for a selection of applied static electrical bias levels (as labeled). The inset shows the spectral dispersion of absolute transmission around the resonance wavelength for zero and 2 V bias settings. b) Numerically simulated cross-sectional map in the *xz* plane of the static electric field amplitude over a single period of the metamaterial array for a gap size d_1 = 100 nm and an applied bias of 1V between the ITO sections of the two nanowires. c) Maximum electric field amplitude (at the midpoint of the gap between the nanowires) as a function of gap size, for a fixed 1V bias.

$\Delta T = T_\alpha - T_0$, T_α being the absolute transmission at an applied bias of α Volts. At 2 V bias, the induced change reaches maximum values of +7% and –4% at wavelengths of 1497 and 1544 nm, either side of the 1520 nm zero-bias transmission resonance wavelength. Two volts represent a conservative upper limit on the operational range of applied bias within which electrostatic control of nanowire separation provides continuous and reversible tuning of transmission. Beyond this, there comes a point at which the elastic restoring force on a nanowire (which increases linearly with displacement from its equilibrium position, i.e., with increasing gap size d_1) is surpassed by the electrostatic force of attraction to its oppositely biased neighbor (which grows as d_2^{-2}; see Figure 3b,c). At this point, the gap will abruptly close and, by virtue of van der Waals forces, remain closed even when the applied bias is removed. An order-of-magnitude estimate for this irreversible switching threshold can be obtained analytically[48] (assuming a symmetric pair of beams in a material with Young's modulus E) as $\alpha^* \approx \sqrt{32Ehw^3d^2/(\pi\varepsilon_o L^4)}$, and is found experimentally for the present sample geometry to be ≈3V. The change in transmission associated with this irreversible deformation of the metamaterial structure (i.e., reduction of gap size d_2 to zero) is unsurprisingly much larger than those observed within the reversible tuning range, as illustrated by the vertically scaled dashed line in Figure 3a.

For the purposes of studying the high-frequency alternating bias (AC) EO modulation characteristics of the Si/ITO metadevice, the metamaterial is mounted in a low-vacuum microscope stage to reduce air damping of induced nanowire oscillations (see Experimental Section). The relative change in metadevice transmission is monitored at a fixed wavelength of 1550 nm while varying the frequency f of an applied sinusoidal electrical bias with an amplitude α of up to 500 mV (**Figure 4**). At low frequencies, the induced displacement of the nanowires, and therefore the magnitude of the induced change in transmission, is small. Both however are enhanced when the nanowires are driven at their natural mechanical resonance frequency. In the

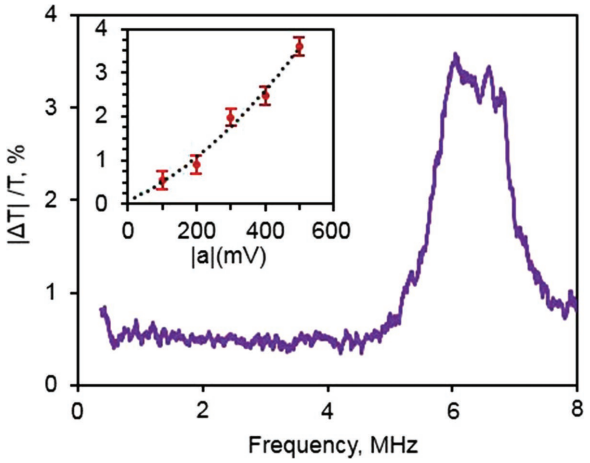

Figure 4. Dynamic electro-optic modulation of Si/ITO metamaterial transmission. Relative change in transmission at 1550 nm of the Si/ITO nanowire metamaterial shown in Figure 1 as a function of the drive voltage modulation frequency, for a fixed peak bias $\alpha = 500$ mV. The inset shows the peak magnitude of induced transmission change at 6 MHz as a function of peak bias voltage α.

present case, $\Delta T/T_0$ reaches 3.5% at a frequency of 6 MHz for a drive amplitude of 500 mV, as compared to only ≈0.5% off resonance. Transmission modulation amplitude increases super-linearly with drive voltage as shown in the inset to Figure 4. One might anticipate the presence of a double peak in the frequency spectrum, by virtue of the fact that there are nanowires with two different widths (and therefore Eigenfrequencies) within each unit cell of the metamaterial. From numerical simulations, employing Young's moduli E and densities ρ for Si and ITO from refs. [49,50], these frequencies are estimated to be 4.07 and 6.10 MHz for the 200 and 300 nm wide nanowires, respectively. The observation of a single peak, extending at full-width half-maximum, from 5.7 to 6.8 MHz, is attributed to the coupled nature of the oscillations (which may include components of out-of-plane and twisting motion), stress within the bilayer derived from the Si membrane fabrication and/or ITO annealing processes, and spectral broadening associated with manufacturing imperfections (up to 10% variation in $w_{1,2}$ over the metamaterial array).

The nanomechanical functionality of the metamaterial can be understood as a form of artificial electrostriction at the unit cell level, in that it comprises a structural deformation dependent upon the magnitude of an applied electric field E. Specifically, strain s should exhibit a quadratic dependence on the applied field: $s = ME^2$, where M is the electrostrictive coefficient. (In bulk materials, M is a fourth ranked tensor; here we evaluate what, in these terms, would be the longitudinal electrostriction coefficient M_{11} under an assumption that the applied field, resulting stress and deformation are all unidirectional and parallel).

We quantify strain as the change Δd in the size of the gaps between Si/ITO nanowires (the magnitude of the increase in d_1 or decrease in d_2), relative to the mean equilibrium gap size $\overline{d} = (d_1^* + d_2^*)/2$, where $d_{1,2}^*$ are the zero-bias gap sizes of 100 and 200 nm respectively, in the present case. Numerical simulations demonstrate that for small values of Δd, metamaterial

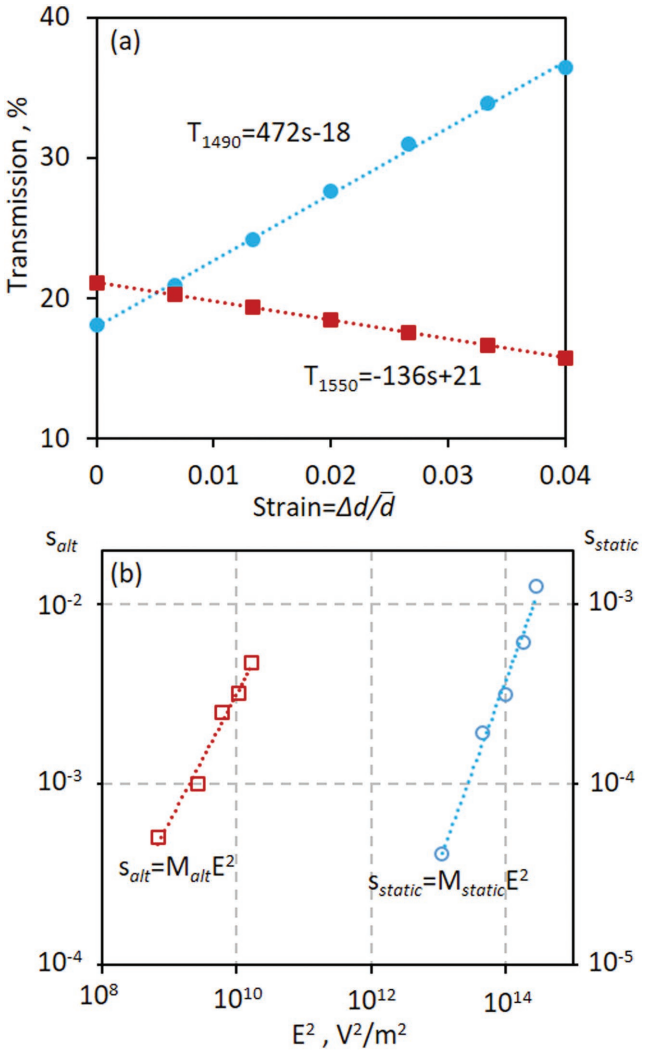

Figure 5. Si/ITO metamaterial electrostriction. a) Numerically simulated spectral dispersion of Si/ITO nanowire metamaterial transmission as a function of strain, defined as the relative change in the size of the gaps between nanowires, for wavelengths of 1490 nm (blue) and 1550 nm (red) at which maximally positive and negative proportionalities are observed. b) Strain induced within the metamaterial structure [from experimental measurements of optical transmission at 1490 nm for static bias and 1550 nm for alternating bias, via proportionalities derived from panel (a)] as a function of applied static and peak alternating ($f = 6$ MHz) electric field squared.

optical transmission is, to a very good approximation, a linear (of course spectrally dispersive) function of strain in these terms, as illustrated in **Figure 5**a. Experimentally measured dependences of transmission upon applied bias α can thus be translated into dependences of strain upon applied electric field $E = \alpha/\overline{d}$ as shown in Figure 5b, from which effective electrostriction coefficients for both static and high-frequency dynamic modes of excitation can be derived.

The metamaterial's static effective electrostriction coefficient is found to be $M_{\text{static}} = 4 \times 10^{-18}$ m^2 V^{-2}—a value somewhat smaller than the largest coefficients found in bulk dielectric media.[37,51] However, this value is enhanced by five orders of magnitude

when the structure is driven to oscillate at its mechanical resonance frequency, reaching $M_{alt.} = 3 \times 10^{-13}$ m^2 V^{-2}, a value three orders of magnitude larger than that can be found in bulk dielectrics. It should further be noted that these values represent conservative estimates of the electrostriction coefficients: strain is underestimated because higher resonance quality factors in simulation (as compared to experiment) exaggerate the dependence of transmission upon strain; and at the same time electric fields are overestimated because the bias applied to the device terminals is assumed across the gaps between nanowires with no account taken of Ohmic losses in the ITO.

The change in optical properties brought about by the electrostrictive deformation of the metamaterial can be described by an effective electro-optic coefficient $r = \Delta n L/\alpha$, where Δn is the effective refractive index change induced over an interaction length L (the thickness of the metamaterial, $h_1 + h_2 = 170$ nm) under an applied bias of α V. Numerical simulations indicate a phase shift in transmission at 1550 nm of up to $\pi/9$ at a nanowire displacement $\Delta d = 3$ nm (strain of 2%, achieved at a static bias of 2 V). This corresponds to an effective index change $\Delta n \approx 0.5$, giving $r \approx 10^{-6}$ m V^{-1}—a value approximately five orders of magnitude larger than in typical electro-optic media such as lithium niobate, which has an EO coefficient of 3×10^{-11} m V^{-1}.[52]

In summary, we have demonstrated a free-standing, all-dielectric metamaterial electro-optic modulator of substantially subwavelength thickness ($<\lambda/8$), manufactured from CMOS-compatible materials—a high-index–low-loss semiconductor and a transparent conductive oxide. The device provides continuous and reversible electrically actuated nanomechanical tuning of near-infrared transmission, at wavelengths selected by design, presenting effective electrostriction and electro-optic coefficient orders of magnitude larger than those of bulk dielectric media: electrostatic forces are harnessed to control the separation between elements of a nondiffractive Si/ITO nanowire array and so to deliver, in the present case, relative transmission changes of up to 7% at 1550 nm under an applied static bias of 2 V. In this low frequency limit, power consumption is dominated by leakage resistance of 500 kΩ and amounts to only 8 μW at a bias of 2 V. Optical modulation amplitude is enhanced when structures are driven by an alternating bias to oscillate at their few-MHz mechanical resonance frequencies. Depending on application requirements, an appropriate balance among modulation amplitude, power consumption, and speed of response may be engineered. For example, longer nanowires would have a lower mechanical resonance frequency but they would be displaced further at a given bias voltage than shorter wires, producing a larger change in transmission. Greater modulation contrast may be achieved via optimization of the metamaterial nanofabrication procedure, whereby reduction of dimensional inhomogeneity will enhance both optical and mechanical resonance quality factors.

Experimental Section

Metamaterial Fabrication: Devices were manufactured on commercially sourced polycrystalline silicon membranes (1 × 1 mm windows supported in 200 μm thick silicon frames). These were coated (including the frame) with 70 nm of indium tin oxide by radio-frequency sputtering from an In_2O_3/SnO_2 (90/10 wt%) alloy target. A base pressure of 4×10^{-5} mbar was achieved before deposition and a high-purity argon gas flow of 70 ccpm was used to strike the plasma. A 20:5 argon:oxygen deposition gas mixture was used to maintain the plasma and ensure sufficient oxygen content in the deposited ITO film. The membrane substrate was held on a rotating platen ≈150 mm from the target where it was subjected to a temperature increase of <10 °C during deposition, ensuring minimal stress in the film, which was subsequently annealed at 200 °C for 60 min under an oxygen atmosphere to increase conductivity (measured sheet resistance decreased from 3.4×10^6 to 1×10^3 Ω sq^{-1}; carrier concentration increased from 3.5×10^{16} to 10^{21} cm^{-3}).

Metamaterial arrays of asymmetric nanowire pairs were fabricated by focused ion beam (FIB) milling from the ITO side of the bilayer membrane, cutting through both layers of the material. The pattern of electrodes required to alternately bias pairs of nanowires (as indicated in Figure 1b) was then defined by FIB milling in the ITO layer only.

Numerical Simulations: Full-wave electromagnetic simulations of the metamaterial structure, based on the geometry presented in Figure 1c, were performed using the finite element method in COMSOL Multiphysics. Calculations employed periodic boundary conditions in the *x* and *y* directions (i.e., effectively assuming an infinite array of infinitely long nanowires). They utilized refractive indices for polycrystalline silicon and for ITO from ellipsometric measurements (both materials have weakly dispersive indices in the near-IR spectral range above ≈1300 nm: 3.45 + 0.005i for Si and 1.9 + 0.08i for ITO), and assumed normally incident, narrowband, linearly polarized plane wave illumination.

The electrostatic field distribution and its dependence on gap size, as presented in Figure 3b,c, were modeled using the AC/DC COMSOL module, assuming a pair of parallel, free-standing 18 μm long wires, with the ITO surface of one held uniformly at a given bias voltage against the other at 0V (ground).

Nanowire mechanical Eigenfrequencies were obtained from finite element models of single, isolated 18 μm long wires with fixed ends and rectangular cross sections as presented in Figure 1c. These assumed Young's Moduli E and density ρ values for Si and ITO[49,50]: $E_{Si} = 150$, $E_{ITO} = 190$ GPa; $\rho_{Si} = 2300$, $\rho_{ITO} = 7300$ kg m^{-3}.

Microspectrophotometry (Including Static EO Modulation Measurements): Transmission and reflection spectra (Figure 2) were obtained using a microspectrophotometer (CRAIC QDI2010), with a 15 × 15 μm sampling aperture via a 15× objective with numerical aperture of 0.28. All data were normalized to reference levels for air (100% transmission), a silver mirror (high reflector), and a "Vantablack" vertically aligned carbon nanotube array (zero reflection/transmission), and averaged over 15 repeated measurement cycles, each with a 500 ms integration time. A source measure unit (Keithley 2636) was employed to apply a static bias across the metadevice terminals.

High-Frequency EO Modulation Measurements: The metamaterial sample was mounted in a low-vacuum (≈1 mbar) microscope stage equipped with an RF electrical feedthrough via which a control bias signal from an electrical network analyzer (Agilent Technologies E5071C) could be applied to the metadevice terminals. Optical transmission was monitored at a wavelength of 1550 nm using a diode laser providing a continuous-wave intensity of 70 μW cm^{-2} at the sample and an InGaAs photodetector (New Focus 1811) connected to the network analyzer. Data were averaged over five frequency scans at each setting of peak bias voltage; error bars in the inset to Figure 4 were calculated as the standard error.

Acknowledgements

This work was supported by the UK Engineering and Physical Sciences Research Council [grants EP/M009122/1 and EP/N00762X/1] and the Singapore Ministry of Education [grant MOE2016-T3-1-006]. Following a period of embargo, the data from this paper can be obtained from the University of Southampton ePrints research repository: http://dx.doi.org/10.5258/SOTON/D0663. The authors thank J. Y. Ou for assistance with electro-optical measurements and M. E. Rizou for helpful discussions.

Note: Figure 5 was replaced on January 3, 2019 to correct the units on the x-axis scale in Figure 5b. This correction to the axis scale does not affect any of the other results reported here.

Conflict of Interest

The authors declare no conflict of interest.

Keywords

electro-optic modulation, electrostriction, nanomechanics, photonic metamaterials

Received: July 26, 2018
Revised: September 21, 2018
Published online: November 6, 2018

[1] G. T. Reed, G. Mashanovich, F. Y. Gardes, D. J. Thomson, *Nat. Photonics* **2010**, *4*, 518.
[2] E. A. Donley, T. P. Heavner, F. Levi, M. O. Tataw, S. R. Jefferts, *Rev. Sci. Instrum.* **2005**, *76*, 063112.
[3] T. Bifano, *Nat. Photonics* **2011**, *5*, 21.
[4] W. M. Zhu, A. Q. Liu, T. Bourouina, D. P. Tsai, J. H. Teng, X. H. Zhang, G. Q. Lo, D. L. Kwong, N. I. Zheludev, *Nat. Commun.* **2012**, *3*, 1274.
[5] Z. Zhang, Z. You, D. Chu, *Light: Sci. Appl.* **2014**, *3*, e213.
[6] K. Shih, P. Pitchappa, M. Manjappa, C. P. Ho, R. Singh, B. Yang, N. Singh, C. Lee, *Appl. Phys. Lett.* **2017**, *110*, 161108.
[7] N. I. Zheludev, Y. S. Kivshar, *Nat. Mater.* **2012**, *11*, 917.
[8] A. M. Urbas, Z. Jacob, L. D. Negro, N. Engheta, A. D. Boardman, P. Egan, A. B. Khanikaev, V. Menon, M. Ferrera, N. Kinsey, C. DeVault, J. Kim, V. Shalaev, A. Boltasseva, J. Valentine, C. Pfeiffer, A. Grbic, E. Narimanov, L. Zhu, S. Fan, A. Alù, E. Poutrina, N. M. Litchinitser, M. A. Noginov, K. F. MacDonald, E. Plum, X. Liu, P. F. Nealey, C. R. Kagan, C. B. Murray, D. A. Pawlak, I. I. Smolyaninov, V. N. Smolyaninova, D. Chanda, *J. Opt.* **2016**, *18*, 093005.
[9] Y.-W. Huang, H. W. H. Lee, R. Sokhoyan, R. A. Pala, K. Thyagarajan, S. Han, D. P. Tsai, H. A. Atwater, *Nano Lett.* **2016**, *16*, 5319.
[10] L. Kang, Y. Cui, S. Lan, S. P. Rodrigues, M. L. Brongersma, W. Cai, *Nat. Commun.* **2014**, *5*, 4680.
[11] N. K. Emani, T.-F. Chung, A. V. Kildishev, V. M. Shalaev, Y. P. Chen, A. Boltasseva, *Nano Lett.* **2014**, *14*, 78.
[12] J. Li, P. Yu, H. Cheng, W. Liu, Z. Li, B. Xie, S. Chen, J. Tian, *Adv. Opt. Mater.* **2016**, *4*, 91.
[13] Z. Li, W. Liu, H. Cheng, S. Chen, J. Tian, *Opt. Lett.* **2016**, *41*, 3142.
[14] T. Driscoll, H.-T. Kim, B.-G. Chae, B.-J. Kim, Y.-W. Lee, N. M. Jokerst, S. Palit, D. R. Smith, M. Di Ventra, D. N. Basov, *Science* **2009**, *325*, 1518.
[15] Z. L. Sámson, K. F. MacDonald, F. De Angelis, B. Gholipour, K. Knight, C. C. Huang, E. Di Fabrizio, D. W. Hewak, N. I. Zheludev, *Appl. Phys. Lett.* **2010**, *96*, 143105.
[16] A. Minovich, J. Farnell, D. N. Neshev, I. McKerracher, F. Karouta, J. Tian, D. A. Powell, I. V. Shadrivov, H. Hoe Tan, C. Jagadish, Y. S. Kivshar, *Appl. Phys. Lett.* **2012**, *100*, 121113.
[17] O. Buchnev, J. Y. Ou, M. Kaczmarek, N. I. Zheludev, V. A. Fedotov, *Opt. Express* **2013**, *21*, 1633.
[18] N. I. Zheludev, E. Plum, *Nat. Nanotechnol.* **2016**, *11*, 16.
[19] P. Moitra, Y. Yang, Z. Anderson, I. I. Kravchenko, D. P. Briggs, J. Valentine, *Nat. Photonics* **2013**, *7*, 791.
[20] S. Jahani, Z. Jacob, *Nat. Nanotechnol.* **2016**, *11*, 23.
[21] A. I. Kuznetsov, A. E. Miroshnichenko, M. L. Brongersma, Y. S. Kivshar, B. Lukyanchuk, *Science* **2016**, *354*, aag2472.
[22] I. Staude, J. Schilling, *Nat. Photonics* **2017**, *11*, 274.
[23] O. Yavas, M. Svedendahl, P. Dobosz, V. Sanz, R. Quidant, *Nano Lett.* **2017**, *17*, 4421.
[24] A. Karvounis, V. Nalla, K. F. MacDonald, N. I. Zheludev, *Adv. Mater.* **2018**, *30*, 1707354.
[25] J. Sautter, I. Staude, M. Decker, E. Rusak, D. N. Neshev, I. Brener, Y. S. Kivshar, *ACS Nano* **2015**, *9*, 4308.
[26] P. Gutruf, C. Zou, W. Withayachumnankul, M. Bhaskaran, S. Sriram, C. Fumeaux, *ACS Nano* **2016**, *10*, 133.
[27] A. Karvounis, B. Gholipour, K. F. Macdonald, N. I. Zheludev, **2016**, *109*, 051103.
[28] B. Gholipour, A. Karvounis, J. Yin, C. Soci, K. F. MacDonald, N. I. Zheludev, *NPG Asia Mater.* **2018**, *10*, 533.
[29] M. R. Shcherbakov, P. P. Vabishchevich, A. S. Shorokhov, K. E. Chong, D. Y. Choi, I. Staude, A. E. Miroshnichenko, D. N. Neshev, A. A. Fedyanin, Y. S. Kivshar, *Nano Lett.* **2015**, *15*, 6985.
[30] Y. Yang, W. Wang, A. Boulesbaa, I. I. Kravchenko, D. P. Briggs, A. Puretzky, D. Geohegan, J. Valentine, *Nano Lett.* **2015**, *15*, 7388.
[31] A. Karvounis, J. Y. Ou, W. Wu, K. F. Macdonald, N. I. Zheludev, *Appl. Phys. Lett.* **2015**, *107*, 191110.
[32] K. N. Pham, A. Hussain, C. W. Ahn, W. Kim, S. J. Jeong, J. S. Lee, *Mater. Lett.* **2010**, *64*, 2219.
[33] F. Li, L. Jin, Z. Xu, S. Zhang, *Appl. Phys. Rev.* **2014**, *1*, 011103.
[34] W. Lehmann, H. Skupin, C. Tolksdorf, E. Gebhard, R. Zentel, P. Krüger, M. Lösche, F. Kremer, *Nature* **2001**, *410*, 447.
[35] F. Bauer, E. Fousson, Q. M. Zhang, *IEEE Trans. Dielectr. Electr. Insul.* **2006**, *13*, 1149.
[36] V. V. Kochervinskiĭ, *Crystallogr. Rep.* **2009**, *54*, 1146.
[37] B. Kim, Y. D. Park, K. Min, J. H. Lee, S. S. Hwang, S. M. Hong, B. H. Kim, S. O. Kim, C. M. Koo, *Adv. Funct. Mater.* **2011**, *21*, 3242.
[38] M. Lallart, P. J. Cottinet, D. Guyomar, L. Lebrun, *J. Polym. Sci., Part B: Polym. Phys.* **2012**, *50*, 523.
[39] J. Galvagni, *Opt. Eng.* **1990**, *29*, 1389.
[40] A. Kholkin, B. Jadidian, A. Safari, in *Encyclopedia of Smart Materials* (Ed: M. Schwarz), John Wiley & Sons Inc., New York, USA **2002**.
[41] T. Khudiyev, J. Clayton, E. Levy, N. Chocat, A. Gumennik, A. M. Stolyarov, J. Joannopoulos, Y. Fink, *Nat. Commun.* **2017**, *8*, 1435.
[42] M. J. A. Smith, B. T. Kuhlmey, C. M. De Sterke, C. Wolff, M. Lapine, C. G. Poulton, *Phys. Rev. B* **2015**, *91*, 214102.
[43] A. Singh, M. J. A. Smith, C. Martin De Sterke, *J. Opt. Soc. Am. B* **2017**, *34*, 1573.
[44] J. Li, N. Rao, *Appl. Phys. Lett.* **2002**, *81*, 1860.
[45] B. Guiffard, L. Seveyrat, G. Sebald, D. Guyomar, *J. Phys. D: Appl. Phys.* **2006**, *39*, 3053.
[46] V. V. Khardikov, E. O. Iarko, S. L. Prosvirnin, *J. Opt.* **2012**, *14*, 035103.
[47] B. Zeng, A. Majumdar, F. Wang, *Opt. Express* **2015**, *23*, 12478.
[48] J.-Y. Ou, E. Plum, J. Zhang, N. I. Zheludev, *Nat. Nanotechnol.* **2013**, *8*, 252.
[49] W. N. Sharpe, B. Yuan, R. Vaidyanathan, R. L. Edwards, in *The Tenth Annual International Workshop On Micro Electro Mechanical Systems. An Investigation of Micro Structures, Sensors, Actuators, Machines and Robots (MEMS97)*, IEEE, Piscataway, NJ, USA **1997**, 424.
[50] B.-K. Lee, Y.-H. Song, J.-B. Yoon, in *Proc. of the 22nd IEEE Int. Conf. on Micro Electro Mechanical Systems (MEMS 2009)*, IEEE, Piscataway, NJ, USA **2009**, 148.
[51] R. Korobko, A. Patlolla, A. Kossoy, E. Wachtel, H. L. Tuller, A. I. Frenkel, I. Lubomirsky, *Adv. Mater.* **2012**, *24*, 5857.
[52] E. K. Turner, *IEEE J. Quantum Electron.* **1966**, *2*, 128.

nature COMMUNICATIONS

ARTICLE

DOI: 10.1038/s41467-018-06360-5 OPEN

Reconfigurable MEMS Fano metasurfaces with multiple-input–output states for logic operations at terahertz frequencies

Manukumara Manjappa [1,2], Prakash Pitchappa[1,2], Navab Singh[3], Nan Wang[3], Nikolay I. Zheludev[2,4], Chengkuo Lee [5,6] & Ranjan Singh [1,2]

A broad range of dynamic metasurfaces has been developed for manipulating the intensity, phase and wavefront of electromagnetic radiation from microwaves to optical frequencies. However, most of these metasurfaces operate in single-input–output state. Here, we experimentally demonstrate a reconfigurable MEMS Fano resonant metasurface possessing multiple-input–output (MIO) states that performs logic operations with two independently controlled electrical inputs and an optical readout at terahertz frequencies. The far-field behaviour of Fano resonance exhibits XOR and XNOR operations, while the near-field resonant confinement enables the NAND operation. The MIO configuration resembling hysteresis-type closed-loop behaviour is realized through inducing electromechanically tuneable out-of-plane anisotropy in the near-field coupling of constituent resonator structures. The XOR metamaterial gate possesses potential applications in cryptographically secured terahertz wireless communication networks. Furthermore, the MIO features could lay the foundation for the realization of programmable and randomly accessible metamaterials with enhanced electro-optical performance across terahertz, infrared and optical frequencies.

[1] Division of Physics and Applied Physics, School of Physical and Mathematical Sciences, Nanyang Technological University, 21 Nanyang Link, Singapore 637371, Singapore. [2] Centre for Disruptive Photonic Technologies, The Photonics Institute, Nanyang Technological University, 50 Nanyang Avenue, Singapore 639798, Singapore. [3] Institute of Microelectronics, 11 Science Park Road, Singapore 117685, Singapore. [4] Optoelectronics Research Centre and Centre for Photonic Metamaterials, University of Southampton, Highfield, Southampton SO17 1BJ, UK. [5] Department of Electrical & Computer Engineering, National University of Singapore, 4 Engineering Drive 3, Singapore 117576, Singapore. [6] Center for Intelligent Sensors and MEMS (CISM), National University of Singapore, E6 #05-11F, 5 Engineering Drive 1, Singapore 117608, Singapore. Correspondence and requests for materials should be addressed to R.S. (email: ranjans@ntu.edu.sg)

Recent trends in the metamaterial research have advanced towards the realization of functional and reconfigurable metasurfaces[1–3] that enable real-time control over their geometrical and optical properties, thereby creating exceptional opportunities in the field of active and tuneable metamaterials. Over the years, various approaches have emerged in realizing tuneable metamaterials through reconfiguring their structure and geometry via external stimulus such as electrical control[4–7], magnetic field[8,9], thermal gradient[10–12] and optical pulse[13–18]. A specific class of structurally reconfigurable metasurfaces based on micro/nano electromechanical systems (MEMS/NEMS) have given a unique advantage for active manipulation of the near-fields in all the three spatial directions by exploiting sensitive changes to their micro/nano scale movements. Near-fields[19] are the most significant components of the scattered fields that stay closer to the object surface and fail to radiate freely to the far-field. The omnipresent nature of the near-field and the finest information that it entraps, makes it a vital component in the light–matter interactions. Therefore, dynamic control over the near-fields provides a new paradigm of manipulating the light–matter interactions, which makes them more resilient and merits their applications in future generation state-of-the-art active photonic devices. At the terahertz (THz) and infrared frequencies, the MEMS/NEMS metasurfaces have enabled dynamic manipulation of near-field entities thereby showing an active reconfiguration of intriguing features like magnetic response[4,10], transparency[20], near-perfect absorption[21], phase engineering[22], resonance modulation[23], anisotropy[5] and THz invisibility[24]. However, apart from these useful advancements, the ability to control and tailor the near-field interactions by establishing multiple controls at the unit-cell level has remained elusive.

The bright prospects of functional metamaterials lie in achieving multiple controls within the unit cell of the metamaterial, which could provide a flexible platform for realizing extremely versatile devices manifesting enhanced electro-optical performance. Multiple controls within the unit cell would enable precise tailoring of near-field interactions between the meta-atoms by relatively manoeuvring their structural properties, thereby obtaining the optical properties on demand[25]. Recently, the MEMS/NEMS switchable metamaterials[2,7] have provided a promising pathway to control near-field coupling between the metamolecules by establishing independent/multiple controls over the structural reconfiguration of the constituent resonators within the unit cell of the metamaterials. However, most of these metamaterial designs operate in single output configurations. In the hindsight of enhancing their multifunctional capabilities in digital[26–28] and multichannel signal processing applications, one way is to establish a multi-valued dependency between the input and output characteristics of the metamaterial. In the past, the multiple output states signifying the hysteresis behaviour has been shown in various hybrid metamaterial systems composed of vanadium dioxide (VO_2)[12] and graphene–ferroelectric polymer[29] that demonstrated the memory effects and logic gate functionalities at THz frequencies. However, these results were based on single input control and depend on the properties of the integrated natural material that dictates their output efficiencies along with limiting their operation to specific frequencies.

Here, we experimentally realize the excitation and active tuning of sharp Fano resonances in a MEMS reconfigurable metasurface exhibiting multiple-input–output (MIO) characteristics in its near-field as well as far-field optical properties. These MIO states are created by establishing anisotropic nature in the near-field coupling between the asymmetric resonators in the out-of-plane (z-axis) reconfigurable metasurface that excites a sharp Fano-type resonance feature. The reconfigurable geometry of the MEMS Fano-metasurface provides various structural meta-stable states by using two independently controllable electrical inputs and an optical/near-field readout that enables the realization of digital logic gates. Here, we demonstrate exclusive-OR (XOR), XNOR and NOT logic gates in the far-field optical states, and the NAND logic gate operation in the near-field characteristics of the device at THz frequencies. Fundamentally, XOR is an important secondary Boolean (logic) operation that is a composite of the basic logic functions and is not linearly separable. This property makes it more resilient and practically useful in the information and computational technologies as parity generators, one-time pad (OTP)-based unbreakable cryptography protocols[30,31], pseudorandom number generators and digital encoders or decoders in signal processing. On the other hand, the NAND logic operation is a functionally complete set logic operator which can be used to express all the basic set logic operations by defining a network of NAND gates. The multiple-logic operations together with the volatile and nonvolatile[32,33] regimes of MEMS actuation can enhance the digital functionalities of the device in realizing optical memory registers to encode, harvest, process and send secured information in the form of encoded/decoded optical bits at THz frequencies.

Results

Design and fabrication. To precisely elucidate the operation of logic gate functionalities through active control of Fano resonances, we fabricated a MEMS-based metasurface consisting of two split ring resonators (we term them SRR-1 and SRR-2) that are independently and sequentially actuated by applying the voltages V_1 and V_2 (shown in Fig. 1a). The device is fabricated using the photolithography technique, where periodic array of bimorph SRRs (900 nm thick aluminium (Al) deposited on top of 50 nm aluminium oxide (Al_2O_3) layer) possessing mirror-symmetry are patterned on a lightly doped silicon (Si) substrate (refer to the Methods section and Supplementary Figs. 1–5 for the device fabrication details and characterization). Due to the residual stress in the bimorph layers, the cantilevers are bent up, thereby increasing their released heights (h). Scanning electron microscope (SEM) image of the fabricated MEMS Fano-metasurface is shown in Fig. 1a in the coloured scale that illustrates the maximum asymmetric state of the device with SRR-1 snapped down on the substrate using voltage $V_1 = 35$ V and SRR-2 is retained in the released state of the bimorph cantilevers with $V_2 = 0$ V. The out-of-plane reconfiguration of the released cantilevers is achieved through electrostatic actuation, by applying voltage across the Al layer and silicon substrate. Metal lines connecting the SRR-1 and SRR-2 cantilevers are electrically isolated from each other and this allows for the independent reconfiguration of heights h_1 and h_2 through the application of voltages V_1 and V_2, respectively. The selective reconfiguration at the sub-unit cell level provides the flexibility to introduce dynamically tuneable structural asymmetry along the out-of-plane (z)-axis of the sample. The out-of-plane structural asymmetry parameter is defined as $\delta = \frac{|h_1 - h_2|}{s} \times 100\%$, where s is the length and h_1, h_2 are respectively the released heights of SRR-1 and SRR-2 cantilever arms. Figure 1b–d are the SEM images of the unit cell showing the sequential control of SRR cantilevers by applying voltages V_1 and V_2 across the Al-metal lines and the silicon substrate.

Active control of Fano resonance. Persistent control of resonance features in the MEMS Fano-metasurface is experimentally characterized by using the photoconductive antenna-based THz-time domain spectroscopy setup in the transmission mode (refer to the Methods section for more details on experimental

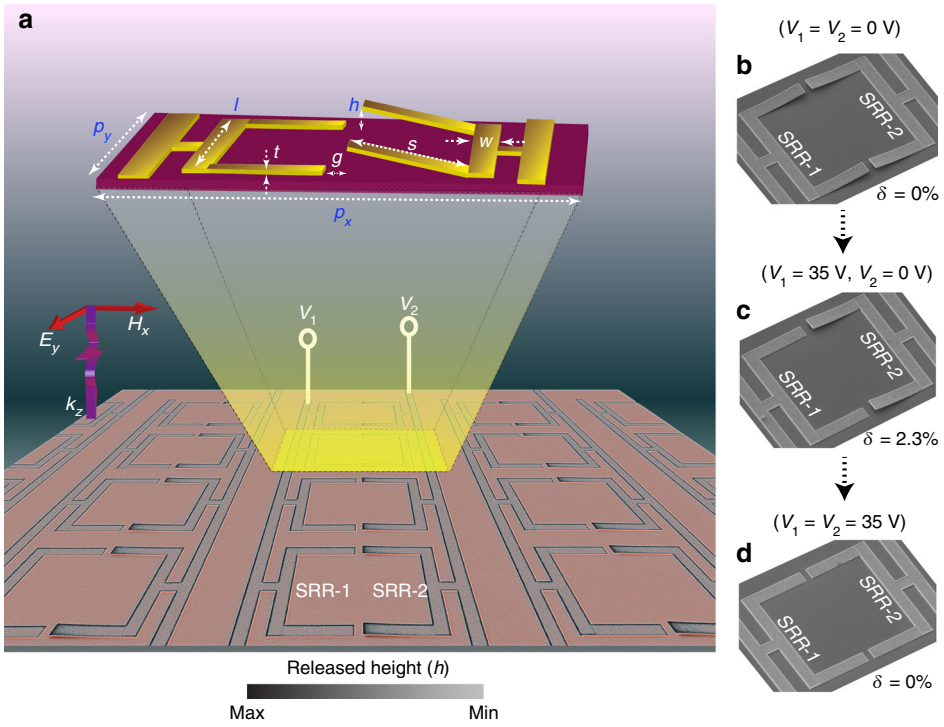

Fig. 1 Fabricated sample images and the sequential operation of the device. **a** Coloured scanning electron microscope (SEM) image of the MEMS Fano-metasurface. The unit cell comprises of two SRRs separated by a gap *g*, where SRR cantilever arms of length *s* are released at a height *h*. The unit cell dimensions are depicted in the inset, where p_x: 110 μm; p_y: 75 μm; *l*: 60 μm; *s*: 25 μm; *w*: 6 μm; *g*: 4 μm; and *t*: 900 nm. V_1 and V_2 are the input voltage ports to achieve the independent actuation of SRR-1 and SRR-2, respectively. **b**–**d** SEM images of the unit cell showing the sequential actuation of SRRs with voltage V_1 and V_2 applied across the two SRRs, where the sequence from (**b**) to (**c**) represents the increasing asymmetry (δ) and (**c**) to (**d**) represents the decreasing asymmetry configuration

procedure). The measured transmission spectra for increasing voltage V_1 with $V_2 = 0$ V are shown in Fig. 2a. The inset diagram in Fig. 2b presents the experimentally measured mechanical deformation profile of the cantilever by applying the voltage on one of the SRRs (details on the device characterization are given in the Methods section). Initially, for the case where no voltage is applied across the resonators, i.e. $V_{1,2} = 0$ (see Fig. 1b), the cantilever arms of the two SRRs are symmetrically inclined at same heights $h_1 = h_2 = h$ ($\delta = 0$) along the *z*-axis. Such symmetric configuration of resonators results in the excitation of strong dipole type of resonance at 0.77 THz for the incident THz radiation polarized in the $\mathbf{E_y}$ direction. When voltage (V_1) is applied across the Al lines of the released cantilevers (say, SRR-1) and Si substrate, the suspended SRR-1 cantilevers gradually bend towards the substrate due to the attractive electrostatic force. This deformation in the height of the SRR-1 cantilevers creates a structural asymmetry (δ) along the *z*-axis of the metasurface sample. As a result, near-field coupling between the asymmetric structures excites a sharp and weak Fano resonance[34–37] feature (at 0.58 THz, red curve in Fig. 2a) within a broad dipolar resonance. Upon continuously increasing V_1 across the SRR-1, strength of Fano resonance grows and reaches its maximum amplitude for $V_1 = 35$ V (at 0.56 THz, where $V_2 = 0$ V), with a slight red shift in its resonance frequency. Subsequently, when the voltage V_2 is applied across SRR-2 by keeping SRR-1 on the substrate, the cantilever arms of SRR-2 are gradually pulled towards the substrate, which decreases the asymmetry in the system. Due to this decrease in asymmetry, the Fano resonance starts to weaken with increasing V_2 and completely diminishes at $V_2 = 35$ V, as shown in Fig. 2b (both SRR-1 and SRR-2 are snapped down on the substrate with $V_{1,2} = 35$ V (see Fig. 1d)). Thereby, the symmetry of the structures is restored in the system that now shows only a dipolar resonance (at 0.67 THz). The observed red-shift in the frequency of the dipole and the Fano resonance is due to enhanced capacitance in the air gap between the cantilever and the substrate, as the cantilever is gradually bent down onto the substrate. We also fabricated the samples with various metal thicknesses of cantilevers (300, 500 and 700 nm) possessing different released heights. The THz transmission measurements were performed on the samples and are shown in Supplementary Fig. 4. The cantilever with thinner metal film possesses larger release height (*h*) (see Supplementary Fig. 5), and hence aids in achieving larger structural asymmetry (δ) in the system, which in turn results in stronger Fano resonance amplitude. The main reason for using the 900 nm thick aluminium resonator sample for our detailed analysis is the enhanced structural stability offered by thicker cantilevers during the persistent tuning of their released heights. This factor aids in precise control and continuous active tuning of Fano resonance feature in the proposed MEMS Fano-metasurface structure.

The correspondence between the transmission spectra obtained by the sequentially applied voltages (V_1 and V_2) and the structural asymmetry (δ) of the MEMS Fano-metasurface is established by the numerical simulations. The transmission spectra for varying δ are shown in Fig. 2c, d, which are calculated using finite difference time domain (FDTD) simulations offered by the commercially available Computer Software Technology (CST) microwave studio using unit-cell boundary conditions (refer to the Methods section for more details). The value of structural asymmetry parameter (δ) is estimated using the defined expression for δ based on the experimentally measured inclined heights (h_1, h_2) of the cantilevers of resonators SRR-1 and SRR-2 (as shown in the inset of Fig. 2b). The insets in Fig. 2c, d represent the sequential actuation of SRR-1 and SRR-2 resonators that

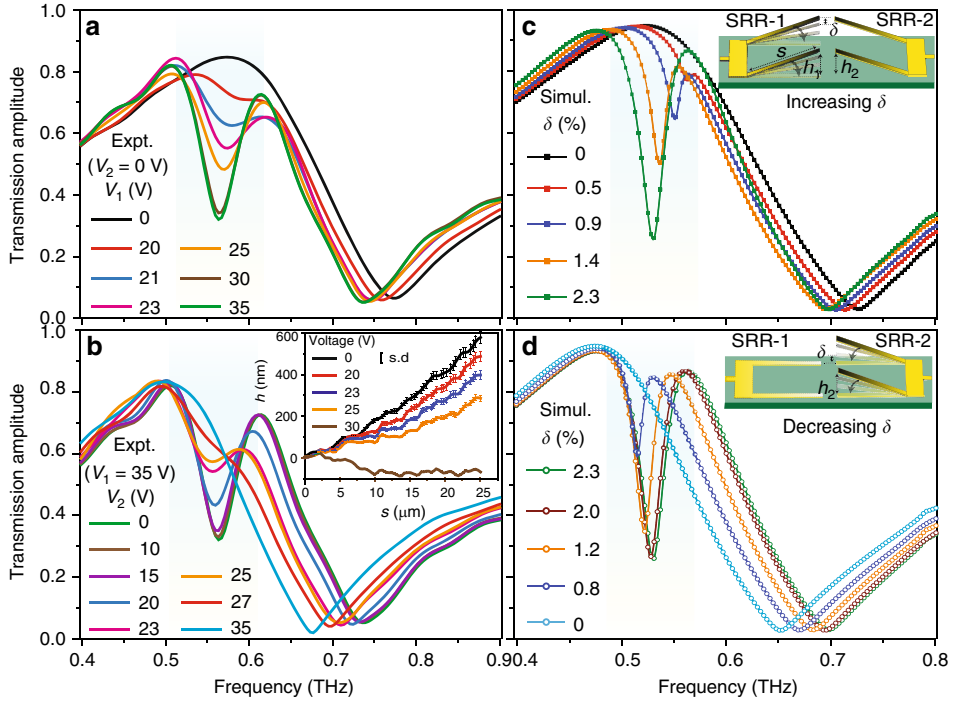

Fig. 2 Active tuning of Fano resonances in MEMS metasurface. **a** Depicts the experimentally measured THz transmission spectra showing the evolution of Fano resonance for continuous actuation of SRR-1 by varying voltage V_1, while keeping $V_2 = 0$ V. **b** Represents the measured spectra resulting from the actuation of SRR-2 by increasing V_2, while keeping $V_1 = 35$ V. Inset figure depicts the experimentally mapped actuation angles (with the error bars) of the SRR cantilevers of metal thickness 900 nm under the applied voltage (V) for the designed MEMS Fano-metasurface. **c**, **d** Numerically simulated THz transmission spectra for increasing and decreasing structural asymmetry configurations of the proposed MEMS Fano-metasurface. The values of the depicted asymmetry parameter (δ) in (**c**) and (**d**) show one-to-one correspondence with the voltage values of V_1 and V_2 varied in (**a**) and (**b**), respectively. The insets in (**c**) and (**d**) signify the sequential actuation of SRR-1 and SRR-2, respectively, showing the increasing and decreasing structural asymmetry configurations

correspond to the continuous increase and decrease in δ, which signifies one complete ramp cycle of asymmetry parameter (δ). As a first actuation sequence, asymmetry in the structure is increased by decreasing the released height (h_1) of SRR-1, which results in strengthening of the Fano resonance feature that reaches its largest resonance amplitude at the maximum asymmetry of $\delta_{max} = 2.3\%$. In the next actuation sequence, upon decreasing the released height (h_2) of SRR-2, amplitude of the Fano resonance diminishes and eventually disappears as the cantilever of SRR-2 touches down on the substrate ($\delta = 0$). Therefore, sequential actuation of the resonators SRR-1 and SRR-2 alters the symmetry of the structure from a symmetric configuration to an intermediate asymmetric state and finally bringing it back to the symmetric state thereby controlling the excitation of Fano resonance in one complete ramp cycle of δ.

Multiple-input–output (MIO) characteristics. The most striking feature of the excitation of the Fano resonance in MEMS Fano-metasurface is the observed anisotropic nature in the near-field coupling between the resonators at a given asymmetry parameter (δ). The anisotropic Fano coupling exhibits two distinctive pathways (in the output states) for the far-field and the near-field optical characteristics with respect to the sequential application of two voltage inputs V_1 and V_2, respectively on SRR-1 and SRR-2 or for increasing and decreasing pathways of δ. The distinctive pathways in the far-field response of the device are analysed using the peak to peak transmission intensity ($|\Delta T|$) of Fano resonance, which is discussed in Supplementary Fig. 6. As a input control parameter, we define the sequential voltage operation of V_1 and V_2 in terms of the differential voltage applied between the two resonators SRR-1 and SRR-2, defined as $\Delta V = |V_1 - V_2|$ that directly corresponds to the asymmetry parameter (δ) of the structure. We plot the variation in $|\Delta T|$ with respect to increasing and decreasing values of ΔV applied across the resonators in Fig. 3a, where the $|\Delta T|$ exhibits distinctive values for the increasing and decreasing configuration of input parameter ΔV. This scenario showing the distinctive pathways for $|\Delta T|$ closely resembles the hysteresis-type behaviour as observed in many natural phase change materials such as VO_2[12] and Ferrites[29]. However, here it is indeed two stable output states observed for two input controls (V_1 and V_2) that forms a closed loop in $|\Delta T|$ with respect to $|\Delta V|$ signifying the multiple-input–output states in the electro-optical characteristics of the metasurface. This hysteresis-type behaviour constituting MIO states is artificially created by the induced anisotropic near-field coupling observed in the tuning of Fano excitation by varying δ or ΔV. Further, similar MIO states are observed for the measured Q-factors of Fano resonance features for increasing and decreasing values of ΔV, as shown in Fig. 3c. We observe that for a given value of ΔV, the Q-factors during the increasing configuration of ΔV follow a different variation and possess larger values compared to the decreasing pathway of ΔV. The maximum Q-factors of 19.73 and 19 are experimentally measured for the lower ΔV (i.e. for extremely small asymmetry parameter (δ) cases), respectively during the increasing and decreasing configuration of ΔV. In the numerical simulations, the differential voltage (ΔV) is expressed in terms of asymmetry (δ) of the structure, which is a critical parameter in controlling the nature and excitation of Fano resonances. In Fig. 3b, d, the peak to peak transmission intensity ($|\Delta T|$) and Q-factors of Fano resonance are plotted for the

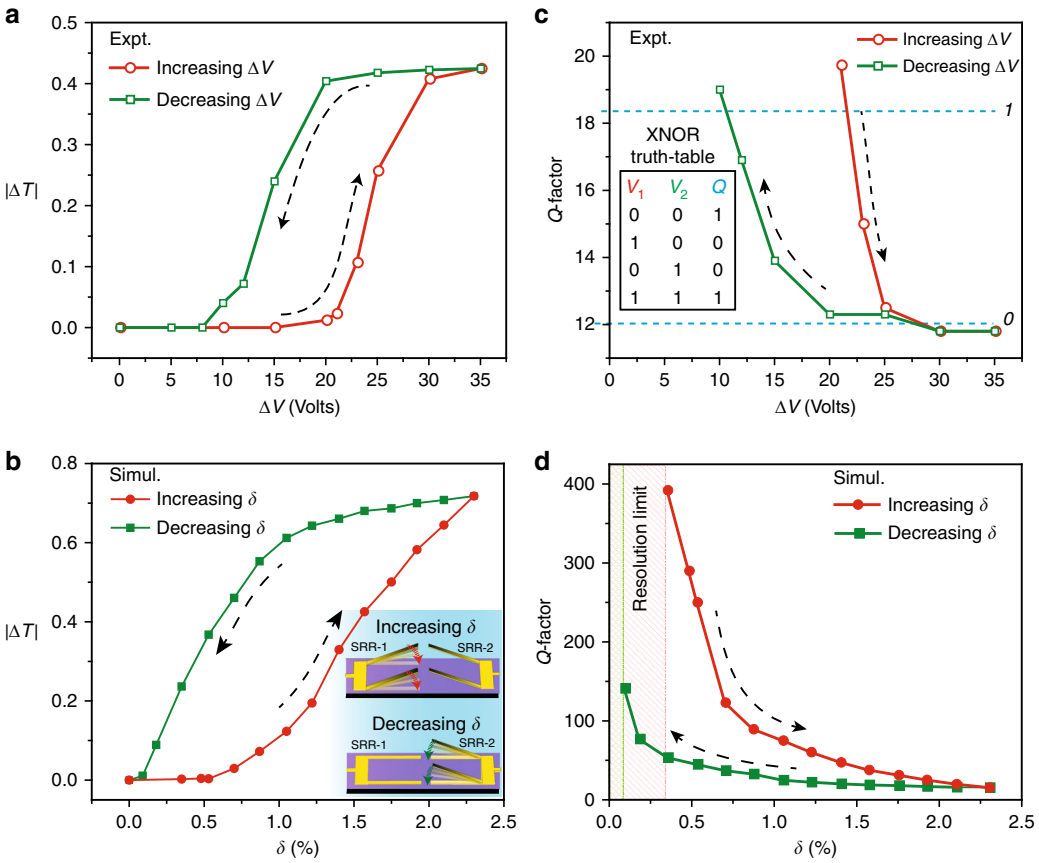

Fig. 3 Multiple-input-output electro-optical characteristics in the far-field features of MEMS Fano-metasurface. **a** Measured Fano resonance transmission intensity ($|\Delta T|$) with respect to differential voltage (ΔV) calculated for the curves shown in Fig. 2a and b, respectively. The red circles represent increasing order of Fano resonance strength by increasing the ΔV applied on the structures (applying V_1 on SRR-1 with $V_2 = 0$ V), whereas green squares represent decreasing state of Fano resonance in the presence of V_2 on SRR-2 with $V_1 = 35$ V that decreases the ΔV applied on the structure. **b** Simulated Fano resonance intensity ($|\Delta T|$) showing two intensity states for a single asymmetry value (δ) of the system. The inset figure represents the sequential actuation of SRR-1 and SRR-2 that governs the observed multiple-input-output (MIO) states for the MEMS Fano-metasurface. **c** Experimentally and **d** numerically calculated *Q*-factors of the Fano resonance are shown that exhibits the MIO configuration for sequential actuation of the SRR-1 and SRR-2 resonators. Inset table in (**c**) represents the truth-table for the logic exclusive-NOR (XNOR) operation that can be visualized in the proposed MEMS Fano-metasurface device in the form of high (*'1'*) and low (*'0'*) values for *Q*-factors of Fano resonance in the far-field

increasing and decreasing scenario of structural asymmetry parameter (δ), where the SRR-1 and SRR-2 are actuated sequentially (as shown in the insets of Fig. 3b). The simulation results agree well with the MIO characteristics observed in the experimental data. Further detailed plots on the figure of merit[38] (FoM) of Fano resonance showing the MIO characteristics are provided in Supplementary Figs. 10 and 11. These MIO states enacted by the out-of-plane (three-dimensional) symmetry breaking induced Fano resonances provide a unique advantage of creating a closed-loop behaviour in the electro-optical properties with tuneable area under the loop, which could help in precise tailoring of energy dissipation in the system. The tuneable MIO states for the intensity, *Q*-factors and FoM of Fano resonance are depicted in Supplementary Figs. 12–14. This tuneable MIO feature could lead towards the realization of multiple (more than two) output states favouring the possibility of digitizing the optical response through the system with two (or more) independent input-voltage control parameters.

MEMS Fano-metasurface enacted logic gates. The uniqueness of digitizing the excitation of Fano resonance in terms of its far-field optical states using two electrical controls constitutes digital XOR, XNOR, PASS and NOT logic functions in the far-field spectrum at THz frequencies. As discussed earlier, the structural states ('up' or 'down') of the constituent resonators SRR-1 and SRR-2 are independently reconfigured using the voltage inputs V_1 and V_2, respectively in determining the output state of Fano resonance (*F*). The structural metastable states of the resonators determined by the electrical inputs ($V_{1,2}$) are represented by the logic binary digits, where 'up-state' of the resonator corresponds to binary '*0*' ($V_{1,2} = 0$ V) and the 'down-state' corresponds to binary '*1*' ($V_{1,2} = 35$ V). True (ON) and false (OFF) states of the Fano resonance amplitude in the far-field are represented by the binary digits '*1*' and '*0*', respectively. The measured THz far-field transmission spectra showing the XOR logic feature for the various metastable structural states (*00*), (*10*), (*01*) and (*11*) of the MEMS resonators are given in Fig. 4a–d. The voltage inputs (V_1 and V_2) applied to the individual resonators (SRR-1 and SRR-2) can be programmed using sequential trigger bits {*0,1*} that controls the actuation heights (up/down) of SRR-1 and SRR-2, respectively. However, in our experiments, the limitations posed by the well-known problem of stiction[39] in our fabricated MEMS devices disrupt the repeatable operation of the device. Hence, we consider two devices and prepare their cantilevers in their respective metastable states (*10*) and (*01*) by applying the corresponding voltage inputs and perform the transmission measurements in the far-field. Since the Fano resonance feature

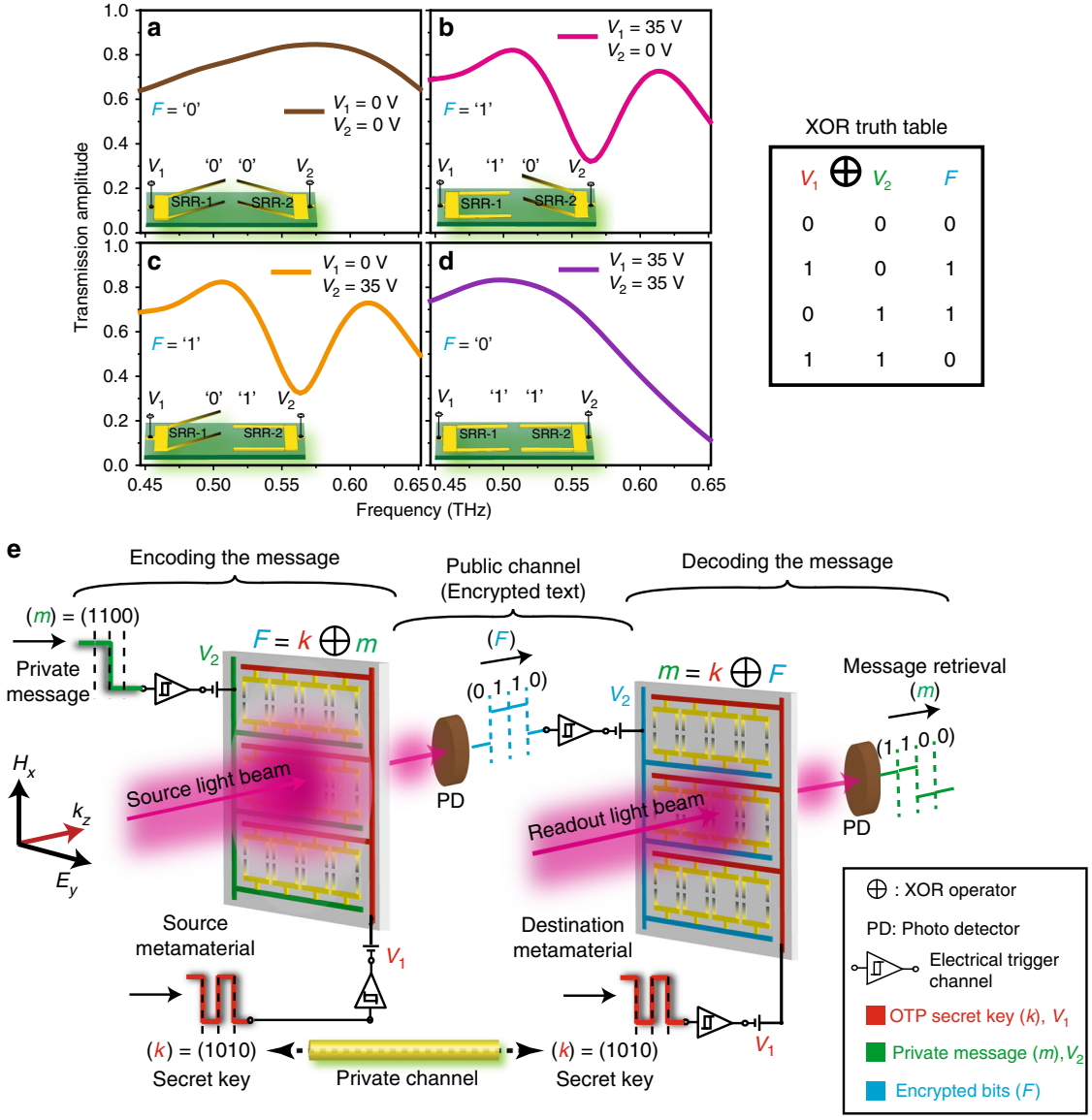

Fig. 4 Exclusive-OR (XOR) logic operation with MEMS Fano-metasurface and its significance in cryptographic wireless communication networks. **a**–**d** Measured far-field THz transmission spectra of the MEMS Fano-metasurface showing the XOR logic feature in the form of presence/absence of Fano resonance (at 0.56 THz) for various structural/voltage states of the SRRs. **a**, **d** show the symmetric configuration of the structures (*00* and *11*) that signifies the absence of Fano resonance excitation ($F = 0$), whereas **b**, **c** represent the asymmetric configuration of the structures (*10* and *01*) that results in the excitation of Fano resonance feature ($F = 1$) in the sample. **e** Pictorial representation of realizing the OTP secured wireless communication channel by performing the XOR logic operation to encode the private message (m) with the secret key (k) and is sent through the public channel as optical signals. The message is retrieved securely (decrypted) at the destination end by performing the inverse XOR operation on the measured optical states (F) with the secret key (k). The structural/voltage states of SRR-1 and SRR-2 are expressed as OTP secret key (k) and the private message (m), respectively, whereas the secured data is transmitted through public channel in the form of optical bits (F)

results due to the asymmetry in the structural configuration of the metasurface, for input voltages ($V_1 = 0$, $V_2 = 35$ V and $V_1 = 35$ V, $V_2 = 0$ V) there exist two asymmetric structural configurations 'up–down' (*01*) and 'down–up' (*10*) that results in the true state for the Fano resonance condition (i.e. $F = 1$), as shown in Fig. 4b, c, respectively. On the other hand, for symmetric structural configurations of the device ($V_1 = V_2 = 0$ V and $V_1 = V_2 = 35$ V), 'up–up' (*00*) and 'down–down' (*11*) results in the absence of Fano resonance ($F = 0$) state, as shown in Fig. 4a, d. Resulting truth table is presented in the inset of Fig. 4, which resembles the digital XOR logic operation, where the Fano output is true ($F = 1$) if the input voltage states differ, otherwise Fano output results in a false state ($F = 0$) (i.e. when both the inputs are either true (*11*) or false (*00*), then output state $F = 0$). As discussed in Supplementary Fig. 7, intensity contrast between the output states $F = 0$ and $F = 1$ is measured to be equal to $\Delta T = 0.61$ (normalized to the input intensity of 1) at a frequency of 0.56 THz. The proposed XOR logic functionality based on the Fano resonance exhibits substantial improvement in the intensity contrast ratio compared to earlier demonstrations at THz frequencies[29,40]. Furthermore, another logic functionality that represents the XNOR truth table is derived from the MIO characteristics observed in the Q-factors of the Fano resonance, as shown in Fig. 3c. The XNOR logic operation signifies the true output if both the inputs are either true or false, which is complementary to the XOR logic operation. In our measurements, by defining the threshold values to the input voltages (V_1, V_2) and the output states in the form of Q-factors (inverse of loss-factors), we construct the XNOR

functionality of the device. Here, with either very low (*00*) or high (*11*) voltage inputs, the system exhibits extremely high values of *Q*-factors showing the true output state ($Q = 1$) for the low structural asymmetry region. In the case of large structural asymmetries, where one of the voltage input is high and other input is low (*10* or *01*), results in the false output state ($Q = 0$) with low *Q*-factors for the Fano resonance feature.

The proposed design further provides a flexibility of controlling the asymmetry of the structure to show either anisotropic or isotropic way of tuning the coupling between the adjacent resonators just by adequately coding the input electrical (voltage) signalling sequence. Supplementary Fig. 15 represents the experimentally measured variation in the intensity of the Fano resonance with respect to the voltage V_2 applied on SRR-2, by keeping SRR-1 in contact with the substrate with $V_1 = 35$ V (decreasing pathway of the asymmetry). This configuration of Fano resonance tuning signifies the single-input–output (SIO) characteristics in the MEMS Fano-metasurface, which is due to the isotropic nature of coupling between the resonators during the increasing and decreasing pathways of asymmetry (δ). The ability of converting the electro-optical response of the system from MIO configuration (anisotropic tuning of coupling) to the SIO configuration (isotropic change in coupling) aids in realizing the NOT and PASS logic operations. By closing the input with high (*1*) and low (*0*) logic states, respectively and varying the other input, the pre-selection of the states with an added control enables a switch between NOT to PASS logic functions. These NOT and PASS logic operations are the special cases of XOR functionality of the MIO states. The NOT or negation operation represents the formation/annihilation of a Fano mode in the far-field spectrum of the device in the absence/presence of external stimulus, signifying the switching between the coupled and uncoupled regime of the metasurface system. On the other hand, by closing the input having the low ('*0*') logic state, the buffer/PASS gate can be realized, where the operation does not alter the input state and hence the output logic state stays the same as the input logic state. The details on the NOT and PASS logic functionalities of the proposed design is provided in Supplementary Fig. 15.

In addition to the XOR, XNOR, NOT and PASS logic operations using the far-field characteristics, the near-field characteristics reveal the NAND logic operation in the form of confined electric fields in their ON (snapped) and OFF (released) states. Numerically calculated electric field amplitude distributions for various structural states of the MEMS Fano-metasurface are plotted in Fig. 5a–d. The absolute **E**-field amplitude for structural configurations shown in Fig. 5a–c represents enhanced field strengths when at least one of the structural states is in released (OFF) state compared to structural configuration (shown in Fig. 5d), where both cantilevers are prepared in snapped (ON) states. Variation in the amplitude of the confined electric fields is plotted in Fig. 5e that highlights the distinctive pathways for the increasing and decreasing configuration of the asymmetry. For the symmetric state with both the cantilevers in the OFF state (Fig. 5a), the electric field confinement is nearly an order of magnitude greater than the symmetric configuration, where both the cantilevers are in the ON states (Fig. 5d). Whereas, for the two asymmetric configurations of the cantilevers (Fig. 5b, c), the field confinement in the structure shows similar amplitude to the symmetrically prepared OFF states (Fig. 5a) of the structure. Higher amplitude value of the electric field confinement is labelled as binary '*1*', whereas lower electric field amplitude is represented by binary '*0*', as shown in Fig. 5e. Therefore, the change in confined near-field electric amplitude measured at the tip of the cantilevers in their various metastable structural states constitutes a logic NAND function as described by the truth table given in Fig. 5f. Experimental extraction of the near-field information in the THz part of the spectrum is challenging,

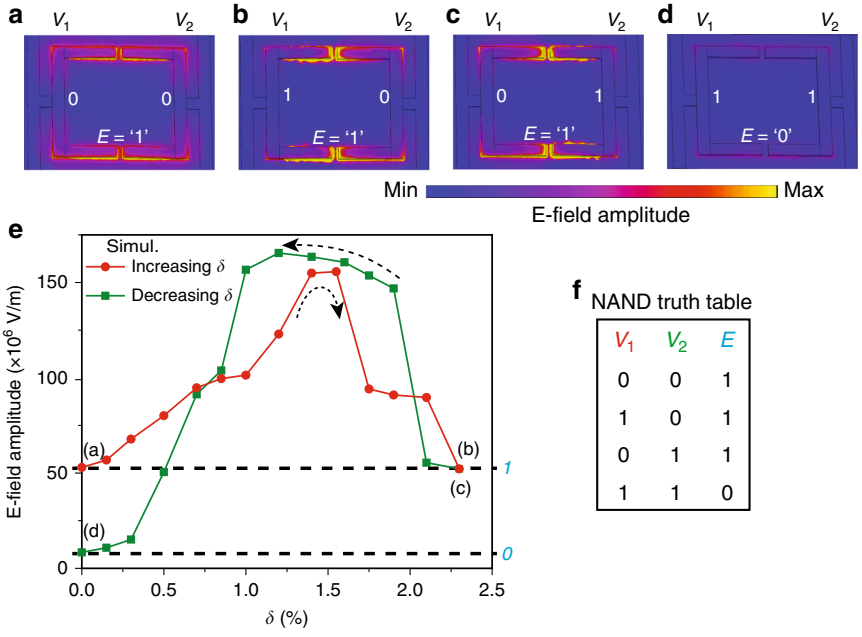

Fig. 5 NAND logic gate and multiple-input-output states in the near-field confined energy of MEMS Fano-metasurface. **a**–**d** The numerically calculated electric field distributions at 0.55 THz, where **a**–**c** represent the true states of the electric field confinement ($E = 1$), whereas **d** shows the false state of *E* (i.e. $E = 0$), signifying the construction of NAND logic operation that is tabulated in (**f**). The input logic states *0* and *1* for V_1 and V_2 represent the 'up' and 'down' actuation states of SRR cantilevers, respectively. **e** Distinctive variations shown for the enhanced spatially confined electric near-field strengths in the device at Fano frequencies (0.55 THz) that possess MIO behaviour during sequential actuation of the SRR-1 (increasing δ) and SRR-2 (decreasing δ). The electric field strength is measured at the tip position of the SRR cantilevers. **f** NAND logic truth table generated from the electro-optical operation of proposed MEMS Fano-metasurface

however, recent demonstrations using tip based THz near-field microscopy[41–43] can be used as one of the ways to retrieve the near-field information in terms of output field intensity states that in turn can be used to sequentially trigger the input voltage of the cascaded NAND device. This could enable the near-field cascading of the logic gates in the complementary metal-oxide-semiconductor (CMOS) configuration. Furthermore using numerical simulations, we conceptually show the NAND and OR logic operations in the far-field spectrum using the same geometrical design of MEMS Fano-metasurface but combining two unit-cells to make one composite unit-cell (super-cell) consisting of two Fano meta-molecules (a pair of SRR-1–SRR-2 and SRR-3–SRR-4), as shown in Supplementary Figs. 16 and 17. By independently controlling the SRRs present within the two Fano meta-molecules using the voltage sources (V_1 and V_2) the NAND and OR logic operations can be realized by the THz readout pulse in the form of presence or absence of Fano resonance ($F = 1$ or 0) in the far-field amplitude or intensity spectrum. The NAND logic operation is significant owing to its unique feature of functional completeness (universal gate), as any Boolean function can be implemented by using the combination of several NAND gates, where the concept is schematically presented in Supplementary Fig. 18 to show the construction of AND and OR logic gates by cascading the NAND metasurface gates in the far-field.

Discussion

The excitation of sharp Fano resonance feature in metamaterials has been pivotal in enhancing the confinement of near-field energy in the structures to aid the strong nonlinearity and sensing applications[36]. However, so far, such resonances have been realized by breaking the in-plane symmetry of the structures that was restricted to the SIO behaviour in the optical properties of the metamaterial. In this work, by breaking the structural symmetry in the out-of-plane (third) dimension of metamaterial allows us to probe the intriguing features resulting from the exponentially decaying nature of out-of-plane fringing near-fields. This nonlinear spatial extension of near-fields in the third dimension of the sample aids in the anisotropic tuning of Fano resonance during its increasing and decreasing asymmetry (δ) pathways, which leads to the observed MIO states in the excitation of Fano resonance (Fig. 3). This anisotropic type of Fano tuning is a result of contrasting coupling strengths between the resonators (SRR-1 and SRR-2) for same δ, depending on whether the interacting resonator cantilevers are closer to or farther away from the surface of the substrate. For instance, in the region of low structural asymmetry (δ), during the increasing δ configuration, the cantilevers of deforming SRR-1 and fixed SRR-2 are positioned away from the substrate, where the spatial extention of the near-field is weak (refer to inset of Fig. 3b). Therefore, the near-field interaction between the cantilever arms of SRR-1 and SRR-2 lays in the region of weak spatial field distribution. Hence, it requires larger structural asymmetries (higher threshold) to excite the Fano resonance, which also results in the observed relatively higher Q-factors for a specific value of δ, as shown in Fig. 3c, d. Whereas, while decreasing the asymmetry by actuating SRR-2 cantilevers, the SRR-1 that is positioned on the substrate is in the strong near-field spatial region and is likely to possess greater influence on the near-field coupling between the resonators and hence results in a stronger excitation of Fano features possessing relatively lower Q-factors (lower threshold). Hence, the resulting MIO states in the electro-optical characteristics of the proposed MEMS Fano-metasurface fundamentally exploits the intrinsically present exponentially decaying spatial distribution of near-fields extended along the z-axis of the sample.

One of the important aspects of MEMS-based metasurface device is that it could be operated in both volatile as well as in non-volatile regimes depending on the partial or complete actuation of the constituent resonator cantilevers in the unit cell. This directly reflects on the persistent repeatability of the demonstrated logic gate functionalities of MEMS Fano-metasurface. As emphasized earlier, the results on XOR logic operation of the proposed device discussed in Fig. 4a–d represent non-volatile operation regime of the MEMS Fano-metasurface, where due to stiction in the MEMS devices, the cantilevers remain stuck to the substrate even after the input voltage is removed (refer to Supplementary Movie 1). This non-volatile property of the device affects the speed and repeatability of the device operation, but enables the memory features in the device, which could potentially be used as memory registers in data storage and processing techniques[33]. On the other hand, the volatile feature of MEMS Fano-metasurface enabled by the partial actuation of SRR-1 and SRR-2 cantilevers (applied voltage of $V_{1,2} < 25$ V, i.e. less than the pull-in voltage of the device) assures persistent repeatability of the XOR and other logic operations (refer to Supplementary Movie 2). Most interestingly, the volatile feature of XOR functionality in the device possesses unique property of pseudorandom generation and serves as a key component in OTP encryption/decryption techniques in establishing theoretically secured cryptographic protocols in the communication systems. In Fig. 4e, we provide a schematic for the secured OTP cryptographic channel that can be achieved by performing the XOR logical operations using the MEMS Fano-metasurface in the volatile operation regime of the cantilevers. The input/output states of the XOR logic operation are listed by the truth table shown in Fig. 4. The two inputs (secret key) $k = \{0,1\}^n$ and (private message) $m = \{0,1\}^n$ are expressed as the strings of binary digits that represent the structural states of resonators SRR-1 (V_1) and SRR-2 (V_2). The transmitted optical (THz) bits are represented by F that signifies absence (binary '0') or presence (binary '1') of Fano intensity states. At the source (Alice's end), for each bits of $k = (1010)$ and $m = (1100)$, a XOR operation ($F = k \oplus m$) is carried out by performing an optical readout using THz beam that encrypts the private message (m) in the form of transmitted optical bit, $F = (0110)$, which is sent as a ciphertext (encrypted message) through the unsecured public channel. At the destination (Bob's end), the optical bits (ciphertext) are detected using a photo-detector (PD) and the resulting voltage states ($F = 0110$) from the PD are directly fed through a trigger channel to the voltage source V_2 that controls the actuation states $\{0,1\}$ of SRR-2 of MEMS Fano-metasurface. Finally, the ciphertext (F) containing the information of private message is decrypted to retrieve original private message (m) at the destination end by performing the inverse XOR operation, $m = k \oplus F$, as shown in Fig. 4e. The secret OTP key (k) contains the information of the structural state of SRR-1 (V_1) and is pre-shared between the source and the destination ends via a private (secure) channel. Thus, the proposed far-field XOR functionality of the MEMS Fano-metasurface could open-up new avenues for realizing cryptographically secured wireless THz communications[44,45].

In summary, we demonstrated excitation of sharp Fano resonances in a reconfigurable MEMS metasurface using two independent voltage controls that constitutes digital XOR, XNOR, NOT, NAND and OR logic gates at THz frequencies. Formation of MIO states resembling the hysteresis loop is observed in the electro-optical properties of the MEMS Fano-metasurface that results from the anisotropic variation in the near-field coupling of Fano resonance excitation during increasing and decreasing out-of-plane asymmetry of the system. The XOR operation of the device reveals that the concept can show potential prospects in super-encryption techniques in i-banking sectors, short

messaging services (SMS), defence, national data security systems and high speed cryptographically secured wireless communication networks, which are now being pushed towards THz frequencies. The NAND logic operation being the universal logic function would enable the construction of all the other Boolean logic operations, thereby providing a flexibility of enhancing the digital functionalities of the device. The reported multi-functionalities of the proposed MEMS Fano-metasurface are largely suitable for real-world applications such as active sensors possessing tuneable mode volumes, nonlinear devices and modulators. Alongside, the MIO characteristics of the MEMS Fano-metasurface could potentially provide a flexible platform for developing the next generation randomly accessible, digital and programmable metamaterials for precise tailoring of electro-optical properties and multichannel data processing at higher bit rates.

Methods

Sample fabrication. The MEMS Fano-metasurface was fabricated using a CMOS compatible process as described below. First, the lightly doped 8 in. silicon substrate of 725 µm thickness was cleaned and a 100 nm thick sacrificial SiO_2 layer was deposited using low pressure chemical vapor deposition (LPCVD) process. Following this, conventional photolithography process was used to pattern the anchor region. With the designed pattern, the parts of sacrificial SiO_2 for anchor regions were dry etched using reactive ion etching process. After this, a 50 nm thick Al_2O_3 layer was deposited using the ALD process, followed by the sputter deposition of Al metal of thicknesses 300, 500, 700 and 900 nm. Note that the bimorph layers (Al/Al_2O_3) were in physical contact with Si substrate at the anchor region, and in the remaining part of the wafer, it was on top of the sacrificial SiO_2 layer. Then, the second photolithography step was carried out for defining the cantilevers and metal lines of metasurface patterns. Following this, both Al and Al_2O_3 layers were dry etched to form the designed metasurface. Finally, vapor hydrofluoric acid (VHF) was used to isotropically etch the SiO_2 sacrificial layer underneath the bimorph structures, thereby suspending it over the Si substrate with an air gap between them. At the anchor region, since the bimorphs were in physical contact with Si substrate; the VHF release process was not time controlled, and this ensured higher yield of the devices. Due to the residual stress in the bimorph cantilevers, the released cantilevers were bent up, thereby increasing the initial tip displacement.

Electromechanical characterization of the MEMS device. The deflection/actuation profiles of released cantilevers were measured using Lyncee Tec. reflection digital holographic microscope (R-DHM). The released chips are wire-bonded to a printed circuit board (PCB). Separate voltage supplies (V_1 and V_2) are used for the actuation of SRR-1 and SRR-2 cantilevers, respectively. Silicon (Si) substrate was chosen as the ground potential, and the cantilevers were positively biased. When voltage is applied across the released cantilevers and Si substrate, the attractive electrostatic force deforms the suspended cantilevers towards the fixed Si substrate. This mechanical deformation of cantilevers induces a restoring force that opposes the electrostatic force causing the deflection at the first place. Hence, the final position of the cantilever at a given voltage is determined by the equilibrium position, where the electrostatic force and restoring force balances each other. As the applied voltage increases, the electrostatic force exceeds the restoring force and at a critical value known as the pull-in voltage (>25 V), thereby bringing the cantilevers to be in physical contact with Si substrate (shown in the inset of Fig. 2b) (refer to Supplementary Movie 1). The pull-in can be clearly observed through the optical microscope fitted on the R-DHM. The Al_2O_3 layer beneath the Al layer ensured that there is no current flowing from Al layer to Si substrate, when pull-in occurs. Current flow through the Al/Si junction is forbidden as that could permanently damage the device due to the increase in the local temperature.

THz measurements. The MEMS Fano-metasurface is optically characterized using the conventional GaAs photoconductive switch-based THz-time domain spectroscopy system operating in the transmission mode. The wire-bonded MEMS metasurface sample is positioned at the focus of the THz beam. The electrical connections to the SRR-1 and SRR-2 resonators structures are established using a two channel DC voltage source. For four configurations of the voltages ($V_1 = 0$ V, $V_2 = 0$ V; $V_1 = 35$ V, $V_2 = 0$ V; $V_1 = 0$ V, $V_2 = 35$ V; and $V_1 = 35$ V, $V_2 = 35$ V), the THz wave of beam spot 4 mm impinges on the sample at normal incidence and the transmitted THz pulse is captured using the THz detector connected to the lock-in amplifier. THz response through the bare silicon substrate is measured as the reference. In the post-processing steps, the detected THz pulses measured through the sample and the bare substrate are fast Fourier transformed (FFT) to obtain the corresponding THz spectra. Later, the transmitted THz spectrum through the sample ($\boldsymbol{T}_S(\omega)$) is normalized with respect to the transmission through the substrate ($\boldsymbol{T}_R(\omega)$), i.e. $\boldsymbol{T}(\omega) = |\boldsymbol{T}_S(\omega)/\boldsymbol{T}_R(\omega)|$, and the normalized spectrum is shown in Figs. 2a, b and 4a–d.

Numerical simulations. FDTD numerical simulations were conducted to calculate the THz transmission spectra and the confined electric near-fields and surface current distributions corresponding to the resonance modes for the normal incident of THz waves of TE polarization. Full-field electromagnetic wave simulations were performed using the commercial simulation software CST microwave studio. For the material property, aluminium (Al) of thickness 900 nm was modelled as a lossy metal with a conductivity of 3.57e7 S/m. Aluminium oxide and Silicon were modelled as lossless dielectric materials with a dielectric constant of 9.5 and 11.9, respectively. In the simulation, a single unit cell of the metasurface structure was simulated with periodic boundary conditions employed in axial directions orthogonal to the incident waves. The perfectly matched layers are applied along the propagation of the electromagnetic waves. Plane waves were incident onto the unit cell from the port on the metal side, while the transmission spectrum was determined from the probe placed at the other side of metasurface. The experimentally measured (inset in Fig. 2b) deformation (released) angles for the cantilevers establishes the congruence between the values of applied voltages in the measurements and the structural asymmetry parameter used in the simulations. For the numerical simulations, the deformation angle of the cantilevers is calculated using the expression, $\theta = \sin^{-1}(h/s)$, where h is the released height of cantilevers and s is the length of cantilever. In the meanwhile, field monitors are used to collect the electric fields, magnetic fields and the respective surface currents at Fano resonance frequencies for varying asymmetry values.

Code availability. The transmission responses and the electric field distribution plots were numerically computed using CST microwave studio.

Data availability

The data that support the findings of this study could be made available upon request to the corresponding author. The data from this paper is also available from the University of Southampton ePrints research repository: https://doi.org/10.5258/SOTON/D0612

Received: 20 November 2017 Accepted: 30 July 2018
Published online: 03 October 2018

References

1. Zheludev, N. I. & Kivshar, Y. S. From metamaterials to metadevices. *Nat. Mater.* **11**, 917–924 (2012).
2. Zheludev, N. I. & Plum, E. Reconfigurable nanomechanical photonic metamaterials. *Nat. Nanotechnol.* **11**, 16–22 (2016).
3. Fan, K. & Padilla, W. J. Dynamic electromagnetic metamaterials. *Mater. Today* **18**, 39–50 (2015).
4. Zhu, W. M. et al. Switchable magnetic metamaterials using micromachining processes. *Adv. Mater.* **23**, 1792–1796 (2011).
5. Zhu, W. et al. Microelectromechanical Maltese-cross metamaterial with tunable terahertz anisotropy. *Nat. Commun.* **3**, 1274 (2012).
6. Kan, T. et al. Enantiomeric switching of chiral metamaterial for terahertz polarization modulation employing vertically deformable MEMS spirals. *Nat. Commun.* **6**, 8422 (2015).
7. Pitchappa, P. et al. Active control of electromagnetically induced transparency analog in terahertz MEMS metamaterial. *Adv. Opt. Mater.* **4**, 541–547 (2016).
8. Bi, K. et al. Magnetically tunable Mie resonance-based dielectric metamaterials. *Sci. Rep.* **4**, 7001 (2014).
9. Valente, J., Ou, J. Y., Plum, E., Youngs, I. J. & Zheludev, N. I. A magneto-electro-optical effect in a plasmonic nanowire material. *Nat. Commun.* **6**, 7021 (2015).
10. Tao, H. et al. Reconfigurable terahertz metamaterials. *Phys. Rev. Lett.* **103**, 147401 (2009).
11. Ou, J. Y., Plum, E., Jiang, L. & Zheludev, N. I. Reconfigurable photonic metamaterials. *Nano Lett.* **11**, 2142–2144 (2011).
12. Driscoll, T. et al. Memory metamaterials. *Science* **325**, 1518–1521 (2009).
13. Zhang, J., MacDonald, K. F. & Zheludev, N. I. Nonlinear dielectric optomechanical metamaterials. *Light Sci. Appl.* **2**, 96 (2013).
14. Padilla, W. J., Taylor, A. J., Highstrete, C., Lee, M. & Averitt, R. D. Dynamical electric and magnetic metamaterial response at terahertz frequencies. *Phys. Rev. Lett.* **96**, 107401 (2006).
15. Manjappa, M., Srivastava, Y. K., Cong, L., Al-Naib, I. & Singh, R. Active photoswitching of sharp Fano resonances in THz metadevices. *Adv. Mater.* **29**, 1603355 (2016).
16. Gu, J. et al. Active control of electromagnetically induced transparency analogue in terahertz metamaterials. *Nat. Commun.* **3**, 1151 (2012).

17. Manjappa, M. et al. Hybrid lead halide perovskites for ultrasensitive photoactive switching in terahertz metamaterial devices. *Adv. Mater.* **29**, 1605881 (2017).
18. Lim, W. X. et al. Ultrafast all-optical switching of germanium-based flexible metaphotonic devices. *Adv. Mater.* **30**, 1705331 (2018).
19. Pendry, J. B. Manipulating the near field with metamaterials. *Opt. Photonics News* **15**, 32–37 (2004).
20. Pitchappa, P. et al. Active control of near-field coupling in conductively coupled microelectromechanical system metamaterial devices. *Appl. Phys. Lett.* **108**, 111102 (2016).
21. Liu, M. et al. Ultrathin tunable terahertz absorber based on MEMS-driven metamaterial. *Microsyst. Nanoeng.* **3**, 17033 (2017).
22. Cong, L., Pitchappa, P., Lee, C. & Singh, R. Active phase transition via loss engineering in a terahertz MEMS metamaterial. *Adv. Mater.* **29**, 1700733 (2017).
23. Bai, Y., Chen, K., Bu, T. & Zhuang, S. An electrically tunable terahertz metamaterial modulator with two independent channels. *J. Appl. Phys.* **119**, 124505 (2016).
24. Manjappa, M., Pitchappa, P., Wang, N., Lee, C. & Singh, R. Active control of resonant cloaking in a terahertz MEMS metamaterial. *Adv. Opt. Mater.* **6**, 1800141 (2018).
25. Zheludev, N. I. Obtaining optical properties on demand. *Science* **348**, 973–974 (2015).
26. Giovampaola, C. D. & Engheta, N. Digital metamaterials. *Nat. Mater.* **13**, 1115–1121 (2014).
27. Cui, T. J., Qi, M. Q., Wan, X., Zhao, J. & Cheng, Q. Coding metamaterials, digital metamaterials and programmable metamaterials. *Light Sci. Appl.* **3**, e218 (2014).
28. Papaioannou, M., Plum, E., Valente, J., Rogers, E. T. F. & Zheludev, N. I. All-optical multichannel logic based on coherent perfect absorption in a plasmonic metamaterial. *APL Photonics* **1**, 090801 (2016).
29. Kim, W. Y. et al. Graphene–ferroelectric metadevices for nonvolatile memory and reconfigurable logic-gate operations. *Nat. Commun.* **7**, 10429 (2016).
30. Croft, N. J. & Olivier, M. S. Using an approximated one-time pad to secure short messaging service (SMS). In *Proceedings of the Southern African Telecommunication Networks and Applications Conference*. South Africa, 26–31 (2005).
31. Subramanyan, P., Ray, S. & Malik, S. Evaluating the security of logic encryption algorithms. In *Proceedings of the 2015 IEEE International Symposium on Hardware Oriented Security and Trust (HOST)*. Washington, DC, 137–143 (2015).
32. Xiang, W. & Lee, C. Nanoelectromechanical torsion switch of low operation voltage for nonvolatile memory application. *Appl. Phys. Lett.* **96**, 193113 (2010).
33. Lee, S. W., Park, S. J., Campbell, E. E. B. & Park, Y. W. A fast and low-power microelectromechanical system-based non-volatile memory device. *Nat. Commun.* **2**, 220 (2011).
34. Fedotov, V. A., Rose, M., Prosvirnin, S. L., Papasimakis, N. & Zheludev, N. I. Sharp trapped-mode resonances in planar metamaterials with a broken structural symmetry. *Phys. Rev. Lett.* **99**, 147401 (2007).
35. Singh, R., Al-Naib, I. A. I., Koch, M. & Zhang, W. Sharp Fano resonances in THz metamaterials. *Opt. Express* **19**, 6312–6319 (2011).
36. Luk'yanchuk, B. et al. The Fano resonance in plasmonic nanostructures and metamaterials. *Nat. Mater.* **9**, 707–715 (2010).
37. Limonov, M. F., Rybin, M. V., Poddubny, A. N. & Kivshar, Y. S. Fano resonances in photonics. *Nat. Photonics* **11**, 543 (2017).
38. Cong, L. et al. Fano resonances in Terahertz metasurfaces: a figure of merit optimization. *Adv. Opt. Mater.* **3**, 1537–1543 (2015).
39. Buchnev, O. et al. Controlling stiction in nano-electro-mechanical systems using liquid crystals. *ACS Nano* **10**, 11519–11524 (2016).
40. Ho, C. P., Pitchappa, P. & Lee, C. Digitally reconfigurable binary coded terahertz metamaterial with output analogous to NOR and AND. *J. Appl. Phys.* **119**, 153104 (2016).
41. Adam, A. J. L. Review of near-field terahertz measurement methods and their applications. *J. Infrared Millim. Terahertz Waves* **32**, 976 (2011).
42. Mitrofanov, O. et al. Near-field terahertz probes with room-temperature nanodetectors for subwavelength resolution imaging. *Sci. Rep.* **7**, 44240 (2017).
43. Sang, Y. et al. Broadband multifunctional plasmonic logic gates. *Adv. Opt. Mater.* **6**, 1701368 (2018).
44. Koenig, S. et al. Wireless sub-THz communication system with high data rate. *Nat. Photonics* **7**, 977–981 (2013).
45. Nagatsuma, T., Ducournau, G. & Renaud, C. C. Advances in terahertz communications accelerated by photonics. *Nat. Photonics* **10**, 371–379 (2016).

Acknowledgements

M.M., P.P. and R.S. acknowledge the funding support from Ministry of Education, Singapore, MOE2017-T2-1-110 (S) grants and National Research Foundation (NRF) Singapore and Agence Nationale de la Recherche (ANR), France-NRF2016-NRF-ANR004 (M4197003) grant. M.M., P.P., N.I.Z. and R.S. acknowledge the funding support from Ministry of Education, Singapore, MOE2016-T3-1-006 grant. N.I.Z. acknowledges the support from the UK's Engineering and Physical Sciences Research Council (grant number EP/M009122/1). C.L. acknowledges the grant support from NRFCRP15-2015-02 "Piezoelectric Photonics Using CMOS Compatible AlN Technology for Enabling the Next Generation Photonics ICs and Nanosensors" at NUS, Singapore.

Author contributions

M.M., R.S. and P.P. conceived the idea and designed the experiments. P.P. and N.W. fabricated the experimental samples. M.M. carried out the THz measurements and numerical simulations. M.M., P.P., N.I.Z., N.S., C.L. and R.S. analysed the results. M.M. and R.S. prepared the manuscript with inputs from the co-authors. R.S. supervised the overall project.

Additional information

Supplementary Information accompanies this paper at https://doi.org/10.1038/s41467-018-06360-5.

Competing interests: The authors declare no competing interests.

Reprints and permission information is available online at http://npg.nature.com/reprintsandpermissions/

Publisher's note: Springer Nature remains neutral with regard to jurisdictional claims in published maps and institutional affiliations.

Applied Physics Letters

Optical bistability in shape-memory nanowire metamaterial array

Cite as: Appl. Phys. Lett. **113**, 021105 (2018); https://doi.org/10.1063/1.5025400
Submitted: 09 February 2018 . Accepted: 08 June 2018 . Published Online: 13 July 2018

Yusuke Nagasaki, Behrad Gholipour, Jun-Yu Ou, Masanori Tsuruta, Eric Plum, Kevin F. MacDonald, Junichi Takahara, and Nikolay I. Zheludev

Optical bistability in shape-memory nanowire metamaterial array

Yusuke Nagasaki,[1,2] Behrad Gholipour,[1,3] Jun-Yu Ou,[1,a)] Masanori Tsuruta,[1,4] Eric Plum,[1] Kevin F. MacDonald,[1] Junichi Takahara,[2,5] and Nikolay I. Zheludev[1,6]
[1]*Optoelectronics Research Centre and Centre for Photonic Metamaterials, University of Southampton, Highfield, Southampton SO17 1BJ, United Kingdom*
[2]*Graduate School of Engineering, Osaka University, 2-1 Yamadaoka, Suita, Osaka 565-0871, Japan*
[3]*Department of Chemistry, University of Southampton, Highfield, Southampton SO17 1BJ, United Kingdom*
[4]*Asahi Kasei, Energy and Environment R&D Center, 2-1 Samejima, 416-8501 Fuji, Japan*
[5]*Photonics Advanced Research Center, Osaka University, 2-1 Yamadaoka, Suita, Osaka 565-0871, Japan*
[6]*Centre for Disruptive Photonic Technologies, SPMS, TPI, Nanyang Technological University, Singapore 637371, Singapore*

(Received 9 February 2018; accepted 8 June 2018; published online 13 July 2018)

Non-volatile temperature-induced structural phase transitions such as those found in chalcogenide glasses are known to lead to strong changes in optical properties and are widely used in rewritable optical disk technology. Herein, we demonstrate that thermally activated optical memory can be achieved via the nanostructural reconfiguration of a metallic nanowire metamaterial array made from a shape-memory alloy: A nickel-titanium film of nanoscale thickness structured on the subwavelength scale exhibits bistability of its optical properties upon temperature cycling between 30 °C and 210 °C. The structure, comprising an array of NiTi nanowires coated with a thin film of gold to enhance its plasmonic properties, can exist in two non-volatile states presenting an optical reflectivity differential of 12% via nanoscale mutual displacements of alternating nanowires in the structure. Such all-metal shape-memory photonic gratings and metamaterials may find applications in bistable optical devices. *Published by AIP Publishing*. https://doi.org/10.1063/1.5025400

Structuring of materials on length scales comparable to or smaller than the wavelength of electromagnetic radiation enables the design of metamaterials, photonic crystals and gratings with engineered or enhanced optical properties, including properties that are not available in natural materials.[1,2] Periodically structured surfaces may be referred to as metamaterials or metasurfaces when they interact with radiation that has a wavelength longer than the said period. In respect of shorter wavelengths of radiation, the same structures function as diffractive gratings. Several approaches for tuning, modulating and switching the functionalities of such structured materials have emerged, including (i) mechanical actuation of the internal structure of metamaterials,[3–9] (ii) inclusion of phase-change media (e.g., chalcogenide glasses, vanadium dioxide, gallium)[10–12] or nonlinear materials,[13] and (iii) all-optical "coherent control" of the interaction of ultrathin metamaterials with light.[14] Here, we introduce a reconfigurable photonic nanostructure which exhibits optical memory behaviour underpinned by the shape-memory effect. Shape-memory alloys are binary or ternary metallic alloys that exhibit thermally induced reversible transitions between structural phases with different mechanical properties. Temperature-activated shape-memory effects were first observed in gold-cadmium alloys[15,16] and became widely used with the discovery of nickel-titanium alloys,[17,18] leading to a variety of applications ranging from actuators and valves to stents.[19,20]

To demonstrate thermally activated optical memory with a shape-memory alloy, we developed a device structure, in which an array of nickel-titanium (NiTi) nanowires supported on silicon nitride nano-beams is covered with a gold layer of nanoscale thickness (Fig. 1). The purpose of the plasmonic gold layer is to enhance the resonant optical characteristics of the nanostructure, while the SiN–NiTi bimorph provides for the hysteretic temperature-activated reconfiguration of the nanostructure that leads to non-volatile changes in the composite's optical properties. The NiTi alloy was chosen as the active medium because it retains shape-memory properties on the nanoscale.[21,22] The beams of the

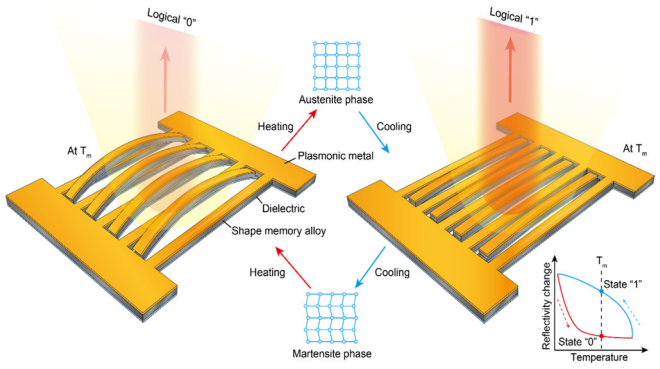

FIG. 1. A shape-memory photonic nanostructure. For a given temperature T_m, the nanostructure has two different stable shapes as shown, depending on the phase of the NiTi alloy component forming the nanostructural framework. Transition between these shapes can be achieved in a temperature cycle within which NiTi transforms between its martensite and austenite phases in a hysteretic fashion. The change in the shape of the nanostructure leads to a change in its plasmonic response and thereby its optical properties, which are dominated by the gold coating on the NiTi framework. (Note that in these artistic sketches, the structural deformation is highly exaggerated and in fact happens at a level comparable to or smaller than the thickness of the nanowires.)

a)Author to whom correspondence should be addressed: jo2c09@orc.soton.ac.uk

array are anchored to the unstructured part of the membrane and every second beam of the array has trenches cut through the gold into the NiTi layer at either end close to the anchor points (see inset to Fig. 2). Temperature variations cause stress in the beams due to differential expansion of the constituent layers. The stress causes a larger deformation of weakly anchored beams (with trench cuts) than strongly anchored beams (without). As the optical properties of the array are sensitive to the mutual positions of the beams, a change in temperature leads to a change in the array's optical properties. The central NiTi shape-memory alloy layer of the structure undergoes a hysteretic transition between martensite and austenite solid phases upon temperature cycling. This leads to a hysteresis in the thermal expansion that drives beam deformation, in turn, giving rise to hysteretic changes in the optical properties of the array.

The shape-memory nanowire array was manufactured on a silicon nitride (SiN) membrane by sputtering of the NiTi alloy, thermal evaporation of gold and subsequent nanostructural patterning by focused ion beam milling. 175 nm of NiTi (42% Ni, 58% Ti) was deposited on a commercially sourced SiN membrane of 50 nm thickness by radio-frequency sputtering (Kurt J. Lesker Nano 38) from 99.999% purity NiTi and Ni targets (Testbourne), providing for accurate control over the deposited film's composition.[22–24] A base pressure of 4.0×10^{-5} mbar was achieved before deposition. A flow rate of 10 cubic centimetres per minute (SCCM) of high purity argon was used to strike the plasma on both targets. The substrate was held on a rotating platen with a target-substrate distance of approximately 150 mm, which ensures the deposition of low stress films. A working pressure of 2×10^{-3} mbar was achieved during deposition. The sputtering rate was fixed at 3.50 nm/min. The deposited film was subsequently annealed (Jipelec rapid thermal annealer) at 400 °C for 30 min in argon at atmospheric pressure[24,25] with heating and cooling rates of 50 °C/min and 1 °C/min, respectively (the annealing chamber having first been purged with Ar for 2.5 h to remove air). The final composition of the shape-memory alloy film was determined, by energy-dispersive X-ray spectroscopy, to be 42% Ni and 58% Ti. The 50-nm-thick gold layer was deposited on top of the shape-memory alloy by resistance evaporation (Edwards Auto 306) with a base chamber pressure of 2.0×10^{-6} mbar at a deposition rate of 0.05 nm/s. The nanowire pattern was manufactured by focused ion beam milling (FEI Helios NanoLab 600), cutting through the layers to produce an array of 400-nm-wide freestanding suspended beams separated by 100-nm-wide gaps (Fig. 2). In order to avoid over-milling the gold layer, the nanowires were first milled from the SiN membrane side. Then, the sample was turned over and the trenches were milled from the gold side, to a depth of 150 nm, at both ends of every other beam, as shown in the inset to Fig. 2.

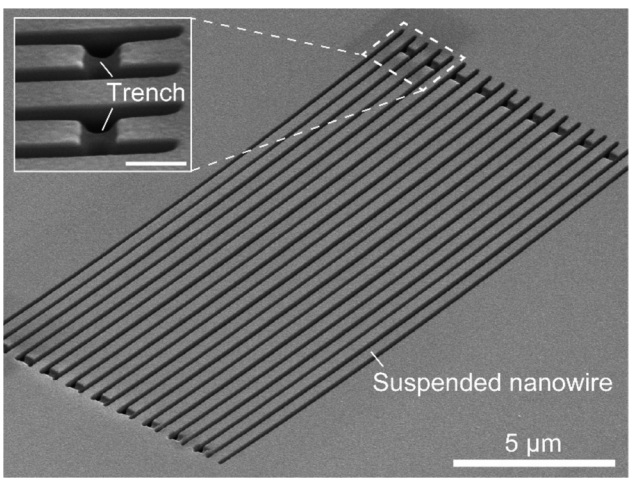

FIG. 2. A shape-memory photonic nanowire metamaterial array. Scanning electron microscopy image of the nanostructure fabricated on a Au-NiTi-SiN nano-membrane. The inset shows the trenches fabricated at the ends of every other beam (scale bar = 500 nm).

In order to confirm the reversible martensite-austenite transitional behavior of NiTi,[21] the temperature dependence of resistance of a 175-nm-thick NiTi control sample deposited on a SiO_2 substrate was measured. A 4-probe measurement (Keithley 2636B Sourcemeter) was performed under vacuum at a pressure of 4.0×10^{-6} mbar to prevent sample oxidation. The probes were fixed to the sample with conductive adhesive to prevent separation during temperature cycling, which may otherwise occur due to differential thermal expansion of the sample substrate and probes. Upon temperature cycling between ~30 °C and 220 °C, the resistance shows a clear hysteresis loop, which is a characteristic feature of the martensite-to-austenite phase transition for this alloy (Fig. 3). This behaviour is maintained through repeated temperature cycling (tested here up to 7 heating-cooling cycles).

To demonstrate the hysteretic behaviour of the shape memory plasmonic nanostructure's optical properties, reflection spectra were recorded at various points in the heating/cooling temperature cycle using a microspectrophotometer (CRAIC QDI2010) with a 15× objective (numerical aperture 0.28). The nanowire structure was illuminated with light linearly polarized perpendicular to the nanowires. Spectra were recorded with an aperture size of 5 μm × 5 μm (i.e., smaller than the 25 μm × 9.5 μm size of the array).

In the absence of deformation, the structure is a metamaterial for wavelengths longer than 500 nm. However, as the differential displacement of every second nanowire doubles the period to 1000 nm, the structure becomes diffracting over

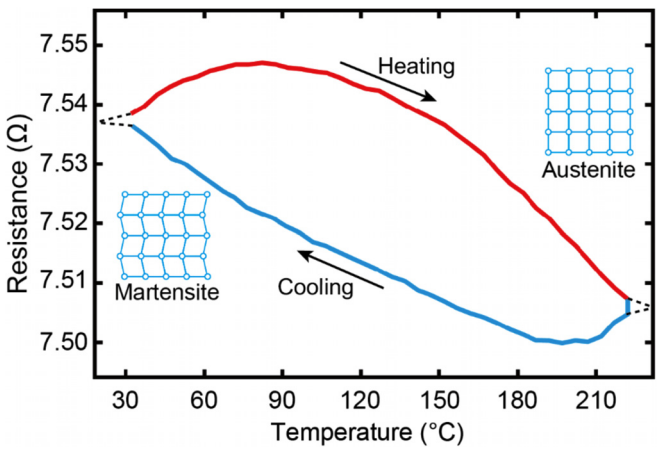

FIG. 3. Hysteretic dependence of resistance on temperature for a 175-nm-thick NiTi film on a fused silica (SiO_2) substrate.

the experimental wavelength range (500 nm–870 nm). In reflective measurements, both illumination of the sample and collection of reflected light occur through an objective with a numerical aperture of 0.28—giving a maximum angle of incidence for illumination and detection of light equal to 16°. As such, the microspectrophotometer does not detect diffracted light from a grating of 1000 nm period at wavelengths greater than 560 nm.

The reflectivity spectrum of the nanostructure shows a local maximum at ∼500 nm [Fig. 4(a) inset] corresponding to the lattice mode associated with the nanowire spacing. The increase in reflectivity towards the long wavelength end (870 nm) of the measurable spectral range suggests the presence of another reflectivity maximum at longer wavelengths, which may be the lattice mode associated with the 1000 nm spacing of identical nanowires.

To measure the temperature dependence of the nanostructure's reflection properties, it was mounted on a thermostatic sample stage. The stage temperature was varied from 30 to 210 °C in 20 °C steps, allowing 5 min for the system to reach thermal equilibrium at each temperature. The optical properties of the shape-memory nanowire array are found to be strongly temperature-dependent and hysteretic, which is to say that the nanostructure presents different reflection spectra depending on whether it has been heated or cooled to a given temperature.

Figure 4(a) shows the differential reflectivity spectra of the nanowire array after heating (red) and cooling (blue) to a temperature of 110 °C, relative to the reflectivity at a reference temperature of 210 °C. Figure 4(b) shows the hysteretic temperature-dependence of reflection at a given wavelength (835 nm). The shape-memory nanowire structure is up to 12% more reflective after cooling to a stage temperature of 110 °C (a state that may be denoted logical "1") as compared to having been heated to the same temperature (logical "0"). Starting at room temperature, the decrease in reflectivity with increasing temperature is consistent with increasing deformation of the nanostructure causing more light to be diffracted. This trend is reversed as the sample is heated above 110 °C, implying a gradual phase transition in the NiTi layer. As the nanostructure is cooled, its reflectivity at 835 nm is higher (implying reduced diffraction due to reduced nanowire deformation) than at the same temperature during the heating process, until the reflectivity returns to its original value close to room temperature, indicating that the nanowires have returned to their original state.

We conclude that the observed temperature hysteresis (memory) of optical properties is related to the martensite-austenite cycle in NiTi, which results in the existence of two different stable shapes for the nanostructure. Indeed, finite element analysis (COMSOL Multiphysics) indicates that the midpoint of a nanowire with trenches on either end is displaced out of plane by 105 nm at 110 °C when NiTi is in the martensite phase and by 70 nm at the same temperature in the austenite phase [Fig. 4(c)], while the displacement of nanowires without trenches is negligible (<5 nm) for both NiTi phases. The simulations assume flat nanowires at room temperature, with nanowire ends at a fixed position and a fixed orientation, and martensite and austenite phases with thermal expansion coefficients of 7×10^{-6} and $11 \times 10^{-6} K^{-1}$ (Ref. 26), Young's moduli of 28 and 83 GPa, and Poisson's ratio of 0.33 (Ref. 22). As illustrated schematically in Fig. 1, the change in the shape of the nanostructure leads to a change in its plasmonic response and thus in its optical properties, which are dominated by the gold coating on the NiTi framework. An additional contribution

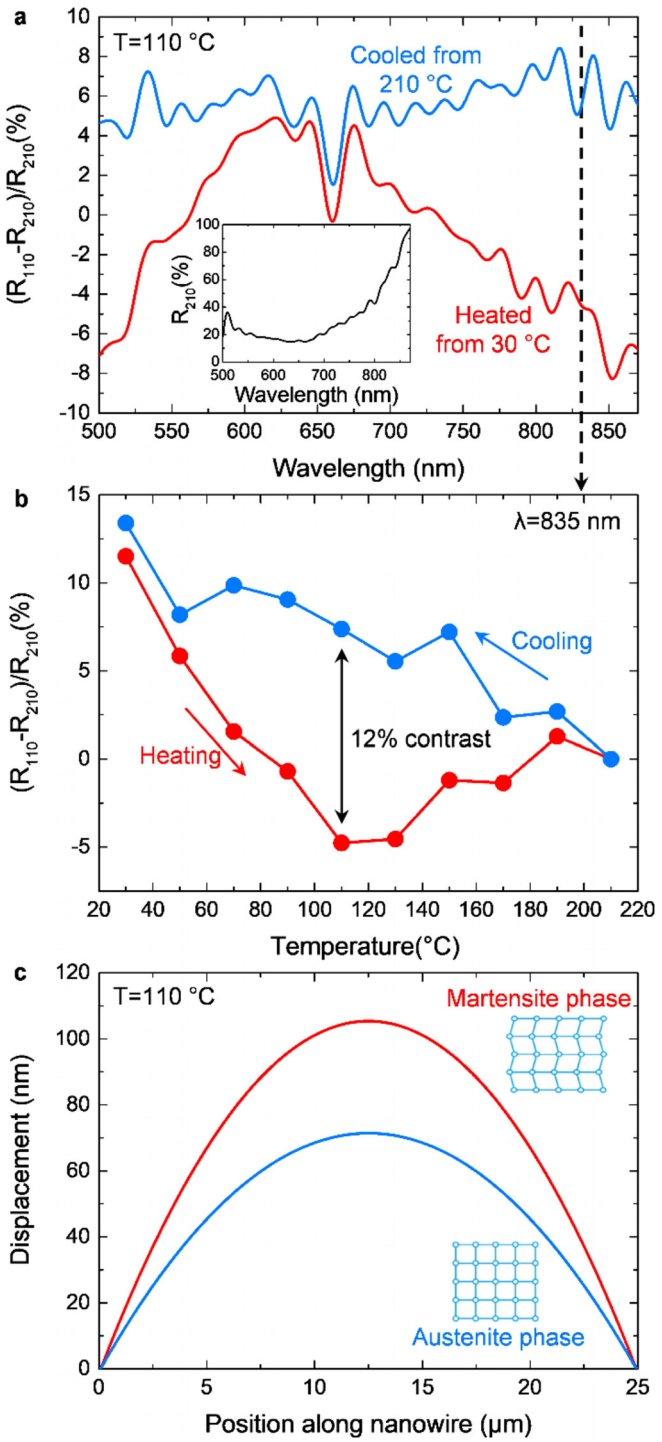

FIG. 4. Deformation-dependent optical properties of the shape-memory nanowire array. (a) Spectral dispersion of the difference between reflectivities of the nanostructure measured at 110 °C and 210 °C, relative to the reflectivity at 210 °C. Blue and red curves correspond to the cooling and heating parts of the hysteresis cycle, respectively. The inset shows the reference reflectivity spectrum at 210 °C. (b) Difference between the sample reflectivity at temperatures T and 210 °C relative to the reflectivity level at 210 °C at a wavelength of 835 nm. (c) Simulated out-of-plane deformation profile of a nanowire with trench cuts at each end for NiTi in the martensite (red) and austenite (blue) states at a temperature of 110 °C.

to the change in the nanostructure's optical response may come from a temperature-dependent change in the optical properties of NiTi.

The shape-memory nanowire array reported here demonstrates how non-volatile memory characteristics can be achieved in reconfigurable metamaterial nanostructures based on bimaterial bridge actuators.[6–9] More generally, shape-memory materials provide a broad range of opportunities for active/adaptive plasmonic devices, metamaterials, gratings and photonic crystals: For example, shape-memory materials could be used to add hysteretic switching and memory functionalities to thermally actuated metamaterials,[6,8,27,28] which are typically deformed only by differential thermal expansion of different materials rather than phase transitions. Two-way shape-memory alloys[19] could enable pronounced thermal switching of photonic structures between two distinct states, even without relying on differential thermal expansion. This could allow the realization of thermally switchable, bistable magnetic metamaterials based on three-dimensional split ring resonators.[27–29] Shape-memory polymers, offering reversible strains of up to 800%[30] and multi-shape memory,[31] could act as elastic shape-memory substrates for gratings, photonic crystals and metamaterials reconfigured by stretching.[5] Furthermore, shape-memory polymers, loaded with nanoparticles to achieve a high refractive index, could even serve as nanoimprint substrates, where imprint in regimes of elastic and plastic deformation[32] could be exploited to create temporary and permanent bas-relief metamaterials and gratings,[33] allowing thermal recovery of the latter.

Our proof-of-principle demonstration highlights the opportunity that shape-memory materials provide for reconfigurable photonic nanostructures. The engineering of optimized devices will require systematic studies to achieve an optimal performance of alloy and nanostructures and investigations of device behaviour over a large number of temperature cycles.

In summary, we demonstrate a shape-memory-alloy-based nanomechanical reconfigurable grating. By introducing a phase-change material into a mechanically reconfigurable nanowire array, we realize a mechanically reconfigurable photonic nanostructure with rewritable memory functionality. We believe that shape-memory photonic nanostructures and metamaterials can enable a variety of advanced optical functionalities: In principle, they can be programmed by permanent deformation into complex shapes, tuned by reversible actuation under the influence of thermal, electrical, magnetic or optical control signals, and reset with heat.

The authors are grateful to João Valente for fruitful discussions. This work was supported by Asahi Kasei, the UK's Engineering and Physical Sciences Research Council (Grant Nos. EP/M009122/1 and EP/N00762X/1), the UK's Defence Science and Technology Laboratory (Grant No. DSTLX1000064081), and the Ministry of Education Singapore (Grant No. MOE2016-T3-1-006). Y.N. was supported by Research Fellowships of the Japan Society for the Promotion of Science (JSPS) for Young Scientists and the Interactive Materials Science Cadet Program of Osaka University and by the JSPS Core-to-Core Program, A. Advanced Research Networks. Following a period of embargo, the data from this paper can be obtained from the University of Southampton ePrints research repository: https://doi.org/10.5258/SOTON/D0557.

[1]N. I. Zheludev, Science **348**, 973–974 (2015).
[2]A. F. Koenderink, A. Alù, and A. Polman, Science **348**, 516–521 (2015).
[3]M. Lapine, D. Powell, M. Gorkunov, I. Shadrivov, R. Marqués, and Y. Kivshar, Appl. Phys. Lett. **95**, 084105 (2009).
[4]H. Tao, A. C. Strikwerda, K. Fan, W. J. Padilla, X. Zhang, and R. D. Averitt, Phys. Rev. Lett. **103**, 147401 (2009).
[5]I. M. Pryce, K. Aydin, Y. A. Kelaita, R. M. Briggs, and H. A. Atwater, Nano Lett. **10**, 4222–4227 (2010).
[6]J. Y. Ou, E. Plum, L. Jiang, and N. I. Zheludev, Nano Lett. **11**, 2142–2144 (2011).
[7]J.-Y. Ou, E. Plum, J. Zhang, and N. I. Zheludev, Nat. Nanotechnol. **8**, 252–255 (2013).
[8]J. Valente, J.-Y. Ou, E. Plum, I. J. Youngs, and N. I. Zheludev, Appl. Phys. Lett. **106**, 111905 (2015).
[9]N. I. Zheludev and E. Plum, Nat. Nanotechnol. **11**, 16–22 (2016).
[10]T. Driscoll, H.-T. Kim, B.-G. Chae, B.-J. Kim, Y.-W. Lee, N. M. Jokerst, S. Palit, D. R. Smith, M. D. Ventra, and D. N. Basov, Science **325**, 1518–1521 (2009).
[11]B. Gholipour, J. Zhang, K. F. MacDonald, D. W. Hewak, and N. I. Zheludev, Adv. Mater. **25**, 3050–3054 (2013).
[12]R. F. Waters, P. A. Hobson, K. F. MacDonald, and N. I. Zheludev, Appl. Phys. Lett. **107**, 081102 (2015).
[13]M. Lapine, I. V. Shadrivov, and Y. S. Kivshar, Rev. Mod. Phys. **86**, 1093–1123 (2014).
[14]J. Zhang, K. F. MacDonald, and N. I. Zheludev, Light Sci. Appl. **1**, e18 (2012).
[15]G. V. Kurdyumov and L. G. Khandros, Dokl. Akad. Nauk SSSR **66**, 211–214 (1949).
[16]L. C. Chang and T. A. Read, Trans. AIME **189**, 47–52 (1951).
[17]W. J. Buehler, J. V. Gilfrich, and R. C. Wiley, J. Appl. Phys. **34**, 1475–1477 (1963).
[18]K. Otsuka and X. Ren, Prog. Mater. Sci. **50**, 511–678 (2005).
[19]K. Otsuka and C. M. Wayman, *Shape Memory Materials* (Cambridge University Press, 1999).
[20]J. M. Jani, M. Leary, A. Subic, and M. A. Gibson, Mater. Des. **56**, 1078–1113 (2014).
[21]*Thin Film Shape Memory Alloys: Fundamentals and Device Applications*, edited by S. Miyazaki, Y. Q. Fu, and W. M. Huang (Cambridge University Press, 2009).
[22]Y. Q. Fu, S. Zhang, M. J. Wu, W. M. Huang, H. J. Du, J. K. Luo, A. J. Flewitt, and W. I. Milne, Thin Solid Films **515**, 80–86 (2006).
[23]A. Ishida, A. Takei, and S. Miyazaki, Thin Solid Films **228**, 210–214 (1993).
[24]P. Surbled, C. Clerc, B. L. Pioufle, M. Ataka, and H. Fujita, Thin Solid Films **401**, 52–59 (2001).
[25]J.-L. Seguin, M. Bendahan, A. Isalgue, V. Esteve-Cano, H. Carchano, and V. Torra, Sens. Actuators A **74**, 65–69 (1999).
[26]J. Uchil, K. P. Mohanchandra, K. G. Kumara, K. K. Mahesh, and T. P. Murali, Physica B **270**, 289–297 (1999).
[27]C. C. Chen, C. T. Hsiao, S. Sun, K.-Y. Yang, P. C. Wu, W. T. Chen, Y. H. Tang, Y.-F. Chau, E. Plum, G.-Y. Guo, N. I. Zheludev, and D. P. Tsai, Opt. Exp. **20**, 9415–9420 (2012).
[28]Y. Mao, Y. Pan, W. Zhang, R. Zhu, J. Xu, and W. Wu, Nano Lett. **16**, 7025–7029 (2016).
[29]C.-C. Chen, A. Ishikawa, Y.-H. Tang, M.-H. Shiao, D. P. Tsai, and T. Tanaka, Adv. Opt. Mater. **3**, 44–48 (2015).
[30]W. Voit, T. Ware, R. R. Dasari, P. Smith, L. Danz, D. Simon, S. Barlow, S. R. Marder, and K. Gall, Adv. Funct. Mater. **20**, 162–172 (2010).
[31]T. Pretsch, Smart Mater. Struct. **19**, 015006 (2010).
[32]Q. Zhao, W. Zou, Y. Luo, and T. Xie, Sci. Adv. **2**, e1501297 (2016).
[33]J. Zhang, J.-Y. Ou, K. F. MacDonald, and N. I. Zheludev, J. Opt. **14**, 114002 (2012).

ADVANCED SCIENCE Open Access
www.advancedscience.com

Mechanochromic Reconfigurable Metasurfaces

Artemios Karvounis, Nikolaos Aspiotis, Ioannis Zeimpekis, Jun-Yu Ou, Chung-Che Huang, Daniel Hewak, and Nikolay I. Zheludev*

The change of optical properties that some usually natural compounds or polymeric materials show upon the application of external stress is named mechanochromism. Herein, an artificial nanomechanical metasurface formed by a subwavelength nanowire array made of molybdenum disulfide, molybdenum oxide, and silicon nitride changes color upon mechanical deformation. The aforementioned deformation induces reversible changes in the optical transmission (relative transmission change of 197% at 654 nm), thus demonstrating a giant mechanochromic effect. Moreover, these types of metasurfaces can exist in two nonvolatile states presenting a difference in optical transmission of 45% at 678 nm, when they are forced to bend rapidly. The wide optical tunability that photonic nanomechanical metasurfaces, such as the one presented here, possess by design, can provide a valuable platform for mechanochromic and bistable responses across the visible and near infrared regime and form a new family of smart materials with applications in reconfigurable, multifunctional photonic filters, switches, and stress sensors.

Up to date, control of electromagnetic properties of photonic metamaterials and/or metasurfaces, artificial media structured on the subwavelength scale, have been achieved via nanomechanical reconfiguration of its building blocks,[1–3] structural phase change in the material of constituting elements,[4–7] carrier injection effects,[8–11] application of liquid crystals,[12,13] chemical modification,[14] and by stretching the elastic substrate supporting plasmonic or dielectric metamolecules.[15,16]

Mechanochromism is the color change, upon mechanically induced reorganization of crystal structure or mechanically induced structural phase transition.[17] Such effects have been studied in a number of materials,[17,18] where strongest effects are seen in polymers,[19] liquid crystal elastomers,[20–22] nanofibers,[23] and photonic crystals.[24] Recently, chromic effects have been used as tuning mechanisms for photonic metasurfaces and plasmonics related devices with thermochromic and electrochromic responses, respectively.[25,26]

In recent years, strain engineering of optical and mechanical properties of solids, in particular silicon and 2D solids have attracted considerable attention.[27–33] 2D materials, such as graphene, oxides, nitrides, and transition metal dichalcogenides are of particular interest as constitutive elements for reconfigurable metamaterials and metasurfaces, as the extreme electron confinement inherits them with unique dielectric properties that can be controlled by external stimuli.[32,34]

In particular, molybdenum disulfide, MoS_2 is formed from the covalent bond between transition metal atoms (Mo) sandwiched by two layers of chalcogen atoms (sulfur), while every sheet is bound via weak van der Waals interaction. Several theoretical reports have indicated that the energy bandgap renormalization can occur on MoS_2 upon stress, where microscopic parameters like carrier mobility and effective mass of carriers upon mechanical deformation can lead to substantial changes on refractive index. Furthermore, excitonic peak emission wavelengths have been observed to be sensitive to mechanical stress in its monolayer form.[35–40] MoS_2 has excellent mechanical properties because its large Young modulus (330 GPa) and high elastic limit which makes it an attractive material for nanomechanical and mechanochromic devices.[41]

In this paper, we introduce a previously unexplored mechanism of tuning the optical properties of photonic metasurfaces that exploits the phenomenon of mechanochromism. We show that elastic strain in a $MoS_2/MoO_{3-x}/Si_3N_4$ nanomechanical photonic metasurface causes a profound change in its optical properties, which originates from the strain-sensitive refractive index of MoS_2, enhanced by electromagnetic resonances created by nanostructuring. Specifically, heat activated nanomechanical deformation of the array of nanowires lead to profound reversible changes of its transmission, reflection

Dr. A. Karvounis, N. Aspiotis, Dr. I. Zeimpekis, Dr. J.-Y. Ou, Dr. C.-C. Huang, Prof. D. Hewak, Prof. N. I. Zheludev
Optoelectronics Research Centre
University of Southampton
Southampton SO17 1BJ, UK
E-mail: karvounis@phys.ethz.ch
Dr. A. Karvounis
Optical Nanomaterial Group
Institute for Quantum Electronics
ETH Zurich
8093 Zurich, Switzerland
Prof. N. I. Zheludev
Centre for Disruptive Photonic Technologies & The Photonics Institute
School of Physical and Mathematical Sciences
Nanyang Technological University
Singapore 637371, Singapore
The ORCID identification number(s) for the author(s) of this article can be found under https://doi.org/10.1002/advs.201900974.

DOI: 10.1002/advs.201900974

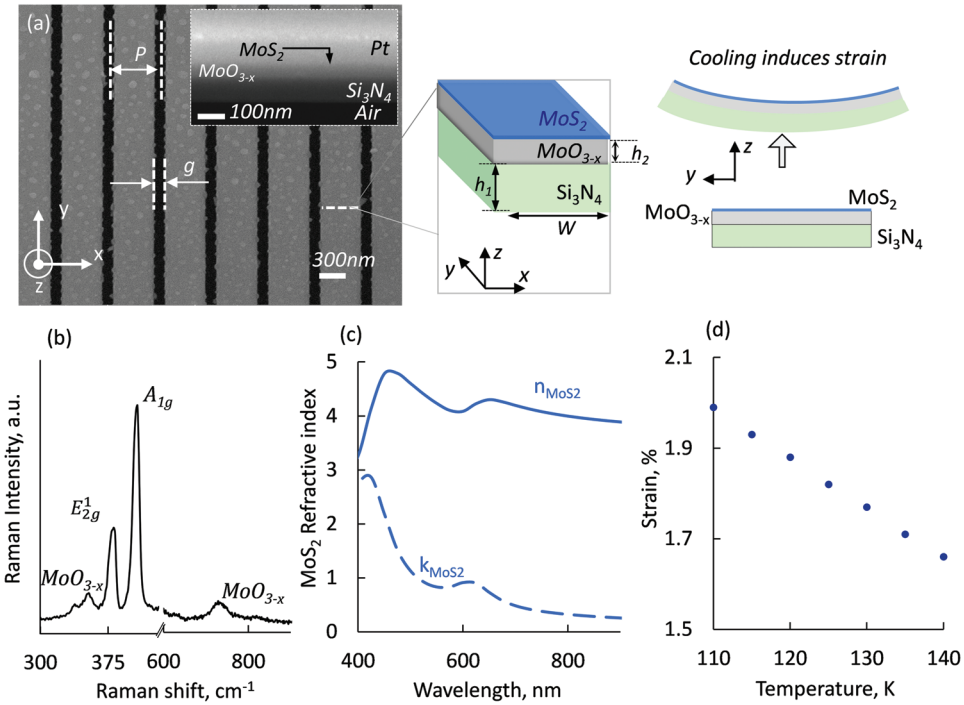

Figure 1. Mechanochromic metasurface. a) Scanning electron microscope image of the metamaterial formed by a nanowire array manufactured on a $MoS_2/MoO_{3-x}/Si_3N_4$ trilayer free-standing membrane, schematic of a single nanowire [$P = 500$, $g = 100$, $h_1 = 90$, $h_2 = 50$, $h_3 = 5$, $W = 400$ nm], scale bar 300 nm. Inset: cross section of the trilayer sample, coated with platinum to improve contrast. b) Raman spectra of metamaterial shows the composition of the sample; c) ellipsometric data of a few layer MoS_2 film; d) strain induced in a single nanowire upon cooling, deformation of the nanowire is caused by the large thermal expansion mismatch between Si_3N_4 and MoO_{3-x}.

and absorption in the visible part of the spectrum operating either as a photonic filter or as a mechanically bistable element. Transmission changes up to 197% are obtained at 654 nm upon 2% of mechanical strain, while two nonvolatile states presenting a difference in optical transmission of 45% achieved at 675 nm. The response of the system is controlled via the speed of induced mechanical stress. This type of devices can serve not only as photonic elements but also as strain sensors with an optical readout. Recently, more trilayer metasurfaces have been reported.[42]

The metasurface was fabricated on a 90 nm thick Si_3N_4 membrane which was patterned as an array of nanowires 22 µm long, 400 nm wide with gaps of 100 nm separating them (see **Figure 1**). The prepatterned Si_3N_4 membrane, was coated with a 60 nm thick layer of MoO_{3-x} and a 5 nm layer of MoS_2 by atmospheric pressure chemical vapor deposition (APCVD). Figure 1a shows a top view of the metasurface, while the insets present a cross-section of the trilayer film. The white dots seen on the scanning electron microscopy (SEM) are caused by the film growth and device fabrication process; The short term roughness of the film is in the order of 1 MoS_2 layer whereas the suspected contamination adds a waviness in the order of 3 nm (rms), verified by atomic force microscopic (AFM) measurements. The period of the contamination is in the order of 2–4 µm so this is beyond our wavelength of interest. The height of the individual contaminants is a maximum of 13 nm so with the refractive indices of our materials this translates to less than 1/10 of the wavelength of interest so it can be considered optically flat. More details related with transmission electron microscopy (TEM) and X-ray power diffraction (XRD) analysis of MoS_2 films grown via APCVD method can be found in our previous publication,[43] while the growth methods of the films are included in the Experimental Section. The composition of the sample has been evaluated using reflective Raman spectroscopy. Figure 1b shows the Raman spectrum of the nanowire indicating its crystallinity: the 381 cm^{-1} line relates to the in-plane vibration mode, while the 407.5 cm^{-1} line corresponds to the out-of-plane vibration A_{1g} mode of MoS_2.[44] The 353 and 733 cm^{-1} lines indicate the presence of MoO_{3-x} in the structure.[45] Furthermore, we measured the complex refractive index of MoS_2 layer of the composite nanomembrane by spectral ellipsometry (Figure 1c). The refractive index of our films is similar to previous literature,[46] demonstrating MoS_2 as a high index dielectric material. These results were used to computationally model the optical properties of the nanowire array, as presented in **Figure 2**b.

Measured and computed optical properties of the metamaterial are presented in Figure 2. At optical wavelengths longer than the structure period of 500 nm the nanowire array does not scatter light and acts as an optically homogeneous metamaterial layer, that can be fully characterized in terms of its transmission, reflection and absorption. However, the periodic structuring, results in reflection and transmission resonances at 654 and 810 nm for linearly polarized light parallel to the wires, with a quality factor of $Q \approx 25$. The experimental spectra are well reproduced in computational modelling, as shown in Figure 2b. The field maps in Figure 2c,d reveal that on resonance, displacement currents running through the nanowires

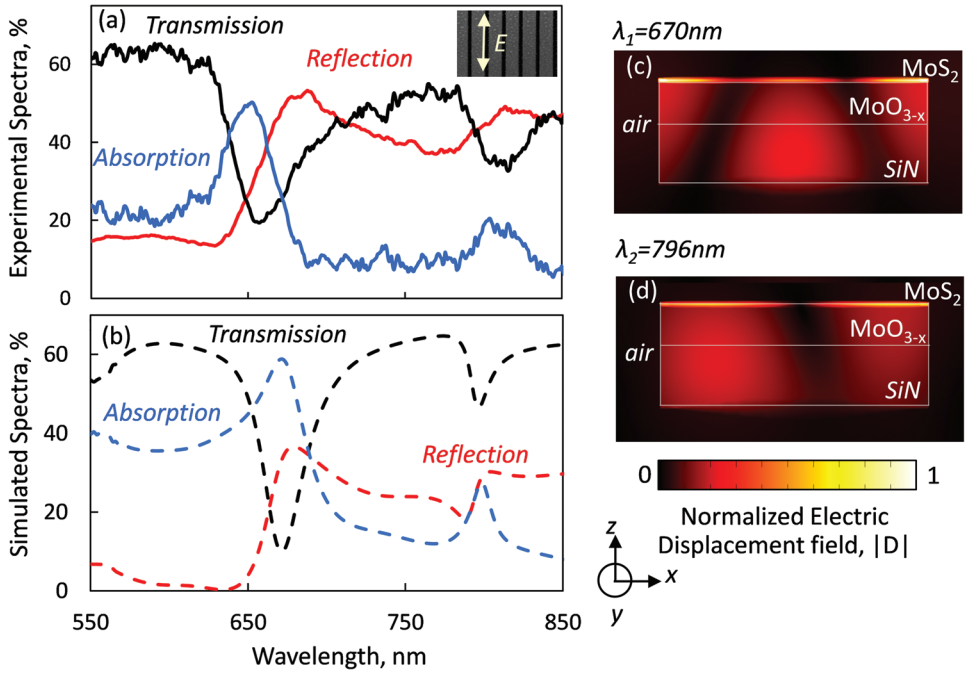

Figure 2. Optical properties of mechanochromic metasurface. a) Reflection, transmission, and absorption spectra of mechanochromic metamaterial under linear polarized illumination, as indicated on inset to plate. b) Numerically simulated reflection, transmission, and absorption spectra of the metamaterial. c,d) Numerically simulated distribution of the electromagnetic field in the metamaterial nanowire. Color maps show the magnitude of the electric displacement field in the *x*–*z* plane.

with a higher concentration within the high index MoS_2 part, interfere constructively with incident light and block transmission over this wavelength, as studied in the past.[6,47,48] Small discrepancies between measured and computed spectra can be attributed to fabrication tolerances and accuracy of the refractive index values used in the modeling.

Optical properties of such metasurfaces are expected to be strongly dependent on temperature, given the stress-induced modifications of the band structure of MoS_2 component. Indeed, heat activated nanoscale reconfiguration of the metamaterial induces nanomechanical deformation of the wires. Since the MoS_2 is much thinner than Si_3N_4 and MoO_{3-x} layers, the thermal expansion mismatch between the Si_3N_4 and MoO_{3-x} is the main mechanism of the bow-like deformation of the nanowires upon cooling/heating (the thermal expansion coefficients are 2×10^{-6} and 6×10^{-5} K^{-1},[49] respectively). This deformation in its own turn leads to the stress-induced modification of the optical properties of the MoS_2 layer. Stress-induced change of optical properties of the wide band gap materials Si_3N_4 (E_g = 4.5 eV)[50] and MoO_{3-x} (E_g = 3.1 eV)[51] is insignificant in the part of the spectrum of interest.

Our finite element method (FEM) mechanical stress calculations—based on the linear momentum balance equation and the linear stress–strain relation—are displayed in Figure 1d, employing a single nanowire. Strain ε is the ratio of the deflection of the MoS_2 layer from the neutral plane, γ over the radius of curvature, R, $\varepsilon = \gamma/R$. They show that the decrease of the temperature on a nanowire array from 300 to 110 K results in a bow-like deformation of 50 nm that induces a compressive stress of 2.05% to the MoS_2 layer. This is a finite element method simulation, as a result stress levels may differ upon grown methods of the films and nanostructuring techniques.

Since thermal cooling of the metasurface induces mechanical strain upon the MoS_2 layer, the transmission spectra were measured at different temperatures using a microspectrophotometer, to test its mechanochromic response. We first studied the induced changes in optical transmission as a function of applied strain. **Figure 3** presents the optical transmission of the mechanochromic metasurface for various strain levels, at the cooling rate of 5 K min^{-1}. We define the relative transmission change $\Delta T/T_0$, where $\Delta T = T_\varepsilon - T_0$; T_ε being the absolute transmission at an applied strain ε and T_0 the transmission for zero strain. For small strain levels—below 1%—the transmission change is small, however larger strain upon MoS_2 induces change in Transmission spectra of the sample. At 2% strain the induced change reaches maximum values of 197% and 80% at 657 and 810 nm, accompanied with the sample's color change, inset Figure 3a. Since, some semiconductors show a variation of their bandgap with temperature, we test if the response in color change is related with the amount of stress applied on the metasurface, or due to temperature. Figure 3b shows the relative transmission difference of the metasurface, for several levels of stress reaching up to 200%, while the trilayer films, where no elastic strain exist, provide transmission changes of the level of 2% between room temperature and 110 K as shown in the inset of Figure 3. Furthermore, no change of the lineshape is recorded, since the relative change is flat. In this work, we did not study the limits of elastic deformation and therefore we did not exceed the 2% applied strain level in pursuit of higher transmission change to avoid irreversible nanomechanical deformations. This performance is already exceptionally

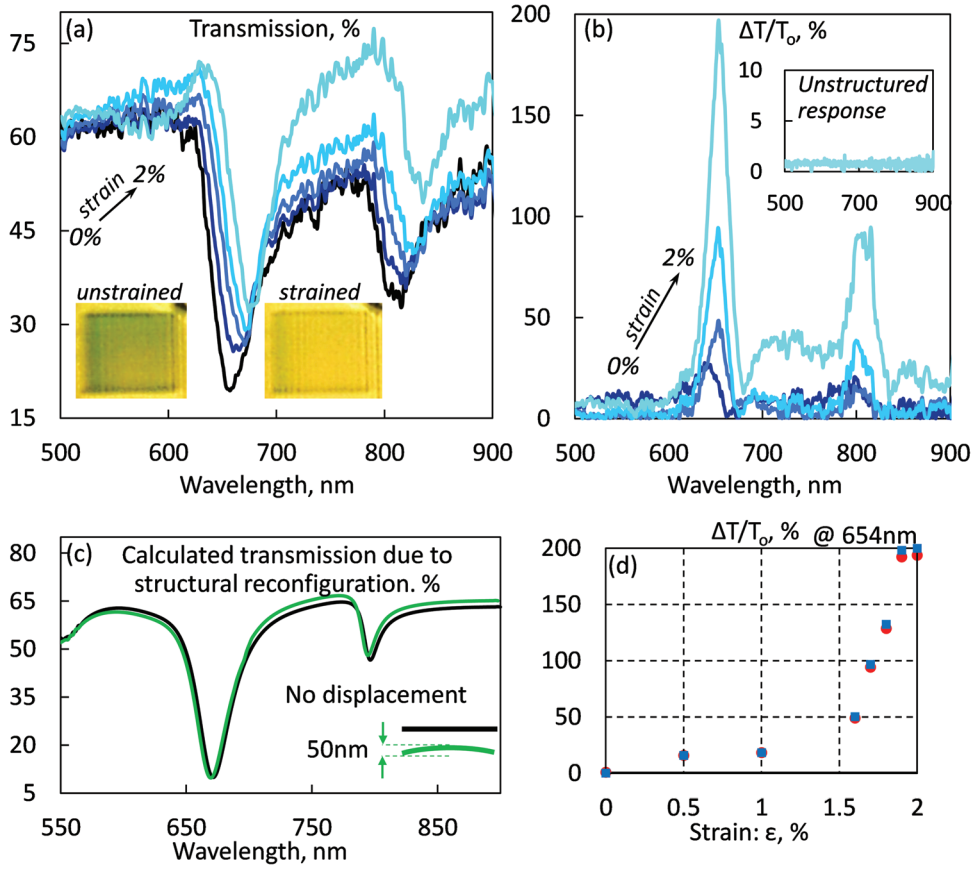

Figure 3. Mechanochromic reconfigurable metasurface. Variation of the optical properties of MoS_2 metamaterial under stress caused by slow cooling [5 K min^{-1}]. a) Spectral dispersion of transmission of the metamaterial for different levels of strain up to maximum strain of 2%. Insets shows the perceived colors of metamaterial sample for zero and 2% strain. b) Relative transmission change for different strain levels. Inset: transmission change of the reference trilayer film. c) Calculated transmission of no displacement, black, and 50 nm displacement of the central part of the sample, green, assuming only structural reconfiguration and no stress dependent refractive index of the nanostructure. d) Reversibility of induced mechanochromic effect—at 654 nm—for the full strain cycle, strain up-red circular markers, strain down-cyan rectangular markers.

high as the metasurface's transmission minimum shifts from $\lambda_o = 657$ nm to $\lambda_1 = 681$ nm—providing giant mechanochromic sensitivity, which is defined by the ratio of the wavelength shift over the applied strain $\Delta\lambda/\varepsilon$ [nm%$^{-1}$] and is found to be as high as 12, one order of magnitude larger than other polymeric mechanochromic systems.[24] More interestingly, our device outperforms recent reports on polymer based mechanochromic devices.[21] The mechanochromic metasurface demonstrates transmission difference of 200% under 2% strain at 645 nm wavelength. In contrast, in ref. [21] on Figure 1h it is recorded 77% transmission difference under 50% strain at the wavelength of 600 nm, thus our work outperforms on the transmission contrast achieved. At this and slower cooling rates the change in transmission do not show any hysteretic response.

Upon a faster cooling rate, 15 K min^{-1}, a hysteretic behavior of metamaterial's transmission is observed. **Figure 4**a presents a selection of spectra for different strain levels. For increasing strain, the metasurface demonstrates a red-shift of its spectrum similar to Figure 3. However, on the level of 1.9% strain the second dip of transmission mode is recorded, as transmission jumps from 31% to 41% for the wavelength of 680 nm, see Figure 4b. In Figure 4b we show the full strain cycle over transmission at the wavelength of 680 nm. Upon decreasing strain—blue line—the optical spectra are different from those of the same strain level for increasing strain—red line. At the level of 1% strain the hysteretic loop closes. Furthermore, we define the differential hysteresis: $\Delta h = \mathrm{Abs}[\mathrm{Tr}_{up}(\lambda) - \mathrm{Tr}_{down}(\lambda)]/\mathrm{Tr}_{up}(\lambda)$ as the relative transmission difference between the two nonvolatile states for increasing–decreasing strain, with the largest value recorded at the wavelength of 678 nm equal to 47%. This response is mainly driven by the mechanical buckling of the metasurface;[52,53] an effect accompanying flexible parts when subject to large applied mechanical load and therefore demonstrate mechanical bistability.

The experimentally observed red-shift of the optical response of the metamaterial spectrum depending on temperature can be satisfactorily explained in terms of mechanocromism. The red-shift of the spectrum is related to the mechanochromic nature of device rather than the structural reconfiguration of the sample. We have designed the metamaterial to keep its optical response invariant upon deflection of the nanowires. Upon cooling, nanowires bend in the same fashion, as a result, the metamaterial's response is expected to provide negligible transmission changes for small deformations between neighboring nanowires, since most parameters remain the same such as the

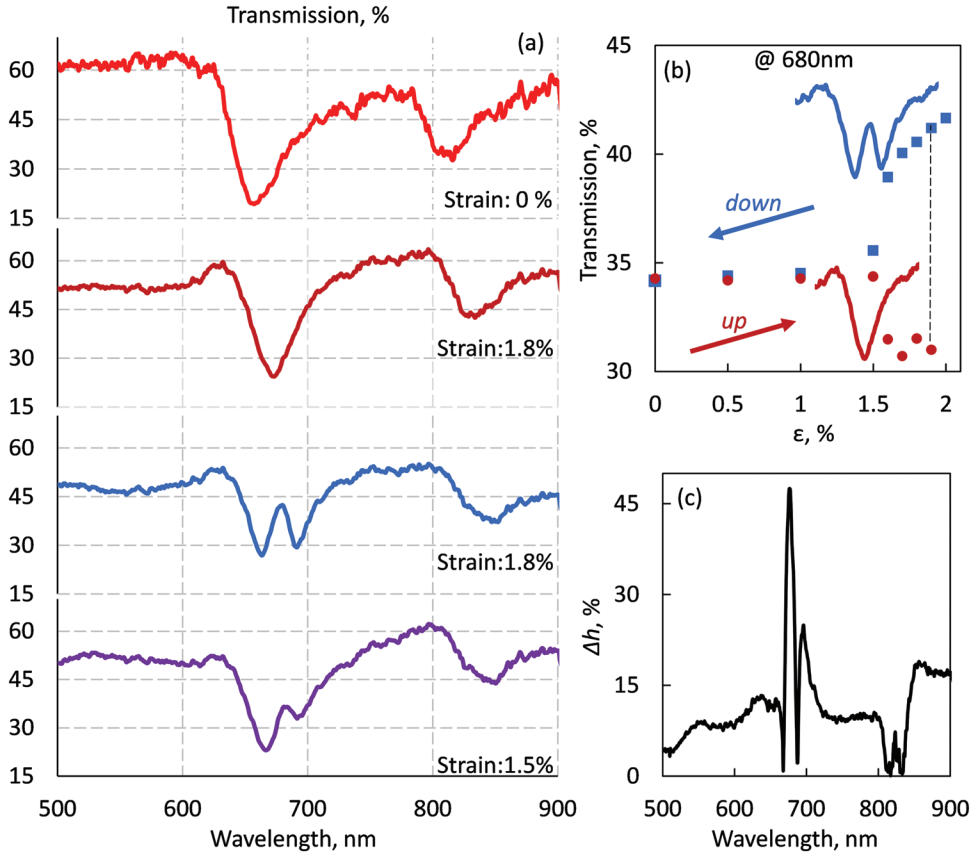

Figure 4. Hysterisis of mechanochromic metasurface. a) Transmission spectra for different strain levels in the regime of rapid cooling [15 K min^{-1}]. b) Variation of the metamaterial transmission at 680 nm during the full strain cycle. A hysteresis of optical properties is observed at strain levels exceeding 1.5%. c) Span of the hysteresis loop. Differential hysteresis: $\Delta h = |Tr_{up}(\lambda) - Tr_{down}(\lambda)|/Tr_{up}(\lambda)$ as a function of wavelength at strain level of 1.8%.

distance between the nanowires and the period of the metasurface. This is in contrast to previous works that present substantial changes in the optical properties due to the doubling of metamaterial's period or by controlling the gap between the nanowires.[1,54,55] Our mechanical FEM calculations (COMSOL) indicate that the midpoint of each nanowire is displaced out-of-plane by ≈50 nm when strain is at 2% and temperature at 110 K. For this deflection, the optical FEM modeling indicates that solely the 50 nm mechanical deformation of the central part of the array of the nanowires can induce relative transmission changes smaller than 5% (see Figure 3c). Moreover, the simulation without MoS_2 film reveals a similar response with Figure 3c, with the transmission difference at 645 nm to be less than 3%, in contrast to experimentally observed change of 200%, at Figure 3b. Furthermore, the fact that the transmission change is nonlinear with the applied strain, Figure 3d as well as the observed hysteresis related to the applied stress rate over an increasing-decreasing thermal cycle, Figure 4, further verifies the mechanical nature of the effect over any thermal effects, that might exist, negligible in the current study.

In summary, we have reported a new mechanism to tune the optical properties of photonic metamaterials. We have studied the mechanochromic response of MoS_2 metasurfaces and identified the conditions under which they can operate either as photonic filters or switches. The proposed device provides continuous and reversible optical tuning of visible transmission with relative transmission change of more than 190% actuated by a strain level of 2%, which is translated into great mechanochromic sensitivity. For example, materials with larger thermal expansion coefficient difference or longer nanowires can improve mechanochromic sensitivity. Moreover, new designs of mechanochromic metasurfaces should be developed to improve the bandwidth of the response. Even though we apply a heat-actuated method to induce stress on the mechanochromic metasurfaces, equivalent strain effects are also achievable via electrically means in nanomechanical metamaterials, such as electrostriction.[56] We also believe that other types of transition metal dichalcogenides should be studied as strain dependent refractive index materials for metamaterials, targeting different operational wavelengths. Overall, the use of photonic metasurface technology for creating mechanochromic devices based on transition metal dichalcogenides, can be used as a general platform for force responsive materials with optical readouts and form a new family of ultrathin color displays and multifunctional devices.

Experimental Section

Metamaterial Fabrication: Nanograting metamaterial patterns, with a fixed gap width g = 100 nm and period P = 500 nm, covering

an area of ≈22 µm x 25 µm, were directly etched via focused ion beam (FIB) milling, using a FEI Helios NanoLab 600 dual beam system, on a commercially available 90 nm thick Si_3N_4 membrane from Norcada Inc. Then, an APCVD synthesis method was used for the deposition of the MoS_2 on the prepatterned membrane, with two separate precursors: MoO_3 and sulfur loaded in two 3 cm quartz tubes in a CVD chamber. A silicon nitride membrane was placed at the center of the furnace and a quartz boat containing the MoO_3 precursor was placed upstream at a distance of 3 cm. The sulfur powder is placed in a separate quartz boat outside the furnace at a distance of 30 cm with controlled ambient temperature. Prior to the deposition, the quartz tube was flushed with 500 sccm of Ar gas for 1 h. The temperature of the furnace was first ramped up to 500 °C with a rate of 20 °C min^{-1} and subsequently up to 700 °C with 4 °C min^{-1} under constant flow of Ar at 200 sccm allowing the evaporation and deposition of MoO_3. At the temperature of 700 °C the sulfur zone was heated up to 170 °C for 15 min. During the process, a sulfur rich time window, the as-deposited MoO_3 was partially converted to MoO_{3-x} and MoS_2 progressing in a layer by layer manner while MoS_2 in the gas phase was codeposited. After the 15 min time window, the gradually sulfur deficient environment resulted in the deposition of a metal oxide rich layer.

Variable-Angle Spectroscopic Ellipsometry: The complex relative permittivity/refractive index APCVD deposited MoS_2 was evaluated by spectroscopic ellipsometry (J. A. Woollam 4000) over the wavelength range from 400 to 900 nm.

Numerical Simulations: Full-wave electromagnetic simulations of the metamaterial structure, based on the geometry presented in Figure 1a, were performed using the finite element method in COMSOL Multiphysics. Calculations employ periodic boundary conditions in the *x* and *y* directions (i.e., effectively assuming an infinite array of infinitely long nanowires). They utilize refractive indices for silicon nitride and MoO_{3-x} assumed to be nondispersive and equal to 2, while for MoS_2 ellipsometry data used are presented in Figure 1c. Furthermore, numerical spectra were integrated over the numerical aperture of the objective in the experiment, assuming linearly polarized plane wave illumination; nanowire mechanical deformation was obtained from finite element models of a single, isolated 22 µm long wire with fixed ends and rectangular cross sections as presented in Figure 1. These assumed Young's moduli E and density ρ values for Si_3N_4, MoO_{3-x} and MoS_2: E_{SiN} = 200 GPa; E_{MoO} = 80 GPa; E_{MoS} = 320 GPa; ρ_{SiN} = 3170 kg m^{-3}, ρ_{MoO} = 4690 kg m^{-3}, ρ_{MoS} = 5060 kg m^{-3}.

Raman Spectroscopy: Raman measurements under 532 nm laser excitation indicate the deposition on the prepatterned membrane of both MoO_{3-x} and MoS_2. The bulk MoS_2 was confirmed by the Raman mode at ≈381 cm^{-1} and A_{1g} mode at 407.5 cm^{-1};[44] and the MoO_{3-x} the Raman peaks at 353 and 733 cm^{-1}.[45]

Microspectrophotometry (Including Low Temperature Measurements): Transmission and reflection spectra (Figure 2) were obtained using a microspectrophotometer (CRAIC QDI2010), with a 11 µm × 11 µm sampling aperture via a 15× objective with NA 0.28. All data are normalized to reference levels for air (100% transmission), a silver mirror (high reflector), and a "Vantablack" vertically aligned carbon nanotube array (zero reflection/transmission), and averaged over 15 repeated measurement cycles, each with a 500 ms integration time. For the low temperature measurements, a cryogenic stage (model No THMS600) with temperature control was used. Pressure level is monitored throughout the experiment at 10^{-3} mbar. Measurements performed while temperature level were stabilized with fluctuation of less than 0.1 K.

Acknowledgements

The support of the UK's Engineering and Physical Science Research Centre is gratefully acknowledged, through grants EP/M009122/1 The Physics and Technology of Photonic Metadevices and Metasystems and EP/N00762X/1 National Hub in High Value Photonic Manufacturing. Following a period of embargo, the data from this paper can be obtained from the University of Southampton ePrints research repository: https://doi.org/10.5258/SOTON/D1040.

Conflict of Interest

The authors declare no conflict of interest.

Keywords

mechanochromism, metasurfaces, nanomechanics, photonic metamaterials, van der Waals materials

Received: April 25, 2019
Revised: August 9, 2019
Published online: September 12, 2019

[1] J. Y. Ou, E. Plum, L. Jiang, N. I. Zheludev, *Nano Lett.* **2011**, *11*, 2142.
[2] A. Karvounis, J.-Y. Ou, W. Wu, K. F. MacDonald, N. I. Zheludev, *Appl. Phys. Lett.* **2015**, *107*, 191110.
[3] J. Canet-Ferrer, A. Afridi, L. Philippet, R. Quidant, J. Osmond, P. Berto, *ACS Photonics* **2018**, *5*, 4497.
[4] T. Driscoll, H.-T. Kim, B.-G. Chae, B.-J. Kim, Y.-W. Lee, N. M. Jokerst, S. Palit, D. R. Smith, M. Di Ventra, D. N. Basov, *Science* **2009**, *325*, 1518.
[5] A. Tittl, A. K. U. Michel, M. Sch??ferling, X. Yin, B. Gholipour, L. Cui, M. Wuttig, T. Taubner, F. Neubrech, H. Giessen, *Adv. Mater.* **2015**, *27*, 4597.
[6] A. Karvounis, B. Gholipour, K. F. Macdonald, N. I. Zheludev, *Appl. Phys. Lett.* **2016**, *109*, 051103.
[7] Q. Wang, E. T. F. Rogers, B. Gholipour, C.-M. Wang, G. Yuan, J. Teng, N. I. Zheludev, *Nat. Photonics* **2016**, *10*, 60.
[8] K. M. Dani, Z. Ku, P. C. Upadhya, R. P. Prasankumar, S. R. J. Brueck, A. J. Taylor, *Nano Lett.* **2009**, *9*, 3565.
[9] M. Ren, B. Jia, J. Ou, E. Plum, J. Zhang, K. F. Macdonald, A. E. Nikolaenko, J. Xu, M. Gu, N. I. Zheludev, *Adv. Mater.* **2011**, *23*, 5540.
[10] Y.-W. Huang, H. W. H. Lee, R. Sokhoyan, R. A. Pala, K. Thyagarajan, S. Han, D. P. Tsai, H. A. Atwater, *Nano Lett.* **2016**, *16*, 5319.
[11] M. Morea, K. Zang, T. I. Kamins, M. L. Brongersma, J. S. Harris, *ACS Photonics* **2018**, *5*, 4702.
[12] A. Minovich, J. Farnell, D. N. Neshev, I. McKerracher, F. Karouta, J. Tian, D. A. Powell, I. V Shadrivov, H. Hoe Tan, C. Jagadish, Y. S. Kivshar, *Appl. Phys. Lett.* **2012**, *100*, 121113.
[13] O. Buchnev, J. Y. Ou, M. Kaczmarek, N. I. Zheludev, *Opt. Express* **2013**, *21*, 1633.
[14] F. Sterl, N. Strohfeldt, R. Walter, R. Griessen, A. Tittl, H. Giessen, *Nano Lett.* **2015**, *15*, 7949.
[15] I. M. Pryce, K. Aydin, Y. A. Kelaita, R. M. Briggs, H. A. Atwater, *Nano Lett.* **2010**, *10*, 4222.
[16] P. Gutruf, C. Zou, W. Withayachumnankul, M. Bhaskaran, S. Sriram, C. Fumeaux, *ACS Nano* **2016**, *10*, 133.
[17] M. K. Beyer, H. Clausen-schaumann, *Chem. Rev.* **2005**, *105*, 2921.
[18] J. X. X. Zhang, Z. Chi, Y. Zhang, S. Liu, *J. Mater. Chem. C* **2013**, *1*, 3376.
[19] B. R. Crenshaw, C. Weder, *Chem. Mater.* **2003**, *15*, 4717.
[20] E. Lee, M. Zhang, Y. Cho, Y. Cui, J. Van Der Spiegel, N. Engheta, S. Yang, *Adv. Mater.* **2014**, *26*, 4127.
[21] S. Zeng, D. Zhang, W. Huang, Z. Wang, S. G. Freire, X. Yu, A. T. Smith, E. Y. Huang, H. Nguon, L. Sun, *Nat. Commun.* **2016**, *7*, 11802.
[22] E. Ducrot, Y. Chen, M. Bulters, R. P. Sijbesma, C. Creton, *Science* **2014**, *344*, 186.

[23] M. Raisch, D. Genovese, N. Zaccheroni, S. B. Schmidt, M. L. Focarete, M. Sommer, C. Gualandi, *Adv. Mater.* **2018**, *30*, 1802813.
[24] E. P. Chan, J. J. Walish, A. M. Urbas, E. L. Thomas, *Adv. Mater.* **2013**, *25*, 3934.
[25] K. Sun, C. A. Riedel, A. Urbani, M. Simeoni, S. Mengali, M. Zalkovskij, B. Bilenberg, C. H. De Groot, O. L. Muskens, *ACS Photonics* **2018**, *5*, 2280.
[26] G. J. Stec, A. Lauchner, Y. Cui, P. Nordlander, N. J. Halas, *ACS Nano* **2017**, *11*, 3254.
[27] A. Castellanos-Gomez, R. Roldán, E. Cappelluti, M. Buscema, F. Guinea, H. S. J. Van Der Zant, G. A. Steele, *Nano Lett.* **2013**, *13*, 5361.
[28] N. Papasimakis, S. Mailis, C. C. Huang, F. Al-Saab D. W. Hewak, Z. Luo, Z. X. Shen, *Appl. Phys. Lett.* **2015**, *106*, 061904.
[29] X. Fu, C. Su, Q. Fu, X. Zhu, R. Zhu, C. Liu, Z. Liao, J. Xu, *Adv. Mater.* **2014**, *26*, 2572.
[30] H. Gao, Q. Shi, D. Rao, Y. Zhang, J. Su, Y. Liu, Y. Wang, K. Deng, R. Lu, *J. Phys. Chem. C* **2017**, *121*, 22105.
[31] Q. Guo, Z. Di, M. G. Lagally, Y. Mei, *Mater. Sci. Eng., R* **2018**, *128*, 1.
[32] Y. Zhang, W. Liu, Z. Li, H. Cheng, Y. Zhang, G. Jia, S. Chen, J. Tian, *Appl. Phys. Lett.* **2017**, *111*, 111109.
[33] S. Chen, Z. Li, W. Liu, H. Cheng, J. Tian, *Adv. Mater.* **2019**, *31*, 1.
[34] G. V. Naik, V. M. Shalaev, A. Boltasseva, *Adv. Mater.* **2013**, *25*, 3264.
[35] Y. Li, Z. Zhou, S. Zhang, Z. Chen, *J. Am. Chem. Soc.* **2008**, *130*, 16739.
[36] L. Kou, C. Tang, Y. Zhang, T. Heine, C. Chen, T. Frauenheim, *J. Phys. Chem. Lett.* **2012**, *3*, 2934.
[37] P. Johari, V. B. Shenoy, *ACS Nano* **2012**, *6*, 5449.
[38] H. Peelaers, C. G. Van de Walle, *Phys. Rev. B* **2012**, *86*, 241401.
[39] L. Yang, X. Cui, J. Zhang, K. Wang, M. Shen, S. Zeng, S. A. Dayeh, L. Feng, B. Xiang, *Sci. Rep.* **2015**, *4*, 5649.
[40] F. Kafi, R. Pilevar Shahri, M. R. Benam, A. Akhtar, *J. Electron. Mater.* **2017**, *46*, 6158.
[41] A. Castellanos-gomez, M. Poot, G. A. Steele, H. S. J. Van Der Zant, *Adv. Mater.* **2012**, *24*, 772.
[42] B. Yang, W. Liu, Z. Li, H. Cheng, D. Y. Choi, S. Chen, J. Tian, *Nano Lett.* **2019**, *19*, 4221.
[43] C. C. Huang, F. Al-Saab, Y. Wang, J. Y. Ou, J. C. Walker, S. Wang, B. Gholipour, R. E. Simpson, D. W. Hewak, *Nanoscale* **2014**, *6*, 12792.
[44] C. Lee, H. Yan, L. Brus, T. Heinz, J. Hone, S. Ryu, *ACS Nano* **2010**, *4*, 2695.
[45] M. Dieterle, G. Mestl, *Phys. Chem. Chem. Phys.* **2002**, *4*, 822.
[46] C. Yim, M. O'Brien, N. McEvoy, S. Winters, I. Mirza, J. G. Lunney, G. S. Duesberg, *Appl. Phys. Lett.* **2014**, *104*, 103114.
[47] B. Gholipour, G. Adamo, D. Cortecchia, H. N. S. Krishnamoorthy, M. D. Birowosuto, N. I. Zheludev, C. Soci, *Adv. Mater.* **2017**, *29*, 1.
[48] B. Gholipour, D. Piccinotti, A. Karvounis, K. F. Macdonald, N. I. Zheludev, *Nano Lett.* **2019**, *19*, 1643.
[49] S. K. Deb, *Proc. R. Soc. London, Ser. A.* **1968**, *304*, 211.
[50] Y.-N. Xu, W. Y. Ching, *Phys. Rev. B* **1995**, *51*, 379.
[51] W. Yang, Z. Wei, X. Zhu, D. Yang, *Phys. Lett. A* **2009**, *373*, 3965.
[52] J. W. Jiang, *Nanotechnology* **2014**, *25*, 355402.
[53] S. K. Singh, M. Neek-Amal, S. Costamagna, F. M. Peeters, *Phys. Rev. B* **2015**, *91*, 14101.
[54] J. Valente, J.-Y. Ou, E. Plum, I. J. Youngs, N. I. Zheludev, *Nat. Commun.* **2015**, *6*, 7021.
[55] Y. Nagasaki, B. Gholipour, J.-Y. Ou, M. Tsuruta, E. Plum, K. F. MacDonald, J. Takahara, N. I. Zheludev, *Appl. Phys. Lett.* **2018**, *113*, 021105.
[56] A. Karvounis, B. Gholipour, K. F. MacDonald, N. I. Zheludev, *Adv. Mater.* **2019**, *31*, 1804801.